Electric Field Optimisation for Cryogenic nEDM Experiments

Jacob Aaron Thorne

Department of Physics and Astronomy
University of Sussex

This dissertation is submitted for the degree of
Doctor of Philosophy

June 2018

To who ever read this thesis... Good luck and thanks for all the fish !

Declaration

I hereby declare that this thesis describes my own original work, expect where explicitly stated. No part of this work has previously been submitted either in the same or different form, to this or any other University in connection with a higher degree or qualification.

Signature:

Jacob Aaron Thorne
June 2018

Acknowledgements

I would like to thank my supervisor, Clark Griffith, for all the support and finding all the resources to get the experiments done in just enough time for submission. Thanks for all the help getting everything sorted behind the scenes, without that this thesis would not have been possible.

The biggest thanks goes to Mike Hardiman, despite him being retired, he came in to help wherever was needed throughout this PhD, providing invaluable advice and guidance, without him this work would have been very different.

I would also like the thank Ian Wardell, he came in every Thursday without fail to assist and provide advice and knowledge that I was lacking in key aspects of the experiment throughout this PhD.

Thanks also goes to Phil Harris, he helped push me to get the thesis written in time which for that I am grateful.

Estelle Chanel, thanks for all the distractions during your summer placement, drawing random stuff on the white board, and the fun times we had when we saw each other in collaboration meetings and visits. I really appreciate the help you provided in the final days to submitting the thesis, could not have gotten it done in time without you.

Thanks to Nick Ayres for the help in explaining the physics to me when I needed it. Nick your requirements to go drinking at all times left me with numerous hangovers. Side note, your snoring still haunts me.

Chris Abel you helped me with a many mechanical issues, not only on my car, but also with my experiments too. You also helped with good chats while in the lab, thanks for everything. I'll find something in the tunnel as a token of my appreciation.

Matthew Musgrave you provided me with someone to talk to during my first few collaboration meetings and socials at Sussex, thanks for being there. One day I'll beat you at

Love Letter.

Dave Shiers thanks for the help with electronics and machining knowledge, I would have struggled otherwise. I also enjoyed our conversations in the lab, helped to distract me when I needed it.

Peter Smith, thanks for the helpful printing advice, general help, and entertainment.

Thank goes to all the project students I had, Tom Rehaag, Shek Fan Ho, and Nathan Udy, you guys helped me progress on a number of experiments in this thesis and provided a laugh in the lab.

Massive thanks goes to the technicians in the workshop: Alan Mayers, Michel Sacre, Ian Wallis, Dan Bartlett, Chris Moore, Liam Killeen, and Bob Woodhouse. Everyone helped in some form to produce quality work, even in the situations where I needed things urgently they helped get it made. The apparatus would not have been completed in time without their contributions.

Thanks to my housemates, THOA mark 2.5: Ridwan for being my first friend at Sussex; Daniel for introducing me to board games, all that money spent, worth it; Alex for constantly beating me at squash was fun, Ausfall!; Panka for an introduction to the wonders of halloumi; Benoit for being entertaining us with this Frenchness and I acknowledge your skills in triggering people.

Special mention goes to my friends at University of Sussex Lacrosse club, the socials, matches, trainings, and good times we all had I will remember always, it helped to get me through this and I may not have been able to finish the PhD without you all.

David Charles, thanks for the good times we had, drinking and playing lacrosse. You setting up the lacrosse club really helped keep me around at Sussex, thanks for everything you've done.

Thanks to Mark Winter, Billy Camuso, and Andew Majoran for all the times we played lacrosse together at the weekends throughout my PhD and times we spend hanging out afterwards.

Finally to all my family and friends you've helped get me through this.

Abstract

This thesis presents details of the design, construction and measurements of an apparatus (Blue Elbow cryostat) for high voltage testing of a full-size cryogenic nEDM cell in liquid helium at 4.2 K SVP. The test cell is cylindrical and of 24 cm internal diameter with stainless steel electrodes and an insulating borosilicate glass spacer. The cylinder axis of the cell is vertical and the insulator is located in grooves in the electrodes. The electrode separation can be varied from 0.2 cm to 2.6 cm and a voltage of up to 260 kV can be applied across the cell. It has long been expected that a nEDM cell immersed in superfluid LHe at 0.5 K should permit E-fields much greater than room temperature experiments. Long et al. (1) showed that over 400 kV/cm was obtainable in a large cell without an insulating spacer at 4.2 K, but that this was reduced dramatically as the temperature, and hence pressure, was reduced to below 2 K in a pumped LHe bath. Subsequent work by Davidson (2) in this laboratory on small spacerless cells showed that the dielectric strength in the superfluid at 1.9 K could be restored to its 400 kV/cm value by pressurising the LHe to 1 bar.

Further work in this laboratory by Davidson (2) and Hill (3) shows that the introduction of a dielectric spacer reduces the value of the breakdown field, E_{bd}, for a given geometry. However, measurements presented here on smaller scales than the Blue Elbow cryostat, overcame the reduced fields through careful groove optimisation and insulator material choice.

E_{bd} data as a function of separation with the Blue Elbow cryostat in LN_2 show a clear reduction compared to data from smaller scale cells, due to surface area effects. Breakdown fields in LHe at 4.2 K SVP with this apparatus indicate fields at 120 kV/cm were achievable at 6 mm separation but dropped off dramatically as separation was increased to 12 mm then 16 mm. The reason for the drop off is attributed to the geometry of the electrode. This result, together with Davidson's pressure dependence data, should inform the design of a future cryogenic nEDM experiment.

Table of contents

List of figures

List of tables

Chapter 1

Introduction

The universe is primarily made of matter with no evidence for anti-matter existing in large clusters anywhere. After the Big Bang, matter and anti-matter were created in equal quantities. However, nature decided that regular matter was the preferred over anti-matter when they annihilated, the normal kind left. The mechanism that causes this is called **CP** violation as understood through the Sakharov conditions for baryogenesis. One potential source of this **CP** violation could be the presence of a finite neutron Electric Dipole Moment (nEDM).

The goal of this thesis is to investigate the possibility of being able to achieve an order of magnitude higher electric fields in a cryogenic environment compared to what is currently possible in the room temperature nEDM experiment. This represents an increase in the sensitivity to the nEDM by an order of magnitude. Achieving this goal is a significant technical achievement in the steps towards a fully realised cryogenic nEDM experiment.

Chapter 2 discusses the nEDM further stating the source of **CP** violation in the Standard Model (SM) of particle physics. The origin of a nEDM in the SM will be covered and how it can help with searches for beyond SM theories. The comparison between other EDM's in other systems besides the neutron will be discussed as well for a complete picture.

Chapter 3 will cover the methodology for a nEDM experiment. This includes the process of generating UCN (Ultra-Cold Neutrons), storing them, and performing a Ramsey method to measure the nEDM. The current nEDM experiment being performed at PSI will be described as well as the planned upgrade, n2EDM which is aims to be online by 2020. A number of other nEDM experiments under development, which use different techniques will be described for comparison.

The sensitivity of the nEDM is linearly proportional to the applied electric field, therefore, being able to maximise this will greatly increase the sensitivity to a finite nEDM. In room temperature nEDM experiments, like at PSI, the applied electric field is limited by the presence of an insulator between the electrodes, around 10-20 kV/cm in vacuum. In the case of a LHe medium, the electric fields can potentially be dramatically increased in value, to perhaps greater than 100 kV/cm. The added benefit of using this as a medium is it can also be used as a superthermal UCN source, hence, potentially reducing loss factors from transport and further increasing the sensitivity of the experiment. However, this thesis only focuses on the question of the maximum electric field possible in a LHe medium.

In chapter 4 past publications on the breakdown behaviour of LHe and LN_2 will be reviewed. This will determine the variables that effect the breakdown voltage in a cryogenic medium. Surface area and volume effects, as well as the presence of an insulator are potentially the limiting attributes. The insulator creates a region in which the electrode surface, liquid medium, and insulator meet called the cathode triple junction (CTJ). The presence of the CTJ lowers the electric field by a factor of ~ 2-3, according to previous measurements. In some experiments with ~ 1 mm separation between plane-plane geometry, ~ 50 mm diameter electrodes without an insulator, electric fields as high as 400 kV/cm can be achieved in LHe and 180 kV/cm for LN_2. This dielectric strength can decrease dramatically due to these variables stated. These attributes are particularly important for a nEDM experiment as it requires a large volume filled with a high density of UCN. Electrodes usually form the top and bottom of the UCN chamber and an insulator is placed in between acting as a wall to store them.

The main goal of this thesis is to determine the maximum electric field on a realistically sized cryogenic nEDM mock Ramsey Cell. An apparatus has been constructed to hold 360 mm diameter electrodes with an adjustable separation from 2-26 mm with a cylindrical insulator between the electrodes. The variable separation enables the measurement of surface area effects and of the achievable electric field with increasing separations. The groove profile of the electrodes was carefully optimised in order to reduce the constraints linked to the CTJ. The design allows HV to be applied to both electrodes, giving total electric field at maximum separation of 100 kV/cm. The details of the apparatus and simulations for optimising the electrode geometry are given in chapter 5.

A series of initial measurements in LN_2 were performed, on smaller electrodes and insulators with varying radial separations and materials to determine factors contributing to breakdowns due to the presence of an insulator. This setup is detailed in chapter 5.

The 360 mm diameter electrode measurements in LN_2 showed a surface area effect when compared to the smaller electrode measurements. It was also used as a preliminary breakdown measurements to check performance of the system prior to LHe measurements.

The results for the measurements performed on Al_2O_3 and BG insulators on all the electrodes in LN_2 are presented in chapter 6. The measurements in LHe on the 360 mm diameter electrodes are also detailed in chapter 6.

Data from chapter 6 are analysed in chapter 7. The optimised electrode geometry with an insulator has the same breakdown voltage as previous results without the spacer, for measurements on the scales performed in this thesis. However, despite the recovery, some Al_2O_3 insulators would get damaged catastrophically and then limit the breakdown voltage. This is attributed to the radial separation between the groove wall of the electrode and the insulator wall. It was also noticed that upon switching to BG insulators the damage was mitigated. The cause of the damage is associated with the material of the insulator having a much higher dielectric constant which creates high fields in the CTJ.

The surface area effect data is compared to past measurements which are given in chapter 4, showing comparable breakdown fields; despite the presence of the insulator in this work, the breakdown values were unaffected compared to previous data without insulators.

The LHe measurements are currently being performed, however, preliminary results and discussion on the anticipated fields is given at the end of chapter 7.

The conclusion is given in chapter 8. The issue of the CTJ can be overcome with careful design of the groove region. The material choice of the insulator seems to have an effect on the damage observed. The simulations in chapter 5 hinted that the dielectric constant on the material would be a major difference but experimentally this was not the case. These results in LN_2 indicate that one could expect to observed high electric fields in LHe without the reduction in breakdown voltages due to the insulator presence. This can have implications for various nEDM experiments with the work on the geometry potentially useful to optimise the electric field in room temperature experiments as well. This is discussed in more detail at the end of chapter 8.

Appendix A is the results of magnetic scanning of potential material that could be

used to construct a high voltage feedthrough for n2EDM.

Appendix B is the design of the n2EDM HV feedthrough with notes on its construction. Simulations were performed to optimise the geometry and ensure that it would hold 200 kV in vacuum. The material which was found to be suitable is PTFE or PEEK for the insulation and the conductors made out of aluminium.

Appendix C is the results from the simulations of the electric fields inside the PSI nEDM Ramsey chamber and determines the uniformity of the E field within the UCN volume. This is important information for evaluating the actual nEDM sensitivity and for analysis of electric field related systematic effects.

Appendix D is the determination of the characteristics for the ballast resistors used in the dual HV supply results in this thesis. The resistors are designed to protect the power supplies during breakdown measurement when they are put back to back.

Appendix E details the Blue Elbow cryostat performance with LHe. The process of improvements is detailed.

Appendix F gives a summary of all the KEK and Blue Elbow cryostat breakdown data runs.

Appendix G details performance measurements taken at PSI and on a test setup for the mercury co-magnetometer with applied electric fields. At PSI the relaxation time of the mercury will drop with reversal of electric field. This effect was found to be asymmetric with applied polarity. The effect was attempted to be replicated in the test setup in order to investigate the mechanism which causes the issue at PSI.

Appendix H includes the drawings of the Blue Elbow cryostats storage vessel (SV) for the electrodes as well as their geometry.

Chapter 2

The neutron Electric Dipole Moment (nEDM)

2.1 Introduction

In this chapter the history of symmetry violation will be discussed as well as the relation to the nEDM, as a violation of time reversal. The theoretical origin of the nEDM in the Standard Model will be demonstrated, with **CP** violation sources also discussed. The nEDM can also be used as a probe for beyond Standard Model physics which will be discussed. The nEDM is not the only EDM that can be searched for, every particle also theoretically has one. Searching for each EDM is required to pin point the exact values for the sources of **CP** violation outside of the Standard Model. This will be discussed at the end of the chapter.

An electric dipole moment (EDM) of is a measure of the asymmetry of the electric charge distribution along the spin axis of the particle. Similar to the effect of the magnetic dipole moment of a particle, where the application of an external magnetic field will generate a torque on the neutron, aligning the neutron's spin with the magnetic field, the presence of an electric dipole moment would generate a torque with the application of an electric field.

The observation of any non-zero EDM is of significant importance as it could indicate one of the origins for the baryon asymmetry of the universe, which requires asymmetry in the laws of physics. There are three discrete symmetry transformations, charge conjugation (**C**), parity (**P**), and time reversal (**T**), which can all be considered singularly or in combination with each other. The existence of a non-zero EDM within this context results in the violation of **P** and **T** (or equivalently (**CP**) symmetry if the combination of **CPT** is conserved). This breaking of fundamental symmetries can help explain the

physical processes in the early universe leading to the excess of matter over anti-matter in the universe, due to a bias for one "direction" over the other. It is theoretically well established that the combination of all symmetries, **CPT**, should be conserved in nature (4) (5).

The Standard Model of particle physics includes some **CP** violation from the CKM quark mixing matrix, however, it is too small to generate the observed baryon asymmetry and the Standard Model predicts values of all EDM's to be many orders of magnitude smaller than what experiments can currently or even expect to reach in the coming decades. The nEDM is thought to be in the range $10^{-31} \rightarrow 10^{-34}$ $e$cm based on the Standard Model. However, many BSM theories predict values for EDM's much larger than that of the Standard Model. This makes probing EDM's a valuable test for such theories.

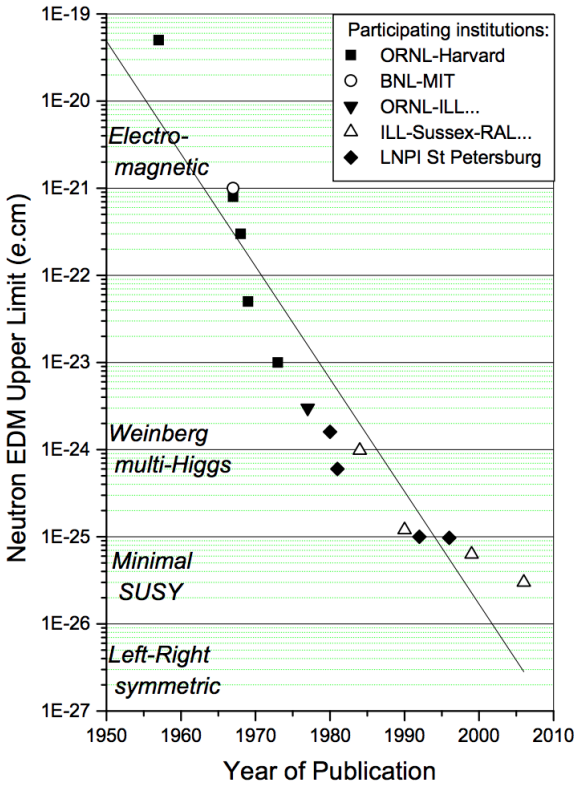

Fig. 2.1 Improvement in the nEDM sensitivity limit over time with comparison to theoretical models (6).

Beyond the Standard Model theories predict the nEDM of order $\sim 10^{-28}$ $e$cm, the next generation of nEDM experiments should cover this sensitivity region (7).

2.2 C, P, and T symmetries

The operation of charge conjugation (**C**) results in the change of matter to antimatter but the dynamics of the particles would remain the same. In order to conserve this operation the generation of matter and anti-matter must occur with the same probability. It was found in the 1950's, however, that all forces, except the weak force were invariant under this operation. Goldhaber et al.(8) found that free neutrinos (antineutrinos) were left-handed (right-handed) i.e. had their spin antiparallel (parallel) to their momentum. Goldhaber was able to do this by analysing circular polarization and resonant scattering of γ rays following orbital electron capture from their source in order to measure the helicity of the neutrino, which they found to be negative. This observation meant that all neutrinos are "left-handed", and right-handed neutrinos do not exist. On the other hand, anti-neutrinos are always right-handed; left-handed anti-neutrinos have not been observed. This difference between neutrinos and anti-neutrinos violates charge conjugation symmetry.

Parity (**P**) transformation acts to invert the coordinates of a system. The best analogy for parity is that it acts like a mirror view of the system its being applied to; for example ($\mathbf{P}: x, y, z \rightarrow -x, -y, -z$). Therefore, invariance under this transformation means that a process should be equivalent in both states; all that has changed is its coordinates. However, this was proven to also be violated by Wu et al.(9) and theorised by Lee and Yang (10) in 1957 and 1976. Lee and Yang postulated that parity might be violated in weak interactions and suggested a number of experiments in order to prove this. Wu et al. performed one of these experiments, measuring the angular distribution of electrons coming from beta decays of polarized ^{60}Co nuclei. It was found that the angular distribution was asymmetric, showing that weak interactions also violate parity.

The discovery of **C** and **P** violation was a surprise to most physicists in the 1950s, as both were strongly believed to be conserved at the time. Fortunately the combination of **C** and **P** seemed to restore symmetry to the weak interaction. Landau (11), therefore went further, stating that **CP** symmetry must be preserved by all forces. However, in 1964 Christenson et al.(12) indirectly observed **CP** violation in decaying long-lived kaons $K_L^0 \rightarrow \pi^+\pi^-$. The experiment measured the branching ratio of decaying neutral K^0 to 2π versus 3π modes. The existence of $K_L^0 \rightarrow 2\pi$ decays violates **CP** symmetry. This was due to an asymmetry in the neutral kaons with quark mixing in the kaon creating unequal amounts of matter and anti-matter. Further evidence followed from direct **CP** violation observed in CERN in 1988 (13) and subsequently again by the BELLE collaboration (14) and BABAR collaboration (15). They looked at decay rates of the natural B^0 and $\bar{B}^0$ mesons to K_L^0 and K_S^0. It was found that there was a difference between the matter

and anti-matter B mesons decay with less detected events for the anti-matter decays. Therefore, **CP** violation was also broken in weak interactions.

Experimental evidence for violations of all the previous symmetries motivated theorists to find some form of symmetry that nature obeys. This led Lüders (16) and Pauli (17) to determine that the product of charge conjugation, parity, and time reversal will hold for any system. The **CPT** theorem is strongly theoretically believed to hold with all experiments to date supporting this (Ahmadi et al.(18) and others). One of the consequences of this theorem is that if a pair of symmetries is violated then the third must also be violated so that **CPT** invariance is up held in nature. Therefore, if **CP** is violated then **T** symmetry is violated.

Direct observation of **CP** violation in B meson systems was well established while **T** violation was strongly believed to occur it had not been experimentally observed. However, in 2012, this violation was observed by the BABAR collaboration (19) by measuring **T**-violating parameters in the time evolution of neutral B mesons. The experiment compared the probabilities of $\bar{B}^0 \to B^-$, $B^+ \to B^0$, $\bar{B}^0 \to B^+$, and $B^- \to B^0$ transitions, to their **T** conjugates. Their measurements were also consistent with **CP**-violating measurements inferring experimental support for **CPT** invariance.

2.3 Baryon Asymmetry of the Universe

The observable universe is made up of stars, planets, gas clouds, etc., but all this material is matter. This presents a fundamental question: why is there are no anti-matter observed?

The Big Bang model describes that matter and anti-matter are created equally, however, somehow the antimatter annihilates asymmetrically with matter after the Big Bang, with matter the dominant type remaining. This distribution of matter in the observable universe can be measured experimentally from the CMB (20), giving the level of baryon asymmetry, η, in the universe:

$$\eta = \frac{\eta_B - \eta_{\bar{B}}}{\eta_\gamma} = 6.1 \cdot 10^{-10}, \tag{2.1}$$

where η_B is the number density of baryons, $\eta_{\bar{B}}$ is the number density of anti-baryons, and η_γ is the number density of background photons. This value for η should be zero if all symmetries of the universe are conserved (21) (22).

A theoretical explanation for evolution of the early universe was formulated by Sakharov

(23) in 1967. Sakharov stated that in order for the current universe to exist then three things had to have occurred: baryon number violation, **C** and **CP** symmetry breaking, and interactions out of thermal equilibrium.

The first statement says that at some initial condition the baryon number would be conserved, then over time this changed, resulting in more matter baryons over the anti-matter baryons. If the baryon number was the only violation then over long periods of time, symmetries would equate the number of baryons equal to the number of anti-baryons. The implication is that **C** and **CP** symmetries are broken in order for the rate of baryon generation to be larger than that of anti-baryons. The departure from thermal equilibrium would also have to have occurred for baryogenesis, otherwise **CPT** would equate for the asymmetry processes increasing or decreasing baryon number. The consequence of Baryogensis before thermal equilibrium means that the generated asymmetry is then established after thermal equilibrium, resulting in a breaking of **T** symmetry (24).

The nEDM represents a possible candidate for a probe for the **CP** violating mechanism which caused this baryonic asymmetry.

2.4 nEDM as a Classical Depiction

The neutron is made up of quarks which each have an EDM. The combination of these EDMs gives an overall EDM of the neutron. Under the application of a strong electric field the neutron's spin will change. The effect is similar to the neutron's finite magnetic moment, μ_n = -1.91μ_N, where μ_N is the nuclear magneton 5.05×10^{-27} J/T (25). Under the application of a magnetic field, strong enough to affect is magnetic moment, the neutron will align its spin. The existence of an EDM, however, would result in a direct violation of **P** and **T** (equivalent **CP**) symmetry.

Quantity	Parity (**P**)	Time Reversal (**T**)
Spin, $\vec{s}$	$\vec{s}$	$-\vec{s}$
Angular momentum, $\vec{l}$	$\vec{l}$	$-\vec{l}$
Time, t	t	$-t$
Electric field, $\vec{E}$	$-\vec{E}$	$\vec{E}$
Magnetic field, $\vec{B}$	$\vec{B}$	$-\vec{B}$
Position, $\vec{x}$	$-\vec{x}$	$\vec{x}$
Velocity, $\vec{v}$	$-\vec{v}$	$-\vec{v}$

Table 2.1 Transformation of various physical quantities under parity and time reversal.

The Hamiltonian of the neutron, in a classical sense, can be represented by the following equation in an electric, $\vec{E}$, and magnetic field, $\vec{B}$:

$$\hat{H} = -d_n \vec{\sigma} \cdot \vec{E} - \mu_B \vec{\sigma} \cdot \vec{B}, \tag{2.2}$$

where $\vec{\sigma}$ are the Dirac spinors, μ_B the Bohr magnoton (9.27×10^{-24} J/T) (25), and d_n is the nEDM.

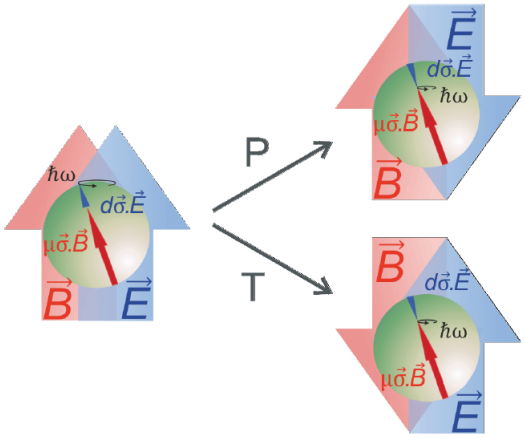

Fig. 2.2 Representation of **P** and **T**-violation of the nEDM (7).

Applying the Parity transform to the Hamiltonian, the electric field will reverse direction but keep the others the same, resulting in a **P** violating product,

$$\mathbf{P}(\hat{H}) = -d_n \vec{\sigma} \cdot (-)\vec{E} - \mu_B \vec{\sigma} \cdot \vec{B} = d_n \vec{\sigma} \cdot \vec{E} - \mu_B \vec{\sigma} \cdot \vec{B} \neq \hat{H}. \tag{2.3}$$

Performing the time reversal transform to the Hamilton results in the Dirac spinors and the magnetic field changing sign. This transform results in the same product if **CP** transformation were to be applied instead,

$$\mathbf{T}(\hat{H}) = \mathbf{CP}(\hat{H}) = -d_n(-)\vec{\sigma} \cdot \vec{E} - \mu_B(-)\vec{\sigma} \cdot (-)\vec{B} = d_n \vec{\sigma} \cdot \vec{E} - \mu_B \vec{\sigma} \cdot \vec{B} \neq \hat{H}. \tag{2.4}$$

The application of parity and time reversal from these equations shows that under either transform the Hamiltonian is not equivalent, hence, a nEDM is a violation of **P** and **T** for a non-zero d_n value.

2.5 nEDM in the Standard Model

There are two potential sources for the nEDM. In the Standard Model there is a **CP** violating term present in the Kobayashi-Maskawa quark mixing matrix. This term is what gives the electroweak sector its **CP** violating behaviour. The other is present in

QCD. The Lagrangian of the neutron produces an asymmetric term which gives rise to the "strong **CP** problem". This potentially gives rise to a **CP** violating term from the strong sector. Violation of **CP** has not been observed in strong interactions to date, however, the observation of a nEDM could be the example of this.

2.5.1 Electroweak Interactions

The source of **CP** violation in the weak sector that is present in the standard model comes from a phase δ term in the KM matrix of quark flavour mixing in the charged current interaction:

$$(\bar{u},\bar{c},\bar{t}) = \begin{pmatrix} c_1 & s_1c_3 & s_1s_3 \\ -s_1c_2 & c_1c_2c_3 - e^{i\delta}s_2s_3 & c_1c_2s_3 + e^{i\delta}s_2c_3 \\ S_1s_2 & -c_1s_2c_3 - e^{i\delta}c_2s_3 & -c_1s_2s_3 + e^{i\delta}c_2c_3 \end{pmatrix} \begin{pmatrix} d \\ s \\ b \end{pmatrix}, \tag{2.5}$$

where $c_i = \cos\theta_i$, $s_i = \sin\theta_i$, θ_i (i = 1, 2, 3) are mixing angles (26).

In the KM model it was realized that the nEDM cannot occur to first order in G_F (the Fermi weak interaction constant) (27)(28)(29). Therefore, in the SM the nEDM can, at lowest order, arise in a second order effect of approximately order G_F^2 (30). The nEDM is controlled in the standard model by long-distance contributions weakly interacting within the neutron. This weak interaction creates a **CP**-odd vertex in the Feynman diagram which generates the nEDM.

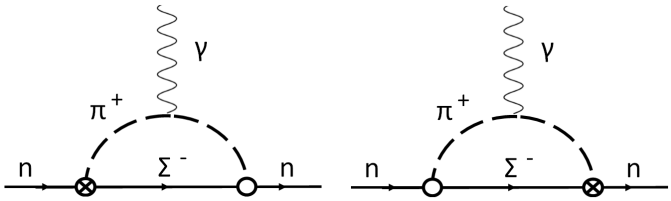

(a) CP violating 1st vertex (b) CP violating 2nd vertex

Fig. 2.3 Feynman diagrams for quark weak interaction contributing to the nEDM (31).

In the Figure 2.3, the ∘ vertex represents the non-leptonic weak interaction, **CP**-even term. The ⊗ vertex is the contribution to the nEDM. It's the **CP**-odd term for which the operator is essentially the so-called "penguin" diagram. The calculation of the nEDM starts with the interaction of $\Sigma^-\pi^+ n$ by calculating the matrix element $\langle\Sigma^-\pi^+|H_\otimes|n\rangle$. Using this matrix element and the Hamiltonian of the ∘ vertex, the following is the contribution to the nEDM from Figure 2.3:

$$d_n = -eG_F^2 \sin\delta\ (s_1s_2s_3c_2)\frac{\alpha_s}{\sqrt{2}\,27\pi^3}\ln\frac{m_t^2}{m_c^2}\,\frac{f_\pi m_\pi^2}{m_s(m_u+m_d)}A(2\alpha-1)\,g_A\ln\frac{m_K}{m_\pi}. \tag{2.6}$$

The terms m_t, m_c, m_π, and m_K are mass of t, c quarks, π and K meson respectively. The $G_F = \frac{1.027 \cdot 10^{-5}}{m_p^2}$ is the Fermi weak interaction constant, $\alpha \approx 0.64$ is the relative weight of the D coupling in the interaction of the baryon and meson octets, $g_A = 1.26$, A is the non-leptonic hyperon decay amplitude, and $f_\pi = 130$ MeV the pion decay constant. The δ term is present in this calculation; if there was no **CP** violation in the SM then this value would be zero, hence d_n would also be zero. From K and B meson decay experiments, $\delta = 1.2$ rad.

Therefore, an estimate for the nEDM can be calculated as (31):

$$d_n \approx 10^{-32} - 10^{-31} ecm. \tag{2.7}$$

2.5.2 The Strong CP-problem

The other potential source of **CP** violation in the SM comes from QCD. The Lagrangrian for the neutron gives an asymmetric term which is controlled by an angle, θ. This **CP**-violating term gives rise to the nEDM as an experimental test for **CP**-violation in the strong sector. The QCD Lagrangian can be written as:

$$\mathscr{L}_{QCD} = \mathscr{L}_0 + \mathscr{L}_\theta \tag{2.8}$$

In the QCD Lagrangian the $\mathscr{L}_0$ describes the dynamics and interactions of the quarks and gluons. The $\mathscr{L}_\theta$ Lagrangian is the term that contains the **P** and **CP**-violation in QCD, given as:

$$\mathscr{L}_\theta = -\theta \left(\frac{g^2}{32\pi^2} \right) \tilde{G}^\alpha_{\mu\nu} G^\alpha_{\mu\nu} \tag{2.9}$$

where g is the strong coupling constant and $0 \leq \theta \leq 2\pi$. It can be seen from the equation above that the field strength tensors $G^\alpha_{\mu\nu}\tilde{G}^\alpha_{\mu\nu}$ will not cancel out, resulting in an asymmetry. The amount of asymmetry is therefore determined by the θ term.

This results in **CP** violation in the strong sector between the pion and a nucleon, details are given in (32)(33)(34)(35)(36). This interaction is represented in the Feynman diagram in Figure 2.4.

In the Figure 2.4 the two vertices are the **CP**-even, $\circ$, and **CP**-odd, $\otimes$. This interaction is a virtual transformation of an up quark to down quark and then back again which then breaks the symmetry. In order to determine the contribution to the nEDM from this interaction, the calculation of the coupling constants at each vertex are required (33)(36). The CP-even vertex is well known, $g_{\pi NN} = 13.6$, however, the CP-odd vertex has to

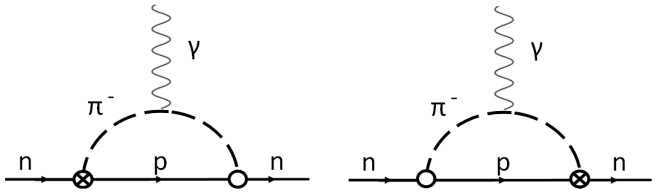

(a) **CP** violating 1st vertex (b) **CP** violating 2nd vertex

Fig. 2.4 Feynman diagrams for strong **CP** violation contributing to the nEDM (33).

be calculated:

$$\langle p\pi^-|\delta L_{CP}|n\rangle = -\theta \frac{m_u m_d}{m_u + m_d} \frac{\sqrt{2}}{f_\pi} \frac{M_\Xi - M_\Sigma}{m_s} = \bar{g}_{\pi NN} \approx -0.027\,\theta, \tag{2.10}$$

where M_Ξ and M_Σ are the masses of the hyperons Ξ and Σ.

The contribution to the nEDM can now be formalised from the coupling constants of the vertices from the Feynman diagrams:

$$d_n = \frac{e}{m_p} \frac{g_{\pi NN}\bar{g}_{\pi NN}}{4\pi^2} \ln\frac{m_\rho}{m_\pi}. \tag{2.11}$$

From the equation above it is clear that θ will contribute to the nEDM, therefore, from the experimental limits $d_n < 3.0 \cdot 10^{-26}$ ecm (37), the sensitivity limit of θ can be determined:

$$|\theta| < 10^{-10} \tag{2.12}$$

Hence the CP-odd coupling constant is:

$$\bar{g}_{\pi NN} < 10^{-12} \tag{2.13}$$

The extremely small limit on θ is why it's called the "strong CP problem". Without fine tuning, naturalness would assume any angle parameter would be of order ~ 1, however, the value is unnaturally small due to the nEDM constraints. There are models (38) (39) (40) that resolve this problem by setting the θ value to zero, however, this presents a new problem in the "existence" of axions. Unfortunately thus far no axion has ever been observed (41).

2.6 Beyond the Standard Model contributions to the nEDM

The SM predicts that the nEDM is of order $\sim 10^{-31} \rightarrow 10^{-34}$ which is unreachable for any current experiment. However, BSM theories predict values for the nEDM much larger, by several orders of magnitude, than that of the SM, adding in additional **CP** violating terms via introduction of new forces/particles. The observation of the matter-antimatter asymmetry in the current universe indicates that the SM severely underestimates the amount of **CP** violation of the universe, therefore, BSM theories ideally include new sources of **CP** violation.

For example, the MSSM (minimal supersymmetric standard model) acts as an extension to the SM which adds a sparticle (spin differs by $\frac{1}{2}$ and opposite parity) partner for every SM particle. The additional presence of sparticles leads to additional **CP** violating processes occurring which in turn would mean the occurrence of an nEDM would be observed at larger values. The number of free parameters in MSSM is large: 169 free parameters. Removing some parameters due to globel symmetries leaves 80 real and 44 imaginary physical parameters, of which one of them is the CKM δ term, therefore, there are 43 new **CP** violating terms which could all contribute to the nEDM.

Experimental searches for the nEDM has led to sensitivity limits which put constraints on the MSSM, which in its most basic form predicts $d_n \sim 10^{-25}$ ecm. This value is in conflict with the current experiment limit for the nEDM of $d_n < 3.0 \times 10^{-26}$ ecm (37). This affectively rules out 'natural' MSSM as an answer to BSM physics.

There have been a number of modifications to the MSSM to fix the problem of nEDM values being too large compared to experimental results. The biggest problem of the MSSM is the number of free parameters; it is experimentally impossible to determine the value of all of them, therefore, modifications were made to fix this. One such fix cuts down the number of **CP** violating parameters to those just in the CKM matrix; no new **CP**-violation sources (additional particles result in more possible **CP** violating interactions), no flavour changing neutral currents, and 1st and 2nd universality. For this such model, it predicts an nEDM at $10^{-27} \rightarrow 10^{-29}$ ecm, see (42), (40), and (43) for more details.

An alternative to SUSY models is the Weinburg multi-Higgs model. This theory states that there is an extra charged Higgs to the SM Higgs. The addition of an extra Higgs would result in further **CP**-violation in the leptonic sector. This would result in a modification to the δ term in the CKM matrix, increasing its value. The larger the δ term the larger the nEDM; this model predicts a value to be $d_n \approx 10^{-24}$ ecm, which is well above

current experimental limits (44) (45).

Another alternative BSM theory is the Left-right symmetry model. In this model it states that the V-A structure of weak interactions only occurs at low energies, therefore, CP-violating processes are confined to lower then GUT scale at about 10^3 GeV. Above this scale, all interactions are defined by a single gauge coupling constant and are CP conserving. At this low energy scale a new gauge and Higgs field is thought to be created which is what mediates the CP-violating processes. L-R models predict nEDM values of $d_n \approx 10^{-26} \rightarrow 10^{-27}$ ecm (46) (47).

2.7 Comparision with other EDMs

Fundamental particles such as the proton, electron, and muon (atomic EDMs can arise from various parameters which generate EDMs in particles) also have EDMs which are required for complete BSM physics searches. EDMs probe multiple **CP**-odd parameters that can all contribute towards symmetry violation. In order to achieve an effective theory for **CP**-odd phases at the highest energy scales, contributions from every EDM searches are required.

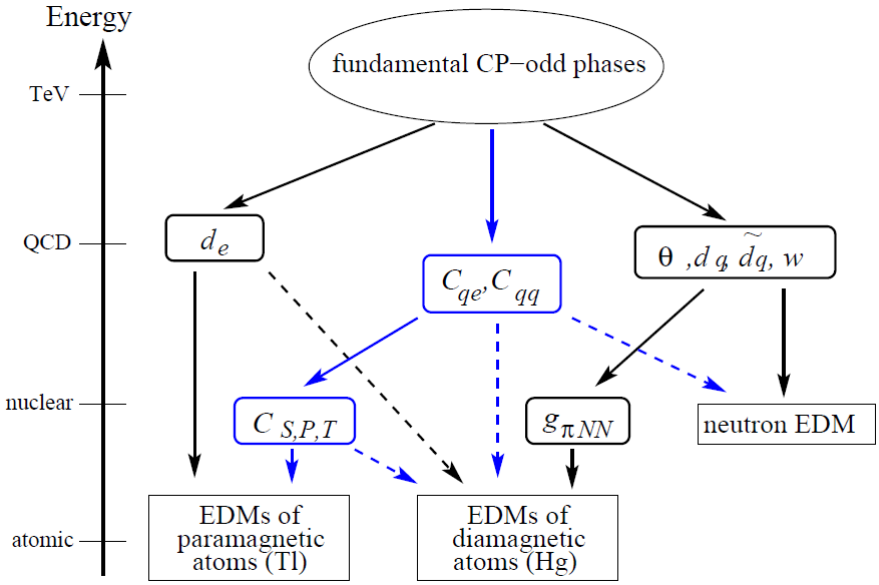

Fig. 2.5 Schematic plot relating the EDMs to CP-odd sources. The EDMs are split into three catagories that probe different sources of CP violation. The dashed lines represent weaker connection to the various parameters (40).

The EDMs of paramagnetic atoms, primarily systems with one unpaired electron, are most sensitive to an electron EDM. However, in some cases there can be contributions from the nucleon EDM.

In the case of diamagnetic atoms in which total electron angular momentum is equal to zero, the EDM arises due to nuclear finite-size effects. Misalignment in the nucleus of the atom between the distribution of the charges will generate a EDM in nucleus. This is more visible on larger atoms. The induced atomic EDM is considerably suppressed relative to the underlying EDM of the nucleus. In these systems the contributor to a nuclear EDM would come from either the proton or neutron EDM or from CP violating nucleon-nucleon interactions.

The final catagory is neutron EDM (direct measurement).

Futher information of the theoritical details of comparisions are given in Pospelov (40) and Khriplovich (5).

Thus far an EDM of non-zero has not been observed. Table 2.2 gives the results of all competitive searches for EDMs from various catagories. There are some EDM measurements that are not mentioned here, but details can be found in (48) and the references in the table.

System	Year/ref	Result
	Paramagnetic systems	
Cs	1989 (49)	$d_A = (-1.8 \pm 6.9) \times 10^{-24}$ ecm
		$d_e = (-1.5 \pm 5.6) \times 10^{-26}$ ecm
Tl	2002 (50)	$d_A = (-4.0 \pm 4.3) \times 10^{-25}$ ecm
		$d_e = (6.9 \pm 7.4) \times 10^{-28}$ ecm
YbF	2011 (51)	$d_e = (-2.4 \pm 5.9) \times 10^{-28}$ ecm
ThO	2014 (52)	$\omega^{NE} = 2.6 \pm 5.8$ mrad/s
		$d_e = (-2.1 \pm 4.5) \times 10^{-29}$ ecm
		$C_s = (-1.3 \pm 3.0) \times 10^{-9}$
	Diamagnetic systems	
^{199}Hg	2016 (53)	$d_A = (-2.2 \pm 4.2) \times 10^{-30}$ ecm
^{129}Xe	2001 (54)	$d_A = (0.7 \pm 3) \times 10^{-27}$ ecm
TlF	2000 (55)	$d = (-1.7 \pm 2.9) \times 10^{-23}$ ecm
Neutron	2015 (37)	$d_n = (-0.2 \pm 1.8) \times 10^{-26}$ ecm

Table 2.2 EDM results presented by authors, showing comparision in sensitivity for various experiments (48).

Currently, Hg result gives the smallest upper bound for an EDM in any system. Because of the link between various EDMs, one can interpret the Hg result as a limit on the nEDM d_n $1.6\times \leq 10^{-26}$ $e$cm, which is lower then the current limit. However, there are very large uncertainties in the nuclear theory calculations interpreting the Hg EDM. This limits

the ability to probe for BSM physics. The paramagnetic atoms and molecules don't have the same nuclear contributions to deal with and instead rely on atomic/molecular theory, which is easier to calculate. However, these have limitations too, originating from atomic structure. The neutron can be considered the easiest to interpret an EDM from as its a direct observation of a fairly fundamental particle. However, this has limitations to extracting more fundamental quantities like the quark EDM, due to 'messy' QCD derivations.

This is why its important to pursue improvements in sensitivities in all systems, so that when a non-zero result is eventually found, the different contributions to various EDMs and determined the origin for any underlying **CP** violation.

Chapter 3

Neutron EDM Measurement

3.1 Introduction

This chapter looks at how to perform a nEDM experiment in order to determine its magnitude. The measurement typically involves storage of polarised UCN in a bottle with a stable magnetic field applied to the volume. Then an electric field is applied to the bottle during the measurement as the neutron spin precesses around the stable magnetic field. In order to observe the nEDM an NMR technique is used to measure the neutron spin precession frequency. The presence of an nEDM would result in a slight shift in that precession frequency during the application of the electric field. The details of the techniques used are given in this chapter.

The generation of UCN in LHe at 0.5 K which is relevant for a cryogenic nEDM experiment is also covered. The reason for using a cryogenic nEDM experiment is through improvements in sensitivity. These improvements come from better UCN numbers and higher E fields.

Examples of nEDM experiments that are either running or planning to come online within the next decade are also discussed. These range from room temperature experiments with external UCN sources to cryogenic experiments with in-situ sources.

3.2 General nEDM experimental technique

3.2.1 Neutrons in a magnetic field

Neutrons have a magnetic moment (μ_n), which is how the neutron can be influenced in a magnetic field (56).

The interaction between the magnetic moment and magnetic field results in a torque

on the neutron spins leading to spin precession around the magnetic field ($\vec{B}$).

$$\vec{\tau} = \vec{\mu_n} \times \vec{B}, \text{and} \tag{3.1}$$

$$\mu_n = -1.91\mu_N = -9.66 \cdot 10^{-27}\ \text{J T}^{-1}, \tag{3.2}$$

where μ_N is the nuclear magneton.

$$\mu_N = \frac{e\hbar}{2m_p} = 5.05 \cdot 10^{-27}\ \text{J T}^{-1}, \tag{3.3}$$

where e is the elementary charge and m_p is the proton mass.

The rate of the precession of the neutron in this field is determined by the gyromagnetic constant (γ_n) and the magnitude of the field. The rate at which the neutron will precess in the field is called the Larmor precession frequency (ω_L),

$$\omega_L = \gamma_n \cdot B, \text{and} \tag{3.4}$$

$$\gamma_n = \frac{2|\mu_n|}{\hbar} = 1.83 \cdot 10^8\ \text{rad s}^{-1}\ \text{T}^{-1}. \tag{3.5}$$

Taking the magnetic field used in the PSI nEDM experiment of 1 μT:

$$\omega_L = \frac{v}{B} = 183\ \text{rad s}^{-1} = 29.1\ \text{Hz} \tag{3.6}$$

3.2.2 Neutrons in magnetic and electric fields

Application of an electric field in the storage bottle containing UCN will create an extra torque on the precession of the neutron if a nEDM exists. The applied electric field can be parallel or anti-parallel and is normally varied between cycles (UCN enter, measurement is performed, UCN drained to detector) in conjunction with varying of the magnetic field. The nEDM can be positive or negative, therefore, varying the direction of the applied electric or magnetic fields can help eliminate systematics.

By looking at the interaction Hamiltonian energy from the Zeeman and Stark splitting it can be seen that:

$$\mathscr{H} = hv = 2\mu_n \vec{\sigma} \cdot \vec{B} \pm 2d_n \vec{\sigma} \cdot \vec{E}. \tag{3.7}$$

Therefore, by finding the frequency with parallel magnetic and electric fields, $v_{\uparrow\uparrow}$, and where the electric field is anti-parallel to the magnetic field, $v_{\uparrow\downarrow}$:

$$v_{\uparrow\uparrow} - v_{\uparrow\downarrow} = \Delta v = \frac{(4d_n \cdot E)}{h}. \tag{3.8}$$

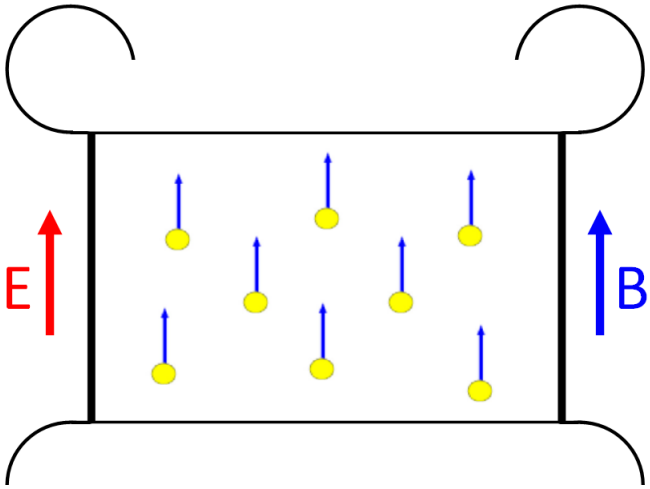

Fig. 3.1 Bottle with spin polarised neutrons parallel with B_z field and E field. Top of the bottle is the HV electrode with the bottom being the ground electrode.

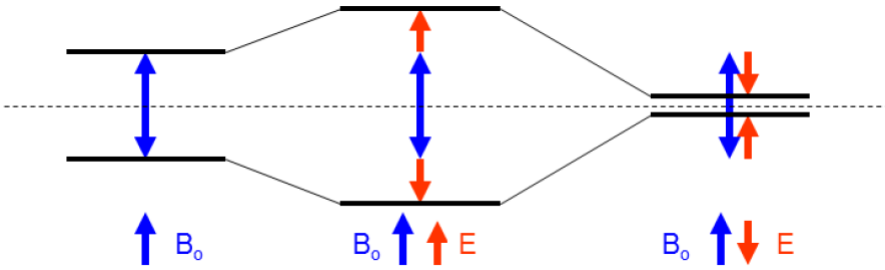

Fig. 3.2 Zeeman splitting for B and E field parallel and Stark shift for B and E anti-parallel.

Therefore, the magnitude of the shift between the parallel and anti-parallel frequency due to the presence of a nEDM can be determined. Assuming a nEDM of order $1 \cdot 10^{-27}$ $e$cm and application of an electric field of 100 kV/cm:

$$\Delta \nu = 96 \text{ nHz} \tag{3.9}$$

Clearly at nHz range the stability of the magnetic field needs to be very stable, as a shift of 96 nHz corresponds to a 3 fT B field, so a small shift would mimic the presence of a nEDM (generally called a false nEDM). Generally the aim is to limit any potentially magnetic contributions to be at least one order of magnitude less than that coming from the EDM sensitivity of that experiment. In order to observe such a small frequency shift, the Ramsey technique is used.

3.2.3 Ramsey Method of Separated Oscillating Fields

The small shift from the presence of the nEDM means that a standard NMR technique cannot achieve the sensitivity required for a shift of the nHz range on top of the 29.1 Hz signal. Therefore to observe this shift the Ramsey method of separated oscillating fields

is used (57).

A spin polarised neutron entering the storage volume with its spin aligned in the same direction of the static magnetic field B_z (spin-up state) will precess around it with frequency $\omega_z = \gamma B_z$. The electric field is continuously applied, either parallel or anti-parallel with the B_z magnetic field. Using a pair of AC coils in opposite directions, so their components in the z axis cancels, an additional oscillating magnetic field B_{xy} perpendicular to the static B_z field is introduced. This field can be considered as two rotating fields at ω_{rot} (at Larmor frequency) but in opposite directions. The neutron will see this B_{xy} field as a rotating field with its spin at the Larmor frequency. As a result it will start to precess around the B_{xy} field with frequency $\omega_{xy} = \gamma B_{xy}$. This causes the neutron to spiral out of alignment with the static B_z field, towards the x-y plane. This process is allowed to occur for $\tau = \frac{1}{4\gamma B_{xy}}$. After this time the neutron has been flipped by 90° ($\frac{\pi}{2}$ pulse), and is aligned with the x-y plane. This B_{xy} field is then switched off, but the oscillation of the field is still monitored.

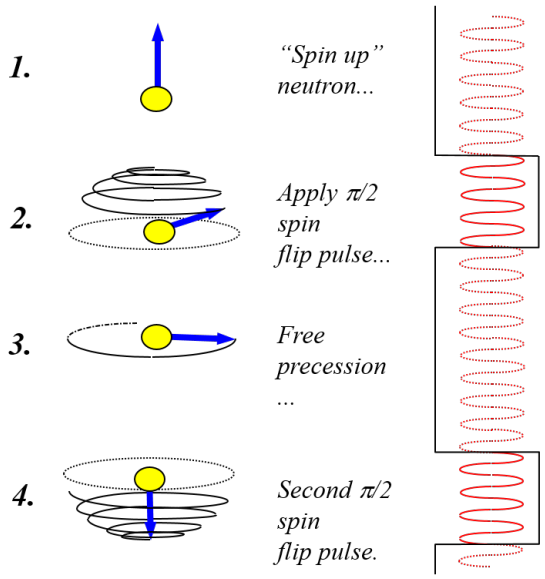

Fig. 3.3 Ramsey technique of separated oscillating fields (6).

The neutron is now in the free precession period, precessing around the B_z axis. After a length of time which is dependent on the experiment, with the maximum time restricted by τ_n (lifetime of the neutron), another $\frac{\pi}{2}$ pulse is applied which is in the same phase as the first one. This second pulse will cause the neutron to precess downwards towards the opposite direction from its initial position, spin-down, if its spin is still in phase with the applied RF pulse. The sequence of pulses at resonance frequency $\omega_{rot} = \omega_z$, results in the minimum number of neutrons in the initial spin-up state.

If the nEDM exists then the application of the electric field, $\omega_{rot} \neq \omega_z$, will cause an accumulation of phase. The final state of the z-component is strongly dependent on the spin vector ($\vec{\sigma}$) of the neutron and the oscillating field B_{xy}. If the additional phase shift causes the angle between $\vec{\sigma}$ and B_{xy} to exceed $\frac{\pi}{2}$ then the second pulse will cause the neutron to tend back towards the initial position. To determine the change in phase, the number of neutrons in the initial and final states are detected and measured against the applied field frequency, υ_{rot}.

At the resonance frequency, υ_0, the number of neutrons is either all spin-up or spin-down, depending on the orientation of their polarisation opposite their initial spin state (if perfect polarisation). In an nEDM experiment the polarisation of the neutron is switched in different cycles in order to eliminate systematics, if the nEDM exists then a phase shift will be visible in both spin states, shifting the Ramsey resonance curve left or right.

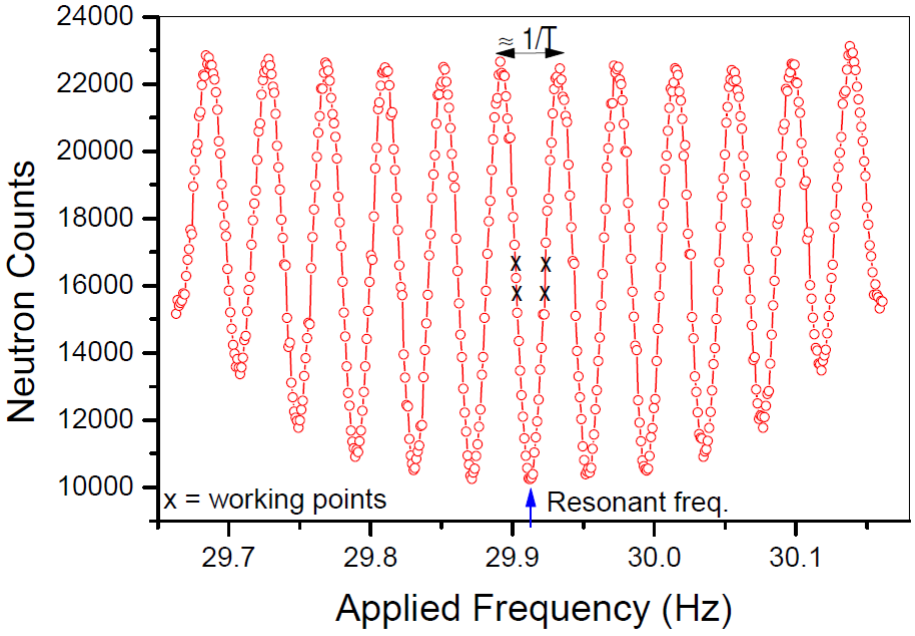

Fig. 3.4 Ramsey resonance curve. The x axis is the working points of the curve which is where $N_\uparrow$ is measured against $N_\downarrow$ to pinpoint the resonant frequency. The working points are at the position of largest gradient in order to maximise sensitivity to a frequency shift. If a nEDM exists then these points will shift left or right depending on the sign of the EDM (6).

The number of neutrons in the spin up state ($N_\uparrow$) and down ($N_\downarrow$) as a function of applied frequency υ_{rot} is given by:

$$\overline{N_{\uparrow\downarrow}}(\upsilon_{xy}) = \overline{N_{\uparrow\downarrow}} \mp \alpha_{\uparrow\downarrow}\overline{N_{\uparrow\downarrow}} \cos\left(\frac{\pi(\upsilon_{rot} - \upsilon_0)}{\Delta\upsilon_{rot}}\right), \tag{3.10}$$

where $N_{\uparrow\downarrow}$ is the average number of neutrons in a given spin state:

$$\langle N_{\uparrow\downarrow} \rangle = \frac{N_{\uparrow\downarrow max} - N_{\uparrow\downarrow min}}{2}. \tag{3.11}$$

The polarisation or visibility of the fringes is given by:

$$\alpha_{\uparrow\downarrow} = \frac{N_{\uparrow\downarrow max} - N_{\uparrow\downarrow min}}{N_{\uparrow\downarrow max} + N_{\uparrow\downarrow min}}. \tag{3.12}$$

Δv_{rot} is the width of the central fringe at half height which is determined by the free precession time and the time in which the oscillating field is applied.

3.2.4 UCN generation and storage

nEDM measurements require the generation of UCN. These types of neutrons are made by various methods, but for the purposes of this thesis only generation of UCN by superfluid LHe will be discussed. For more details on UCN generation see (58).

For a superfluid LHe superthermal source a polarised cold beam of neutrons (8.9 Å) is required, which are normally produced in a Maxwellian spread of energies. However, in order to store them they need much lower energies $\sim 10^{-7} eV$ (59).

Neutrons interact via the strong, weak, gravitational, and magnetic forces. Therefore, when UCN come into contact with a surface they will interact via the strong nuclear force. If the Fermi potential (V_f) of the material experienced by the neutron over the total sampling area is greater than that of the kinetic energy of the UCN then it can be reflected by the surface.

$$V_f = \left(\frac{2\pi\hbar^2}{m_n}\right) \sum_i N_i a_i, \tag{3.13}$$

where m_n is the mass of the neutron, N_i is the molecular density, and a_i is the scattering length.

If the UCN does experience an inelastic interaction with a surface then the neutron will be up scattered, gaining energy from the surface, therefore, no longer bound in the storage volume so is lost.

As UCN have such low energy they can be accelerated under gravity and gain enough energy to above V_f, and so can be lost. UCN move at ~ 5 ms^{-1}, hence are strongly affected under gravity.

$$V_g = mgh, \tag{3.14}$$

where V_g is gravitational potential and m is the neutron mass.

If the neutron free falls under gravity for 1 metre it will gain energy of $\sim 1.03 \cdot 10^{-7} eV$ which could increase there kinetic energy to overcome V_f of many surfaces, hence, careful design for storage does need to be considered (56).

The time the UCN spends in the storage bottle is ultimately dependent on the lifetime of the free neutron. The neutron decays through β decay into a proton via the weak interaction.

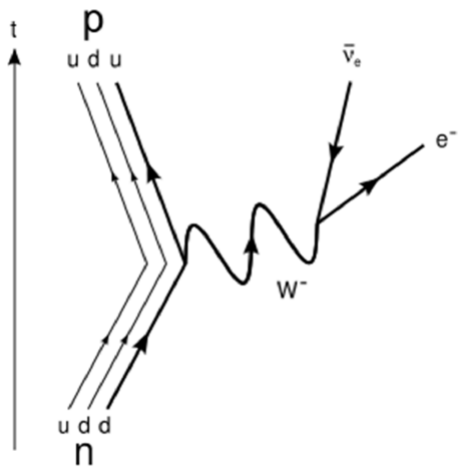

Fig. 3.5 Diagram of the β decay of the free neutron (60).

However, the full neutron lifetime cannot be completely exploited due to a number of loss mechanisms (more details given in (58)).

Pendlebury and Golub (61) theoretically investigated the production of UCN with cold neutrons interacting with He II. It was found that the dispersion curves for a free neutron and He II crossed at two points.

The dispersion curve shows that the maximum temperature of the LHe volume will convert the neutron to UCN at 0.8 K. This occurs as the free neutron will emit a phonon to the He II, losing virtually all of its energy. One advantage of this process is that the polarisation of the free neutron will be maintained.

However, the upscattering rate of UCN in LHe is proportional to T^7 below 1 K, therefore, at 0.8 K UCN are generated but the storage time is limited $\tau \sim 300$ s. But if the temperature of the He II is $\leqslant 0.5$ K the upscattering rate suppressed by the Boltzman factor, dramatically reducing it, so the the maximum UCN production occurs at this

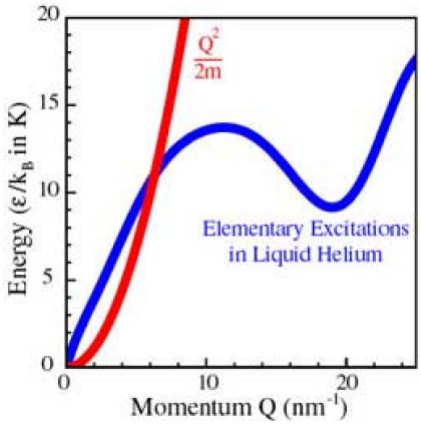

Fig. 3.6 Phonon dispersion curve for the (red) free neutron and LHe (blue). Free neutrons have 8.9 Å and E = 1.03 meV. At 0.8 K LHe will downscatter the free neutron, losing all their phonons to the fluid (62).

temperature for a given cold neutron beam. The UCN see the He II as an inert matrix and do not interact with it.

In a room temperature nEDM experiment the walls of the storage vessel are warm, therefore, when a UCN at 2 mK interacts with the surface it has a higher probability it will gain energy and be upscattered, being lost from the storage vessel. The neutron could also be captured by the material of the wall. The same thing can happen in a cryogenic vessel on walls at 0.5 K, but with significantly less probability; the long wavelength of the neutron interacts with $\sim 10^7$ particles on the surface. The total centre of mass velocity of the $\sim 10^7$ particles in this case is far less than that of the UCN, therefore, the UCN is coherently scattered from its surface back into the He II medium.

The total number density of UCN (63) in He II volume is given by:

$$\rho_{UCN} = P\tau_n, \tag{3.15}$$

where P is production rate of the UCN $\mathrm{cm}^{-1}\mathrm{s}^{-1}$ and τ_n is the experimental UCN lifetime determined from the experiment and includes all loss mechanisms.

3.2.5 Polarisation

The magnetic interaction of the neutron with a magnetic surface is strongly dependent on its spin. This adds an additional term, V_f, to the potential U of the neutron when it interacts with the magnetic material's surface,

$$U = V_f \pm \vec{\mu}_n \cdot \vec{B}. \tag{3.16}$$

The second term is spin dependent, which is measured relative to the B field. This can be exploited to extract neutrons of a certain spin state. Interacting with magnetic material surfaces with the spin aligned parallel to the B field will result in a high U which causes it to be reflected back, while if the neutron is aligned anti parallel it will have energy greater than the potential barrier so can pass through the magnetic material.

Total reflection of a neutron will occur from a magnetic surface material at any angle of incidence to the surface up to a critical angle θ_c (59).

$$\sin\theta \leqslant \lambda\left(\frac{Na}{\pi} \pm \frac{m_n}{2\pi\hbar^2}\mu B\right)^{\frac{1}{2}} = \sin\theta_c, \tag{3.17}$$

where λ is the neutron wavelength. Therefore, for high energy neutrons the small glancing angles of incidence to a magnetic foil can create spin polarised UCN.

3.2.6 Transport of UCN

In the current room temperature experiment at PSI the UCN are generated in an external spallation source and then transported to the Ramsey Cell via guide tubes. The UCN act like an ideal gas in this case, therefore, they will fill the cell and the guides according to kinetic theory. The guides have high Fermi potential which direct the UCN to the bottle. In a cryogenic nEDM measurements, such as SNS nEDM (64), the source is in-situ with the Ramsey Cell in order to maximise UCN counts and avoid transport losses. Experiments on LHe sources of UCN by Zimmer indicate that high UCN densities (> 100 cm^{-3}) are possible in the storage volume (65).

3.2.7 nEDM Statistical Uncertainty

The statistical uncertainty for nEDM experiments (σ_{d_n}) is given by:

$$\sigma_{d_n} = \frac{\hbar}{2\alpha E T_s\sqrt{N}}, \tag{3.18}$$

where E is the applied electric field in the storage volume, T_s is the storage time of the UCN, and N is the neutron count.

$$\alpha = \frac{(N_\uparrow - N_\downarrow)}{(N_\uparrow + N_\downarrow)}, \tag{3.19}$$

where $N_\uparrow$ is the number of spin up neutrons and $N_\downarrow$ is number of spin down neutrons. The full derivation is given in (58).

The storage time (T_s) is limited by neutron losses, therefore, in general this number is

100-300 seconds. Polarisation (α) is the percentage of neutron counts in $N_\uparrow$ or $N_\downarrow$ state, and this value is from 0-1. These factors can't make orders of magnitude improvements to nEDM sensitivity, therefore, large sensitivity gains can only come from improving E and N. The neutron count can be improved by having a better UCN source but the sensitivity gains are inhibited by the square root, so very large source improvements are required to make substantial sensitivity gains.

Therefore, the factor which is the 'easiest' to make the biggest improvements to the sensitivity is the electric field, E, which gives a linear improvement in sensitivity.

3.3 nEDM experiments

This section will cover some of the many current nEDM efforts around the world. For more details on other experimental efforts currently being undertaken are given in (7).

3.3.1 PSI experiment

The current PSI experiment which finished running as of August 2017 operates using similar concepts as already stated, however there are a number of differences that will be briefly covered here. Full details are given in (66).

The UCN are generated in an external source then transported to the experiment. The High Intensity Proton Accelerator (HIPA) (67) at PSI accelerates protons to 590 MeV energy with a peak intensity of up to 2.4 mA. The beam is directed to a spallation target for about 7 ms to 8 s.

The target is made of lead which contains 756 Zircalloy tubes. The target is surrounded by heavy water at room temperature which causes the neutrons to undergo thermalisation, significantly slowing the neutrons down from energies of range 2 MeV to a few hundred MeV . The fast neutrons are thermalized in the heavy water by losing a significant about of kinetic energy to the deuterons. This leaves them with a thermal spectrum peak at 313 K with 27 meV for the neutron (68) (69).

The solid deuterium moderator vessel is another heavy water tank which contains purified deuterium cooled to 5 K with liquid helium. The heavy water is then cooled as to crystallise. This crystal is where the neutrons from the heavy water tank are downscattered and lose almost all their remaining kinetic energy to become UCN. The UCN then leave the crystal at its surface into a storage vessel. Full details of the source are given in (70).

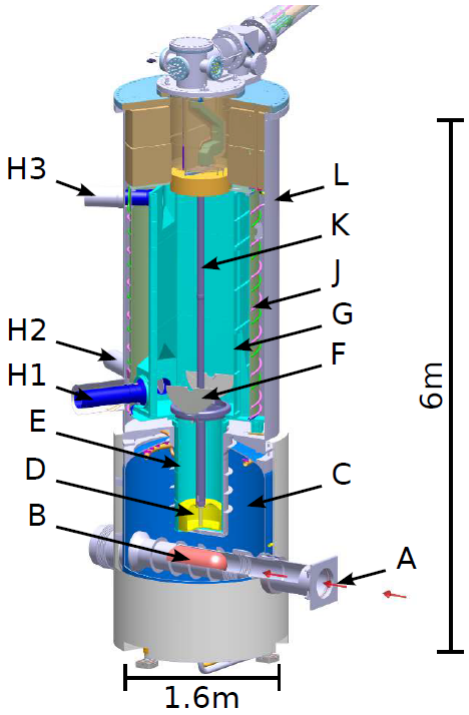

Fig. 3.7 CAD drawing of the central part of the UCN source at PSI. A - incoming photon beam, B - Spallation target, C - Heavy water tank, D - Solid deuterium moderator vessel (crystal is formed inside), E - Vertical UCN guide, F - Central storage vessel window, G - Central storage vessel, H1-H3 - UCN ports, J - Thermal shield, K - Deuterium and helium supply lines, L - Vacuum vessel (68).

The UCN are transported through guide tubes which are made of glass and coated with nickel and molybdenum (NiMo); this ensures the UCN are contained within the guide, due to the high Fermi potential.

The UCN are then polarised by using a superconducting 5 T solenoid to accelerate UCN in one spin state and decelerate those of another spin state towards a foil. Those with a higher kinetic energy will be transmitted through while those of the opposite spin state will be reflected back into the source.

The UCN are then transported to the Ramsey Cell were the nEDM measurement is performed. The storage bottle contains two aluminium electrodes separated by an insulating spacer made of Rexolite. The electrodes and insulator walls are coated in DLC (diamond like carbon), giving a high Fermi potential for the UCN. The electric fields for the experiment are generated by applying HV to the top electrode to give a field of 11.67 kV/cm on average.

Polarised ^{199}Hg is produced and allowed into the storage volume during a nEDM mea-

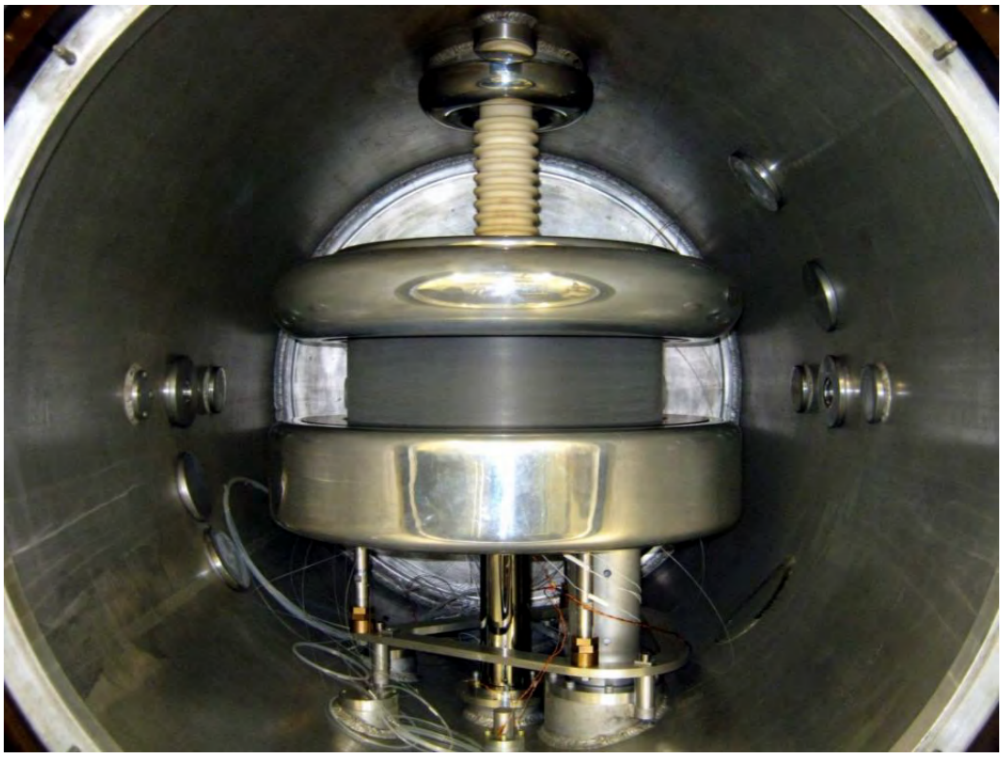

Fig. 3.8 Picture of the PSI nEDM experiment, as viewed from the side with the front of the mu-metal shield removed (71).

surement in order to monitor the stability of the magnetic fields over the Ramsey Cell. The mercury is probed by a laser which emits photons at 254 nm on to the precessing mercury atoms which absorb the light depending on their spin orientation, the transmitted light is detected by a PMT in the UV range.

The Ramsey Cell is contained within a vacuum chamber which contains $\sim 10^{-3}$ mbar helium gas. The vacuum chamber is then surrounded by the magnetic field coils, with the field inside the cell at 1 μT. Surrounding all this is four layers of mu-metal shielding.

The standard cycle for the experiment is one filling of UCN and one Ramsey sequence. The UCN are then emptied into a detector, after the free precession time, to determine the number of neutrons in the opposite spin state to there initial, giving the Ramsey curve.

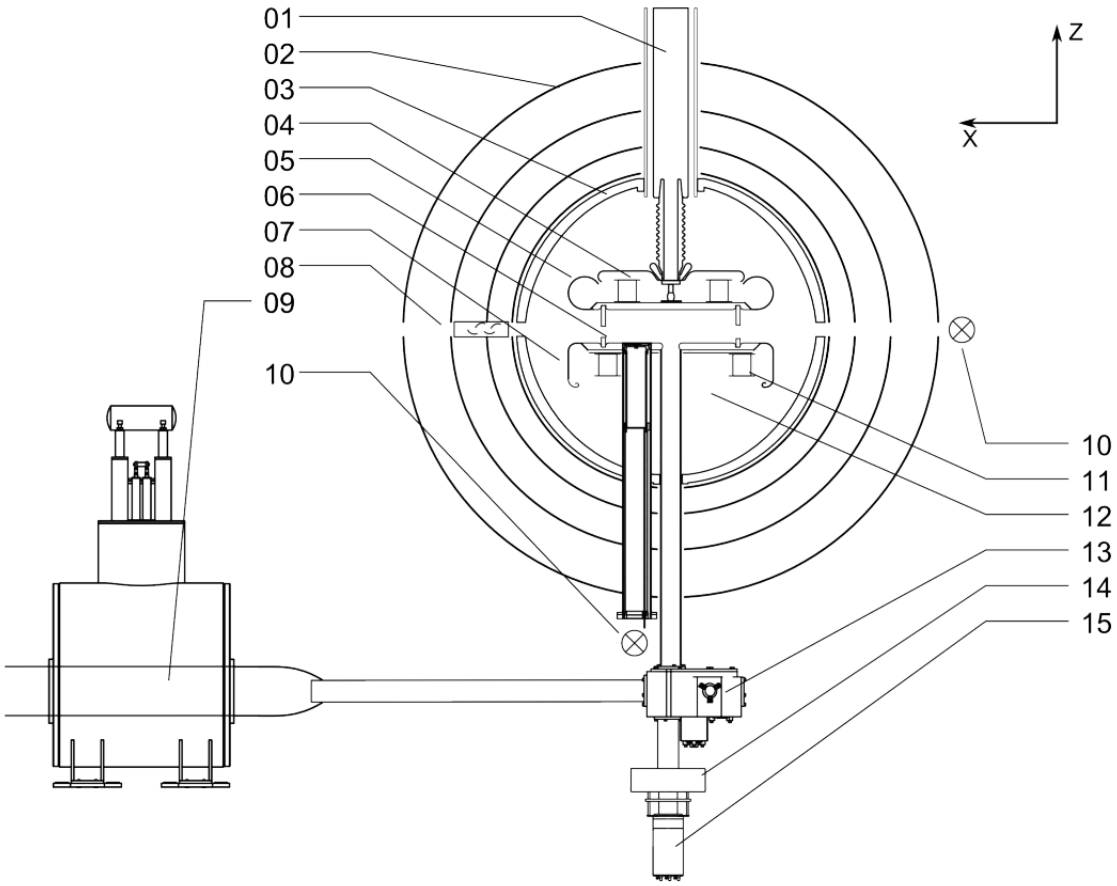

Fig. 3.9 Sketch of the nEDM experiment at PSI. The labelled components are as follows: (1) High voltage feedthrough, (2) 4 layer mu-metal shield, (3) vacuum tank with main magnetic coils and correction coils, (4) cesium magnetometer array, (5) high voltage electrode, (6) insulator ring, (7) ground electrode, (8) PMT, (9) superconducting polariser magnet, (10) ^{204}Hg discharge lamp, (11) second cesium magnetometer array, (12) vacuum, (13) neutron switch, (14) spin analyser, (15) neutron detector (71).

3.3.2 n2EDM

n2EDM is the replacement for the nEDM experiment which has just shutdown at PSI. It will start construction in February 2018 with data taking in late 2020. The advantage of n2EDM over the previous experimental setup is that it uses a double chamber geometry with electrode diameter larger previous experiment. This means it is able to do measurements with much larger the numbers of UCN's, hence improved sensitivity. The experiment will use the same source as the previous experiment.

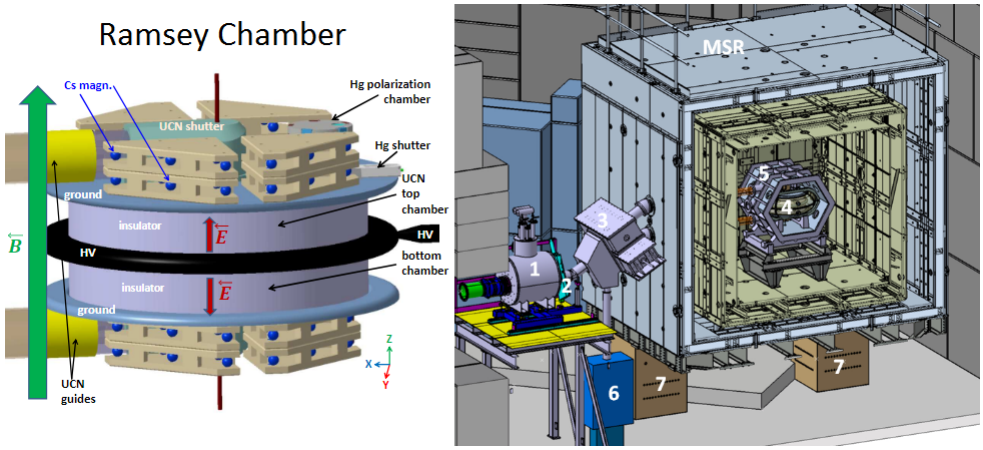

Fig. 3.10 CAD drawings of the n2EDM experimental setup, Ramsey Cell (left) and complete setup of the Ramsey Cell inside the magnetically shielded room, MSR, at PSI (right). The MSR is mounted on granite pillars (7) for stability. The 5 T superconducting-magnet polariser (1) and beamport (2) are left of the MSR, which bring the UCN's from the source into the switch (3). The switch directs the UCN to both chambers or into the UCN detector (6). The UCN enter the Ramsey Cell (4) via the vacuum tank (5) from the switch. After the measurement is performed the UCN extracted into the UCN detector (72).

3.3.3 SNS nEDM experiment

The SNS nEDM collaboration are seeking to construct a full scale cryogenic nEDM experiment to attempt to measure to a sensitivity of $\sim 3 \times 10^{-28}$ $e$cm. In order to do this improvements in E, N and T_s are planned. Their full experiment will generate UCN using an 8.9 Å cold neutron beam at the Oakridge National Laboratory which can create UCN in-situ which in turn should generate larger density of UCN than current experiments (61). The advantage over a room temperature nEDM experiment is having the UCN source in-situ, which will eliminate UCN losses from transportation and provide larger N. The use of the LHe bath at 0.4 K will also suppress some of the loss mechanisms for stored UCN which in turn provides longer T_s (73) (74). The electrodes will have the cells sit between them with a double chamber geometry with 2 neutron beams coming in horizontally to the cryostat. The cryostat is made of non-magnetic materials

with SQUID magnetometry placed in the LHe vessel outside of the electrodes. This is surrounded by a large superconducting shielding in order to eliminate any external magnetic fields.

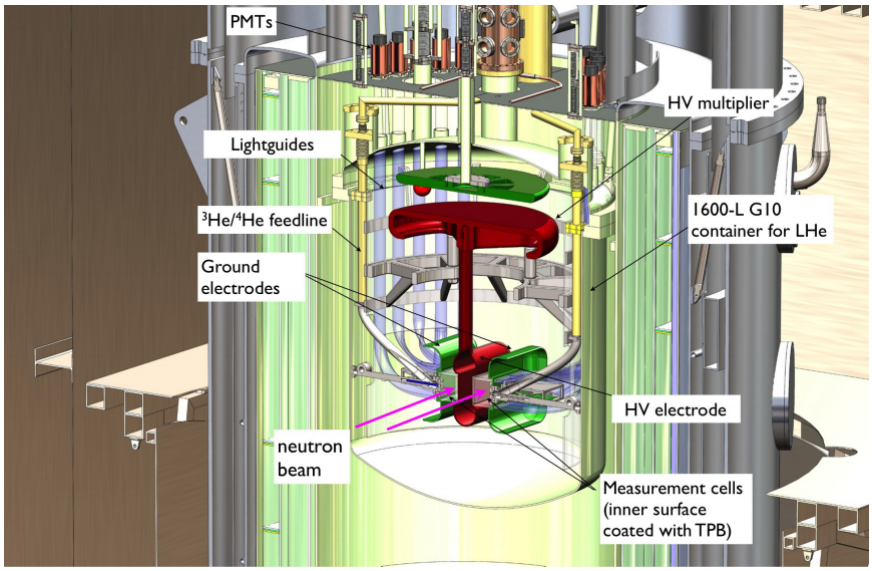

Fig. 3.11 CAD drawing of the planned SNS nEDM experiment.

The SNS collaboration plan to use a 100 kV power supply to provide the voltage they require. However, the separation between the electrodes is significent (10 cm), therefore, at this voltage it would not generate a large enough E field for a competitive nEDM experiment. In order to get the desired 600 kV on the HV electrode without having massive HV delivery systems which could provide a large thermal input to the LHe volume, they will use a HV multiplication technique: the Cavallo's multiplier method (75). This involves having two isolated conducting plates, charging one of them up to the maximium voltage, isolating it from HV, then moving it in contact with the other plate. As they touch, the charge on one will migrate to the other distributing charges evenly on both plates. They repeat this process multiple times till enough charge builds up on the secondary plate to get the required E field. The design goal for the E field is 80 kV/cm in L^{4}He at 0.4 K.

The experiment will also use a unique method for measuring the magnetic field's stability within the Ramsey Cell, with the use of spin-polarized ^{3}He atoms as a co-magnetometer. SNS will purify the L^{4}He bath then dope the volume with a known quantity of ^{3}He. ^{3}He has one less neutron, therefore, has a large absorption cross-section for free neutrons, if their spins are aligned. However, in the SNS nEDM experiment they plan to exploit this property to capture the spin polarised UCN onto the ^{3}He in order to measure the neutron precession. They plan to use a technique called critical spin dressing, full details here (76). The process modifies the Larmor precession frequency of

both the ^{3}He and the free neutron so that they both will possess the same gyromagnetic ratio and, therefore, precess at the same rate in a static magnetic field. As the neutron is captured by the ^{3}He they will then generate scintillation light. The photons emitted have their energy down shifted by a film coating on the aryllic vessel in order to be detected by a PMT.

The presence of a nEDM would result in a variation in the number of photons detected as the spins of the ^{3}He and the free neutron will be out of phase. This method of detecting the nEDM means that T_s can be a lot longer then other nEDM experiments, however, it will be limited to 1400 s due to wall collisions as well as ^{3}He losses. The polarisation is close to 1, due to the spin conserving properties of such a source for generating UCN (64).

3.3.4 TRIUMF nEDM

The TRIUMF nEDM collaboration are planning on performing a measurement using UCN in a room temperature setup, similar to that used in the PSI experiment. Their goal is to achieve sensitivity of 10^{-27} $e$cm with measurements starting in 2020. The difference with TRIUMF's experiment from PSI is they plan on using superfluid helium as the UCN source, a Hg/Xe co-magnetometer, and double cell geometry. As with PSI the UCN source uses a spallation of 480 MeV protons at initially 1 μA but instead to a tungsten target. The neutrons are then moderated by 300 K then a 10 K D_2O volume. This moderation slows the fast neutrons to cold neutron. At these energies they can be down scattered via phonon excitation in superfluid helium. The helium bath is then kept at a lower height then a UCN guide to the experiment in order to confine the liquid by gravity. This results in the UCN going to room temperature by leaving the LHe surface. The UCN are then extracted to the experiment. The use of the dual co-magnetometer is to correct for a false EDM caused by the geometric phase effect. The use of two elements results in the determination of both B_0 and the B_0 gradient (77) (78).

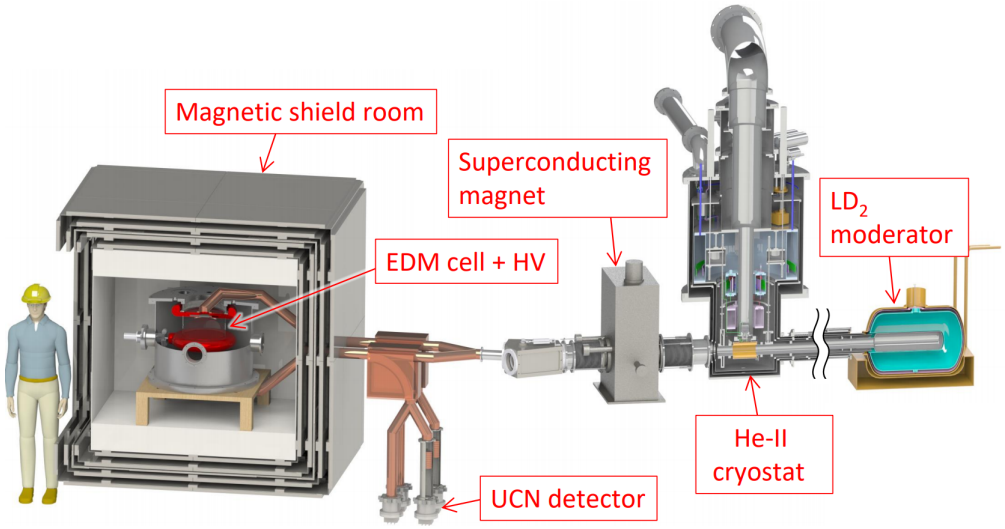

Fig. 3.12 CAD model of the planned TRIUMF room temperature nEDM experiment. The neutrons are extracted from the superfluid helium bath then polarised with a superconducting magnet. The neutrons then travel through guide tubes into the double chamber setup for measurements. Once completed they are removed into the UCN detector (77).

3.3.5 PanEDM

PanEDM is a planned experiment to search for the nEDM to a sensitivity of 7×10^{-28} $e$cm in a room temperature environment. They plan to use a double Ramsey chamber with a ^{199}Hg magnetometer, with plans to also use either Cs, Xe, ^{3}He. The experiment would eventually switch to cryogenic Ramsey Cell, after operation at room temperature, with use of SQUID's magnetometers. The benefit of switching to cryogenic setup would enable higher E fields achievable compared to room temperature experiments. PanEDM plans to be operating with UCN at Institut Laue-Langevin (ILL) in 2019. The unique aspect of this nEDM experiment is the UCN source.

This source is a superthermal UCN source, using superfluid LHe with a cold neutron beam at 8.9 Å wavelength to generate them. The advantage of this source is its size and portability. SuperSUN uses a small LHe volume in which the cold neutron beam enters. The beam is then down scattered, creating UCN which are then magnetically trapped by a Hallback array. The UCN are then extracted to room temperature to be delivered to the PanEDM experimental apparatus. The claim of this source is it is predicted to deliver much larger densities of UCN, expected to achieve 1670 n/cm^3 inside the magnetic trap. However, the densities expected in external cells is unknown at this point (65)(79).

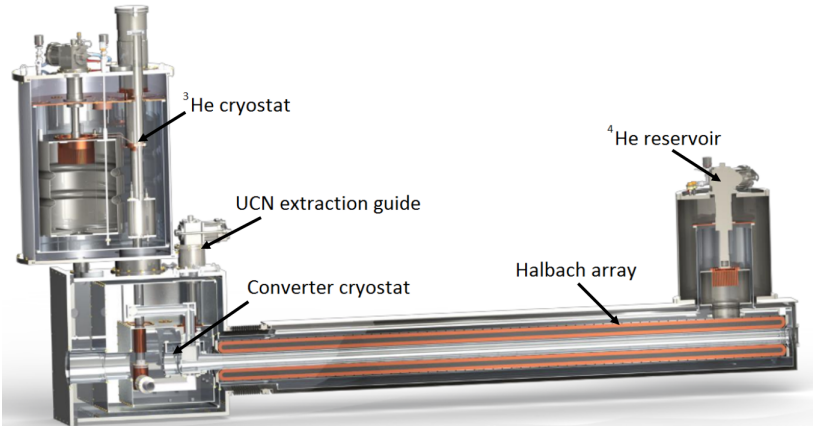

Fig. 3.13 CAD model of SuperSUN, prototype UCN source. Cold neutron beam enters the Halbach array and converted to UCN due to loss of phonon's to the superfluid volume. The UCN can then be extracted to a room temperature guide to the experiment through the port on the back of the converter cryostat (79).

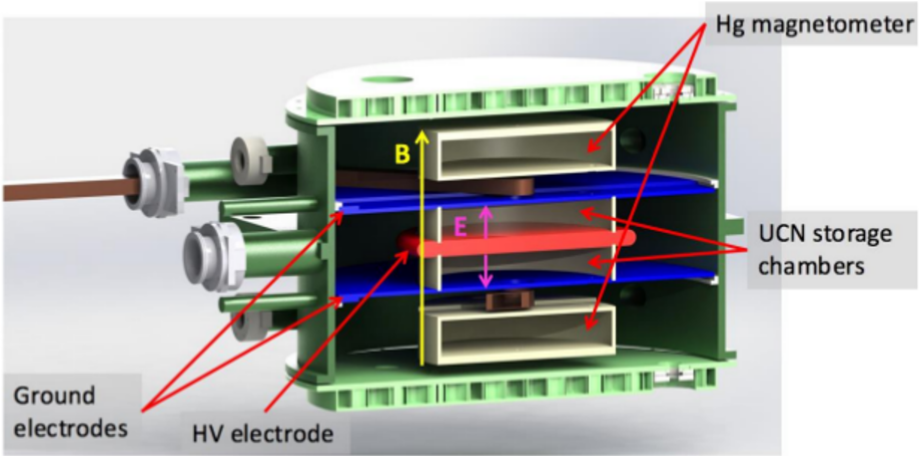

Fig. 3.14 CAD model of planned double chamber Ramsey Cell for PanEDM. The setup is enclosed in G10 vacuum chamber with ports on the sides to deliver the UCN to the chambers (brown component is UCN guide). The magnetic fields in this setup are monitored by Hg magnetometers (however, can in future use different elements like ^{3}He) above and below the ground electrodes.

Chapter 4

High Voltage Breakdown

4.1 Introduction

A high voltage breakdown is a process that occurs when the charge on a cathode exceeds the dielectric strength of the medium between it and the anode. This process results in a very quick, order nano-second, flash of charge to the other electrode, akin to lightning. The high voltage region is classified as DC voltage greater than 1.5 kV.

In this chapter, breakdowns in various mediums will be discussed for context in later sections. I will then discuss properties of LHe and breakdown behaviour in this cryogen, establishing a mechanism for the breakdown and expected values for given geometry. Breakdown measurements with LN_2 are also discuss to establish the mechanism for breakdowns in that cryogen. The behaviour of the two liquids can be compared to check if effects which influence the breakdowns are applicable to both.

The conclusion from the work of various authors is that the mechanism that limits breakdown voltages in LHe to the range of kV/cm, instead of MV/cm, is the generation of bubbles by local heating of the electrode surface. The bubble that is created becomes ionised by the high fields which causes an electrostatic stretching of the surface until it crosses the gap between the two electrodes. The breakdown then occurs through the gas within the bubble, collapsing it. This breakdown process is similar in LN_2 but charges can flow through the liquid volume which is suppressed in LHe. The formation of the bubble can be mitigated if the liquid volume is pressurised, increasing the breakdown field. There are a number of variables that can cause the bubbles to form at lower voltages; purity of the liquid, condition of the electrode surface, material of the electrode, surface area of the electrode, and breakdown repetition rate.

The presence of an insulator also limits the applied voltage between the electrodes.

High field regions exist at the point where the electrode, insulator, and liquid meets called the cathode triple junction. This region can limit the breakdown field in the liquid and in some cases damaging the insulator.

4.1.1 Breakdown in solid

Breakdowns through solids is dependent on the material separating the charged component to ground. It has two ways to breakdown: tracking on surfaces and breakdown through the solid.

Tracking is a process that results in carbonisation of the solid's surface. As carbon has formed on the surface this creates a short circuit as current is then able to flow from the cathode to the anode. This occurs as electrons are able to travel along a solid's surface, accelerated by the electric field, or aided by the presence of conductive contamination, like water vapour. The surface is the weakest point of the system while the bulk of the material normally has a dielectric strength many orders of magnitude higher than the surface.

However, tracking can be overcome with proper design by ensuring the length of the insulator is sufficient; this is referred to as the 'tracking length'. Normally in HV insulator design, the surface length is increased dramatically by adding castellations (ridges) so electrons have to travel further to ground, hence higher fields are required to enable the electrons to travel the extra distance.

Breakdown occurring through a solid is rare, however, this can happen due to poor design by not making sure the insulator is sufficiently thick enough to hold such a voltage. There can also be breakdown through a solid due to mechanical faults, resulting in a path for the electrons to flow to ground.

4.1.2 Breakdown in gas

Breakdown in a gas is dependent of the pressure of the gas and electrode separation:

- At very high pressures, i.e. atmospheric, the mean free path is very short. Therefore, electrons do not have enough time to be accelerated to ionization energies before hitting atoms or molecules. At these high pressures a HV breakdown processes needs to create a plasma to bridge across the gap to ground, which will come from charge carriers in the surrounding gas.

- However, at low pressures even though the mean free path is very long and the electrons have time to be accelerated to ionisation energies, the lack of charge carriers in the medium means that in order to create a plasma all the charge carriers need to come from the surface of the electrodes instead. This is what makes vacuum a very good insulator.

This behaviour is represented in the Paschen curve in Figure 4.1. The dip in the middle is the "Paschen minimum", which depends on the gas present and the electrode separation.

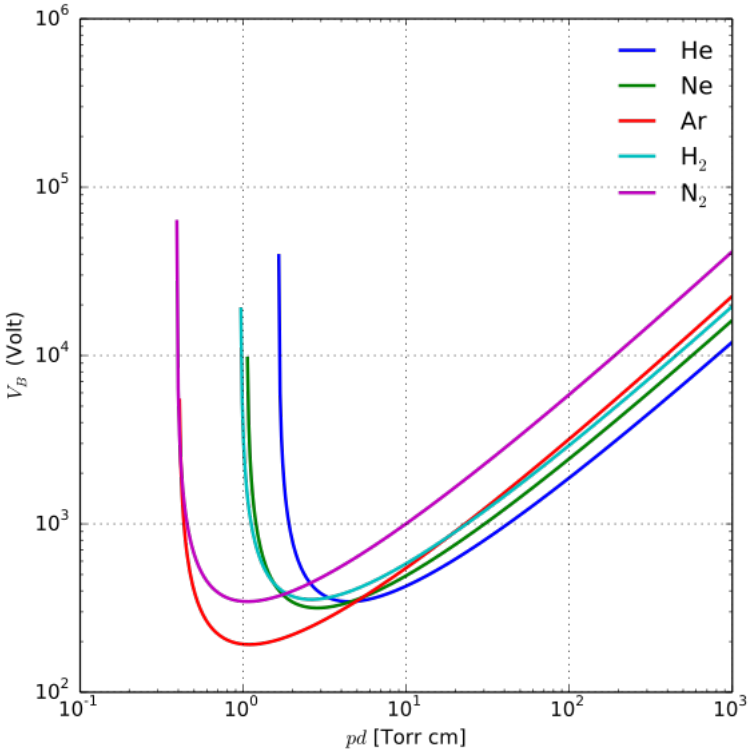

Fig. 4.1 Paschen curve for Helium, Neon, Argon, Hydrogen, and Nitrogen (80).

The behaviour of a breakdown is completely different on the right hand side of the Paschen minimum compared to the vacuum region on the left. There are two processes in which breakdown can occur: avalanche or streamers.

Avalanche breakdown is where an electron is released from the electrode surface and accelerates under the applied electric field. The electron has enough energy to ionise the gas. At this point the electron ionises the neutral atoms and molecules, producing more electrons. These products then start ionising more atoms and molecules, exponentially increasing the number of electrons travelling to the anode, as shown in Figure 4.2. This is the moment of inception of high voltage breakdown; if the conditions are right then it

will result in a flashover.

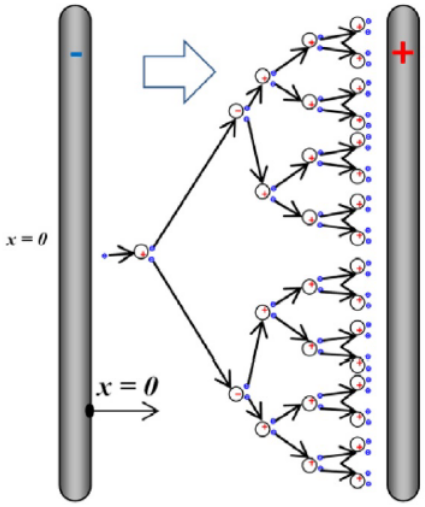

Fig. 4.2 Diagram of an avalanche breakdown process (81).

Figure 4.3 shows the distribution of particles in a single avalanche. This single avalanche changes the electric field between the electrodes, with a negative head tending towards the positive electrode and a positive tail tending towards the negative electrode. The change in electric field is caused by the slower moving positive ions, hence why they form a long tail.

Streamers form when a single avalanche emits photons that ionise local atoms or molecules, creating more free electrons to make further avalanches, as can be see in Figure 4.4. The constant creation of avalanches eventually forms a chain of avalanches which is then a streamer. They propgate in both directions, till they chain and bridge the gap between the electrodes creating an ionised conductive channel and thus a flashover.

This behaviour near the Paschen minimum it leads to a counterintuitive phenomenon: electrodes further apart will have lower breakdown voltages as this larger separation gives the electrons more space to form an avalanche.

The previous two sections are a summary of breakdown in different mediums, more details can be found in the following: (81), (82), (83), (84), (85), (86), and (87).

4.1.3 Vacuum breakdown

The previously mentioned processes only occur to the right of the Paschen minimum, left of this minimum is the vacuum breakdown region. As Figure 4.1 shows, the voltages required to breakdown rapidly increase with decreasing pressure. The mechanisms

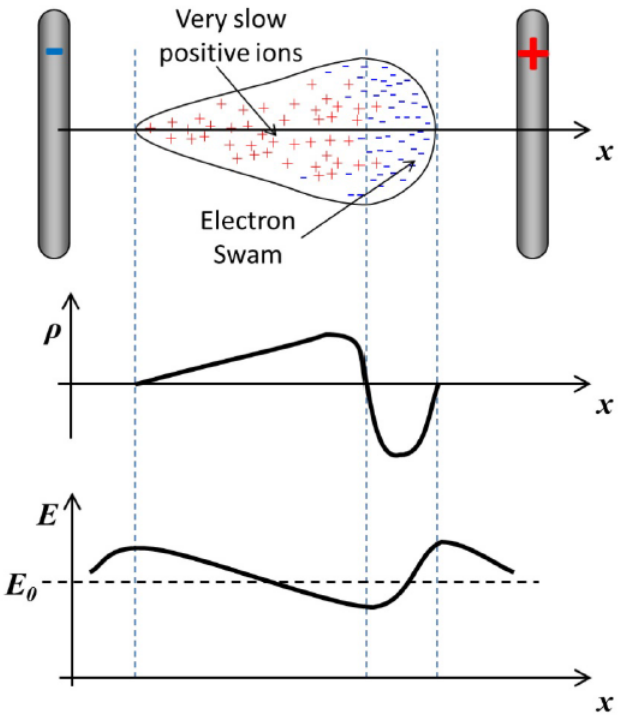

Fig. 4.3 Diagram of a single avalanche event, as well as the distribution of charge density (ρ), and value of the electric field, E, in the gap (81).

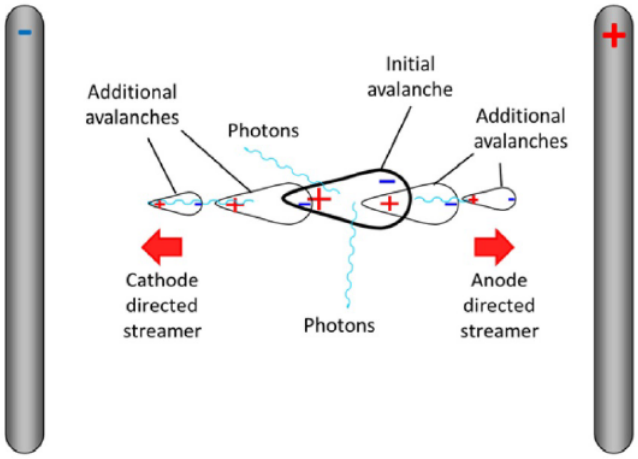

Fig. 4.4 Diagram of a streamer event, chain of avalanches together propograting in both directions till the gap is crossed (81).

for this to occur originate from the electrode instead. The surface of a material will always have a roughness on it to some degree, therefore, these protrusion can initiate HV breakdown. These protrusions cause localised field enhancements, which results in an emission of electrons through quantum tunnelling processes. This causes a localised current flow which heats the protrusion, eventually resulting in it exploding and creating a vapour that ionises causing a breakdown.

First applying HV to a system in vacuum generally results in a large amount of electron emission at low voltages. This is normally due to protrusions on the electrodes and requires a conditioning process. Therefore, HV is applied to the electrode till a spark occurs which will vaporise the protrusion. This process is continued till higher voltages can be reached at which point the maximum electric field can be obtained.

If an insulator is present between the electrodes in a vacuum high voltage system, it will usually be the weakest point. As previously mentioned, in section 4.1.1, the insulator surface can result in charge travelling along to the surface to ground, causing a breakdown. In a vacuum system this problem is exacerbated as there is no gas to prevent the electrons travelling so the breakdown voltage is much lower. The electrons will travel along the insulator surface due to such a high mean free path and they can ionise regions on the surface creating more electrons till eventually enough travel that it creates a short circuit, dumping all the charge to the anode, and creating a track on the surface.

Further details can be found in the following: (81), (82), and (83).

4.2 Breakdown in liquids

Breakdown in liquids is much more complex and varies from liquid to liquid. The liquid is normally used as a coolant and dielectric insulation for HV systems. The advantage in using liquids is that they are self-healing from a breakdown, were as a solid would need to be replaced. The causes of the breakdown in a liquid can occur due to many different parameters, such as; liquid state, impurities, stressed volume, electrode geometry and material, surface condition, breakdown repetition rate, and if the volume is pressurised.

In this thesis, we are interested in the breakdown behaviour of liquid helium at 4.2 K between two large electrodes in a plane-plane geometry with a fairly large gap between them. Understanding this behaviour should help inform any cryogenic effort for a possible future nEDM experiment. A cryogenic nEDM experiment would require the LHe to be at < 0.7 K, however, as will be demonstrated in this Chapter, breakdown values at < 0.7 K can be recovered to that at 4.2 K.

4.2.1 Properties of liquid helium

Liquid helium is an extremely low temperature fluid with a 4.2 K boiling point at SVP with a density of 0.125 g/cm^3. The temperature of LHe is so low due to the weak in-

teraction between the atoms. Because of this it will remain liquid, at SVP, down to absolute zero. Solidification of helium can only occur at extremely low temperatures and incredibly high pressures (~ 25 bar). The liquid is unique for its low viscosity (30×10^{-7} kg m^{-1} s^{-1}), low latent heat (2.6 MJ/m^3), and low permittivity (1.05).

Natural ^{4}He which is the most common isotope, is not completely pure, containing trace amounts of ^{3}He, the only other stable isotope of helium. The abundance ratio of ^{3}He to ^{4}He is 1:10^7. This lack of natural abundance of ^{3}He is why it is very rare. It is only produced in 'large' amounts through beta decay of tritium, an isotope in itself that is rare too. The boiling point of ^{3}LHe is just below that of ^{4}LHe at 3.2 K.

The most physically interesting phenomena of ^{4}LHe is the fact that it can become a superfluid. This phase transition occurs at the lambda transition point, T_λ = 2.17 K. The superfluid phase is commonly referred to as LHe II with LHe I the phase before the transition. The specific heat of the liquid rapidly increases as the fluid approaches the transition. This also results in vigorous bubbling as the volume reaches the transition, then as the volume crosses this temperature threshold the bubbling immediately ceases and the fluid is still, even if there is still heat input to the volume. The immediate ceasing of bubbling of the LHe II volume is due to the thermal conductivity of the liquid which dramatically rises. This means that the whole volume absorbs heat, resulting in bubbling only occurring on the surface of the fluid. Superfluids exhibit strange characteristics such as zero viscosity, flow without resistance, meaning it will creep up walls in which it is stored. This behaviour means that sealing a volume of LHe II needs to be done correctly as the fluid will flow through holes as small as ~ 0.7 nm, 3 times the classical diameter of helium atoms. At below 1 K the entire volume is converted to LHe II, which is important for maximising UCN production, as seen in Figure 4.6. ^{3}LHe does not pass the superfluid transition till ~ 2.6 mK.

The presence of ^{3}LHe in ^{4}LHe is useful: at 0.9 K the two isotopes separate out, with the lighter ^{3}LHe rising to the top of the heavier ^{4}LHe liquid. This behaviour is exploited for use in cryogenic refrigerators in order to purify the ^{4}LHe volume by syphoning off the ^{3}LHe. The ^{3}LHe can then be used to further cool the ^{4}LHe volume to mK range. However, for the use in a cryogenic nEDM experiment the presence of ^{3}He is problematic. ^{3}He has a high absorption cross section for neutrons, therefore, it will capture any free neutrons in a Ramsey cell volume resulting in potentially a high neutron loss factor.

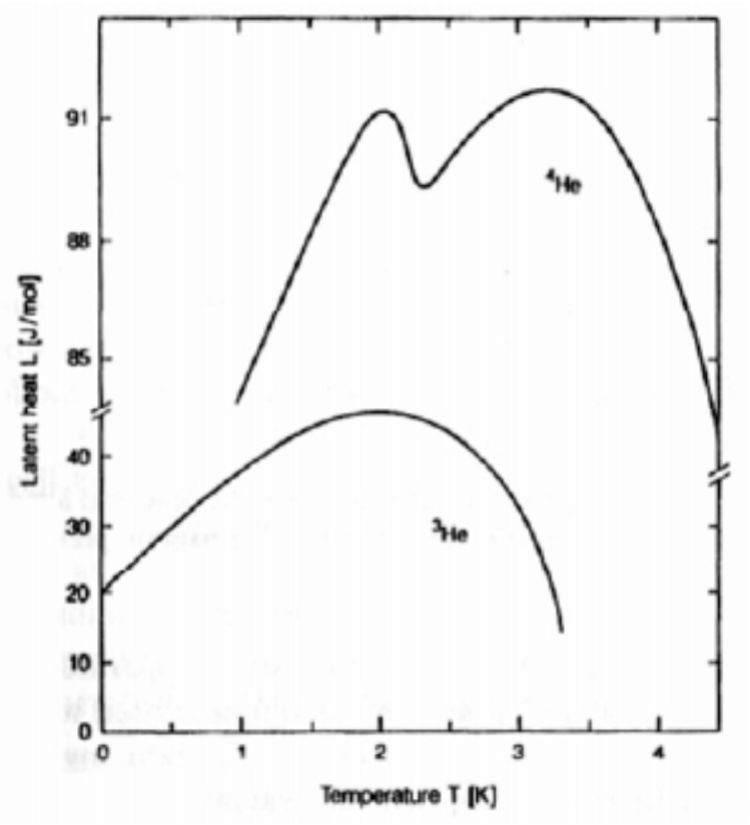

Fig. 4.5 Latent heat of ^{3}He and ^{4}He (88).

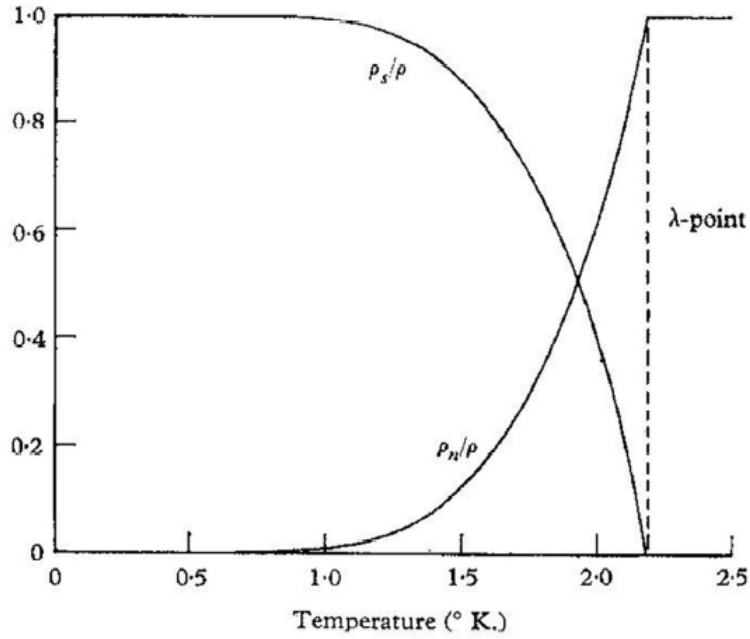

Fig. 4.6 Normalised density for LHe I and LHe II (89).

4.2.2 Breakdown in LHe

The dielectric strength of LHe is very high with fields of greater then 100 kV/cm being reported, seen in Figure 4.7. This is due to the mechanisms that cause breakdown within the liquid. An electron entering the fluid loses all its kinetic energy by ionisation and excitation of helium atoms and by the production of elementary excitations of the liquid (rotons and phonons). Upon the electron losing all its energy it will form a cavity within the fluid and becomes trapped. The electron is confined to the bubble as this state is lower energetically then that required to move through the bulk liquid. The energy of the electron bubble can be calculated using the following from Maris (90):

$$E_{bubble} = \frac{h^2}{8mR^2} + 4\pi R^2\alpha + \frac{4}{3}\pi R^3 P, \tag{4.1}$$

where α is the surface tension of helium, m is mass of electron, h is planks constant, and P is the applied pressure. In the absence of any applied pressure the bubble radius R at minimum energy is:

$$R_{min} = \left(\frac{h^2}{32\pi m\alpha}\right)^{1/4}. \tag{4.2}$$

Therefore, the minimum energy is:

$$E_{min} = h\left(\frac{2\pi\alpha}{m}\right)^{1/2}. \tag{4.3}$$

Using surface tension of helium at low temperature of 3.75×10^{-4} N/m gives a radius for the bubble of 18.9 Å and energy 0.21 eV. As this electron energy in the bubble is so low this means that impact ionisation on an electrode surface is suppressed. It also means that the electron bubble also cannot ionise the helium (24.6 eV ionisation energy) to create further sources for breakdown. If the electron was to escape the bubble structure it would also be unable to cause electron impact ionisation due to the relatively small scattering length of the helium, with a mean free path for electrons of 100 nm. This small scattering length for a free electron also limits the electron bubble from accelerating under high electric fields.

In the superfluid state, however, the electron bubble transfers its energy to the fluid by creation of vortex rings or rotons, depending on the pressure. This will slow or even trap the electron bubble in these rings, lowering the kinetic energy of the bubble (90).

Belevtsev (91) has done detailed theoretical calculation of electron multiplication in liquid helium from induced electric fields and found that breakdown caused by electron impact would occur in the MV/cm region, which is well above what has been experimentally reported.

Another breakdown mechanism is the presence of positive ions in the fluid, also called 'snowballs'. This occurs as the helium forms around the ion due to electrostriction effects. As this snowball has quite a large number of helium formed around the ion, its relative mass is very large so its acceleration under an electric field is slowed by the same processes that slow the electron bubble. The presence of snowballs and electron bubbles has been experimentally demonstrated by Li et al. (92).

The reason for the lower observed breakdown fields in LHe is thought to be due to the creation of vapour bubbles within the fluid. The breakdown then corresponds to the dielectric strength of the He vapour instead of the bulk fluid. However, a small vapour bubble still needs to span the gap in order for the breakdown to occur with the electrons then able to travel through the vapour column to the anode.

The inception of the bubbles is thought to occur due to local heating on the surface of an electrode caused by a region of high electric fields. The origin of this high field region can be due to a number of factors that will be discussed further in this Chapter.

Previous work on studying HV breakdown in LHe have mostly been done under SVP. The measurements normally are performed on pumped helium baths between 4.2 K (760 torr) and 1.2 K (< 1 torr). To reduce the temperature to below 4.2 K the LHe bath is pumped on in order to reduce the pressure which will then lower the temperature via evaporative cooling. Karamath collated all the available data on breakdowns in LHe at the time, shown in Figure 4.7.

Karamath's own work studied the breakdown voltage as a function of temperature and found that for quasi-parrallel plate electrodes the reduction in breakdown voltage would decrease by factor ~ 2 from 4.2 K to 1.4 K at SVP. The total pressure in the helium, between the electrodes is determined from:

$$P_{total} = pgh + P_{SVP} \tag{4.4}$$

where pgh is the hydrostatic pressure and P_{SVP} is SVP. Figure 4.8 can be interpreted that the breakdown voltage is temperature dependent, however, it has been noted that the estimated hydrostatic pressure in this experiment is ~ 10 torr, therefore, pressure contributions could also possibly explain the lower field values.

McClintock (94) (95) investigated field emission in liquid helium, however, the apparatus used is not clearly described but it can be inferred that it is a tip-plane geometry

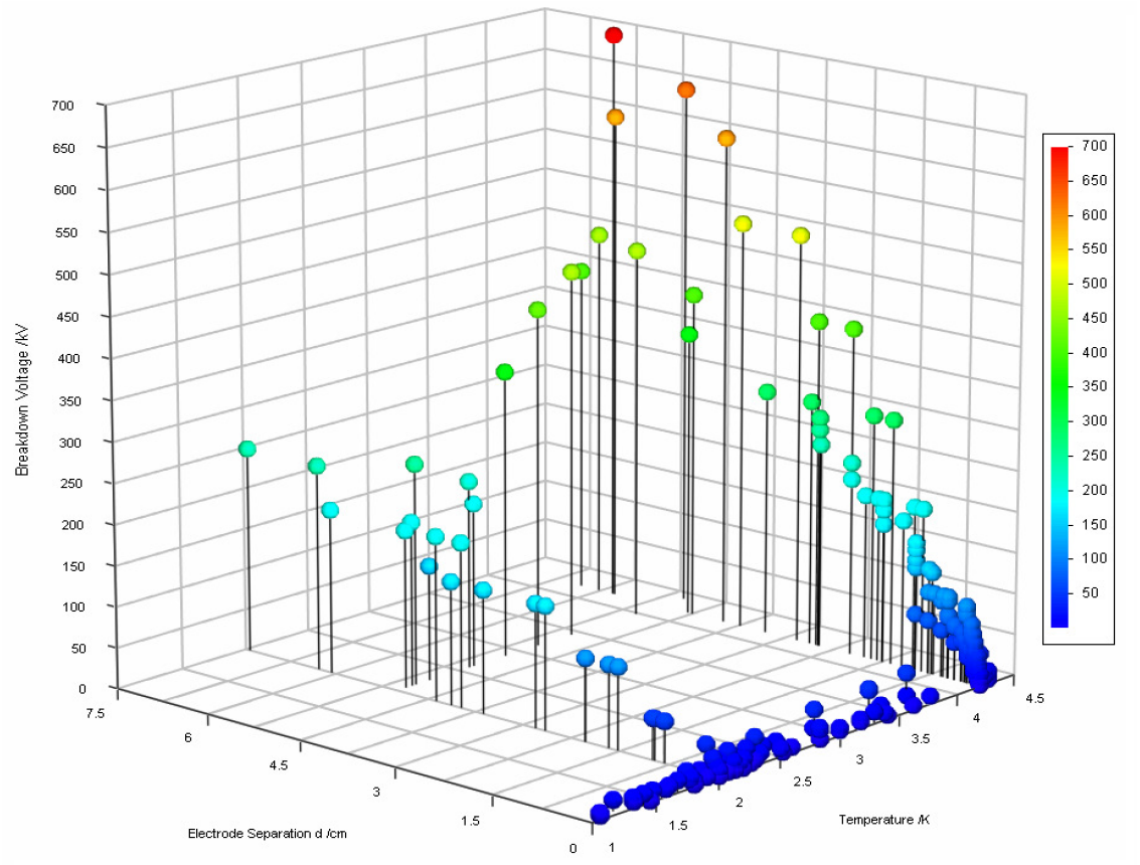

Fig. 4.7 Karamath (93) HV breakdown data for all known previous experiments in LHe as a function of voltage, electrode separation, and temperature.

at a separation of 0.2-1.0 cm. The electrons are injected into the liquid from the tip by varying the current delivered to it. It was assumed that at positive polarity the He atoms are ionised. McClintock describes that at lower temperatures, < 1.7 K, the electron mobility is increased by the presence of more vortex rings in the liquid resulting in a higher current required for a given voltage at these temperatures.

The results given in Figure 4.9, McClintock claims that at 1.7 K the required current is much higher for a given voltage in comparison to temperatures above or below this value (1.2 K and 4.2 K, respectively). The implication of these results is unclear, however, it implies that discharges occur more at 1.7 K, hence a temperature dependence on the breakdown in liquid helium. The transition of the helium from normal to superfluid state, shown in Figure 4.6 shows the crossing point is close to 1.7 K for which McClintocks measurements show is where the highest field emission is present. It is difficult to infer why this would happen, but is potentially due the lower pressure of the liquid creating a bubble enabling the electrons to cross the gap.

There is also evidence for a polarity dependency, showing that the primary mecha-

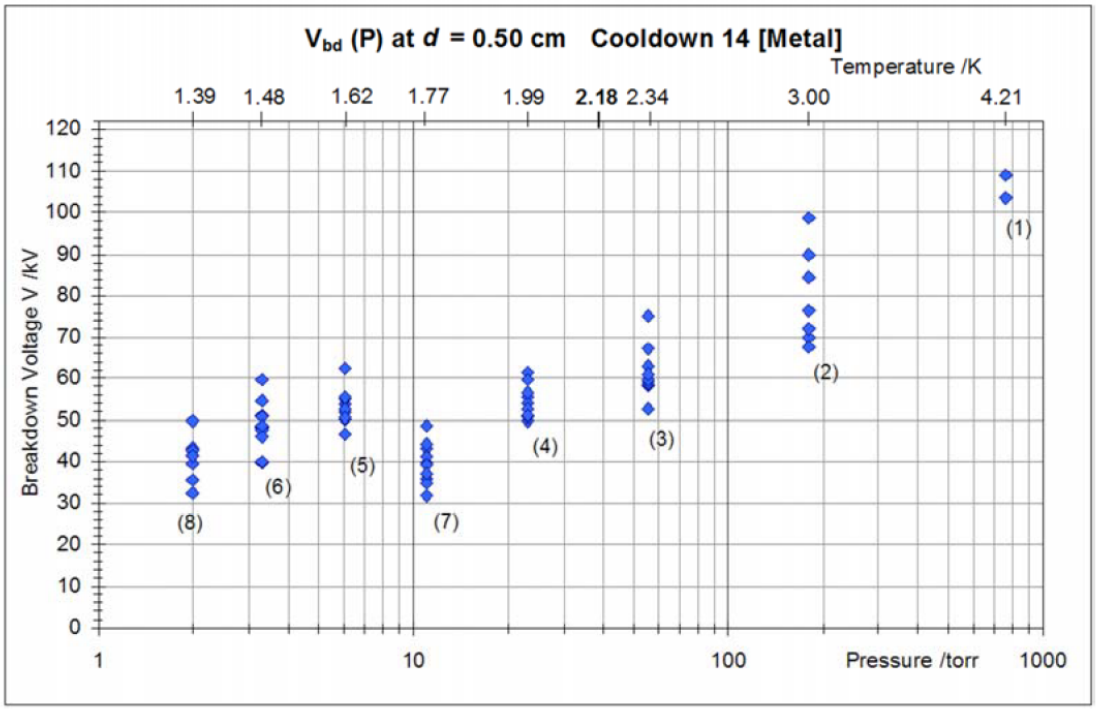

Fig. 4.8 Karamath (93) HV breakdown data as function of temperature and pressure with quasi-parallel plate electrodes at 5 mm separation in LHe.

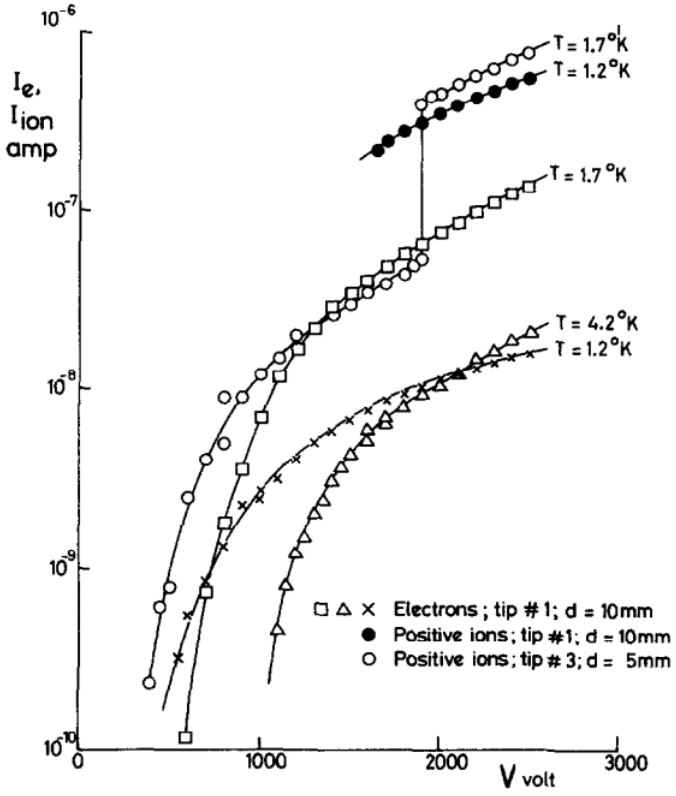

Fig. 4.9 Emission current into LHe of electrons I_e and positive ions, I_{ion}, as a function of tip potential V at various temperatures and electrode separations.

nism for breakdown occurs at the cathode between the injection of electrons or positive ions, with the ions requiring higher currents and voltages. An explanation for this behaviour could be the formation of a corona discharge at the tip. McClintock states that this is likely due to the amount of heat on the tip of the electrode ~ 1 W/cm^2 which would lead to vapour formation. McClintock observed these bubbles and noticed that the size of the bubble varies with the applied current and the discharge at lower currents would lead to a helium-gas like discharge. It is also stated that not all the bubbles were spherical but some were elongated. McClintock states that the field emission of electrons into LHe will form a corona discharge which can create a stable bubble. If corona discharge is the breakdown mechanism then it still does not explain why at 1.7 K it requires the highest current injected into the volume. It could be due to the transition to superfluid which may make a bubble occur easier as the whole volume wold not be superfluid, so the heat will not be completely absorbed into the bulk superfluid volume.

Blank et al. (96) investigated breakdowns in liquid helium at 4.2 K and 1.2 K at SVP in order to determine pre-breakdown current. The setup used was $\frac{3}{8}$ inch diameter steel electrodes at separations between 0.15 to 1 mm with a geometry of point-plane, sphere-sphere, or plane-plane.

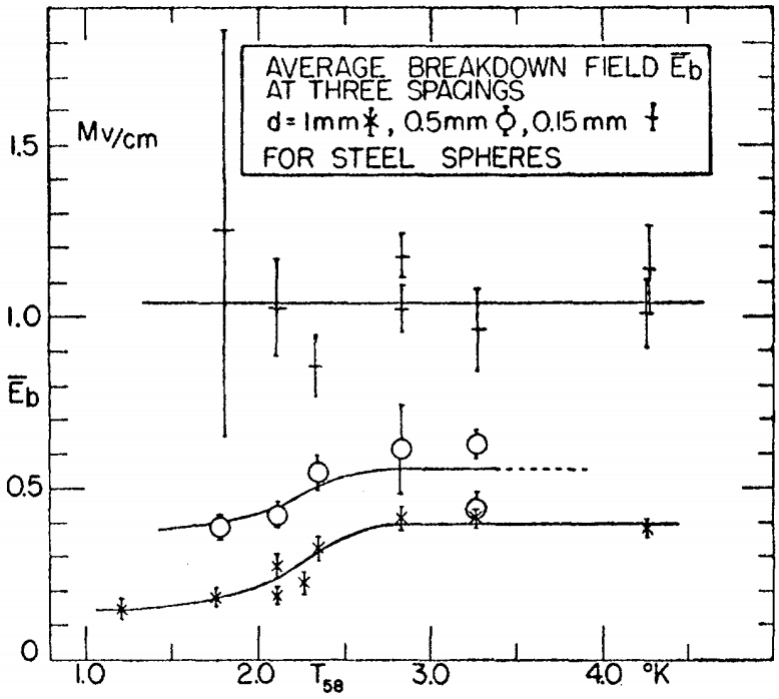

Fig. 4.10 Average dielectric field strength, $\bar{E}_b$, using negative polarity in liquid helium for three different separations as a function of temperature (96).

In Figure 4.10, at the smallest separation the electric field is constant over a range of temperatures. However, at the larger separations the electric field drops off below ~ 2.5

K. The drop off is by about factor of 2-3. There is also a drop off as the separation is increased from 0.5 mm to 1 mm. The current was also monitored for this experiment, only one pre breakdown current was observed. This pre-breakdown current was a constant current observed of the order 10^{-13} A, 10 seconds before the breakdown occurred. This implied a resistivity of the liquid of 10^{16} Ωm. It could be that the reason this was only observed once is due to some impurity in the liquid or a bubble crossing the gap and allowing current to flow. Inspection of the electrodes after the measurements showed significant cratering, bumps, and pits on the surface due to the breakdown, as seen in Figure 4.12.

Breakdowns were also performed with point-plane and plane-plane geometry. The point-plane geometry shows a discrepancy between the two polarities with the breakdown values half that for negative than positive. It implies that the breakdown occurs at the cathode which is in agreement with what McClintock saw. The plane-plane electrodes were noted to have sharp edges to them which would act like tips, which may lower the breakdown voltage to something more like a point-plane geometry.

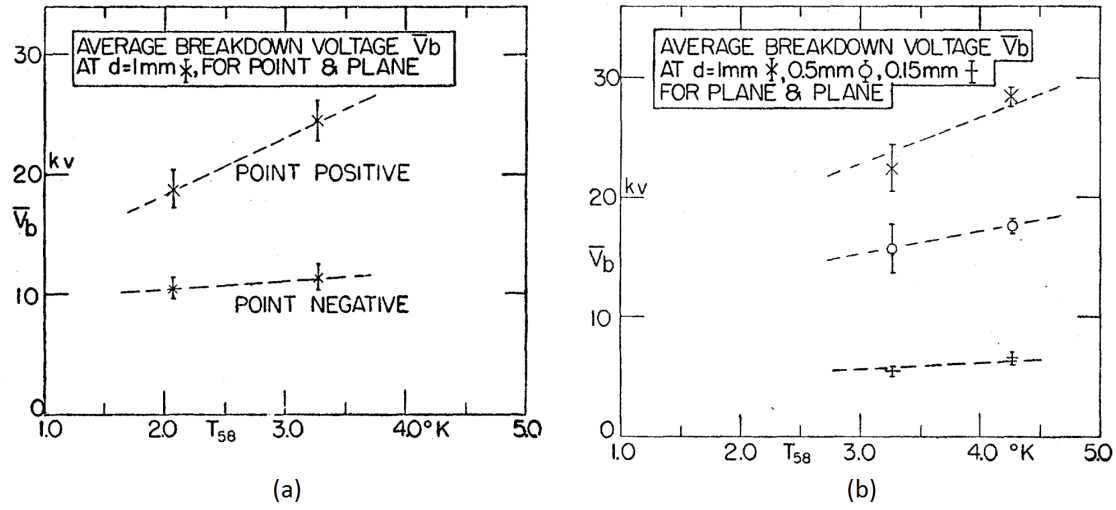

Fig. 4.11 Average breakdown voltage, $\bar{V_b}$ in liquid helium for: (a) steel point-plane electrodes , and (b) steel plane-plane geometry a function of temperature (96).

For all the measurements taken the breakdown voltage is reduced as the temperature is decreased. Blank states that the breakdown occurs by injection of the electrons into the liquid which would then form electron bubbles. This would then drift across the gap leaving behind a density hump formerly associated with it, then moving with reduced mass but increased velocity. This electron could then further ionise the He leading to electron multiplication causing the breakdown. It should be stated that these measurements were performed in the MV/cm region which as Belevtsev states should result in breakdown via field emission rather than bubble creation. However, it is difficult to

believe that field emission is the primary effect for breakdown as other experiments demonstrate lower breakdown voltages which is then associated with bubble formation.

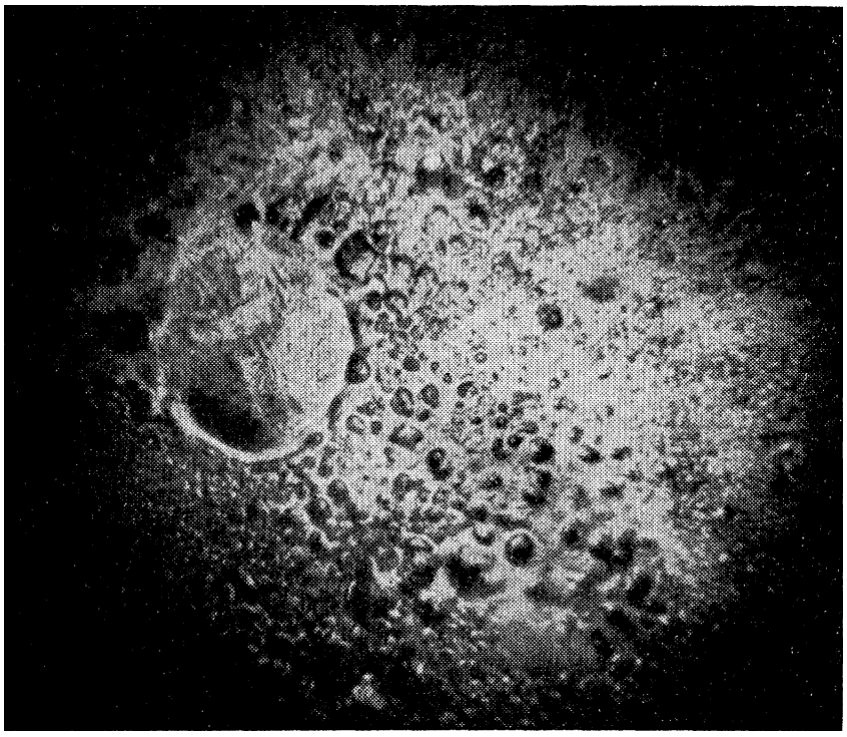

Fig. 4.12 Photomicrograph of a 0.1 mm diameter region on Blank's cathode surface, showing detail near one large crater. It is implied that this was observed on the sphere-sphere geometry measurement (96).

Schmidt (97) reviews the theory of breakdown mechanisms in liquid helium and liquid neon. The author investigates other experiments performed in LHe using point-plane geometry and determines that the breakdown is always initiated at the cathode due to the polarity difference. Schmidt also comes to the conclusion that the positive tip breakdown will develop a corona discharge, which will shorten the effective gap between the electrodes, causing an enhancement of the local field to facilitate electron emission. However, Schmidt does state that this would require fields of MV/cm in order to breakdown across a gap, which is in agreement with Belevtsev (91).

4.2.3 Electrode roughness

As previously stated for breakdowns within a vacuum system, a major cause can be due to the condition of the electrode surface. It is well know that for vacuum systems the best treatment to maximise the electric field is to electro-polish the surface. This process minimises burrs, sharp microscopic metal strips that protrude from the surface. These burrs occur in the machining process, with subsequent mechanical polishing just pushing them back down into the surface which does not necessarily remove them.

These techniques are common for vacuum high voltage systems but in a cryogenic fluid is this still true?

May and Krauth (98) did measurements of different surface finishes in liquid helium to see if roughness as well as micro cracks and oxide layers will decrease the breakdown voltage. They used spherical electrodes of 50 mm in diameter and made of niobium, brass, and different types of steel. The brass and stainless steel electrode were mechanically polished with Al_2O_3 the grains were 300 nm in diameter. The niobium was electro-polished.

The experiments ran with 10 to 20 breakdowns for each electrode type, recorded at constant electrode separation with the mean of the breakdowns taken for the plots.

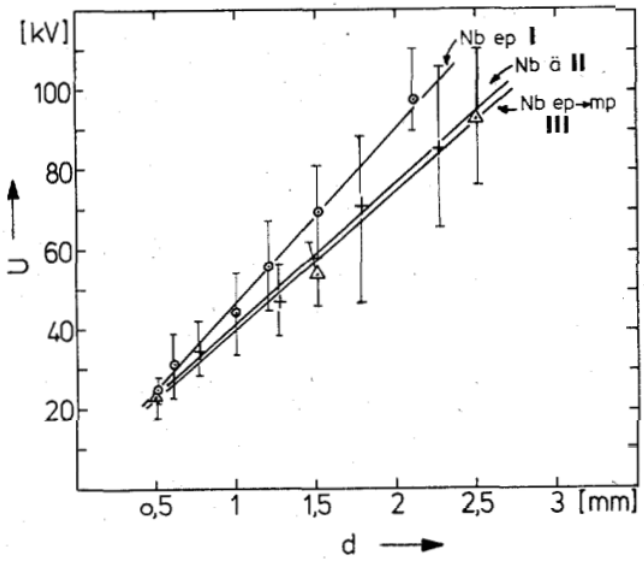

Fig. 4.13 AC breakdown voltages, U, versus gap distance, d, with niobium electrodes. Nb ep I was electro-polished (roughness of ~ 10 nm), Nb a II was etched, Nb ep → mp III was electro-polished then mechanical polished (98).

The stainless steel, in Figure 4.14, resulted in lower breakdown voltages compared to the niobium, and that is attributed to imperfections on the surface and imply that a different type with smoother finish would result in a higher breakdown voltage. However, interestingly the ball bearing produces a much higher value, one that is comparable to the niobium. The ball bearing is not very smooth so they attribute this increase to an oxide layer of a few microns on its surface.

In Figure 4.15 the slowly cooled brass electrodes, upper curve, were done with gas cooling before liquid was introduced. This seems to give similar results to steel and niobium from Figure 4.13 and 4.14. The rapidly cooled brass electrodes, the lower curve,

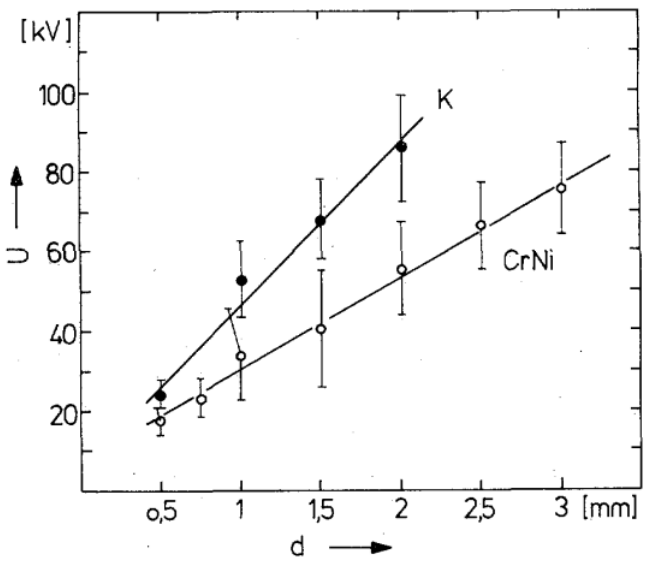

Fig. 4.14 AC breakdown voltages, U, versus gap distance, d, with steel electrodes. The labels are for the types of steel; K was ball bearing, CrNi is stainless steel (98).

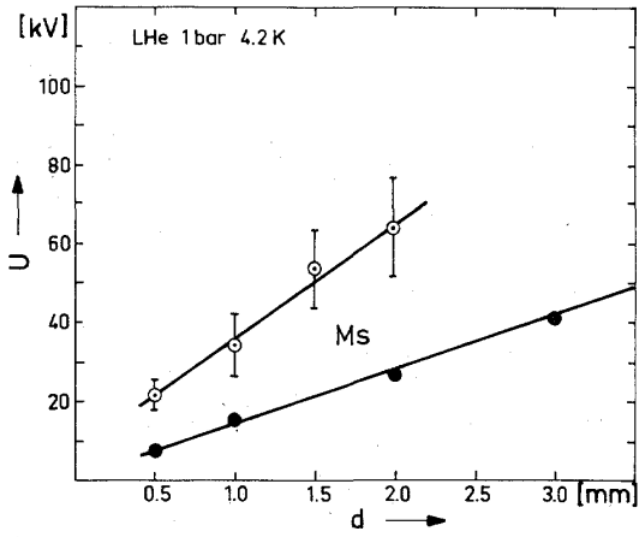

Fig. 4.15 AC breakdown voltages, U, versus gap distance, d, with brass electrodes. The upper curve is with slowly cooled brass electrodes, the lower curve is with rapidly cooled electrodes (98).

shows a significant drop off. The thought it that this caused micro cracks in the surface which leaves sharp edges. The origin of these micro cracks are thought to be due to thermal gradients during the rapid cooling or from the machining process. These micro cracks where not observed on the steel or niobium samples.

May and Krauth also found that the breakdown voltage can vary from the peak breakdown value by as much as 40%, this is attributed to a random distribution in breakdown events.

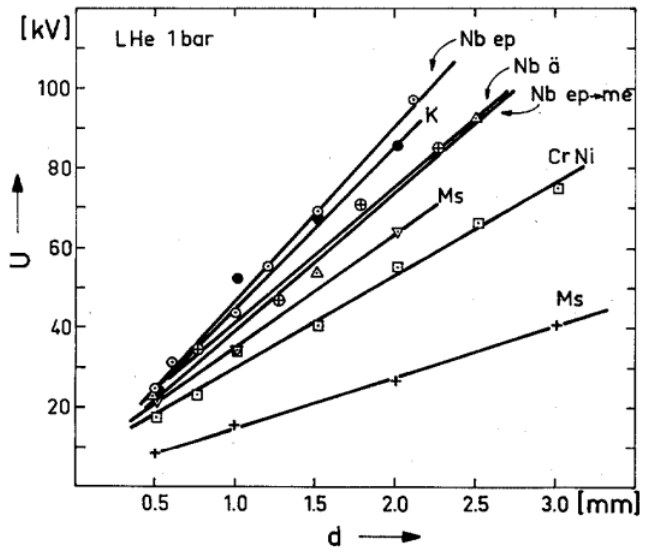

Fig. 4.16 AC breakdown voltages, U, versus gap distance, d, for all data by May and Krauth, 'Ms' is brass electrodes with the lower one being the rapidly cooled one (98).

They also found that there is a dependence on the time interval between breakdown measurements. If within a relatively short time period between breakdowns the values would be lower, while using a time interval of 4-5 minutes would more consistently reach peak breakdown value. From visual observation they determined that this was due to gaseous bubbles in the liquid helium dissipating within 10 seconds of the breakdown. However, leaving the system for the extra time would guarantee all the heat on the surface as dissipated.

Interestingly, they also found that if the applied voltage that would have resulted in a breakdown was kept constant over ling periods of time it would eventually breakdown. They associated this with thermal effects within the liquid.

Gerhold (99) also investigated the effect of electrode roughness on high voltage breakdown in LHe I at 4.2 K SVP. Gerhold used a model, anti-bubble (AB) barrier, to explain the cause of the breakdown in LHe. The initiation of the breakdown starts with the rough cathode surface.

The AB model states that asperities on the surface of the cathode create a high local electric field which results in the emission of electrons into the LHe volume. This results in a vacuous cavity at the asperity for which the electrons on the cathode can flow into. The model then states that the cavity will collapse due to any instability. The energy stored in the cavity as it collapses is then transferred to forming vapour bubbles which can elongate. These bubbles can collapse if the latent heat of the liquid exceeds

the electrical energy of the moving charge carriers. The thought is that these bubbles will bridge the gap and then result in a flow of charge from the cathode to the anode.

The AB model is for a single asperity, however, a real surface will have asperities of arbitrary shapes and sizes and this can increase substantially when the surface area is increased. There can also be a greater chance of breakdown if any particles in the bulk liquid attached to the cathode, also resulting in vapour bubbles being created.

Gerhold's model could explain the results that May and Krauth found. The rougher surfaces they measured resulted in low breakdown voltages that could be attributed to one of the factors for causing the discharge. The measurements with brass, by May and Krauth, had micro cracks that would give sharp edges, potentially seeding the creation of these bubbles when high voltage is applied. They also observed the damage caused by the breakdown in the form of craters which for the brass were sharp but for the stainless steel was smooth. However, this does not explain why the ball bearing had higher breakdown voltages than machined stainless steel, despite the rougher surface of the ball bearing. The presence of an oxide layer may prevent the formation of these bubbles, creating some potential barrier which stops electrons traveling into the vapour bubbles.

Yoshino et al. (100) performed breakdown measurements in LHe at 4.2 K using a pulsed voltage source and needle-plane geometry (tip radius ~ 3 μm). In one experiment he looked at the condition of the surface of the electrode and the affect it would have on HV breakdown.

Figure 4.17 shows that there is a relation between the breakdown voltage and the condition of the electrode: the rougher surface will result in lower breakdown values for the positive needle as the electrons travel from the plane cathode. The case with the negative needle shows negligible difference between the smooth and rough surfaces.

Yoshino states that this process cannot be the result of simple gas bubble creation by heating effects as the same results are observed in the superfluid state. The argument he uses is that because superfluid thermal conductivity becomes extremely large, the generation of bubbles only occurs on the surface of the fluid. This is true but it applies only to the bulk liquid, with a local spot of heating it can result in the generation of a gas bubble; this is evident in the work on pressurising the liquid volume which will be discussed in section 4.3.1. The processes that limit free electron and positive ion travel through the LHe volume still applies at lower temperatures. Therefore, bubble

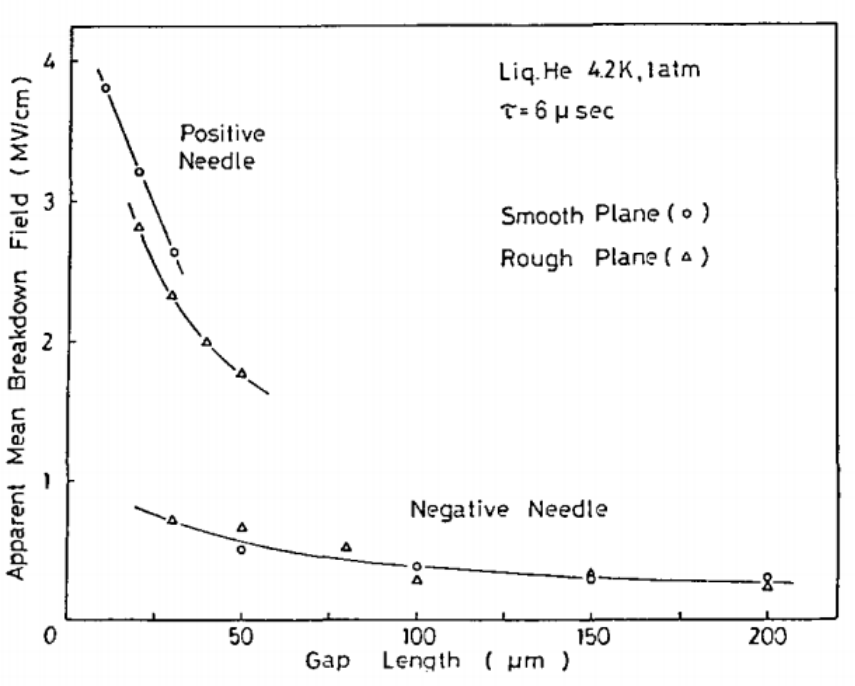

Fig. 4.17 Apparent mean breakdown voltage against gap length in LHe at 4.2 K for smooth and rough surfaces with needle-plane geometry (100).

formation on the source for breakdown can be the only possible cause of breakdown in superfluid.

4.2.4 Electrode material

As previously mentioned, the material used for electrodes can result in very different effects on the surface after an initial breakdown event. The damage left behind after this initial event can then effect the voltage of subsequent events. This discharge is a highly energetic event, which results in a local heating spot on the surface of the electrode, vapourising the metal and creating a crater. The shape and condition of the crater can influence the breakdown voltage.

Olivier (101) investigated the performance of electrode material on the initial breakdown in LHe as well as the conditioning effect of repeated sparking of the electrodes.

These measurements were performed in a cryostat with a 350 mm inner diameter. It was able to simultaneously cool 17 spark gaps with sphere electrodes made of brass or steel, of 20 mm diameter with separation of 0.5 mm. These sphere pairs would revolve cylindrically in order to place each pair to an optical window for the measurement. The separation of the electrodes are measured optically before and after, with resolution of 5 μm. The electrodes were mechanically polished. Special care went into ensuring the system and electrodes were thoroughly clean. The system was then pre-cooled,

after which liquid helium was admitted till thermal equilibrium was reached and then breakdowns were performed.

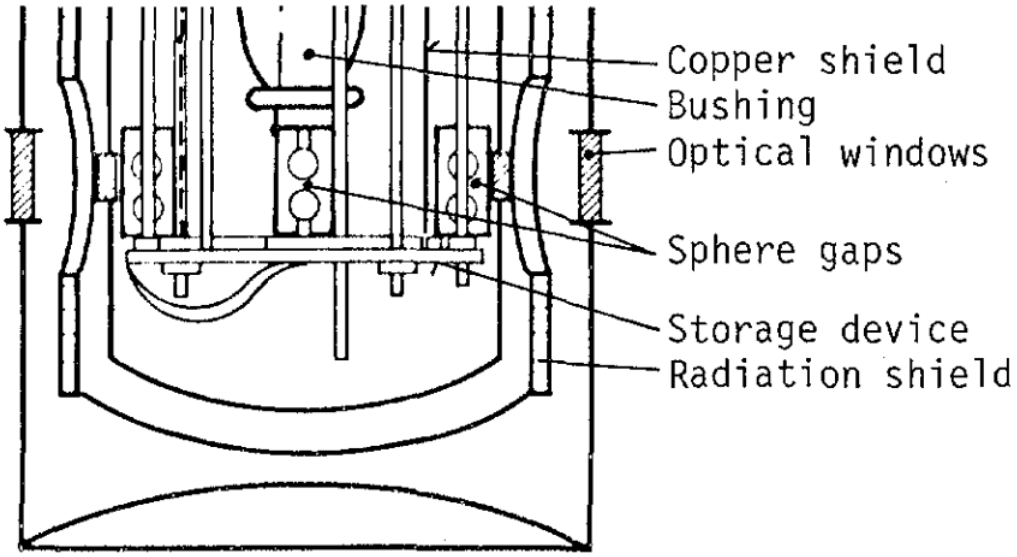

Fig. 4.18 Lower end of cryostat and insert comprising of 17 sphere pairs separated by 0.5 mm separation (101).

The results Olivier found are shown in Figure 4.19, 4.20, and 4.21. There is two different kinds of behaviour: spark gaps reach highest voltage at first application in brass, and reached highest voltage after conditioning phase with steel. In the case of steel it reached this highest value after 5 breakdowns, after conditioning. According to Olivier, the reason for lower breakdown voltages for the brass is the presence of sharper edges around the craters on the surface of the electrodes, observable afterwards with a microscope.

Interestingly they also performed measurements with mixed material setup (shown in Figure 4.21), where the brass was the upper sphere and the steel one the bottom, this was also done in reverse too. In both cases there was strong polarity dependence. The majority of breakdowns they observed occurred with the brass electrode as the cathode, resulting in similar data set to that of both electrodes being brass.

They conclude that the initial breakdown, material dependent, will result in damage to the electrode that will in turn influence the following breakdown measurements, and that this behaviour is not solely due to the liquid helium properties but the condition of the electrode surface. They also note that the cathode is the key to initiation of the breakdown event. They argue that the difference between the electrode materials condition after the conditioning phase results in crater structures, which for the brass

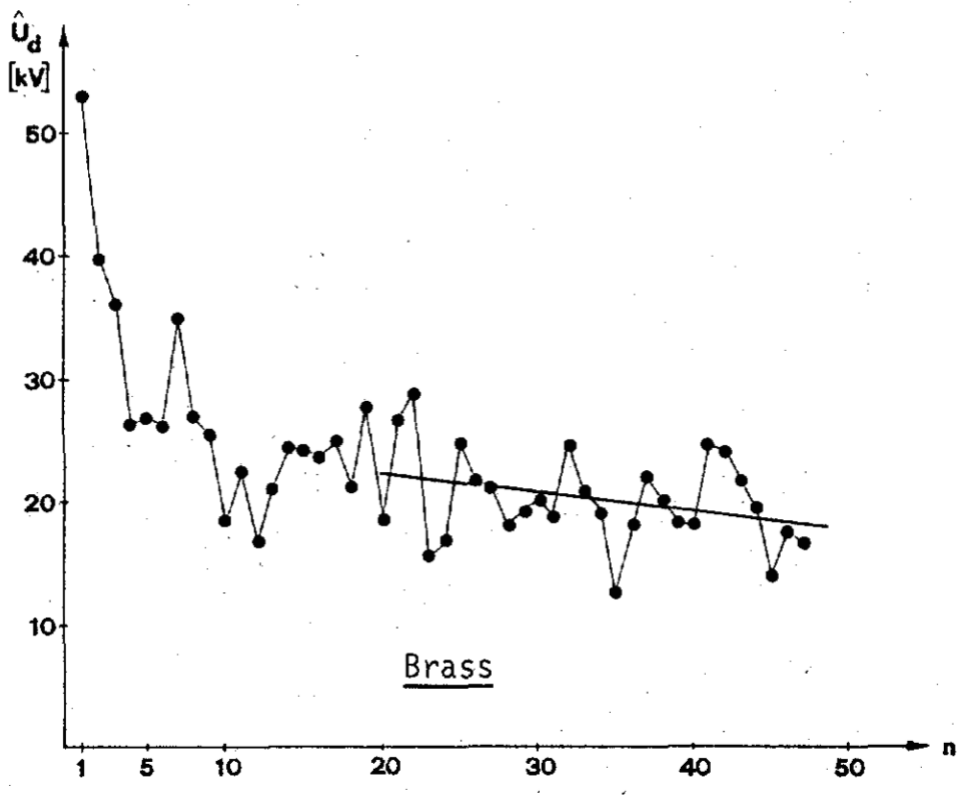

Fig. 4.19 Breakdown voltage, $\hat{U}_d$, versus number of events for brass electrodes in LHe (101).

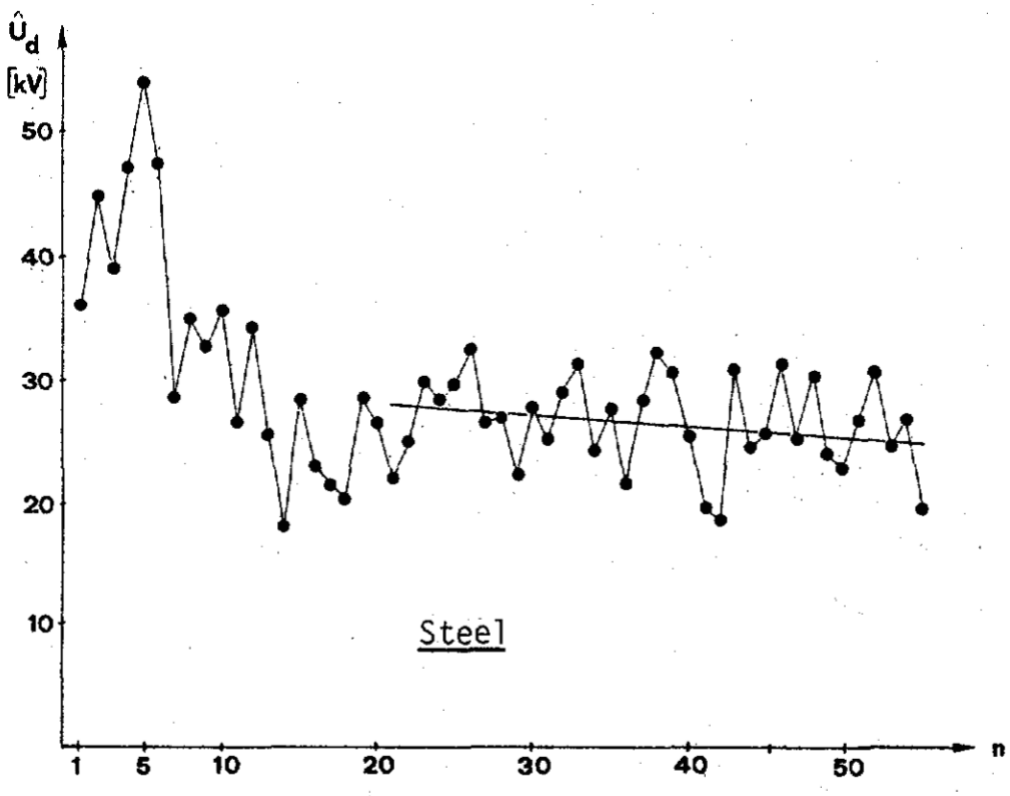

Fig. 4.20 Breakdown voltage, $\hat{U}_d$, versus number of events for steel electrodes in LHe (101).

are much sharper due to faster solidification of the molten brass because of higher heat conductivity, and hence the reason for the lower breakdown voltages.

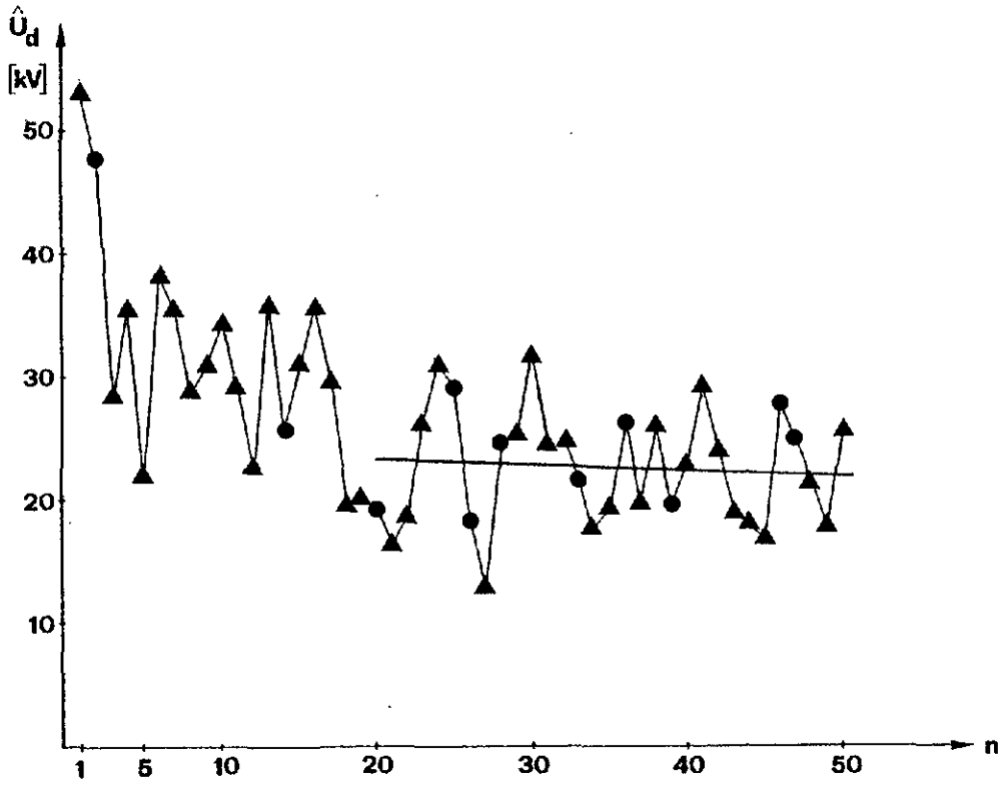

Fig. 4.21 Breakdown voltage, $\hat{U}_d$, versus number of events for brass cathode (triangles) and brass anode (dot), other electrode made of steel (upper brass, lower steel) (101).

These results are comparable to May and Krauth, showing that brass electrodes result in lower breakdown voltages then steel.

K. Yoshino et al. (100) performed breakdown measurements in LHe at 4.2 K using a pulsed voltage source and needle-plane geometry (tip radius ~ 3 μm). They used a number of different materials as the plane electrode: copper, iron, silver, and aluminium. The needle material was steel.

In Figure 4.22 that data is shown for LHe at 4.2 K, however, they comment that the same was observed for LHe for a wide range of electrode separations and temperatures (4.2 K – 1.8 K). The results show a dependence on the electrode material with positive polarity. In the case of the positive needle the electrons will be flowing from the plane electrode, therefore the structure and initial condition of the surface is critical. Copper seems to drop off fast, probably due to the initial breakdown severely damaging the surface. Iron and silver have comparable breakdown voltages. They are soft metals so the breakdowns probably will create a crater with smoother edges compared to copper. Aluminium

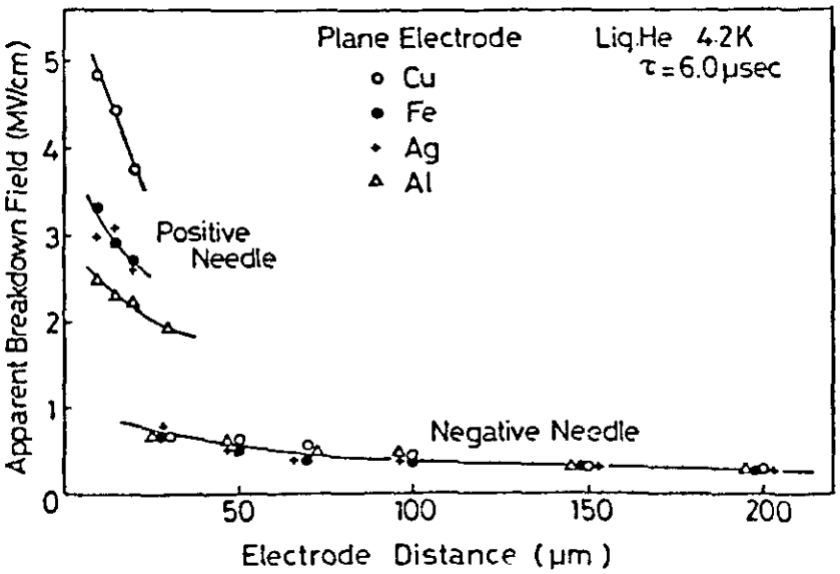

Fig. 4.22 Apparent breakdown field versus electrode separation with needle-plane geomtry for different plane electrode materials (100).

starts saturating which would imply the first few breakdowns are conditioning of the surface.

The paper also notes that the reason for different breakdown voltages for various materials is due to their work functions, hence why copper gives the highest value initially.

This supports the results Olivier found in LHe: the surface/condition of the cathode is highly correlated with breakdown voltage.

4.2.5 Liquid purity

K. Yoshino et al. (100) studied HV breakdowns in various cryogenic liquids: Ar, Kr, N_2, Ne, and He. Yoshino et al. claims that all have their own unique breakdown behaviours. For their setup they use a pulsed voltage source. All liquids are either commercial grade or purified. The geometry used is a plane-needle non-uniform (tip radius ~ 3 μm) and plane-sphere, nearly uniform electrode system made of stainless steel.

Yoshino et al. suggests that impurities in the liquids play three different roles:

- electro-negative impurities like O_2 capture electrons, supressing high energy electrons,
- impurity molecules with internal degrees of freedom may scatter electrons with inelastic collisions and act to reduce the electron energy,

- impurities of low ionisation potential play an important role to supply the free electrons by the collision of high energy electron with this impurity.

Interestingly, Yoshino found that doping of liquid nitrogen with oxygen would cause the breakdown voltage to increase. However, for the liquid helium case this would dramatically reduce the breakdown voltage. The explanation for this is probably due to the different mechanisms in which either fluid breaks down. The purification of helium compared to commercial grade results in a higher breakdown value as seen in Figure 4.23.

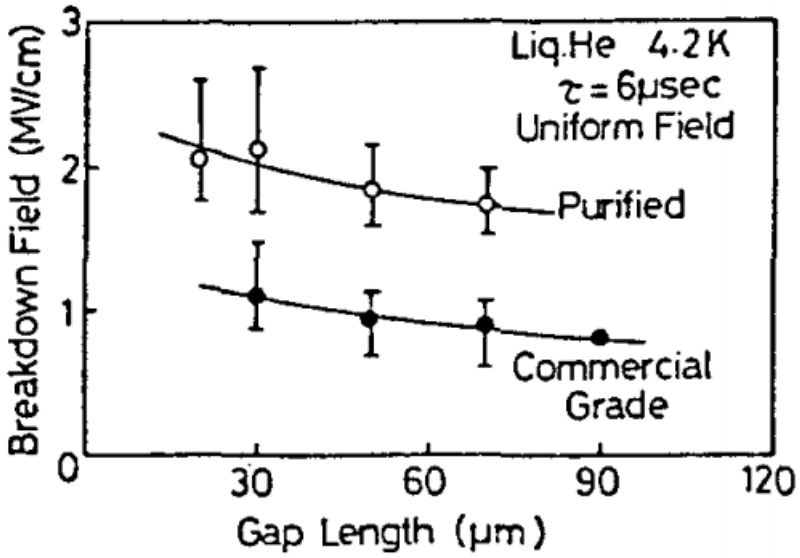

Fig. 4.23 Breakdown strength for LHe at 4.2 K with commercial grade and purified fluid (100).

Study of breakdown as a function of liquid impurity in LHe was performed by Wu (102). The setup consisted of a parallel plate geometry with 1 mm gap and particles of sizes 50 μm to 200 μm were introduced into the liquid helium. The particles were non-metallic fiberglass (G10) and showed no effect on the breakdown field. However, when adding in conductive particles of aluminium particles or solder, similar sizes to the G10, it reduced the breakdown fields by a factor of 2. The experiments were carried out at 4.2 K and 2.15 K under 1 bar pressure, and there was no evidence for any temperature dependence.

The increase of breakdown voltage with more purified liquid helium occurs due to the removal of impurities. The presence of conductive matter within the volume will help to trigger breakdown through the liquid. This occurs as the particle is accelerated in high fields which will then result in impact with the electrode surface creating further electron emission. If the particle remains on the surface, it could trigger bubble formation as it will look like sharp asperities on the surface of the electrode from the

perspective of the electric fields.

This idea as to why impurities cause lower breakdown values is different to what Yoshino suggests as the mechanisms. Even though his theory as to the mechanisms are different to that of Wu, Yoshino's data still shows evidence that agree ideas Wu presents.

Hara et al. (103) investigated the breakdown behaviour in LHe over a range of temperatures and pressures with the presence of metallic particles in the volume. The setup involved two electrodes with a separation of 6.5 mm with a glass spacer of ϕ 28 mm in order to see the metallic particles placed between the electrodes through an observation port in the cryostat.

In order to test the effect of metallic particles in the volume, various shapes were used, stationary needle with flat-cut tip (SNF), a stationary needle with a hemi-sphere tip (SNS), a free sphere (FS), and free needle with flat-cut tip (FN). The dimensions of each particle is length (l), diameter (D), and tip radius (r_p). Various materials were used which includes steel, copper, and aluminium. The dependence on material only applied to whether it was lifted under the influence of an electric field.

Previous work by Hara et al. (104), found with FS particles that:

- Small particles will cross the gap by electrostatic forces prior to breakdown.
- Microdischarges and bubbles are generated on all occasions of particle collision with the electrode.
- Generated bubbles grows up to a critical size and then collapse.
- Bubble behaviour depends strongly on state of LHe: in LHe I bubbles will remain for a long time and rise to form gaseous layer on the upper electrode, but in LHe II it disappears completely upon liquefaction of bubble gas in a short time.

In these investigations it was found that the energy released by moving FS particles in the fluid would collide with the electrode surface, dissipating much of the energy in form of micro-discharging and frictional heat. This collision would then generate bubbles.

In the case of FN particles, shown in Figure 4.24, the electric field lifts the particle from a lying position to vertical, which then travels towards the upper electrode. The impact of the particle with the electrode would cause light emissions and current pulses which were associated with micro-discharges and bubble behaviour.

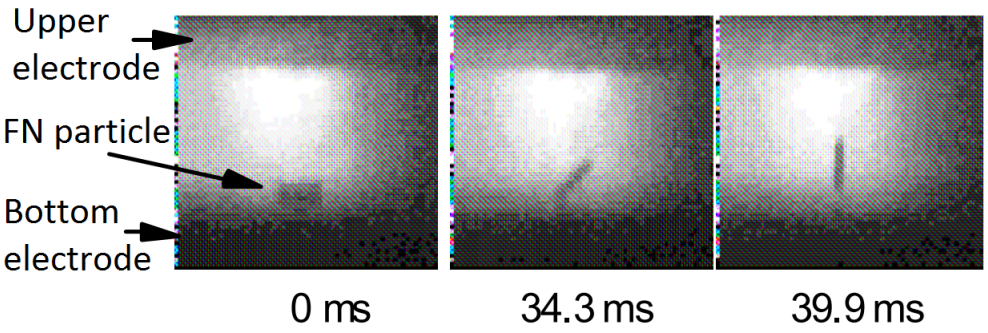

Fig. 4.24 Motion behaviour of FN particle in volume after initial HV application for given time (V_{app} = 4.5 kV, p = 101.3 kPa, l = 2 mm, D = 0.5 mm) (103).

The micro-discharge behaviour is associated with the initial collision with the electrode and if any double impact collisions occurred, the second would not give additional micro-discharging. However, every collision with the surface by the PN particle would generate bubbles.

Experiments with the SNF and SNS particles observed different behaviour. It was noted that higher voltages were possible but prior to breakdown fine bubble generation from unknown sources occurred. It was observed that corona discharges would accompany the fine bubbles. The bubbles would rise and then remain on the upper electrode.

Hara lists the expected factors for each particle as follows:

- SNF: no bubble generated by the particle collision and there is high stress fields at the particle tip.
- SNS: no bubble generated by particle collision and smooth change in field at particle tip with tip radius.
- FS: micro-discharge occurred, followed by bubbles due to the particle collision with electrode surface. No high stress fields present on the particle.
- FN: micro-discharge occurred, followed by bubbles due to the particle collision. High stress fields are present on the particle tips.

Hara shows that a key trigger of breakdown in LHe is from the generation of bubbles due to the collision of particles with the electrode surface.

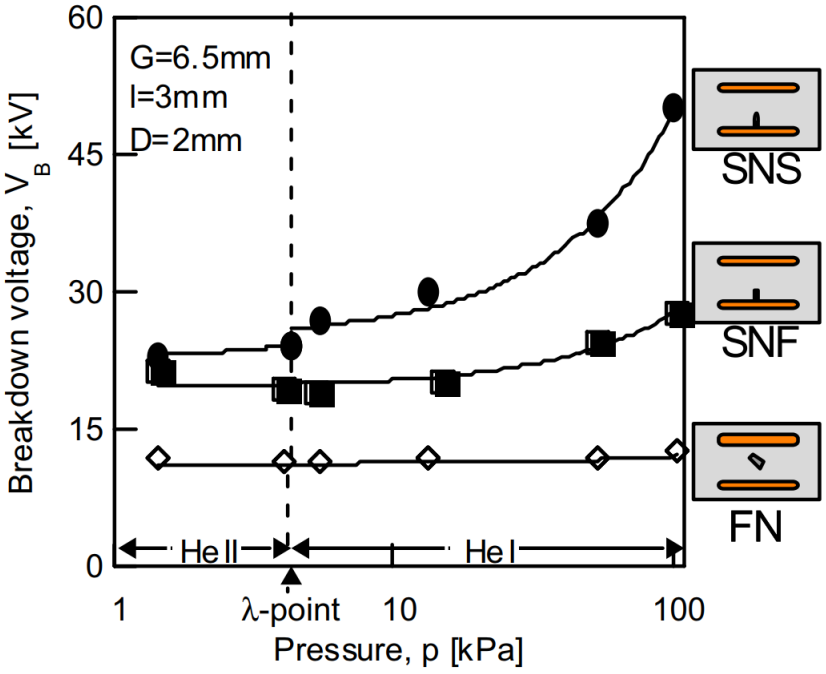

Fig. 4.25 Breakdown voltage, V_b, as a function of pressure, p, with different particle conditions. Particle used is a copper needle particle of various shapes (103).

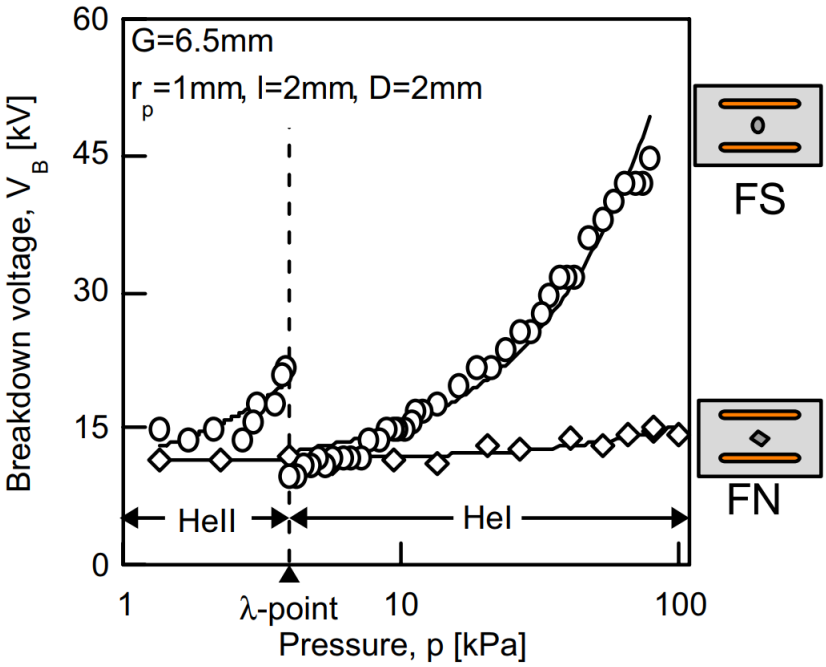

Fig. 4.26 Breakdown voltage, V_b, as a function of pressure, p, with different particle conditions. Particles used were steel FS or copper FN particle. The lower breakdown voltages before the kink after the lambda transition is most likely due to the rapid bubbling of the LHe I as it approaches that point (103).

The purity of the fluid, therefore, is critical to ensuring the maximum voltage can be applied to the system. In Figure 4.25 and 4.26 it is also shown that as the pressure is dropped the breakdown voltage decreases, which could be associated with either the larger diameter of the bubbles that are able to form or the kinetic energy that is transferred to the surface of the electrode from the particle generating more bubbles due to the lower latent heat of vaporisation of LHe II.

4.2.6 Breakdown repetition rate, polarity, geometry

Coletti et al. (105) looked at the effect of breakdown repetition rate in liquid helium. The breakdown measurements were performed in a 3 litre LHe bath in which two stainless steel Rogowski (106) electrodes, 36 mm in diameter, are placed. The finish on the electrodes is not commented on. The liquid helium was commercial grade and meticulous care was made to ensure as little contamination as possible. The first run of tests were done with separation of 0.4 mm and time interval of 1 to 8 minutes. Coletti et al. found that the smallest time internal that did not affect the breakdown value was 4 minutes, seen in Figure 4.27.

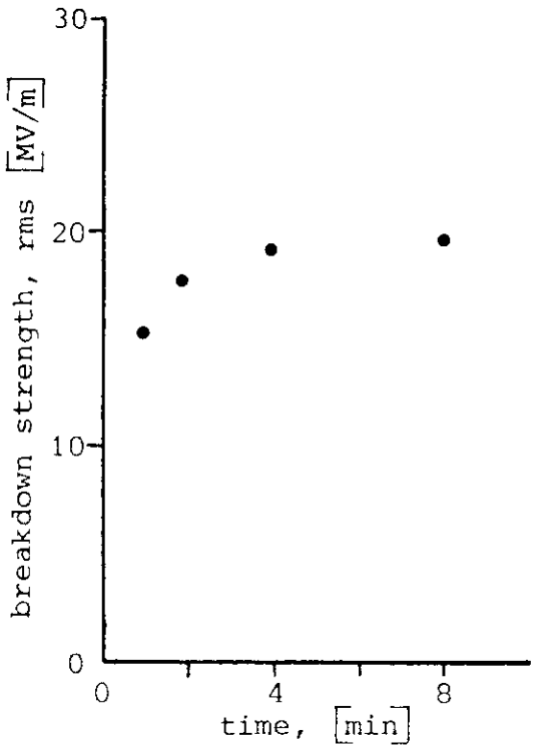

Fig. 4.27 Mean values of breakdown strength of groups of 70 tests against time interval between tests with Rogowski electrodes at 0.4 mm separation (105).

The likely reason for having to wait some time interval between breakdowns is the liquid is probably disturbed from the energy input from the breakdown. Energy released

during the breakdown possibly heats a spot on the electrode surface so after the breakdown occurs it will have to be cooled again. The breakdown event also causes some vaporisation of the liquid, therefore, the gas in the volume will need to be released or condensed otherwise a bubble with a lower dielectric strength will be present.

Coletti also looked at the spark conditioning of electrodes in liquid helium (Figure 4.28) and compared them to the mean breakdown voltage to see if the conditioning effect is present. This shows the first breakdown voltage value and compares it to the mean, maximum, minimum of the following tests at that separation. Coletti shows that the first breakdown can be above or below the mean voltage.

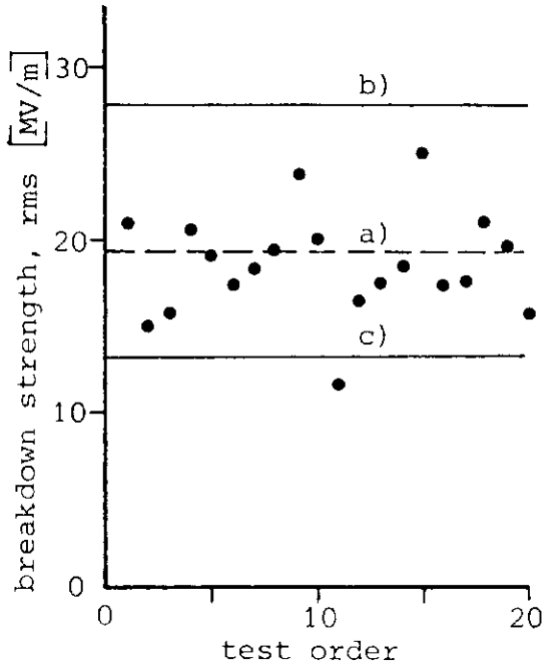

Fig. 4.28 Spark conditioning (initial breakdowns) in liquid helium with Rogowski electrodes at 0.4 mm separation. Time interval was 4 minutes. The horizontal lines are the mean breakdown (a), maximum breakdown (b), minimum breakdown (c) values following 80 tests (105).

S. Kim et al. (107) made measurements in liquid helium to look at the conditioning effect for HV breakdown. Kim used a sphere-plane configuration and a 3 μm needle-plane configuration. The voltage supply was pulsed source and breakdown was confirmed visually.

The results show that the positive polarity with non-uniform field has a steadily decreasing breakdown value. The negative needle increases steadily after continuous breakdowns.

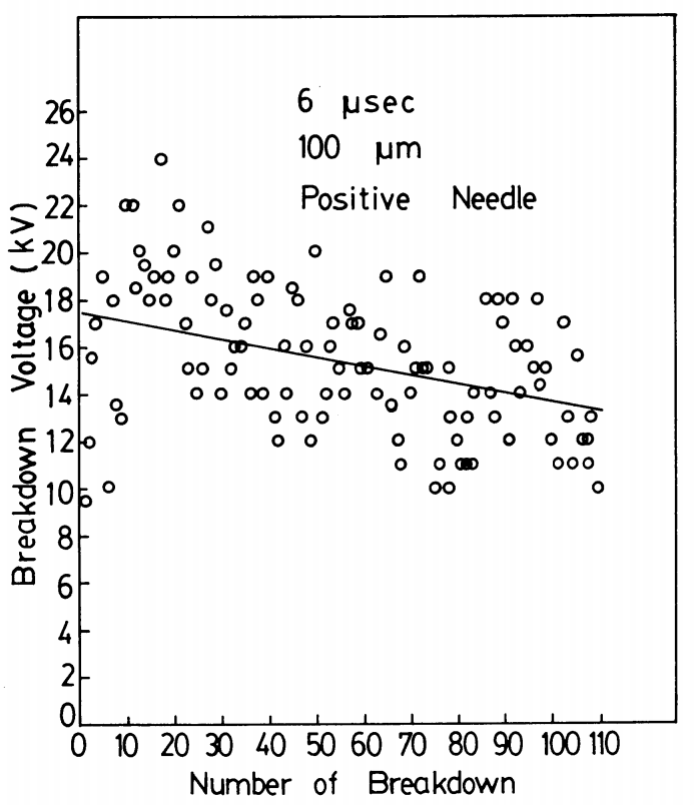

Fig. 4.29 Conditioning effect of breakdowns in liquid helium under positive needle-plane geometry (107).

For the case with a uniform field, negative polarity was first applied and then positive was applied after 90 breakdowns. Both the negative and positive show an initial increase in breakdown values then it drops off, but saturates at that the latter breakdowns. In the positive needle run and the negative sphere run there are approximately 10 initial breakdowns which are at lower values to the average. This is attributed to the conditioning of the system which can also occur in vacuum breakdowns. The source of this is normally considered to be impurities or contamination on surfaces of the electrodes.

S. Kim et al. explains the process they believe is the cause of the breakdown: electron emission from the cathode. This is evident as in the positive needle condition they state that it will start at the plane cathode which will damage it from He+ bombardment increasing the roughness and thus decreasing the breakdown voltage. In the negative case they state the opposite is true, the needle will get smoother increasing the breakdown voltage. For the uniform field case the negative breakdowns damage the cathode which will decrease the breakdown voltage with the number of events. The anode is not as badly damaged so upon switching to positive polarity the breakdown voltage will increase as it is known that the cathode is the source of the breakdown event. On average for the uniform field case, the positive values are a bit lower than the negative; this could be due to contamination in the fluid from the negative breakdowns.

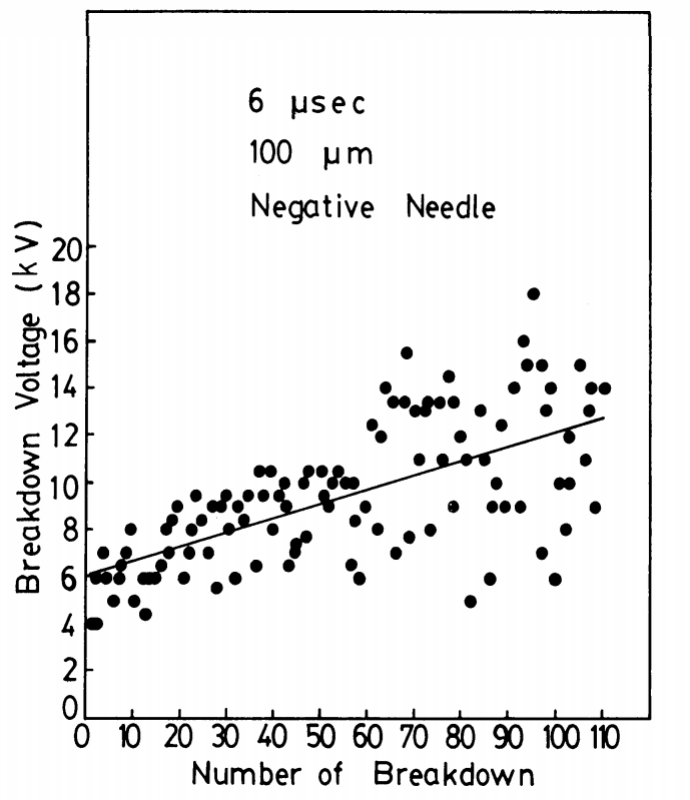

Fig. 4.30 Conditioning effect of breakdowns in liquid helium under negative needle-plane geometry (107).

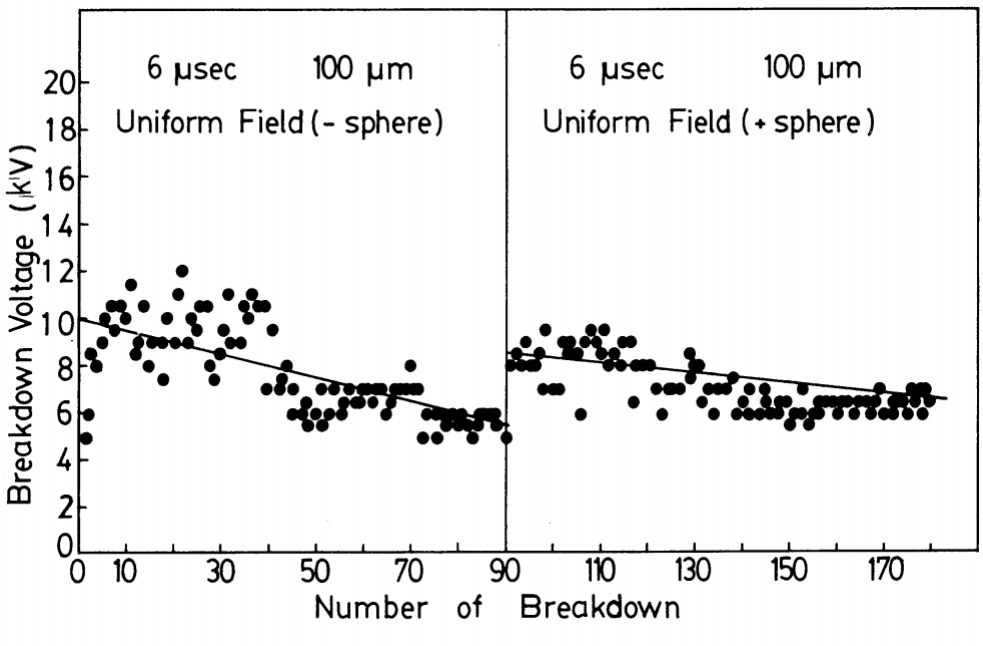

Fig. 4.31 Conditioning effect of breakdowns in liquid helium under uniform field sphere-plane geometry. Polarity switched after 90 breakdowns (107).

The statement by Kim that the cathode is the emitter of electrons is likely true, however, the charge will then flow to the anode and damage it, which the Kim seems to disagree with. In the case of vacuum breakdown it is well know that where the discharge travels to is where the damage will occur. The idea of electron emission being the reason for breakdown is questionable as the free electrons in liquid helium is suppressed so should not accelerate in an electric field. Now this may not apply for the case in very small gaps such as this. If the volume is boiling then bubbles are present which is known to be the primary cause of breakdown in liquid helium.

The conditioning behaviour observed with the S. Kim et al. setup is at odds with what Coletti found. The lack of an initial conditioning effect with Coletti's setup is possibly because either the conditioning runs were taken out or the electrodes were left in the system after each run, therefore, had already been conditioned after the measurements seen in Figure 4.27.

K. Yoshino et al. (100) investigated the change of polarity with the experimental setup previously mentioned section 4.2.5 but in liquid nitrogen, using the non-uniform setup. The application of pressure was performed on both polarities. The breakdown values for the two polarities are different, with positive needle starting higher then saturating, while the negative needle starts lower then increases dramatically. Yoshino attributes this to bubble formation being suppressed at higher pressures for negative while the positive polarity streamer breakdown is the primary characteristic.

The data presented in Figure 4.32, suggests that the primary behaviour for breakdown is through seeding of a bubble, otherwise there would not be a pressure dependence. Therefore, what could be happening is that the needle forms a bubble around the tip and becomes ionised, the electric fields elongate the bubble till it crosses the gap. However, it is not clear that in the positive polarity case that a streamer is responsible as it does still rise with pressure. The difference in polarity could be due to the larger surface area on the plane electrode, resulting in more asperities to seed more bubbles.

The Olivier (101) results previously shown above also comments on the conditioning effect and behaviour of repeated breakdown events. Olivier measures the conditioning effect on steel and brass electrodes. Olivier demonstrated that for brass there is no conditioning phase: the highest value is the first breakdown and then there is a large drop off followed by a steady decline. As for steel it has a short conditioning phase, about 5 breakdowns, then the highest value is reached then the breakdown value saturates.

The difference in behaviour is attributed to the condition of the surface after vari-

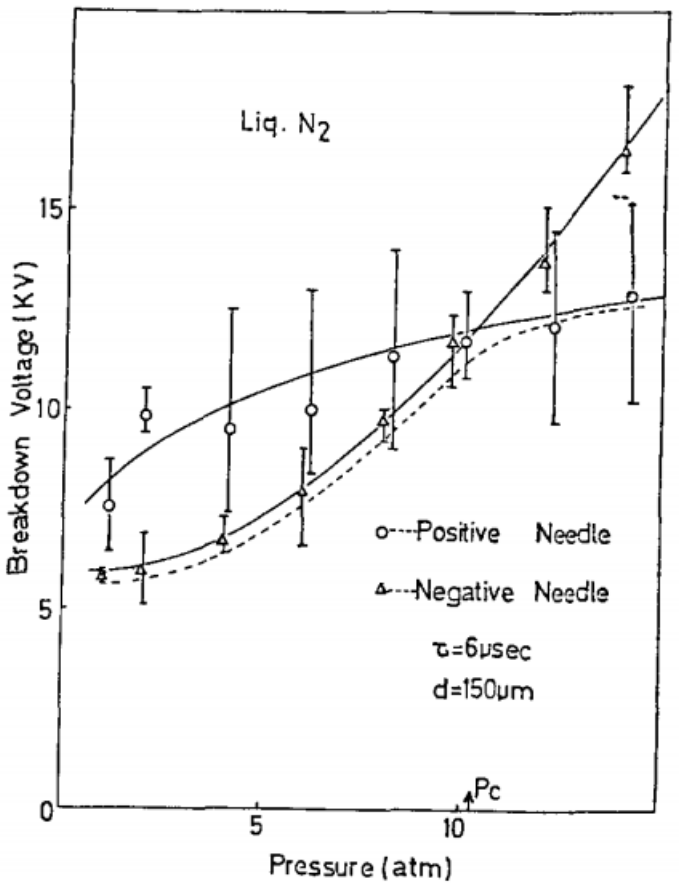

Fig. 4.32 Pressure dependence of breakdown in LN_2 using positive and negative polarities for needle-plane geometry (100).

ous breakdowns. The brass as already discussed will create sharper edges on the craters while the steel will be smoother. The data here for steel though is comparable to other papers already discussed, which shows that breakdowns will saturate after a number of breakdown events. The drop off is likely due to the material ejected off the electrode surface into the fluid volume which contaminates it, reducing the breakdown value over time as more is ejected.

Weber and Endicott (108) investigated the statistical distribution of breakdown voltages for a given electrode geometry in transformer oil. They used uniform field Rogowski electrodes of four different diameters: 3-inch, 2-inch, 1-inch, and 0.7-inch. The electrode spacing for all were set to 0.025 mm. In order to measure the distribution accurately, the electrodes and oil volume was meticulously cleaned after each breakdown to ensure that contamination from the breakdowns did not effect the results.

Weber and Endicott show in Figure 4.33 and 4.34 that the breakdown voltages are skewed. This implies that the lower voltages are more frequent then the voltages above the peak voltage. This probably occurs as the breakdown values can always get worse once the

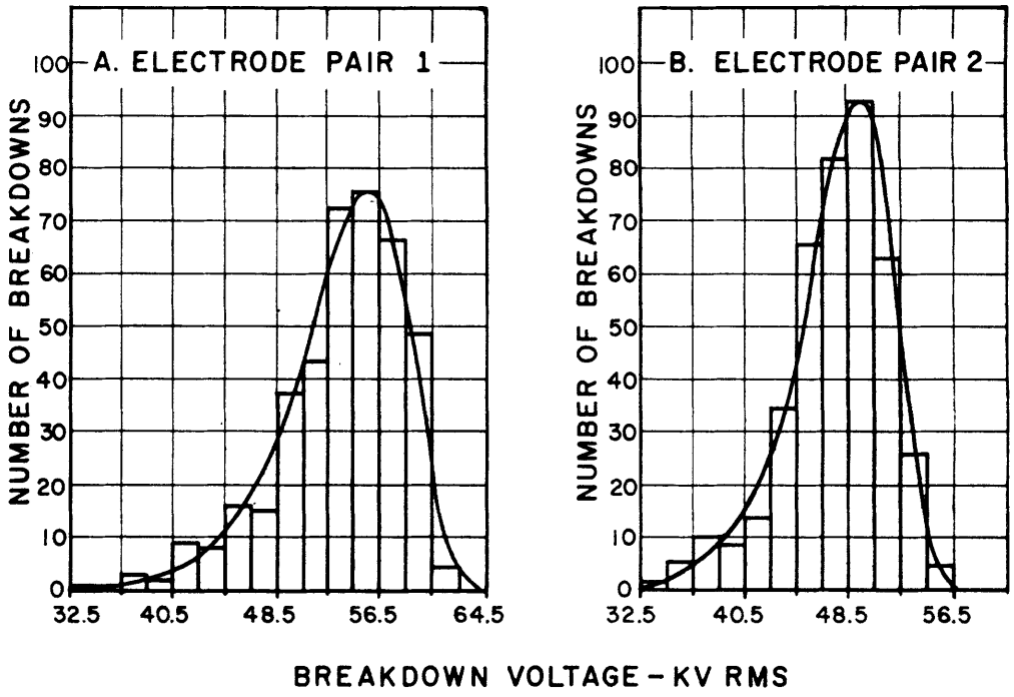

Fig. 4.33 Histograms for breakdown voltage distributions for the 0.7-inch electrode pair (A) and 1-inch electrode pair (B). Smooth curves are corresponding theoretical exponential (extreme value) distributions (108).

peak voltage has been reached due to deteriorating surface condition. The conditioning effect could also effect the results as these values in general will be lower then the peak voltages.

4.2.7 Electrode area effect and stressed volume

Weber and Endicott (108) also investigated the surface area effect on breakdown voltages.

In Figure 4.35 it shows that as the surface area is increased the breakdown voltage decreases logarithmically. This would be expected, as the larger the surface area, the number of asperities will increase exponentially, resulting in a greater probability to cause a breakdown.

N. Hayakawa et al. (109) investigated breakdown events in LN_2 with varying area and volume effects. The breakdown mechanisms in LN_2 are different from LHe, however, in this experiment the generation of thermal bubbles, micro-protrusions on the electrode surface, and impurities were regarded as weak points in the system at the scale these measurements were performed.

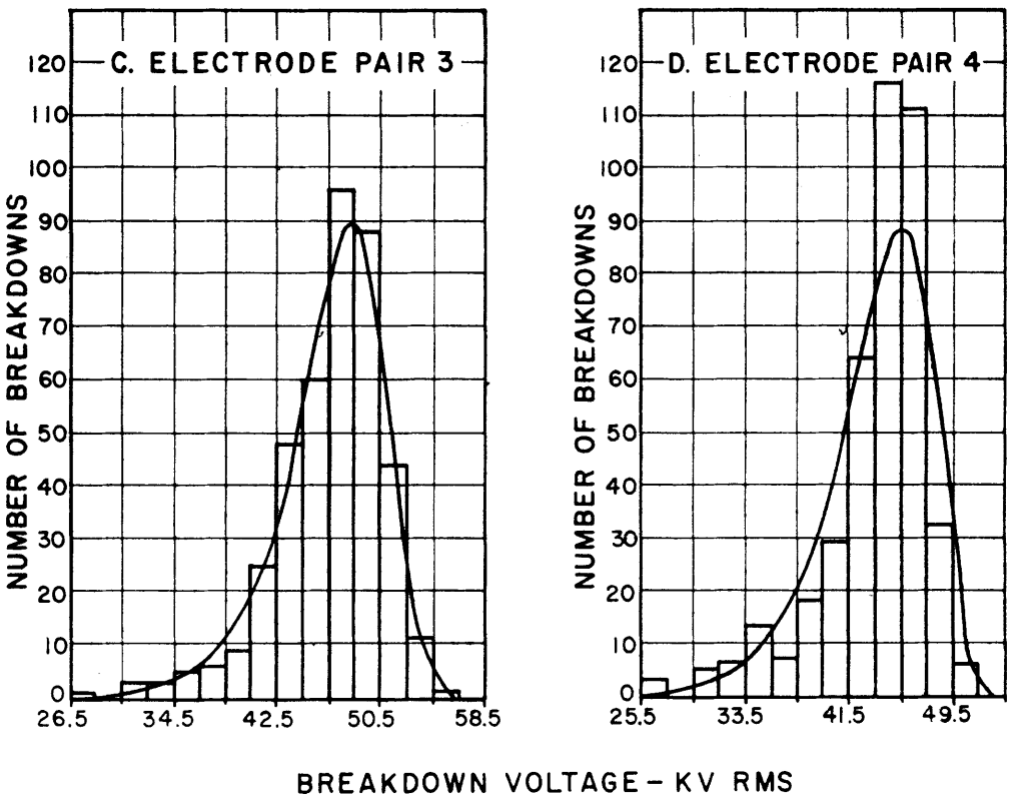

Fig. 4.34 Histograms for breakdown voltage distributions for the 2-inch electrode pair (C) and 3-inch electrode pair (D). Smooth curves are corresponding theoretical exponential (extreme value) distributions (108).

N. Hayakawa et al. used two different geometries: sphere-plane and coaxial cylindrical configurations. The roughness of the stainless steel sphere-plane surfaces were < 1 μm while for the coaxial it was ~ 200 μm. The surface area was varied from 10^0 to 10^5 mm^2 and volume 10^{-1} to 10^5 mm^3. This variation was achieved by changing the sphere diameter or gap length for the sphere-plane geometry, or by changing the gap length, inner cylindrical radius, or electrode length in the coaxial case.

N. Hayakawa also included measurements from other published data for comparison, as seen in Figure 4.37. The data shows that there is an exponential relation between breakdown voltage with respect to the surface area and volume of the fluid, this is comparable to Weber and Endicott (108). The results obtained make sense with expected breakdown behaviour, in that surface condition is very important, therefore, as the exposed surface is increased in size then it is more likely for an asperity to be present and cause a breakdown event to initiate. The stressed volume will be more dependent on impurities in the fluid or the size of a vapour bubble created in the breakdown process. An issue with the data presented is that it is comparing two different types of geometry and orientation. The sphere-plane geometry will be less dependent on the condition of the cathode surface as the stressed area is very small. In the coaxial

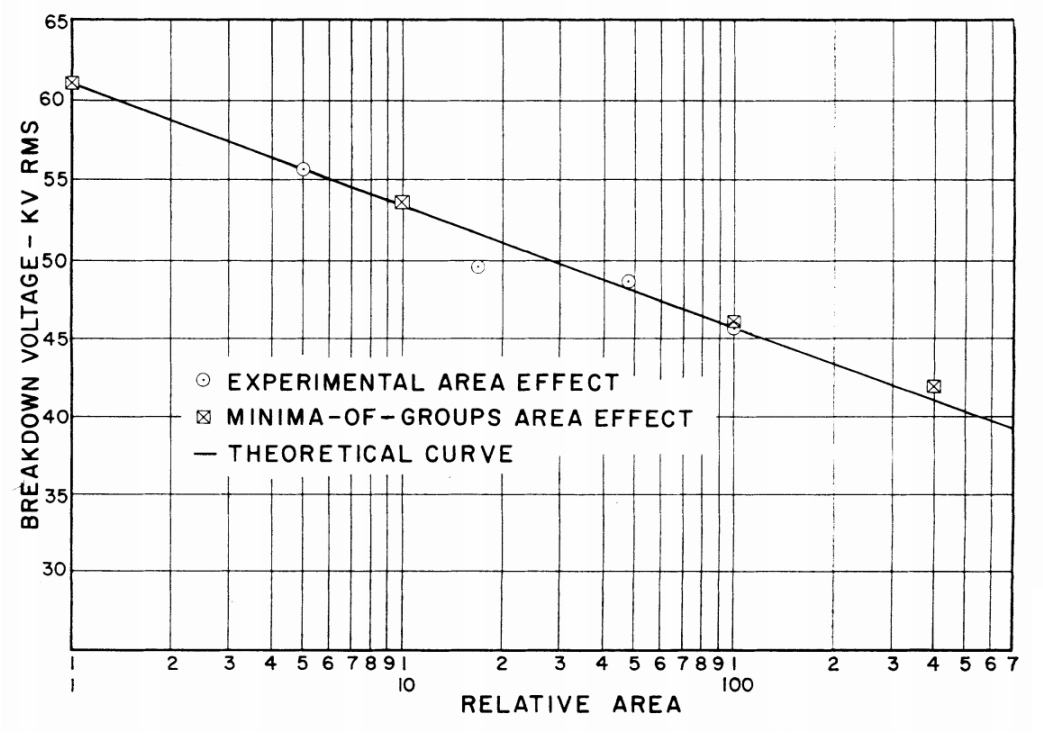

Fig. 4.35 Effect of electrode area on breakdown voltage of transformer oil. Relative area is the ratio of surface area between the four electrodes used (108).

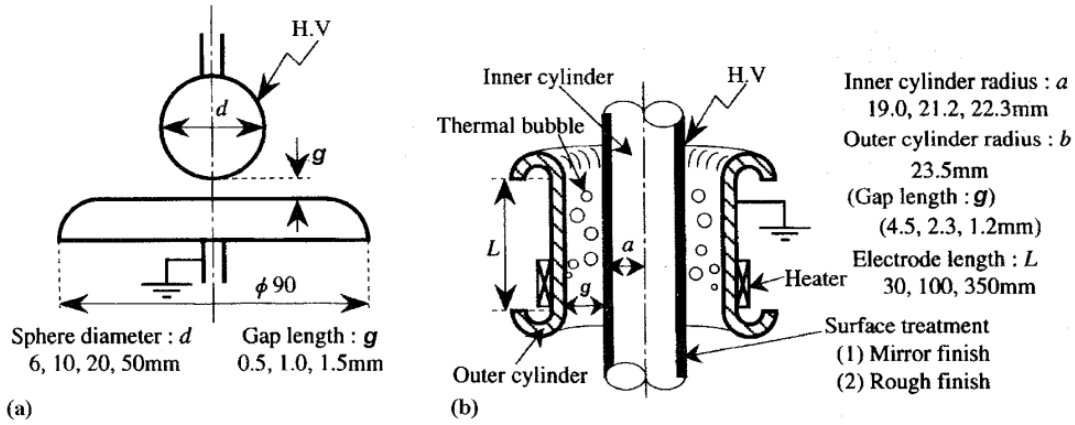

Fig. 4.36 Electrode configuration for breakdown voltage measurements in LN_2. (a) is sphere-plane, (b) is coaxial cylindrical geometry (109).

case, bubbles generated from the surface will rise upwards, not necessarily towards the ground electrode, so breakdown is more dependent on the bubble being charged, to get elongated in the field, which it may not necessarily the case.

Measurements were also performed with a heater to measure the breakdown voltage with bubble size. The heater was present on the outside of the ground electrode on the coaxial setup.

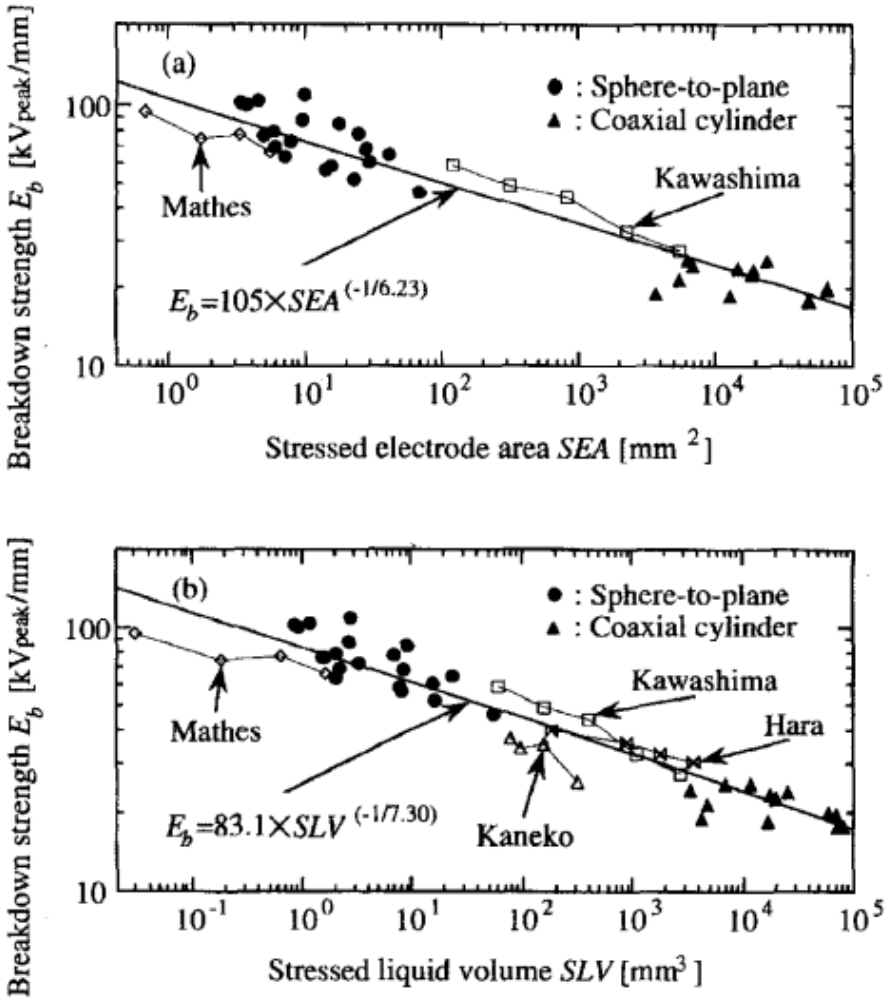

Fig. 4.37 AC peak breakdown fields, E_b, in LN_2 at atmospheric pressure versus stressed electrode area (SEA) for (a) and stressed liquid volume (SLV) for (b) (109).

Figure 4.38 shows that the breakdown voltage is dependent on the size of the bubble. As the bubble size increases it is more comparable with the dielectric strength of vaporised LN_2 given in section 4.3.3. The effect is even worse at smaller gaps, where the bubble is more easily able to span the gap. The surface condition is also discussed: when the central electrode is positive with a mirror finish the breakdown will occur through the thermal bubble, but when the central electrode is rough and at negative polarity the breakdown value is lower as micro-protrusions (asperities) are present so it is more likely to initiate a breakdown event.

4.3 Bubble formation in liquids

Bubble dynamics is a complex physical problem even in a classical fluid. It is still a challenging theoretical problem due to the number of parameters involved. The complexity comes from the dynamics of bubble like surface tension, pressure of the fluid, external

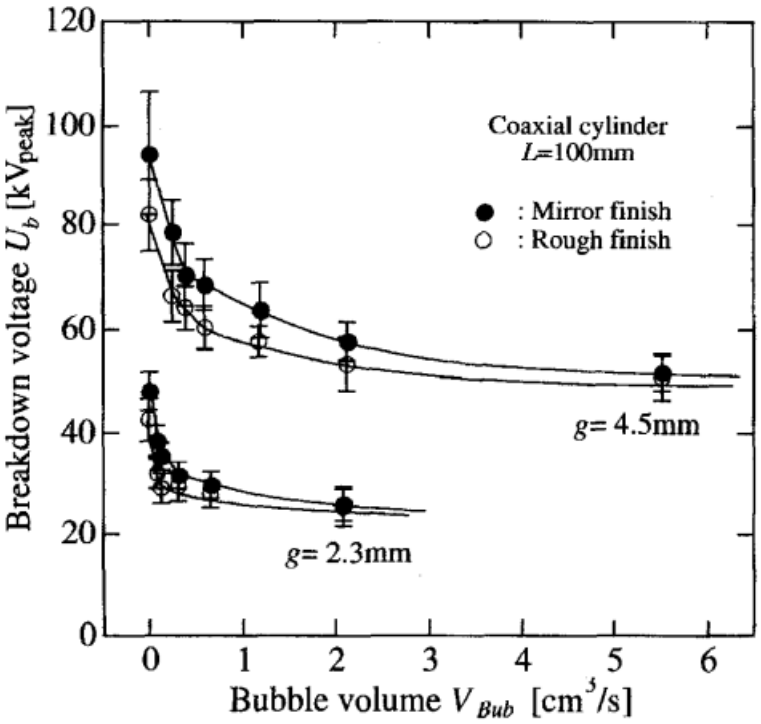

Fig. 4.38 AC breakdown voltage, U_b, as function of bubble volume, V_{Bub}, for different electrode surface conditions. The value g represents the electrode separation (109).

pressure applied, and pressure of the gas inside the bubble. In addition, there is also the hydrodynamic properties of the fluid itself. An idealised model for bubble dynamics is described by the Rayleigh-Plesset equation (110).

The initial formation of a bubble due to presence of an electric field will be discussed later in this section. Once the bubble is formed in a fluid the bubble can then grow and elongate. It is able to do this as the gas inside the bubble becomes ionised from electrons off the surface of the electrode. This creates a conductive bubble which under the application of electric fields will grow and elongate. However, this does mean that it is unstable, and it could collapse under the stress of the electric fields. Garton and Krasucki (111) investigated the behaviour of bubbles under electric fields for insulating liquids. They compared theoretical models to measured data to produce a general form for the stability of a bubble in a uniform E field, expressed as:

$$P_{(hydro)} + P_{(applied)} + P_{(electrostrictive)} + \sigma C - P_{(bubble)} = 0, \tag{4.5}$$

where $P_{(hydro)} = \rho gh$, $P_{(applied)}$ is the pressure applied to the fluid, σ is the surface tension, C is the radius of curvature of the bubble, and $P_{(bubble)}$ is the pressure of the gas inside the bubble. The $P_{(electrostrictive)}$ is given by the function of the permittivity of the fluid and the gas:

$$P_{(electrostrictive)} = \frac{1}{2}\left[\left(\epsilon_{(liquid)} - \epsilon_{(bubble)}\right)\left(\frac{\epsilon_{liquid} + 2\epsilon_{bubble}}{3\epsilon_0}\right)\right] E^2. \tag{4.6}$$

Graton and Krasucki showed that in mineral oil the general behaviour of the electrostrictive pressure is to elongate the bubble in the direction of the electric field, from one electrode to another. The bubble will always deform and become unstable. For a non-conducting bubble with neutral gas the difference in the permittivity is very small, therefore, the elongation under an electric field is minimal.

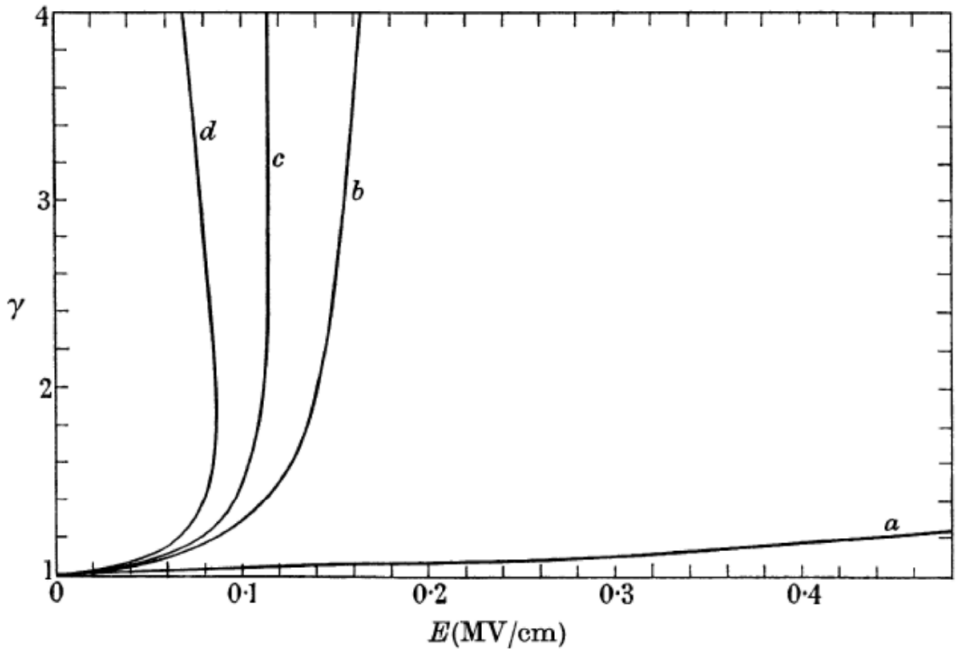

Fig. 4.39 Elongation of bubble under various conditions. γ, the ratio of the major and minor axis of an ellipse for compressible bubbles in a dielectric liquid, against applied electric field, E. $\epsilon_{liquid} = 1.883$, $\sigma = 18.42 \times 10^{-3}$ Nm^{-1}, $P_0 = (P_{hydro} + P_{applied}) = 1$ bar, $r_0 = 10$ μm. Curvature: (a) $\frac{\epsilon_{(bubble)}}{\epsilon_{(liquid)}} = 0.534$; (b) $\frac{\epsilon_{(bubble)}}{\epsilon_{(liquid)}} = 10$; (c) $\frac{\epsilon_{(bubble)}}{\epsilon_{(liquid)}} = 20$; (d) $\frac{\epsilon_{(bubble)}}{\epsilon_{(liquid)}} = \infty$ (2) (111).

Garton and Krasucki conclude that for a non-conducting bubble for which $\frac{\epsilon_{(bubble)}}{\epsilon_{(liquid)}} < 20$, the bubble will maintain a stable shape at all field values. But if the bubble becomes conducting it will elongate to a critical stable shape corresponding to $\gamma = 1.85$ (ratio of major to minor axis of the bubble) and will increase above this if the permittivity decreases from ∞.

However, if the bubble becomes ionised it would result in a change to the permittivity, leading to the bubble to elongate further which limits the applied field. This work was performed in a classical fluid, however, does this applied in LHe? Due to the thermal conductivity LHe II there is also a question if a bubble can form within the bulk volume? The permittivity of helium gas is also very close to that of liquid helium ($\epsilon_{(gas)} = 1.00007$,

$\epsilon_{(liquid)}$ = 1.05 (97) (112)), therefore, the question if the ionisation of the bubble will dramatically change its permittivity to elongate it under applied electric field is also not clear.

4.3.1 Vapour Bubble Formation in Liquid Helium

Evidence discussed previously shows that the sources of breakdowns are heavily dependent on formation of bubbles in the cryogenic fluid. The question that will be first addressed is if bubbles can be formed in LHe I and LHe II. The high thermal conductivity of LHe II means that the heat to the volume will cause bubble formation on the surface rather then in the bulk volume, in general.

Abe et al. (113) investigated the formation of bubbles in various states of liquid helium: normal ^{4}LHe, pure superfluid ^{4}LHe and a superfluid mixture of ^{4}LHe and ^{3}LHe.

Abe performed the experiment in a ^{3}He – ^{4}He dilution refrigerator with optical windows in order to observe the bubbles forming. The bubbles were formed by the presence of two ultrasonic transducers, opposite each other in the helium volume. During the measurement the transducer was set to a certain voltage at which a bubble would form on the surface. As the voltage is increased above a threshold voltage the induced bubble is enlarged. This threshold voltage is described as the critical value at which nucleation occurs. The behaviour of the bubble is reported on when it reaches macroscopic size.

Bubble behaviour in normal liquid LHe was observed at a temperature of 3.2 K under SVP. A large bubble was able to form on the surface of the transducer, shown in Figure 4.40. This bubble was able to grow and detach from the surface, proceeded by many small bubbles ~ 70 μm in size.

The behaviour is stated as like boiling to due warming from the transducer surface. Abe et al. states that the presence of the small bubbles is due to the local boiling which is possible due to the low heat conduction in the normal state. It can be imagined that if the bubble had become conductive it could carry charge across the gap with the small bubbles creating an easier gas path for the breakdown.

In the pure superfluid ^{4}LHe state, at temperature of 300 mK, the bubble forms on a point on the surface of the transducer as seen in Figure 4.41. Unlike in normal ^{4}LHe the bubble seems to be more spherical in natural while in contact with the surface. As the bubble grows it becomes more irregular in shape till it detaches from the surface.

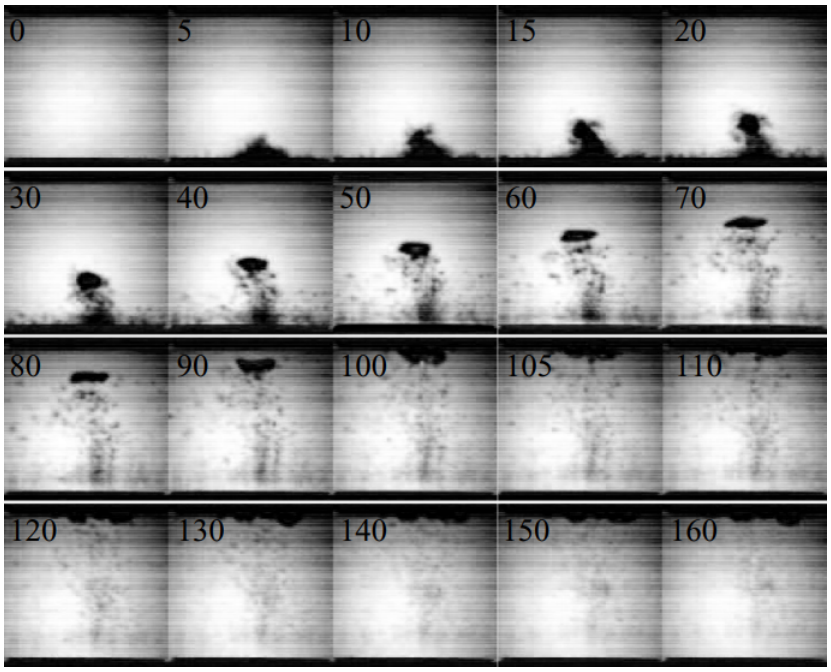

Fig. 4.40 Images of sound-induced bubble formation on the surface of a piezoelectric transducer (bottom plane). The LHe is normal state at 3.2 K SVP. The frame width is 10 mm with the time between each frame stated at the top corner of each picture in micro seconds. The main bubble width is 2.5 mm. The pulse width of the transducer is 0 ms to 5 ms. Applied voltage of the transducer is 7.2 V (113).

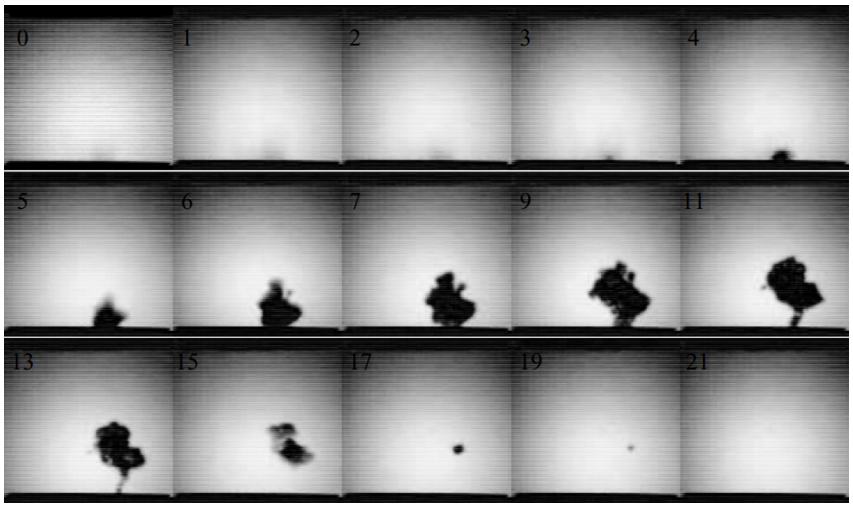

Fig. 4.41 Images of sound-induced bubble formation on the surface of a piezoelectric transducer (bottom plane). The volume is LHe II at 300 mK. The frame width is 10 mm with the time between each frame stated at the top corner of each picture in micro seconds. The pulse width of the transducer is 0 ms to 5 ms. Applied voltage of the transducer is 7.2 V (113).

In the normal ^{4}LHe as the bubble detached it became elliptical in natural while in this case it is very irregular. Abe et al. notes that the formation of the bubble only occurs on the active region of the transducer and not the whole surface like as in LHe I. In the superfluid case the heat is dissipated to the volume, therefore, the active spot at which

the bubble is formed can only be one point source on the surface. The superfluid state also seems to cause a more rapid collapsing of the bubble across the gap.

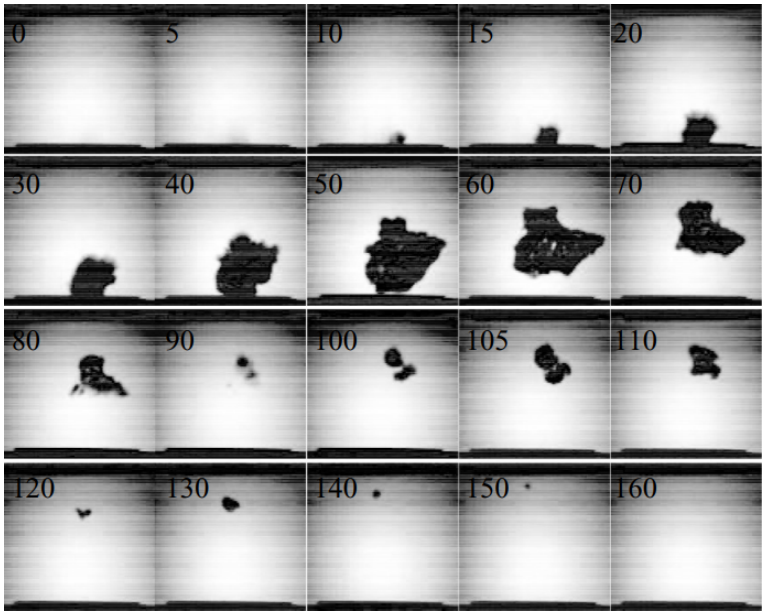

Fig. 4.42 Images of sound-induced bubble formation on the surface of a piezoelectric transducer (bottom plane). The volume is LHe II at 300 mK. The frame width is 13 mm with the time between each frame stated at the top corner of each picture in micro seconds. The pulse width of the transducer is 0 ms to 5 ms. Applied voltage of the transducer is 8.2 V (113).

For the pictures in Figure 4.41, the voltage is lower than in Figure 4.42, which results in less energy transfer to the bubble, hence why it is smaller in Figure 4.41. The lower voltage would have allowed the heat input to the surface to stop more rapidly, allowing the fluid to equilibrate with the surface. This can be seen in Figure 4.41 for frame 11-13, the bubble grows then the tail of the bubble collapses as the surface is cooled, leaving the bubble which then collapses very quickly and disappears. The irregular shape of the bubbles in LHe II is thought to be due to turbulent flow around it, distorting the shape.

It is surprising that a bubble can form on a surface in bulk superfluid helium. It would naturally be thought that the heat will dissipate to the volume too quickly to create this local heating effect. However, this does occur at a small point on the surface. Considering the case with HV application it is known that in a vacuum a small asperity, on a surface will generate a breakdown event, by heating the asperity till it explodes. If this local heating of this spot occurs in the fluid case it could easily generate a bubble.

Comparing Figure 4.40 to 4.41 shows that the bubble diameter will be larger than in the LHe I case. Past data does show that as the pressure of the liquid helium is reduced (required to lower the temperature of the bath) then the breakdown voltage of

the helium will be lower. Hence if an electric field were applied in this case then the gaseous bubble would more easily create a vapour column to the opposite electrode, potentially making a breakdown event more likely.

4.3.2 Bubble generation in cryogenic liquids with electric fields applied

Hara (114) performed breakdown measurements in LN_2 for a rod to plane geometry with a heater attached to the rod in order to generate a local hot spot to generate bubbles. The HV is applied to the plane electrode with separations of 2.6 mm. The volume was also pressurised for various measurements to observe the effect on the bubble formation. It was observed, before HV was applied, that there was a relation between the heater power and the bubble diameter: the more power the larger the diameter, as seen in Figure 4.43.

However, if the pressure is increased the bubble diameter is also reduced and the bubble will collapse quickly when it has left the surface of the electrode. If HV is applied, it is found that the bubble shape will always deform in a way that is dependent on the magnitude of the electric field, heater power, and ambient pressure, as shown in Figure 4.44. It was noted that the bubble behaviour was independent of the polarity. Hara notes that there are different behaviours of the bubble formation with applied electric fields when pressure is varied.

The first behaviour stated is a “no bubble region”, at which the low heater power is not enough to form a bubble, however, breakdown does occur once the breakdown voltage is reached. It is unclear if this is because of electron emission from the surface initiating the breakdown, which is assumed to occur through the liquid volume.

In Figure 4.43 (a), a discrete bubble is first observed. As the heater power is increased many additional bubbles are generated. But compared to Figure 4.44, application of the electric field slows this down and the bubble turns abruptly into round bubbles. Increasing the voltage further causes the bubble to elongate, forming a cone. It flattens gradually and occasionally collapses before breakdown. It’s implied that the breakdown occurs through a combination of gas and liquid phases.

Application of higher heater power causes more bubbles to form. As the electric field increases the bubbles coalesce quickly to form a vapour column, parallel to the electric field, between the electrodes. As the voltage increases it forms a cone instead with small bubbles streaming from its tip before breakdown occurs.

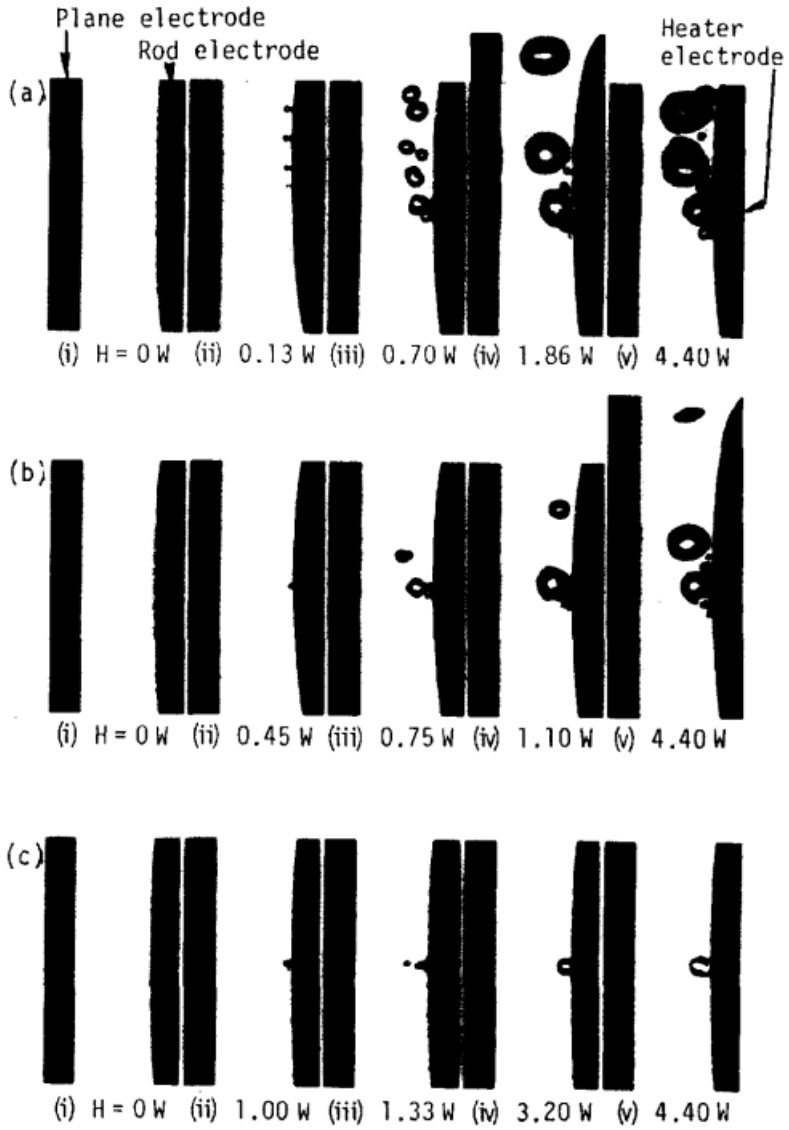

Fig. 4.43 Shadow photograph of bubbles under different heater powers and pressures when no voltage is applied to the electrode, (a) P_e = 0.1 MPa; (b) P_e = 0.2 MPa; (c) P_e = 0.4 MPa (114).

At higher pressures, with much more heater power (Figure 4.44 (c)), the voltage is 5 kV higher before the vapour column bridges the gap. The bubble also shrinks at higher voltages, despite the significantly higher heater power.

At the highest heater power with reduced pressure (Figure 4.44 (d)), the bubbles are formed very easily and have the largest diameters. The vapour column is formed and maintained at lower voltages, and breakdown also occurs at lower voltages.

It seems that in the relation between the heater power and the applied pressure there is a non-linear behaviour for the breakdown voltage. At larger heater powers, a more

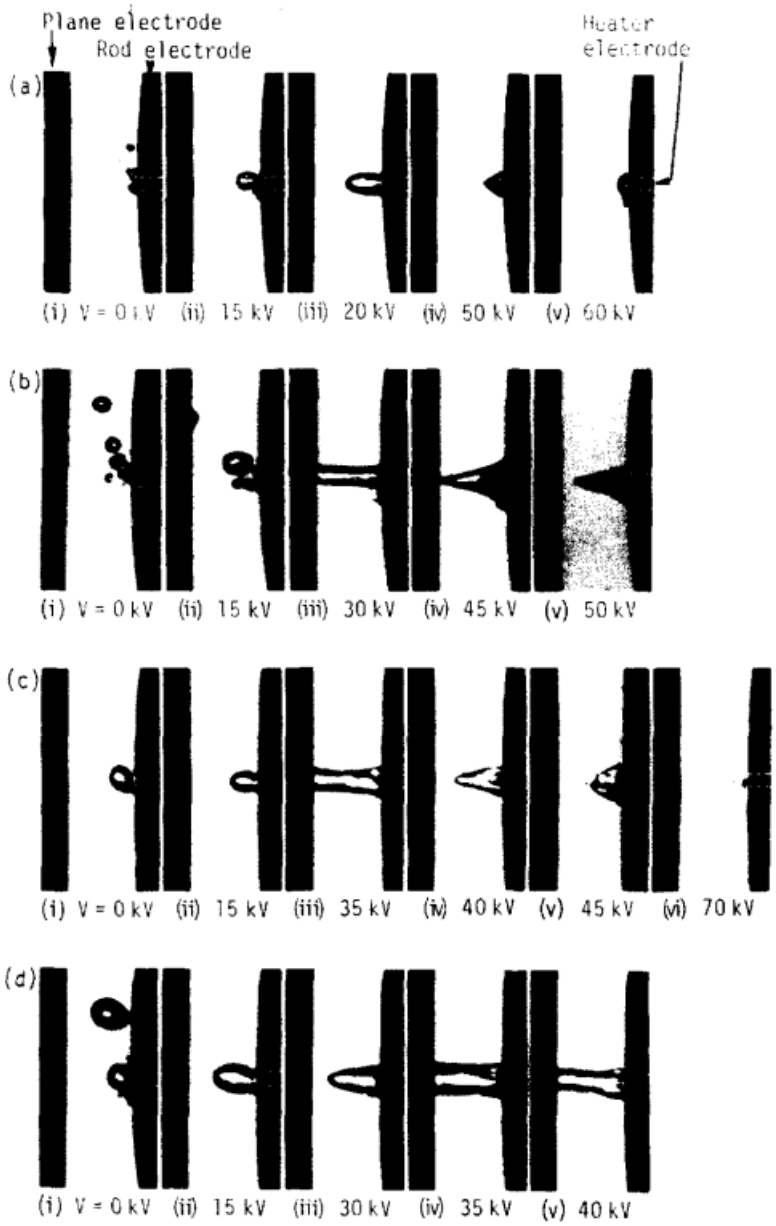

Fig. 4.44 Shadow photograph of bubbles under different heater powers and pressures when voltage is applied to the electrode, (a) P_e = 0.15 MPa, H = 0.55 W; (b) P_e = 0.15 MPa, H = 0.8 W; (c) P_e = 0.25 MPa, H = 1.58 W; (d) P_e = 0.15 MPa, H = 1.58 W (114).

solid, larger bubble is formed regardless of the applied pressure. However, clearly at higher applied pressures the highest voltages can be achieved even with greater heater power. This implies that the bubble formation does have some effect on the breakdown voltage.

Hara comments that for larger bubbles observed they are elongated by the electric field, overcoming the pressure effect, and thus follow the calculations of Garton and Krasucki (111).

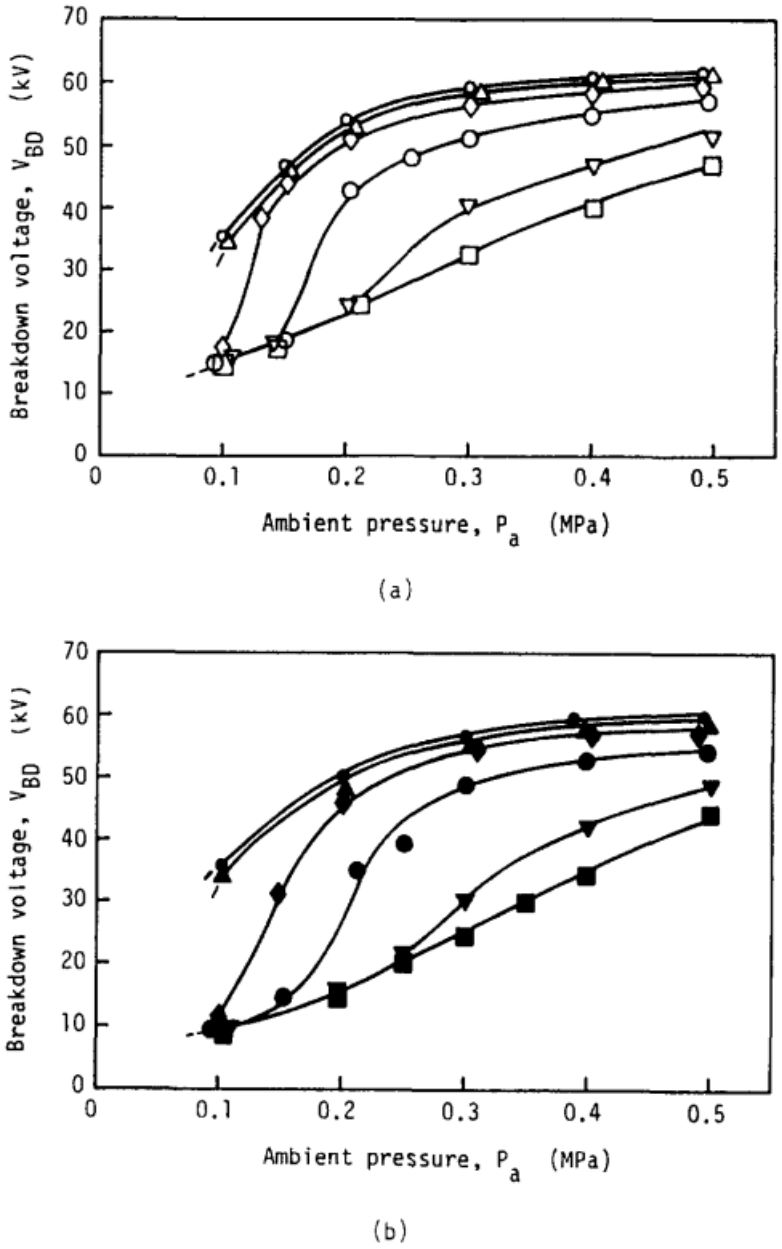

Fig. 4.45 Breakdown voltage as a function of ambient pressure for six heater powers at separation of 1.2 mm, (a) is positive rod electrode, (b) is negative rod. Small circles are with no heater power; triangles, H = 0.05 W; diamond, H = 0.50 W; large circles, H = 1.1 W; cone, H = 3.2 W; square, H = 4.4 W (114).

Hara found that the breakdown voltage with increasing pressure would increase even with higher heater power, seen in Figure 4.45. This is possibly due to the applied pressure decreasing the bubble size, meaning it is unable to span the gap and result in breakdown. It is noted that the breakdown for positive rod voltage is higher than for the negative polarity rod when breakdown appears through a vapour column or through series of bubbles.

The electrical breakdown strengths can be predicted approximately by Garton and Krasucki's model for low heater power, Hara concludes. However, for higher heater power the breakdown occurs through a vapour column, and streamer theory fits this type of discharge.

Hara (115) also performed measurements in a LHe bath at SVP using a parallel plane stainless steel electrode geometry with a separation of 1 mm in a vertical arrangement. The purpose of the system was to investigate breakdown phenomena initiated by thermally generated bubbles in LHe. In the setup bubbles were generated using a heater which was placed on one of the plane electrodes. Bubbles produced for a vertical electrode orientation without applied electric field are shown in Figure 4.46. HV is only applied to the heater electrode and at positive polarity in all cases.

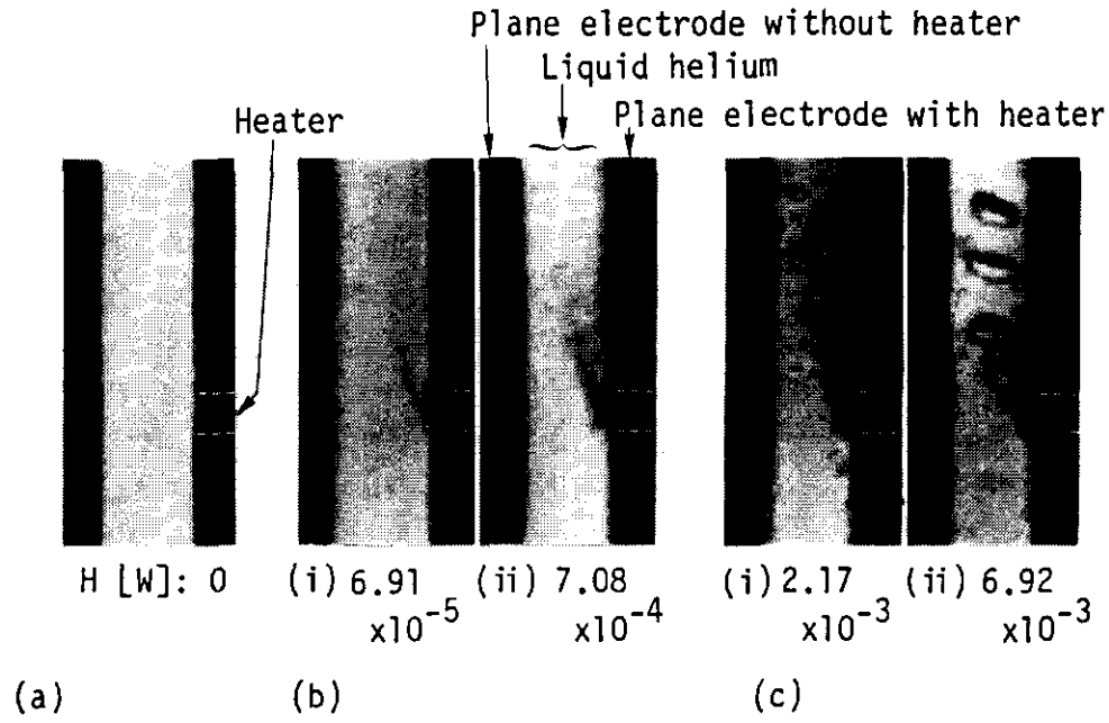

Fig. 4.46 Plane-plane vertical electrode geometry with no electric field. Only the heater power is varied, with values (in W) displayed in each picture. The pictures show (a) no boiling occurring, (b) nucleate boiling, (c) film boiling (115).

It is observed that there are two types of bubble generation observed in this case: nucleation boiling and film boiling. The nucleation is occurring at the point of the heater, with small heat input coming from a point source, forming a bubble. The film boiling is clearly causing the heat input to be spread more across the volume, hence larger bubble generation. Hara then applies electric fields in the case for nucleation boiling and observes the following in Figure 4.47.

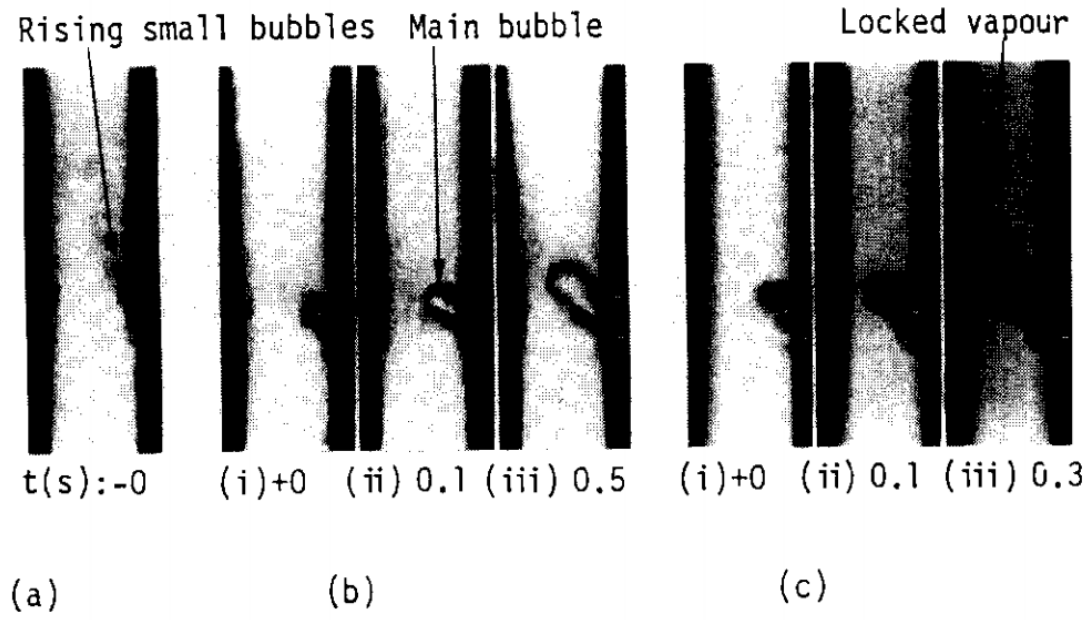

Fig. 4.47 Plane-plane vertical electrode geometry for given heater power of 5.42×10^{-4} W. The following represents: (a) V = 0 kV, (b) V = 6 kV, (c) V = 11 kV (115).

At the start of electric field application, bubbles break off the electrode surface and rise due to buoyancy. A bubble forms on the heater and grows with fixed electric field. At some critical size the bubble breaks off again and the process starts over. At higher applied voltages the bubble is completely removed and instead a vapour channel between the electrodes is formed. It is noted that at this stage the breakdown may occur.

This vapour bubble region is investigated in Figure 4.48. In these cases, the heater power is varied and higher electric fields are applied. As a higher heater power is used, the bubble switches to a film boiling. As voltage is increased, the bubble on the surface swells till it eventually bridges the gap before breakdown occurs. It is noted that in any case where the heater power is non-zero then a bubble can form which may detach from the surface, but it will always form a vapour bridge between the electrodes, followed by a breakdown.

Hara also performed measurements on a horizontal setup with the heater with the heater on either the top or bottom electrode. In the case of the bottom electrode with the heater in absence of electric field, bubbles would break off the surface and rise to the upper electrode where they are trapped. Bubbles would eventually merge on the upper surface creating a larger bubble which is then removed by convection currents in the LHe, as seen in Figure 4.49.

Figure 4.50 and 4.51 show when HV is applied to the horizontal setup bottom electrode.

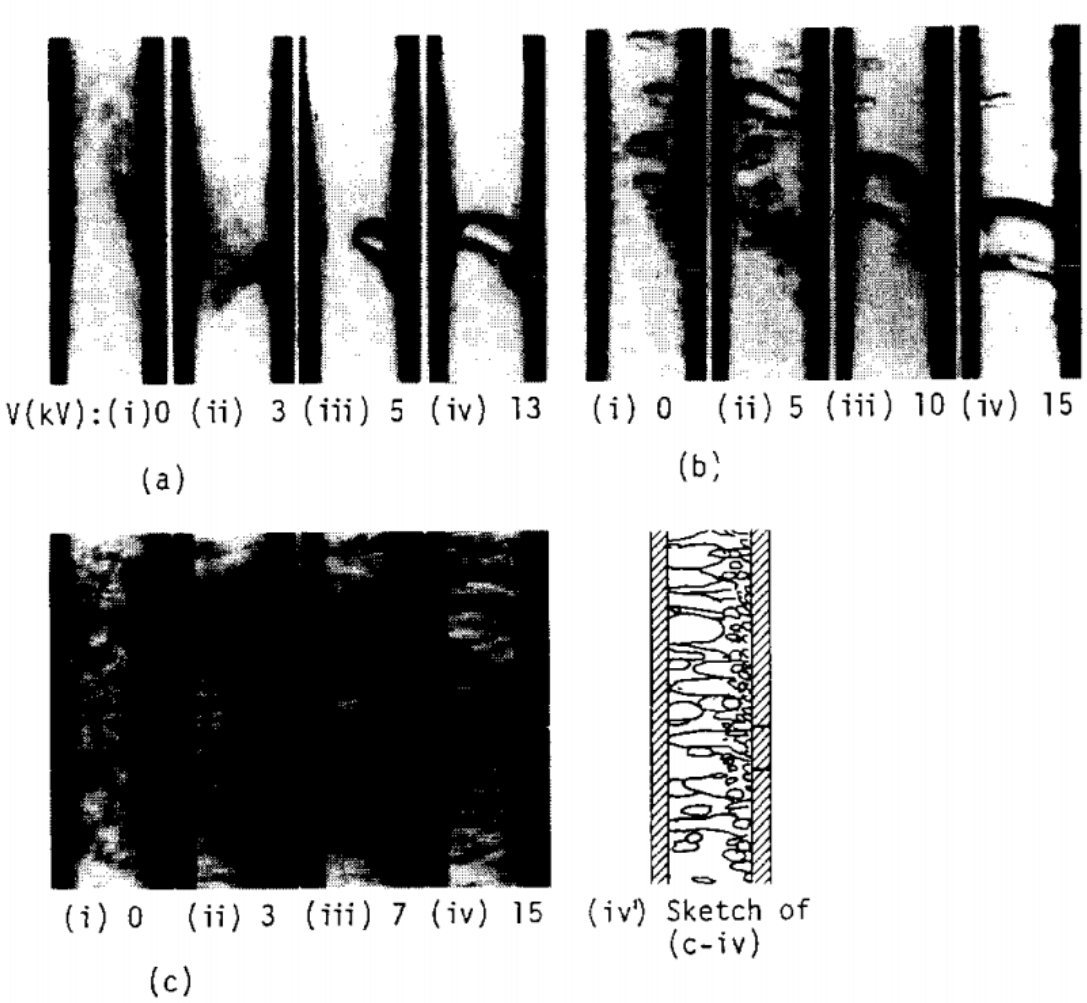

Fig. 4.48 Plane-plane vertical electrode geometry for given electric field, heater power is varied. The following represents: (a) H = 5.42×10^{-4} W, (b) H = 5.35×10^{-3} W, (c) H = 1.78×10^{-2} W (115).

In this case, a main bubble is developed on the upper electrode in the gap, with larger bubbles forming on the edge of the heater surface. Application of the electric field causes bubbles to break off and merge with the trapped bubble on the upper surface. At this point the bubble breaks off an is driven out of the gap. This causes new bubbles to form with the main bubble on the upper electrode surface forming again. The application of higher E fields causes the bubbles opposite each other to merge forming a vapour bridge and breaking down. It is noted that the limiting size of the main bubble is due to the magnitude of the electric field and not the heater power. The bubbles are also held in place on the electrode surfaces by the electrostatic forces overcoming buoyancy when electric field is applied.

Experiments with the heater on the upper electrode yield similar behaviour to before, but with the main bubble forming on the heater, as seen in Figure 4.52. However, no bubbles are formed on the lower electrode. The main bubble growth is much slower and

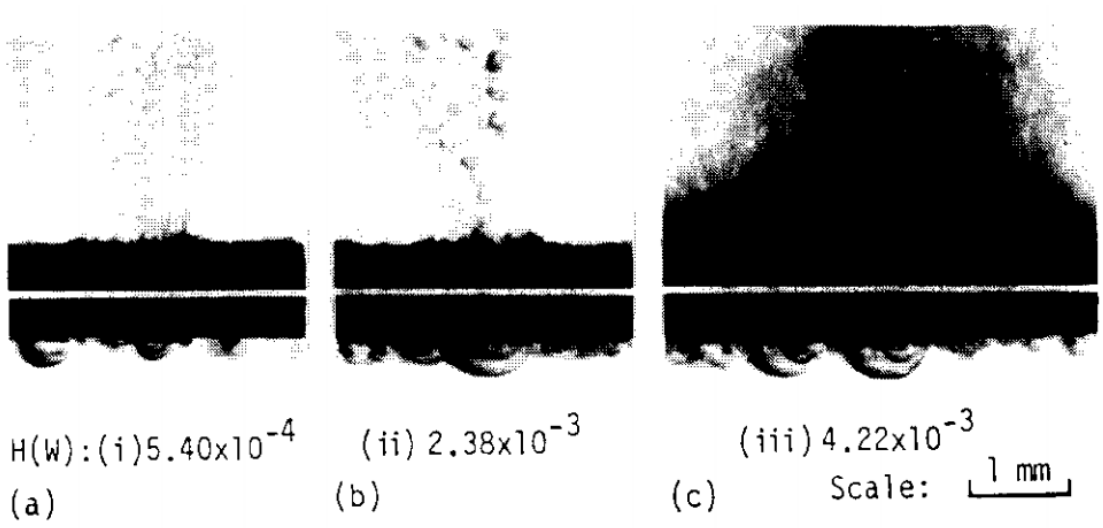

Fig. 4.49 Plane-plane horizontal electrode geometry without electric field. Boiling occurring at both sides of the electrode with heater at different powers. The following represents: (a) Nucleate boiling on upward heater surface, (b) start of film boiling on upward heater surface, (c) active film boiling on upward heater surface (115).

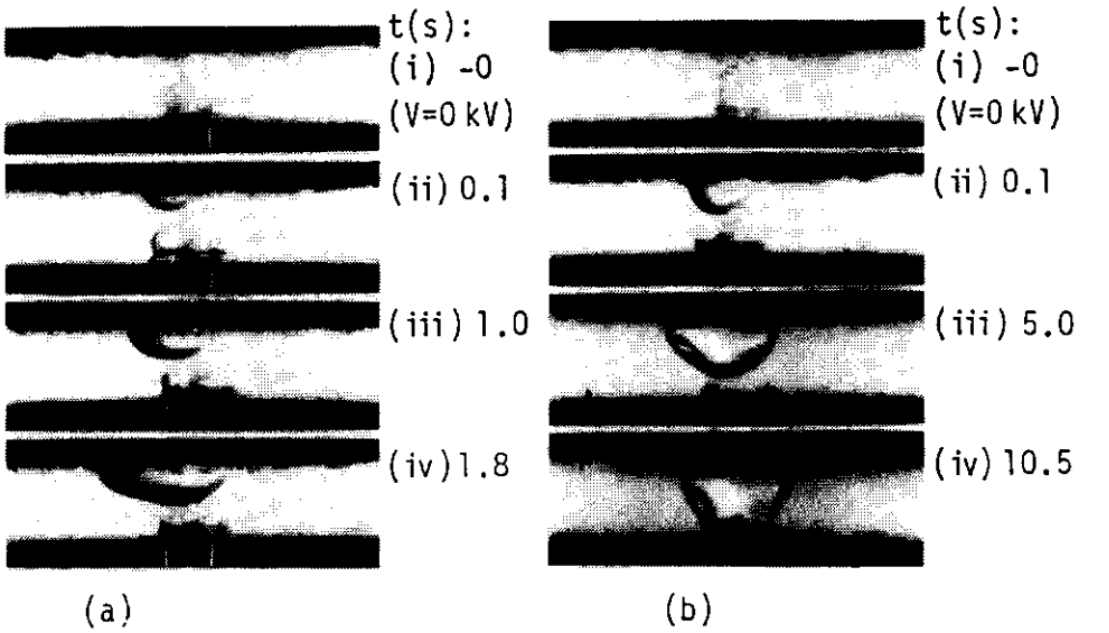

Fig. 4.50 Plane-plane horizontal electrode geometry with electric field and heater on top electrode, H = 5.42 × 10^{-4} W. The following represents: (a) V = 3.7 kV, (b) V = 5 kV (115).

being driven by the heater, with it reaching a critical size and breaking off and driven out of the gap. It should be noted that the onset voltage which forms the bubble and creates the vapour bridge is higher than in the previous setup.

Hara goes further in this paper to relate his work to that of Garton et al. (111). The bubbles generated in Hara's setup are elongated under the application of the higher

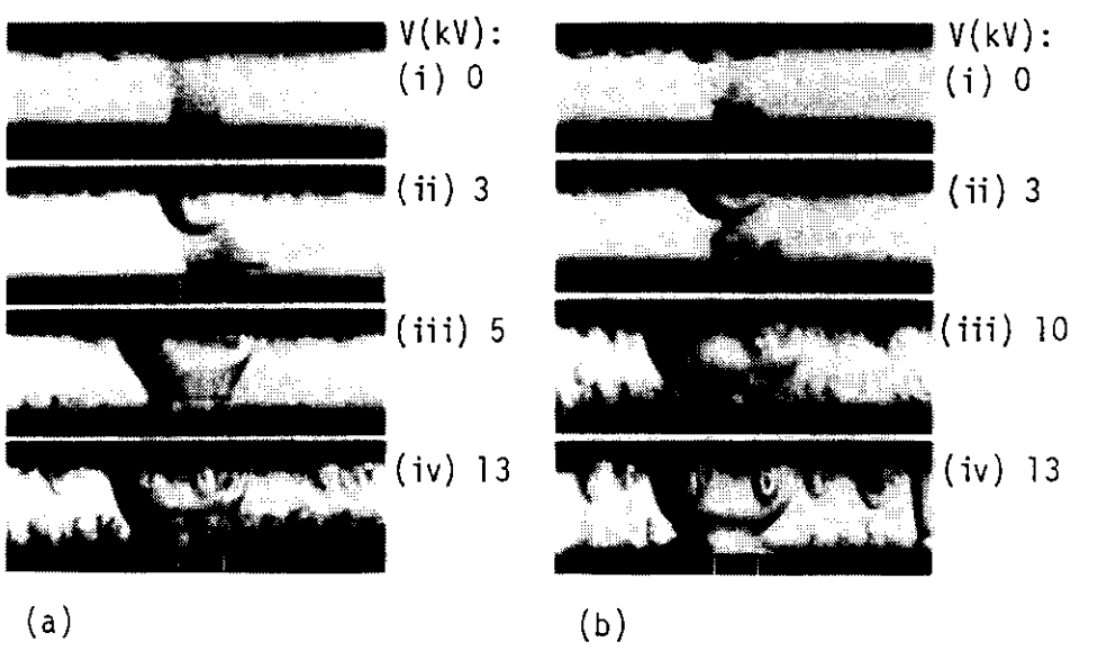

Fig. 4.51 Plane-plane horizontal electrode geometry with electric field and heater on top electrode, H = 5.42 × 10^{-4} W. The following represents: (a) V = 3.7 kV, (b) V = 5 kV (115).

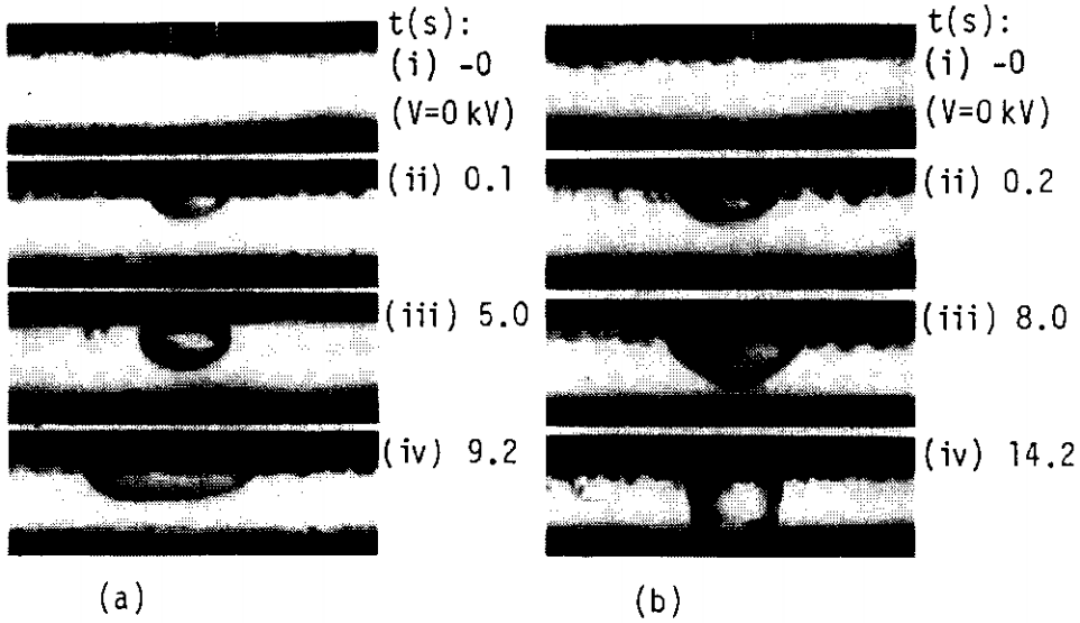

Fig. 4.52 Plane-plane horizontal electrode geometry with electric field and heater on bottom electrode, H = 5.42 × 10^{-4} W. The following represents: (a) V = 5 kV, (b) V = 8 kV (115).

electric fields. Hara calculates the elongation of a bubble due to electric fields in LN_2 and LHe, seen in Figure 4.53. The implication is that the bubble shape in LN_2 is elongated more than in LHe, which could potentially more easily form a vapour bridge, leading to lower achievable electric fields.

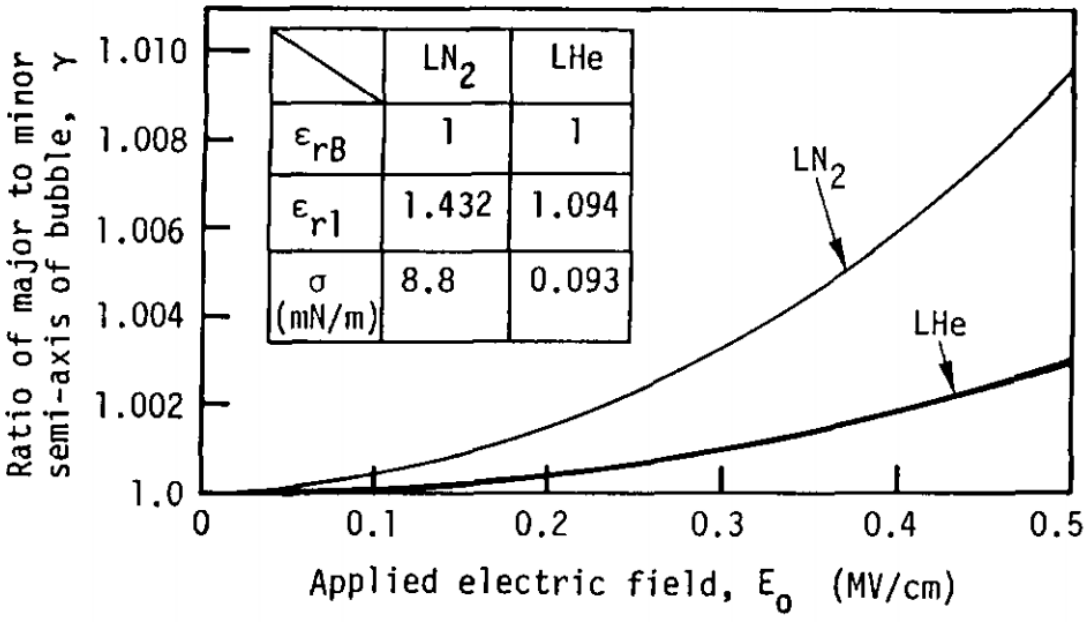

Fig. 4.53 Calculated ratio of the major to minor semi-axis, γ, of isolated bubble in the presence of uniform electric field, E_0. ϵ_{rB} = relative permittivity of He gas, ϵ_{rl} = relative permittivity of LHe, and surface tension of LHe (115).

Hara concludes that the DC electrical breakdown voltage occurs through the locked vapour channel which is caused by thermal bubbles. This produces values for breakdown fields that are comparable to that of helium gas, indicating that bubble generation is the limiting factor.

Cevallos et al. (116) performed breakdown measurements in transformer oil using a needle-plane geometry with a gap of 2.5 mm using a negative polarity on the needle. The needle has a radius of 5.0 μm as seen in Figure 4.54.

The initial direction of the streamer is not reproducible. This random direction could be due to collisions with particles in the liquid, ionising them. This behaviour is not seen in the positive polarity case, implying that the high field at the tip of the needle is what generates the bubbles. Breakdowns at higher pressures that form the initial streamer are suppressed, its radius smaller, while at the lower pressures the diameter of the bubble is much larger. The growth across the gap is also more significant at lower pressures. Once the streamer crosses the gap, the breakdown occurs inside the vapour column which is very clear in Figure 4.54 at 300 torr and 2.4 μs. This also seems to cause a shock wave through the fluid, in the wake of the discharge. However, the voltage of the breakdown in Cevallos's experiment is not stated.

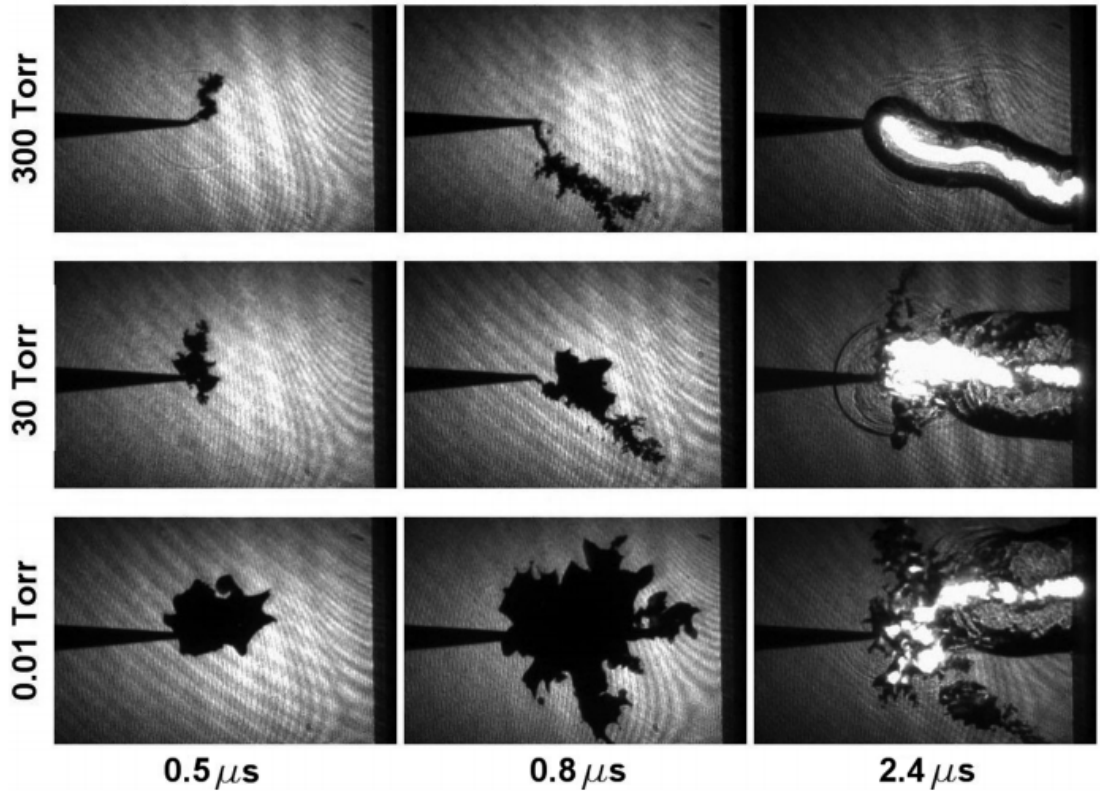

Fig. 4.54 Shadowgraph image of streamer expansion as a function of time and pressure for a negative needle-plane geometry.

Hong (117) performed measurements in LN_2 to investigate if the limiting effect of HV breakdown was the formation of bubbles between two electrodes. Hong varied the pressure and bubble diameter (via heater power). The setup could achieve 200 kV which could be applied to the electrodes, which were 7 cm in diameter. The HV electrode was flat, however, the ground electrode was slightly curved and had a heater glued into the centre of it. The experiment used a camera to observe the formation of the bubbles on the electrode surface.

In Figure 4.55 and 4.56 it can be seen that increasing heater power results in larger bubbles, and higher pressures will these bubbles smaller without an electric field applied. Applying the electric field leads to the bubbles staying longer on the surface before detaching. The bubbles also elongate in a direction, parallel to the electric field. Eventually, as the field is increased, a vapour column forms between the electrodes for a long period of time. If the electric field is raised further then the breakdown occurs through the vapour column.

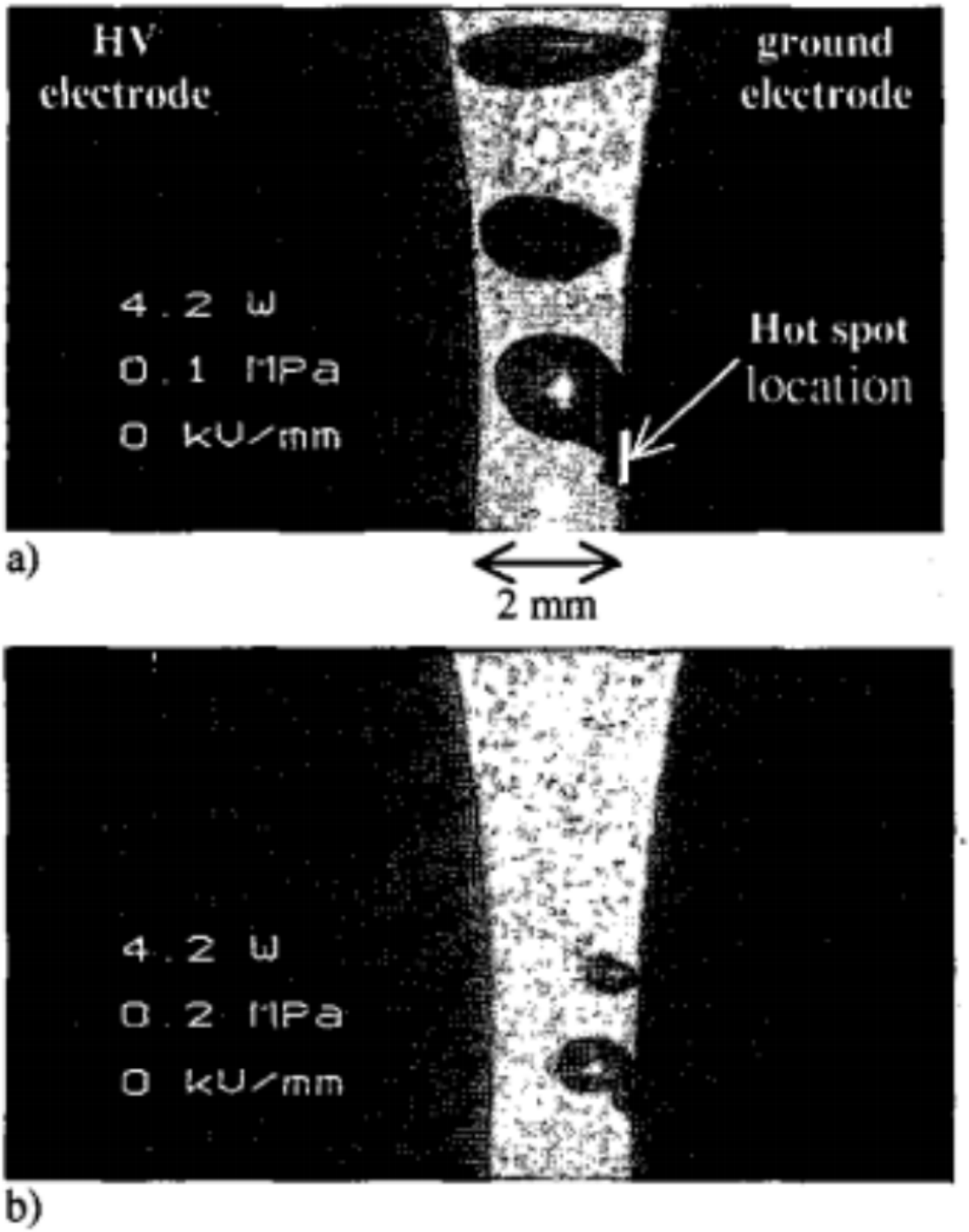

Fig. 4.55 Bubble formation in liquid nitrogen without electric field applied between two electrodes. In this case the heater power is 4.2 W with pressures at: (a) 0.1 MPa, and (b) 0.2 MPa (117).

In the case where the vapour bridge is formed and the pressure is raised while it bridges the gap, then it will form a conical shape. Further increasing the pressure the vapour bridge is reduced to a thin layer on the surface of the hot spot. It was found that the breakdown voltage would reduce as the heater power was increased. This is expected as

it would mean more bubbles are generated on the surface.

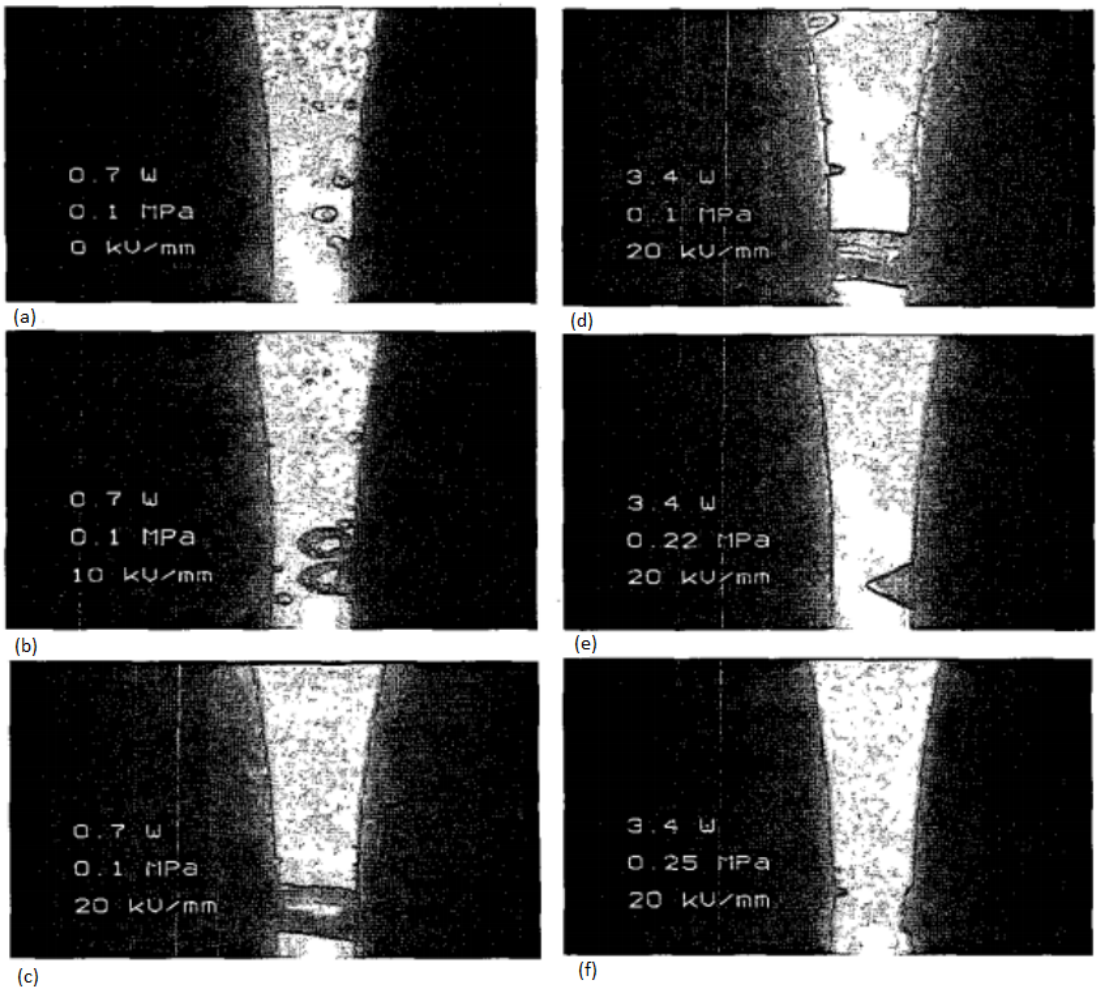

Fig. 4.56 Bubble formation in liquid nitrogen with electric field applied between two electrodes. In cases (a)-(c) the heater power is 0.7 W and pressure of 0.1 MPa, electric field is varied in steps of 10 kV/mm. For (d)-(f) the heater power is 3.4 W and electric field is 20 kV/mm, only pressure is varied. (117).

The breakdown voltage was also found to increase as the applied pressure is increased. This is expected as the higher the pressure the harder it is to generate a large bubbles in the liquid. They found that the breakdown behaviour has two pressure dependent regimes. Between 0.1 and 0.2 MPa a vapour bridge exists and the breakdown value is correlated with the Paschen voltage of gaseous nitrogen in Figure 4.1. At pressures 0.4 to 0.5 MPa a thin vapour layer on the heater is present, which is about 0.1 mm thick. It was determined that a breakdown occurs in this thin gas layer which then triggers a breakdown across the whole gap.

The results found here are similar as those by Hara (114). Both experiments demonstrate that there are two regimes to the bubble formation which is in agreement with Garton

and Krasucki (111). The bubble becomes incompressible after a certain pressure and instead it becomes elongated under the applied electric field to result in a breakdown. Comparing the breakdown voltages, in Figure 4.45 and 4.56, shows that there is a discrepancy between the values, even though the behaviours described are the same. For Hara's data the heater power of 3.2 W, which is comparable to that Hong uses (3.4 W), achieved higher fields for equivalent pressures. The implication is that the condition of the electrode surface could be causing this discrepancy.

Hong finds that the measurement breakdown voltage is lower than that predicted by Paschen's law, but it is unclear if this calculation takes into account the actual pressure in the vapour bridge rather than using the external pressure applied.

LHe can form bubbles at 4.2 K and also below the superfluid transition temperature. If the bubble is formed then has been experimentally demonstrated that it will grow and initiate the breakdown, via a vapour column from one electrode to another in LN_2. The exact mechanism that seeds the initial bubble in the LHe is not clear. As has been previously discussed the breakdown voltage can be limited by impact collisions with impurities in the volume. However, in a purified volume with as little contamination as possible, how is the bubble formed? If the process is the same as that in transformer oil then it will be generated by a sharp point on the electrode. Similar to vacuum breakdown, asperities on the electrode surface will create sharp points. These sharp points could create local spots of heating from the high electric fields which is what could seed the bubble initially.

4.3.3 Pressurising LHe and other liquids

N. Hayakawa et al. (109) also looked at the effect of pressurising LN_2 while bubbles are being generated on the surface with a coaxial and sphere-plane electrode setup.

Hayakawa et al. shows that as pressure is increased there is a sharp increase in breakdown voltage till it saturates (Figure 4.57). From visual observation they state that almost all the bubbles disappeared at these higher pressures and the primary breakdown was due to impurities in the volume instead. The mirror finish results in Figure 4.57 are better than the rough surface finish, which is expected even if impurities are present. The breakdown voltage for the sphere-plane geometry is much higher than coaxial, due to the smaller surface area and volume.

N. Hayakawa compared the data of various other authors on comparable geometries with increasing pressure, shown in Figure 4.59. The results are similar in that as pres-

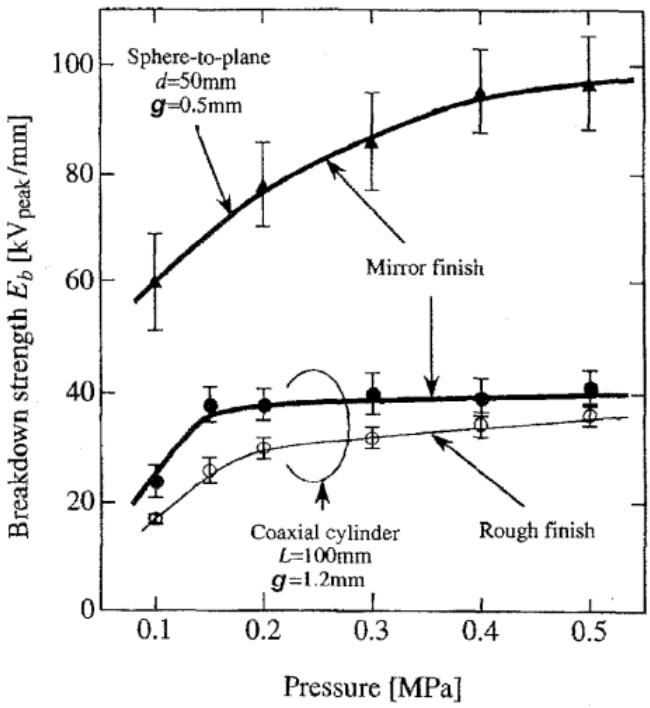

Fig. 4.57 AC breakdown strength, E_b, as a function of pressure for difference electrode conditions (109).

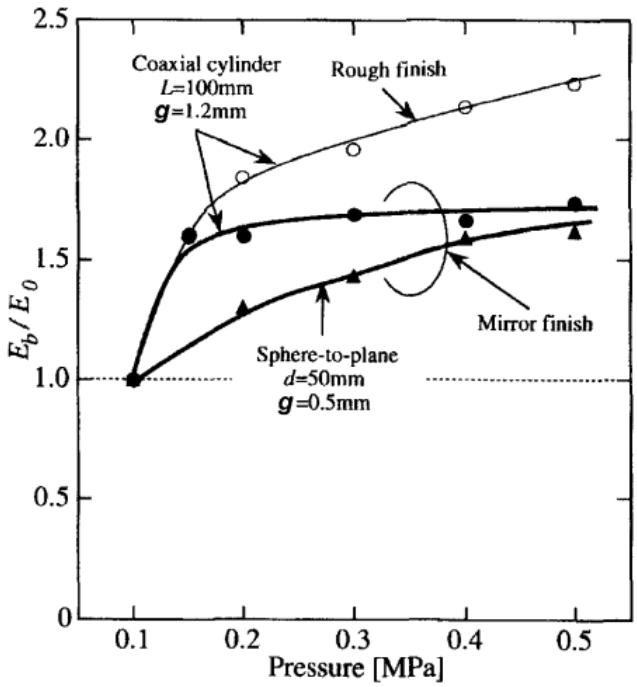

Fig. 4.58 Normalised AC breakdown strength as a function of pressure for different electrode conditions (109).

sure is increased the breakdown voltage increases sharply then saturates at higher pressure. The similar data is evidence that at larger pressures the thermal bubbles are suppressed, with the primary breakdown cause being from impurities instead. It should

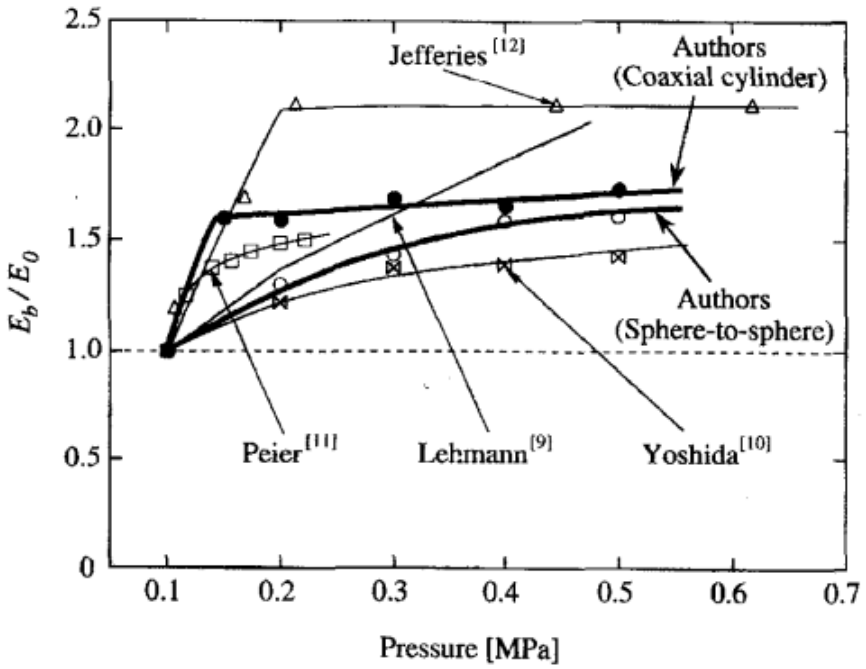

Fig. 4.59 Normalised AC breakdown strength as a function of pressure for various experiments (109).

be mentioned that Hayakawa's results is limited in its scope for discussing possible breakdown processes. In LN_2 the emission of bubbles causing breakdown is not the only process for breakdown to occur. Evidence from previously discussed experiments suggest that electrons can also travel through the fluid in LN_2, therefore, electron emission can also influence breakdown which may be why the saturation at higher pressures.

Blaz et al. (118) investigated pressurising LN_2 in order to reduce bubble size for HV applications. In order to do this, breakdown measurements were performed on two Rogowski profile electrodes with the pressure of the system being varied from 3 bar to 5 bar. The electrodes were ϕ 108 mm with a homogeneous region of ϕ 40 mm, with electrode separation being able to reach up to 25 mm.

Prior to the measurements the system was conditioned with several breakdowns; this conditioning data was not used in the results.

The parallelism of the electrodes was confirmed from the distribution of the resulting craters, scattered randomly across the surface. The craters observed would range in height of about 20 μm. They state that the roughness did not seem to effect the discharge behaviour permanently, though they do comment that after a breakdown the following breakdown voltage would be lower but then recover after that. Blaz states that this is due to protrusions on the surface resulting from the previous breakdown being

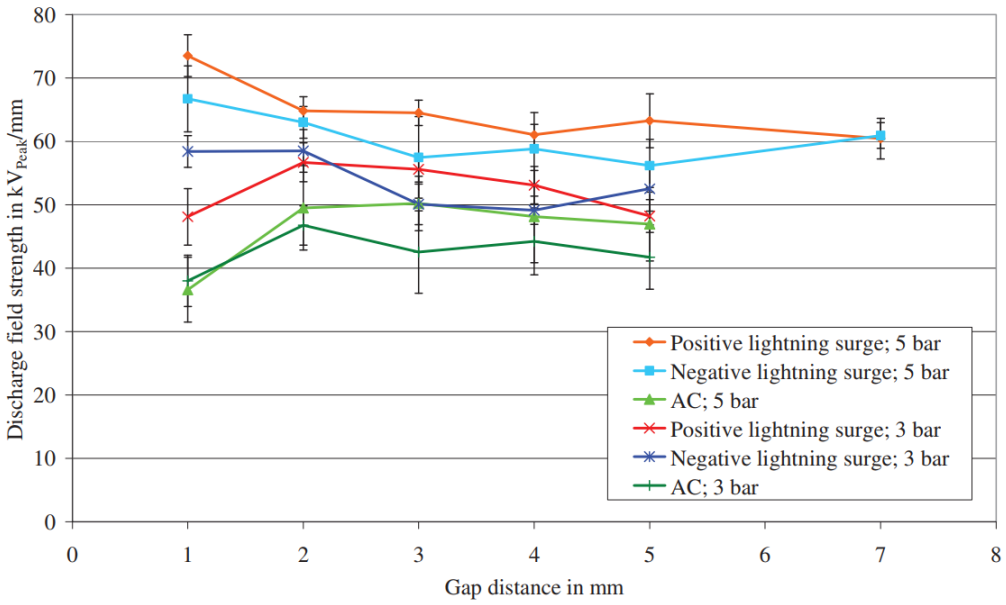

Fig. 4.60 Breakdown field strength for increasing gap lengths at ambient pressures of 3 and 5 bar (118).

vaporised.

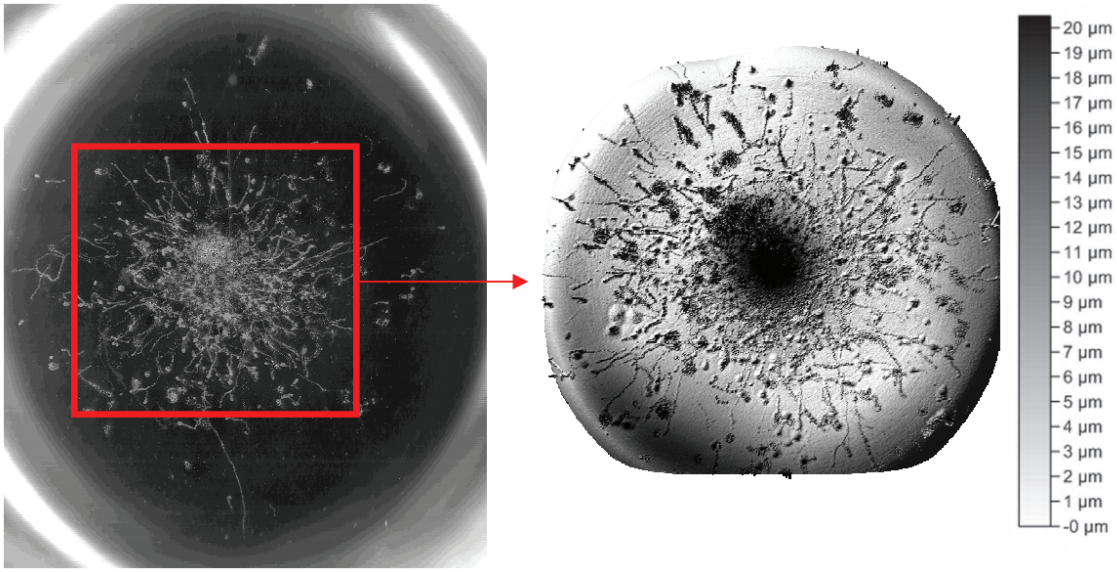

Fig. 4.61 Picture of the homogeneous part of the electrode after breakdown measurements (left) and height profile of the electrode (right) (118).

Blaz also states that in the first measurements, particles were present on the surface of the electrode which could have lowered the results, however, after the following measurements no particles were observed again.

Blaz concludes that upon pressurising breakdown voltage is increased by 15%, as seen in Figure 4.60.

In a follow up paper, Blaz et al. (119), investigated breakdown voltages using the same pressures in LN_2 with a heater to generate bubbles. The heater, supplying constant power, is added to the ground electrode.

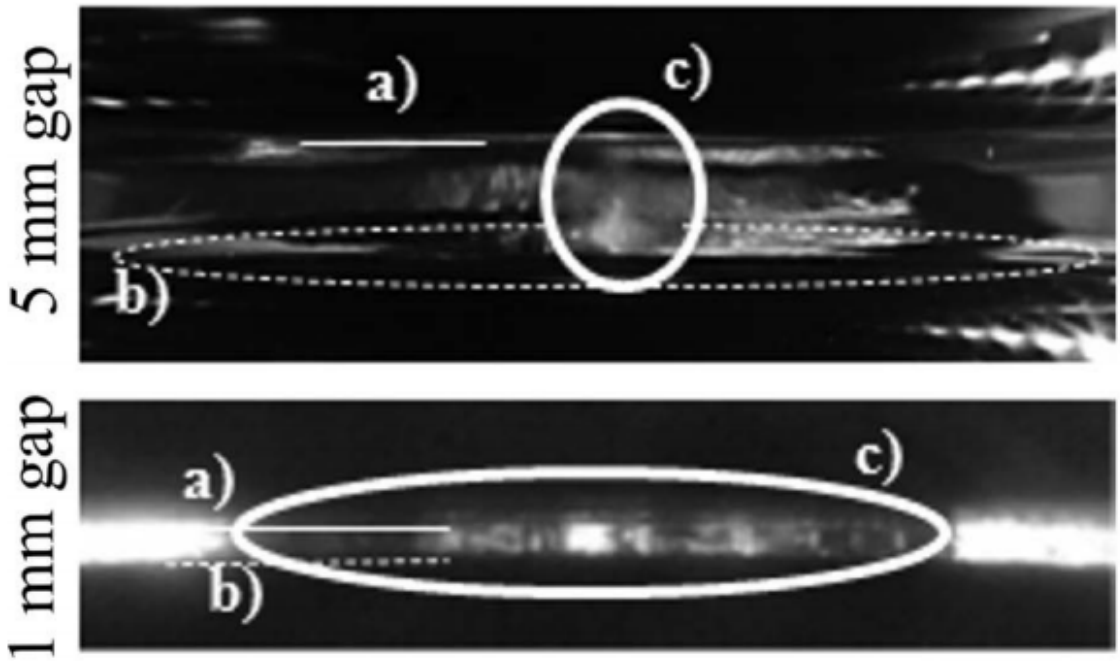

Fig. 4.62 Electrodes setup with bubbles being generated from the bottom electrode from a heater. (a) upper HV electrode, (b) bottom ground electrode, (c) thermally induced gas bubble (119).

The amount of gas bubbles between the electrodes depends on the ambient pressure of the nitrogen and the gap separation, see Figure 4.62. Decreasing the pressure of the volume causes the bubbling to increase, while if the gap is reduced the voltage will decrease due to larger vapour column between the electrodes. The results of the experiment show that with bubble generation the discharge field strength at 3 bar is reduced to 32%-50% of the value without bubbles and at 5 bar it is reduced to 43%, as can be seen in Figure 4.63 and 4.64.

Blaz suggests a model for breakdown behaviour by assuming the discharge field strength will be similar to that of a cryogenic gas. This is calculated from Paschen's law:

$$E_d = \frac{U_d}{2 \cdot r} = \frac{B \cdot p}{ln \frac{A \cdot p \cdot 2 \cdot r}{k}}, \tag{4.7}$$

where p is ambient pressure, r is the radius of the bubble ~ 500 μm, k is the Townsend coefficient of values 2.5 and 18 across the discharge path, $A = 510$ bar^{-1}mm^{-1}, and $B =$

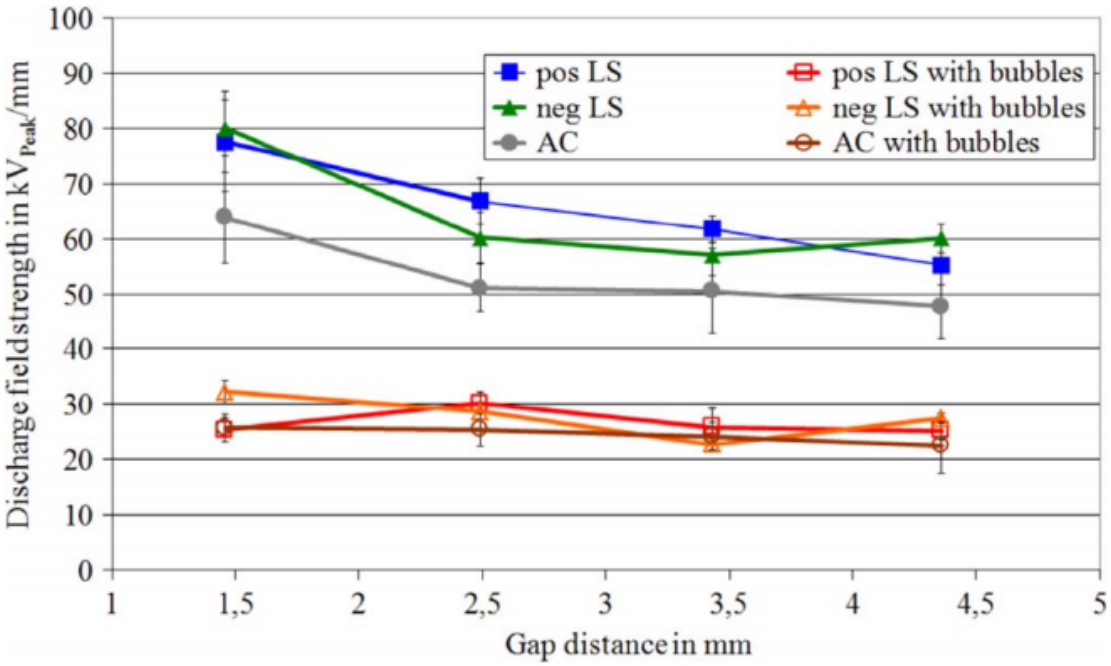

Fig. 4.63 Breakdown field strength at 3 bar for positive and negative lightening surge and AC ramp, with and without thermal bubbles (119).

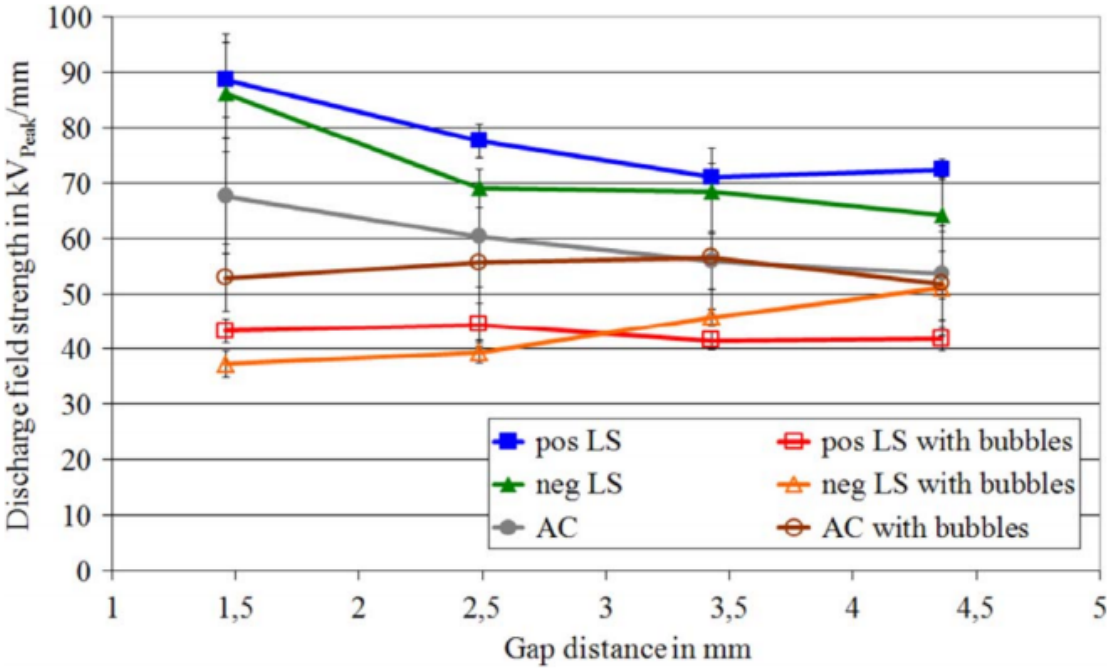

Fig. 4.64 Breakdown field strength at 5 bar for positive and negative lightening surge and AC ramp, with and without thermal bubbles (119).

19.65 kV bar^{-1}mm^{-1} are for nitrogen gas. Temperature is not taken into account in this calculation although the density of the gas is instead, as this will be higher for cryogenic gases, giving a value of 11 bar for p_{flc}.

$p_{ambient}$ in bar	T_{Gas} in K	p_{flc} in bar	Calculated E_d k = 2.5	in kV/mm for k = 18
3	87.9	11	28	37.6
5	94	17.9	43.9	56.5

Table 4.1 The field strengths are calculated for a bubble with a radius of 0.5 mm using Equation 4.7.

Blaz performed a calculation of the electric field enhancement of the bubble compared to the homogenous field in the liquid:

$$E_{bubble} = E_0 \frac{3 \cdot \epsilon_{rLN_2}}{\epsilon_{rN2} + 2 \cdot \epsilon_{rLN_2}}, \tag{4.8}$$

where ϵ is the permittivity of the gas or fluid. In the homogenous field region the electric field is 25 kV/mm, therefore, using Equation 4.8 the field strength in the bubble is 27.8 kV/mm. This is comparable to the calculation of the breakdown field strength in Table 4.1 at 3 bar, assuming an ideal sphere.

In Figure 4.64 for the negative polarity measurements it shows that the breakdown voltage is rising continuously and will have a discrepancy compared to the positive at 5 mm. Blaz states that an explanation for this polarity effect could be space charges in the gas bubble. For a positive electrode there will be positive space charges in the bubble on the cathode surface (heater electrode). Positive space charge is caused by faster movement of the electrons, due to higher mobility in the gas. If the charge is high enough it will create a field enhancement creating secondary electrons till breakdown occurs.

For the negative polarity, positive space charges are created due to discharges in the bubble which weakens the field strength. Then, these positive ions have to travel through the liquid phase which will take a long time, due to low mobility, till it hits the electrode to generate secondary electrons. Therefore, it's stated that this can only occur if the streamer criteria is met.

The issue with Blaz's explanation of the charge carriers in the vapour column is the bottom electrode has no charge unless positive voltage is applied to the upper electrode, therefore, in the case of negative voltages the breakdown process should only occur when the bubble has sufficiently bridged the two electrodes, hence the delay. While for the positive breakdown the charge is built up within the bubble till the breakdown field strength (as it will be lower in a gas) is exceeded, leading to a breakdown.

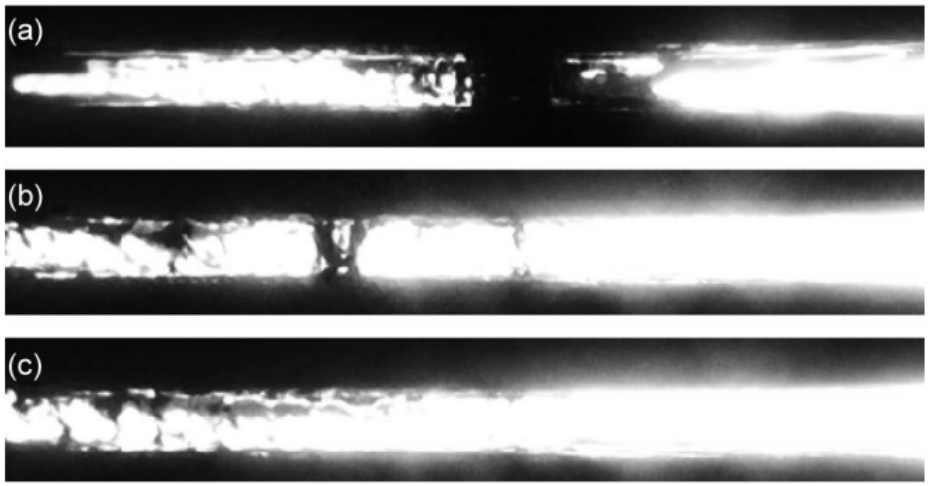

Fig. 4.65 Thermally induced bubbles at a 2 mm gap, with (a) no voltage applied, (b) and (c) 10 kV RMS applied to the gap. The picture seems to show that electrostrictive forces move the bubbles to the left of the gap.

The AC voltage breakdown data presented at 5 bar shows that at larger gaps the values are even the same without bubbles. The reason for this is attributed to electrostrictive forces which move the bubbles to areas of lower fields. This seems to occur as the permittivity of the gas is lower than that of the liquid, therefore, the bubbles move to regions of lower fields while the liquid will move towards regions of higher fields.

Blaz et al. presents some interesting results on pressurised liquid nitrogen at small gaps. The bubble dynamics involved at higher pressures it more complex than initially realised due to additional forces from electrostatic contributions.

4.4 Studies of HV breakdown for cryogenic nEDM experiments

4.4.1 Davidson - Pressure dependence of breakdown in LHe

Previous high voltage breakdown measurements in LHe shows a drop off by about a factor ~ 2-3 as temperature of the fluid is lowered below 4.2 K to ~ 1 K (93). This is problematic for a cryogenic nEDM experiment as the LHe bath needs to be at 0.5 K. However, the previous measurements all lowered the LHe temperature by pumping on the bath, which also lowers the temperature. Therefore, Davidson (2) investigated the cause of this drop off in breakdown voltage. The setup consisted of a cryostat in which an insert is placed. The insert consists of a pressure cell containing the electrodes in superfluid tight LHe bath, shown in Figure 4.66 and 4.67. During the experiment the cryostat is filled with LHe, the pressure cell is submersed and thermally anchored to the

bottom of the cryostat. At the same time the pressure cell is filled. The pressure cell is held of the bottom of two pipes which hold the HV feeds, these are evacuated. On the bottom of the pipes are vacuum feedthroughs with one attached to the HV and the other to ground electrode inside the pressure cell. The electrode setup is a Rogowski profile with spacerless plane-plane geometry using a separation of 1.27 mm to 2.9 mm. The ground electrode is held off one of the pipes via a G10 support structure. The ground is then connected to a return line on the other pipe containing another HV feed from 4.2 K to room temperature. Davidson performed breakdown measurements in this experimental system as a function of pressure with fixed temperature between 1.7 K and 4.2 K.

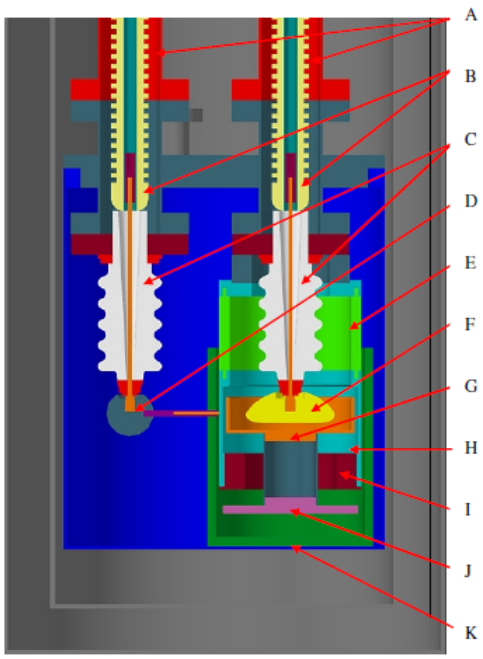

Fig. 4.66 AutoCAD model of Davidson's pressure cell. A - HV feed vacuum tubes, B - HV feeds, C - ± 30 kV commerical ceramic feedthroughs, D - Return line ball connector, E - G-10 middle section of the pressure cell ground electrode support, F - HV Rogowski profile electrodes, H - Lower section of the pressure cell ground electrdoe support structure, I - ground electrode positioning ring, J - ground electrode positioning plate, K - Insulating PTFE bucket (2).

Davidson found that the general form for breakdown voltage at constant temperature is that it will increase with increasing pressure. However, there are two regimes; at lower pressure just above SVP a rapid increase in breakdown voltage is observed (region 2), while at higher pressures breakdown voltage increases gradually (region 1), this can be seen in Figure 4.69. The point at where this transition occurs is labelled the pressure kink.

Fig. 4.67 The pressure cell without the outer can (2).

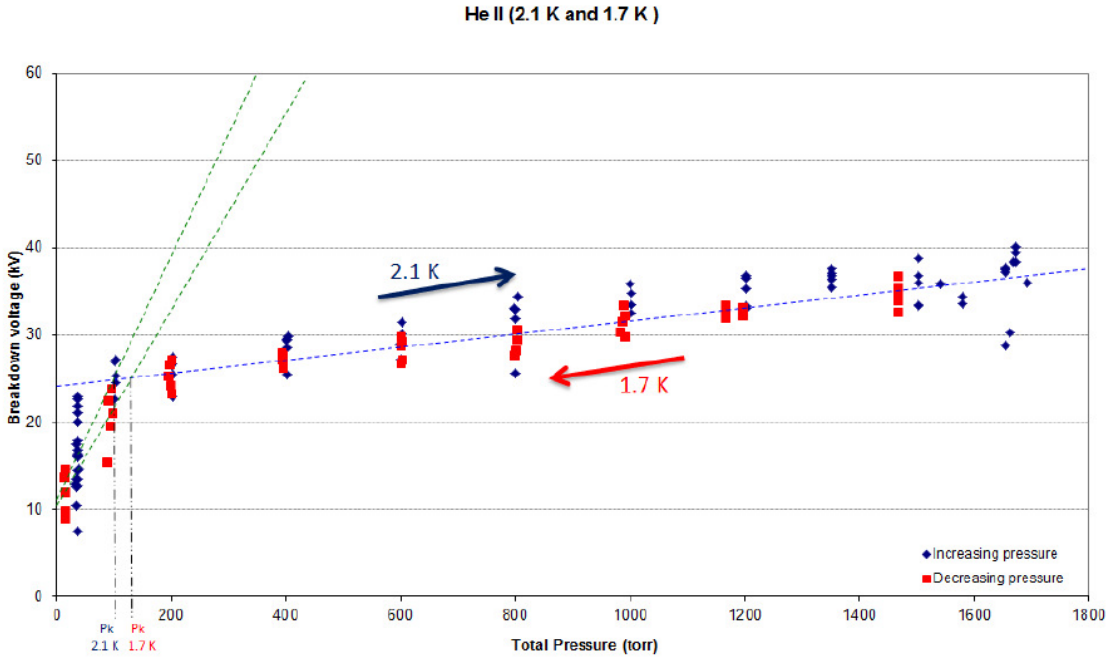

Fig. 4.68 Breakdown voltage as a function of pressure at 2.1 K and 1.7 K. Green dashed lines are the region 2 regime for two different temperatures, and the blue dashed line is region 1. Black dashed lines indicate the pressure kink. Arrows are the pressurisation direction as function of time (2).

These measurements were taken over a wide pressure range from 1200 to 100 torr intervals of about 200 torr. The measurements were taken while increasing and decreasing the pressure. The data points lie in the same place whether pressuring or de-pressuring.

Davidson's electrodes took about ~1165 breakdowns for the majority of the experiment. This resulted in a a decline in the mean breakdown voltage as seen in Figure 4.71.

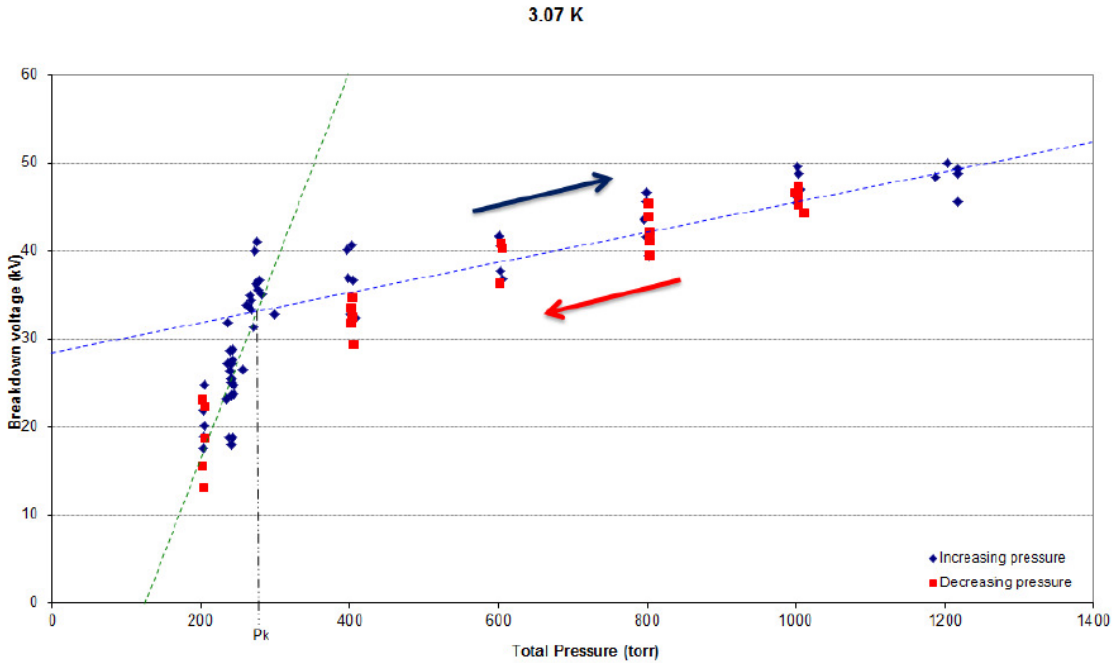

Fig. 4.69 Breakdown voltage as a function of pressure at 3.07 K. Green dashed lines are the region 2 regime for two different temperatures, and the blue dashed line is region 1. Black dashed lines indicate the pressure kink. Arrows are the pressurisation direction as function of time (2).

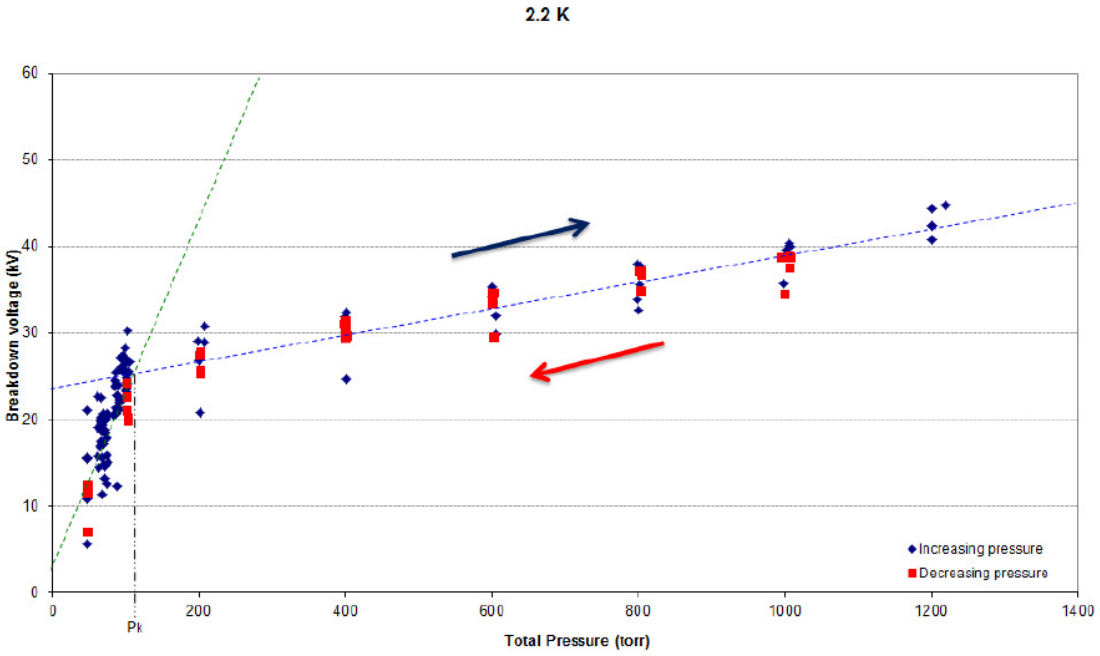

Fig. 4.70 Breakdown voltage as a function of pressure at 2.2 K. Green dashed lines are the region 2 regime for two different temperatures, and the blue dashed line is region 1. Black dashed lines indicate the pressure kink. Arrows are the pressurisation direction as function of time (2).

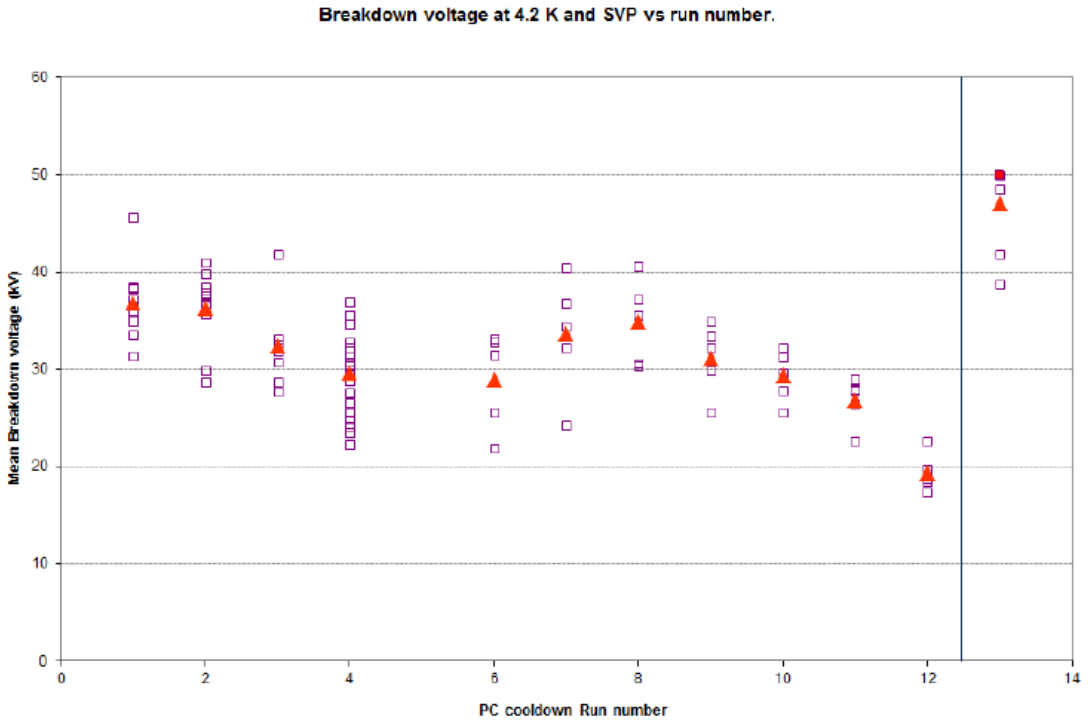

Fig. 4.71 Mean breakdown voltage as a function of pressure cell run number. Orange triangles are the mean values and pink squares are the breakdown events. The black line is where the electrodes where polished (2).

Upon inspection after the first 8 runs, the electrodes were found to be not completely parallel with one side being 1.84 mm and the other 1.61 mm at room temperature. Observing the condition of the electrodes after removal showed significant damage to the surface in the form of cratering. The fact that the electrodes were not parallel was clear as the breakdowns tended to be more to one side of the electrode surface. The decreasing mean breakdown over time is thought to be due to the increasing roughness of the electrode surface from breakdowns. The breakdowns leave craters as the material is heated with particles ejected into the volume. This also leads to an increasingly impure volume surface which is well known to limit the breakdown voltage.

Davidson presents a model for the cause of the reduced breakdown voltages observed in his experiment. The normal method for lowering the temperature of LHe bath involves pumping on the system which reduces the pressure. The primary process for breakdown in LHe, that Davidson presents, is from initiation of a bubble from local heating on the electrode surface. This creates a seed bubble which is uncharged. The vapour within the bubble is then ionised from the high electric fields and this then causes it to elongate to the anode. A streamer is then created and this results in a full breakdown.

The reduction of pressure from pumping to get to lower temperatures for LHe means that the size of any vapour bubble within the fluid can have a larger volume due to lower hydrostatic pressure of its surface than at 4.2 K at SVP, hence why breakdown voltage is limited.

Pressurising the fluid then should reduce the size of the bubble formed during the initiation process. However, this alone does not explain why there are two regimes. In Figure 4.68 where the breakdown voltage rises rapidly with increasing pressure (region 2) is argued to be occurring due to the applied hydrostatic pressure which limits the diameter for which the bubble can form. After the pressure kink the applied pressure no longer becomes the predominate process that limits the breakdown values. Davidson argues that the pressure caused by electrostriction becomes the more predominate effect. Such high electric fields cause the ionised bubble to elongate with increasing pressure having a diminishing return. This can be explained by Equation 4.5 from Graton and Krasucki (111).

It should be stated that this was done without the presence of an insulator. The addition of an insulator, which will be discussed later, potentially results in a different source of breakdown which limits the achievable voltage. However, if the problem of the insulator limitation can be mitigated or overcome then it is been demonstrated that pressurising LHe at any temperature below 4.2 K will recover the breakdown value back to that 4.2 K , or potentially exceed it.

4.4.2 Long - Area and volume dependence of breakdown in LHe

In a study by Long et al. (1) as an initial HV test for the SNS nEDM collaboration they performed measurements in LHe on large scale electrodes (ϕ 45.8 cm). The primary goal was to test the effectiveness of the high voltage multiplication method for SNS nEDM as well as the lower limit on the dielectric strength of LHe. A big problem for SNS is how to achieve ~100 kV/cm in LHe without using massive feedthroughs to deliver ~ 600 kV which could transfer large amounts of heat to the LHe bath. Therefore, they originally planned to achieve high voltages by adjusting the capacitance of the system in-situ,

$$C = C_1 + C_2 = \frac{Q_1}{V_1} + \frac{Q_2}{V_2}, \tag{4.9}$$

for capacitors in parallel, where C_1 is the capacitance on one electrode pair and C_2 is the capacitance on the other. If the charge $Q_1 = Q_2$, then as the capacitance is proportional to the voltages V_1 and V_2, decreasing C_2 will increase V_1.

The apparatus for the experiment consists of a two cylindrical electrodes, mounted hori-

zontally on the central axis in a LHe tank. The electrodes are made of hollow aluminium shells. The HV electrode is fixed by G10 stand-offs, while the ground electrode is fixed by an aluminium rod to bellows allowing horizontal displacement. The HV electrode is charged by a smaller (ϕ 7.6 cm) moveable solid aluminium electrode which is connected to a commercial 40 kV ceramic feedthrough through vacuum. This then connects to a 100 kV commercial ceramic feedthrough to atmosphere. The inside of the LHe tank is 66 cm and 44 cm long to hold a LHe volume of 180 L.

The separation of the HV and ground electrode can be adjusted from 0 to 10 cm while the HV to the charger electrode can be adjusted from 0 to 7 cm. The separations can be determined visually through a series of 5 cm quartz view ports in the side walls of the central volume and vacuum chamber.

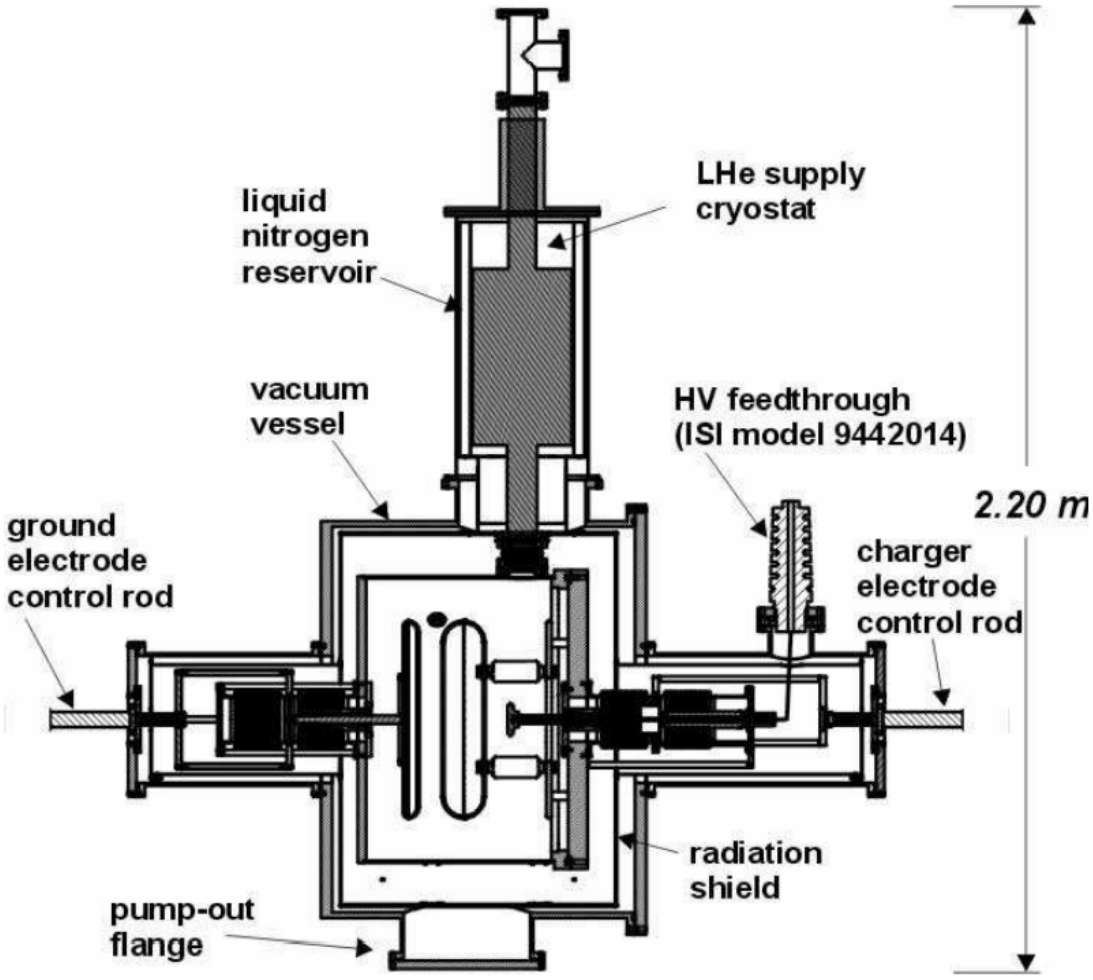

Fig. 4.72 Assembly drawing of the LANL HV test system (1).

The electric field is determined by using the charger electrode as a capacitive probe of the voltage between the HV and ground electrode. In an initial amplification measurement the charger electrode is at 50 kV while in contact with the HV electrode. The ground electrode is retracted to 2-3 mm from the HV electrode for reference. The stability of the field on the two electrodes is achieved after several sparks occurring across the gap which was attributed to conditioning behaviour of the system after which, it reached 50 kV. At this point the voltage amplification can begin. The charger electrode is retracted from the HV electrode to a reference position several centimeters away, then switched from the power supply to a sensitive current amplifier. The ground electrode is then retracted which causes a change in capacitance, amplifying the voltage on the HV-ground electrode gap. Long uses the charging current to estimate the capacitance of the system in order to measure the voltage between the HV-ground electrode gap, as seen in Figure 4.73.

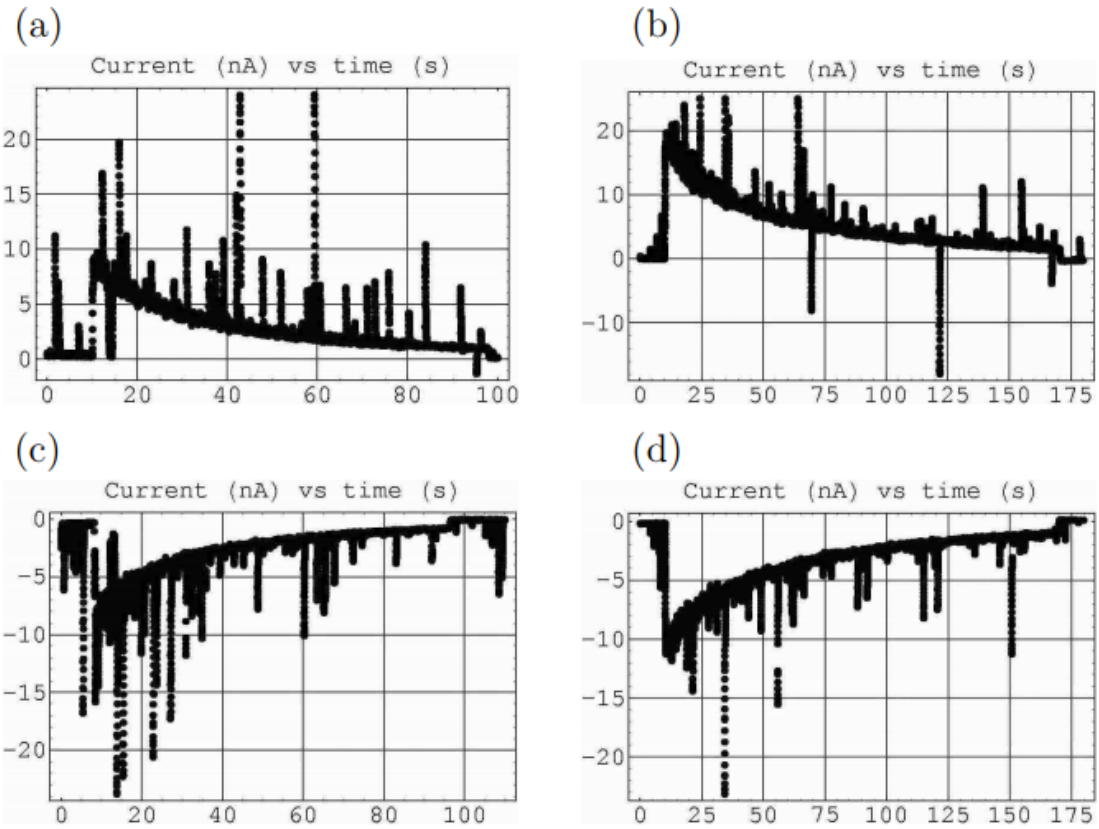

Fig. 4.73 Current (nA) vs time (s) for various runs. (a) LHe at 34.5 torr (2.14 K), initial gap 2.9 mm, potential 13 kV. (b) LHe at 880 torr (4.38 K), initial 3.0 mm, potential 42 kV. (c) LHe at 31.9 torr (2.11 K), initial 3.0 mm, potential -11.5 kV. (d) LHe at 654 torr (4.06 K), the initial gap 3.1 mm, potential -31 kV (1).

These sweeping measurements of the ground electrode were performed for LHe I and LHe II at various temperatures. Long compares his measurements with this system to past data on breakdowns in LHe for different electrode separations. The measurements recorded were the maximum voltages his system was able to achieve using this amplification method; no breakdowns were observed after conditioning.

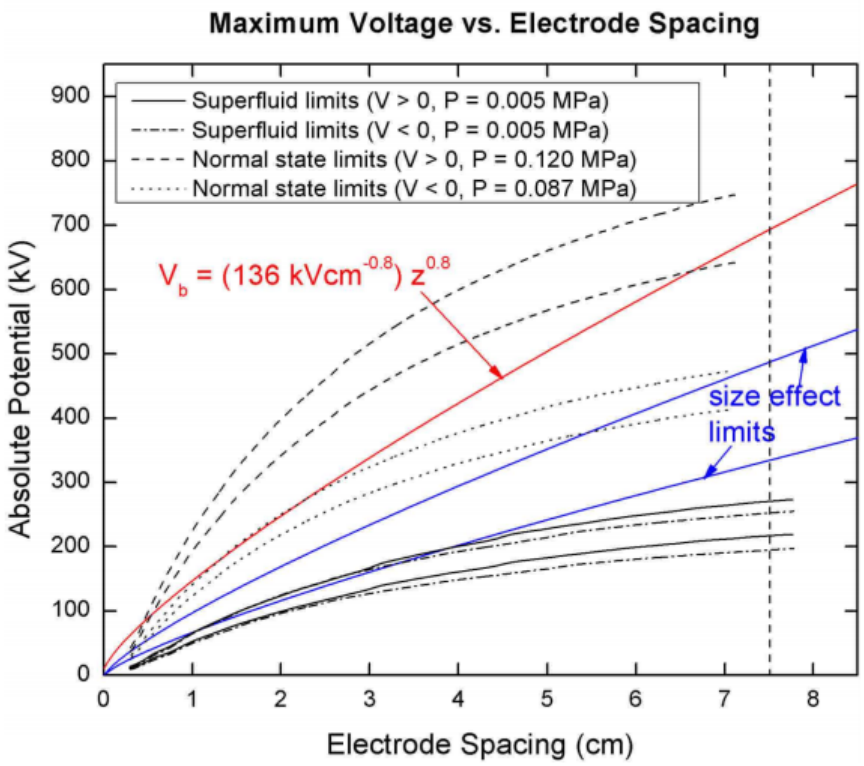

Fig. 4.74 Voltages obtained in HV test system as function of electrode separation. Red and blue curves are extrapolations from Gerhold (120). Black lines are the range within 1-σ error bars for voltages obtained under those conditions stated in the legend (1).

From the determination of the capacitance and charging current the largest positive voltages attained are:

- 240^{+34}_{-14} kV (7.8 cm in LHe II at 2.10 K).
- 688^{+58}_{-41} kV (7.2 cm in LHe I at 4.40 K).

The largest negative voltages:

- - 215^{-37}_{+13} kV (7.8 cm in LHe II at 2.08 K).
- - 443^{-31}_{+27} kV (7.2 cm in LHe I at 4.00 K).

The pressures at which these values are performed are given in Figure 4.75.

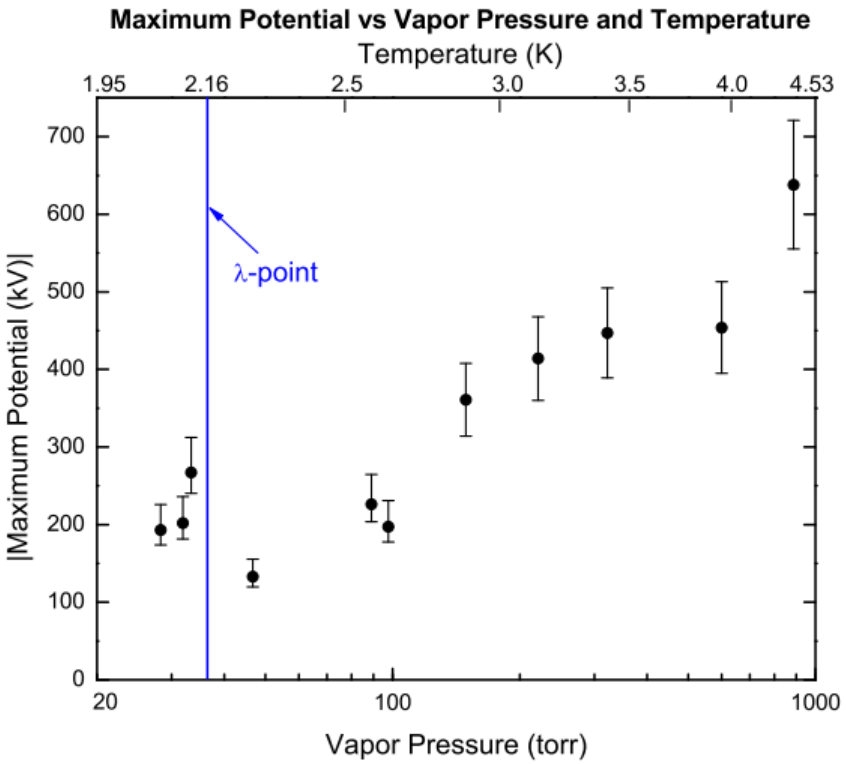

Fig. 4.75 Maximum voltages achieved in the LANL HV test system as a function of pressure and temperature (1).

This is one of the largest scale measurements on high voltage breakdowns in LHe, giving an indication of what voltages can be expected. However, there are a number of problems with the way this experiment not only presents it results but also measures them.

The biggest problem with this voltage amplification method is that it requires precise knowledge of the capacitance of the system, otherwise the voltage cannot be calculated accurately. Long does not take into account the capacitance of the HV electrode to the cryostat walls, which could have values of similar order to that of the moveable ground electrode. This could significantly alter the values determined in the results.

Another issue is that the current is only monitored on the HV charger and ground electrode. Though it is highly suppressed for free charges to flow in LHe the current could move on surfaces much more easily than through the volume, hence current could creep down the G10 stand-offs; this could then be missed when determining the charging current or it might explain the transient currents observed.

There is also the problem of the lack of observed breakdowns. Long's data is attributed to be the maximum electric field maintained within the system but fails to state this if this was because breakdown occurs after achieving this field or not. It could be

that the maximum electric field was achieved, then breakdown occurred but due to the presence of the ballast resistor it limited the energy, hence no spark or damage observed.

The pressure dependence on the HV breakdown is noted upon which is in agreement with Karamath (93) and others observed before Davidson's study (2). However, the results obtained for both LHe II and LHe I also agree with published data that is extrapolated to these separations. However, it would be expected to observe a more substantial drop off for such a large surface area and volume.

4.4.3 Ito - Electrical breakdown measurements in LHe at 0.4 K in mock Ramsey cell

In this paper (64) the SNS nEDM collaboration built and tested an apparatus to study DC electrical breakdowns in LHe at 0.4 K to investigate various parameters for the nEDM experiment. The parameters cover requirements for the sensitivity such as: non-magnetic material investigations, leakage currents in LHe, and dielectric strength of superfluid helium at 0.4 K.

The system constructed consists of a cryostat with a central chamber inside containing the electrodes within the superfluid volume. The high voltage is delivered by two 100 kV commercial feedthrough from atmosphere to 50 kV commercial feedthroughs at 77 K in vacuum. These feedthroughs connect to another at 4.2 K and then a third at 0.4 K. The reason for multiple connections with HV is to ensure proper heat sinking to avoid bubble generation. The use of two feedthroughs means positive voltage can be applied on one electrode and negative in the other for twice the electric field. The central volumes at pressure can be varied from SVP to ~ 600 torr in order to investigate any pressure dependence on the high voltage breakdown. The complete setup is given in Figure 4.76.

The electrodes were designed with a Rogowski profile to ensure the maximum electric field is between the plane-plane surface and not at the edges. The electrodes in this experiment are 12 cm in diameter and can be adjusted to be 1 cm to 2 cm separation between them. At the maximum applied voltage it gives a field of 100 kV/cm at 1 cm separation.

Initial tests used stainless steel electrodes as this is known to give the highest E fields when electro-polished. The electrodes are supported in a horizontal position and remain there to about ~ 0.1° when cooled. The second tests were performed with a PMMA insulator within a stepped groove present between the two electrodes. The size of the

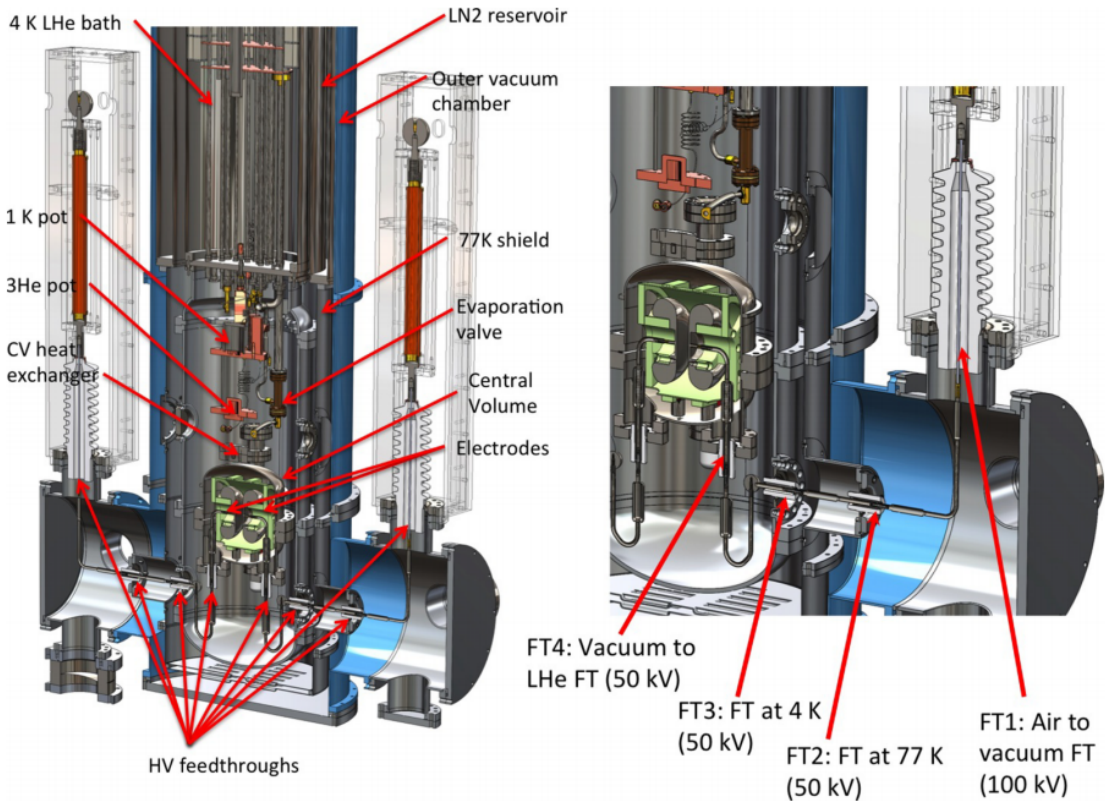

Fig. 4.76 Schematic of the MSHV system (64).

insulator is 6.35 cm OD and 5.08 cm ID. The geometry was optimised in COMSOL to lower the high field regions at the stepped groove where the insulator was placed. They found that high fields are present if the groove of the electrode is too close to the spacer wall. By having a small groove radius this would exacerbate the problem, while a very large radius does not sufficiently protect the high fields at the CTJ, hence compromise was determined.

The HV was applied at rate of 0.5 kV/s or less and paused every 5 or 10 kV. Their initial tests indicated that the performance of the HV feedlines was limiting the applied voltage to ~ ± 40-50 kV. They assume this is occurring in the cryostat from the 50 kV feedthroughs. They never observed any evidence of breakdown on the electrodes with or without grooves and with or without the presence of the PMMA insulator. For the case with the electro-polished Rogowski electrode, without the groove, they achieved 105 kV across a 1 cm gap for a wide range of pressures and temperatures, while with the other electrode with grooves they were able to achieve 80 kV stably over the 1 cm gap. The discrepancy here is attributed to the different setups for the HV feedlines. The data is presented in Table 4.2.

The leakage current of the system was also monitored. This was done by charging

Configuration	Temperature	Pressure	Highest achievable stable field
SS Rogowski electrodes	2.5-2.8 K	72 torr, 90 torr, 785 torr	90 kV/cm
SS Rogowski electrodes	1.1 K	13 torr	90 kV/cm
SS Rogowski electrodes	0.42 K	SVP, 664 torr	105 kV/cm
SS electrodes with a groove without the PMMA insert	2.7 K	620 torr	70 kV/cm
SS electrodes with a groove without the PMMA insert	0.5 K	1.0 torr, 620 torr	80 kV/cm
SS electrodes with a groove with the PMMA insert	2.1 K	614 torr	50 kV/cm*
SS electrodes with a groove with the PMMA insert	0.5 K	SVP, 2.7 torr, 574 torr	80 kV/cm

*Higher voltages were not tired.

Table 4.2 Summary of electric fields achieved in the test setup. In all cases the gap was 1 cm with the highest achievable stable fields stated to be the limitation of performance (64).

up one electrode to 45 kV then monitoring the current on the other electrode using a picoammeter. It is thought that there will be very little charge flowing through LHe as this is suppressed by the electron bubble process. However, the current flowing through the feedthroughs and cables contribute to leakage current and this is likely to be more significant. The measured current was less then 1 pA, although this was limited by the monitoring device.

The paper shows that they clearly demonstrate achieving 100 kV/cm in a 1 cm gap with 12 cm electrodes. However, the voltage is slightly lower for the same gap but with an insulator present. Ito states that the problem of the CTJ is suppressed in LHe due to the properties of the fluid, however, from these results it potentially shows that this may not be the case.

In this measurement there was a high voltage 1GΩ resistor between the 100 kV feedthroughs and the power supplies which will limit the discharging current in the process of a breakdown. This slower dumping of energy into the breakdown could be the reason why there is no evidence of damage on the electrode surface, therefore, it is not entirely clear that the HV feedlines could indeed be the limitation. But, there was no HV correlation when different pressures were applied, regardless of pressures they were still able to achieve the same electric field (in both cases, with or without the insulator).

The odd result from this experiment is that higher stable electric fields were achieved with lower temperatures. This could be occurring as the measurements in this paper are taken close to the λ transition, as the liquid helium approaches this it will bubble much more frantically which could explain why the electric fields are lower. There could also be a contribution here from conditioning of the HV feedlines/electrodes which is why the highest electric fields occur at the lowest temperature.

4.5 Surface flashover in cryogenic liquids

4.5.1 Introduction to breakdown with insulators present

The storage of UCN in a bottle requires walls to contain them, so for a nEDM experiment the presence of an insulator to separate the electrodes and contain those UCN is essential. This, however, creates a new problem the presence of the cathode triple junction (CTJ), which is where the interface of the electrode surface, insulator, and insulating medium meet.

It is well known that in a vacuum the electric field achievable is of order MV/cm, however, the presence of the insulator limits this field to kV/cm range. The mechanism of this process has been studied extensively for the case with vacuum medium ((81), (82), (121), (122)). The effect is caused by the localised geometric field enhancement caused when two insulators of two different permiFtivities meet at an electrode, as seen in Figure 4.77. This change in permittivity causes the equipotential lines to be pushed into the small free space of the CTJ creating high field regions. It is impossible to overcome as it would require a completely flat electrode and insulator surface, which at some level, is impossible. The field enhancement can initiate a catastrophic breakdown in the form of a surface flash over of the insulator, permanently damaging it.

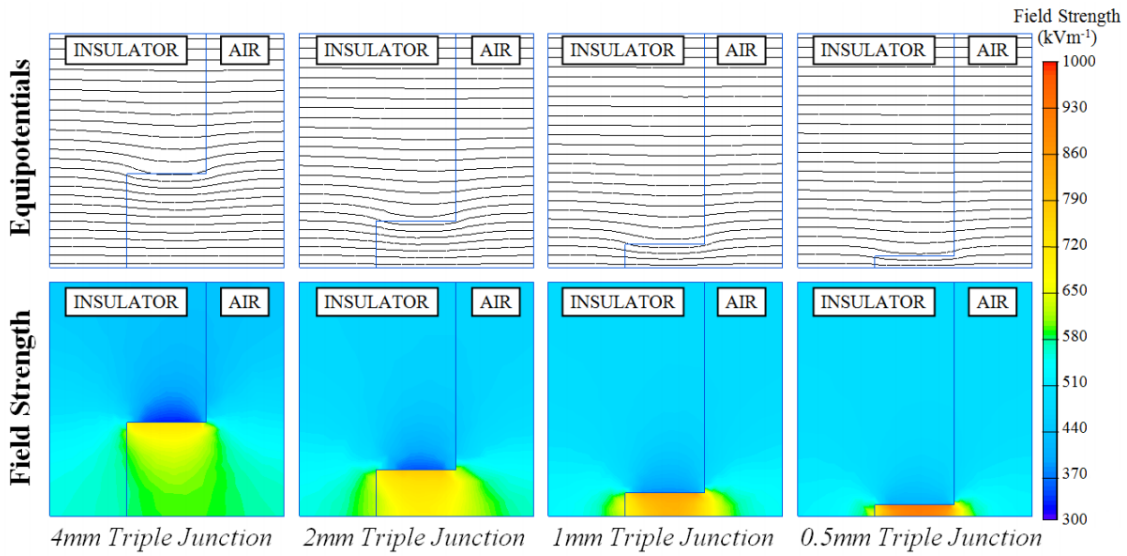

Fig. 4.77 Electric field strength for various sizes of the CTJ (81).

4.5.2 Liquid nitrogen

Rodrigo et al. (123) performed DC and AC breakdown measurements on G10 cylindrical insulators at room temperature in oil and LN_2 at 77 K. The setup consisted of two stainless steel electrodes with a Bruce profile (124) with a diameter of 25 mm. The G10 used was of different diameters, 9.5 mm, 12.7 mm. and 19 mm. Each diameter was cut to 5 mm in height. After each breakdown measurement the electrodes and the insulator were replaced. The oil was also replaced, however, the LN_2 was just topped off between each measurement. The results were formulated using Weibull statistics likelihood of a breakdown occurring at 63.2% time at that given value, shown in Figure 4.78 and 4.79.

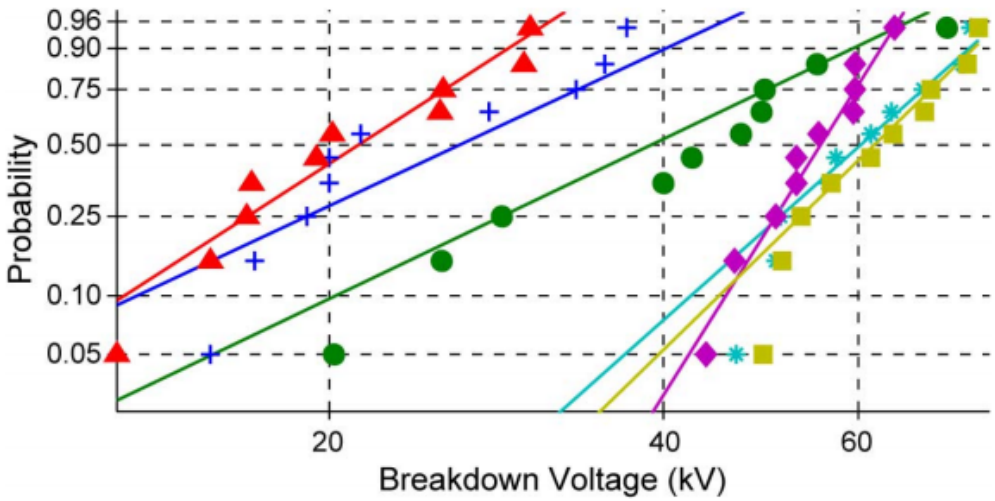

Fig. 4.78 Weibull plots for AC measurements: blue cross - 12.7 mm at 293 K, green circle - 19 mm at 293 K, red triangle - 9.5 mm at 293 K, light blue star - 12.7 mm at 77 K, yellow square - 9.5 mm at 77 K, purple diamond - 19 mm at 77 K (123).

The change of relative permittivity of the G10 from 4.6 at 77 K to 5.7 at 293 K is attributed to the change in breakdown values. The permittivity of the fluid is also different 1.4 for LN_2 and 2.7 for transformer oil. The field enhancement at the CTJ can be affected by the angle at which the insulator rests between the two electrodes. This field enhancement is stated as a source of electron emission and leads to corona discharge, eventually causing breakdown across the gap. It is stated that, because of this, positive and negative ions attach onto the surface of the insulator.

The two smaller insulators were in the completely flat region of the electrodes while the larger 19 mm one extended over the edge of the profile. This leaves a small crevice where the electrode begins to slope away between the G10 and electrode surface. Rodrigo states that the highest field is not at the electrode to insulator surface but a small distance along the electrode profile, the edge of the insulator causing inference with the electric field.

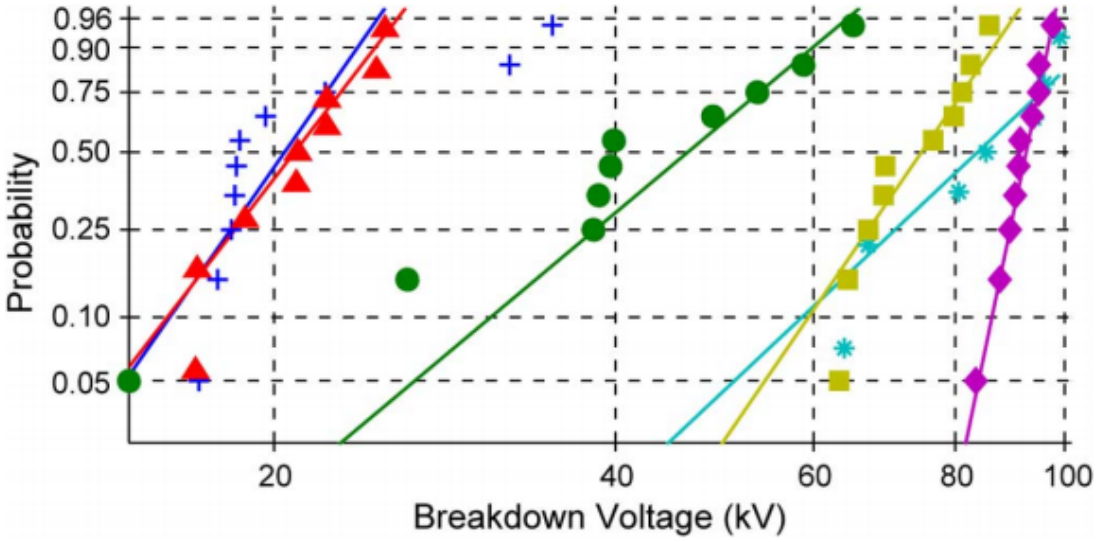

Fig. 4.79 Weibull plots for DC measurements: blue cross - 12.7 mm at 293 K, green circle - 19 mm at 293 K, red triangle - 9.5 mm at 293 K, light blue star - 12.7 mm at 77 K, yellow square - 9.5 mm at 77 K, purple diamond - 19 mm at 77 K (123).

Rodrigo suggests that the breakdown mechanisms are these field enhancements from the CTJ causing corona streamers to develop which eventually forms a spark propagating along the surface of the insulator.

Rodrigo et al. (125) goes further by using epoxy resin samples instead and on two different separations, 3 mm and 5 mm. The same setup is used as stated previously with data presented in Figure 4.80.

Rodrigo goes on to analyses the source of the breakdown mechanism by expanding further on the previous paper, stating that the source is from the misalignment of the insulator creating greater field enhancement of the CTJ. He states that the maximum field will exist on the edges of the insulator which are not in contact with the HV electrode. These results presented go against Miller et al. (122) for the case in a vacuum flashover; as diameter increases the flashover voltage will decrease.

Rodrigo states that misalignment may create a high field region on the insulator but it will still be surrounded by very high dielectric strength insulating material (LN_2) which will suppress breakdowns from that region. The calculations of these high field regions are performed in COSMOL with results given in Figure 4.82. However, these results could be misleading as the CTJ is always the region of highest field. It will possibly also scale with the insulators larger surface that is in contact with the electrode, more rough surfaces which will create more field enhancements on the electrode.

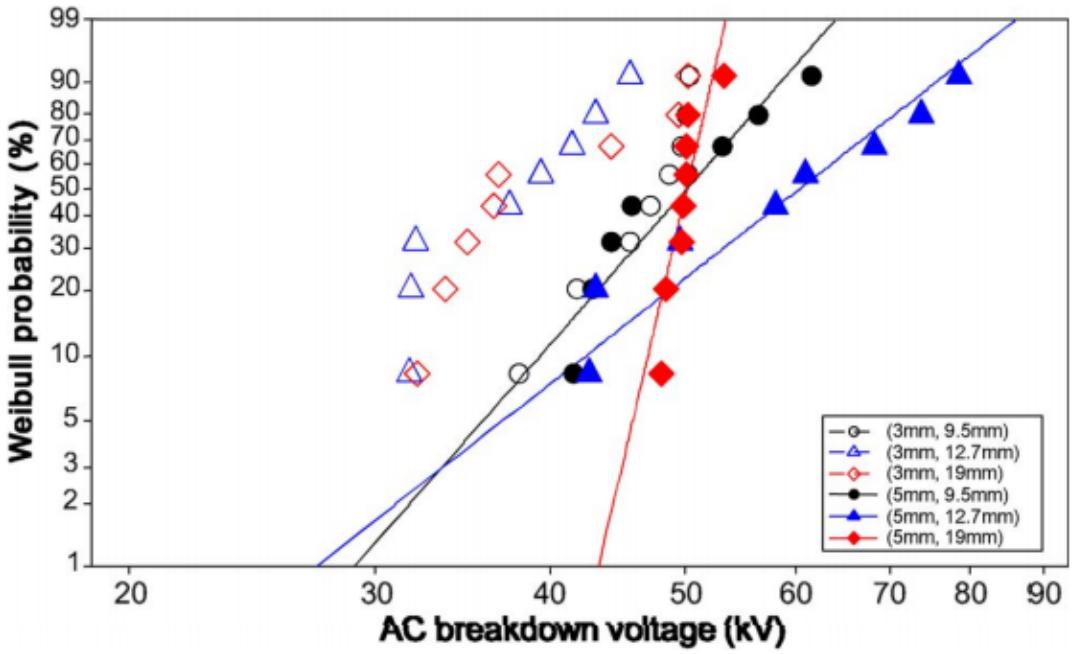

Fig. 4.80 Weibull plots for AC measurements along epoxy surface in LN_2 (125).

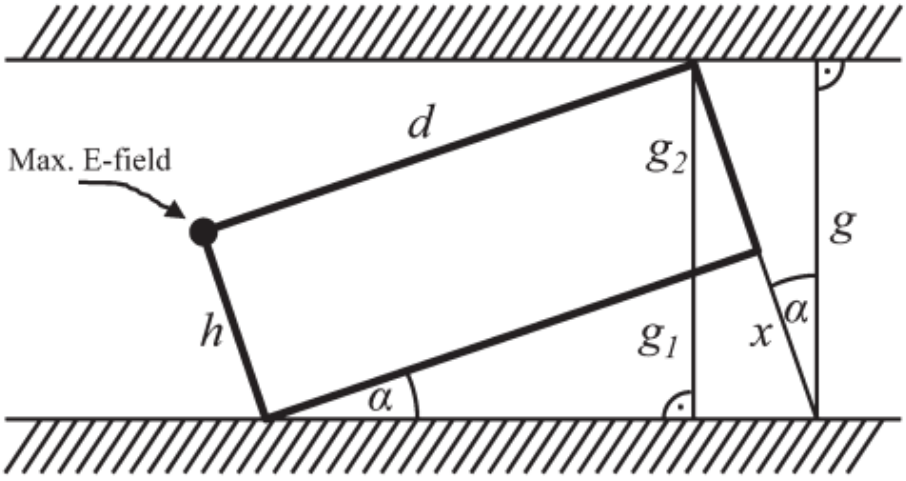

Fig. 4.81 Geometry of a misaligned epoxy sample between the surfaces of perfectly parallel steel electrodes (125).

However, the data for the two different insulating materials can be compared using the AC voltage results. There is a difference in permittivity for G10 and Stycast epoxy insulators; 12.7 mm is the exception, 9.7 and 19 mm measurements show that there is a drop in voltage by ~ 10 kV. The interesting thing to note here is that G10 has an $\epsilon = 4.6$ while Stycast has $\epsilon = 7.7$. This increased permittivity could enhance the field region at the CTJ, reducing the breakdown voltage of the insulator.

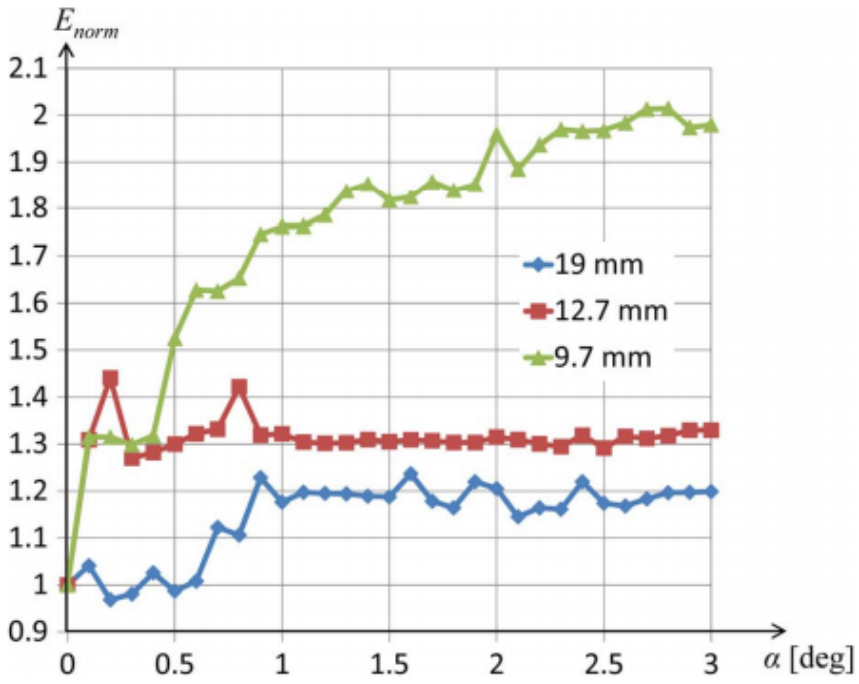

Fig. 4.82 Normalised electric field at the location of the maximum field as a function of misalignment (125).

It should be noted that even though the 19 mm diameter insulator exceeds the uniform field region in size, it would give longer tracking lengths for the electrons to travel to ground. However this seems to limit the breakdown voltage compared to the other insulators which can be seen in Figure 4.80.

Butcher et al. (126) (127) investigated breakdowns in LN_2 with and without insulator. The setup used was a coaxial connection with an inner connector to an apparent plane-plane electrode geometry with a groove to hold the spacer, shown in Figure 4.83.

The measurements were done with an insulator (alumina or lexan) and without, pure LN_2 volume for comparison. The electrode separation was 1.75 mm.

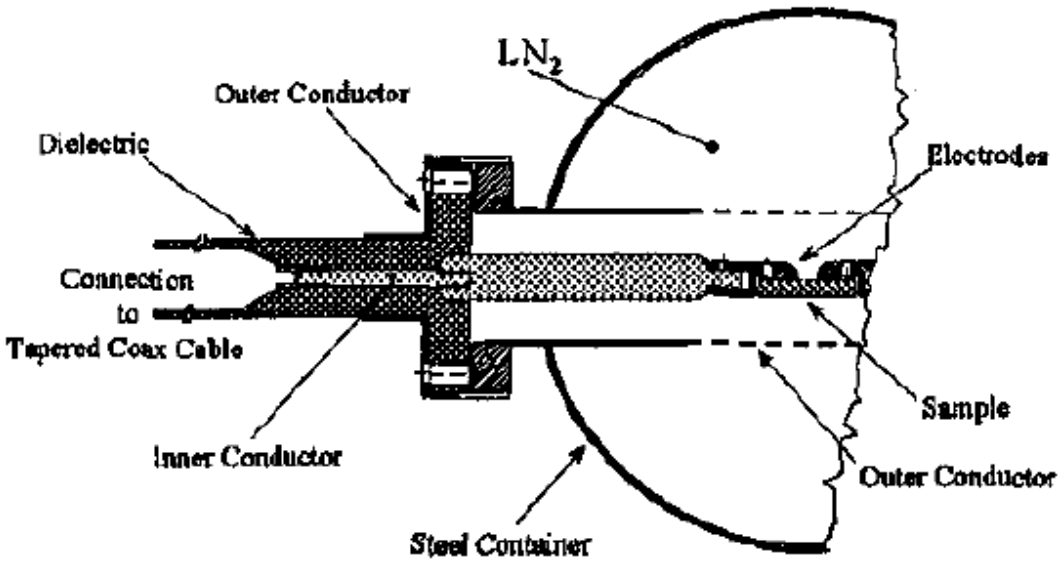

Fig. 4.83 Experimental setup: Feedthroughs and test gap (126) (127).

The breakdown voltage for the pure LN_2 volume shows a constant value of 55 kV which corresponds to an average field of 315 kV/cm, as determined from Figure 4.84. But for both spacer samples the breakdown voltage was significantly reduced to 20-30 kV (115-170 kV/cm) then after subsequent breakdowns is reduced to 10-15 kV (57 -86 kV/cm). The decrease in values for alumina is attributed to surface damage and depositing of electrode material on the surface. This occurs as the alumina is a brittle material so at 20 kV the energy deposited is 1.2 J which is potentially enough to break off chucks of alumina. Butcher states this is observed to occur as pits are visible on the surface of the insulator.

Butcher states that current spikes occur for the majority of discharges for both materials, however, the ongoing surface damage does not seem to result in increased current spikes. Alumina only has current spikes for the first discharge, while for lexan the number of current spikes increased from 2 for the first few discharges to 6-7. In the volume breakdown, this was apparent in 90% of the pre-breakdown spikes. The discharge path along the insulator surface was observed to change with each breakdown event.

Butcher concludes that the introduction of solid insulating mediums between electrodes results in reduction of the breakdown voltage by a factor of 3. He suggests that the initial higher current spikes are associated with bubble formation which is then suppressed after surface damage has occurred, or that the bubble size along with the maximum current associated with a bubble is limited by surface damage.

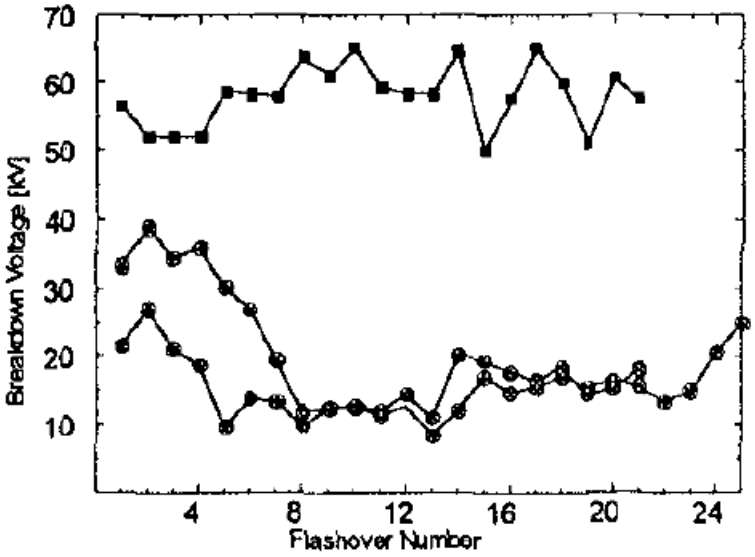

Fig. 4.84 Breakdown voltage against flashover number. Top trace is volume breakdown, bottom two are for lexan and alumnia spacers (126) (127).

It should be noted that the exact geometry of the setup is not mentioned so how the insulator sits in the groove cannot be commented on.

Blaz et al. (128) investigated the surface flashover of cylindrical insulators in liquid nitrogen. The geometry uses plane-plane electrode setup which had a diameter of ϕ 97 mm, similar to that stated by Blaz previously. The cylindrical specimen used was placed in the centre of the electrodes and clamped down between the two planes. The diameter of the specimen was 20 mm and height of 20 mm. A few different materials were tested: PMMA (with a turned surface), G10 (fibre orientation was parallel to that of the E field), and Sivapox HV 401 (synthetic fibre reinforced epoxy). This setup was then placed in a LN_2 bath, results given in Figure 4.85.

The AC voltage measurements show that the presence of the PMMA insulator can influence the breakdown voltage, unlike at atmosphere. Blaz comments that the variation of the breakdown voltage for each measurement had a lot of variation and this is attributed to thermal expansion of the specimen but also due to creation of bubbles. He stated that creation of bubbles due to boiling LN_2 cannot be the only way they are created is due to boundary layer between liquid and gaseous layers. Therefore, the source of breakdown limiting bubbles would be created from small cracks and cavities in which small amounts of gas is present which induces new bubbles. Blaz goes further to suggest that rough surfaces of the specimen in the more electrically stress areas would probably generate more bubbles, with the PMMA specimen being the roughest so having the lowest breakdown voltage.

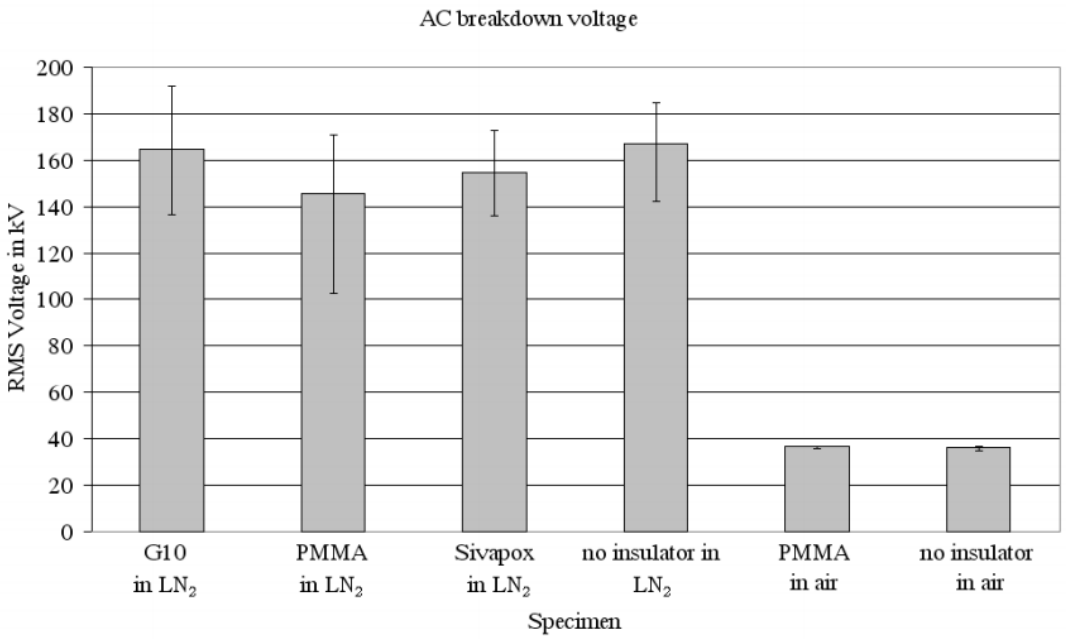

Fig. 4.85 Surface flashover voltage of different materials between electrodes, error bar is the variation of the breakdown voltage (128).

After measurements were taken, damage was observed on the insulators. The PMMA had lots of tracks visible. However, the damage did not limit the breakdown voltage after each event. The materials were different, as after some breakdown events the breakdown voltage would decrease. The G10 was observed to have a single conductive channel along its surface, shown in Figure 4.86. The Sivapox also had a single channel visible but it was not conductive.

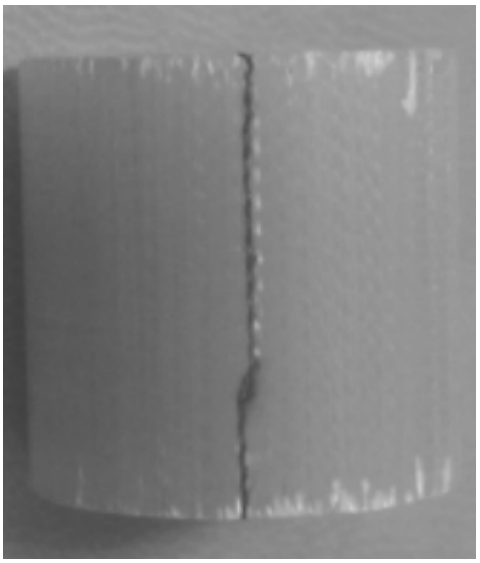

Fig. 4.86 Damage present on the G10 specimen (128).

The mechanism of the breakdown is not expanded upon in detail, instead attributing it to humidity (forming ice) and bubbles which cause a large variation in breakdown values. However, it does show that the presence of the insulator limits the breakdown voltage of the setup, though G10 seems to have less of an effect in lowering the breakdown value but had greater variation.

Kim et al. (129) investigated surface flashover characteristics in LN_2 for superconducting pancake coils. The setup uses a double pancake coil structure that has two disc coils wound around an insulator. The two coils are then separated by two spacers with a slit down the side of both of them with the second slit offset to the first one. The paper states that the highest fields will be on the outside of the HV coil, therefore, adding spacers would increase tracking length.

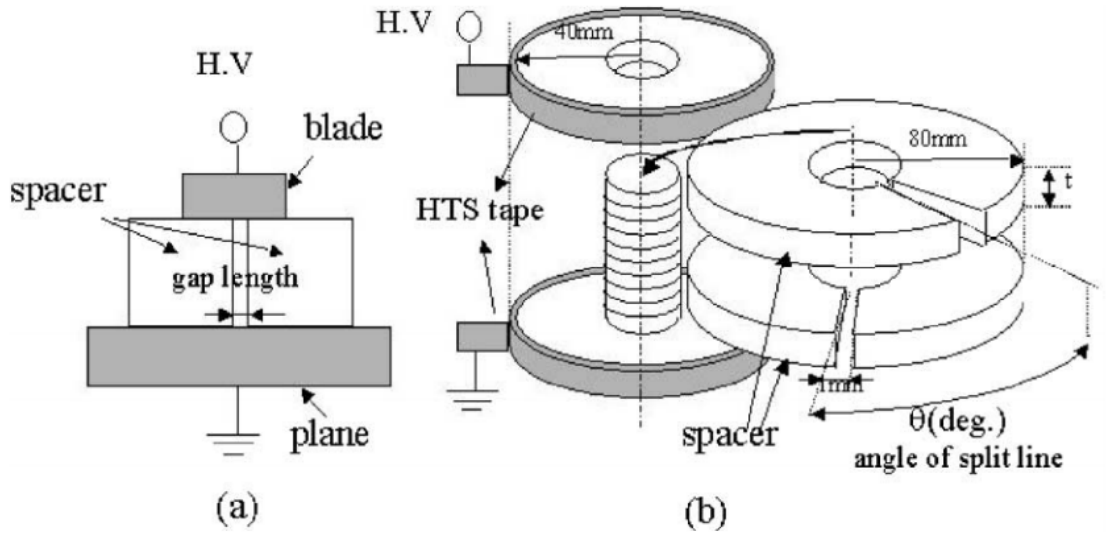

Fig. 4.87 The schematic of the electrode system, (a) the blade-plane geometry, (b) HTS coil setup (129).

It is stated that there are two places at which breakdown can occur: down the slit of the spacer or along the outer surface of it. The blade electrode is a thin plate 20x10 mm^2, 0.11 mm thick and has about an 8° angle between the two slits. The two HTS (high temperature superconductor) loops are a single turn with Ag sheathed Bi-2223 tape (0.25 mm thick, 3 mm wide) on a circular FRP form (40 mm radius, 5 mm thick), setup shown in Figure 4.87.

The surface flashover was measured by changing the gap length of the spacer with the electrodes and by changing the slit offset of the two spacers. The flashover AC voltages of Bakelite, Teflon, and GFRP spacers are measured in LN_2 bath.

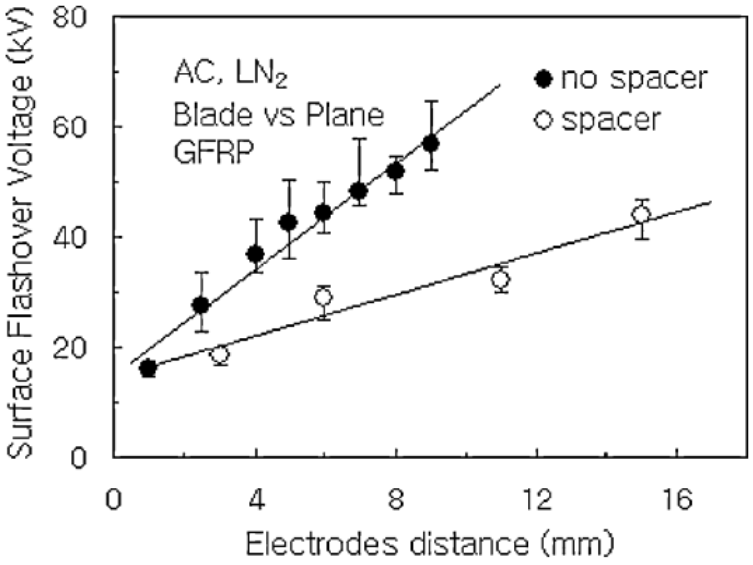

Fig. 4.88 Surface flashover voltages against electrode separation, with and without a spacer in LN_2 (129).

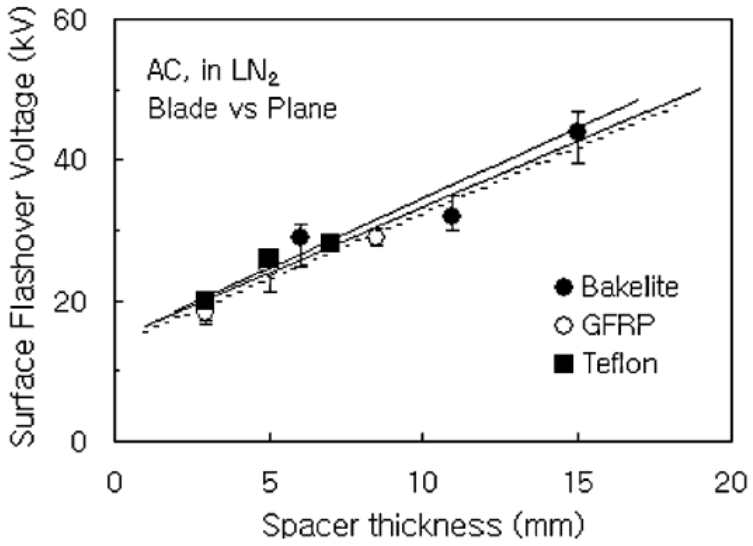

Fig. 4.89 Surface flashover voltages against spacer thickness for various materials (129).

Figure 4.88 shows that the inclusion of the spacer will decrease the voltage attainable in LN_2 without one. The drop in voltage is by a factor of ~ 2. Figure 4.89 shows that the breakdown voltage will be the same regardless of the material. The voltage will increase will increasing thickness of spacer, which is expected due to increasing the tracking length.

The explanation for the mechanisms of this surface flashover behaviour is stated to be caused by bubbles but it does not go into the details of why this conclusion is reached.

4.5.3 Liquid helium

Migliori (130) investigated surface flashover on G10 pieces in LHe and compared this to the breakdown voltages in He gas in an attempt to find the mechanisms of this type of breakdown. The measurements were performed in a sample holder with a plane-plane electrode geometry. The samples consisted of three NEMA G10 circuit boards: first and second being 1.5 cm width and 25 cm long, while the third is 0.6 cm width. Each circuit board was machined with an aluminium oxide wheel to have four regions of differing thickness but equal length.

The first sample was cleaned with no dirt or embedded metal particles on the surface at 10x magnification. The second was rubbed with copper tubing, showing numerous metal chips embedded into the epoxy. The third sample was formed in a mould which results in the presence of sparsely distributed foreign matter in the resin.

Each sample was suspended in LHe with the long axis vertical and thickest section at the top. The stainless steel polished electrode would then be moved along the G10 to regions of different thickness and HV was applied.

Two types of events were observed: first was a hissing sound from within the cryostat and a sample current commensurate with full ionisation (stated as true breakdown). The second type was no noise heard but with a sharp increase in current which then dropped to zero rapidly but did not change the voltage. The second type only occurred on the clean sample twice, while occurring often on the dirty sample. This was attributed to expulsion of particles from the sample surface.

Figure 4.90 is the breakdown electric field strength as function of sample thickness for the three samples. The clean sample showed less scatter then the dirty ones, suggesting that the dirt would lower the voltage. The dirty samples were also on average lower than the clean sample ~ 90%. The typical value of non-boiling LHe at 4.2 K stated

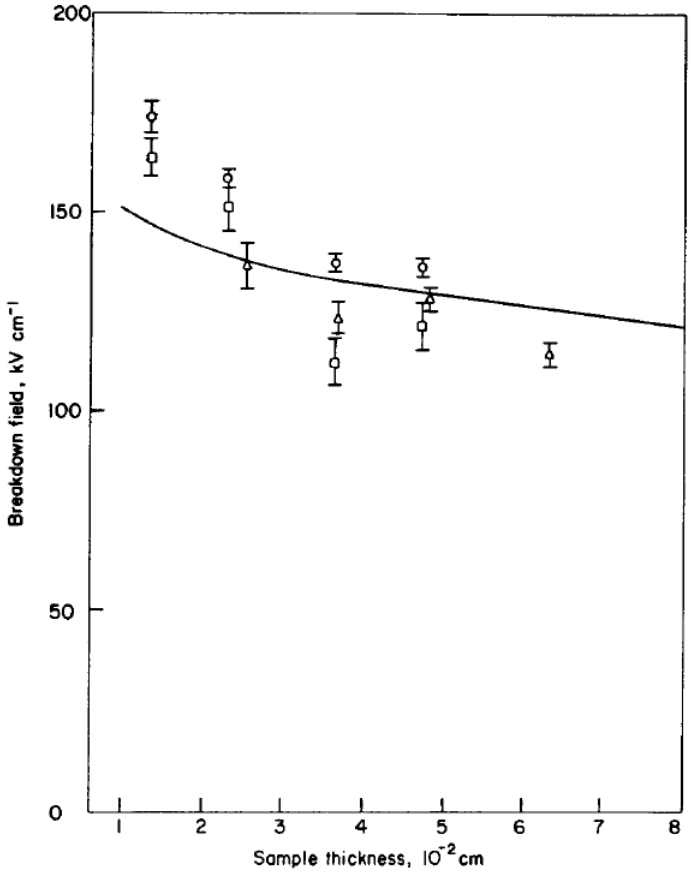

Fig. 4.90 Breakdown field for tracking against tracking distance (sample thickness) for three different samples. Circle - clean G10, sqaure - contaiminated G10 with copper, triangle - crest 475 resin. The lines is from Gerhold (131) for breakdown voltages in He gas (130).

by Migliori is 500 kV cm^{-1} at 5 × 10^{-2} cm or about 4 times the value in Figure 4.90. In comparison the observed results matches that of helium gas. In order to investigate if this electric field value is due to vapour, the presence of bubbles in the helium was eliminated using two techniques: momentary over-pressurisation of the dewar and pumping below the λ point. Only the clean sample was used for these measurements, results shown in Figure 4.91.

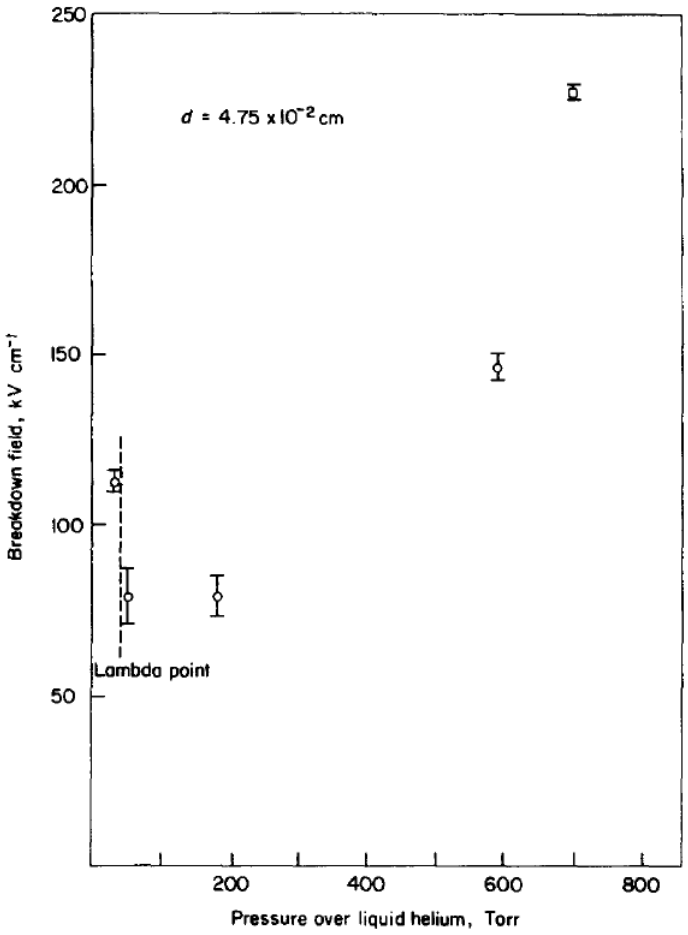

Fig. 4.91 Breakdown field for tracking against pressure applied to the LHe. Clean G10 sample, 4.75 × 10^{-2} cm thick. Circle - at saturated vapour pressure, square - non-boiling helium (130).

Figure 4.91 shows that as the pressure is dropped the breakdown field also decreases in a similar manner to previous data without a spacer. There is also a rise of breakdown field after the λ transition which again is seen in previous data (93). However, the values are still lower than that found without the presence of an insulator by roughly about 2-3. The implication is that bubble generation in having an effect on the breakdown voltage, lower pressure, large the bubble can propagate in the liquid.

Wu et al. (132) (102) also looked at surface flashover in LHe but at temperatures of

1.9 K and 4.2 K. The pressure above the fluid was held at SVP for all tests. The setup consisted of a plane-plane geometry where the electrodes were 7.62 cm in diameter with a 1 mm thick sample of G10-CR of diameter 2.54 cm separating them.

The results were compared to the breakdown voltage without a spacer present but observed no significant difference. However, the bulk breakdown field values for liquid helium was low ~ 120 kV/cm.

Surface tracking measurements with a pin-plane geometry were performed. The horizontal creepage distance is the length of the distance across the surface of the electrode and the thickness of the G10 insulator which was used to determine the tracking length.

The results are not clear. The creepage distance is a fairly arbitrary effect as the distance the discharge travels to ground will vary due to the path along the insulator and it being rougher could increase this value. There is a difference between the two temperatures (4.2 K and 1.8 K) which makes sense that the lower temperature and pressure, bubbles will be more prominently created in that state then at 4.2 K, dereasing the breakdown voltage by ~ 6 kV.

4.5.4 Hill and Davidson measurements

Hill (3) and Davidson (2) both performed measurements in LN_2 and LHe on small (DKHs) and medium (DKHl) electrodes separated by different lengths of Al_2O_3 insulators. The measurements taken for this thesis will directly continue from these measurements.

There were two different cryostats used for these measurements; one was a glass cryostat for the measurements with small DKHs electrodes in LN_2 and LHe. The advantage of using this cryostat was for optical confirmation of HV breakdowns between the electrodes. The cryostat was capable of measuring with a LHe volume down to temperatures of 1.2 K (93).

Due to the risk of HV discharge inside a glass cryostat causing a shockwave that could potentially shatter it, the separation of the glass cryostat DKHs measurements was limited to 3.5 mm.

The other cryostat (KEK cryostat) used is metal with a much larger bore to fit the DKHl electrode setup. This cryostat was capable to reaching temperatures as low as 1.79 K for LHe breakdown measurements. Schematics of the KEK cryostat are given in Davidson (2) and Hill's (3) thesis.

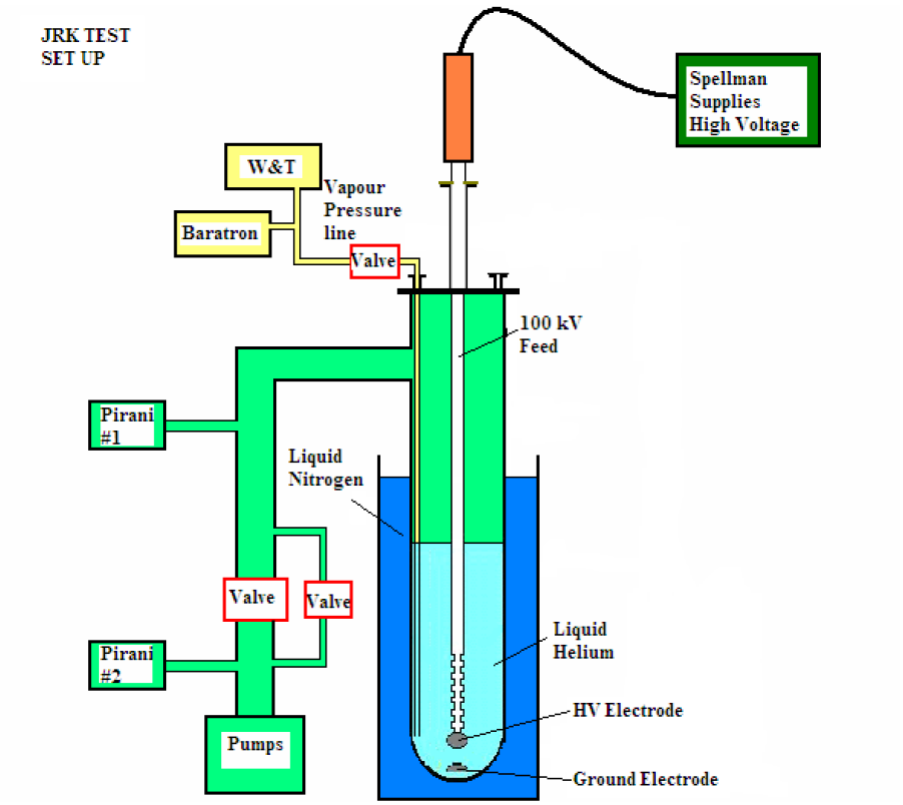

Fig. 4.92 Karamath schematic for setup for HV breakdowns in LHe (3).

Both cryostats were set up for LHe measurements in a similar way to Figure 4.92. The DKHs setup had an insert with baffle assembly attached; this would be lowered into the glass cryostat in which the electrodes were placed on. At the bottom of the insert is a G10 baseplate where the ground electrode is screwed into a return line that goes up to the top of the insert and out through a feedthrough to room temperature. The HV feed then has the HV electrode screwed into it. The feed is guided by a PTFE spyder on the insert structure. The feed is then lowered by a manipulator until the electrode is positioned with the Al_2O_3 insulator between the two electrodes. In order to avoid thermal contraction problems, springs are placed under the baseplate of the ground electrode to mechanically clamp the two electrodes together with the insulator in the middle.

For the KEK cryostat measurements, a different insert was used. This had a much larger G10 base plate in order to hold the DKHl electrodes. The ground electrode was connected to a return line in the same manner as in the glass cryostat. However, the

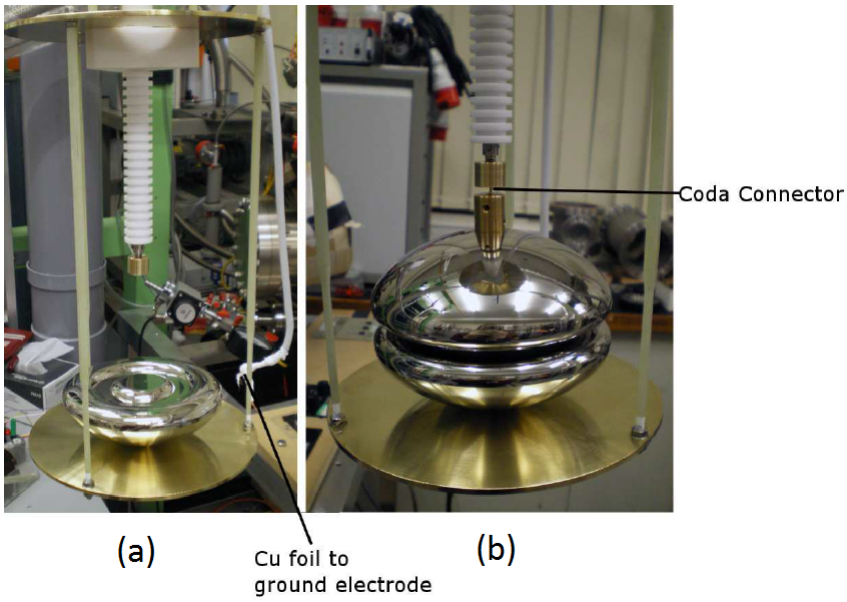

Fig. 4.93 Insert setup for the DKHl electrodes, for DKHs electrodes the base plate and electrodes are smaller to fit the bore of the glass cryostat and the coda connector is replaced with a stud to attach it to the HV feed. (a) is without insulator and HV electrode in place, (b) is with the HV electrode and insulator in place, connected to the HV feed with a coda connector (3).

connection to the HV electrode was done with a coda connector instead of springs below the baseplate, due to the weight of these larger electrodes. In this case the insulator could be placed between the electrodes, then the HV electrode was placed on top.

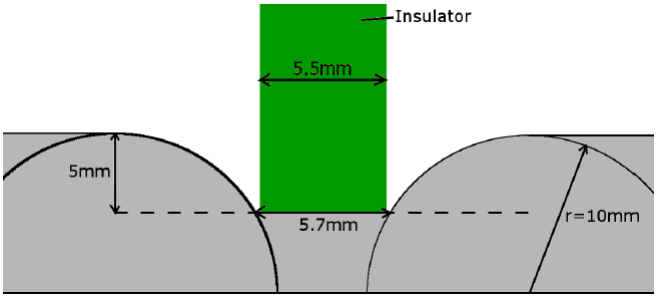

Fig. 4.94 Groove profile selected for the breakdown measurements. The chosen geometry is to minimise the E field on the groove radius; the relation used is the ratio of insulator thickness to groove radius. The insulator has clearance of 0.2 mm at the base of the groove. The grey is the electrode material and green the insulator (3).

However, during machining there were problems which resulted in a modified geometry for DKHs and DKHl electrodes, shown in Figure 5.41.

The material for the insulator was chosen to be Al_2O_3 as an analogue for BeO. BeO has good UCN storage properties, but would create a health risk if breakdowns damaged the insulator surface creating potentially carcinogenic BeO dust. Al_2O_3 was chosen as a good comparison as they both have similar structures, as sintered powder ceramics, as well as similar dielectric constants, which are shown for comparison in Table 4.3.

Property	Al_2O_3	BeO
Purity (%)	99.7	99.5
Density (g cm^{-3}	3.7-3.95	2.85
Max Grain Size (μm)	10	18
Compressive Strength (20°C) (N mm^{-3}	3500	1550
Dielectric Const. (20°C, 10 MHz)	9.2	6.8
Coeff. Thermal Expansion ($10^{-6}K^{-1}$)	8.5	9
Thermal Conductivity (100°C) (W mK^{-1})	30	285-340

Table 4.3 Table of properties for alumina and berylium oxide from Degussit (133) and Materion (134), respectively (3).

The Al_2O_3 tubes are prepared using Aqua Regia, soaked in the solution for half an hour then rinsed in deionised water several times. The electrodes were mechanically polished to a mirror finish and cleaned with isopropanol.

Breakdown measurements were performed for various separations by placing different length alumina insulators between the two electrodes. The DKHs electrodes used 10x15 mm insulators and the DKHl electrodes used 60x70 mm insulators.

In order to identify if the breakdown occurred through the volume between the planes of the electrodes, the electrode surfaces were examined after measurements to look for crater sites. If the crater count matches the number of breakdown events, then all breakdowns can be assumed to have taken place through the liquid volume.

Munday (135) performed an analysis of these structures on the surface of stainless steel electrodes.

The analysis Munday performed, shown in Figure 4.96, estimate a large amount of stainless steel is vapourised and is assumed to then contaminate the liquid volume.

All the breakdown measurements for the DKHs and DKHl electrodes in LN_2 are given in Figure 4.97.

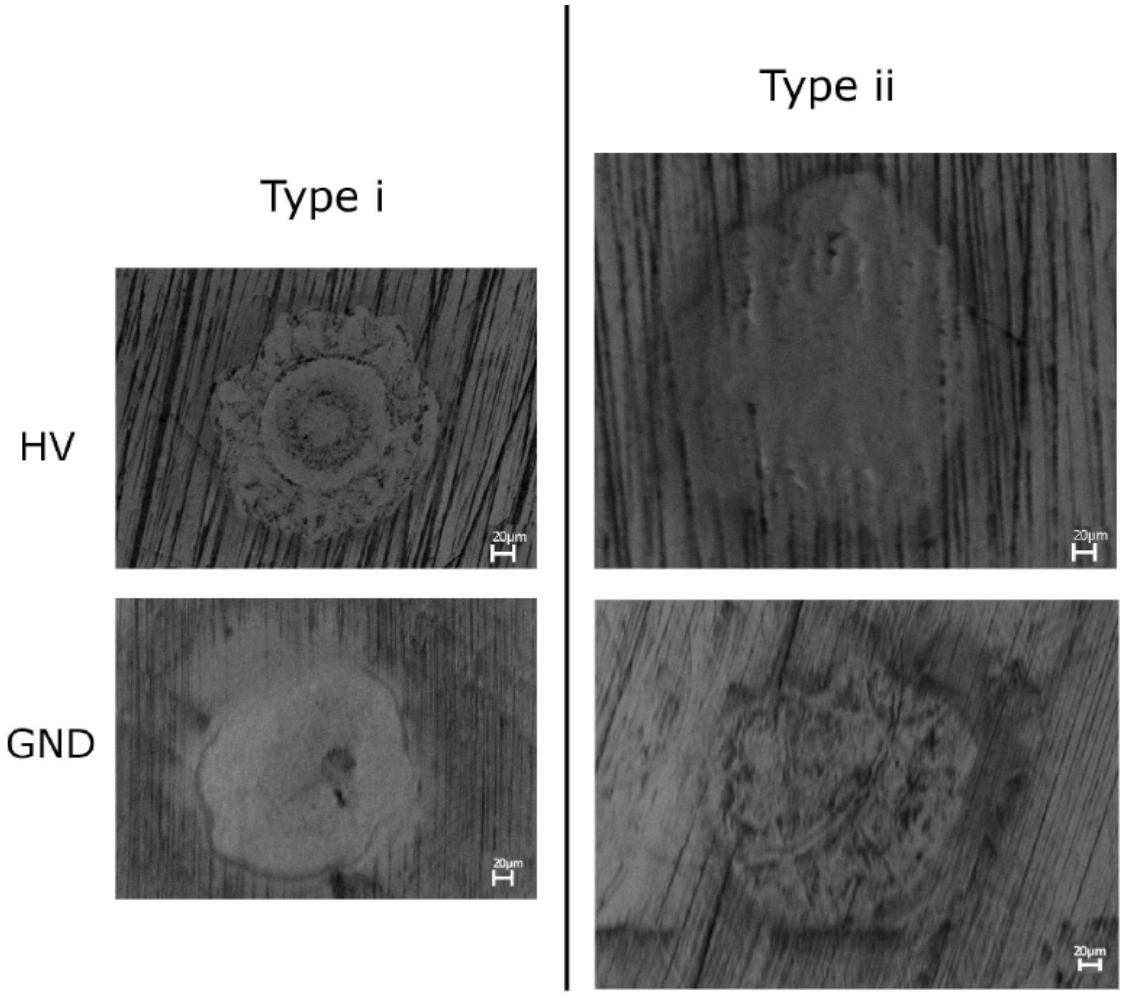

Fig. 4.95 500x magnification SEM (scanning electron microscope) images of breakdown craters that Hill found between two stainless steel electrodes after HV measurements. The craters are ~ 100 μm in diameter (3)(135).

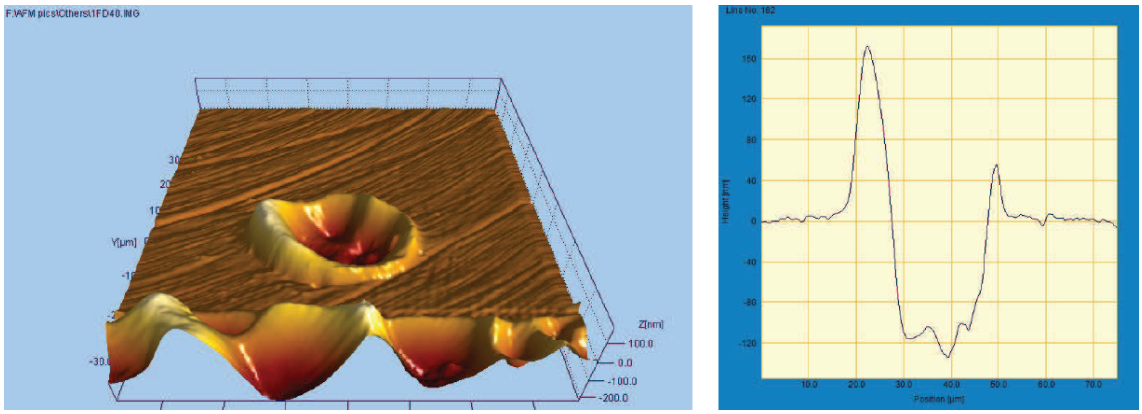

Fig. 4.96 AFM (atomic force microscopy) picture, left, of a crater site on one of the electrodes, (b) is line profile of the crater, right. The breakdown for this crater was performed in LHe at 4.2 K. The depth and width of this crater is 125 nm and 20.75 μm. The estimated loss of material is ~ 60% by volume (135).

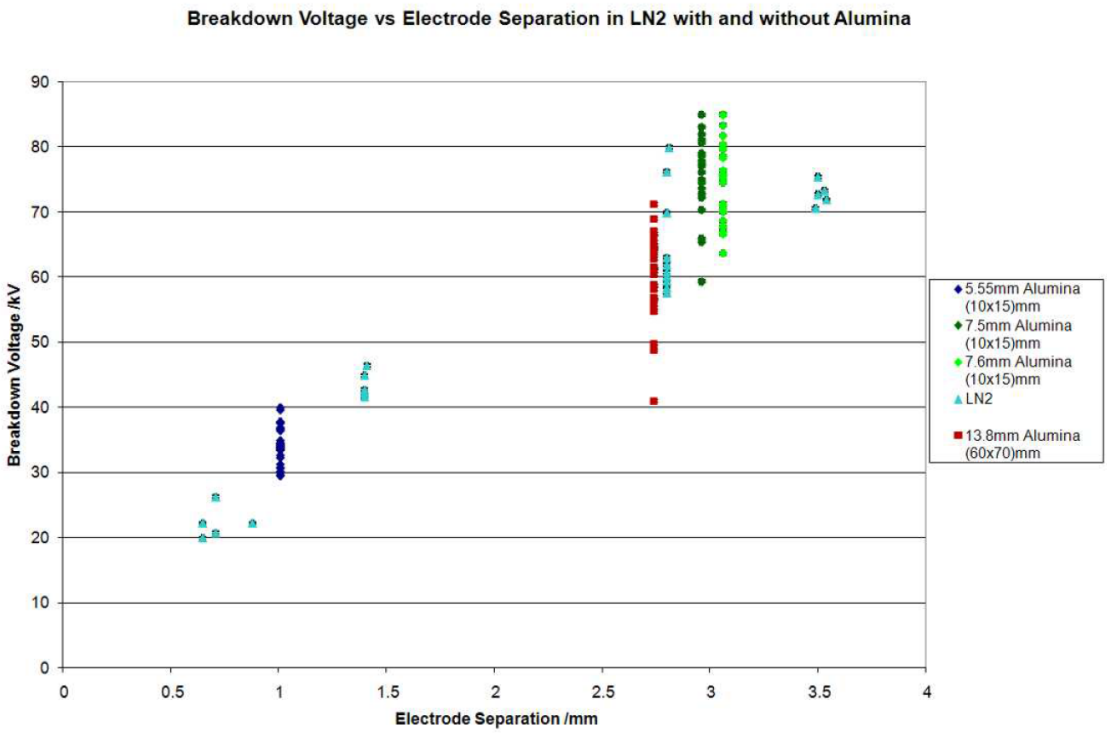

Fig. 4.97 Breakdown voltages for DKHs and DKHl electrodes against electrode separation (mm). Light blue triangles are LN_2 breakdown data using DKHs electrodes without the insulator present (3).

The breakdown measurements with a 5.55 mm Al_2O_3 tube insulator (10x15 mm) resulted in 31 craters for 31 breakdown events. The insulator was not damaged and the breakdown voltage seems to be the same as that without the spacer present. This was performed with negative polarity.

The breakdown measurements with a 7.6 mm insulator (10x15 mm) had 25 breakdowns at positive polarity. Removal of the insert found the insulator had shattered into 8 pieces, with evidence of tracking starting at the Al_2O_3 surface then going underneath the surface and blowing out material, as can be seen in Figure 4.98.

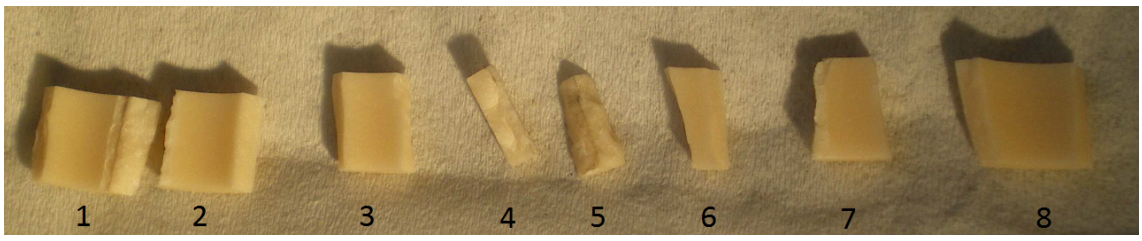

Fig. 4.98 Insulator after breakdowns in LN_2, broke into 8 pieces. The fourth and fifth pieces have tracking marks along the edge of the break (3).

This time the damage to the surface of the electrode was counted to be 54 craters out of 56 with potentially two tracks, seen in Figure 4.98, along the insulator surface. Confirmation that this was not due to mechanical compression was performed by placing the insulator between the two electrodes quickly into LN_2 and applying up to double the pressure the insulator experienced in the cryostat measurements. It was found that the insulators would not break during these tests.

Another measurement was performed on a 7.5 mm insulator (10x15 mm) using negative polarity. The measurements resulted in the insulator being broken into six pieces with one region having blown out a lot of material from the surface, shown in Figure 4.99. The region where the material was ejected had two tracking marks with the other breaks being clean.

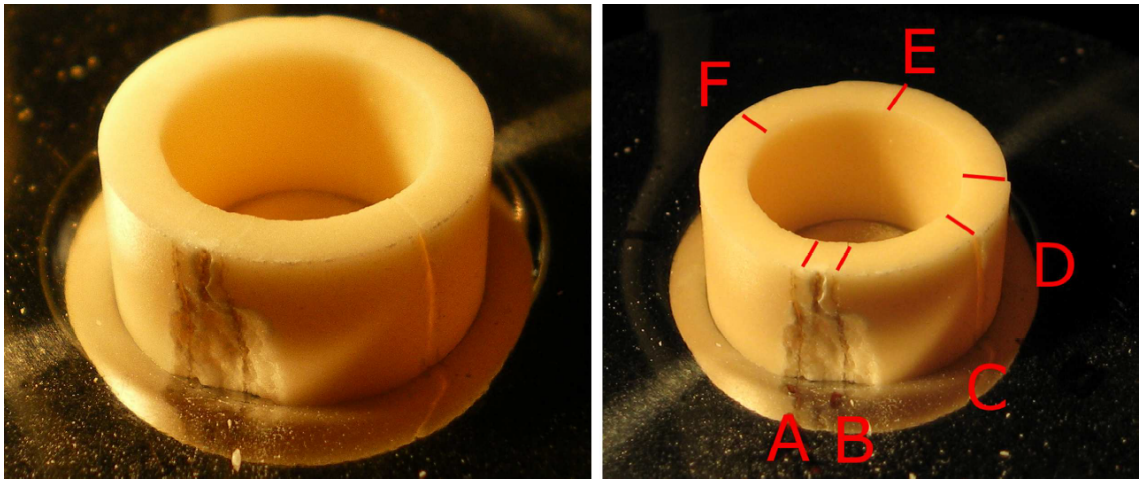

Fig. 4.99 Insulator after breakdowns in LN_2, broke into 6 pieces, labelled A-F. Significent damage is labelled as A and B, where the insulator has been blown out from the surface. Tracking damage was only present here (3).

A single measurement was performed with the larger DKHl electrodes in the KEK cryostat. The Al_2O_3 insulator used was 13.8 mm in length (60x70 mm) and was performed with negative polarity. After the experiment the electrode stack was removed and the insulator was observed for damage. There was no evidence of the damage which had been observed on the 10x15 mm insulator in the DKHs electrodes setup. The damage to the electrode surface was counted to be 25 ± 3 breakdowns out of 30 events.

For comparison, breakdown measurements were performed for DKHs and DKHl electrodes without spacers separating the electrodes. It is not clear how this was performed and the method used to ensure that the separation was exactly as stated, taking into account thermal contraction of the system. It is also not stated how the DKHl electrode would have been connected to the HV feed due to its weight, which may have caused

problems with alignment. However, the measurements showed that for the DKHs electrodes the dielectric strength of LN_2 was 230.4 kV/cm, while with the DKHl electrodes the dielectric strength of LN_2 was 181.7 kV/cm. These numbers are extracted from a linear regression fit (forced through zero) of the mean breakdown measurements. The DKHl electrodes are a factor of 2.2 larger than the DKHs in diameter. The different dielectric strength values of the LN_2 is attributed to a surface area effect for using larger area electrodes.

In these measurements, damage was only ever observed on the outside of the ceramic spacer in the form of tracking and material being blown out, or the insulator shattering completely. The radial separation for these measurements on the DKHs electrodes with an Al_2O_3 insulator is 0.38 mm for the outer separation and 0.25 mm for the inner. For the DKHl electrodes the outer radial separation is 1.76 mm and the inner is 4.5 mm. The DKHl electrode never resulted in any damage to the insulator surface. On the other hand, the DKHs electrodes resulted in damage occurring for all separations at and above 7.5 mm. The radial separation for the inside groove edge is smaller than the outside, yet the damage seemed to mainly only occur on the outside (occasionally on the inside), implying that the trigger for the damage is potentially more due to the condition of the CTJ region. The lack of damage for the smaller separation is possibly due to the highest fields being between the plane-plane surface of the insulator, while at a larger separation, the higher field is elsewhere.

A number of breakdown measurements in LHe at 4.2 K and 1.5 K were also done and compared to Karamath (93) data for the 4.2 K and 1.4 K trend line which he measured in the glass cryostat between spacerless ball electrodes.

The breakdowns were performed on Al_2O_3 insulators with DKHs electrodes for separations of 1.39 mm, 2.01 mm, 3.29 mm and 2.96 mm.

The 1.39 mm separation was done with positive polarity in LHe II at 1.5 K. There was no damage of the degree that was seen in LN_2 experiments, although some dark marks were observed on the ceramic end faces and a bit of chipping to the CTJ and ATJ was present. This can be seen in Figure 4.102.

For the ceramic run with a separation of 2.01 mm using positive polarity in LHe II at 1.5K, there was damage observed to the surface of the insulator. Chipping was present on the CTJ but very small in comparison to the LN_2 measurements, and tracking was also observed, shown in Figure 4.103.

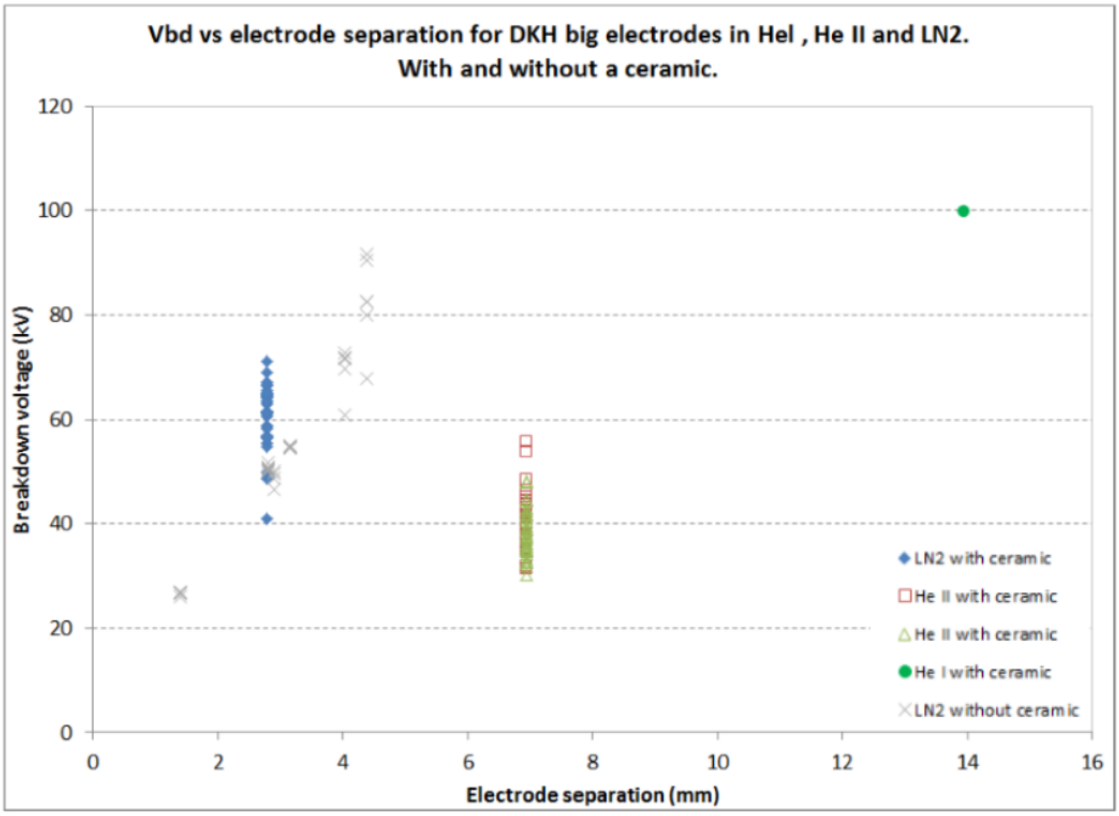

Fig. 4.100 Breakdown measurements with DKHl electrodes in LN_2 and LHe I and II. The green circle at ~ 14 mm separation at 4.2 K in LHe I, only one breakdown occurred before a permanent track meant that the electrodes could not charge up again (2).

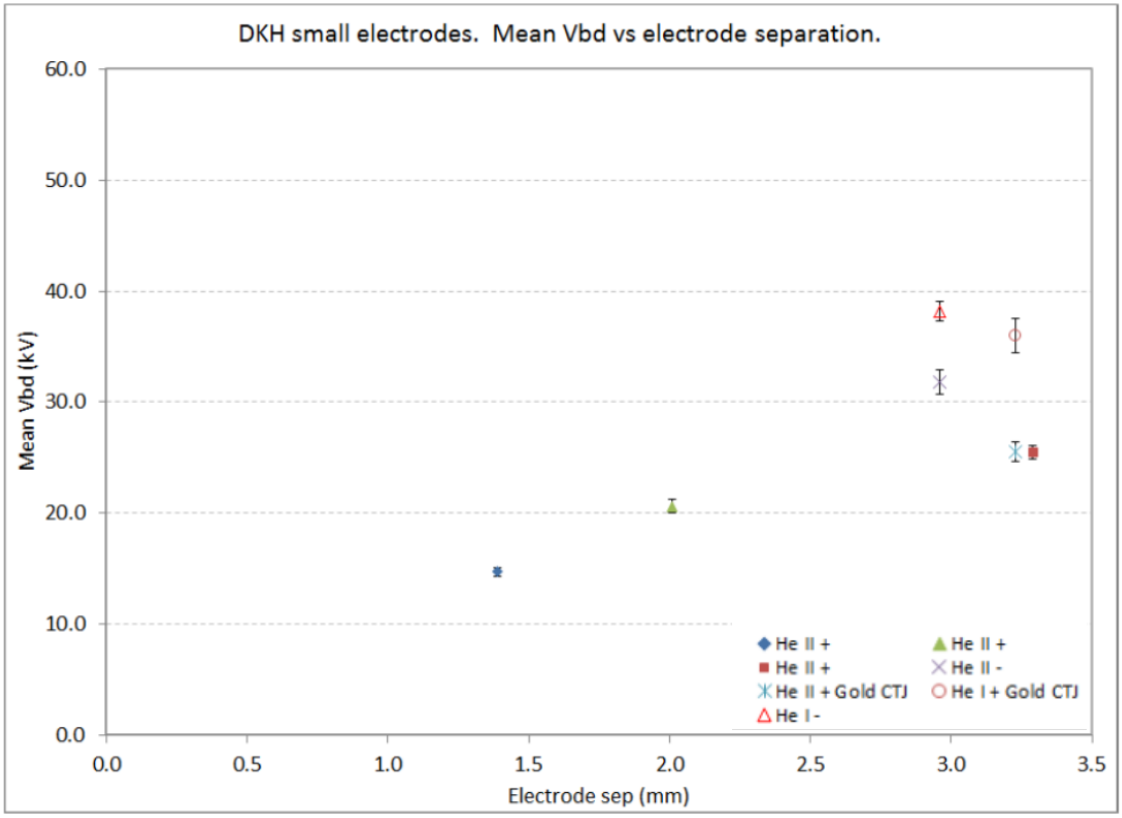

Fig. 4.101 Mean breakdown measurements against electrode separation for DKHs electrodes with Al_2O_3 insulator separating them. The majority of breakdowns were performed in LHe II. Results shown are average breakdowns for a single cool down (2).

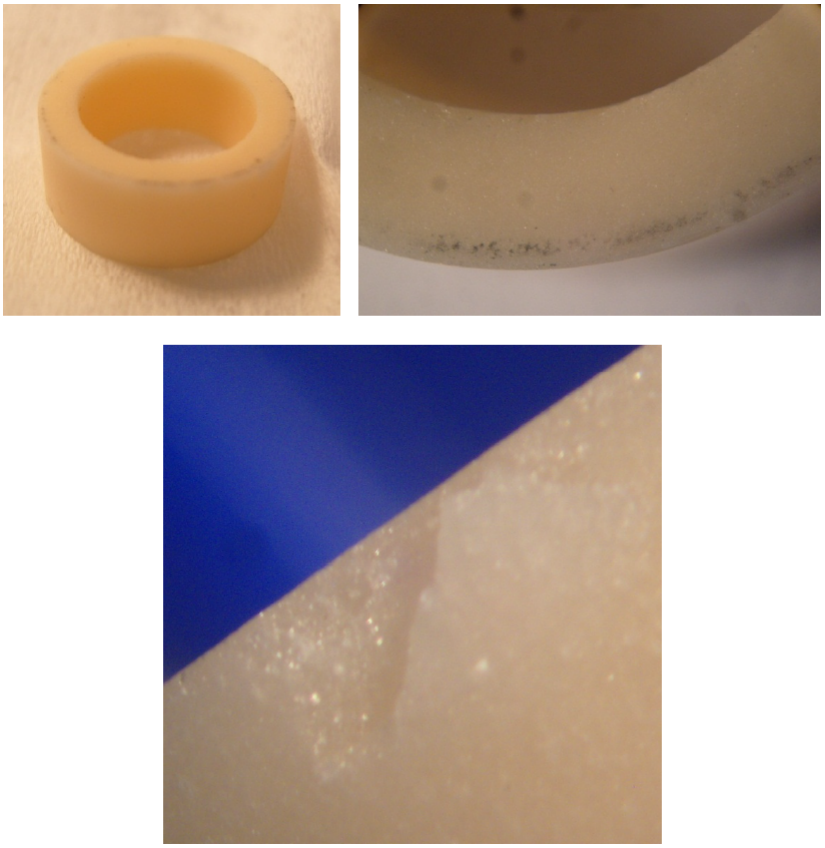

Fig. 4.102 Pictures of ceramic sample tested by Davidson. Overall length of insulator is 5.93 mm. Dark marks are present on the CTJ surface and small chipping had occurred (2).

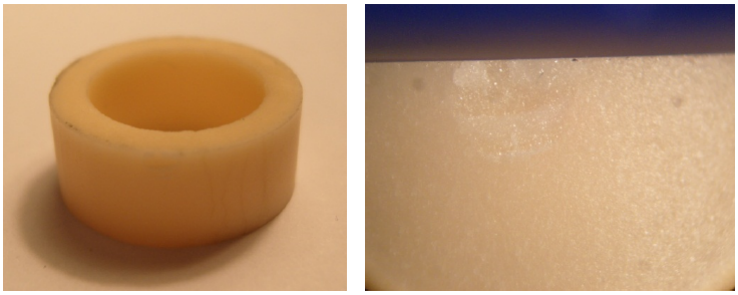

Fig. 4.103 Pictures of ceramic sample of length 6.55 mm. Chipping is visable on the CTJ (right), while on the surface tracking marks are present (left) (2).

The next ceramic measurement was at a separation of 2.96 mm with negative polarity in LHe II at 1.5 K. The damage to the insulator was more prominent than the previous one, presented in Figure 4.104. The tracking was more defined, continuous in nature across the surface from the CTJ to the ATJ. Some small chipping also occurred. Tracking was visible on the inside and outside of the insulator. It is also stated that 90% of breakdowns resulted in a tracking damage.

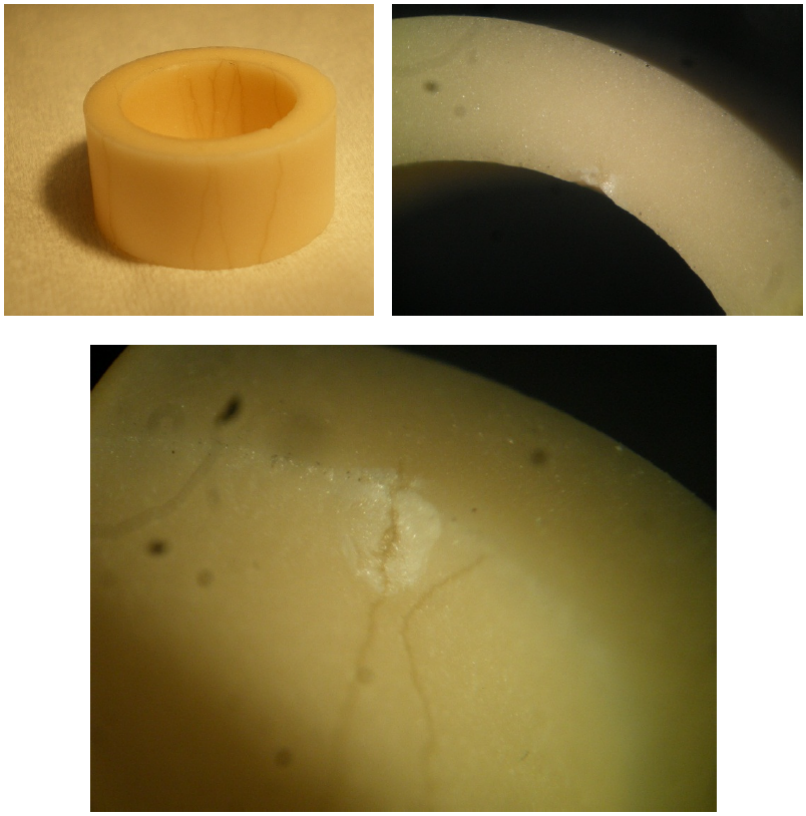

Fig. 4.104 Pcitures of the ceramic sample, overall length 7.50 mm. Clearly tracking had occurred with a small amount of chipping on the CTJ (2).

The last ceramic spacer measured in LHe II at 1.5 K was at separation of 3.29 mm using positive polarity. The results of the breakdown measurement show dark marks again to the face that is in contact with the electrode as well as chipping at the CTJ and the ATJ. There was also small chipping to the outside edge of the CTJ. Tracking was also very present on the surface. The condition of the insulator is shown in Figure 4.105.

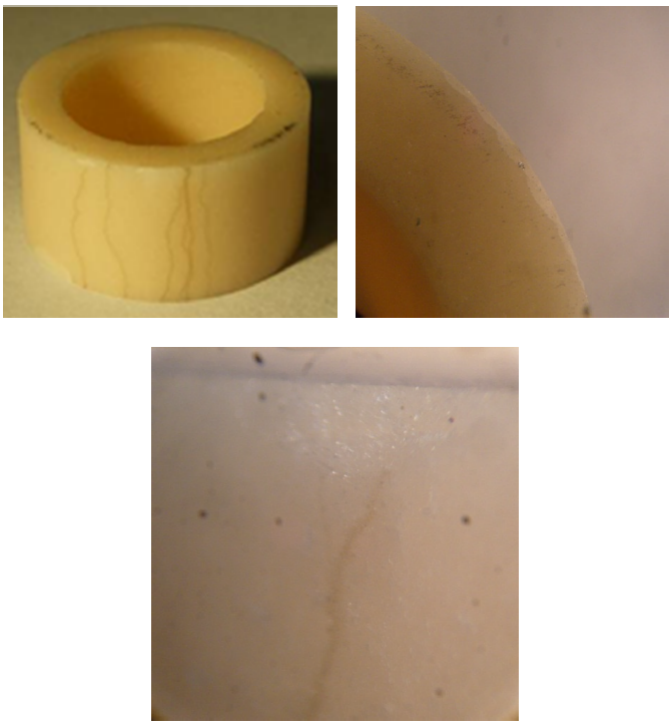

Fig. 4.105 Pictures of the ceramic sample, overall length 7.83 mm. There is tracking visable on the surface of the insulator, as well as dark marks on the CTJ surface and some flaking and chipping (2).

The measurements performed with the DKHs electrodes and Al_2O_3 spacers in LHe at 4.2 K used a separation of 2.96 mm using negative polarity. Damage observed to the insulator was predominately tracking damage, see in Figure 4.106. The difference with this experiment is the tracking is discontinuous, with only a few millimetres along the surface, stopping then occurring again on the other side. Only one track bridges the gap between the electrodes. The number of tracks matched the opposite side. Chipping was also observed, larger in size and depth than what was previously observed in LHe II.

Interestingly a measurement was also performed at first with 4.2 K LHe, then after a number of breakdowns the bath was pumped down to 1.4 K. The electrode separation was 3.23 mm and positive polarity was used. In this case the CTJ was sputtered with gold, which can be seen in Figure 4.107. The thought was that the damage observed on the previously mentioned ceramics was coming from the CTJ. The breakdowns on this gold coated insulator again showed damage, however, it appears to have flakes of gold

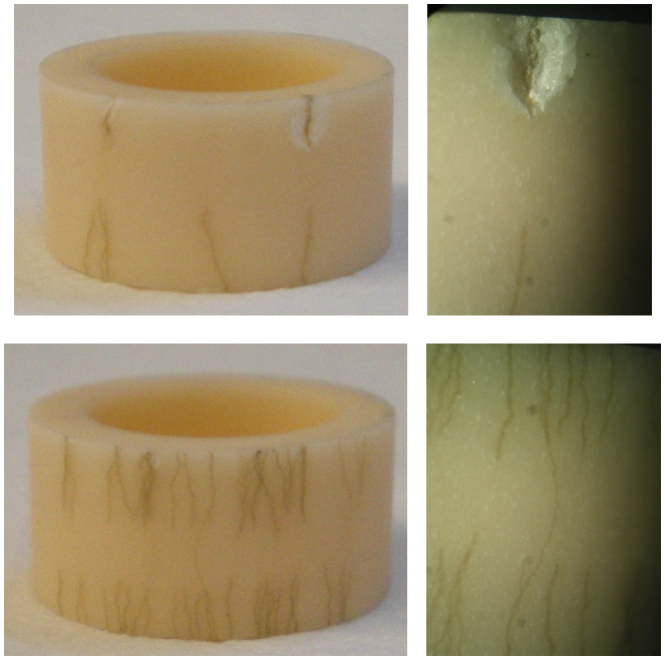

Fig. 4.106 Pictures of the ceramic sample, overall length of 7.5 mm. Discontinuous tracking occurred across most of the outer surface. Chipping also occurred on the CTJ face. Only one continuous track was present (2).

present in the track which has travelled along the surface. Chipping also occurred to the insulator surface where the tracking was present. One track was observed to travelled the full length of the insulator and caused flaking of the alumina surface. This particular track is gold in colour.

The condition observed in LN_2 on the insulators are clearly more damaging than that seen in LHe. This suggests that the mechanism for the damage is different in the two liquids which is not surprising, as LN_2 bubble behaviour is potentially different from LHe. An interesting aspect is the difference between LHe I and II on the type of damage present. The superfluid results have continuous tracking while LHe I has discontinuous tracking. The cause for this is unclear, though the mechanisms as to how a bubble would form and dissipate in either type of helium is probably the reason for difference. The most important measurement, however, is the gold coated insulator. It is clear from the experiment that the origin of the damage is coming from the CTJ taking material from that region in the form of a track. Cratering damage that was observed between the plane-plane surface of the electrodes which results in material in the volume (135). It is possible that the tracking is formed of vaporised stainless steel which has been carried up the insulator surface by the breakdown event. However, it had been mentioned by Davidson that XPS (X-ray photoelectron spectroscopy) measurements were performed on the gold coated ceramic insulators and no trace of stainless steel or gold could be found in the track. The reason is attributed to the small size of the track and the limited

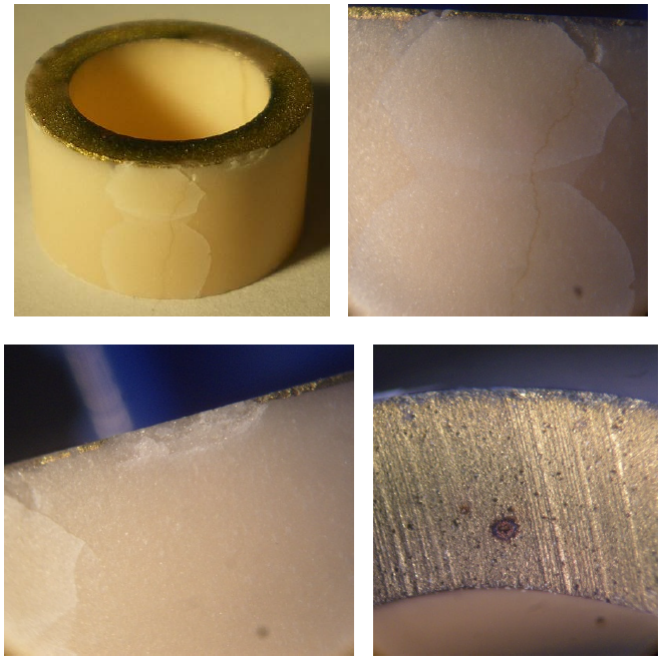

Fig. 4.107 Pictures of the ceramic sample, overall length of 7.77 mm. Gold had been sputtered on to the CTJ surface (top left). Tracking was present inside and outside, some continuous and some discontinuous. Three discontinuous track marks with chipping was present on one side, with a single track on the other which resulted in flaking of alumina from the surface. A single track occurred on the inside (2).

sensitivity of the XPS measurement.

It also appears from Figure 4.108 that for the 4.2 K measurements the presence of the insulator decreases the breakdown voltage by about a factor of 2 compared to the trend line. On the other hand, for the LHe II measurements, on the small scale, it seems to be close to that of the trend line. However, the higher the voltage, the more it also drops off in value to about a factor of 3. It should be mentioned that all those values with the lower breakdown voltage resulted in damage to the insulator which could be why the values are lower than the trend line. The results shown in Figure 4.108 also used different electrode diameters for some of the measurements, therefore, it is hard to compare the JRK trend line with the DKHl electrodes as they are 2.5 times larger (the DKHs electrodes are comparable as they are 58.38 mm in diameter).

The LN_2 measurements in Figure 4.97 seem to stay close to the spacerless breakdown measurements. At the 3 mm separation in LHe the voltage drops off but in the LN_2 case this does not seem to be the case. This is potentially indicating a different mechanism is present resulting in the breakdown across the gap.

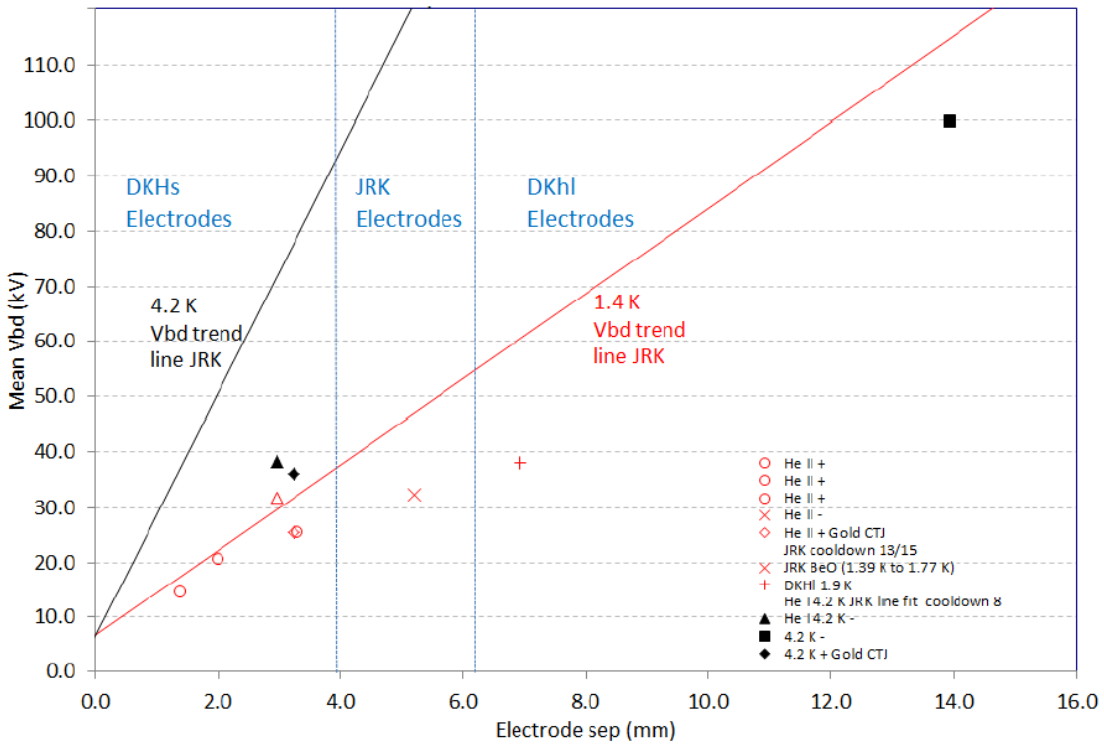

Fig. 4.108 Breakdown measurements against electrode separation for every measurements in LHe performed by Karamath, Davidson, and Hill (93) (3) (2). Ceramic breakdown measurements are compared to spacerless Karamath trendlines for LHe at 4.2 K and 1.4 K.

4.6 Summary

In general the consensus is that the primary breakdown mechanism in LN_2 and LHe is from generation of bubbles between the electrode surfaces with the model by Garton and Krasucki (111) a good representation of the bubble behaviour. These bubbles are seeded by a number of different processes: asperities on electrode surface (roughness and material) (98) (100) (101), purity of the liquid (stressed volume) (100) (103), breakdown repetition rate (105) (107) (108), stressed surface area (109), pressure (118) (2), and presence of the insulator (3) (126) (128) (129) (130) (102).

The electrode surface can be optimised by reducing the roughness present with the best method to do this being electro-polishing. The material that is most common which works well is stainless steel. As the discharge strikes the surface it creates a crater; in stainless steel the edges of these craters are smooth, which means sharp edges are not generated (135). However, this discharge can lead to injection of contamination into the volume. This conductive material is moved under electric fields which collide with the surface to seed bubbles (103). As the bubbles dissipate it takes time, therefore, depending on the frequency of breakdowns, time is required for the volume to stabilise before

electric fields are applied again (98). In addition, surface area effects due to additional asperities present on the electrode surface can increase the chance of a breakdown occurring, hence the breakdown field decreases logarithmically with surface area (109).

Applying pressure to the liquid volume seems to prevent the generation of bubbles. This occurs as the pressure limits the bubble diameter, keeping it smaller so it is unable to traverse the gap between the electrodes. Davidson (2) showed that the drop by a factor of ~ 2-3 in LHe II compared to LHe I is due to pumping of the bath to lower the temperature, which also lowers the pressure, hence the formation of bubbles is more probable. This can be overcome by pressurising the volume, recovering the breakdown voltages to that of LHe at 4.2 K SVP.

Measurements by Davidson (2) and Hill (3) indicate that correct treatment of recesses in the electrode surface to hold the insulator will recover breakdown voltages to that without an insulator present in LN_2. Even if this is the case, the insulator can become heavily damaged during the experiment. In the case of LHe, the breakdown voltage is reduced by a factor of ~ 2-3 (130) (102). These measurements showed that the insulator would also be damaged as well as giving a reduced breakdown voltage. The source of the breakdown is from the CTJ, as demonstrated by Davidson (2) with gold coated ends of the insulator in contact with the electrode. Therefore, correct treatment of this region is critical to avoid the damage and recovering breakdown voltages. Ito (64) demonstrated that 100 kV/cm can be reached in LHe I and II regardless of applied pressure on a 12 cm diameter electrode. This field is comparable with the LHe dielectric strength without an insulator present, taking into account surface area effects. The lack of breakdowns with lowering the applied pressure implies that either electro-polishing of the electrodes, groove optimisation, insulator material, or a combination of all of them makes a difference in being able to achieve high electric fields in LHe.

Chapter 5

Experimental Apparatus and Method

5.1 Introduction

The primary goal of this thesis is to demonstrate that 100 kV/cm is achievable in a mock cryogenic nEDM cell. This measurement was attempted in a 20 litre storage vessel (SV) in which LN_2 and LHe are used as a dielectric medium. Electrodes are placed inside this chamber, which were optimised by using finite element meshing software to ensure the profile does not lead to excessive fields which could induce a breakdown. The electrodes are separated by an insulator to support the upper electrode but also to act as the walls of a Ramsey Cell. This chapter gives details on the design of the SV, electrodes, cryostat modifications, HV delivery system, vacuum system, and how the setup was filled with cryogens. It also details the methodology used to perform the measurements. The results of this chapter provide some interesting information on the effect of the electrode profile on the E field. It also shows that change of dielectric constant of the insulator can enhance the high E fields which may induce an unwanted breakdown.

This chapter also details the setup and methodology for the smaller DKHs/DKHl electrode measurements which are a continuation of that done by Hill (3) and Davidson (2) as mentioned in Section 4.5.4.

The SV was designed in order to investigate the relationship between electrode separation and breakdown voltage with the presence of an insulator between a mock cryogenic nEDM experimental sized Ramsey Cell of diameter 360 mm in LN_2 and LHe. Inside the SV is a pair of electrodes with a plane-plane geometry that can be separated by either alumina, quartz, or borosilicate glass insulators with internal diameters between 250 mm or 240 mm (material dependent). The bottom electrode is held in place by G10 standoffs and connected to a G10/stainless steel low temperature to vacuum feedthrough. This

bottom electrode can be set to ground or HV. The top electrode rests on top of the insulator and is connected to HV via a PTFE/stainless steel room temperature to low temperature cryogenic feed. The electrodes are designed and optimised using Opera (136) simulations. Particular attention was made to the groove geometry where the insulator is centred. In order to measure the behaviour of breakdown voltage and separation, the internal plane of the electrodes can be adjusted by adding spacer plates, giving a range for the internal electrode separation of 2 mm to 26 mm.

The top electrode can have up to positive 130 kV applied to it, while the bottom one was designed to have up to negative 130 kV, therefore, at the maximum separation of 26 mm, a field of 100 kV/cm can be achieved.

5.2 The Blue Elbow Rig

5.2.1 Blue Elbow Cryostat

The Blue Elbow is a large cryostat vertically positioned, 1440 mm tall with an outer diameter of 576 mm. The top of the cryostat has an ISO o-ring sealed flange 770 mm in diameter for internal access. The upper halve of the cryostat contains a tank for ~ 10-20 litres of LN_2. The tank can be filled via a port connecting through the aluminium can with two others for gas blow off. The tank is fixed in place with 3 G10 fittings to the upper halve of the cryostat. Underneath the LN_2 tank is the 100 K copper shield which is thermally anchored to the tank via copper feet. The copper feet have three copper bars bolted to them that extend up to the ISO flange at the top of the cryostat. These bars hold an aluminium shield in place which acts as the internal bore (390 mm) of the cryostat. All joints in which copper to copper or copper to aluminium are bolted together have indium around the bolt to ensure good thermal contact.

The bottom halve of the cryostat has two flanges extending horizontally opposite to each other, positioned in the middle of the cylindrical can. One is a 680 mm diameter o-ring sealed blank flange and the other is a 380 mm diameter o-ring sealed reducer flange to CF 150 to connect to the vacuum system.

The LN_2 tank and 100 K copper shield are both covered in 5 layers of super-insulation in order to reduce thermal radiation to the internal volume.

The cryostat also has two flanges next to the LN_2 ports for feedthroughs.

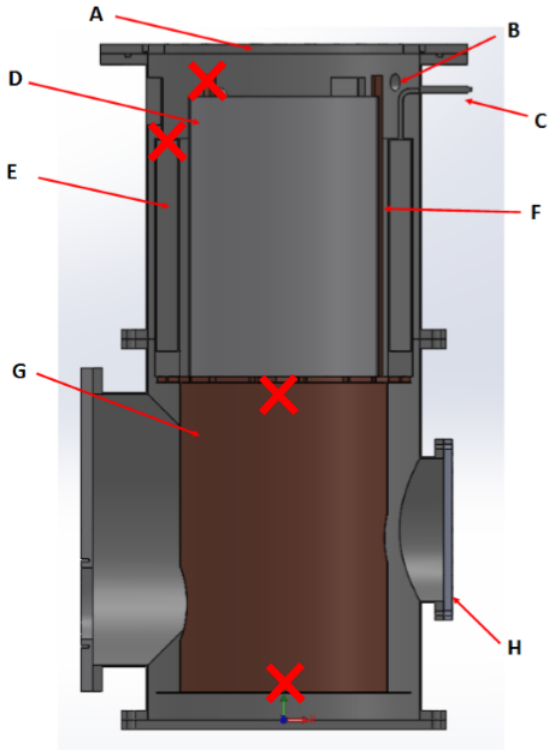

Fig. 5.1 Solidworks drawing of the cryostat. A - ISO flange for access to internal volume, B - CF 38 flange for electronic feedthroughs, C - LN_2 fill/blow-off ports for LN_2 tank, D - aluminum shield, E - LN_2 tank, F - copper support bars for aluminum shield, G - 100K copper shield, H - flange for vacuum pumps. Red crosses are positions for K-type thermocouples.

5.2.2 Vacuum System

The vacuum system used for this cryostat consists of an Edwards E04 vapour diffusion pump and Edwards RV12 oil roughing pump (rate of 12 m^3/hr). The diffusion pump is underneath a cold trap to stop any back streaming of Santovac 5 into the cryostat which could effect the HV delivery to the bottom electrode. During an experimental run the diffusion pump always has LN_2 in the trap. The rotary pump is connected to the backing line of the diffusion pump via a foreline trap with a pirani gauge. The diffusion pump is separated from the rotary pump by two valves, one before the foreline and one after. The rotatory pump is also connected directly to the cryostat via a valve. When pumping the system down initially the backing line to the diffusion pump is closed and left under vacuum from the previous run, while the line to the cryostat is opened to pump from atmosphere. The rotary pump takes about 15-20 minutes to pump the volume in the cryostat to about 0.5 torr, at which point the roughing line is closed and the backing line to the diffusion pump opened. The diffusion pump is allowed to warm till the internal pressure in the pump is $\sim 10^{-7}$ mbar, at which point LN_2 is added to the cold trap. Once this has been done, the cryostat is opened to the diffusion pump by opening the valve between the cryostat and the cold trap. The pressure in the backing

Fig. 5.2 Initial setup of the Blue Elbow Cryostat and insert with frame. Basic setup is shown prior to any modifications detailed in this thesis.

line will rise but falls rapidly once the pressure in the cryostat is dropped from 0.5 torr. The diffusion pump is allowed to run for a few hours before an experimental run till the pressure (from the penning and ion gauge) at the diffusion pump is $\sim 10^{-7}$ mbar.

5.2.3 Electronics for the cryostat

One of the flanges near the LN_2 blow off port was used for thermometry purposes. A CF 38 feedthrough with 4 K-type thermocouple connectors was attached; the thermocouple positions are shown in Figure 5.1. The thermocouples on the vacuum side were attached at various points on the LN_2 tank and 100 K shield in order to measure the temperature gradient of the system during a cool down. One was placed on the top of a copper support bar, another on the top of the LN_2 tank, a third just underneath the copper feet of the LN_2 tank, and finally one at the bottom of the 100 K shield.

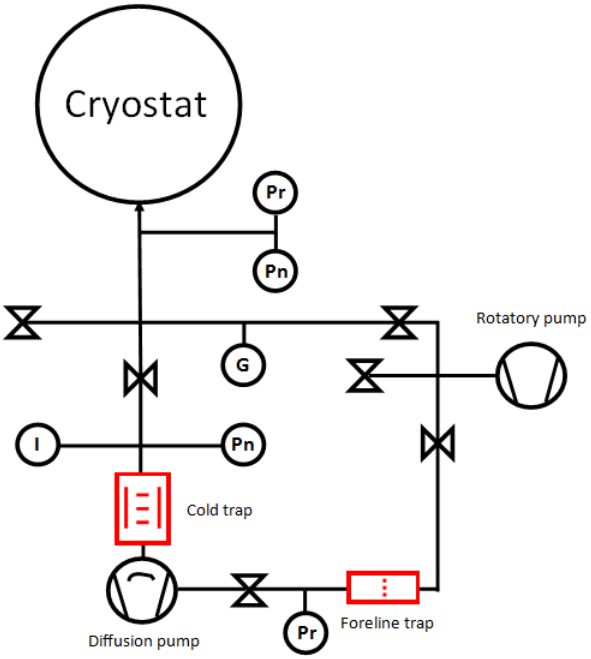

Fig. 5.3 Schematic of the vacuum system. The double triangles represent valves. I = Ion gauge, Pr = Pirani gauge, Pn = Penning gauge, G = Dial gauge (100-1000 mbar). All valves are Edwards speed valves, however, one between cold trap and cryostat is a UHV butterfly valve.

5.2.4 Extensions to the 100 K shield

In order to supply HV to both sides of the SV, extensions were added to the 100 K shield to take a 130 kV feedthrough from room temperature to 4.2 K in vacuum. The large 770 mm blank flange was machined to add a flat surface for an o-ring seal for a CF 150 flange. A tee piece could be added to the blank flange which then had an XYZ manipulator with total travel of 15 cm. The manipulator then has a reducer to CF 38 that interfaces with the vacuum seal on the HV feed. The HV feed is attached to the CF 38 flange on the manipulator with an o-ring seal. The vacuum seal between the HV feed and CF 38 flange is made by a double o-ring seal on the PTFE surface which is held in position by two clamps. The HV feed is then thermally clamped within the copper extension from the 100 K shield, therefore, creating a thermal gradient of 100 K to 4.2 K at the middle of the feed over a distance of 300 mm. The thermal clamp has a radiation baffle attached to it. To support the feed a PTFE ring is held in place inside the copper extension to guarantee the feed will move straight into contact with the G10 feedthrough at the bottom of the SV.

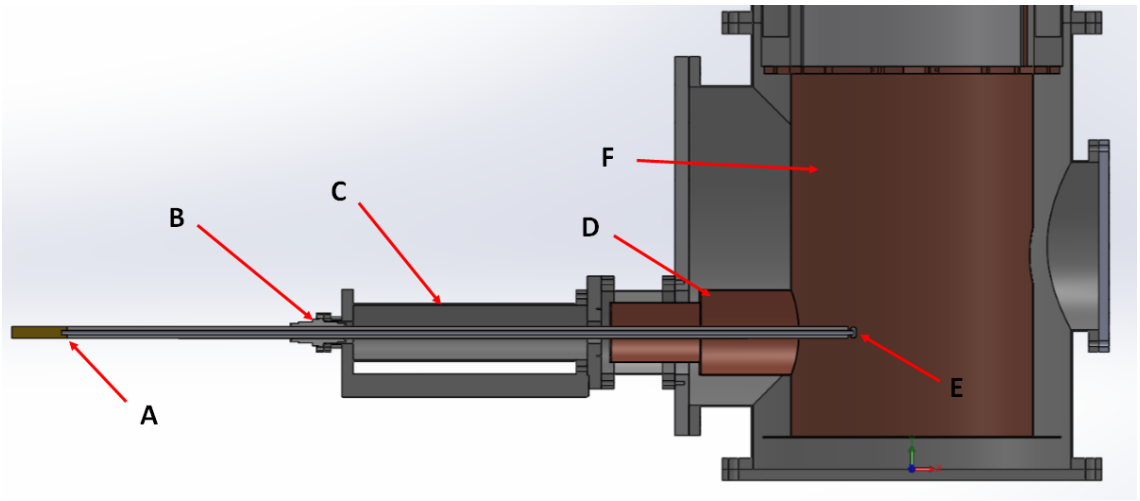

Fig. 5.4 Solidworks drawing of the side feed. A - Brass connector to HV cable, seen in Figure 5.13, B - double o-ring compression seal either side of CF 38 flange, C - long travel XYZ manipulator, D - copper tubulation (thermal clamps for the feed are attached internally), E - ball electrode, F - 100 K copper shield. A K-type thermocouple was added to the thermal clamps on the HV feed at a later staged, details given in Appendix E.

5.3 Insert for Blue Elbow

5.3.1 Storage Vessel (SV)

The SV was designed to fit into the inner bore of the Blue Elbow cryostat while maximising the internal diameter to fit the HV electrodes. The SV is constructed out of 304 stainless steel in order to ensure sufficient strength with vacuum on the outside and atmosphere/cryogen on the inside while keeping the walls thin. The magnetic properties of stainless steel was not a concern for this experiment, however, for a real nEDM measurement non-magnetic materials would need to be used. The SV main body was a cylinder of 380 mm diameter with a wall thickness of 4 mm. The wall has two rings welded on to the top and bottom which are ~ 15 mm x 15 mm cross section with the internal edge machined to a radius of 8 mm, see Figure 5.6. This was done to lower electric fields inside the SV and not cause any breakdowns to occur from the electrode to the SV walls due to sharp edges. These rings also had a groove machined into the external edge in which indium can be placed to make a superfluid tight seal. The seal is formed when the top and bottom plates are bolted down onto the rings. The large plates form the lids and make the vacuum seal. They are 17 mm thick 304 stainless steel. They both have CF 63 flanges on them to attach the SV to the insert at the top plate and the bottom plate for a vacuum feedthrough. The top plate of the SV also has three CF mini ports which connect up to the insert top plate via thin wall tubes. These tubes are used for a fill line, level sensor, and any other electronics required to monitor the liquid.

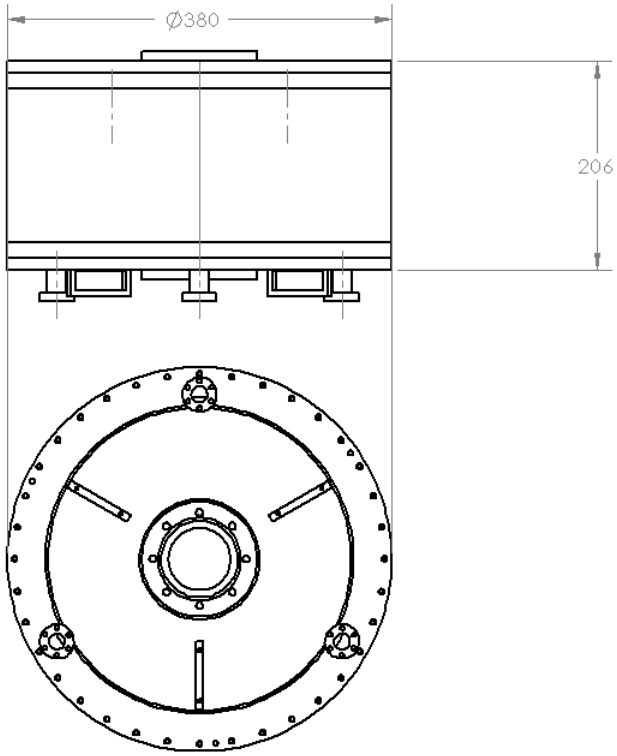

Fig. 5.5 Drawing of the SV, full designs in Appendix H.

The SV is connected to a 550 mm ISO flange at the top of the insert. The flange has a CF 63 fitting coming off the bottom (vacuum side) which is then attached to a thin wall stainless steel tube. This extends 455 mm down to connect to a 220 mm long bellows which then attaches to the top plate of the SV. The stainless steel tube has 8 radiation baffles which are 380 mm diameter and soldered to the tube close to the top of the insert. At the bottom of the baffle assembly is a copper clamp that has 3 thermal straps which connect to the copper bars of the 100 K shield. The room temperature side of the CF 63 central flange of the insert is connected to a tee piece which has a reducer from CF 38 to a CF 38 XYZ manipulator at the top with the HV cryogenic feed sealed with a o-ring compression seal around the PTFE fitting to the manipulator. The other port on the tee piece is a blow off port for LN_2/LHe gas.

The top of the ISO flange has 6 CF 38 ports, three of which are the access ports for the CF minis, the other three are used for thermometry of the SV and heater. The thermometry consists of two K-type thermocouples, one on the top plate of the SV and the other at the copper clamp on the central tube of the insert. For use with LHe there are two silicon diodes (Si410) (137) added to the top plate of the SV and one thermally clamped to the bottom plate of the SV. The silicon diodes were calibrated using another silicon diode used in the Katsika (138) magnetic test setup. This diode was known to read the correct

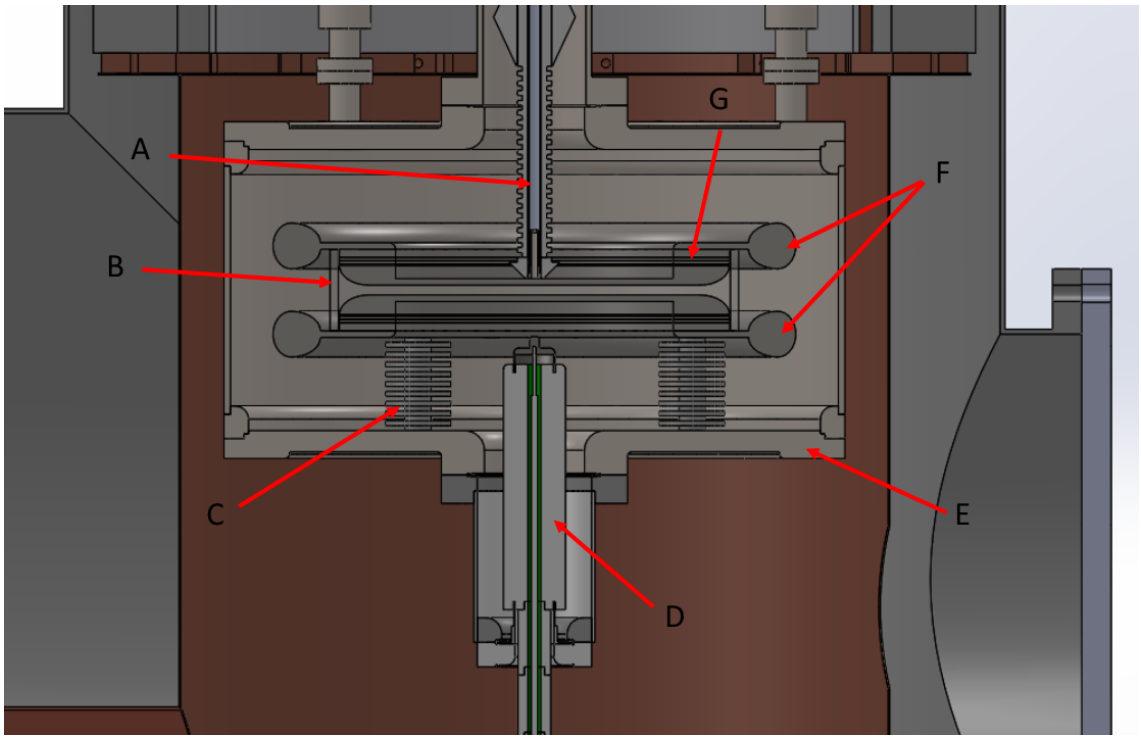

Fig. 5.6 CAD model of the SV. This is a cross sectional view of the SV with the electrodes inside. A - HV room temperature to cryogenic feed shown in Figure 5.11, B - Insulator, C - G10 stand-offs, D - vacuum to cryogenic feedthrough shown in Figure 5.15, E - storage vessel (SV), F - electrodes, G - spacer plates.

temperature to 0.1 K. The heater is three high power resistors 0.33 $\Omega \pm 5\%$ (50 W) bolted to a copper plate that is glued with Stycast 2850FT (139) on the SV top plate. During a warm up, after measurements have been made and the LN_2 has been syphoned from the SV, the heater can be switched on to provide 100 W to slowly warm up the SV to room temperature before the insert is removed. The vacuum is broken to ~ 200 mbar N_2 to allow thermal conduction between the heater and the cryostat walls. The power input is regulated by a CAL 9900 temperature controller (140) (switching the current source on and off using a solid state relay) to 20°C by reading the thermocouple on the top of the SV. This provides a smooth input of heat overnight which avoids any thermal stress on the insert.

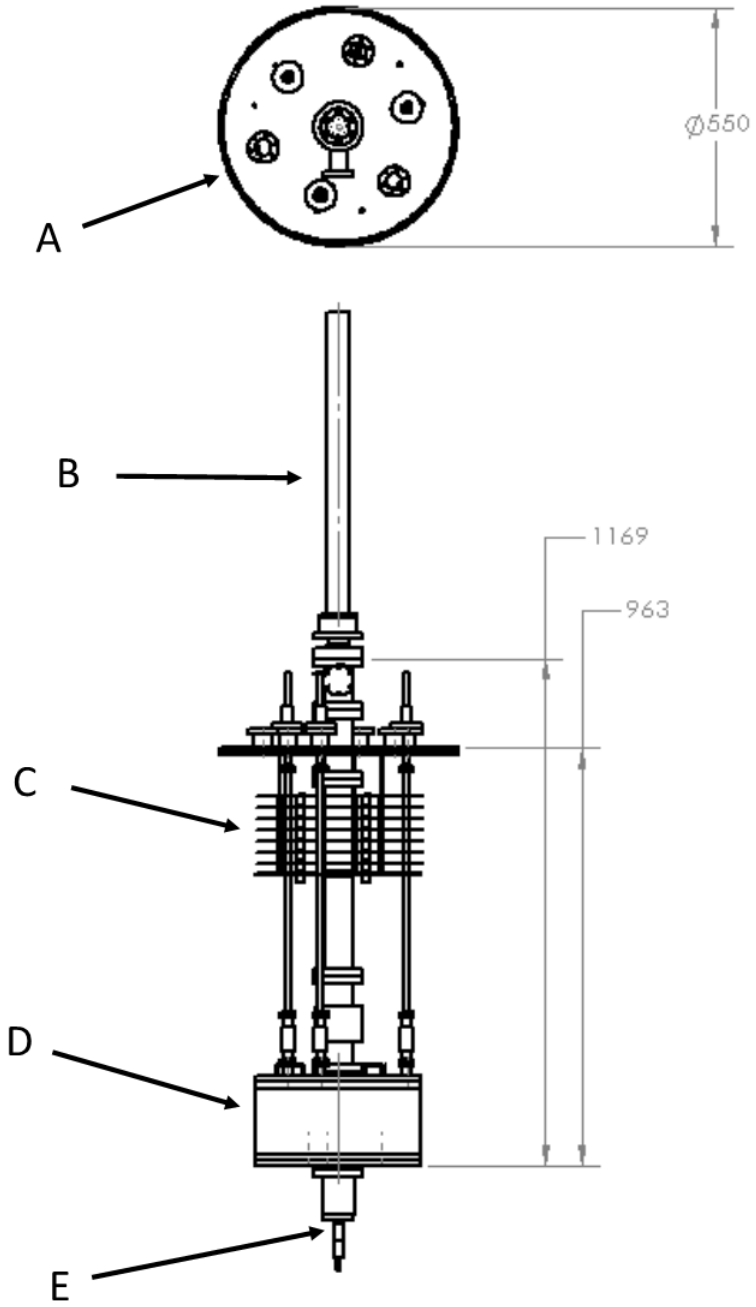

Fig. 5.7 Drawing of the insert with dimensions. A - Insert top plate, B - copper connector shown in Figure 5.12, C - radiation baffles, D - storage vessel (SV), E - vacuum to cryogenic feedthrough shown in Figure 5.15.

5.3.2 Supports

The SV requires supports to hold the weight of the chamber as the thin wall stainless steel will deflect trying to support ~ 100 kg. Therefore, 6 x 3 mm steel studding was used to hold up the SV. They are positioned in pairs with one closer to the central flange and the other closer to the outer edge. This studding is screwed into the ISO flange of the insert on the vacuum side. The studding then passes through the baffles with 20 mm G10 spacers between each baffle to support the assembly. The studding is then screwed into a support bracket that is bolted to the top plate of the SV. In order to avoid swinging of the SV when the insert is lifted into the cryostat, the studding is reinforced by fibre glass tubing below the bottom of the baffle assembly to the bracket. The fibre glass is further strengthened by a flat mat between the pairs of fibre glass tubing of the same material. This stops any translational movement of the SV and deflection of the baffle assembly. Image of supports is shown in Figure E.13.

5.3.3 Filling the SV with LN_2 and LHe

Filling of the SV with LN_2 is done using a stainless steel tube (6 x 8mm) with a compression seal to KF flange. The KF is attached to the fill line port of one of the CF minis on the top plate of the insert. The tube is lowered to the bottom of the SV. A fibre reinforced tube is attached on the end of the tube and the dewer of LN_2 at the other end. Filling is performed with the blow off port on the tee piece fully open as well as the two other CF mini ports.

Filling of the 100 K shield is done through one port on the side of the cryostat. Only one is attached via a fibre reinforced tube to a dewer of LN_2 while the other two are blow off ports.

The insert and cryostat are pre-cooled by filling with ~ 5-10 litres of LN_2 and the gas is allowed to drop the temperature down to ~ 173 K before topping off with more LN_2. The volume is then allowed to cool to 77 K and then filled up. The volume in the SV is filled to up to half way between the copper thermal clamps on the insert and the top plate of the SV. When the liquid is still the measurements are taken.

In the case of the LHe measurements, the cryostat and the SV are both filled with LN_2 till they are at 77 K. The LN_2 is then SV siphoned out and the SV allowed to rise to ~ 80-90 K to ensure all the LN_2 is removed. The LHe is then filled through the same LN_2 fill port of the insert using a transfer tube. The temperature is monitered with the silicon diodes to make sure the SV reaches 4.2 K as its being filled up. The volume of LHe is filled to the same level as for measurements with LN_2.

5.4 High Voltage System

The HV system is a simple RC circuit. The initial tests in LN_2 (2 mm → 8 mm separation) used the same circuit, shown in Figure 5.8, but the ballast resistors were not used and the vacuum feed acted as a ground return line directly to the ground terminal of the Spellman (SL10W) power supply (141). The connection to the bottom electrode is made by having its connective ball, at the end of the feed, touching the G10 feedthrough electrode at the bottom of the SV plate. Before the HV is applied to the system (after cooling) the capacitance is measured between the two feeds at the room temperature side. The capacitance is measured using a RS capacitance meter which is sensitive to ~ 10 pF. The cryogenic feed is moved into contact till there is a slight change in capacitance between the feeds (167 pF with just top feed connected to 260 pF with bottom connected at electrode separation of 6 mm), indicating electrical contact. Then the vacuum feedthrough is moved into contact slowly using the fine thread on the manipulator. A sharp rise in capacitance is observed when contact is made. Each experimental run uses different separations, resulting in different values for capacitance, but the value is in the range of hundreds of pF for all tests.

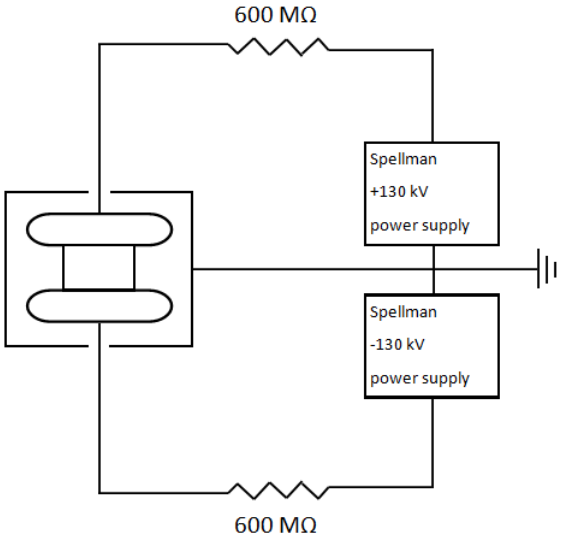

Fig. 5.8 Diagram of the HV system.

The power supplies are run with the positive voltage always on the cryogenic feed and the negative on the vacuum side feed. The reason for this is there are sharp edges present on the 100 K shield, therefore, at positive polarity there would be substantial electron emission.

The internal capacitance of the Spellmans was calculated by Karamath (93) to be ~ 1 nF,

the HV cables (hivolt 2121) have 95 pF/m (142), the HV feeds have ~ 0.1 nF (3), and the electrodes range from ~ 34 pF - 200 pF depending on the selected separation.

5.4.1 HV cryogenic feed

The cryogenic HV feed is based off the design of Karamath (93) which proved reliable to ± 130 kV in vacuum. The construction consisted of ~ 21.2 mm diameter, 1.5 m long PTFE tube with bore of ~ 8 mm to take a 316 stainless steel tube of ~ 8 mm diameter and thin wall of 0.5 mm. The PTFE is then covered in aluminium tape to just above the first castellation at the low temperature side and terminates at the vacuum flange at the room temperature side. However, previous measurements in this lab at low temperature with Karamath's original design of feed only achieved maximum of 100 kV reliably, however, measurements presented in this thesis required achieving voltage of ± 130 kV reliably and consistently. During some measurements presented in this thesis, feeds would fail from a breakdown puncturing through the PTFE at the top castellation on the cryogenic side. At that time the ground sheath was terminated by wrapped in PTFE tape to suppress the sharp edge of the aluminium. The failure occurred more frequently when the level of the LN_2 dropped below this ground termination.

Simulating the feed in Opera, see Figure 5.9, shows that the voltage potential lines start to be pulled out away from the conducting core in the vicinity of the electrode end, creating high field regions shown in red. This starts to occur near the top castellation. As there is a change of dielectric strength, due to the cut out of the castellation, it creates a high field region in this castellation, which the PTFE possibly could not hold.

Therefore, to improve the reliability of the feed a stress cone was added. This was 50 mm in diameter and had a chamfer, to match the diameter of the PTFE feed, on both sides. Initially, the design of the stress cone was made of two halves and screwed together with G10 screws around the feed with the bottom of the cone above the top castellation. The cone is prevented from moving up and down during cooling and warming up by a castellation cut into the feed with the cone having a matching step so it is held in place. The strategy for this design was to prevent high field regions on the sharp ground sheath termination which may create high field regions on the top castellation (see Figure 5.9), hence the thinner region of PTFE being unable to hold the voltage.

It was found that this method did not work, creating a track which meant the electrodes could not charge up. Therefore, the method for fitting the stress cone was redesigned. The cone was fitted by cooling the PTFE tube of the feed in LN_2 while warming the

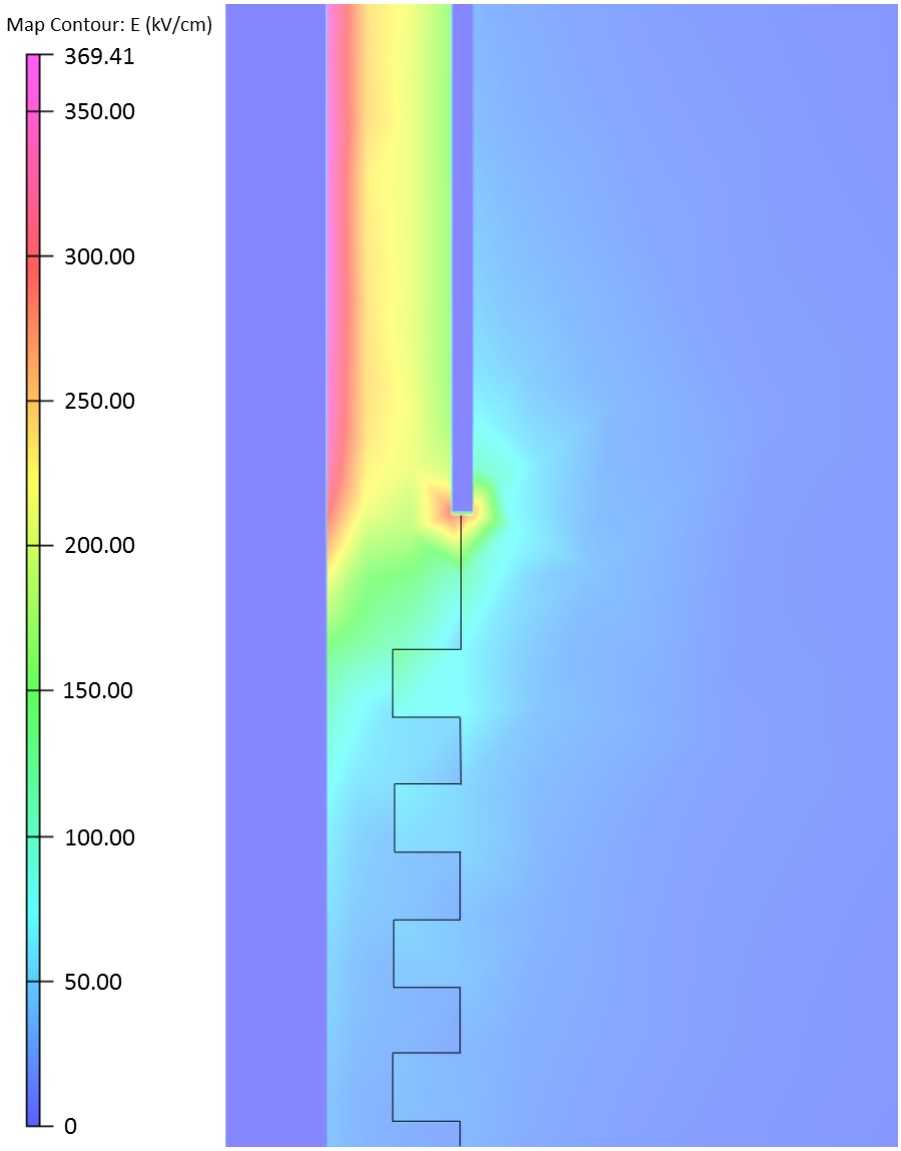

Fig. 5.9 Simulation of Karamath HV feed design. Fields are higher in the top castellation than the others.

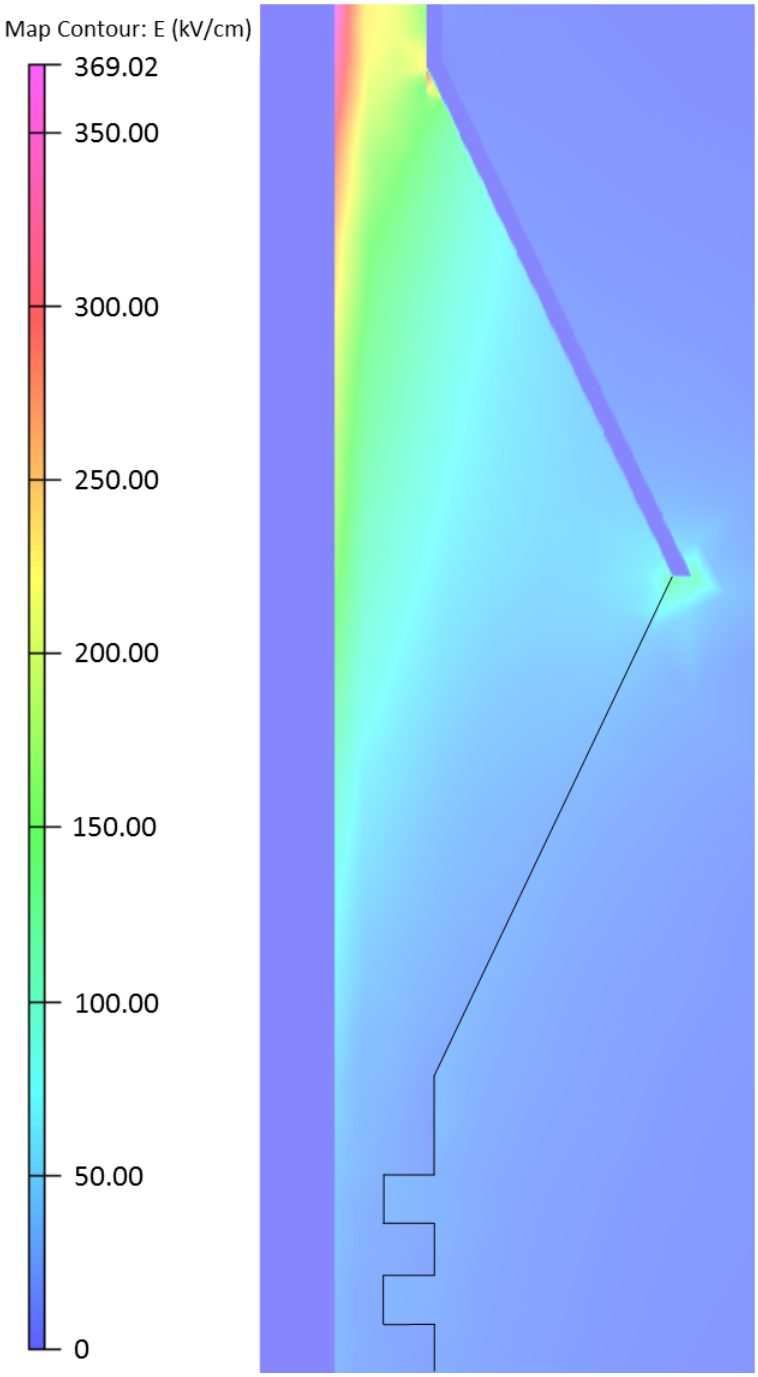

Fig. 5.10 Simulation of new HV feed design. High fields are no longer present on the top castellation.

cone to 393 K. The bore of the cone was 0.2 mm smaller than the feed diameter before cryogenic fitting. The aluminium tape could then cover the top half of the cone and be terminated in the same way as previously stated for Karamath's design.

This modification enabled feeds to be ramped up to 130 kV reliably with either polarity without any damage to the feed.

Fig. 5.11 Prototype feed tested in run 20. The stress cone is made of two halves which are held together with G10 screws. In order to hold it in place, a notch is cut into the feed with a step on the inside of the stress cone halves for them to rest.

The connection to the electrodes is made by lowering the manipulator till the stainless steel feed has made contact. In order to ensure that the feed is guided to the middle of the electrode in the SV, there is a PTFE spyder which sits above the stress cone; this keeps the feed straight in alignment of the bore of the insert. The electrode also guides the feed by the placement of a PTFE block with a chamfer on the electrode surface for a PTFE cone on the end of the feed to guide it straight into contact. The spyder and PTFE guiding blocks are required, in case of thermal contraction which would cause the feed to move out of electrical contact with the electrode.

The room temperature side of the feed required a vacuum seal connection to stop the LN_2 or LHe travelling up the inside of the tube. This was done with a brass connector using a double o-ring seal. The brass connector was held in place with grub screws to the core, shown in Figure 5.13.

A copper tube filled with 50 mm diameter solid PTFE with a bore through the cen-

tre the size of the HV feed, ϕ 21 mm and ~ 350 mm depth. The larger hole is then reduced to take the diameter of the HV cable, ϕ 12.4 mm. This connector is placed on the feed. The cable is then put into the copper tube and completes the electrical connection to the brass connector and the HV power supply.

Fig. 5.12 HV copper connector to shield brass connector to HV cable (2).

Fig. 5.13 HV feed brass connector prior to assembly (2).

A compression o-ring seal around the PTFE tube is made ~ 400 mm from the end of the brass connector. The seal is then attached to a CF 38 flange that is bolted to the XYZ manipulator. The copper tube is also bolted on top of this CF 38 flange to keep a tight fit with the brass connector and HV cable, avoiding thermal contraction problems.

5.4.2 HV vacuum side feed/return line

The side HV feed uses the same design as Karamath's (93).

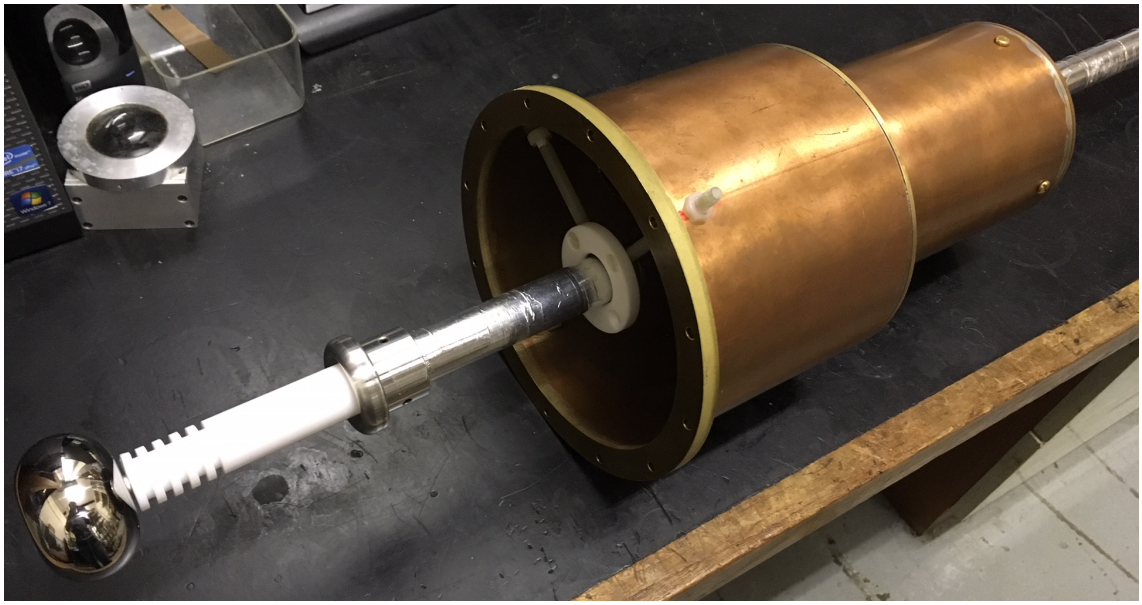

Fig. 5.14 Picture of side feed from atmosphere to vacuum. Copper tubing shown is the extension piece to the 100 K shield.

The vacuum feed seals in a similar manner to the cryogenic feed. There is a double o-ring compression seal around the PTFE tube and between these seals is a CF 38 knife edge in order to attach it to the long travel XYZ manipulator (total travel of 15 cm). The connection to the HV cable uses the same design as the cryogenic feeds but an o-ring compression seal is made around the stainless steel core and PTFE tube to stop vacuum leaks.

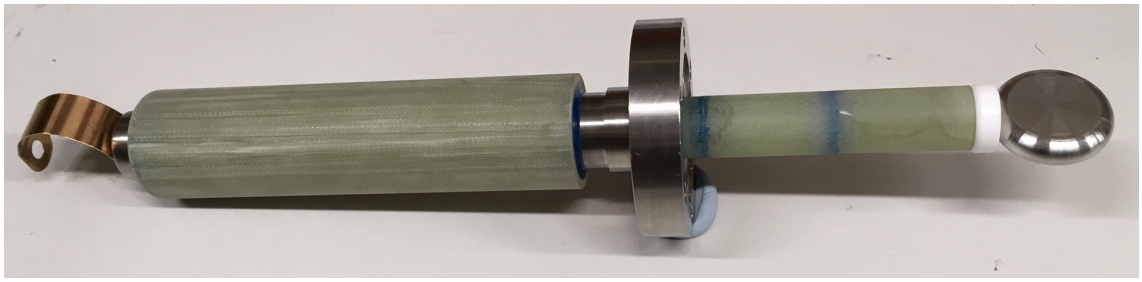

Fig. 5.15 Picture of G10 feedthrough to take HV from vacuum to 4.2 K liquid helium.

The HV is delivered to the bottom electrode via a G10 feedthrough, shown in Figure 5.15. The vacuum feed is moved into contact so that the electrode on the end of it will make electrical contact with the electrode on the bottom of the G10 feedthrough. The G10 feedthrough has a CF 38 flange which has had a tube of G10 (8 x 38 mm) glued in it using

Stycast 2850FT (139). The end has a stainless steel cap which is glued into the G10 tube to seal from the liquid side. The G10 tube then has a smaller tube (8 x 20 mm) coming off the vacuum side which is also glued into the CF 38 flange. In order to connect to the metal cap at the top, a thin stainless steel rod is screwed into the metal cap which reaches down into the vacuum side so a ball electrode can be screwed into that.

5.4.3 Ballast resistors

It was unclear how the Spellman power supplies would cope with a breakdown event that has twice the energy than they were designed to handle. Therefore, for any back to back measurement with them, ballast resistors were required in order to protect them. As the system is an RC circuit an approximation can be made for the criteria of the resistors. But for a circuit without these resistors, assuming a system capacitance of ~ 1 nF and resistance of ~ 60 Ω;

$$\tau = RC = 9 \times 10^{-8} s, \tag{5.1}$$

$$E = \frac{1}{2} C V^2 = 25.35 J, \tag{5.2}$$

which results in an event that is very quick and energetic. In the event of a breakdown the Spellman sees a surge of current which exceeds its safe limit so it shuts itself off. In order to limit this discharge a ballast resistor was required to slow this breakdown event but also to ensure that the charging current would not then take a long time to reach the desired voltage or stop this safety shut off of the power supply. Calculations were performed with this in mind, details given in the Appendix D.

Two ballast resistor each consisting of 6 x 25kV 10W 100MΩ resistors (143) connected in series were constructed.

Tests done in atmosphere with the power supplies back to back and ballast resistor in place (up to 220 kV across a gap) showed that if a breakdown occurred then both supplies shut off at the same time and seemed to suffer no damage.

Fig. 5.16 One of the two dry ballast resistors used in the experiment. Spellman cable is connected through the top and bottom plates, one to power supply, other to HV feeds. The cable connects to a recess inside the corona domes that holds the chain of resistors. The resistor chain is then connected to the other cable insde the opposite corona dome via G10 tubing.

5.5 Electrodes

The electrodes for the SV needed to be able to have a varying separation to measure the breakdown values against separation for a large surface area. For a plane-plane geometry a Rogowski profile (144) (145) (106) is optimum, however, there is not enough space in the SV to hold such electrodes at a separation of 26 mm. Therefore, the geometry needed to be optimised to limit any high field problems that may occur.

5.5.1 Optimisation of electrode geometry

The objectives for optimising the electrodes are to minimise the E field at the groove region (E field along the surface of the groove), limit the E field on the shoulder (point where the curvature of the groove blends into the flat surface and this transition), and maximise E_0 (applied voltage/electrode separation) homogeneity inside the insulator walls.

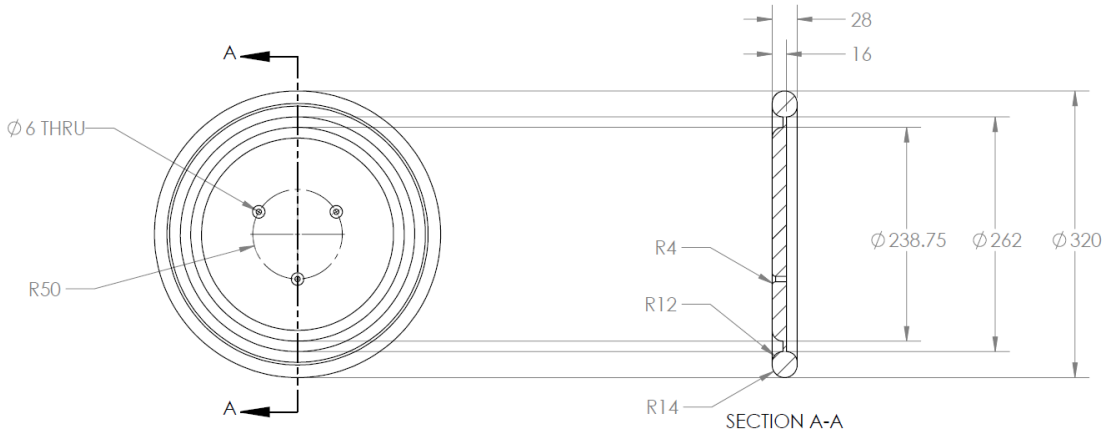

Fig. 5.17 Drawings of the initial electrode design. The groove internal diameter is determined by the internal diameter of the borosilicate glass insulator, outer diameter determined by that of the alumina insulator. The design here is a starting point, non-optimised geometry, based around the PSI nEDM groove geometry with the corona ring curvature equal to its thickness.

These electrodes have an original diameter of 320 mm, 28 mm thick, with grooves 12 mm deep from the surface with 262 ± 0.05 mm (OD) x 238.75 ± 0.05 mm (ID). This gives a R12 (12 mm) radius on the groove, and a corona radius of R14 (14 mm). Simulating the non-optimised groove geometry in Opera with electrode separation 26 mm using an alumina insulator with a radial separation 0.5 mm (distance between insulator walls to the groove base) gives the result shown in Figure 5.18.

Inspecting the contour plot from Figure 5.18, there is a high field present on the groove

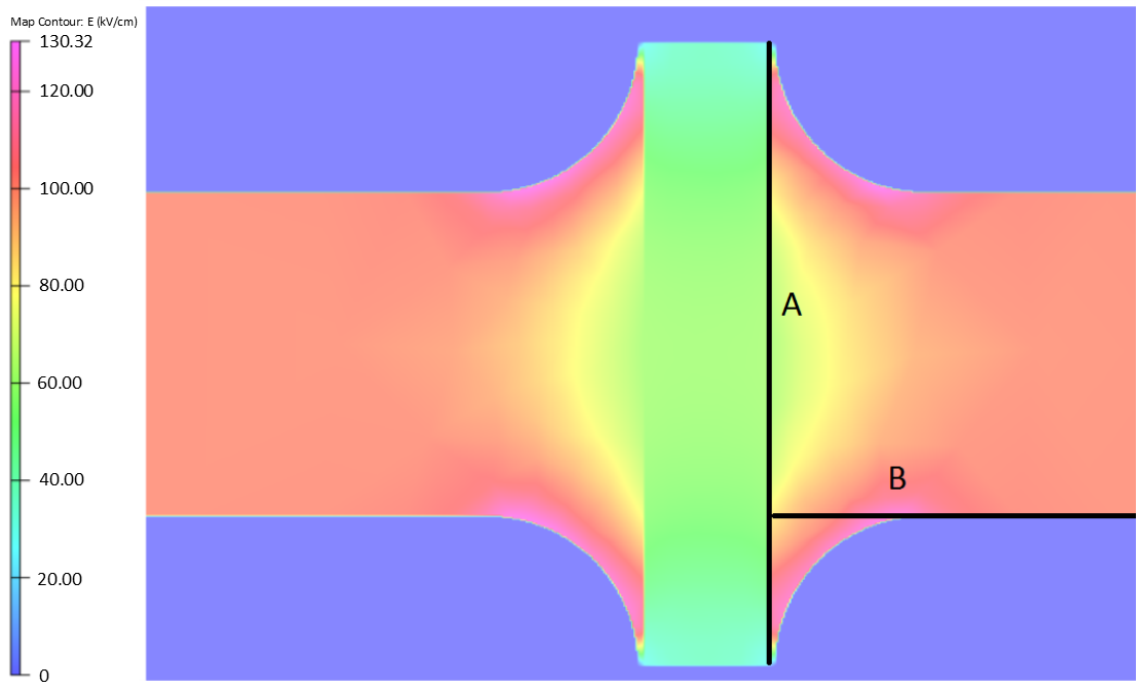

Fig. 5.18 Opera simulation showing a contour plot of the initial groove geometry with R12 profile. The top electrode is charged to negative 130 kV and bottom electrode at positive 130 kV, giving an E_0 field of 100 kV/cm over 26 mm separation. A: Data points taken for simulations along the length of insulator, B: Data points taken for simulations along the shoulder of the electrode.

surface close to the insulator wall. This high field is greater than E_0 which implies that this could be the weak point of the system, hence where the breakdown would be initiated. There is also a high field present on the shoulder of the groove which could also be an initiator for breakdown and is worth investigating if it can be minimised. It's clear that this geometry needs to be optimised to find the ideal geometry to avoid these high fields.

Figure 5.19 shows the variables defining the groove geometry. This leaves a large number of degrees of freedom to explore. Therefore, in order to optimise the profile of the groove I looked at one variable at a time and kept a number of them constant to determine the relation between them all.

Firstly the groove profile will be varied to determine the relation to the field on the surface of the groove (changing a/b). There are two ways to test this; a profile with a constant radius (a=d=12 mm, b and θ varied) and an elliptical profile (a=d=12 mm, b varied, θ = constant). In testing these variables, I kept ϵ_r = 9.3, $\Delta r_i = \Delta r_o$ = 0.5 mm, and d = 12 mm. Keeping the relative permittivity at the highest available value means that the electrodes will be designed for the alumina insulator so that the geometry will be optimal for this material (the other available insulator is borosilicate glass which has a lower

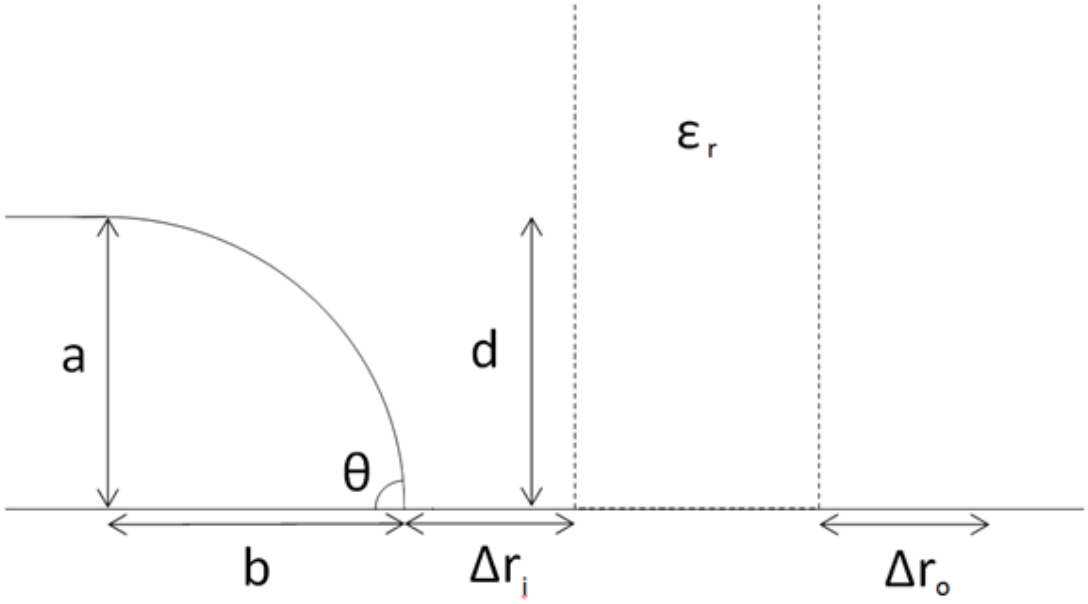

Fig. 5.19 Diagram of variables for the groove profile. Variables a/b are the major/minor lengths, respectively, of the arc. The depth of the groove is d=12 mm. This will be kept constant throughout the following simulations to see if other parameters contribute. θ is the angle of approach of the arc, i.e. if a/b = 1 and d = 12 mm, the radius will be R12, therefore, $\theta = 90°$. Δr_i is the radial separation on the inside groove, with Δr_o the radial separation on the outside. Finally, the relative permittivity of the insulator, ϵ_r, will also need to be considered.

$\epsilon_r = 4.6$). The radial separation is set to 0.5 mm as the insulators will need to be centred on the inside edge for borosilicate glass, and the outside edge for alumina/quartz, due to the dimensions of the available insulators. However, the insulators are not perfectly round so this value should be allowed some extra space between the insulator wall and the groove.

Constructing the model for the simulations, I produced 1000 mm diameter plates with separation 26 mm. The electrode plates are much larger then the actual electrode in order to remove any effects from the edges. At 239 mm ID and 261 mm OD the grooves were created 12 mm deep. Voltage of +130 kV was applied to the top with the other being at -130 kV, giving E_0 of 100 kV/cm. The depth for the groove profile is only 12 mm, so for the constant radius profile a fillet was applied to the edge of the plate of R12, then another simulation of R13, etc... up to R24. This means that the θ variable will change at the point which the arc meets the base, creating a partial curve.

Starting with the constant radius profile, E field plots were created taking values along the insulator wall, shown in Figure 5.18 as path A. These plots are shown in Figure 5.20.

Radius of fillet (mm)	Equivalent value of θ (degrees)
R12	90.0
R13	80.0
R14	76.2
R15	72.8
R16	70.2
R17	67.6
R18	65.6
R19	63.4
R20	61.8
R21	59.8
R22	58.4
R23	57.2
R24	55.8

Table 5.1 Table of values of θ for equivalent radii of the fillet for the profile of the groove.

The choice of taking values at a radial separation of 0.25mm, is to check if the high field is maintained across the gap to the insulator wall, which for the R12 case seems to be true. The high field in this region seems to drop blow E_0 at R14 with diminishing values at the peaks subsequently. From this plot it demonstrates that using less then R14 can potentially cause problems by creating high fields in the gap between the groove and the insulator wall, potentially a weak spot for our system with regard to high voltage breakdowns.

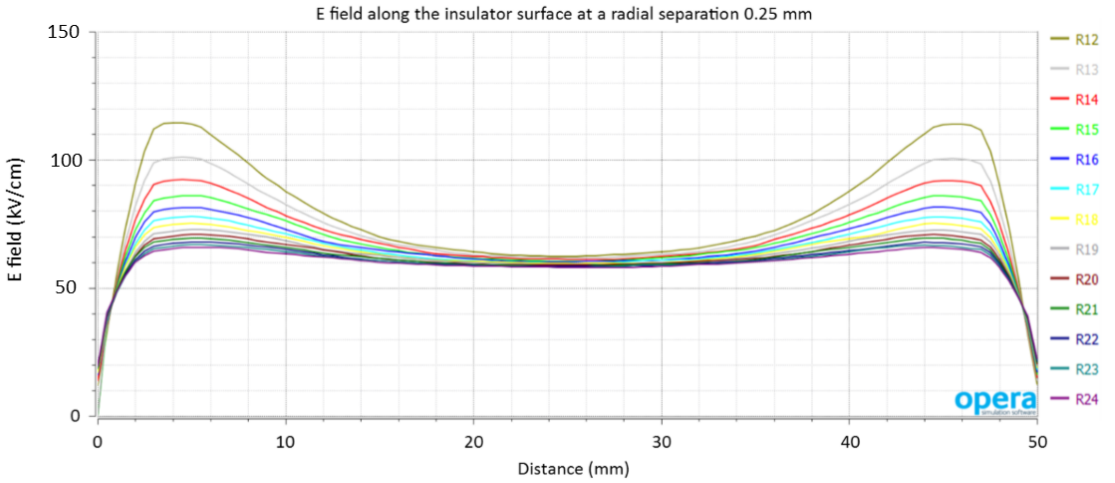

Fig. 5.20 E field plot against distance for along the length of path A in Figure 5.18, the insulator wall from one electrode base to the other at a radial separation of 0.25 mm from the wall, or middle of the gap, between groove and insulator for constant radius profiles, E_0 = 100 kV/cm, distance in mm.

This gap is not the only aspect of interest, as high fields along the groove surface also need to be minimised to move the highest fields away from the wall as much as possible. This region is investigated in the simulations shown in Figure 5.21, which shows that for R12 the transition to the flat surface is very sharp so minimising this will be important to optimise the geometry. The larger radii move the high field region further from the insulator, but again as one gets to the largest radii the improvements to the peak fields are diminishing.

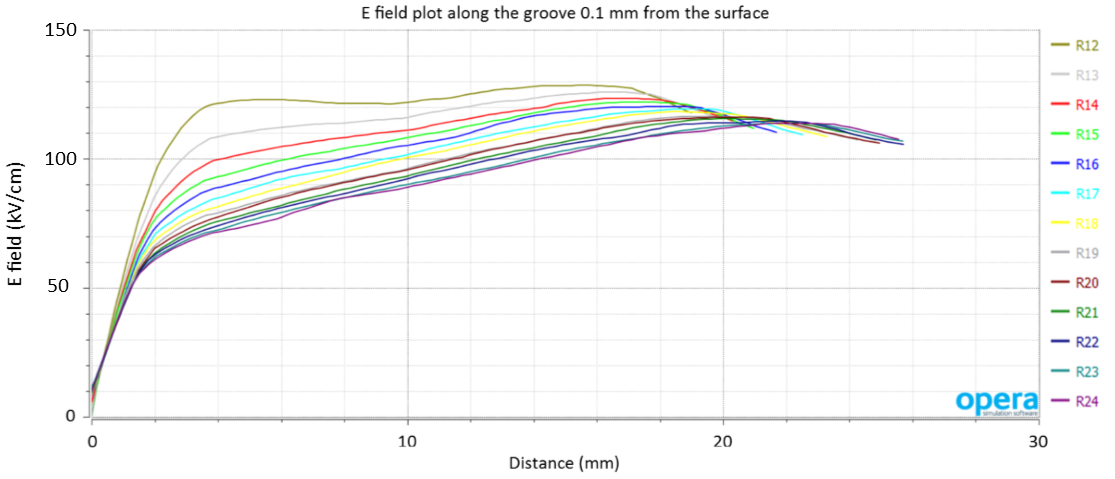

Fig. 5.21 E field plot against arc length along the surface 0.1 mm away from the groove. The choice of 0.1 mm away for the surface is to avoid points formed from the meshing of triangles to the surface, E_0 = 100 kV/cm, distance in mm.

Figure 5.21 also shows that there will be fields higher then E_0 even at larger radii. In-

vestigating this shoulder using the same contour plot, but taking values along the flat plane (path B shown in Figure 5.18) of the electrode to the insulator surface gives the plot shown in Figure 5.22.

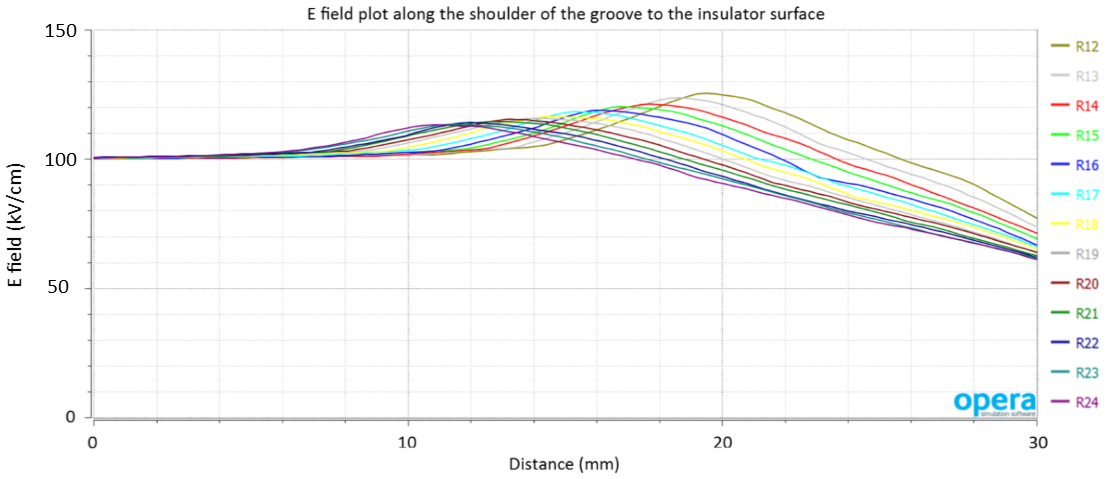

Fig. 5.22 E field plot from 90 mm in from the centre of the electrode to the insulator wall, points taken at 0.1 mm away from the surface of the electrode. The peak value for each radius is higher then E_0.

As Figure 5.22 shows, the presence of high E field on the groove shoulder cannot be avoided, it will always be there but it is not clear whether this will affect our ability to achieve the highest E field possible between the electrodes. However, if this shoulder is the weakest point in the system then the preferential point for breakdown would be at the shoulder, which should remove high fields at the insulator while also allowing the maximum E field to be between the planes of the electrode.

For the elliptical profile, changing θ as well as varying a/b leads to a somewhat complex shape, and it was difficult to generate a model with this geometry as there is not a clear way to generate such a shape profile in Opera. Therefore, Solidworks (146) was used to create the desired geometry and then exported into Opera. In order to check the individual parameter's contribution to the high fields only b will be varied and a = d = 12 mm. The value for b was varied from 12 → 24 mm. The same setup described in the simulation used previously was repeated here for the elliptical geometry. One problem with trying to replicate the same plot as Figure 5.21 is that the E field plots along the surface of the groove are difficult to produce as Opera will not follow the elliptical profile, it can only deal with constant radii. Therefore, I will only focus on path A (Figure 5.23) and path B (5.24) to describe what effect elliptical profile will have.

Compared to Figure 5.20, Figure 5.23 is quite different for the elliptical profile. It shows that the peak values are all above E_0 except R23 and R24. It's clear from Figure 5.20

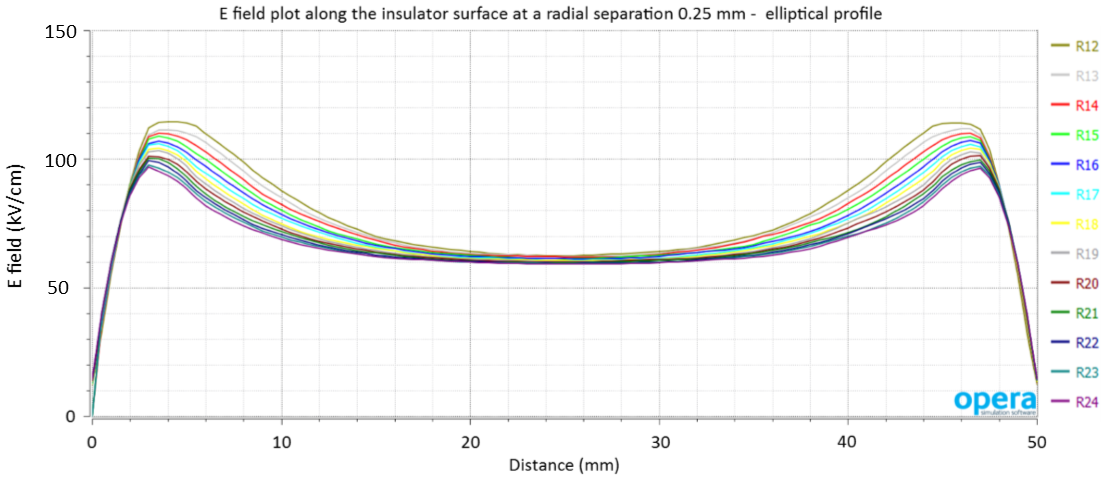

Fig. 5.23 E field plot against distance along the length of the insulator wall from one electrode base to the other at a radial separation of 0.25 mm from the wall, or middle of the gap, for elliptical profiles. E_0 = 100 kV/cm.

and 5.23 that what effects the E field in the groove region is the value of θ, not the minor/major axis of the groove.

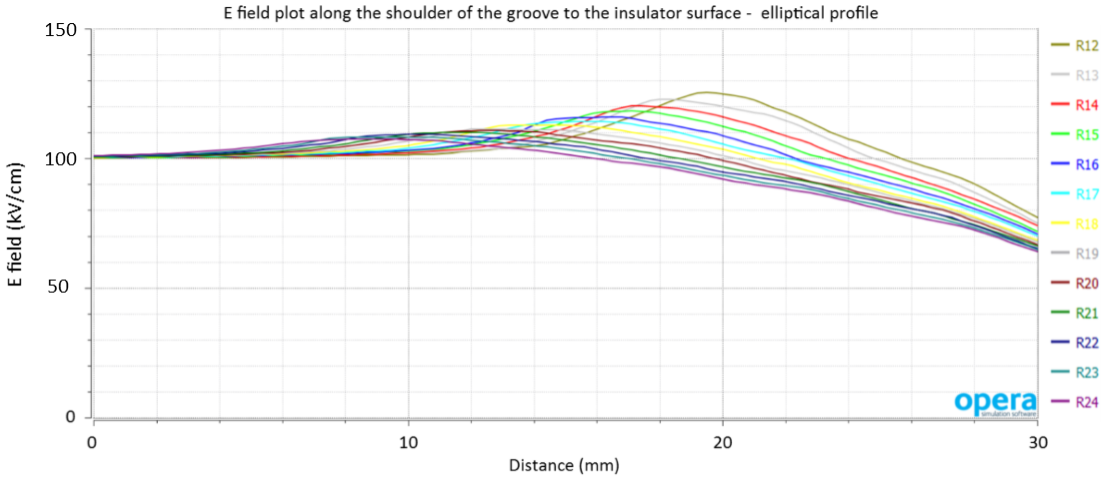

Fig. 5.24 E field plot from 90 mm in from the centre of the electrode to the insulator wall, 0.1 mm away from the surface of the electrode, for elliptical profiles. The peak value for each radius is the highest field in the whole contour plot.

Figure 5.24 shows that the peak E field values at the shoulder will drop off faster compared with the constant radius profile shown in Figure 5.22. This would make sense as the groove blends into the curvature more smoothly with an elliptical profile.

In conclusion, the results of these simulations suggest that the optimal geometry would be an elliptical profile with a θ angle not equal to 90°. This, however, is a very complex shape to machine, and in comparing Figure 5.22 and 5.24, it does not result in too much

difference between the peak E field values on the shoulder: it will always exceed E_0. In fact, it may be optimal to have this higher field value on the shoulder in order to protect the insulator, ensuring that the breakdown occurs at the shoulder compared with the insulator surface. Hence, the chosen geometry for the electrode will have some form of constant radius profile.

5.5.2 Electric field homogeneity

One of the criteria for the electrode geometry is to maximise the homogeneity of the E field in the volume confined by the insulator walls, which for a real nEDM experiment the UCN would occupy. This factor is not relevant for this thesis as the primary goal is to achieve 100 kV/cm across the cell, however, it is important to consider.

The goal for inhomogeneity of the E field for a cryogenic nEDM experiment is quoted for SNS nEDM to be 1%, in order to achieve 10^{-28} ecm sensitivity (147). The origin of this requirement is due to the $v \times E$ effect. Any particle passing through an electric field it will cause a motional magnetic field seen in its rest frame, given by:

$$B_{v\times E} = -\gamma \frac{\mathbf{v}\times\mathbf{E}}{c^2}, \tag{5.3}$$

where $\gamma = (1-\frac{v^2}{c^2})^{-\frac{1}{2}}$. In the case of UCN the value is approximately 1 for γ. The presence of such an effect can cause a mimicking of a nEDM. Normally the electric and magnetic fields are slightly tilted from each other which results in a contribution to the magnetic field gradient $\frac{\delta B_z}{\delta z}$, details given in (7). This leads to the effect being very dependent on the velocity component of the UCN. However, as the general motion of the UCN is random in the volume it is considered that all contributions would average out to zero. But, if there was some small bulk rotation of the UCN cylindrically about the centre of the electrodes (148) this will cause a systematic effect. There is also a component dependent on the angle, $\theta_{v\times E}$ between the electric field and the magnetic field, hence, uniformity of the electric field is important.

The simulations already mentioned can be used to determine the values for the homogeneity of the volume confined by the insulator walls. The idea would be to create a simulation to determine the electric field components at set points throughout the UCN volume. These components could then be compared to measured magnetic field maps of the setup, hence, determining $\theta_{v\times E}$ and producing a systematic limit on this effect.

The change of the groove geometry will affect the homogeneity of the UCN volume as the electric fields become lower at the groove the larger θ is. There are also large holes

for filling the UCN volume in the PSI nEDM which will also lower the electric fields, creating regions of inhomogeneity. This potential issue is just stated here to highlight that there are some constraints on changing the groove geometry which in the case of a real cryogenic nEDM experiment will need to be followed up. But, for the case of this thesis it will only be raised as an issue and included as suggestion for further work to be performed.

5.5.3 Applying the simulation results to the electrodes design

To narrow down the choice of constant radius profiles, further analysis was required. One of the limitations is the dimensions of the chamber in which the electrodes will sit. The internal diameter of the chamber is 372 mm. The diameter of the electrode stainless steel blank to be machined was found to be 332 → 335 mm, therefore, a maximum diameter that we could get out of the blank would be 320 mm. This gives a 26 mm separation to the wall from the electrodes which will be equal to the maximum separation possible between the two electrodes. The alumina insulator, which could be used, has a diameter of 260 mm. As the insulator is not perfectly cylindrical, a radial separation of Δr_0 = 0.5 mm is realistic to assume, for proposes of the simulations. This leaves 29 mm for the groove profile plus the corona profile on the ends of the electrodes. With all this in mind this gives combinations of the following radii: R14 (groove profile) + R15 (corona profile), R15 + R14, R16 + R13 or R17 + R12. The reason for not going to R18 + R11, and so on, is that the highest field in the system will move to the corona profile which is close to the chamber at ground. This will not matter when voltage is applied on both electrodes, where the highest field is between them, but if it's only applied to one side the highest E field will move to the corona edge and limit E_0 as breakdowns will prefer to occur to the chamber.

Simulations are done for these combinations of radii for the groove and corona profile with electrodes at 320 mm in diameter, and a groove of 239 mm ID x 261 mm OD x 12 mm depth. In the groove an alumina insulator 260 x 240 mm was placed at radial separation of 0.5 mm, electrode separation 26 mm with both electrodes charged to ± 130 kV respectively, leading to the contour plots in Figure 5.25 - 5.28.

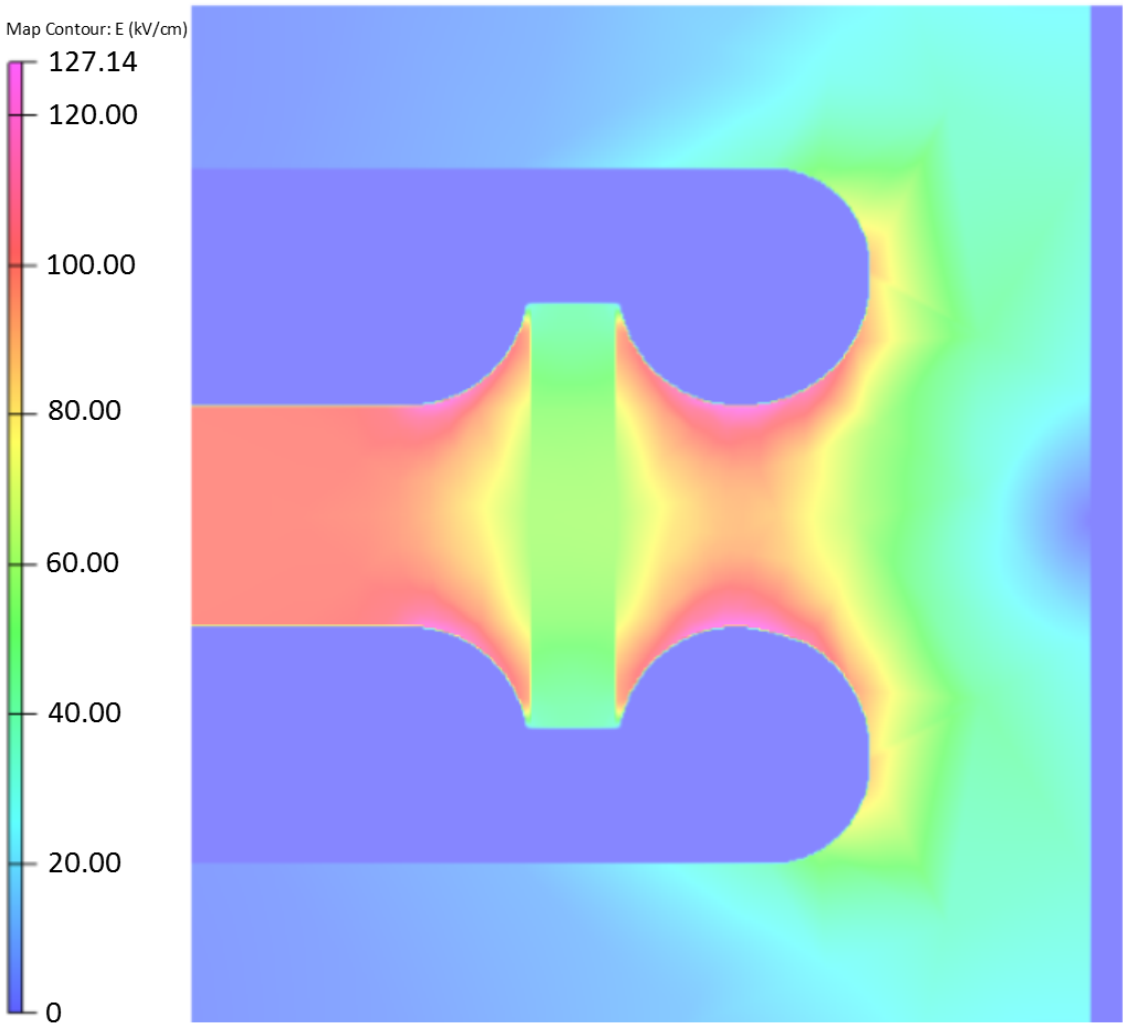

Fig. 5.25 E field contour plot for electrode geometry R14 + R15 where E_0 = 100 kV/cm.

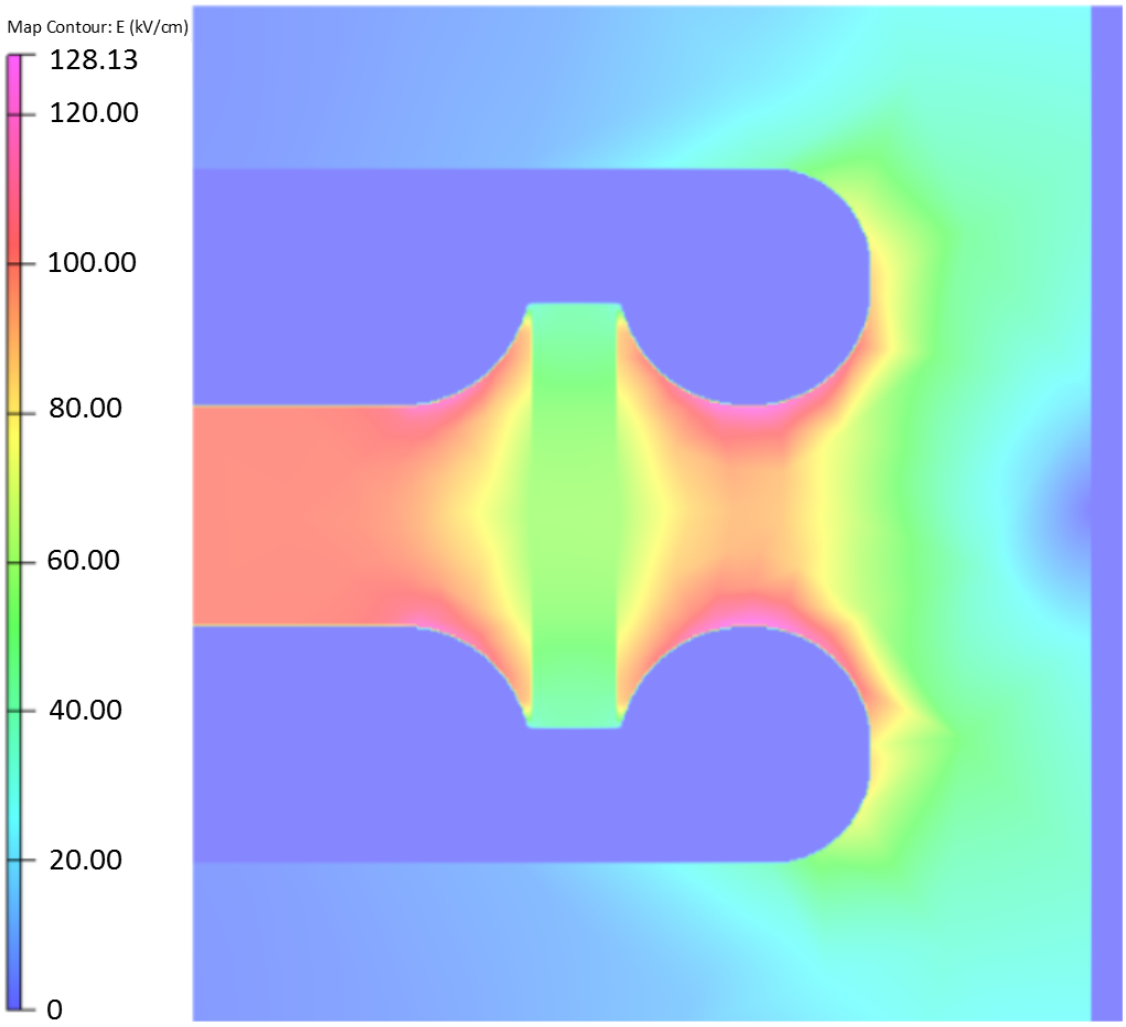

Fig. 5.26 E field contour plot for electrode geometry R15 + R14 where E_0 = 100 kV/cm.

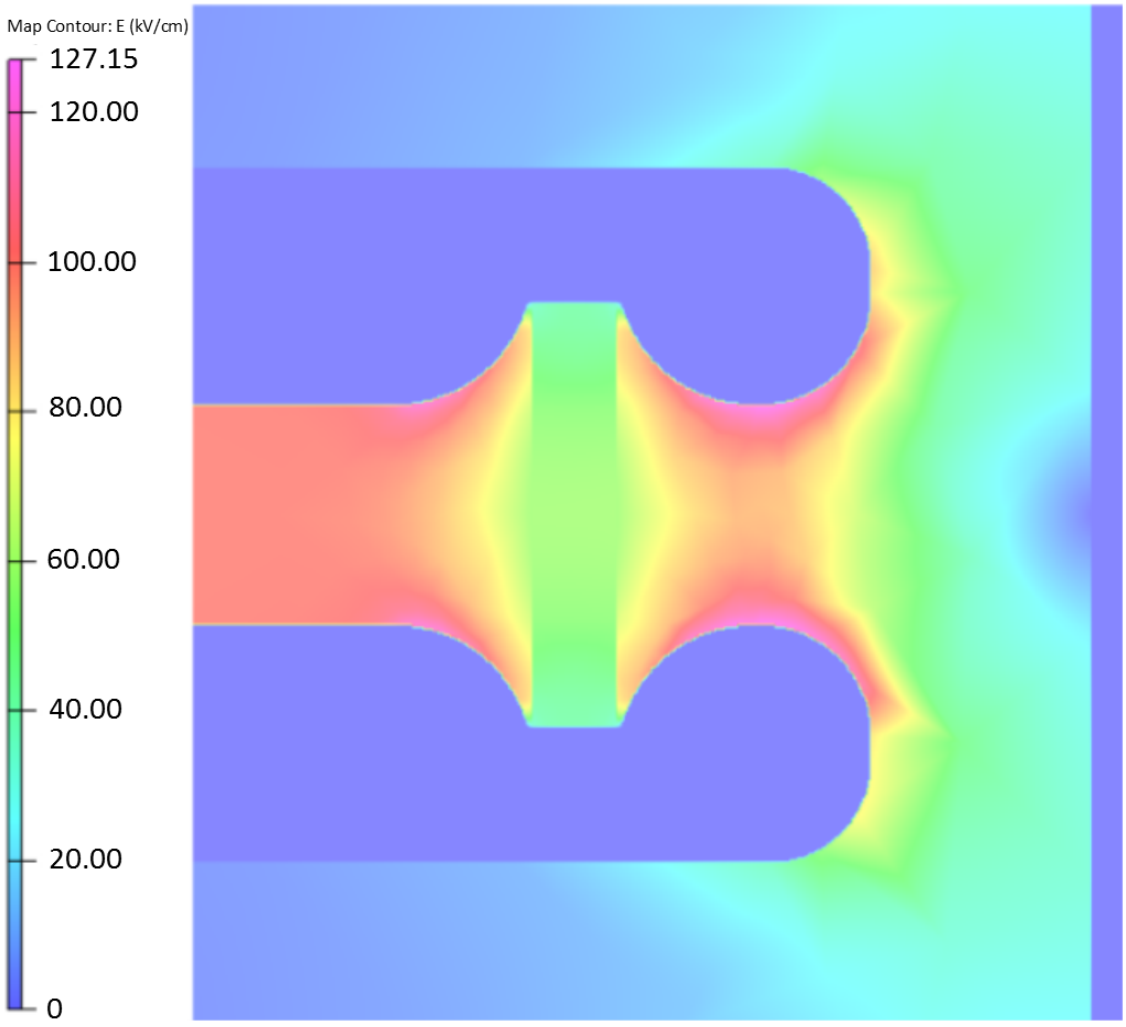

Fig. 5.27 E field contour plot for electrode geometry R16 + R13 where E_0 = 100 kV/cm.

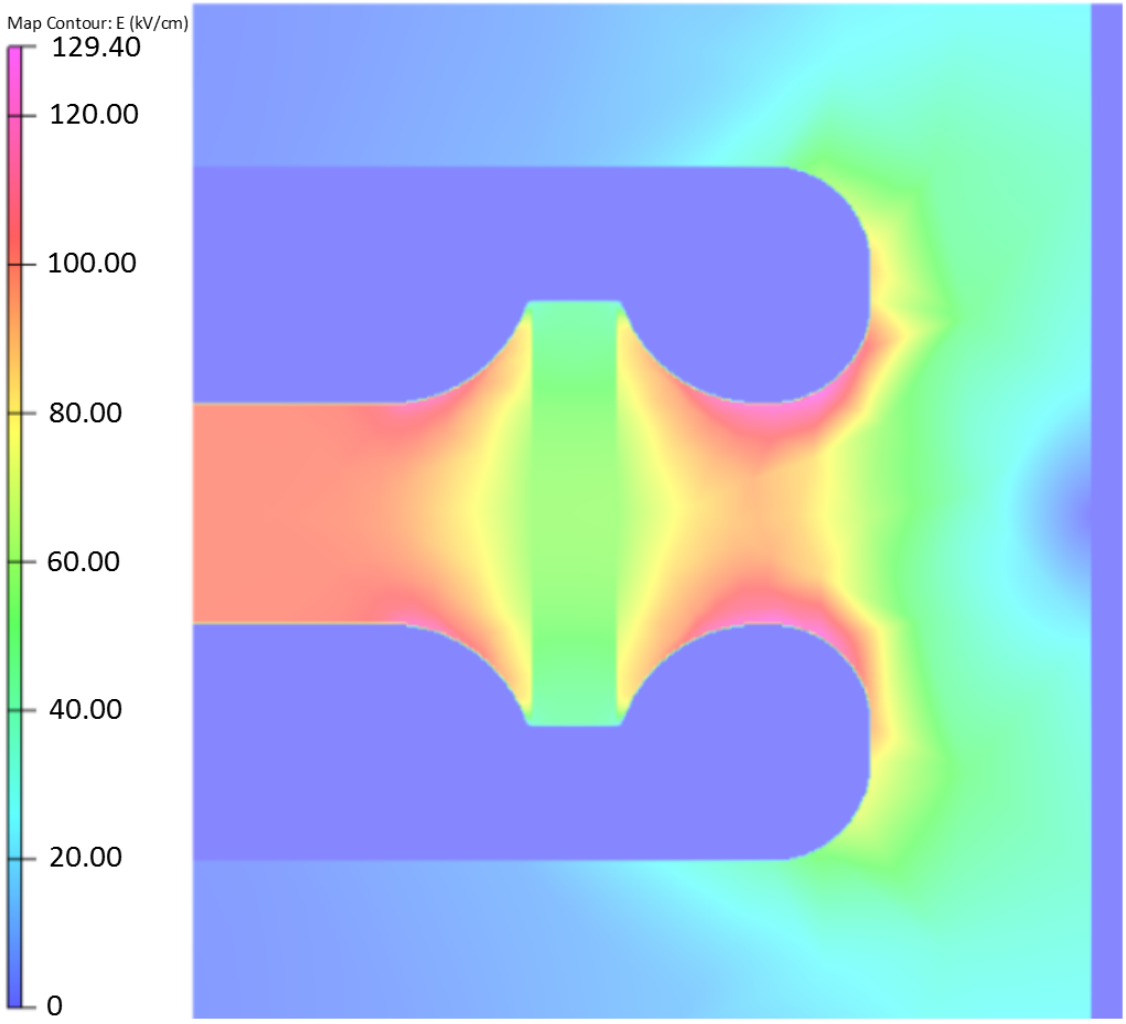

Fig. 5.28 E field contour plot for electrode geometry R17 + R12 where E_0 = 100 kV/cm.

There is not a massive difference in peak E field between Figures 5.25 → 5.27, but Figure 5.28 has a higher peak E field which is located on the corona profile. On Figure 5.25 there is a fairly high E field close to the insulator surface which is concerning, even though Figure 5.20 shows that this field is lower than E_0. This region of high field seems to disappear fairly quickly as the radius increases. To compare these contour plots, the E field along the arc length was taken as well as the E field along the insulator surface for the inside and outside profile.

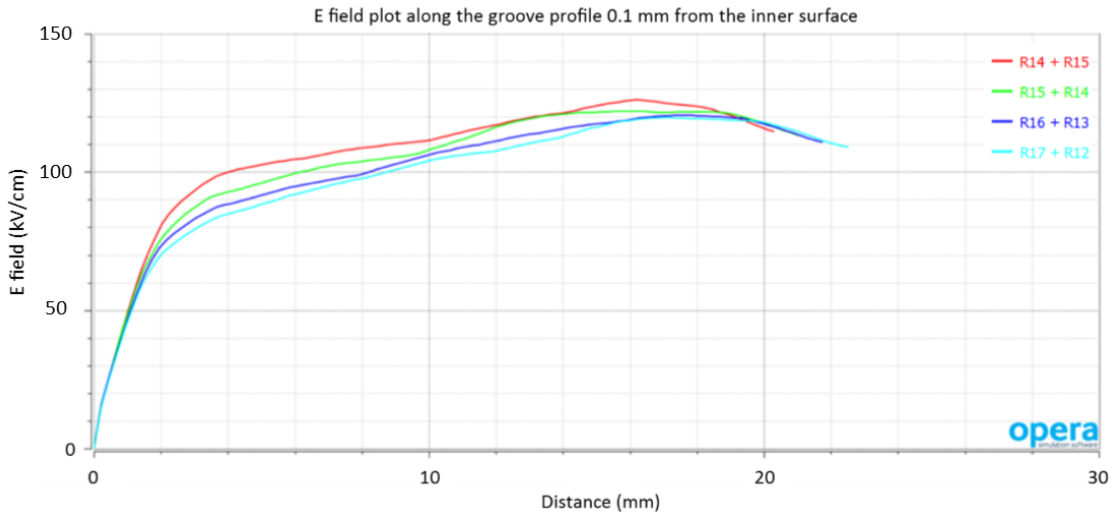

Fig. 5.29 E field plot against arc length along the surface of the groove at 0.1 mm away from the internal groove, E_0 = 100 kV/cm, distance in mm.

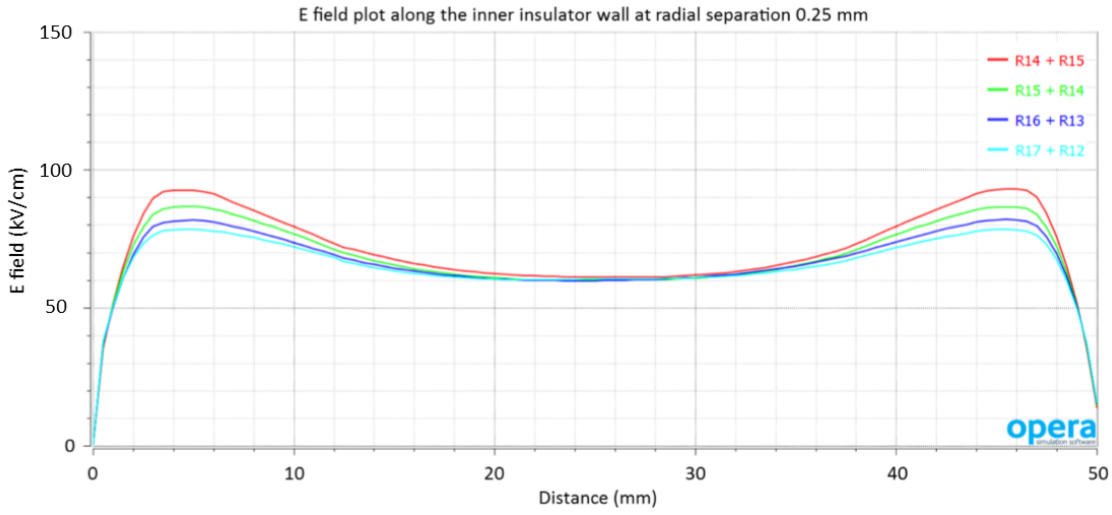

Fig. 5.30 E field plot against distance along the length of the internal insulator wall from one electrode base to the other at a radial separation of 0.25 mm from the wall, or middle of the gap, E_0 = 100 kV/cm, distance in mm.

Figures 5.29, 5.30, and 5.32 are comparable to Figures 5.20 and 5.21; they both show the

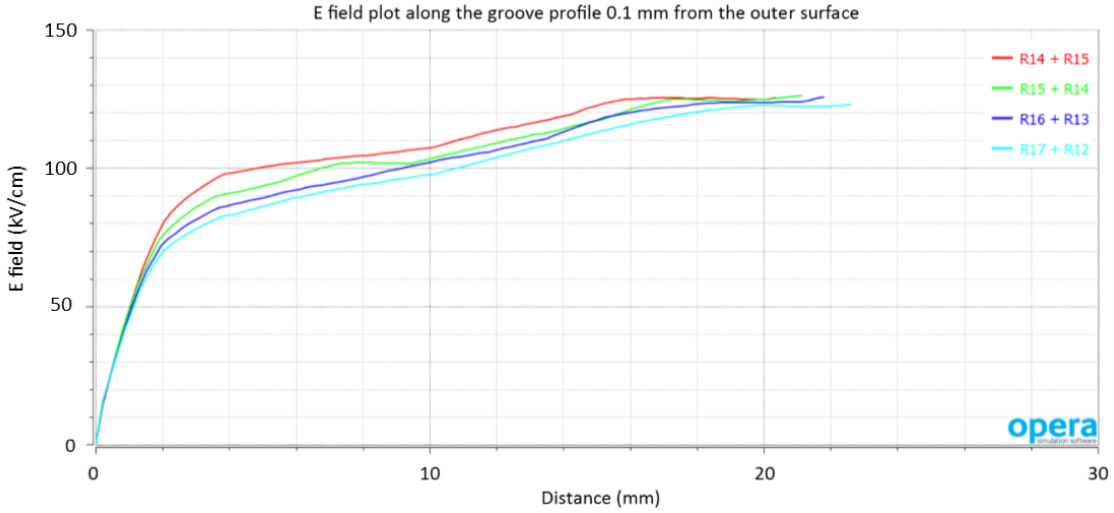

Fig. 5.31 E field plot against arc length along the surface 0.1 mm away from the outer groove, E_0 = 100 kV/cm, distance in mm.

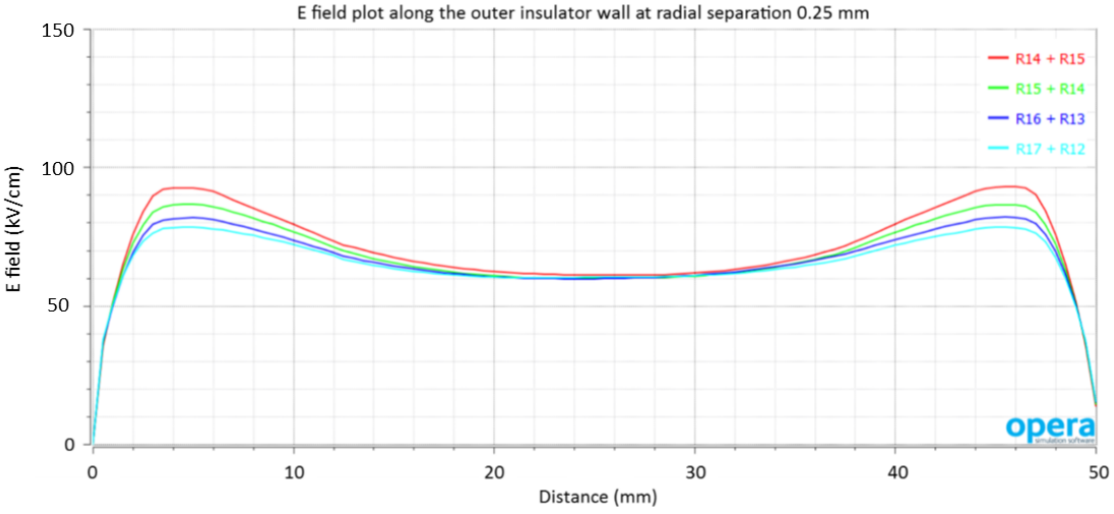

Fig. 5.32 E field plot against distance along the length of the outer insulator wall from one electrode base to the other at a radial separation of 0.25 mm from the wall, or middle of the gap, E_0 = 100 kV/cm, distance in mm.

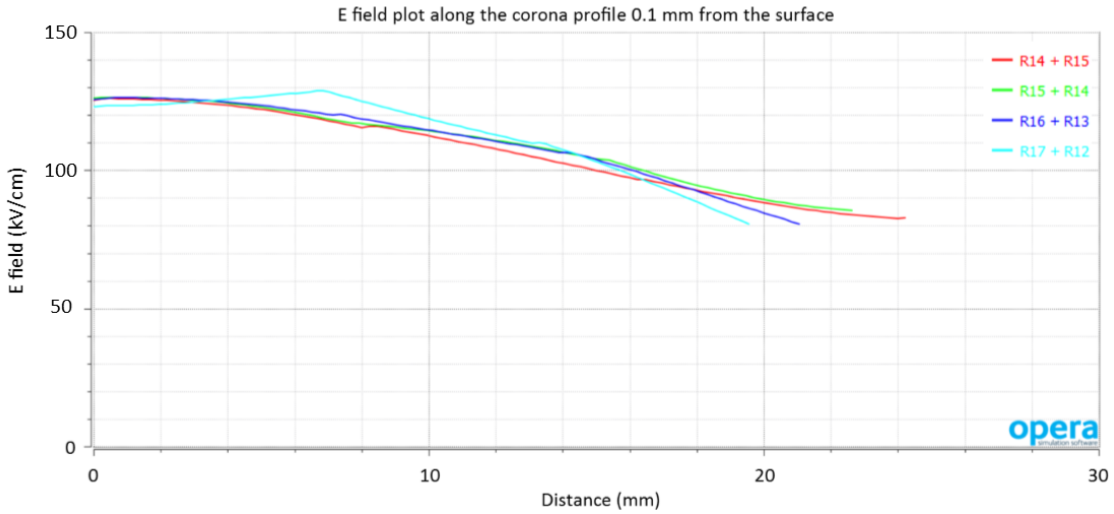

Fig. 5.33 E field plot against arc length along the surface 0.1 mm away from the corona profile, E_0 = 100 kV/cm, distance in mm.

same values, which is to be expected, showing that the outer profile with the corona does not affect the E field on the inside groove or at the insulator surface. However, Figure 5.31 deviates a bit from Figure 5.21 in that it reaches higher values overall which are due to the blend to another radius. Figure 5.33 shows this high E field continues from Figure 5.31. The interesting thing is that all radii start from about the same peak field value which suggests that this high field can't be avoided and is due to this blending of curvatures. This area of high field is concerning as it would at first appear that this would be the weak point in the system with the breakdown occurring across the nodes, but Figure 5.25 → 5.28 all show that the field is not maintained above E_0 across the gap.

5.5.4 Minimising the CTJ field

In order to pin point the geometry to use out of the 4 combinations already stated, it was worth checking what effect they would have on the CTJ. For these simulations the models used to generate Figures 5.25 → 5.28 were used but a cut was made to the base of the insulator, 5 mm in from the outer groove and 0.5 mm up from the electrode base.

The CTJ problem is something that cannot be avoided, it will more than likely be the weak point of the system. However, there are a few things that can be done to increase E_0 before the CTJ will limit it. The value of the relative permittivity has an effect (81). The larger this value the more the potential field lines are pulled towards the CTJ gap, increasing the E field at that region. Therefore, finding a material with low relative permittivity will minimise the problem of the CTJ. Another solution for the CTJ is to polish the electrode and insulator surfaces which should reduce the size of the CTJ. The

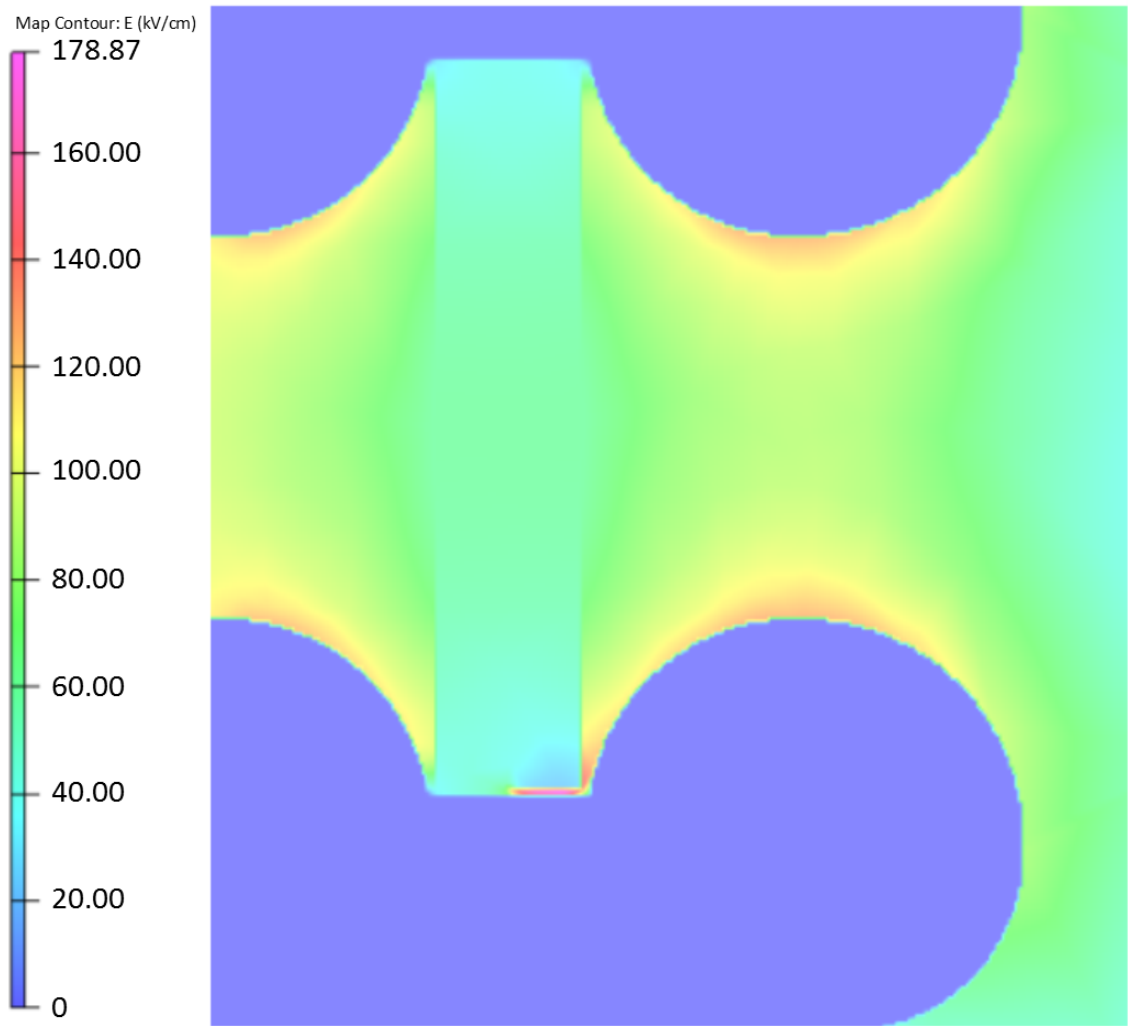

Fig. 5.34 E field contour plot for electrode geometry R14 + R15 where E_0 = 100 kV/cm, with cut for the CTJ at the bottom of the insulator.

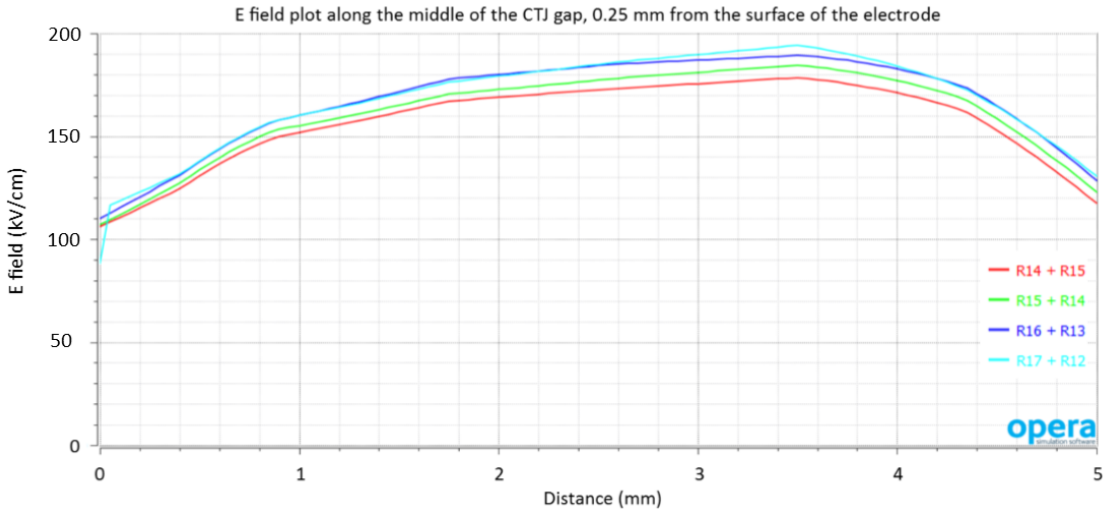

Fig. 5.35 E field plot of values for E field, starting at one end of the CTJ gap to the other, 0.25 mm from the electrode surface (middle of the gap).

fields at the CTJ can also be reduced by increasing the groove depth, therefore, burying the CTJ in the zero field region inside the electrode.

Figure 5.35 shows that as the radius of the profile increases, so will the value of the E field in the CTJ, which is to be expected. However, it does not increase by a large amount, as the profile becomes shallower the insulator will be exposed to higher E fields, however, this is not to the extent as initially thought. This suggests that the smallest radius values would be best in order to avoid any exposure of the CTJ, however, it does not seem to make a massive difference to the value at the junction.

Therefore, at this point R14 + R15 could be eliminated as the R14 profile will create a field that's a bit less then E_0 on the insulator surface. However, that's at 0.5 mm radial separation, and as the insulators could be closer in reality to the groove, they could generate E fields greater then E_0 on the insulator surface in this case.

Alternatively taking the larger radius profile will give a better chance of avoiding this high E field on the insulator surface if the radial separation was to be reduced to less than 0.5 mm, but from the analysis on the CTJ this may not be such a good choice. Figure 5.35 shows that with a large CTJ the field in that region starts to reach $2E_0$ for R17 + R12, therefore, going for lower radii profiles could help to mitigate this problem somewhat. This leaves us with either R15 + R14 or R16 + R13. There is not a good argument to choose one over the other here, therefore, the profile I will go with is R16 + R13 for the reason that if the radial separation decreases to less than 0.5 mm the high E field on the insulator surface will be minimised as much as possible.

5.5.5 Analysis using spacer plates

With the groove profiles determined I went a step further: is it possible to vary the internal separation of the electrodes? In order to take breakdown measurements at different separations and to plot the behavior as a function of separation, multiple electrodes would be required. However, with electrodes at ϕ 320 mm it is very expensive to have multiple made. The same problem applies to using insulators of different lengths to get the desired separation. Therefore, the addition of spacer plates to decrease the separation from 26 mm was investigated. The advantage of these spacer plates will also experimentally test if these groove profile variables will effect the breakdown. This information is then directly comparable to the measurements on the small and medium scale breakdown measurements which will be used to determine the surface area effect for breakdowns in LN_2 and LHe.

Property	Al_2O_3	BG	Quartz
Density (g cm^{-3})	3.7-3.95	2.23	2.20
Dielectric Const. (20°C, 1-10 MHz)	9.2	4.6	3.75
Coeff. Thermal Expansion ($10^{-6}K^{-1}$)	8.5	3.3	0.6
Thermal Conductivity (100°C) (W mK^{-1})	30	1.2	1.4

Table 5.2 Table of insulator properties: alumina (Degussit (133)), borosilicate glass (Glass-solutions (149)), and quartz (Baumbach (150)).

In order to implement this, the internal groove profile is machined on to its own plate, which is then raised and lowered by stepper plates. The stepper plates will fill in the gap between the base electrode and the internal plate. All the plates have been machined in a stack and then polished to the same diameter to ensure a smooth surface. The maximum separation is 26 mm, therefore, in order to cover every combination of electrode separations, the thicknesses of the stepper plates are: 1 mm, 2x2 mm, 5 mm, and 10 mm.

To check if adding in stepper plates would affect the E field on the insulator surface, simulations were done with different electrode separations using the chosen profiles. The models were the same as the one used to create the R16 + R13 one.

Figure 5.36 shows that the highest E field present in the simulation occurs in the gap between the stepper plates and the insulator. This higher than E_0 field is greatest in the intermediate separations but falls off at the smaller ones. The reason this happens is that the insulator wall acts like a CTJ, compressing the potential field lines and thus enhancing the E field in that region. The highest field occurs at the join between the internal plate and the stepper plate. This is a sharp edge creating this field enchantment as well as a CTJ gap. This is concerning as this is what the previous simulations were trying to avoid. The sharp edge where the plates met can be fixed via polishing to an extent. However, this still leaves high fields on the insulator surface. Looking at Figure 5.19, there are a number of other variables present that could solve the problem. Increasing the internal radial separation will take the insulator surface further away from the metal, thus decreasing the high fields in that region, but the problem with doing this is that the insulator will no longer centre on the internal groove. These simulations, however, were done with an alumina insulator which has a high relative permittivity, but in the actual experiment the internal groove diameter is determined by the use of a borosilicate glass insulator. Therefore, redoing the simulations with a lower relative permittivity, ϵ_r = 4.6, gives the plot in Figure 5.38.

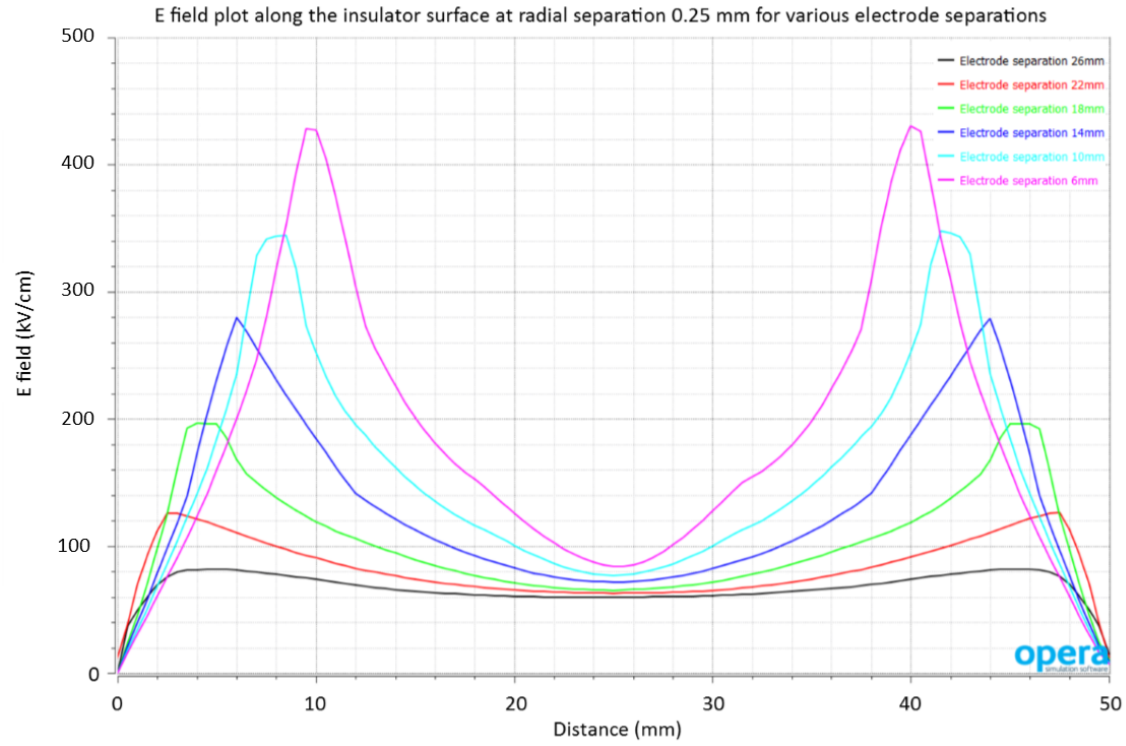

Fig. 5.36 E field plot with varying electrode separations from the base of one electrode to the other at radial separation of 0.25 mm from the insulator wall. Both electrodes at 130 kV. The choice of looking at the separation every 4 mm is arbitrary. E_0 (26 mm) = 100.0 kV/cm, E_0 (22 mm) = 118.9 kV/cm, E_0 (18 mm) = 144.4 kV/cm, E_0 (14 mm) = 185.7 kV/cm, E_0 (10 mm) = 260.0 kV/cm, and E_0 (6 mm) = 433.3 kV/cm.

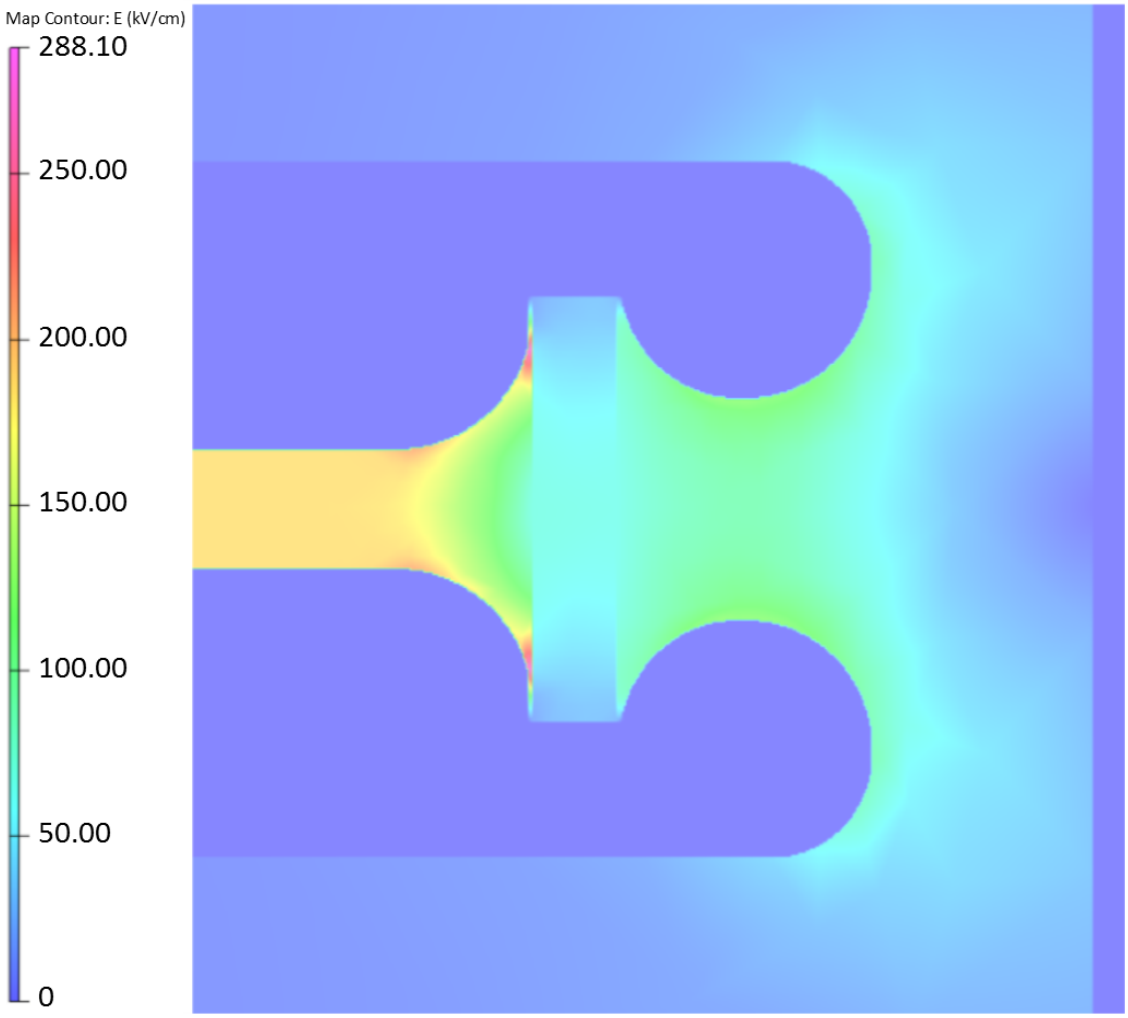

Fig. 5.37 E field contour plot for electrode separation 14 mm with alumina insulator, radial separation 0.5 mm, E_0 (14 mm) = 185.7 kV/cm.

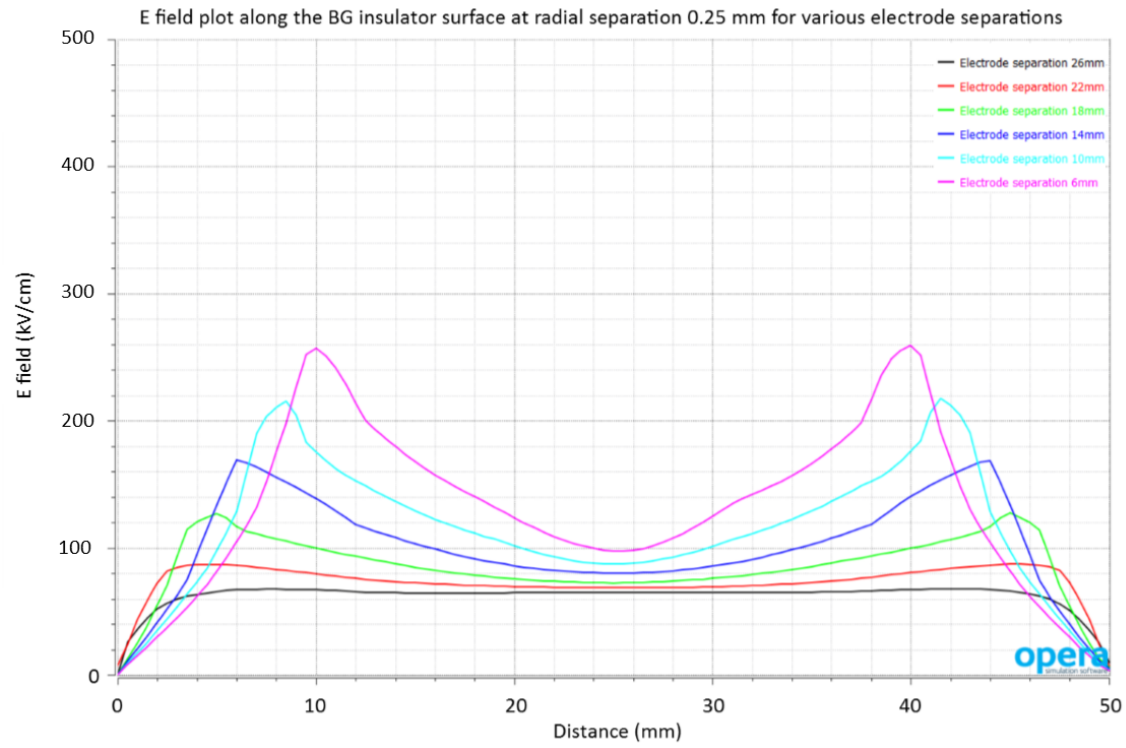

Fig. 5.38 E field plot with varying electrode separations from the base of one electrode to the other at radial separation of 0.25 mm from the insulator wall. The choice of looking at the separation every 4 mm is arbitrary. Insulator used is borosilicate glass. E_0 (26 mm) = 100.0 kV/cm, E_0 (22 mm) = 118.9 kV/cm, E_0 (18 mm) = 144.4 kV/cm, E_0 (14 mm) = 185.7 kV/cm, E_0 (10 mm) = 260.0 kV/cm, and E_0 (6 mm) = 433.3 kV/cm.

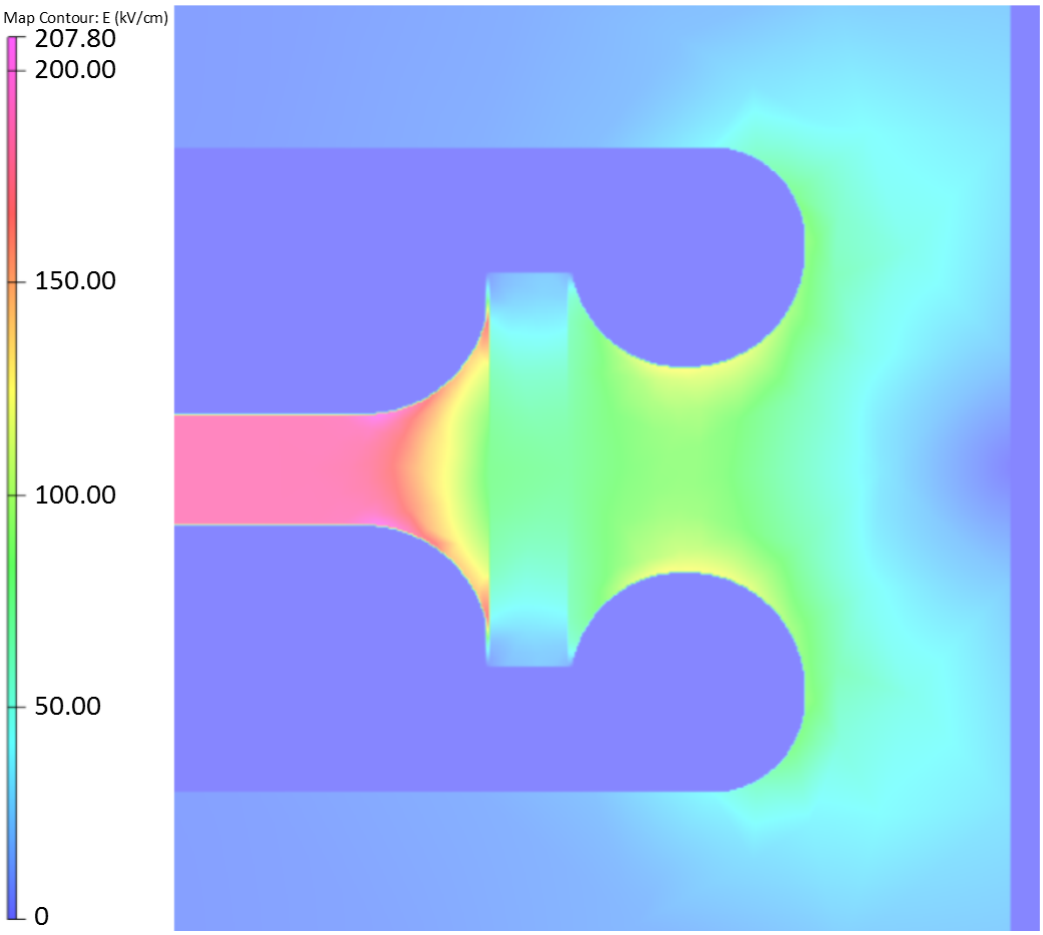

Fig. 5.39 E field contour plot for electrode separation 14 mm with borosilicate glass insulator, radial separation 0.5 mm, E_0 (14 mm) = 185.7 kV/cm.

Figure 5.38 shows that the problem goes away with a lower relative permittivity. However, if the insulator were to get close to the electrode (radial separation < 0.5 mm) then there could be problems, so for intermediate separations the alumina/quartz insulators would be the safest option.

5.5.6 Summary of geometry analysis

In summary this analysis has determined the optimal geometry for the electrodes to be used in the experiment. This could potentially provide 100kV/cm between the electrodes without the risk of a breakdown occurring along the insulator surface, resulting in damage to it, as was observed by Davidson (2) and Hill (3). This analysis should be useful to any bottle nEDM experiment (room temperature or cryogenic) in order to get the maximum E field possible and thus the sensitivity to the nEDM. The final drawings of the electrodes used in the SV are given in the Appendix H.

5.6 Taking breakdown data

Before a breakdown test is performed the capacitance of the system is checked to ensure everything is in electrical contact, after cooling of the system to the cryogenic liquid's temperature. The temperature of the system is also checked and that the liquid volume is not boiling. The ballast resistors are conditioned before an experimental run, up to ± 130 kV, this ensures no discharging from dirt on the surface of the resistors will appear as a breakdown on the data taking run.

For running with one polarity on one electrode, the voltage is slowly ramped up by 5/10 kV from 0 until a breakdown occurs. The charging current from the power supplies is set to 0.5 μA. The voltage is held at a given step for about ~ 5 minutes. Once a breakdown occurs the power supply will trip for a full breakdown or try to charge up the electrodes again for a partial breakdown. If a full breakdown occurs the system is left for 5 minutes at minimum to allow the liquid to settle. This process is repeated for about 15 events, with the level of the liquid checked every so often. If the level gets too low then it is topped off to complete the data run.

When a breakdown occurs, the PC records the momentary value from the power supply before it happens. Extracting this value from the data normally is the highest number before the following value is much lower than the previous, this is used to determine the breakdown value.

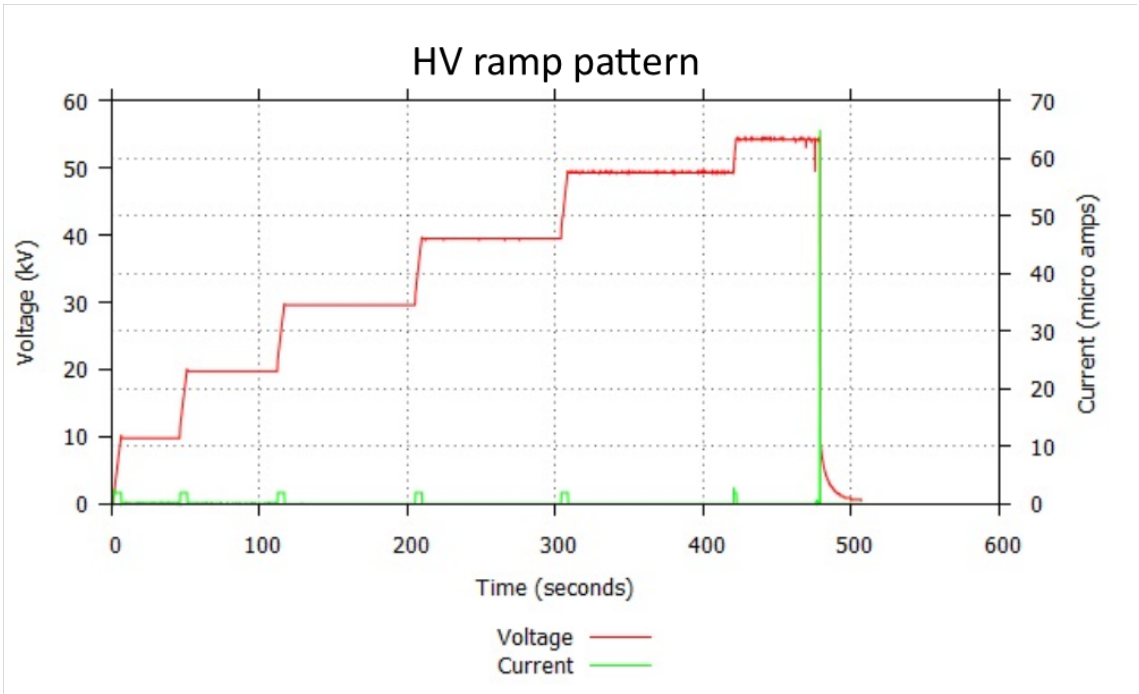

Fig. 5.40 Typical HV breakdown run with the voltage (kV) in red against the number of iterations with current (μA) over laid in green. Time for this run is approximately 30-45 minutes for a single polarity run in the KEK. The sharp drop off in voltage at the end is a full breakdown event.

5.6.1 Methodology

The electrode stack is replaced by removing only one seal, the bottom plate of the SV. The electrodes with the desired separation for the experimental run are placed on the G10 stand-offs, mounted on the bottom of the SV plate, with an insulator (either alumina/quartz/borosilicate glass) separating them. The vacuum to G10 cryogenic feedthrough is attached to the bottom electrode with a CuBe sheet that is bent and acts as a spring connector. The bottom SV plate is then fixed on the insert with a fresh indium seal.

The insert is then put into the cryostat. The vacuum system is turned on and pumped to $\sim 10^{-7}$ mbar. The cryogenic feed is placed into the insert and sealed so that the blow off for the N_2 gas comes up the central bore of the insert so the feed is cooled down. The capacitance is checked between the central and side feeds. At this point the side feed will be in contact with the G10 feedthrough to the bottom electrode.

The pre-cooling of the cryostat can start at this point. The SV and the LN_2 tank of the cryostat is filled with LN_2 at the same time. Approximately 5-10 litres are filled into the SV and allowed to cool the insert. The cryostat has approximately 4/5 separate fills of LN_2 of about 10 litres before the temperature of the shield is less than 100 K. Once the

two systems are cold enough they are topped off. After this point, measurements for LN_2 experiments can be performed with one polarity on the top electrode.

5.6.2 Operation using double polarity

For double polarity measurements the ballast resistors were added in line with the power supplies and the HV feeds. Negative polarity on the side feed and positive on the central cryogenic feed was used. The purpose was to limit the field emission on the vacuum side as there are a lot of sharp edges on the 100 K shield which may limit the applied voltage. The first run with back to back voltage in the system noticed a problem with the controller of the power supplies. At 60 kV range on the positive or negative it would shut down the negative supply. Therefore, the voltage would be ramped asymmetrically. The positive would be increased to its maximum value till a breakdown occurred. The negative would then be increased, bypassing the 60 kV range, straight to 70 kV from 50 kV.

5.7 Tests on small/medium electrodes separated by spacers

5.7.1 Overview

Initial breakdown measurements were performed using a smaller pair of electrodes (DKHs/DKHl) to the ones previously mentioned. These Rogowski electrodes were separated by cylindrical Al_2O_3 or borosilicate glass (BG) spacers in the same manner as the setup previously discussed. All these measurements were made in LN_2 at 77 K. Experiments were performed in a stainless steel cryostat, the KEK, with the same setup as detailed in Davidson's thesis (2).

5.7.2 Electrodes

The two sizes of electrode given in Figure 5.41, DKHs (ϕ 58.38 mm) and DKHl (ϕ 125 mm), are designed to minimise E fields at the CTJ while also locating the spacer. However, the machining of the groove geometry for the DKHl electrodes had a mistake and the spacer is never truly located, either 0.5 mm separation on the outside diameter of the spacer and a significant gap on the inside diameter, ~ 5 mm for 70 mm x 60 mm spacer.

The DKHl electrode has a geometry of 51.00x73.52 mm, which is much wider then the insulators tested, therefore, positioning of the insulator in the groove could not be

achieved accurately. This could lead to one side of the insulator being much closer then the other to the groove wall.

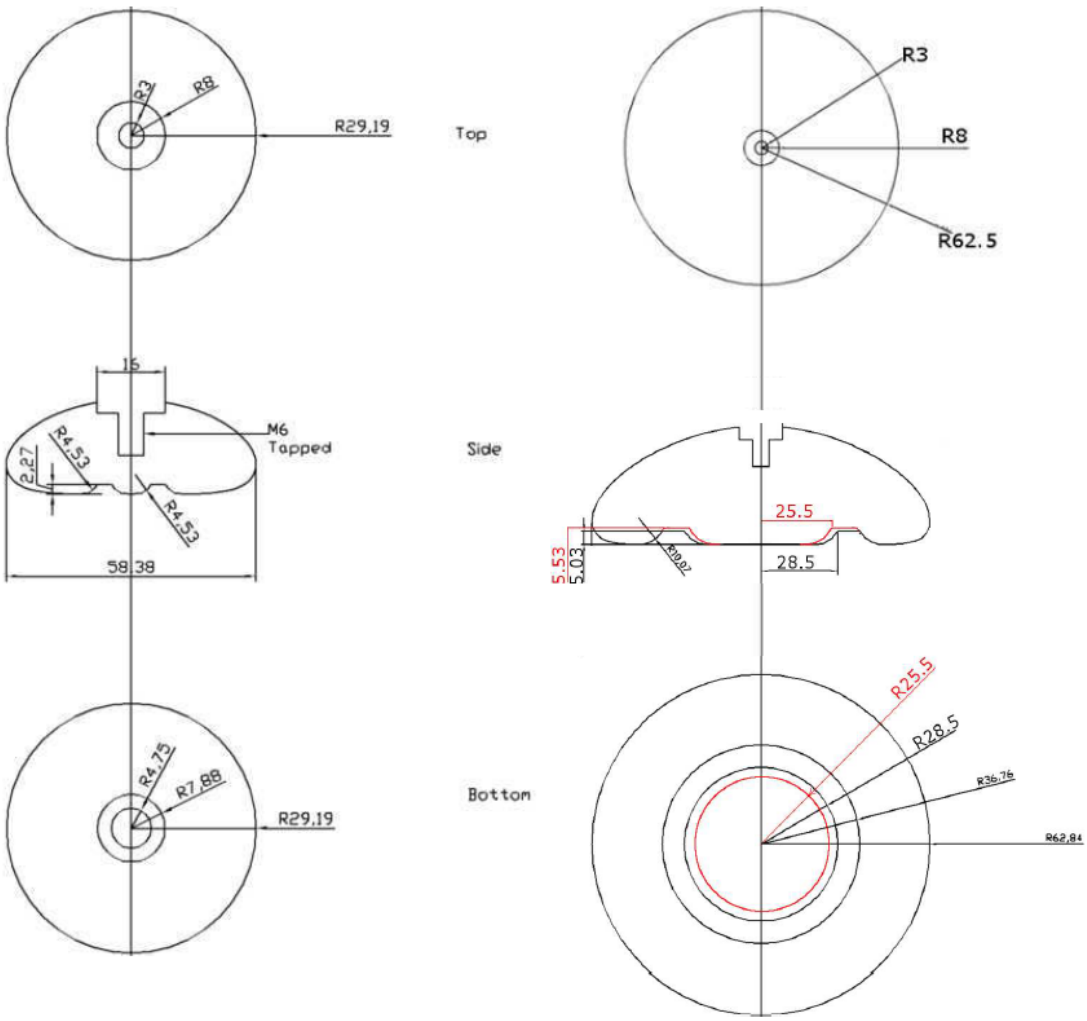

Fig. 5.41 Diagram of electrode geometry for DKHs and DKHl electrodes (3) (2).

5.7.3 Test Rig for DKHs and DKHl electrodes

Hill (3) and Davidson (2) describe the rig used to run with the KEK cryostat. In this setup the bottom electrode rests on a G10 plate which is connected to ground via a copper wire up to the top plate of the insert. The HV electrode rests on top of the insulator which is either alumina or BG of dimensions 70 x 60 mm (smaller Δr_o) or 60 x 50 mm (smaller Δr_i). A coda connector was placed into the HV electrode and a brass stud into the HV feed. The brass stud is bored out on the inside so the coda connector will guide the feed into contact with the HV electrode and the stainless steel tube of the feed to maintain electrical contact.

The HV feed used was the same one that was described by Karamath (93) initially. There

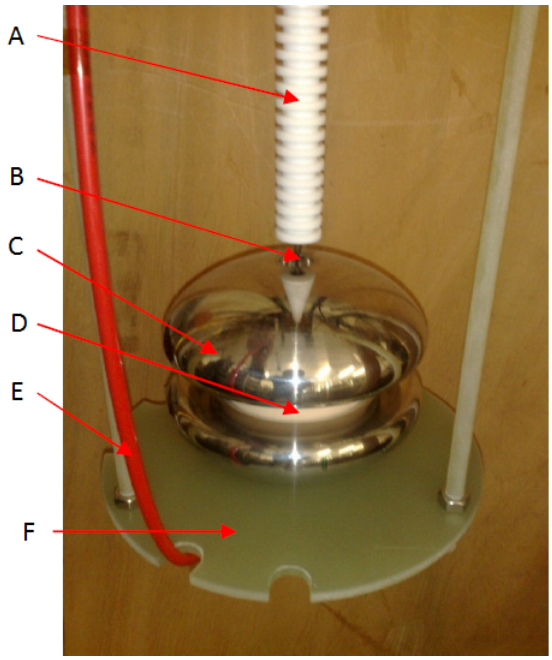

Fig. 5.42 Setup to measure the breakdown behaviour with an insulator between a pair of electrodes. A - HV feed, B - connector to feed and electrode, C - HV electrode, D - alumina spacer, E - return line, F - G10 support plate.

were upgrades made to the feed in order to improve reliability which was described previously in section 5.2.2.

The DKHs electrodes required a modification to the G10 base plate in order to maintain a spring loaded contact with the HV electrode that was screwed into the HV feed. Unlike in Hill's experiment the same insert was used in the KEK. The bottom electrode is fixed to a movable base plate which is sprung loaded, on top of the G10 base plate used with the DKHl electrodes, in order for the electrodes to keep the insulator sandwiched between them. The bottom electrode is grounded by a thin copper sheet which is bolted into the return line and the bottom of the DKHs electrode.

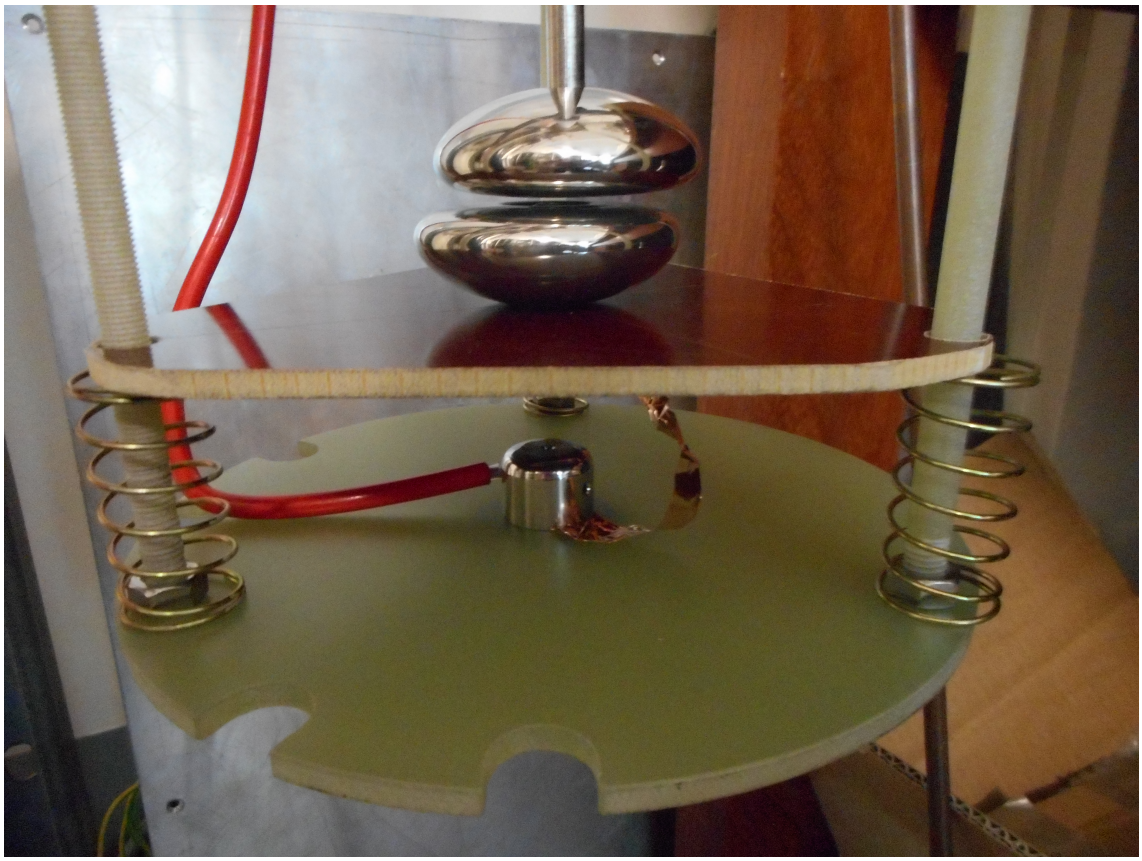

Fig. 5.43 Setup for the KEK insert when using the DKHs electrodes. The ground electrode is screwed into the G10 plate which is sprung loaded when the HV feed is lowered, sandwiching an insulator between the two electrodes. The ground connection to the bottom electrode is made with a thin copper tape. The picture shows the electrodes are not perfectly aligned even with the PTFE guidance blocks above, resulting in some lateral force on the insulator.

5.7.4 Operation of the KEK apparatus

Dimensions of the KEK cryostat are given in Davidson (2) and Hill's (3) thesis.

Before an experiment is performed the ceramics and borosilicate glass are all cleaned in aqua regia for 1 hour then rinsed in deionised water. The electrodes are polished after the surface has been damaged enough, in which about 40-80 craters are visible. The ceramic is then positioned between the electrodes with effort to ensure that it is as central as possible. The ceramic dimensions are also noted down to check the radial separation and to make sure the insulator is as flat as possible.

Filling the KEK with LN_2 is done in the same manner as the SV, until the level of the fluid is sufficiently high enough for the HV feed to get a full experimental. The method of data taking is the same as previously stated.

Chapter 6

KEK and Blue Elbow Breakdown Data

6.1 Introduction

This chapter will present all cryogenic breakdown data taken for this thesis. Experiments were performed on small (DKHs), medium (DKHl), and large (JT) scale electrodes. The DHKs and DKHl electrodes were used in the KEK cryostat in LN_2 and the JT electrodes in the SV inside the Blue Elbow cryostat filled with either LN_2 or LHe. Breakdowns performed with Al_2O_3 insulators in the KEK were found to lead to insulator damage in some cases. Decreasing the radial separation between the groove wall and the insulator would result in the damage occurring on the inside instead of the outside surface. In order to overcome this problem borosilicate glass (BG) insulators were used instead, lowering the dielectric constant of the insulator. However, placement of the glass between the electrodes would result in chipping of the edges. This issue was overcome through polishing of the insulators. Testing of the polished BG insulators in the KEK overcame the damage observed with the Al_2O_3 insulators. Overcoming the damage problem meant breakdowns with the JT electrodes could then be with less worry about catastrophic damage occuring to large insulator rings. During all of the breakdown measurements with the JT electrodes, no damage was observed on the insulator.

Each breakdown run corresponds to a single cooldown of the KEK or blue elbow cryostat from room temperature to 77 K with LN_2 or to 4.2 K with LHe. At 77 K (or 4.2 K) the breakdown measurements are performed with approximately 10-15 breakdowns per cooldown. The insert is then allowed to warm up to room temperature before being removed from the cryostat. The electrodes and insulator condition are then analysed.

Breakdown measurements on the DKHl electrode using a ceramic (Al_2O_3) or BG spacer in LN_2 are presented in section 6.2. These electrodes were used for 27 different breakdown runs, and in order to avoid damage to the surface effecting the results, they were

mechanically polished to a mirror finish between sets of runs indicated by each subsection. Runs 1-24 used the HV feed detailed in Karamath's thesis (93) and the remainder used an improved version detailed in section 5.4.1.

Section 6.3 presents breakdown runs 11-13 using DKHs electrodes. These were separated with thin wall alumina ceramic or quartz insulators for comparison with Hill's (3) measurements.

Section 6.4 investigated if the altered geometry discussed in section 5.5 affects the breakdown voltages with the insulator present. The surface area of the electrodes is much larger then the DKHl or DKHs electrodes, therefore, the surface area effect can be measured. These breakdowns are performed in the Blue Elbow, runs 31-35, which used LN_2. Performing these measurements gave an idea of how the system works and what would be expected for breakdown voltages measurements with LHe. Some of these measurements were performed after upgrades to the Blue Elbow rig as discussed in Section 5.2.2. These measurements were required to determine the ability of the HV system to supply twice the voltage across the gap between the electrodes and work reliably.

Section 6.4.2 covers the measurements with the Blue Elbow cryostat using LHe. This data will provide a comparison at 4.2 K SVP to the results presented by Ito (64).

Run No.	Electrodes	Insulator material	Insulator dimensions IDxODxH (mm)	Separation (mm)	Polarity	Feed/Insulator damaged?
1	DKHl	Al_2O_3	60x70x16	4.94	-	N/N
2	DKHl	Al_2O_3	60x70x16	4.94	+	N/N
3	DKHl	Al_2O_3	60x70x18	6.94	-/+	Y/N
4	DKHl	Al_2O_3	60x70x18	6.94	+/-/+	Y/N
5	DKHl	Al_2O_3	50x60x16	4.94	+/-	Y/N
6	DKHl	Al_2O_3	50x60x16	4.94	+/-	N/Y
7	DKHl	Al_2O_3	50x60x18	6.94	-	N/Y
8	DKHl	Al_2O_3	60x70x16	4.94	+	Y/N
9	DKHl	Al_2O_3	60x70x16	4.94	-	Y/N
10	DKHl	Al_2O_3	60x70x16	4.94	-/+	Y/Y
11	DKHs	Quartz	10x15x7.5	2.96	-	N/Y
12	DKHs	Al_2O_3	11x12x7.5	2.96	+	N/Y
13	DKHs	Quartz	10x15x7.5	2.96	-	N/Y
14	DKHl	BG	60x70x14	2.94	-	N/Y
15	DKHl	BG	60x70x14	2.94	-	N/Y
16	DKHl	BG	60x70x15	3.94	-	N/Y
17	DKHl	BG	60x70x16	4.94	-	N/Y
18	DKHl	BG	60x70x17	5.94	-	N/Y
19	DKHl	BG	60x70x17	5.94	-	N/Y
20	DKHl	BG	60x70x18	6.94	-	Y/Y
21	DKHl	Al_2O_3	60x70x15	3.94	-	N/N
22	DKHl	Al_2O_3	60x70x17	5.94	-	N/Y

23	DKHl	Al_2O_3	60x70x18	6.94	-	Y/N
24	DKHl	BG	60x70x16	4.94	-	Y/Y
25	DKHl	Al_2O_3	60x70x16	4.94	+	N/N
26	DKHl	Al_2O_3	60x70x17	5.94	+	N/N
27	DKHl	Al_2O_3	60x70x15	3.94	+	N/N
28	DKHl	Al_2O_3	60x70x18	6.94	+	N/N
29	DKHl	BG	60x70x14.5	3.44	+	N/N
30	DKHl	BG	60x70x16	4.94	+	N/N
31	JT	BG	240x250x50	6	+	N/N
32	JT	BG	240x250x50	4	+	N/N
33	JT	BG	240x250x50	2	+	N/N
34	JT	BG	240x250x50	8	+	N/N
35	JT	BG	240x250x50	12	+ & -	N/N

Table 6.1 Summary of the breakdown measurements, in LN_2, performed in this thesis. The double line breaks indicate when the electrodes were polished. Table with breakdown values are given in Appendix F.

Run No.	Electrodes	Insulator material	Insulator dimensions IDxODxH (mm)	Separation (mm)	Polarity	Feed/Insulator damaged?
36	JT	BG	240x250x50	12	+ & -	N/N
37	JT	BG	240x250x50	6	+ & -	N/N
38	JT	BG	240x250x50	16	+ & -	N/N

Table 6.2 Summary of the breakdown measurements, in LHe, performed in this thesis. Table with breakdown values are given in Appendix F.

It should be noted that the error bars on the given data is intended to give a representation of the spread in values. The form of the distribution is not Gaussian but more of an extremal with a long tail on the lower voltage side as clearly found by Weber and Endicott, see Figures 4.33 and 4.34. In the following data the errors bars in are calculated from $\frac{\sigma}{\sqrt{n}}$ to represent the spread in voltage and should not be taken as a statistical error bar. The initial application of HV can result in lower values due to conditioning of the system. This data will be included for completeness.

The breakdowns recorded are classified as two types: full breakdown and partial breakdowns. The Spellman power supplies (141) have the 'External Fault Relay Option (EFR)' which cause the power supply to automatically revert to power down mode if the following conditions occur:

- Overvoltage: Greater than 110% of maximum output voltage was produced by the power supply.
- Overcurrent: Greater than 104% of maximum output current was produced by the power supply.

A full breakdown is when the overcurrent condition occurs: this occurs frequently and is the primary breakdown behaviour. A partial breakdown is when the voltage drops but the overcurrent condition is not met. This normally occurs if a leakage current is present, and the current is not able to build to levels that will exceed the overcurrent condition. Both types of breakdowns are recorded as a breakdown event in all the graphs and are used in calculating the mean values of the breakdowns. The number of partial and full breakdowns for each run will be stated for clarity. It was found that the number of partial breakdown increased dramatically if two things occurred: damage on the HV feed or damage to the insulator.

From breakdown run 14 onwards the condition of the electrode surface was examined for damage. A breakdown is a plasma discharge across the gap between the two electrodes and the effect of this event on a metallic surface of an electrode often leads to creation of a crater, see Figure 4.96.

These craters are a good indication for when breakdowns occurs between the electrodes as opposed to the insulator surface. It is very clear that the number of craters on the electrode surface will be equal to the number of breakdowns between the electrodes, therefore, the craters are counted on the plane-plane surface and compared to the overall number of breakdowns.

6.2 DKHl electrodes

Breakdown measurements have been performed with different lengths of Al_2O_3 alumina ceramic tubes with IDxOD of 60x70mm, 50x60mm, and borosilicate glass of 60x70mm. The details of the setup are in section 5.7.4.

These measurements follow on from investigations by Davidson (2) and Hill (3) to look into the effect of the cathode triple junction (CTJ) of the insulator and how this effects the breakdown voltage. The geometry of the grooves for these electrodes are given in Figure 5.41.

The HV feeds had a tendency to creep. As the PTFE shrinks at the HV side due to thermal contraction it clamps onto the stainless steel core, and as the PTFE contracts vertically it tends to push the core back up through the feed. This creeping would result in a gap on the room temperature side between the brass conductor (see Figure 5.13) and the PTFE tube. This problem would leave an exposed gap not insulated which creates high field region and can cause a breakdown like that seen in Figure 6.6. This problem was overcome during run 14, and subsequent runs, by wrapping the exposed core, on the room temperature side, in PTFE which mitigated the issue.

The breakdown runs in which different materials and sizes were used are stated in each subsection. The condition of the electrodes and spacer before and after each run is also stated in order to inform the reason for breakdowns occurring.

Some of the runs performed in this section were left over night after some breakdown events performed before following with additional measurements the following day. The cryostat is topped up whenever the level is too low to well above the level required for the HV feed to work (above the level of the ground termination).

The charging current for all these runs was set to 0.5 μA, however, if the run was unable to achieve higher voltages due to leakage currents limiting it, then the current would be increased. This only was the case in some of the early runs.

6.2.1 Breakdown runs 1-4

The DKHl electrodes were very badly damaged before these experiments were run, with lots of scratching and cratering present. This was possibly from previous experiments carried out with them, and storage in a drawer for several years.

Run 1 was at negative polarity and showed no damage to the HV feed or the insulator,

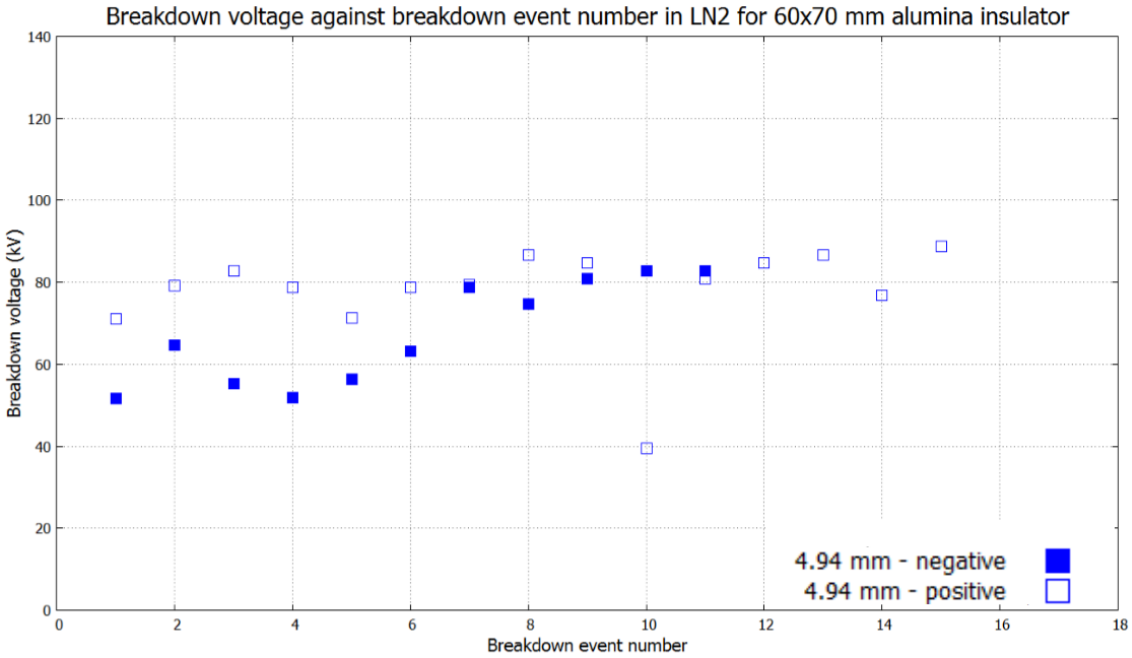

Fig. 6.1 Breakdown voltage versus breakdown event number for runs 1 and 2 using DKHl electrodes with the same 60x70 mm Al_2O_3 insulator 16 mm in length submerged in LN_2. Blue square, filled: V_{bd} LN_2 run 1 (electrode separation 4.94 mm, negative polarity); Blue square, no fill: V_{bd} LN_2 run 2 (electrode separation 4.94 mm, positive polarity).

however, it was observed that there were small grains of possibly alumina in the electrode groove. There was no partial breakdowns recorded. This slight chipping possibly came from the insulator edge where it was cut to length. The breakdown values were scattered around 67.5 kV at 4.94 mm separation. The voltage on this run started out low and got better which successive breakdowns, possibly showing a conditioning effect.

Run 2 at positive polarity with the same insulator as in run 1, also saw no damage to the insulator or HV feed. However, this time 5 partial breakdowns were recorded out of 15 events. The points for this run are scattered around 73.8 kV at 4.94 mm. Comparing the two polarities show that they are comparable to each other, within 5 kV.

Run 3 used a different insulator, 18 mm in length and was run over two days. The second day the polarity was changed from negative to positive. The polarity switch was due to a large amount of leakage current present (> 1 μA). Testing the power supply alone, disconnected from the HV feed, removed the leakage issue, therefore, something inside the setup was causing the problem. This issue is reflected in the number of partial breakdowns occurring. The negative had 10 partial breakdowns out of 18 events, with the positive having 26 partial breakdowns out of 28 events. The insert was removed after the run and the feed was clearly damaged, as can be seen in Figure 6.3.

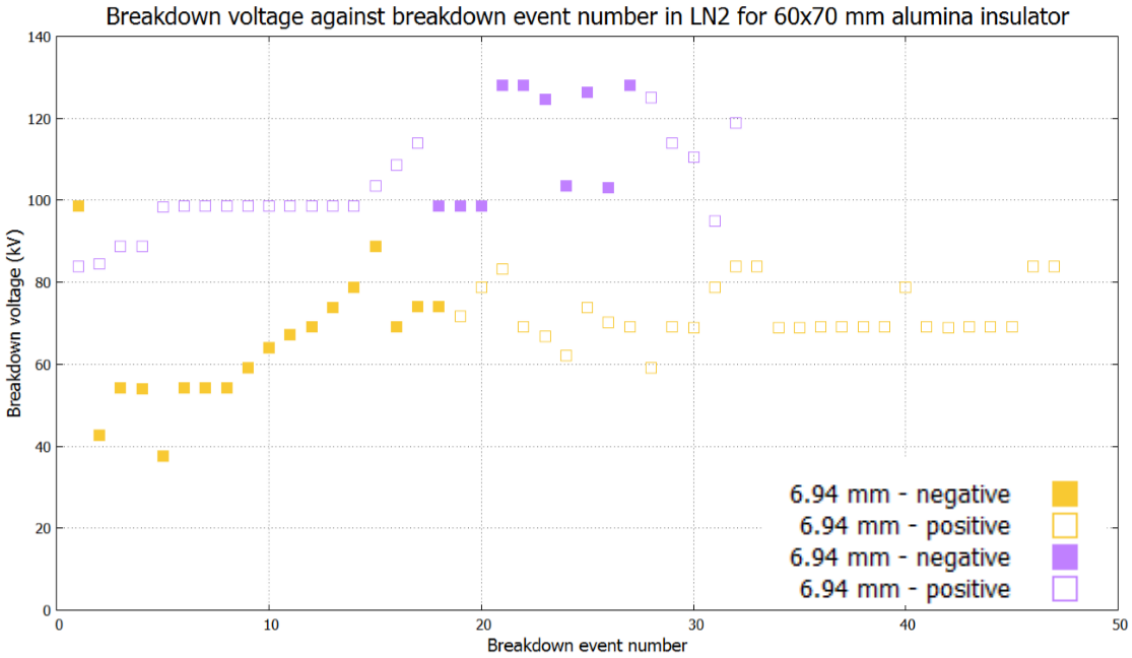

Fig. 6.2 Breakdown voltage versus breakdown event number for runs 3 and 4 using DKHl electrodes with the same 60x70 mm Al_2O_3 insulator 18 mm in length submerged in LN_2. Tan square, filled/no fill: V_{bd} LN_2 run 3 (electrode separation 6.94 mm, negative/positive); Purple square, fill/no fill: V_{bd} LN_2 run 4 (electrode separation 6.94 mm, negative/positive).

Run 4 a new feed was used to replace the damaged one. The experiment was first done at positive polarity. It was then left over night and run again the following day with negative polarity then switched back to negative. The switching was to over come a high leakage current present (> 1.4 μA). This proved some what successful as the number of partial breakdowns decreased, first polarity used had 12 partial breakdowns out of 17 events. Switching to the negative reduced this number to 2 out of 10 breakdowns. The final polarity switch then removed this all together. The same insulator was used between the electrodes as in run 3. The insert was removed and the same damage to the feed shown in the Figure 6.3 above was present again. The insulator did not show any damage. Its likely that the HV feed was damaged in the first few breakdowns and then conditioned afterwards with the final breakdown events at negative having breakdowns possibly occurring between the electrodes.

As mentioned previously the electrodes surface quality was poor. Therefore, to improve the condition of the electrodes it was mechanically polished for the next set of breakdown runs.

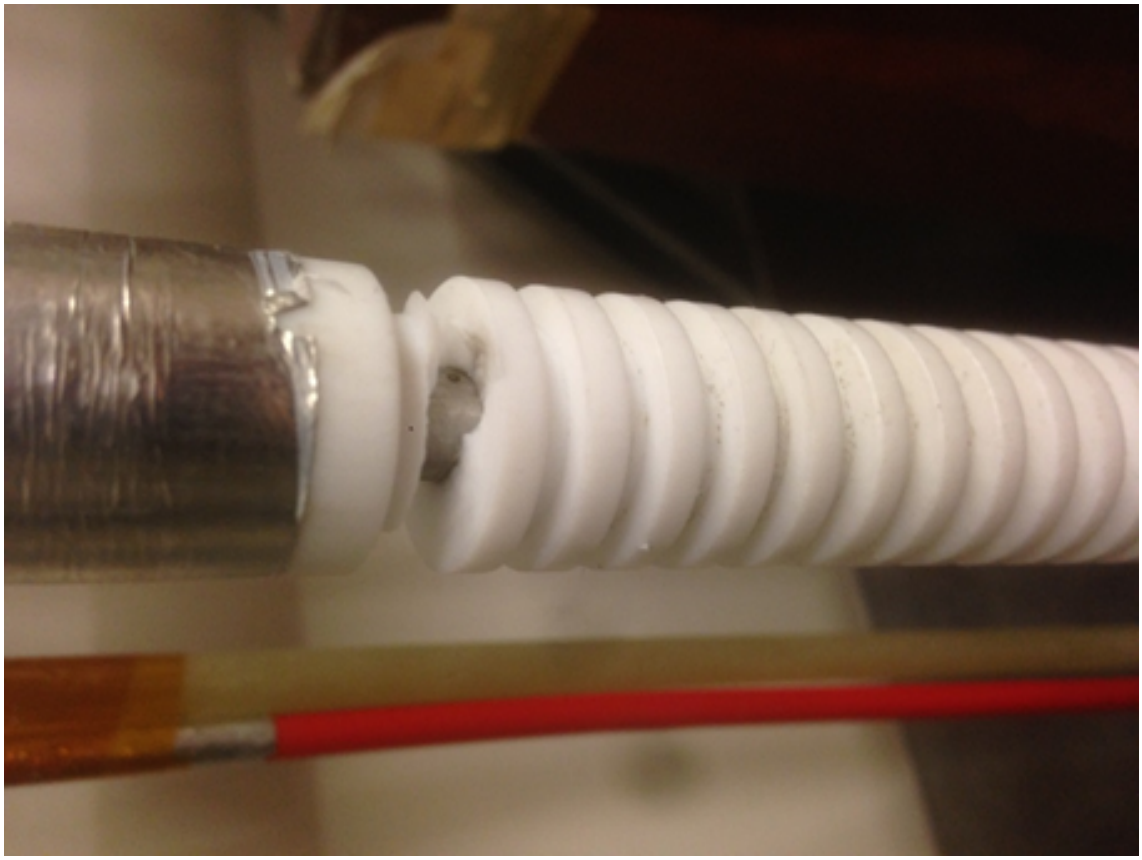

Fig. 6.3 Condition of the HV feed after removal from the KEK cryostat. The PTFE has split at the top castellation. There is a tracking mark along the break with its origin from a burn mark on the stainless steel core. The tracking line has gone to the ground sheath.

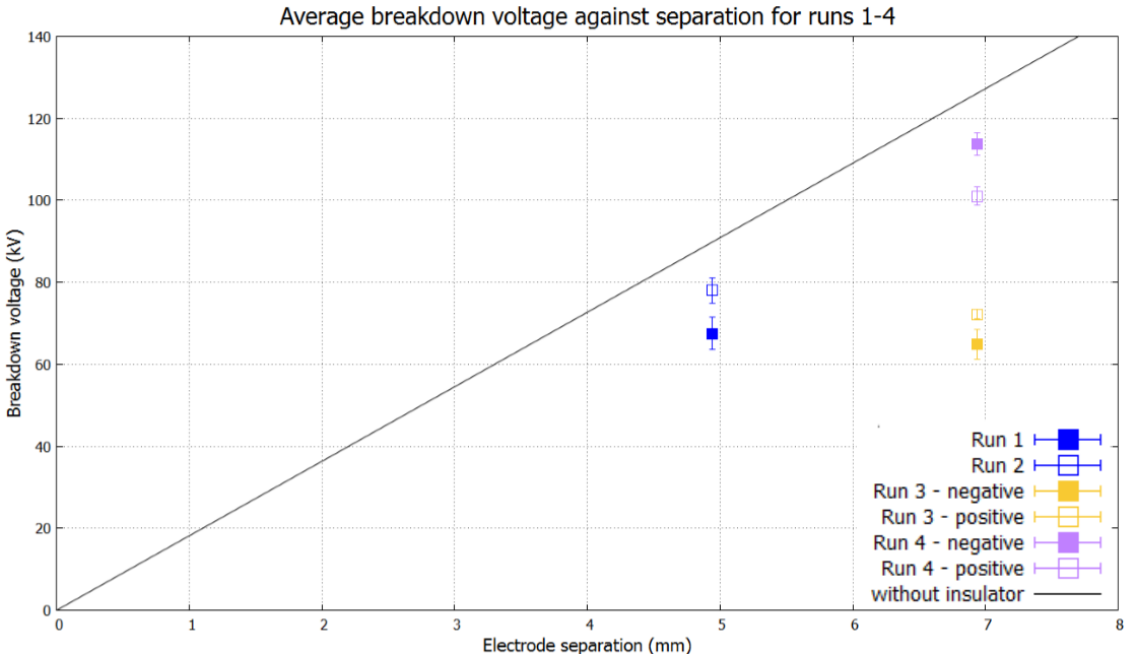

Fig. 6.4 Average breakdown voltage versus separation using Al_2O_3 (60x70 mm) insulator for LN_2 runs 1-4, compared with data from the spacerless breakdown data for DKHl electrodes given in Hill (3) and Davidson's (2) work. Blue square, filled: V_{bd} LN_2 run 1 (electrode separation 4.94 mm, negative polarity); Blue square, no fill: V_{bd} LN_2 run 2 (electrode separation 4.94 mm, positive polarity); Tan square, filled/no fill: V_{bd} LN_2 run 3 (electrode separation 6.94 mm, negative/positive); Purple square, fill/no fill: V_{bd} LN_2 run 4 (electrode separation 6.94 mm, negative/positive); Black trend line is spacerless breakdown data with DKHl electrodes in LN_2.

6.2.2 Breakdown runs 5-10

The alumina insulators were changed at this point as the 60x70 mm size was a loose fit on the electrode outside groove, with radial separation $\Delta r_i \simeq 4.5$ mm and $\Delta r_o \simeq 0.58$ mm. Due to the smaller internal groove diameter, 20 mm smaller then the outer groove diameter, therefore, the effect of the radial separation can be tested (see Figure 5.19) using smaller insulators. Alumina insulators which are diameter 50x60 mm could be tested in the same electrodes, giving a tighter fit on the inner and larger gap on the outer groove (60x70 mm insulators had tighter fit on the outer groove). Their actual internal diameter is $\simeq 51.70$ mm, therefore, the radial separation for these insulators are: $\Delta r_i \simeq 0.35$ mm and $\Delta r_o \simeq 5.79$ mm.

Breakdown runs 5-7 used 50x60 mm alumina spacers, with runs 8-10 switched back to using 60x70 mm insulators.

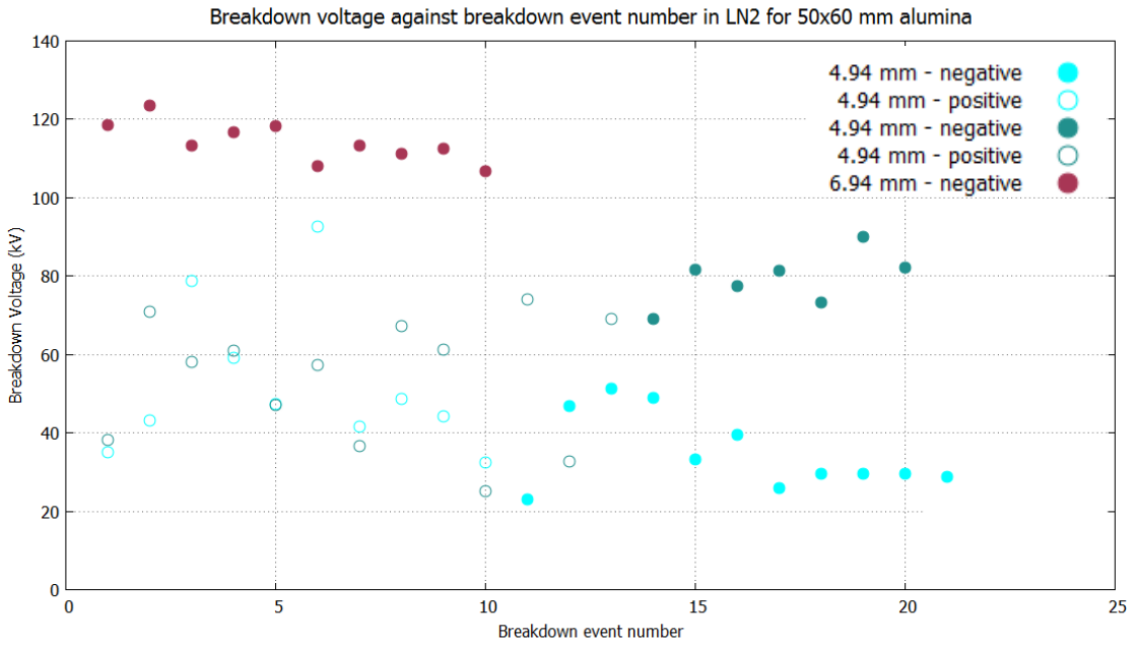

Fig. 6.5 Breakdown voltage versus breakdown event number for runs 5, 6, and 7 using DKHl electrodes with 50x60 mm Al_2O_3 insulator of various lengths submerged in LN_2. Light blue circle, no fill/filled: V_{bd} LN_2 run 5 (electrode separation 4.94 mm, positive/negative polarity); Dark green circle, no fill/filled: V_{bd} LN_2 run 6 (electrode separation 4.94 mm, positive/negative polarity); dark red circle, filled: V_{bd} LN_2 run 7 (electrode separation 6.94 mm, negative polarity).

Run 5 used an electrode separation of 4.94 mm and was performed over two days. No partial breakdowns were recorded. Upon removing the insert after the run, no damage was evident to the insulator or the cryogenic side of the feed, however, the copper connector (details given in Figure 5.12) to the HV cable had tracking damage on it. The

breakdown values were scattered around 43.3 kV. There is a large discrepancy between the data points, with the breakdown voltage dropping off by factor ~ 3 after the 5th measurement and not recovering; it could be assumed that the damage to the HV feed occurred at this point.

Fig. 6.6 Condition of the HV feed after removal from the KEK cryostat. A tracking mark has occurred along the PTFE HV feed at room temperature side, and inside the ground sheath of the Cu connector. The origin is from the stainless steel core to the brass connector, which has become exposed due to creeping of the PTFE, pushing the core up through the feed.

The tracking damage on the inside of the copper connector were removed by using a reamer to take the top layer of damaged PTFE away. The HV cable was cleaned with acetone and the HV feed was then tested to check that it would still operate at 130 kV before the following runs. The feed was tested with a ball electrode on the end, with a large separation to ground surrounded by LN_2 in the KEK. The tests demonstrated that the feed would operate stably to 130 kV.

Run 6 was performed over two days with the same insulator and feed that was used in breakdown run 5. The positive polarity had 3 partial breakdowns for 13 events with the negative having 6 partial breakdowns for 7 events. On this run the feed operated normally with no evidence of damage to it. However, the insulator had damage on it with a number of tracking marks and material blown out from the surface. The damage only occurred on the inside of the insulator's surface. There were 5 continuous tracks which had blown out material half way up the insulator length, with 1 discontinuous track. All the tracks were bunched up on one side of the insulator apart from one which was on the opposite side, a single discontinuous track. This can be seen in Figure 6.7.

Fig. 6.7 Damage present on the 50x60 mm alumina spacer from run 6, after removal from the KEK cryostat. A number of tracking lines are present on the inside of the alumina surface. These lines have one origin but can tend to fork into multiple lines closer to the opposite electrode. There are 6 tracks in total: 5 continuous and 1 discontinuous (with a track line continuing opposite it). The material blown out from the surface all occurs on the bottom half of the insulator. The damage occurring on one side implies that the damage from the discharge is possibly only occurring on one polarity.

The data in Figure 6.5 indicate that the lowest voltages were at positive polarity, possibly indicating that the damage occurred then. The data points are scattered around 53.7 kV for positive polarity and 79.3 kV for negative at 4.94 mm separation.

Run 7 occurred over two days using negative polarity only. No partial breakdowns were recorded. No damage was visible to the feed, however, the insulator had a single discontinuous track about a third of the way up the outside surface, as seen in Figure 6.8. The data points are scattered around 114.2 kV at 6.94 mm separation.

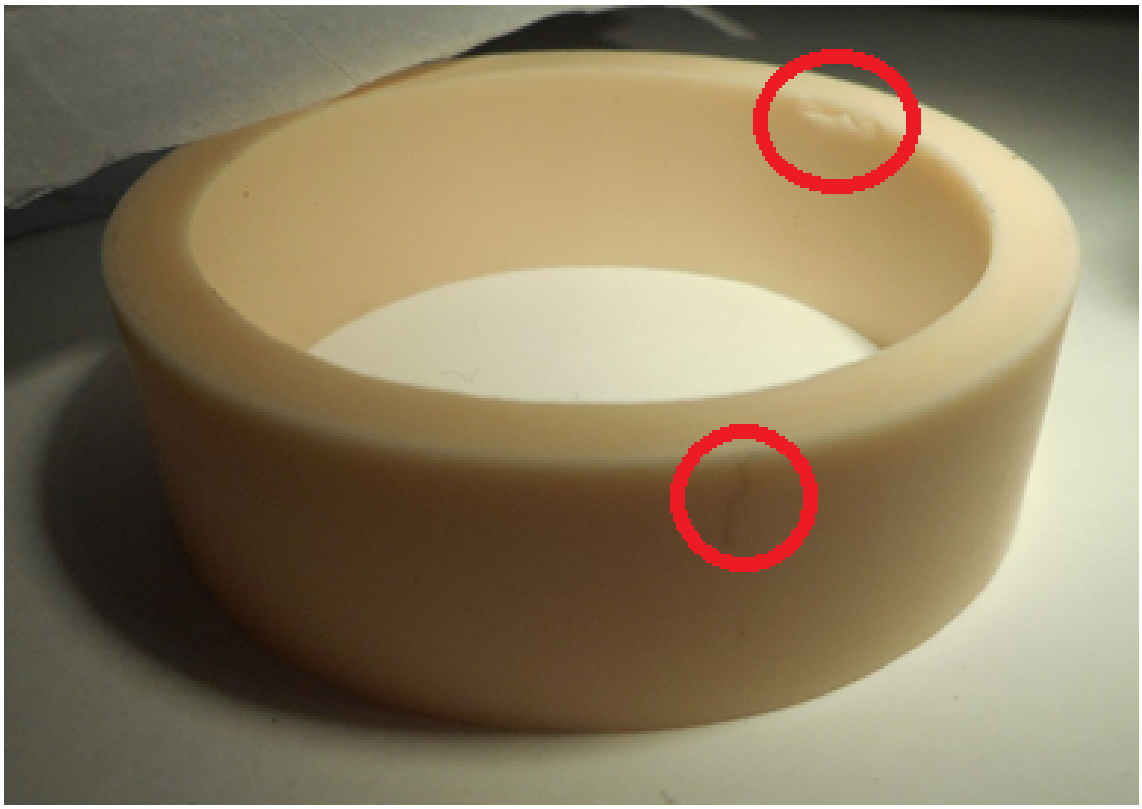

Fig. 6.8 Damage present on the 50x60 mm alumina spacer, from run 7, after removal from the KEK cryostat. Only one discontinuous track line is visible but on the outside. The origin is from the HV electrode which was run with negative polarity during the measurement. There is a large chip also present on the CTJ face. Both are indicated with a red circle.

At this point it was important to check whether this type of damage could occur on the 60x70 mm diameter insulators to pin point if the radial separation was the cause of the damage.

Run 8, only positive polarity was applied to the HV electrode. During the experiment lots of leakage current was present, requiring charging current of (6 μA) in order to achieve voltages above 20 kV. The number of partial breakdowns occurred was 6 for 16

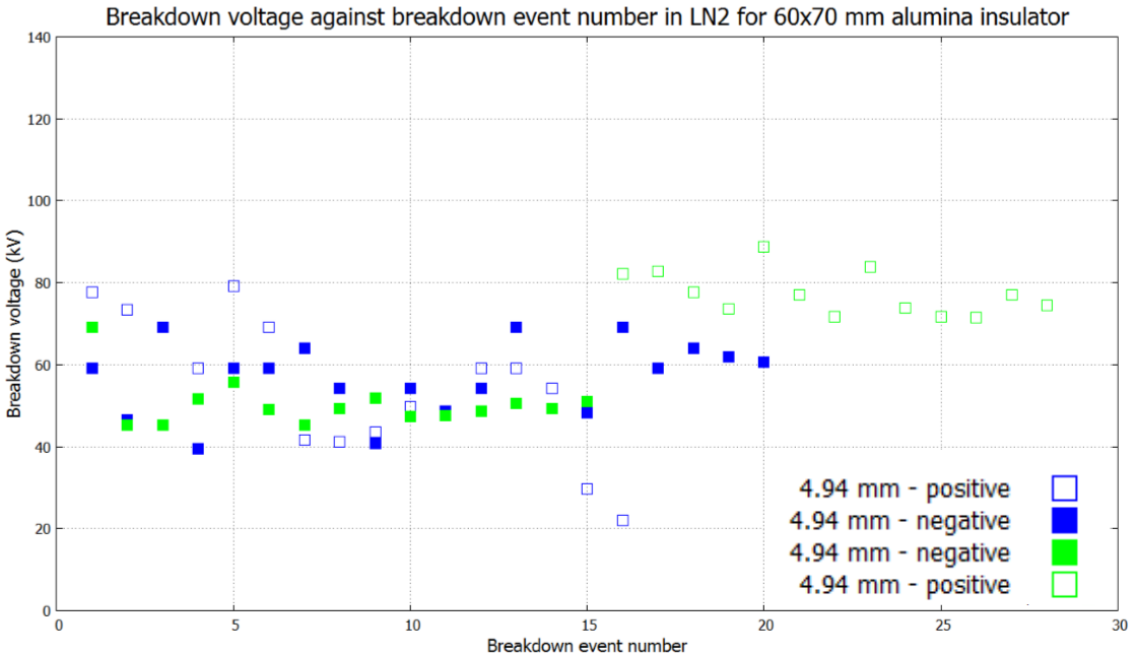

Fig. 6.9 Breakdown voltage versus breakdown event number for runs 8, 9, and 10 using DKHl electrodes with 60x70 mm Al_2O_3 insulators of lengths 16 mm submerged in LN_2. Blue square, no fill: V_{bd} LN_2 run 8 (electrode separation 4.94 mm, positive); Blue square, filled: V_{bd} LN_2 run 9 (electrode separation 4.94 mm, negative); Green square, filled/no fill: V_{bd} LN_2 run 10 (electrode separation 4.94 mm, negative/positive).

breakdown events. The feed at the room temperature side was a problem again with tracking damage present on the PTFE, copper connector, and the HV cable. After about the 10th breakdown event the copper connector was replaced with another that had a fresh PTFE insert inside. The damaged cable side was switched around and put into the Spellman power supply. The tracking was still present on the feed. The aluminium connector and cable components were tested separately and were able to achieve ±100 kV. The data points are scattered around 57.5 kV for electrode separation 4.94 mm. The tracking on the feed was only cleaned with acetone. After the experiment the HV cable was replaced and the delivery system again tested to ±100 kV.

Run 9 used negative polarity only and used the same insulator as the previous. The number of partial breakdowns was 15 out of 20 events. A constant leakage current was present throughout the measurements of (< 0.5 μA). However, extracting the insert showed no damage to the feed on the cryogenic side or on the insulator. The damage from the previous run was still present on the copper connector and room temperature side of the HV feed. The data is scattered around 55.4 kV at 4.94 mm. The KEK cryostat bath was also clearly dirty as there was a lot of material on the G10 support plate. After this run the cryostat was cleaned out with Decon 90 and then washed with water three times to remove any remaining Decon. After the cleaning with water it was allowed to

dry and then the walls were wiped with isopropanol.

Run 10 used the same insulator and HV system as before. The run started on negative polarity. The number of partial breakdowns was 11 out of 15 on the negative, while positive had 3 partials out of 12 events. Leakage currents were present at similar levels as run 9. It should be noted that the switch to positive polarity was performed as negative would struggle to charge to the set voltage. On the positive run, the leakage current was much more substantial (2-3 μA). The data points in Figure 6.9 are all of a similar value for the first 14 points. Afterwards the polarity is switched to positive which gives a higher breakdown voltage. The data points for negative are scattered around 50.5 kV, and around 77.4 kV for positive at 4.94 mm separation.

Extracting the insert showed that the insulator was damaged, similar to that in run 6, except the damage was only on the outside of the insulator surface, as shown in Figure 6.10. All the damage was on one side of the insulator, implying that maybe it was the point which was closest to the groove profile. There were clearly 5 continuous track marks which have material blown out from the insulator surface half way up its length. There are 5 or 6 discontinuous tracks that are between 3-5 mm in length from the CTJ.

In Figure 6.9 the data points for run 10 show that there is a significent difference between the two polarities. This does imply that the HV feed damage could have occurred on the negative polarity, hence reduced voltage. It should be noted that the HV delivery system for runs 8-10 was clearly not operating correctly, therefore, it was hard to distinguish which breakdowns occurred on the insulator or between the electrodes or on the feed.

The electrodes were mechanically polished before the next set of measurements. However, the polishing of the electrodes did not completely remove all the damage from the previous set of breakdown measurements. The number of craters remaining after polishing was counted; ground electrode had 25 and HV electrode had 36.

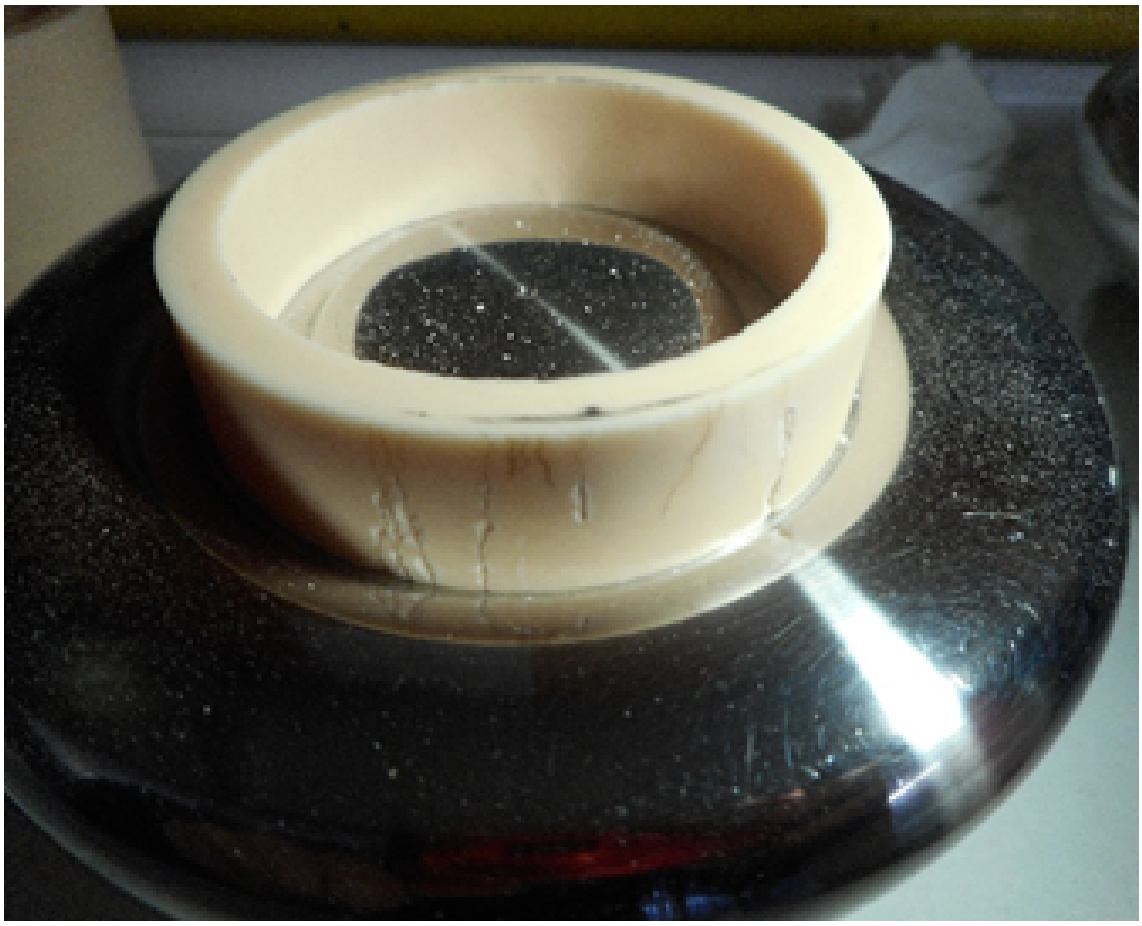

Fig. 6.10 Damage present on the 60x70 mm alumina spacer, from run 10, after removal from the KEK cryostat. A number of tracking lines are present on the outside of the alumina surface. The damage is equivalent to that seen on the 50x60 mm insulator, Figure 6.7. There are 10-11 tracks in total: 5 continuous, 5-6 discontinuous (continuation of the track occurs opposite for every one). The continuous tracks ejected material from the surface on the bottom half of the insulator the same as the previously damaged insulator in run 6. One of the discontinuous tracks started to blow out material before it stops and then the track continues opposite. Both faces that are in contact with the electrode had black marks close to the tracking lines, suggesting the origin for the damage could be coming from the CTJ/ATJ. The length of the discontinuous tracks is ~ 5 mm of vertical length which is equivalent to the groove depth.

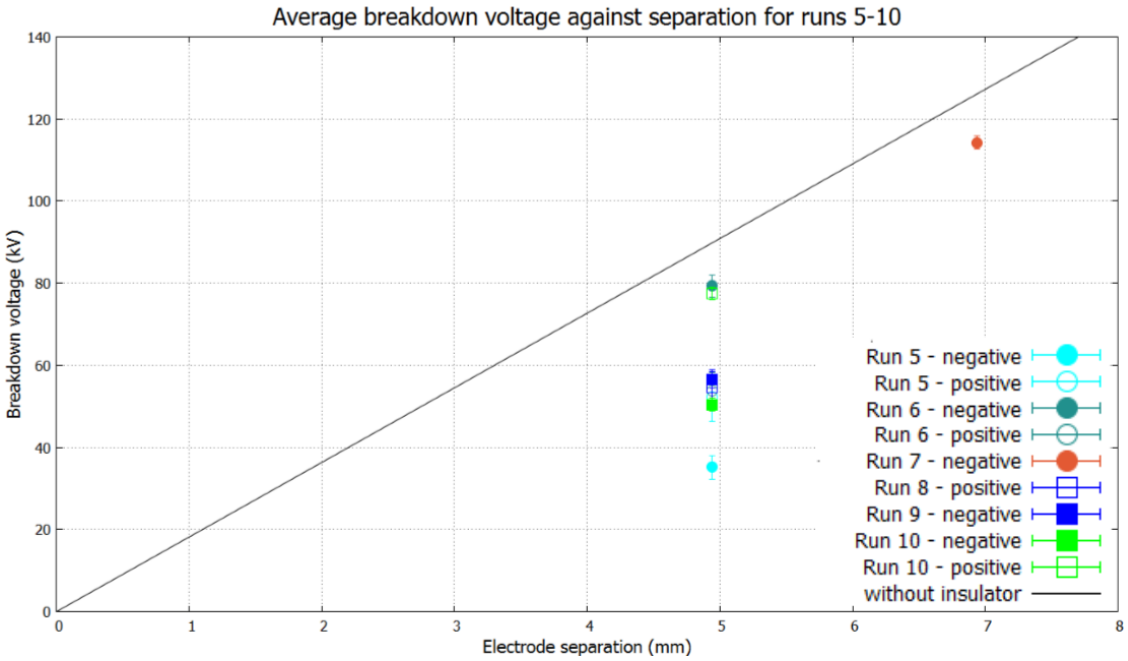

Fig. 6.11 Average breakdown voltage versus separation using Al_2O_3 (50x60 mm and 60x70 mm) insulators for LN_2 runs 5-10, compared with data from the spacerless breakdown data for DKHl electrodes given in Hill (3) and Davidson's (2) work. Light blue circle, no fill/filled: V_{bd} LN_2 run 5 (electrode separation 4.94 mm, positive/negative polarity); Dark green circle, no fill/filled: V_{bd} LN_2 run 6 (electrode separation 4.94 mm, positive/negative polarity); dark red circle, filled: V_{bd} LN_2 run 7 (electrode separation 6.94 mm, negative polarity); Blue square, no fill: V_{bd} LN_2 run 8 (electrode separation 4.94 mm, positive); Blue square, filled: V_{bd} LN_2 run 9 (electrode separation 4.94 mm, negative); Green square, filled/no fill: V_{bd} LN_2 run 10 (electrode separation 4.94 mm, negative/positive); Black trend line is spacerless breakdown data with DKHl electrodes in LN_2.

6.2.3 Breakdown runs 14-17

The effect of changing the dielectric constant of the insulator on the breakdown voltage was investigate by replacing the 60x70 mm alumina with borosilicate glass of the same dimensions. This left a radial separation of $\Delta r_o \simeq 1.75$ mm and $\Delta r_o \simeq 4.32$ mm. After these measurements the number of craters present on the electrode surface was counted.

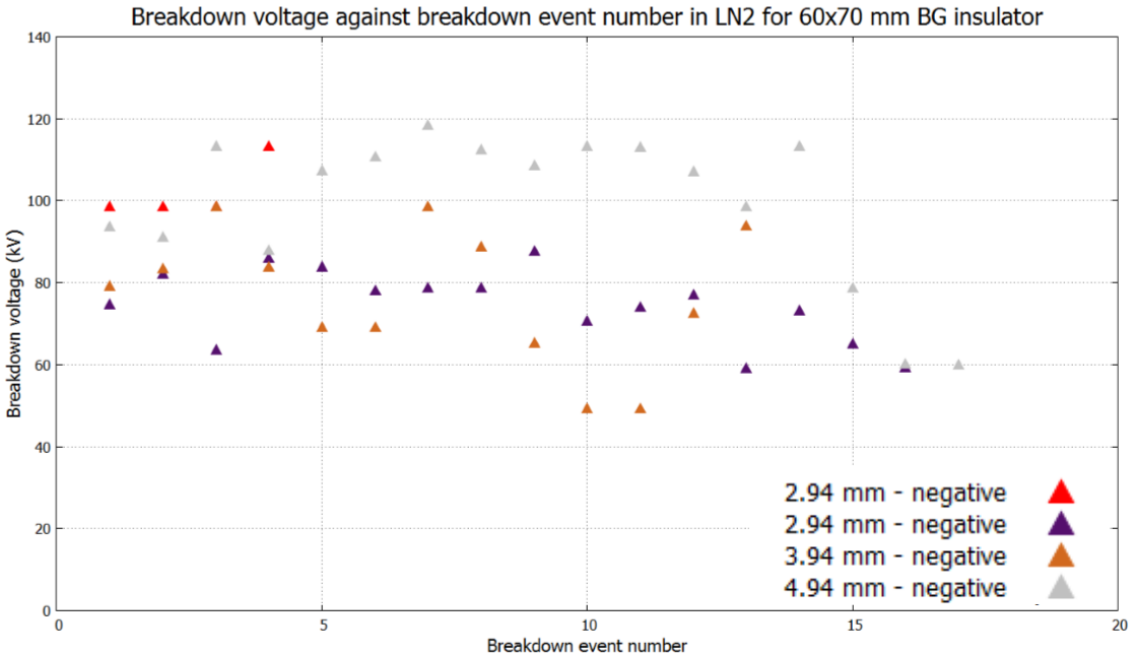

Fig. 6.12 Breakdown voltage versus breakdown event number for runs 14-17 using DKHl electrodes with 60x70 mm BG insulator of various lengths submerged in LN_2. Red triangles, filled: V_{bd} LN_2 run 14 (electrode separation 2.94 mm, negative polarity); dark purple triangles, filled: V_{bd} LN_2 run 15 (electrode separation 2.94 mm, negative polarity); Brown triangles, filled: V_{bd} LN_2 run 16 (electrode separation 3.94 mm, negative polarity); Grey triangles, filled: V_{bd} LN_2 run 17 (electrode separation 4.94 mm, negative polarity).

Run 14 was performed with negative polarity, using a new feed and HV cable from the previous run. Only 4 breakdowns (no partial) were made with this run. The breakdown values were significantly higher than they should be for this electrode separation. It was thought that the feed was not in contact with the electrode. Upon removing the insert, this was clearly the case.

The insulator had become chipped during this run; small shards < 1 mm thick had come away from the surface on the outside of the insulator (5 sites on the CTJ end and 3 on the ATJ end). The chipping had propagated at most 6 mm down the surface, as seen in Figure 6.13.

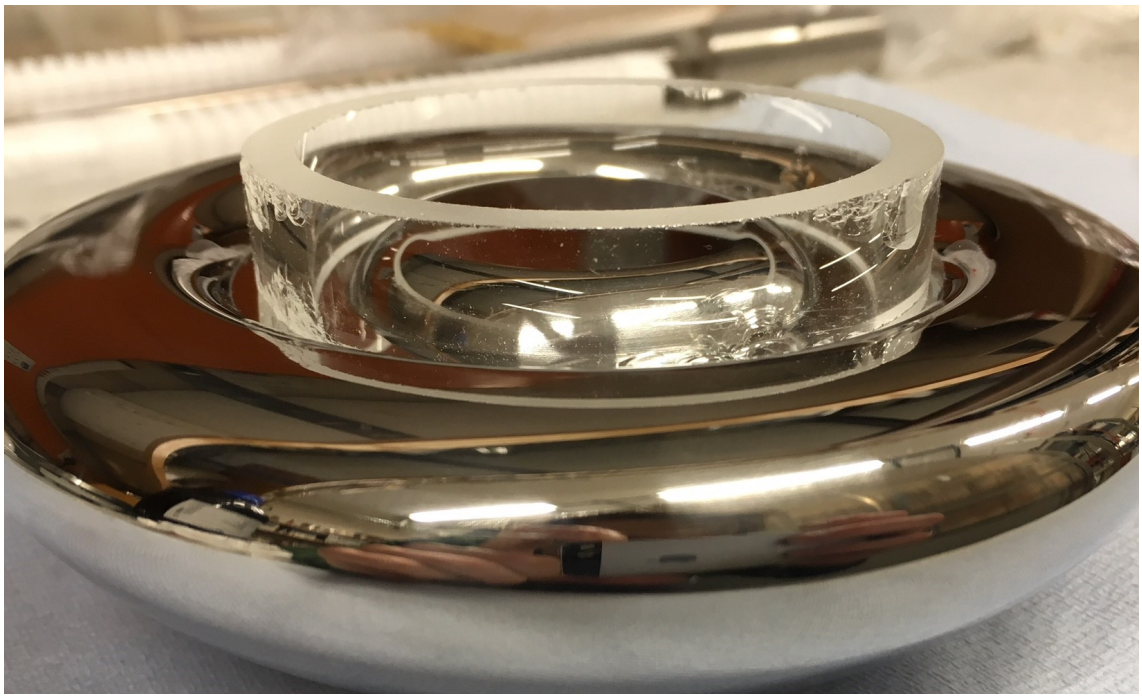

Fig. 6.13 Damage sustained to the borosilicate glass insulator during run 14, insulator is siting in the DKHl electrode.

Run 15 used a new insulator due to the damage on the previous one. This run was also at negative polarity. There was only one partial breakdown for 16 events. It was noticed that when placed between the two electrodes during setup, the insulator would chip, as mentioned previously, in the CTJ region. After the breakdown measurements were performed the insulator and electrodes were removed. The insulator was inspected after the breakdown measurements and showed there was a lot of damage to the insulator. The CTJ region was heavily chipped with shards of glass sitting in the groove of the ground electrode. The cratering on the surface of the HV electrode was found to be 46 (36 initially) which is 10 breakdowns between the electrodes from 16 breakdown events. The ground electrode had 52 (25 initially) craters which is a difference of 27 sites from the number of craters counted on the electrode after polishing. Its likely that some initial craters were missed on the ground electrode, possibly covered by the polish. The damage on this run is seen in Figure 6.14.

Fig. 6.14 Damage sustained to the borosilicate glass insulator during run 15, insulator is siting in the DKHl electrode.

Run 16 used a 15 mm long insulator, breakdown measurements were performed at negative polarity. Upon installing the insulator, 4 chips on the CTJ side occurred. During the experiment, 13 breakdown events were recorded, only one was a partial. Removing the insert after the experiment showed that significant chipping had occurred for this run. Cratering to the HV electrode was counted to be 67 (46 initially) with the ground electrode at 68 (52 initially) sites, giving a difference of 21 and 16 respectively. These numbers are higher then the number of breakdown events, implying those missed previously had now been accounted for. The damage on the insulator is seen in Figure 6.15.

Run 17 was performed with negative polarity on a 16 mm insulator. There was 8 partial breakdowns for 17 events in this run. The HV electrode had 86 (67 initially) craters and the ground electrode 84 (68 initially) sites, a difference of 19 and 16 respectively for 17 breakdowns. Damage to the insulator is seen in Figure 6.16.

Comparing the count of damage between runs 14-17 implies that there was a significant number of craters overlooked originally, simply in the discrepancy between number of breakdown events and craters. The counting being out could have potentially been due to the polishing process obscuring some of the damage that was present previously. However, there still seems to be a continuous increase in cratering damage to the surface, proportional to the number of breakdown events.

Fig. 6.15 Damage sustained to the borosilicate glass insulator during run 16, insulator is siting in the DKHl electrode.

Fig. 6.16 Damage sustained to the borosilicate glass insulator during run 17, insulator is siting in the DKHl electrode.

After all of these runs, no tracking damage was observed on the insulator surface.

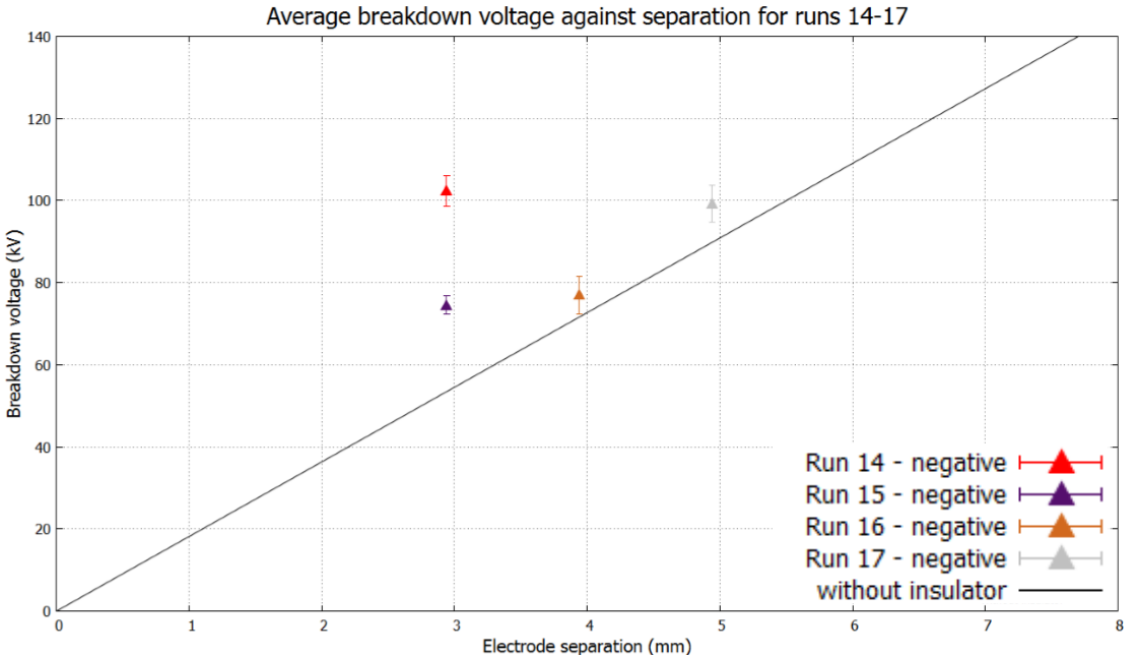

Fig. 6.17 Average breakdown voltage versus separation using BG (60x70 mm) insulators for LN_2 runs 14-17, compared with data from the spacerless breakdown data for DKHl electrodes given in Hill (3) and Davidson's (2) work. Red triangle, filled: V_{bd} LN_2 run 14 (electrode separation 2.94 mm, negative polarity); Dark purple triangle, filled: V_{bd} LN_2 run 15 (electrode separation 2.94 mm, negative polarity); Brown triangle, filled: V_{bd} LN_2 run 16 (electrode separation 3.94 mm, negative polarity); Grey triangle, filled: V_{bd} LN_2 run 17 (electrode separation 4.94 mm, negative polarity); Black trend line is spacerless breakdown data with DKHl electrodes in LN_2.

In Figure 6.17 it shows that all the data points lie close to the expected trend line which is in contrast to the alumina measurements in which they were all below the line. An initial implication is that the change of the dielectric constant of the insulator has played a role in improving the breakdown values. However, all the borosilicate glass runs had damage to the insulator which is a problem. If the chipping is occurring during a breakdown measurement the glass will contaminate the experimental volume. There was also very low number of partial breakdowns occurring, except on run 17. This could be due to the HV feed and insulators not suffering tracking damage during the measurement. As for run 17, there was h a lot of glass shards in the experimental volume possibly causing the increase in partial breakdowns.

After this run the electrodes were again mechanically polished. Inspecting the surfaces of the electrodes after polishing showed that all craters on the HV electrode were removed, while the ground electrode still had two craters visible.

6.2.4 Breakdown runs 18-28

This set of experiments continued the measurements on the borosilicate glass to complete the data set from the available electrode separations. It also contained a number of tests which involved the improved HV feed to attempt to fix the failures of the old design which had left a significant number of breakdown runs potentially compromised. There was also a return to some alumina measurements for a project student Shek Fan Ho to collect data for his master's thesis (151).

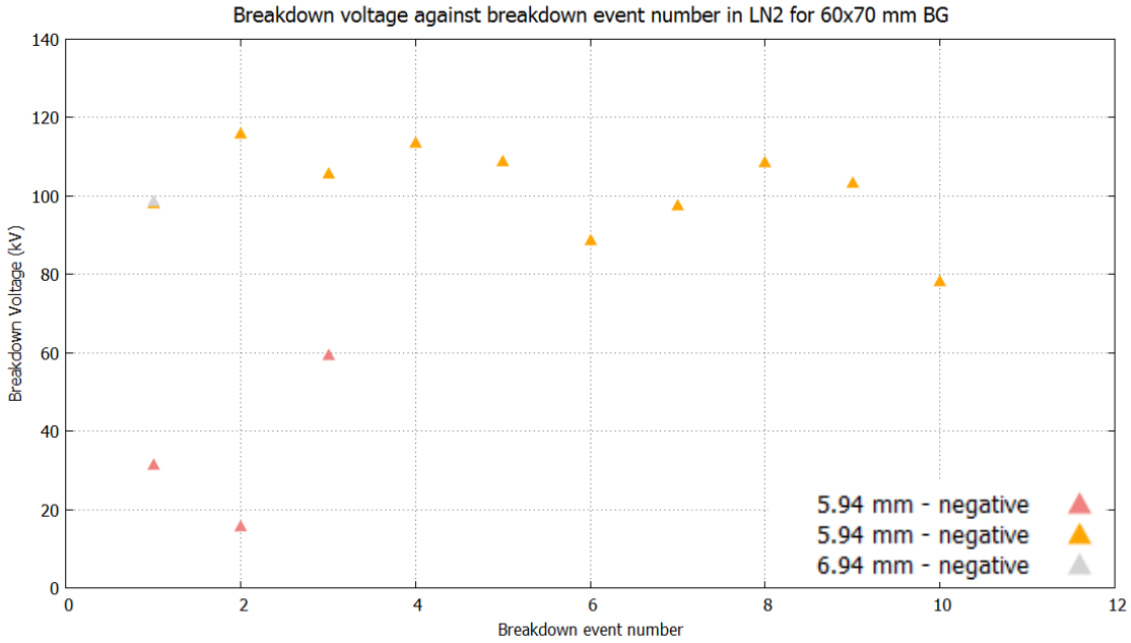

Fig. 6.18 Breakdown voltage versus breakdown event number for runs 18-20 using DKHl electrodes with 60x70 mm BG insulators of various lengths submerged in LN_2. Light red triangle, filled: V_{bd} LN_2 run 18 (electrode separation 5.94 mm, negative polarity); Light orange triangle, filled: V_{bd} LN_2 run 19 (electrode separation 5.94 mm, negative polarity); Light grey triangle, filled: V_{bd} LN_2 run 20 (electrode separation 6.94 mm, negative polarity).

Run 18 used a 17 mm long insulator installed between the electrodes, which resulted in a few chips to the insulator. During the experimental run a leakage current (> 1 μA) was present throughout, which limited being able to reach higher voltages. This occurred continuously on each breakdown attempt, therefore, this run was stopped. There was no partial breakdowns present for this run. The feed was inspected but no damage was observed and the insulator was also still intact. The electrode damage was counted: the HV had 5 craters, and the ground had 5 for 3 breakdown events.

The confidence in the feed to be able to get to the required voltage was questioned, so a test was performed to check its ability to function. The feed was removed from the

insert and suspended in a bucket of LN_2 with the normal connections for HV delivery added. A 50 mm diameter ball electrode was attached to the bottom of the feed with a separation to ground of approximately 10 cm. The feed was able to reach to 130 kV after one breakdown at 110 kV, demonstrating that this was not the limiting factor for the previous run.

One possible explanation for this limiting problem in run 18 is that the electrodes may have had frozen contamination on the surface from the polishing process. The two additional craters to the HV electrode counted could have been hidden by the polishing process.

Run 19 had the previous feed installed back into the insert for the measurements. The polarity was negative and the same insulator from the previous run was placed back into the setup. This time the voltage reached values that were at more acceptable levels so a full run was performed. Only one partial breakdown was recorded. Removing the insert afterwards showed that the insulator had shattered into two pieces with shards of glass covering the ground electrode. However, unlike the alumina breakdown measurements no tracking marks were visible on the surface of the material. The surface of the electrodes were examined for craters with the HV showing 13 sites (5 initially) while the ground had 10 (5 initially) from 10 breakdown events.

Fig. 6.19 Damage present on the 60x70 mm BG spacer, from run 19, after removal from the KEK cryostat. No tracking lines were present on the pieces of the insulator. The fracturing of the glass occurred at multiple sections with no clear origin of the breaks visible. There was also large amount of glass lying on the ground electrode after removal.

Run 20 was the first test to implement a new HV feed design, see Figure 5.11, in which

the normal ground sheath is not terminated by just PTFE tape but a stress cone is added instead. The experimental run used negative polarity with an insulator of borosilicate glass, 18 mm in length. During the run a single full breakdown occurred at 100 kV which seemed to creat a permanent conductive track as the voltage was then unable to get much above 10 kV even at a 5 μA charging current. Removing the insert showed the electrodes and the insulator to be in the same condition as before, with no damage observed on their surfaces. However, the HV feed had black marks around the stress cone. There was what appeared to be a conductive track underneath the stress cone but it was difficult to distinguish between that or contamination on the PTFE surface picked up from the LN_2 volume. It seems likely that the feed was the limitation and that the presence of the G10 screws may have caused problems with the local electric fields, and so the method of how to attach the stress cone to the feed required further investigation.

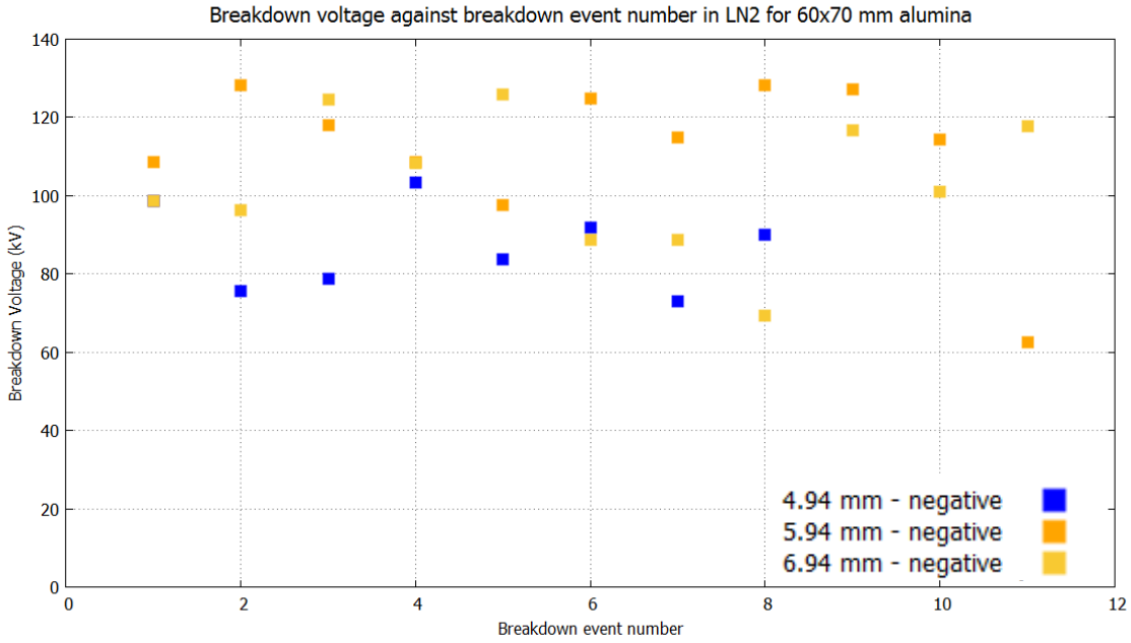

Fig. 6.20 Breakdown voltage versus breakdown event number for runs 21-23 using DKHl electrodes with 60x70 mm Al_2O_3 insulator of various lengths submerged in LN_2. Blue square, filled: V_{bd} LN_2 run 21 (electrode separation 4.94 mm, negative polarity); Orange square, filled: V_{bd} LN_2 run 22 (electrode separation 5.94 mm, negative polarity); Tan square, filled: V_{bd} LN_2 run 23 (electrode separation 6.94 mm, negative polarity).

Runs 21-25 were measurements performed by Shek Fan Ho (151). Run 21 used alumina insulators to see if the damage that was observed previously in the earlier runs could be replicated. It was performed with negative polarity using the Karamath design of HV feed. There was two partial breakdowns for 8 events. After the measurements the feed was inspected but no damage was found, and the insulator also had no damage to it. The surface condition of the electrode was not recorded for this run.

Run 22 used an alumina insulator with negative polarity but at a larger separation of 5.94 mm. During the run the maximum voltage 130 kV was achieved infrequently, but it was unable to hold for long periods of time and partial breakdowns would occur. This resulted in all 11 events being partial. Removing the insert showed that the insulator had suffered significant damage and had broken into 3 pieces. Observation of the breaking points showed that tracking marks were present and even one breakdown had occurred through the insulator material itself to the outside of the insulator, halfway down its length then continuing down the outside of the insulator surface.

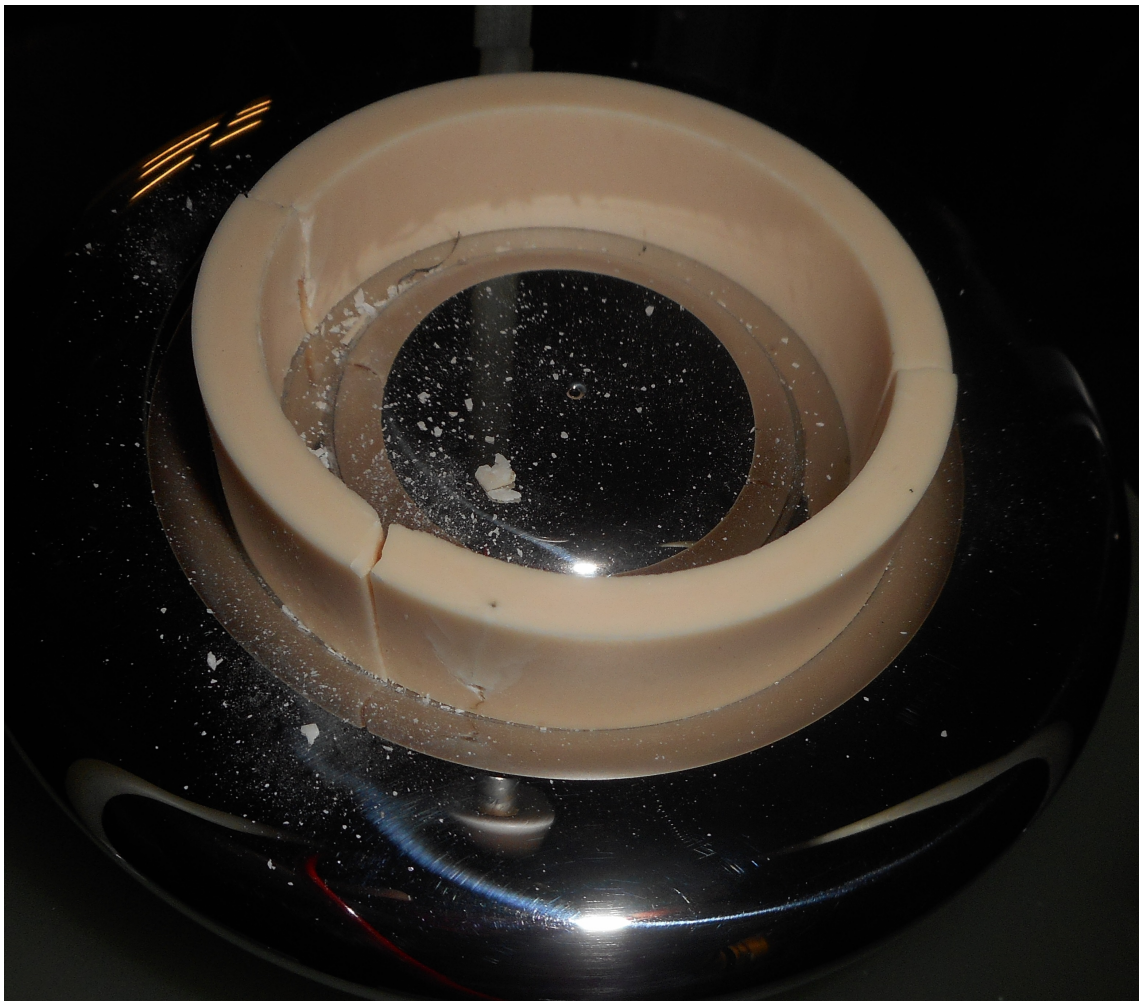

Fig. 6.21 Damage to the 60x70 mm alumina insulator for 6 mm separation in run 22. It has been cracked into three piece which contain tracking marks through the break. One discharge starts at the CTJ, goes through the insulator and appears on the outside surface, then goes down the surface to ground.

Monitoring the damage to the electrode surfaces found that the HV electrode had 26 craters and the ground electrode had 27. Assuming the 8 breakdowns from run 21 left damage between both electrodes, then we can assume the initial number of craters was 18 for the HV and ground electrodes. Therefore, for 11 breakdown events gives 8 and 9

craters for the HV and ground electrodes respectively. There were clearly three tracking marks on the insulator, therefore, some craters would be missing in the count. Shek also noted that 3 craters where found in the base of the groove of the electrode. These are not included in the count as only the ones on the electrode surface indicate bulk fluid breakdown.

Run 23 used an alumina insulator with a length of 18 mm. There were 7 partial breakdown for 11 events. Shek found that the feed failed this time, again in the same place as previous occurrences, see Figure 6.3. There were 4 tracking marks on the split between the two separated pieces of PTFE coming from the conducting core to the ground sheath. The HV electrode was counted to have 36 craters and the ground 31. There were 11 breakdowns observed in this run, while the difference in craters from the previous measurement was 10 for the HV and 4 for ground. This implies that possibly a few craters were missed on the ground electrode or that most of the breakdowns occurred on the HV feed and the number was miscounted on the HV electrode. In Figure 6.20, there are clearly 5 events that are lower than 100kV which for this length of insulator is much lower than expected. These lower voltages could be explained by the breakdown of the feed.

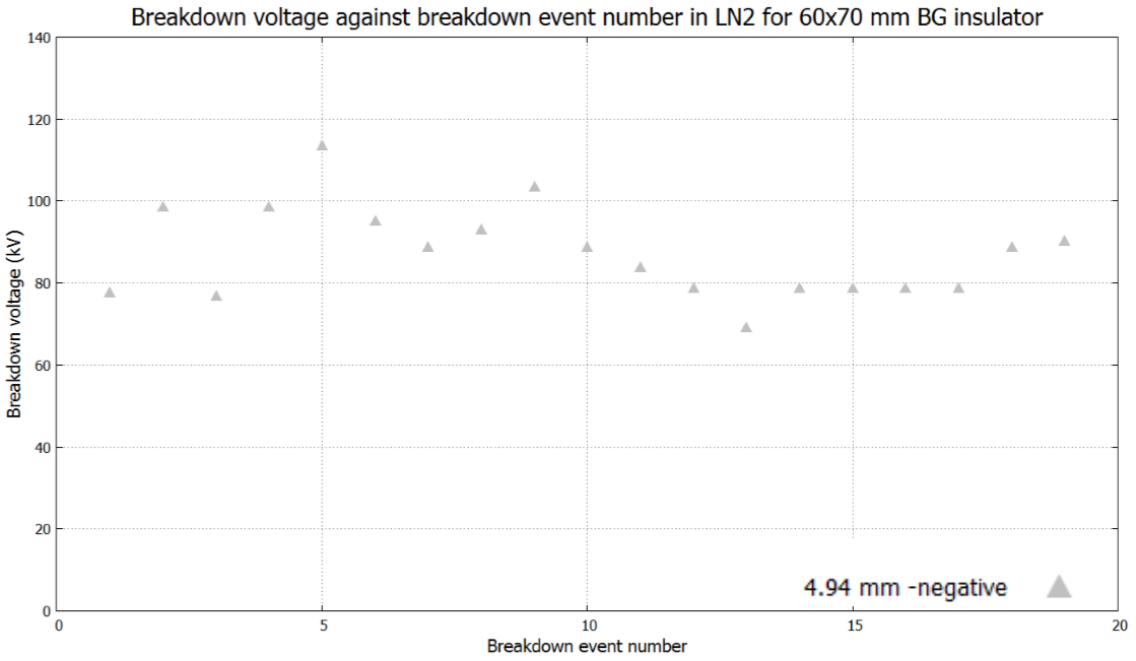

Fig. 6.22 Breakdown voltage versus breakdown event number for run 24 using DKHl electrodes with a 60x70 mm BG insulator (electrode separation of 4.94 mm, negative polarity) in LN_2.

Run 24 the HV feed was replaced with a Karamath HV feed design. The run was performed with negative polarity using a borosilicate insulator of length 16 mm. During

the experiment partial breakdowns were recorded frequently with every breakdown after the 8th being partial. There was 13 partial breakdowns out of 19 events. Removing the insert showed the feed had again failed at the top castellation. The damage to the HV electrode was 38 craters, and the ground had 37 sites. The difference gives 2 additional craters for the HV electrode and 6 for the ground for 25 events, implying that the majority of breakdowns occurred on the feed. In Figure 6.22 it shows that there are a number of breakdowns at values significantly lower than expected, ~90 kV.

The consistent failure of the HV delivery system was becoming increasingly intolerable, therefore, focus was switched to overcome this problem. The feed was redesigned as detailed in section 5.4.1. The design was then tested in LN_2. After conditioning effects in which breakdowns occurred, the feed was able to hold 130 kV for 20 minutes without any leakage current present (to the sensitivity of the power supply, $< \pm 0.1$ μA). This feed was then installed in the KEK cryostat for the next run.

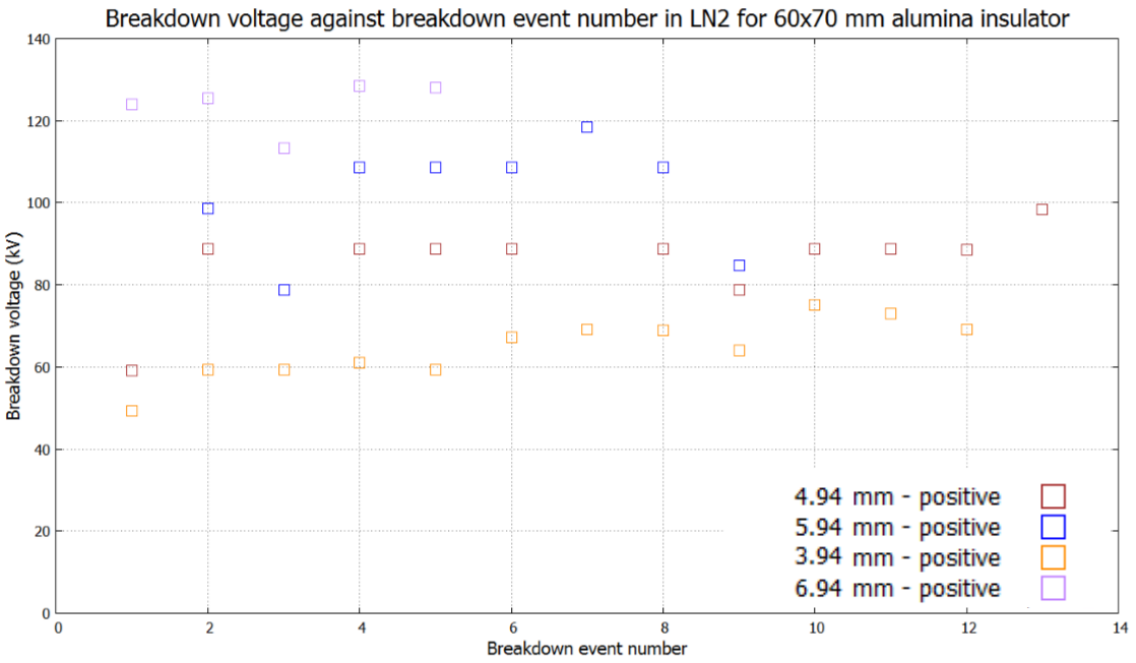

Fig. 6.23 Breakdown voltage versus breakdown event number for runs 25-28 using DKHl electrodes with 60x70 mm Al_2O_3 insulators of various lengths submerged in LN_2. Brown square, not filled: V_{bd} LN_2 run 25 (electrode separation 3.94 mm, positive polarity); Blue square, not filled: V_{bd} LN_2 run 26 (electrode separation 4.94 mm, positive polarity); Light orange square, not filled: V_{bd} LN_2 run 27 (electrode separation 5.94 mm, positive polarity); Light grey square, not filled: V_{bd} LN_2 run 28 (electrode separation 6.94 mm, positive polarity).

Run 25 was performed with an alumina insulator of dimensions 60x70x16 mm at positive polarity. A total of 13 breakdown (no partial) events occurred over two days of measurements. Following the run the insert was removed and the insulator showed no

signs of damage to it. The damage on the surface of the HV electrode was 50 craters and the ground had 49. The difference for both electrodes from the previous run was 12 additional craters compared to the 13 breakdown events recorded.

Run 26 was performed with positive polarity on an alumina 60x70 mm spacer which was 17 mm long. The run resulted in no damage to the insulator or the feed, however, it must be noted that there was some small chipping on the CTJ region on this insulator, possibly due to the method it was cut which left some rough edges. There was no partial breakdowns recorded. The counting of craters on the electrode surface found that the HV electrode had 56 and the ground 57. The HV electrode had 6 new sites and the ground had 8 compared to the 9 breakdown events recorded. The feed for this run had some marks near the stress cone which was attributed to contamination from the LN_2 volume.

Run 27 also was performed at positive polarity with a 15 mm long insulator. There was no partial breakdown recorded. The results of the experiment again showed a slight bit of chipping at the edge of the glass insulator. The craters on the HV electrode were counted to be 65 and the ground had 70 for 12 events, therefore, the HV had 9 new sites and the ground 12.

Run 28 again used positive polarity with an alumina insulator which was instead 18 mm long. During this run there was an occurrence of a spark occurring outside the KEK, near the top of the copper connector to the HV power supply. This happened at 130 kV and seemed to have damaged the electronics controlling the power supply causing some problems through the run. There was 2 partial breakdowns for 5 events. The voltage also had to be stopped a few times during breakdown measurements as it maintained itself at 130 kV between the electrodes for more than 10 minutes without breakdown occurring. Therefore, this run should be considered as conditioning runs for this separation. At the end of this run the craters on the HV electrode were counted to be 76 and 74 for the ground electrode for 11 events.

After this set of runs the electrodes were once again polished and the feed cleaned.

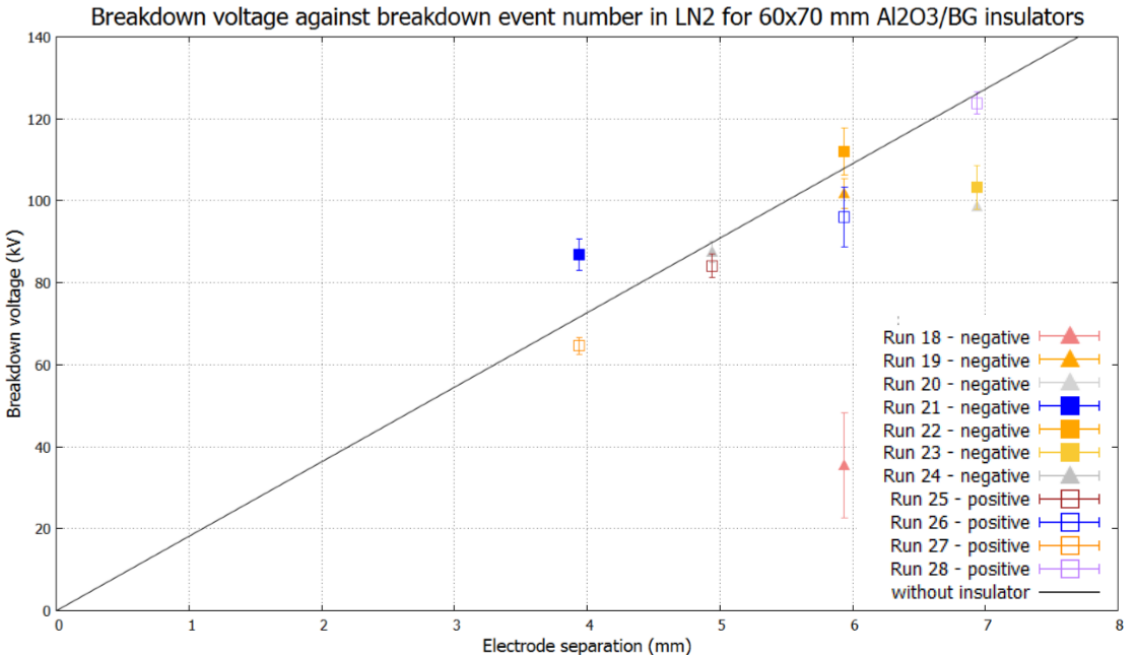

Fig. 6.24 Average breakdown voltage versus separation using BG (run 18-20 and 24) and Al_2O_3 (run 21-23 and 25-28) (60x70 mm) insulators in LN_2, compared with data from the spacerless breakdown data for DKHl electrodes given in Hill (3) and Davidson's (2) work. Light red triangle, filled: run 18 (electrode separation 5.94 mm, negative); Light orange triangle, filled: run 19 (electrode separation 5.94 mm, negative); Light grey triangle, filled: run 20 (electrode separation 6.94 mm, negative); Blue square, filled: run 21 (electrode separation 4.94 mm, negative); Orange square, filled: run 22 (electrode separation 5.94 mm, negative); Tan square, filled: run 23 (electrode separation 6.94 mm, negative); Yellow triangle, filled: run 24 (electrode separation 4.94 mm, negative); Brown square, not filled: run 25 (electrode separation 3.94 mm, positive); Blue square, not filled: run 26 (electrode separation 4.94 mm, positive); Light orange square, not filled: run 27 (electrode separation 5.94 mm, positive); Light grey square, not filled: run 28 (electrode separation 6.94 mm, positive); Black trend line is spacerless breakdown data with DKHl electrodes in LN_2.

6.2.5 Breakdown runs 29-30

Before this set of runs, the electronics problem was fixed. The electrode was again mechanically polished but there was still some damage present on the surface. The HV electrode had about 40 craters and the ground had 35. This set of runs looked at how to overcome the chipping problem with the borosilicate glass. Raw data suggested that the performance, under HV, of the glass was better than the alumina, and stopping the chipping would give a reliable insulator with the benefit of not reducing breakdown voltage. These two runs tested the insulator with two different methods of finishing the CTJ face of the glass. One, run 29, was with a mechanically polished insulator to a 1200 grit and had a 0.5 mm chamfer inside and outside on the faces in contact with the electrode. The other insulator in run 30, was flame polished and also had the same chamfer as the mechanical one. The idea of polishing the insulator is to remove any

stress regions in the glass which could lead to propagation of microscopic chipping which results in the observed damage on previous insulators.

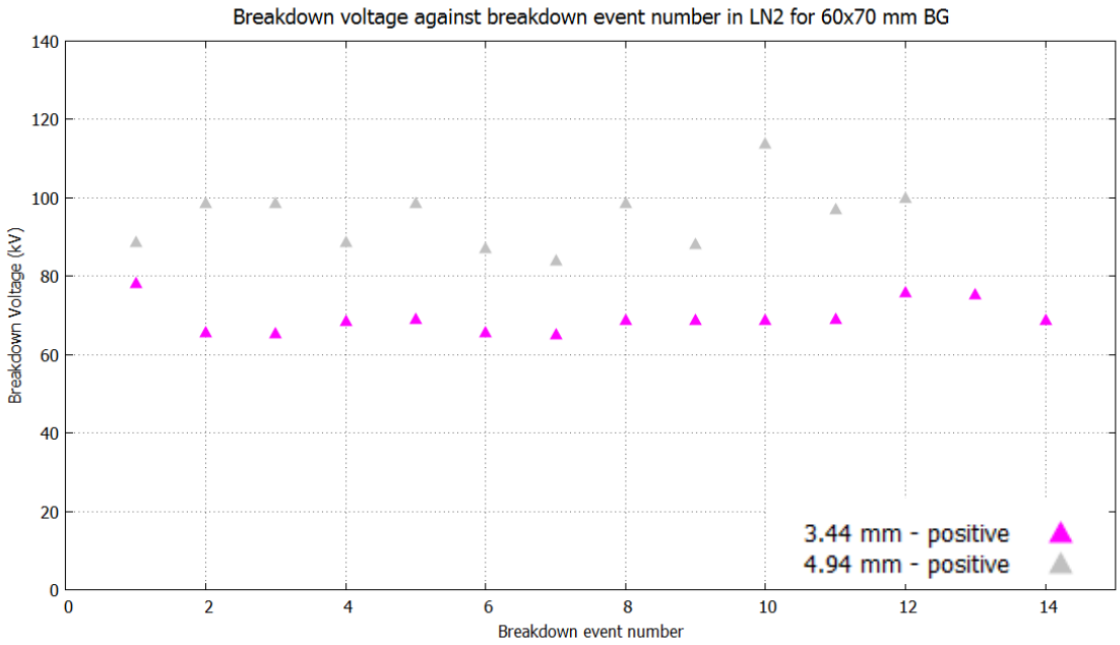

Fig. 6.25 Breakdown voltage versus breakdown event number for runs 29-30 using DKHl electrodes with 60x70 mm BG insulators of various lengths submerged in LN_2. Magenta triangle, not filled: V_{bd} LN_2 run 29 (electrode separation 3.44 mm, positive polarity, mechanically polished); Grey triangle, not filled: V_{bd} LN_2 run 30 (electrode separation 4.94 mm, positive polarity, flame polished).

Run 29 used the mechanically polished borosilicate glass insulator, 60x70 mm in diameter and a length of 14.5 mm. The insulator did not chip upon placing the HV electrode on top. No partial breakdowns were observed during this run. Removing the insert after the run revealed that a crack had occurred at the ATJ that was fairly large. Opposite this was a smaller chip on the chamfer edge of the insulator. However, the occurrence of chipping had been significantly reduced compared to the previous measurements with borosilicate glass. The craters in the HV electrode were counted to be 79 and 75 at the ground electrode, which is a difference of 39 and 40 respectively for only 13 breakdown events. Clearly a large number of craters had been missed in the initial count, probably due to the polish covering it up.

Run 30 used the flame polished insulator which was 60x70 mm in diameter and 16 mm in length. The placement of the insulator did not cause any chipping of the material. Again no partial breakdowns were recorded for this run. After the measurements were performed the insert was removed and showed no damage to the insulator (the damage to the HV electrode was 91 and 90 on the ground for 12 events recorded). The number of craters was almost equivalent to the number of breakdowns recorded.

Fig. 6.26 Condition of the BG insulator, run 29, after removal from the KEK cryostat. The amount of chipping is significantly reduced. Two chips were present, one less than 1 mm^2, and the other slightly larger, 2-3 mm^2.

Figure 6.25 shows a very consistent breakdown voltage for both of the polished borosilicate glass insulators. Even though a large chip occurred on run 29 there does not appear to be a drop in voltage due to this damage. Therefore, it is unclear if this damage occurred during or from mechanical stress when taking it out. However, the flame polished insulator maintained high fields for that separation but also survived without any chipping.

Fig. 6.27 Flame polished insulator, after run 30. There is no damage present on the insulator. It should be noted that the flame polish process does not guarantee the surface is flat.

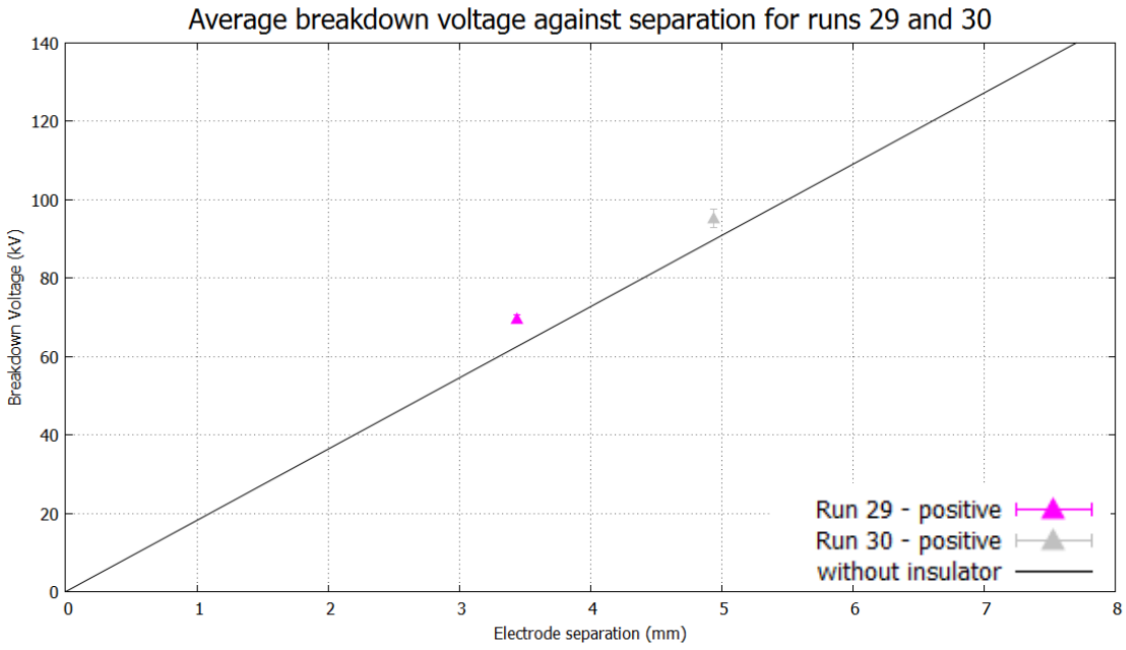

Fig. 6.28 Average breakdown voltage versus separation using BG (60x70 mm) insulators in LN_2 runs 29 and 30 are compared with data from the spacerless breakdown data for DKHl electrodes given in Hill (3) and Davidson's (2) work. Magenta triangle, not filled: V_{bd} LN_2 run 29 (electrode separation 3.44 mm, positive polarity, mechanically polished); Grey triangle, not filled: V_{bd} LN_2 run 30 (electrode separation 4.94 mm, positive polarity, flame polished); Black trend line is spacerless breakdown data with DKHl electrodes in LN_2.

6.3 DKHs electrodes

These measurements were performed in order to ascertain if damage Hill (3) observed on alumina insulators could be replicated on different materials and geometry. Changing the material would change the dielectric constant of the insulator which could influence the damage to the insulator. The change of geometry would affect the local field enhancement at the groove to insulator region, as described in section 5.5. The geometry of these electrodes are given in Figure 5.41.

6.3.1 Breakdown runs 11-13

Two insulator dimensions and materials were tested using the DKHs electrodes: 11x12mm alumina and 10x15mm quartz. The electrode geometry is detailed in Hill's thesis (3). In Hill's experiments only alumina of 10x15 mm was tested, therefore, direct comparison can be made to determine what influences the damage on the insulators Hill observed. The thin wall alumina was used to determine the effect of the radial separation, $\Delta r_o \simeq 1.87$ and $\Delta r_i \simeq 2.44$. The quartz has a radial separation $\Delta r_o \simeq 0.41$ and $\Delta r_i \simeq 0.48$, similar to the 10x15 mm alumina insulators Hill used but with a lower dielectric constant (see Table 5.2).

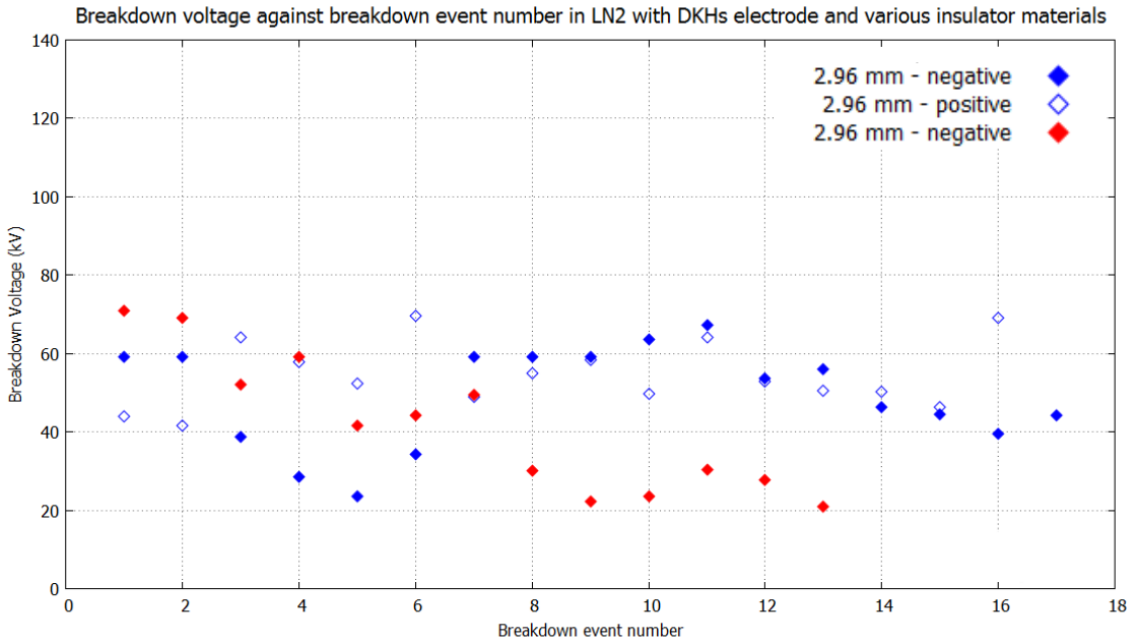

Fig. 6.29 Breakdown voltage versus breakdown event number for runs 11, 12, and 13 using DKHs electrodes with Al_2O_3 (11x12 mm) and Quartz (10x15 mm) insulators of length 7.5 mm, submerged in LN_2. Blue diamond, filled: V_{bd} LN_2 run 11 (electrode separation 2.96 mm, negative polarity); Blue diamond, no fill: V_{bd} LN_2 run 12 (electrode separation 2.96 mm, positive polarity); Red diamond, : V_{bd} LN_2 run 13 (electrode separation 2.96 mm, polarity)

Run 11 was performed at negative polarity with a quartz insulator 10x15 mm in diameter and 7.5 mm in length. The removal of the insert showed that the insulator had completely shattered, however, there was no evidence of tracking present on the surface of the pieces. The damage to the electrode was counted to be 6 on the HV and 8 on ground for 17 events. It should be noted that the electrodes were touching each other once removed. In Hill's (3) thesis, measurements were performed without a spacer present for the DKHs electrodes. This gives a value of ~ 65 kV for the 7.5 mm insulators. In Figure 6.29 the first two breakdowns were at this expected value, however, the voltage clearly dropped off rapidly but recovered. This implies that the damage possibly first occurred here, resulting in reduced breakdown voltages.

Run 12 switched to an alumina insulator but with dimensions 11x12 mm instead and 7.5 mm in length. This run was at positive polarity. Again removal of the insert showed it had completely shattered with pieces on the G10 support structure and bottom of the cryostat. The damage on the electrode was not recorded for this run but there was 16 events. Figure 6.29 shows the data is scattered around ~ 55 kV. The initial two breakdowns are low, and it's possible that this is due to damage from mechanical compression on the insulator. This was checked afterwards, placing the insulator between the two electrodes at room temperature and compressing it between the two DKHs electrodes. It took very little force to cause it to shatter, as alumina is very brittle so with material this thin its unsurprising for this to occur.

Run 13 returned to breakdown measurements with a quartz insulator of the same dimensions as that used in run 11. After the measurements the insulator was found to be broken into multiple pieces. No clear sign of tracking damage was present on the insulator. The craters counted on the electrodes were HV: 25 and Ground: 33, which includes those from the previous run. The electrodes were found to be touching at the end of the run. Figure 6.29 shows a steady drop off of voltage, implying the damage possibly occurred in the first few breakdowns.

In Figure 6.31 the three data point are clearly below the trend line. The quartz and alumina insulators sit at around the same voltage, therefore, the change of material did not make a large difference. The largest of the insulators tested (10x15mm quartz) has a breakdown voltage slightly lower than the other two which may be due to the radial separation influencing the result. The extent of the damage to all the insulators make it difficult to draw many conclusions on these measurements. The cause or when the damage occurred is not clear, though from Figure 6.29 it starts at the expected breakdown voltage and drops off implying subsequent breakdowns could have caused damage resulting in the electrodes snapping together as the insulator structure failed.

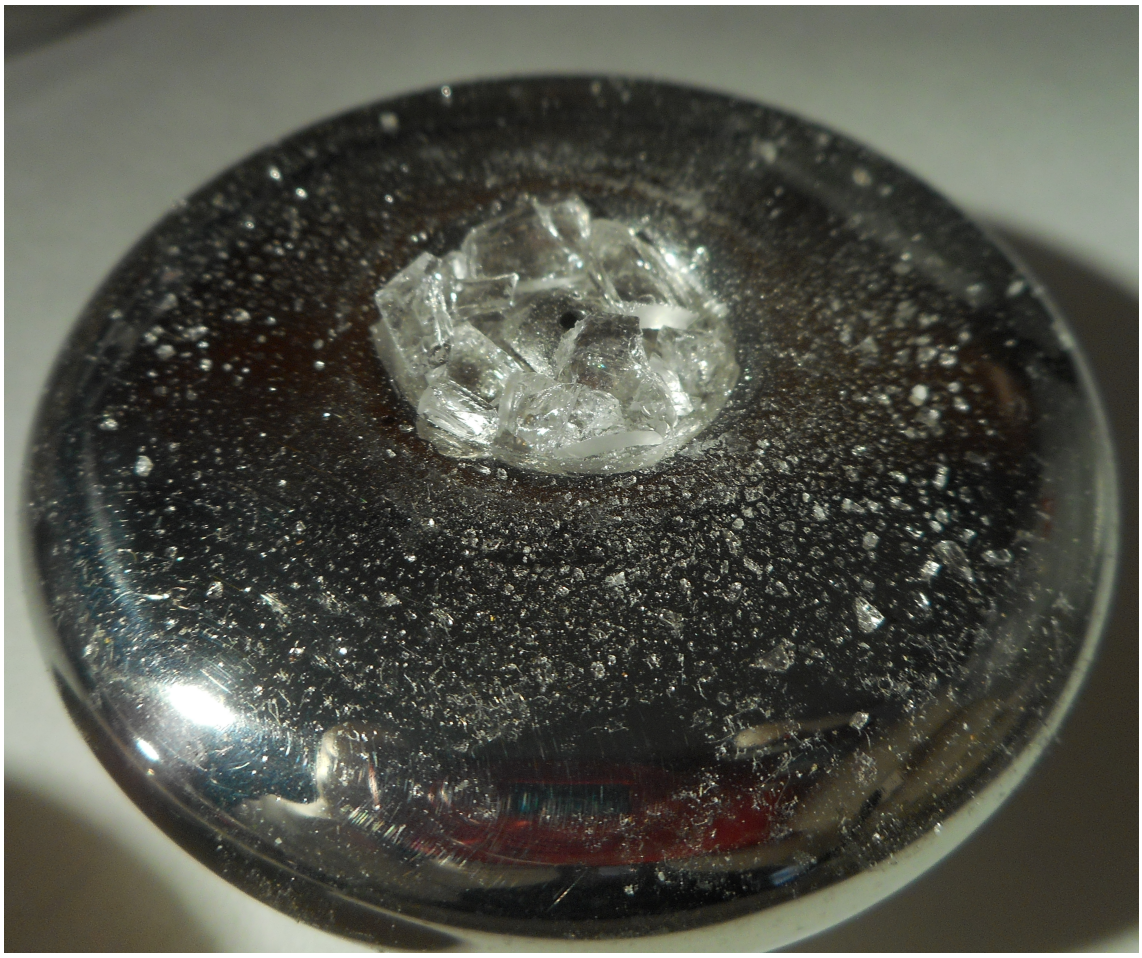

Fig. 6.30 Damage to the 10x15 mm Quartz insulator, from run 13. The insulator had broken into multiple pieces. There were no tracking marks visible on the insulator.

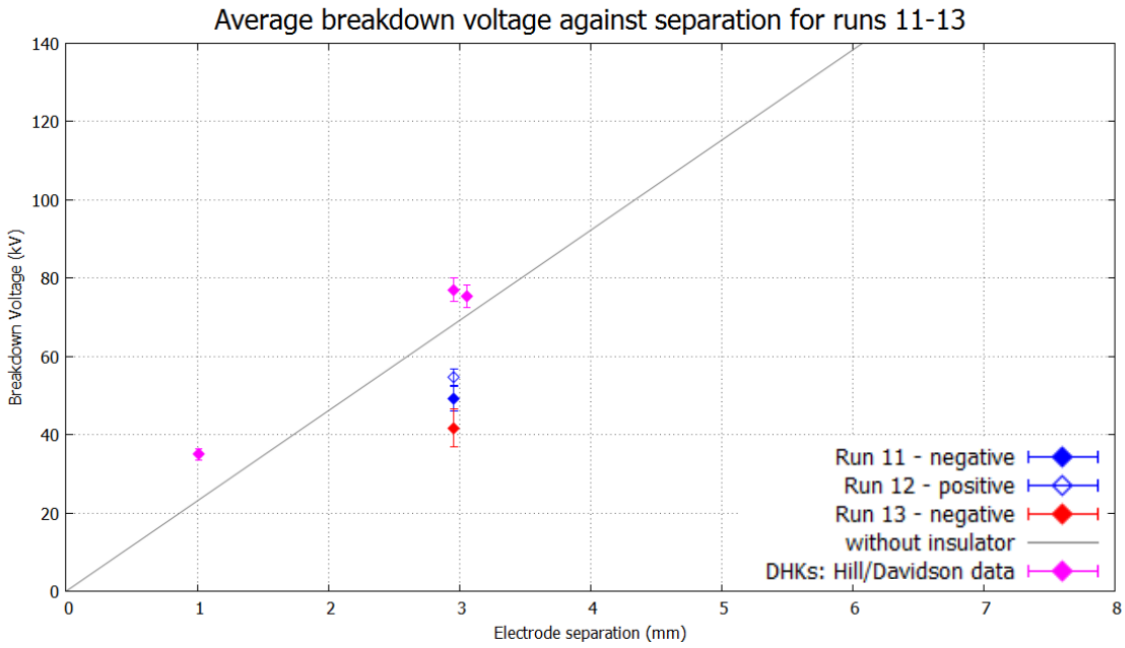

Fig. 6.31 Average breakdown voltage versus separation between DKHs electodes with and without insulators of lengths 7.5 mm made of Quartz 10x15 mm and 11x12 mm Al_2O_3. The standard error on the mean breakdown voltage is shown. Data from LN_2 runs 11, 12, and 13 are compared with data from the spacerless breakdown data for DKHs electrodes given in Hill (3) and Davidsons (2) work. Blue diamond, filled: V_{bd} LN_2 run 11 (electrode separation 2.96 mm, negative polarity); Blue diamond, no fill: V_{bd} LN_2 run 12 (electrode separation 2.96 mm, positive polarity); Red diamond, : V_{bd} LN_2 run 13 (electrode separation 2.96 mm, polarity)

6.4 JT electrodes

Preliminary measurements were performed on the large JT electrode (ϕ 360 mm) in the SV to investigate the effect of increasing electrode separation with an insulator present. These measurements used a borosilicate glass insulator 240x250x50 mm in size. The radial separation is $\Delta r_o \simeq$ 5.52-6.54 mm and $\Delta r_i \simeq$ 0.2-2.15 mm. The geometry of the electrodes is given in Appendix H. The depth of the groove is varied from 24 mm, 23 mm, 22 mm, 21 mm, and 19 mm corresponding to an electrode separation of 2 mm, 4 mm, 6 mm, 8 mm, and 12 mm. The insulator ends were mechanically polished to 1200 grit by hand. Previous measurements using the DKHl electrodes led to damage to the insulator, therefore, one of the primary concerns was to have the insulator survive the breakdown events. The HV system used the same feed from run 30 but with some additions to help centre it and place it in contact with the middle of the HV electrode, details in section 5.4.1. The bottom electrode is grounded via the side vacuum feed. The full apparatus and experimental method is detailed in section 5.2. Measurements were performed in LN_2 with positive polarity applied up to 130kV on the top HV electrode and negative 35 kV on the bottom electrode.

6.4.1 Breakdown runs 31-35

Run 31 was performed at a 6 mm electrode separation with HV applied to the top electrode. This run is the only one in which the insert was not thermally anchored to the 100 K shield. The 100 K shield was not cooled, hence the side feed was potentially providing thermal input to the bottom electrode but also the insert was not as cold as it should be. Before the run, bubbling of the volume could be heard. No partial breakdowns were recorded. The damage to the electrode surface was found to be 10 craters for the HV electrode and 10 on the ground for 13 breakdown events.

This was followed by run 32 at 4 mm separation with HV applied to the top electrode. There was only 2 partial breakdowns recorded. The damage was counted on the surface to be 24 for HV and 23 for ground for 14 breakdown events, which is consistent with the recorded number of breakdowns.

Run 33 was set for 2 mm separation with HV applied to the top electrode. This run there was lots of partial breakdowns, 24 for 39 events. During removal of the electrode stack, it was noticed that the internal surface of one electrode was much closer to the other on one side. Hence, the insulator in which the HV electrode rests was not completely flat; the side with the largest separation was measured as 26.0 mm while the other was 25.2 mm. These measurements were taken between the corona rings. The insulator was then removed and mechanically polished again on one side in order to reduce the deviation.

The deviation was reduced to ~ 25.5 mm separation on one side compared to 25.2 mm on the other side. The damage to the electrodes was counted after the measurements, the HV had 61 sites, and the ground had 64 for 39 breakdowns. It was noticed that normally the craters on the electrode surface are randomly distributed, however, this particular run clearly had most of the breakdowns occur on the side with the shortest separation.

Run 34 was the final run with the top electrode at HV, the separation was 8 mm. There was no partial breakdowns recorded for this run. The damage on the electrode surface was counted to be 76 for HV and 80 for ground for 15 breakdowns.

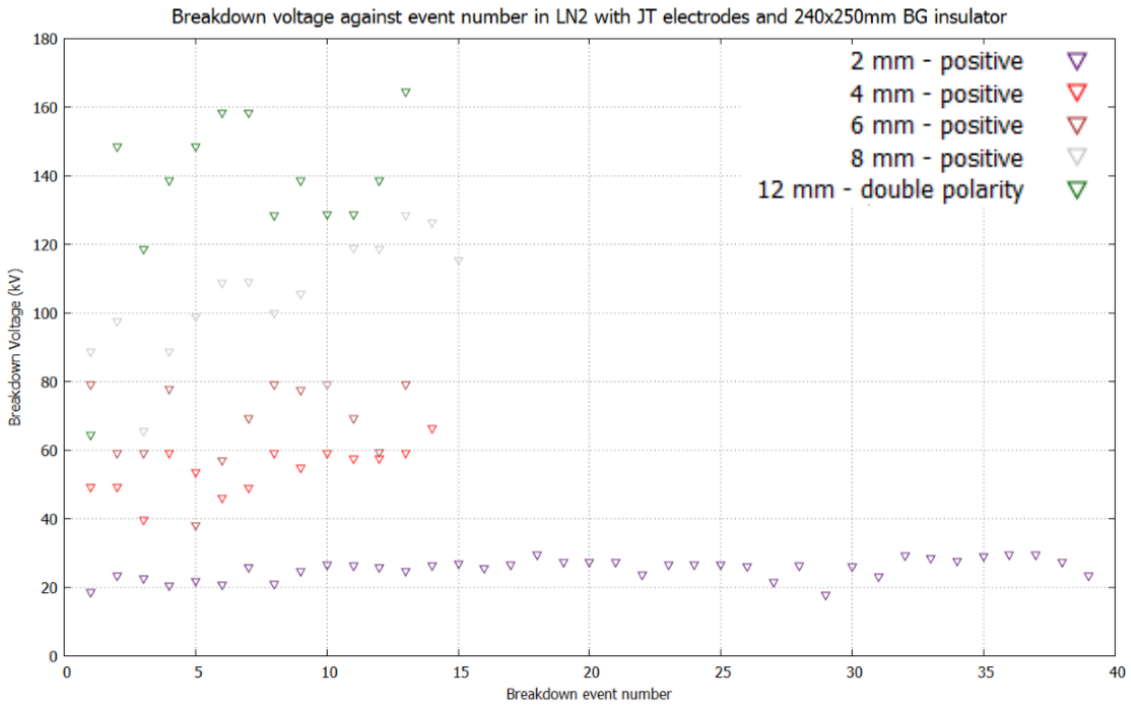

Fig. 6.32 Breakdown voltage versus breakdown event number for runs 31-35 using JT electrodes with BG (240x250 mm) insulators of length 50 mm, submerged in LN_2. Dark red triangle, no fill: V_{bd} LN_2 run 31 (electrode separation 2 mm, positive polarity); Red triangle, no fill: V_{bd} LN_2 run 32 (electrode separation 4 mm, positive polarity); Brown triangle, no fill: V_{bd} LN_2 run 33 (electrode separation 6 mm, positive polarity); Grey triangle, no fill: V_{bd} LN_2 run 34 (electrode separation 8 mm, positive polarity); Dark green triangle, no fill: V_{bd} LN_2 run 35 (electrode separation 12 mm, double polarity).

The large number of breakdowns for 2 mm occurred as partial breakdown where frequent, it is likely that the large number of partial breakdowns at such a low voltage is due to the breakdown mechanism at short electrode separations, bubble crossing the gap much more easily. Alternatively, it could have occurred as the charge on the electrode was never sufficient enough to trigger the full breakdown conditions using such low voltages. Throughout the measurements the HV delivery system operated without any

problems. The insulator also was not damaged throughout this set of measurements.

At this stage it was clear the larger separations would require the side feed to also apply HV to the bottom electrode. Run 35 was performed at 12 mm separation with the top and bottom electrode charged up. However, issues with the side feed started to arise, a large leakage current was present when the voltage was applied ($< 0.5\ \mu$A). This leakage current was persistent throughout the measurement and prevented the system from achieve 40 kV on the bottom electrode. Therefore, to avoid using that feed as much as possible, the top electrode was charged to 130 kV first, before applied voltage to the bottom electrode, which would in some cases breakdown. The run was performed over two days and the volume of LN_2 was topped up three times. Upon removal the insulator was found to be intact. The damage to the HV electrode was 86 and the ground was 89 for 13 events. The first breakdown event for this run was quite low, this was attributed to a condition effect, possibly on the HV feed.

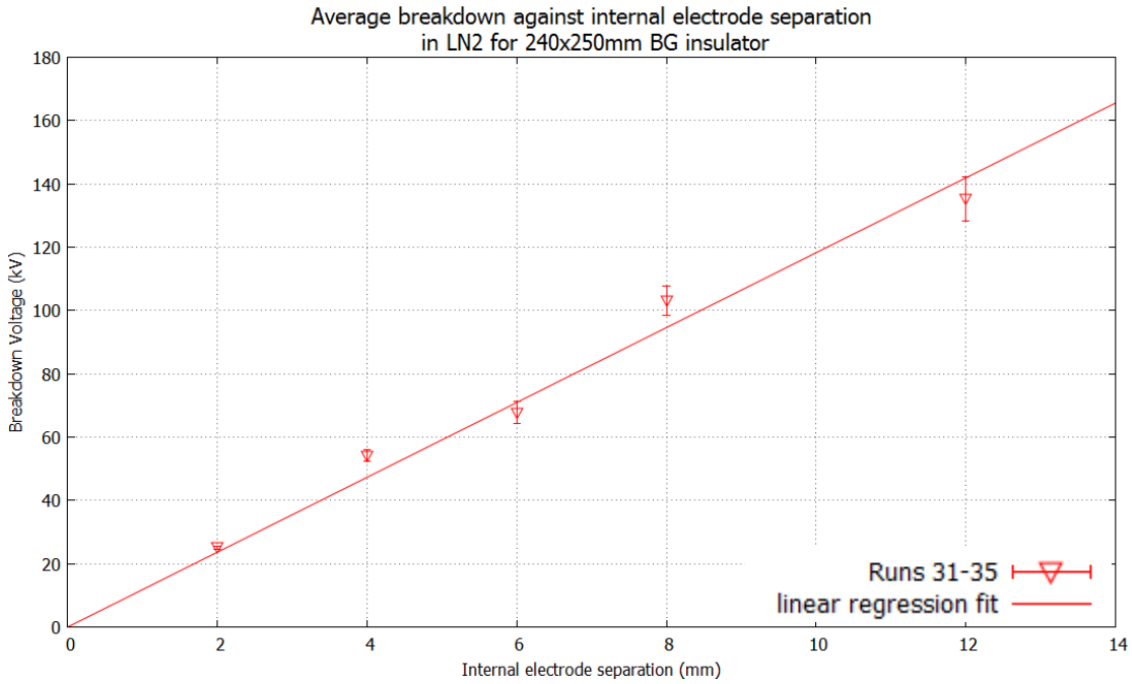

Fig. 6.33 Average breakdown voltage versus separation between JT electodes with 240x250 mm diameter BG insulator of 50 mm in length. The standard error on the mean breakdown voltage is shown. Data from LN_2 runs 31-35 are shown. Red triangles, no fill: V_{bd} LN_2 runs with JT electrodes, single (double for run 35) polarity applied.

Figure 6.33 clearly shows that there is an area effect which is expected from previous data (109). There is also a steady increase in the distribution of the breakdown events, which is attributed to conditioning effect of the system which is what Davidson also found (2).

Run 31 shows that the 6 mm separation run is slightly lower than the overall trend line for the JT electrodes. This is possibly due to it being the first measurement. Even with thorough cleaning of the surfaces, initial conditioning will still be required, after which it will operate as required. That run was also the only one in which the shield was not cooled, possibly resulting in generation of bubbles on the electrode surface which could reduce the breakdown voltage. The deviation in the insulator was present for 2 mm, 4 mm, and 6 mm breakdown measurements which could have affected the overall trend for these breakdowns. The double polarity run is slightly lower then expected which could be because of a drop off in electric field gradient due to volume effect or the mean breakdown voltage is lower due to greater conditioning effects required to achieve that average value.

6.4.2 Breakdown runs 36-38

Switching to LHe volume required a number of cooldowns in order to understand how the cryostat will perform to reach 4.2 K. After successive LHe transfers, improvements were made in order to get LHe inside the SV details of which are given in Appendix E.

A number of breakdowns were performed until the LHe level was too low to continue with more. In total 3 runs where performed with HV applied to both the top and bottom electrode. The HV on both electrodes is applied to attempt to confirm if a breakdown occurs across the cell and not in one of the HV delivery systems. If the discharge occurs across the cell volume, it was found in the LN_2 (run 35) that both Spellman power supplies will respond to this event, shutting themselves off.

Run 36 was performed with 12 mm electrode separation. Breakdowns were observed, however, for the first two the level sensor was left in place, likely reducing the HV performance since it sits close to the electrodes. The level sensor was removed for the subsequent breakdowns.

As detailed in the Appendix E the SV had gone through a number of cooldowns in LN_2 and LHe, therefore, it is quite likely that a lot of contamination was present in the SV for run 36. Interesting behaviour was observed on three of the HV ramps after the level sensor was removed, a partial breakdown occurred which dropped the voltage by $\sim \frac{1}{3}$ but it then recovered back up to the same value. This was quickly followed by a full breakdown. In previous work by Davidson (2) these partial breakdowns are disregarded as conditioning effects but are left in this thesis for completeness. However, they could be some indication of a pre-breakdown event, therefore, more data would be needed to check if they disappeared after the system is conditioned further.

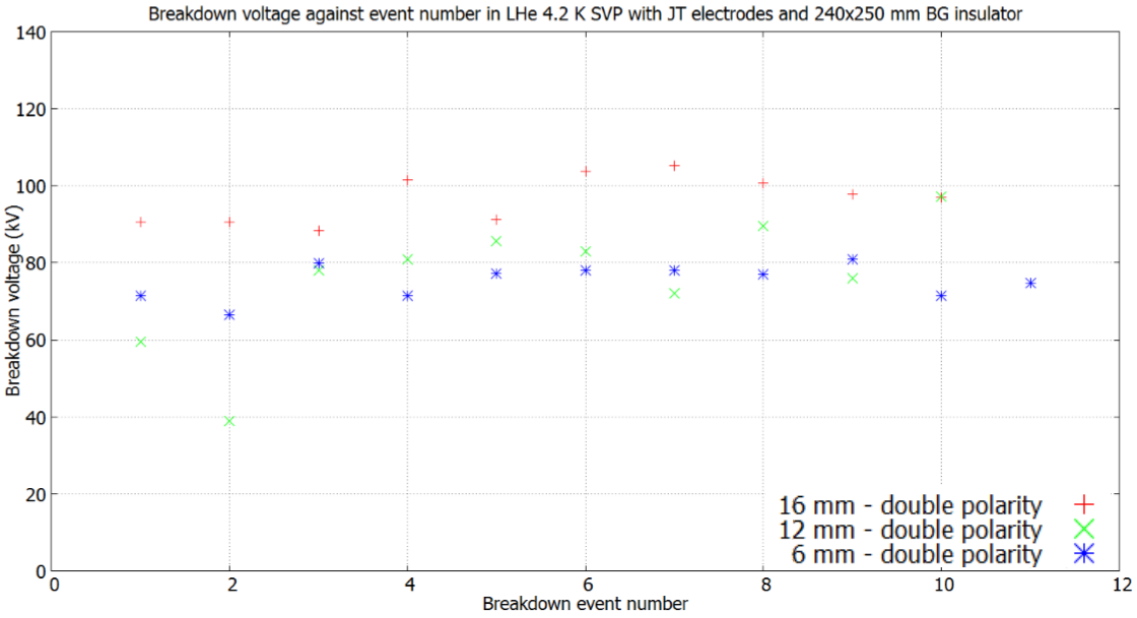

Fig. 6.34 Breakdown voltage versus breakdown event number for runs 36-38 using JT electrodes with BG (240x250 mm) insulators of length 50 mm, submerged in LHe. Red cross: V_{bd} LHe run 36 (electrode separation 12 mm, double polarity); Green cross: V_{bd} LHe run 37 (electrode separation 6 mm, double polarity); Blue star: V_{bd} LHe run 38 (electrode separation 16 mm, double polarity).

Run 37/38 where performed with 6/16 mm electrode separation. At this point running the system was well understood with nothing of note occurring which may affect the results.

Figure 6.34 shows the breakdown voltage in LHe against the number of events. It can be seen that the breakdown voltages all lie close to each other even though the separation is increased.

Chapter 7

Analysis and Discussion

7.1 Introduction

In this chapter, the breakdown data performed in the in the KEK cryostat in LN_2 will be discussed. This includes all the measurements with the DKHl and DKHs electrodes with spacers of different sizes and materials between them. The effect of the presence of an insulator between the electrodes will be discussed, as well as cases where the insulator is damaged. The geometry of the groove walls in relation to the insulator surface will be discussed. Cratering to the electrodes over the course of all the breakdown measurements will be noted and some conclusions drawn. The data observed in this thesis will be compared and added to Hill's and Davidson's data with the same electrodes and insulator materials. Failures of the HV feed and the progression to fixing this issue will be discussed in the context of how this affected the breakdown data.

Following on from the KEK data, measurements performed with the Blue Elbow cryostat for the larger JT electrodes with a borosilicate glass insulator separating them in LN_2 will be discussed. The surface area effect will be demonstrated with a comparison to the KEK measurements and past data discussed in Section 4.2.7. The breakdown measurements in LHe will also be discussed here with comparison to Ito (64), Davidson (2), and Hill (3) measurements.

The final section will suggest the mechanisms that are occurring to cause damage to the insulator surface and the factors that are limiting the breakdown voltage of the system in LN_2 and in LHe.

The results of these measurements performed in LN_2 show that the damage observed on Al_2O_3 insulators can be avoided by replacing them with BG ones instead. It is thought that this occurs due to the high dielectric constant of the material which enhances

the electric fields near the CTJ region. If damage would occur to the Al_2O_3 insulators then a slight drop in average breakdown voltage on one polarity is seen in some cases but not every time, therefore, it is hard to conclude the presence of the insulator is limiting the breakdown voltage. However, the BG insulators did not observe a discrepancy with polarity and the average breakdown voltage generally was consistent with breakdown data without the insulator present. This lead to measurements in LN_2 with much larger JT electrodes. The breakdowns in this case follow a very linear behaviour for increasing electrode separation, however, the gradient is lower then that observed on the DKHl electrodes indicating a surface area effect is present. After LN_2 runs had been performed, breakdown measurements where done in LHe at 4.2 K SVP. Only 3 runs at different separations could be performed. These results showed a very sharp drop off of average breakdown voltage as the electrode separation increased from 6 mm to 16 mm, indicating a non-linear effect. The cause of such behaviour could be due to electrode geometry, spacer plates creating a high field region next to the insulator, or LHe is unable to hold such a voltage at larger separations. In order to determine which of these two options are the cause, more measurements would be required.

The breakdown values are known to be generally linear for "small" separations, however, at some point volume effects will lead to nonlinear behaviour (109). The data presented here seems to follows a linear breakdown vs separation dependence for the separations used, and so linear regression fits will be employed to compare results. The intercept is forced through zero as it would be expected that at a separation of zero there will not be any voltage applied (completes the circuit). However, the behaviour of the breakdown voltage at separations < 2 mm may be non-linear depending on the breakdown mechanisms in small gaps. For the case of this analysis, it won't be taken into account as we are only interested in behaviour at large separations.

The error on the gradients in this analysis is determined by using a linear regression fit and calculating the standard error for that slope using:

$$\sigma_m = \sqrt{\frac{1}{N-1}\Sigma(y_i - \hat{y}_i)^2 \times \frac{N}{\Sigma(x_i - x)^2}}, \tag{7.1}$$

where N is the sample number, y_i is the breakdown voltage, and x_i is the electrode separation. This error does not represent the actual statistical error of the breakdown voltages gradients but instead is an additional representation of the spread of the breakdown values.

7.2 Analysis of the KEK measurements

This section will discuss the effect of an insulator present between the DKHl electrodes in LN_2. The purpose of these measurements was to investigate if the presence of a high dielectric strength insulator as an effect on the breakdown voltage. It was observed that a number of breakdown runs occurred which caused damage to the insulator surface, however, this was not always repeatable. The simulations performed in Section 5.5 indicated that the use of a lower dielectric constant material would lower local field enhancement at the insulator to groove wall region which could be the reason for damage occurring along the alumina insulators. This is compared to the borosilicate glass measurements to see if the material change makes any significant change to the damage mechanism or breakdown voltage.

7.2.1 Al_2O_3 60x70 mm insulator measurements

For all these measurements the data is compared to the breakdown measurements performed by Hill (3) and Davidson (2) for the DKHl electrodes but without an insulator present. Those previous measurements were limited to breakdowns up to 4.5 mm separation, while some of the data presented in this thesis is up to 7 mm separation. It is assumed with the spacerless data that a linear fit is a good representation so this is extrapolated out to larger separations. Some justification for this being the case, can be found from the JT electrode measurements in which the breakdowns are compared to the spacerless data for DKHl and DKHs. The JT electrode data shows that up to 12 mm separations, the data is fairly linear despite the larger surface area. Intuitively if the breakdown measurements started to follow a non-linear behaviour, i.e. start saturating at a given voltage, then this would occur sooner on the larger electrodes due to the greater volume effect present.

The general form for breakdown measurements versus separation is expected to be linear, therefore, if the insulator was to limit the breakdown voltage then it would be expected that the gradient of the linear fit for that data will be reduced compared to that without an insulator.

Figure 7.1 presents all breakdown measurements performed with 60x70 mm insulators, which for completeness includes runs in which there were failures of the HV feed or where the insulator became damaged. It should also be stated that the electrodes were polished at various intervals as well, detailed in Chapter 6. It can be seen that most of the data points lie below the spacerless trend line. The set of runs at 5 mm show a large range in values with non-overlapping error bars. There are also some extreme data points at 4 and 7 mm. This implies that some other effect is varying the

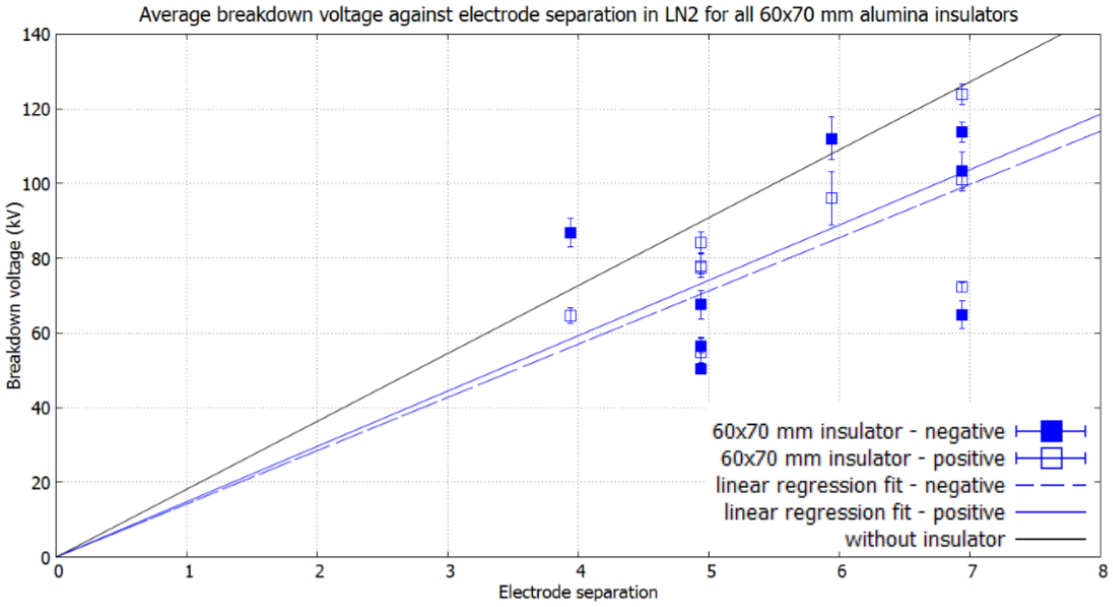

Fig. 7.1 Average breakdown voltage versus separation between DKHl electrodes with and without 60x70 mm Al_2O_3 insulators of various lengths. The standard error on the mean breakdown voltage is shown. Data shows all 60x70 mm insulator runs in LN_2 and is compared with data from the spacerless breakdown data for DKHl electrodes given in Hill (3) and Davidson's (2) work. Blue squares: V_{bd} LN2 (negative filled and positive not filled); Blue line (dashed) is a linear regression fit to all negative for the 60x70 mm breakdown data with the intercept set to zero, giving gradient of 14.25 ± 1.40; Blue line (solid) is a linear regression fit to all positive for the 60x70 mm breakdown data with the intercept set to zero, giving a gradient of 14.82 ± 0.92 kV/mm; Black trend line with gradient of: 18.17 ± 0.37 kV/mm, is spacerless breakdown data with DKHl electrodes in LN_2.

breakdown voltage between runs, one example being the issues with HV feed failures and insulator damage. It should also be stated that the position of the insulator in the groove is not fixed since the groove is very loose for this insulator size, each run can give a different result due to the nature of the position of the insulator in the groove geometry.

As there were a large number of HV feed failures, cuts needed to be made to the data to remove any runs where this could have limited the voltage, and in order to try to guarantee that the included breakdowns only occurred between the electrodes. The indication of a failure is normally due to a high leakage current on the power supply or being unable to charge up to the requested voltage, so any measurements in which the feed was discovered to be broken at the end of the run, or if the leakage current was too high (>1 μA) during a measurement then those data points will be cut. The problem runs can also be identified by large number of partial breakdowns, the presence of any tracking mark on the feed or insulator seems to make partial breakdowns occur more frequently. For the purpose of comparison the cuts still leave some data that contain breakdowns in which the insulator was shattered or had tracking damage.

The data cuts shown in Figure 7.2, have removed many of the more extreme values relative to the trendline. In order to further scrutinise the results, the two polarities were separated for analysis. The negative polarity tend to deviate from positive significantly in general, with two data point that are a number of error bars above the trend line and two negative data points that lie significantly below the trend line. It is not clear experimentally what caused this to occur. Interestingly, the 5.94 mm separation breakdown run which is above the trend line was the only run in which the insulator broke. This particular insulator was from the run were it shattered into three pieces with discharge marks through the breaking point. It is odd that this is higher as this would have contaminated in the liquid volume, leading to a decrease in the breakdown voltage and also generation of a conductive track on the insulator. This could explain why there was so many partial breakdowns for this run. The breakdown voltage is also higher than the positive polarity points, perhaps implying a polarity dependence but there is not enough data to draw a firm conclusion on this. It also could be argued that there was another variable in the system which caused such deviation from the expected trend lines, for example the position of the insulator in the groove.

The positive polarity data points all seem to lie on the same trend line.

It is difficult to draw useful conclusions from the 60x70 mm alumina insulator data due to the large variation between the measurements for negative polarity. The biggest experimental variation between each run is the placement of the insulator in the groove

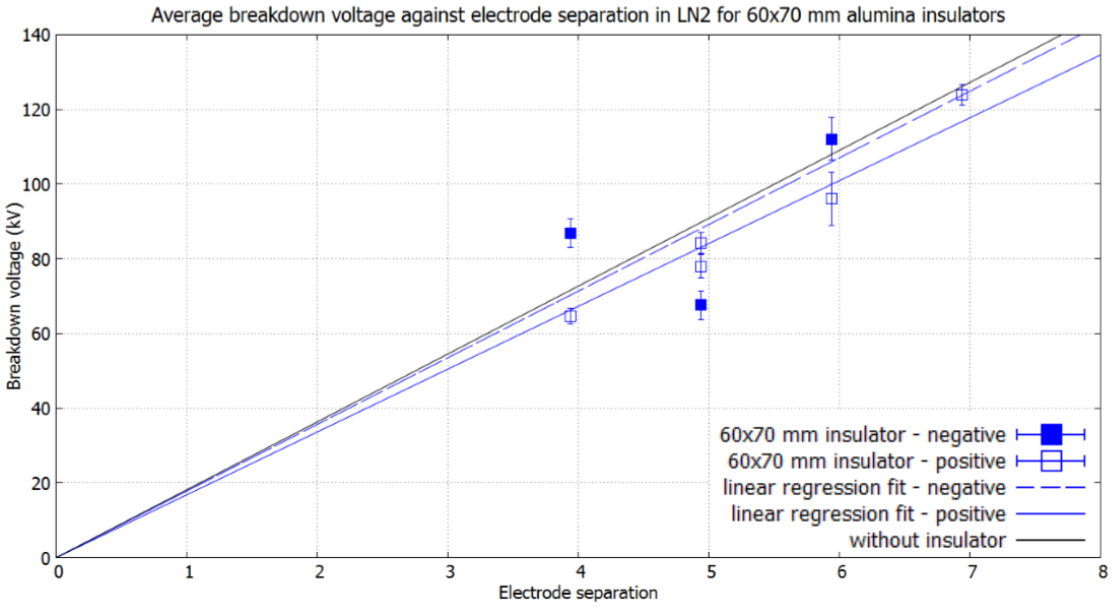

Fig. 7.2 Average breakdown voltage versus separation between DKHl electrodes with and without 60x70 mm Al_2O_3 insulators of various lengths (after cuts made). The standard error on the mean breakdown voltage is shown. Data shows all 60x70 mm insulator runs in LN_2 and is compared with data from the spacerless breakdown data for DKHl electrodes given in Hill (3) and Davidsons (2) work. Blue squares, filled: V_{bd} LN_2 (negative polarity) Blue squares, not filled: V_{bd} LN_2 (positive polarity); Blue line (dashed) is a linear regression fit to the negative data with the intercept set to zero, giving a gradient of 17.84 ± 2.21 kV/mm; Blue line (solid) is the regression line for positive which has a gradient of 16.82 ± 0.40 kV/mm for negative; Black trend line with gradient of: 18.17 ± 0.37 kV/mm, is spacerless breakdown data with DKHl electrodes in LN_2. 7 breakdown runs were removed.

and the electrode condition. If the electrode was too badly damaged then the breakdown voltage could be lower. If the insulator sits too close to the groove edge then, as can be seen from simulations in Section 5.5, there is a local field enhancement which could potentially cause the initiation of the breakdown. This could explain why there is a data point below the trend line, but this is in conflict with the 5.94 mm breakdown which caused the insulator to fail, which we would normally expect to be a much lower value. The amount of partial breakdowns seen in these data sets seems to only occur frequently if a track had formed somewhere in the system (failure of the feed or insulator). This would make sense physically as the conductive track would leak current down it to ground, therefore, when the breakdown occurs that amount of current supplied does not exceed the full breakdown conditions of the power supply.

7.2.2 Al_2O_3 50x60 mm insulator measurements

A few breakdown measurements were also performed on smaller diameter insulators which would fit very tight on to the internal groove of the same DKHl electrode as the previous measurements. The reason for testing with the smaller internal diameter is that the simulations given in Section 5.5 would indicate that the local field enhancement at the groove wall would be more pronounced, and using the smaller insulator can experimentally test if this will affect the breakdown voltage.

In this case the feed failed in one run and the insulator was damaged in two of the runs. The lower breakdown voltage value at 4.94 mm separation was where the HV feed failed, which presumably would have limited the breakdown voltage. The other two runs showed insulator damage, which could explain why their data points are below the trend line. The 4.94 mm breakdown run used positive polarity then negative (see Figure 6.5), so it's unclear at which point the damage would have occurred and whether there is a discrepancy in the result. The 6.94 mm separation breakdown run was all at negative polarity.

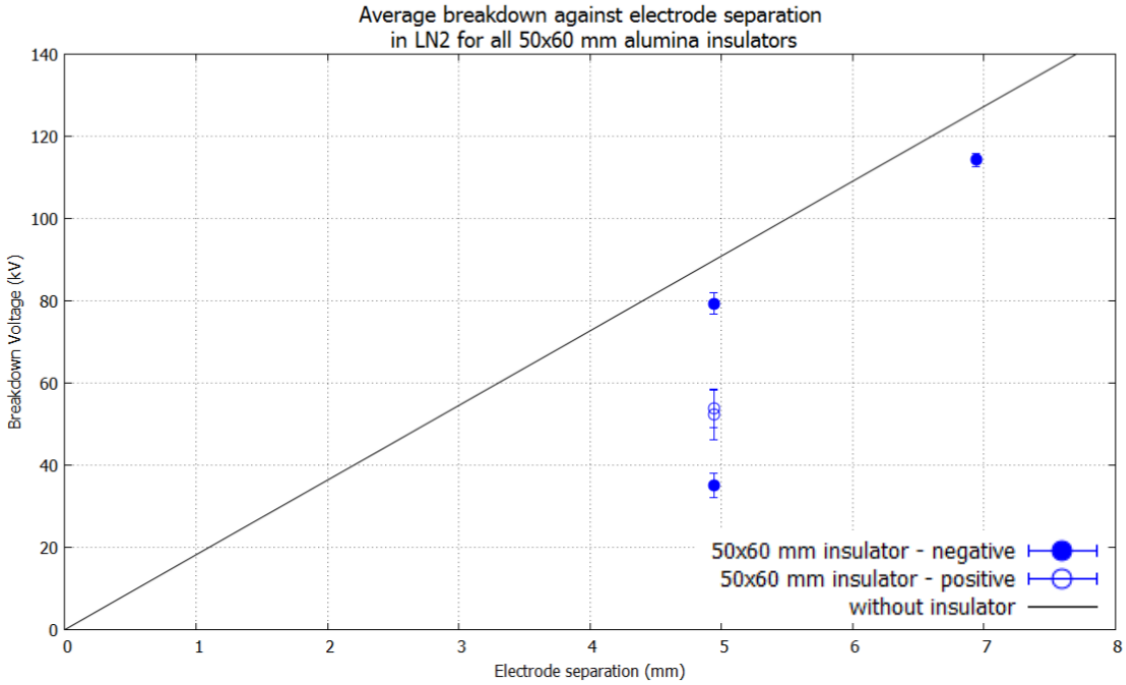

Fig. 7.3 Average breakdown voltage versus separation between DKHl electrodes with and without 50x60 mm Al_2O_3 insulators of various lengths. The standard error on the mean breakdown voltage is shown. Data shows all 50x60 mm insulator runs in LN_2 and is compared with data from the spacerless breakdown data for DKHl electrodes given in Hill (3) and Davidsons (2) work. Blue circle: V_{bd} LN_2 (mix of negative and positive polarity). Black trend line with gradient of: 18.17 ± 0.37 kV/mm, is spacerless breakdown data with DKHl electrodes in LN_2.

There is clearly not enough data points to draw too many conclusions here, however, one can speculate that once the voltage gets to a high enough value then it would cause damage to the insulator, and this seems to limit the voltage compared with the 60x70 mm runs. This hints that the radial separation of the insulator to the wall of the groove will have an effect on the breakdown voltage. On the previous data with the 60x70 mm insulator the radial separation is ~ 3 mm larger than with the 50x60 mm insulators, this seems to cause the damage to occur only on the sides which are closest to the groove wall.

7.2.3 BG 60x70 mm insulator measurements

In Section 5.5 the simulations discussed using different materials with a lower dielectric constant (Al_2O_3: 9.2, BG: 4.6, see Table 5.2 for complete comparison) in order to minimise the local field enhancement at the groove wall to insulator wall region. Therefore, measurements were performed with borosilicate glass in order to determine the effect of changing this value. The insulators used had an issue with chipping at the cut edges, therefore, comparison between the polished and unpolished insulator breakdown data will also be discussed.

The borosilicate glass breakdown data shown in Figure 7.4 clearly has some instances in which there were limitations of some sort, as well as values that exceeded the expected voltage (compared to the spacerless data). There were failures in the ability to deliver HV in a number of breakdown runs as well as run were the feed was not in contact with the electrodes in one incidence. However, compared to the alumina data the borosilicate glass points tend to lie on or above the spacerless data trend line instead of below it. On the other hand, one data point at 5.94 mm is clearly very low compared to the others. There is also variation in the several runs at 4.94 mm separation, implying that something is causing a shift in the breakdown voltage between each run. Again as with the alumina measurements in Section 7.2.1 the insulators are the same dimensions (60x70 mm) giving a few millimeters radial separation on the outside groove edge, which means the insulator cannot be positioned exactly each time a breakdown run is performed.

Data cuts are again applied here to remove the times in which the HV feed failed. After cuts were made, only one measurements had a run with insulator damage (at separation of 5.94 mm). Almost all the insulators used in these runs had chipping occur on them at the their edges. The breakdown measurements at 3.44 mm and 4.94 mm separations with positive polarity were the mechanical polished and flame polished insulators respectively.The data after this cut is applied is shown in Figure 7.5, along with a linear fit (constrained to cross the origin) for the remaining borosilicate glass

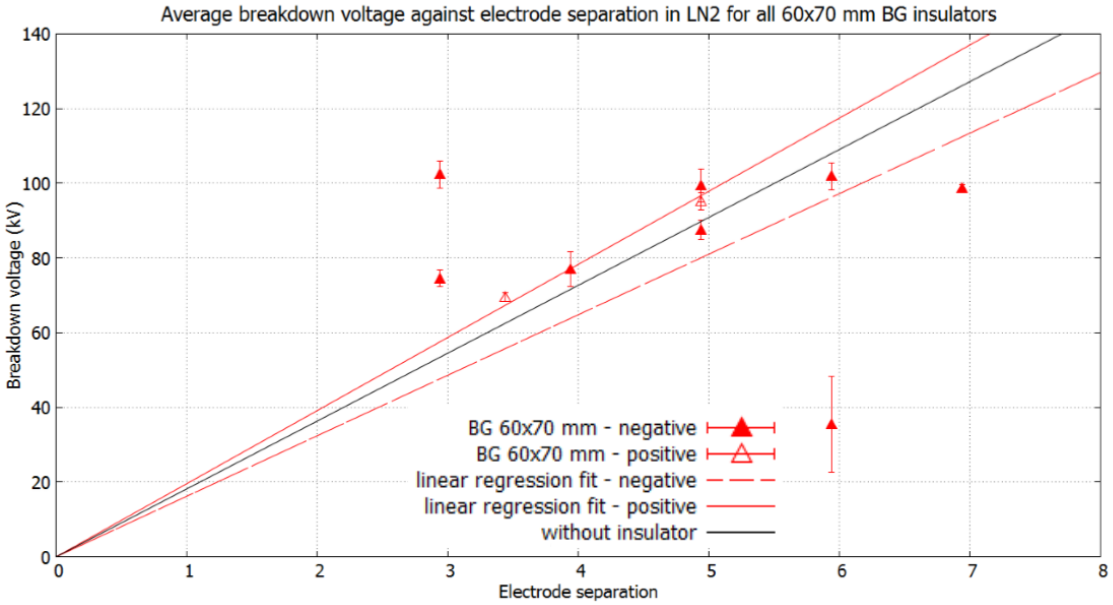

Fig. 7.4 Average breakdown voltage versus separation between DKHl electrodes with and without 60x70 mm BG insulators of various lengths. The standard error on the mean breakdown voltage is shown. Data shows all 60x70 mm insulator runs in LN_2 and is compared with data from the spacerless breakdown data for DKHl electrodes given in Hill (3) and Davidsons (2) work. Red triangles: V_{bd} LN_2 (negative polarity filled and positive polarity not filled); Red line (dashed) is a linear regression fit to the negative data with the intercept set to zero, giving a gradient of 16.20 ± 2.42 kV/mm; Red line (solid) is a linear regression fit to the positive data with the intercept set to zero, giving a gradient of 19.57 ± 0.45 kV/mm; Black trend line with gradient of: 18.17 ± 0.37 kV/mm, is spacerless breakdown data with DKHl electrodes in LN_2.

data.

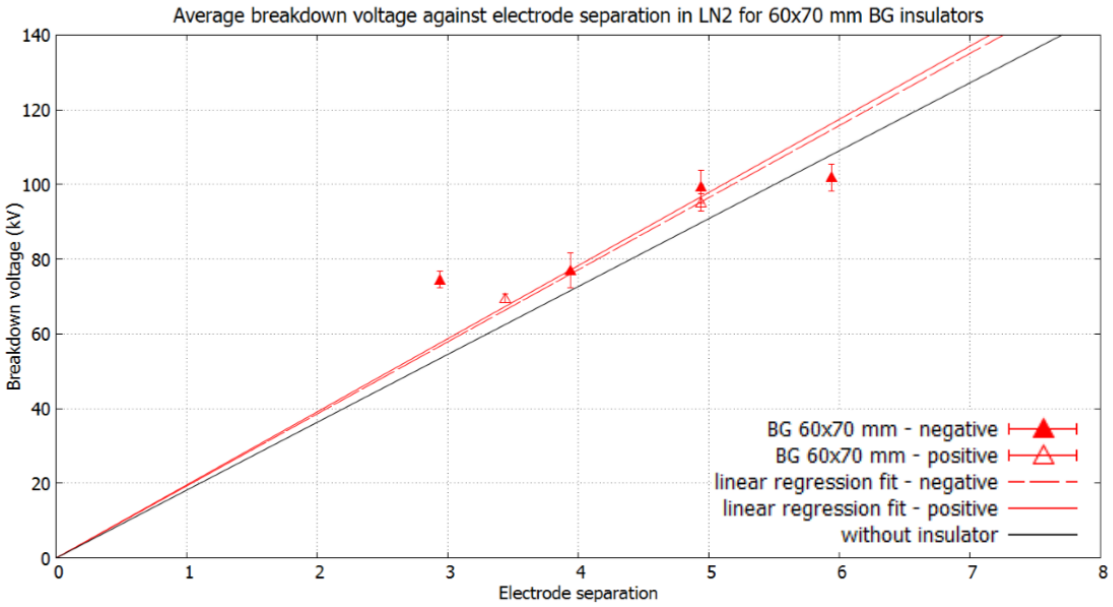

Fig. 7.5 Average breakdown voltage versus separation between DKHl electrodes with and without 60x70 mm BG insulators of various lengths (after cuts made). The standard error on the mean breakdown voltage is shown. Data shows all 60x70 mm insulator runs in LN_2 and is compared with data from the spacerless breakdown data for DKHl electrodes given in Hill (3) and Davidsons (2) work. Red triangles, filled: V_{bd} LN_2 (negative polarity); Red triangles, no fill: V_{bd} LN_2 (positive polarity); Red line (dashed) is a linear regression fit to the negative data with the intercept set to zero, giving a gradient of 19.30 ± 1.40 kV/mm; Red line (solid) is a linear regression fit to the positive data with the intercept set to zero, giving a gradient of 19.57 ± 0.45 kV/mm; Black trend line with gradient of: 18.17 ± 0.37 kV/mm, is spacerless breakdown data with DKHl electrodes in LN_2. 4 breakdown runs removed.

There are two points here of note: the measurements at 2.94 mm and 5.94 mm. The 2.94 mm measurement is significantly above the line even though after the electrode was removed, a large amount of chipping had occurred to the edge of the insulator. This insulator was also rough cut so it was likely that the mechanical compression of the electrodes caused some damage to this surface. It is not clear what caused the higher than expected value at this separation. The 5.94 mm data point was the one which shattered during the experiment, therefore, it would be expected to be below the trend line. It's not clear that the failure of the insulator was due to chipping leading to catastrophic mechanical damage or if the local field enhancement at the groove to insulator wall region was high enough to result in a breakdown that caused the damage. No visual tracking damage was observed on the shattered remains of the insulator. Further breakdown data at 6.94 mm or larger separations would be required to confirm this, as this would presumably lead to larger influence of the insulator compared to bulk breakdown.

The mechanically polished insulator at 3.44 mm is very close to the trend line and the flame polished insulator at 4.94 mm is almost the same as the rough cut edge insulator. An interesting difference here with these values is that the positive polarity is on the same trend line as the negative which for the alumina data this was not the case. From a mechanical view point, the polishing of those insulators only helps to make them mechanically stronger and stop chipping and so does not seem to have affected the breakdown voltage, however, not many data points have been taken to completely justify this.

Interestingly the borosilicate glass data points lie at or above the spacerless data, which indicates that the insulator is not significantly affecting the breakdown voltage for these separations with both polarities. This implies that the CTJ does not seem not to be the limiting factor. All the rough cut measurements resulted in minor to extensive chipping on the insulator edges which does not seem to have dramatically affected the breakdown voltage.

In general the borosilicate glass insulators seem to be equivalent to the spacerless data and only a small improvement over the alumina insulators. Therefore, the dielectric constant of the insulator may not play as large an effect on the breakdown voltage as expected from the simulations.

The gradient in the Al_2O_3 is ~ 16 kV/mm while the BG insulators are ~ 19 kV/mm, compared to ~ 18 kV/mm. The slope of the Al_2O_3 is lower then the other two setups which implies that the insulator is affecting the measurements, by lowering the breakdown voltage. However, it is still difficult to know for sure as the scatter of the data for the negative polarity is causing some dependency. The gradient of the BG is slightly over that of the spacerless data which indicates that the presence of the insulator has not effected the breakdown voltage, which was the goal of these measurements.

7.2.4 Comparison with previous measurements

Hill and Davidson mostly did breakdowns with 10x15 mm insulators using the DKHs electrodes, which will be compared in Figure 7.8, however, they did perform one breakdown run with the DKHl electrodes separated by a 60x70 mm Al_2O_3 alumina insulator which is shown in Figure 7.6.

The extra data point from Davidson's (2) measurements corresponds to a separation of 2.74 mm, and gave a mean breakdown voltage just above spaceless trend line. This is a

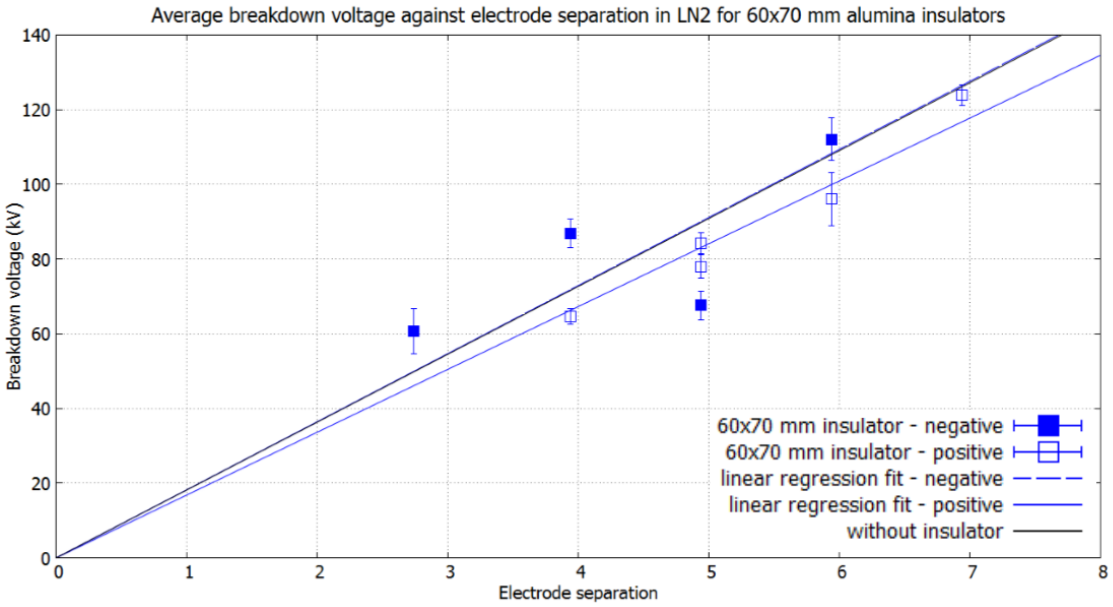

Fig. 7.6 Average breakdown voltage versus separation between DKHl electrodes with and without 60x70 mm Al_2O_3 insulators of various lengths (including measurements by Davidson (2)). The standard error on the mean breakdown voltage is shown. Data shows all 60x70 mm Al_2O_3 insulator runs in LN_2 and is compared with data from the spacerless breakdown data for DKHl electrodes given in Hill (3) and Davidsons (2) work. Blue squares, filled: V_{bd} LN_2 (negative polarity) Blue squares, not filled: V_{bd} LN_2 (positive polarity); Blue line (dashed) is linear regression fit to the data with intercept set to zero, gradient for negative values is 18.23 ± 1.86 kV/mm; Blue line (solid) is linear regression fit to the data with intercept set to zero, gradient for positive values is 16.82 ± 0.40 kV/mm; Black trend line with gradient of: 18.17 ± 0.37 kV/mm, is spacerless breakdown data with DKHl electrodes in LN_2.

negative polarity breakdown result, which adds to the justification that something was limiting the achievable voltage for the 4.94 mm negative polarity runs. It also implies that potentially there is still some polarity effect, particularly for the alumina insulators. The negative polarity breakdown alumina data is similar to the borosilicate glass insulator data. The error on the gradient is much larger for the negative then the positive. This is due to the two data points which lie underneath the spacerless trend line. The implication is that something during this run had possibly limited these values, the only possible cause was the poor condition of the electrode during these runs.

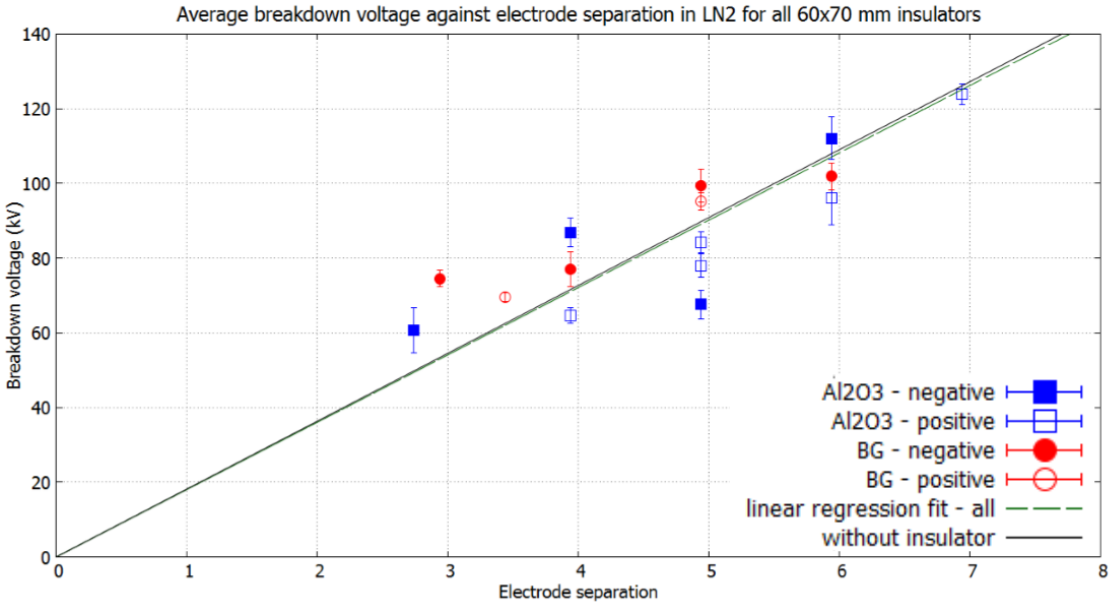

Fig. 7.7 Average breakdown voltage versus separation between DKHl electrodes with and without 60x70 mm Al_2O_3 and BG insulators of various lengths (including measurements by Davidson (2)). The standard error on the mean breakdown voltage is shown. Data shows all 60x70 mm insulator runs in LN_2 and is compared with data from the spacerless breakdown data for DKHl electrodes given in Hill (3) and Davidsons (2) work. Blue squares, filled: V_{bd} LN_2 (negative polarity) Blue squares, not filled: V_{bd} LN_2 (positive polarity); Red triangles, filled: V_{bd} LN_2 (negative polarity); Red triangles, no fill: V_{bd} LN_2 (positive polarity); Green line is linear regression fit to all 60x70 mm data points, intercept set to zero and gradient of 18.03 ± 0.62 kV/mm; Black trend line with gradient of: 18.17 ± 0.37 kV/mm, is spacerless breakdown data with DKHl electrodes in LN_2.

In general the scattering of the data tends to be randomly around the spacerless trendline, which can be seen in Figure 7.7. There is a variation in data above and below the trend line which is comparable to the data for individual breakdown events. As previously noted, the plotted error bars should not be taken in terms of statistical significance, but as a measure of scatter of the individual breakdown events during a run. Interestingly the scatter in values tends to get bigger at the larger separations, maybe hinting that the spread of breakdowns at these separations is much larger. The could

be due to conditioning effects generating smaller breakdown voltage compared to the mean voltage. However, it could be due to a greater occurrence of damage to the insulator at these separations. There are not enough data points present on the low and high ends of the separation values to determine if the data is tending away from linearity.

7.2.5 Al_2O_3/Quartz 11x12 mm & 10x15 mm insulator measurements

These measurements were problematic as the insulator shattered for every measurement performed. It is not clear if this was due to the mechanical stress for the 10x15 mm quartz. However, for the thin wall alumina insulator this was definitely the case over the multiple times they broke once loaded into the electrodes. Nonetheless, these new measurements will be compared to the spacerless measurements and the alumina insulator measurements that Hill (3) and Davidson (2) took.

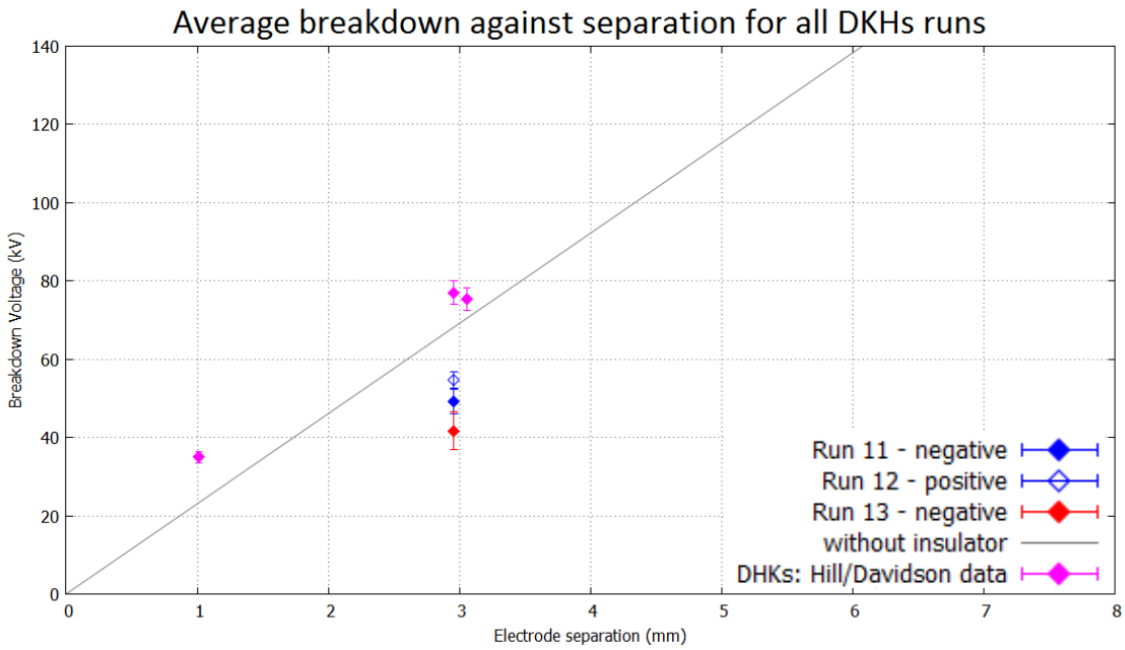

Fig. 7.8 Average breakdown voltage versus separation between DKHs electrodes with and without insulators of various lengths (including measurements by Davidson (2) and Hill (3)). The standard error on the mean breakdown voltage is shown. Orange diamond: V_{bd} LN2 (negative and positive polarity); Purple diamond: V_{bd} LN_2 (Davidson and Hill measurements with insulators); Grey trend line is spacerless breakdown data with gradient 23.04 ~ 1.74 kV/mm for DKHs electrodes in LN_2.

Hill's data tends to fit around the spacerless data points despite the damage that occurred to the insulators during the experiment, as seen in Figure 7.8. A reduction in average breakdown voltage with damage to the insulator was not observed, however, in the measurements performed with the quartz and thin walled alumina it results in a reduced breakdown voltage, giving results that tend to be much lower than the expected.

It is probably unsurprising that this would be the case given that the insulator was in pieces upon removal, likely leading the electrodes to end up with a very small separation afterwards. There would also be lots of particulates in the liquid volume possibly decrease the breakdown voltage. The quartz 10x15 mm insulator (more trustworthy as they were sturdier under mechanical compression) run seems to indicate that this is the case as the first breakdowns occurs on the trend line but steadily drops off more and more until the electrodes could not be charged as the two were in contact. The cause of the damage to the quartz could occur from the chipping on the edges of the insulator in the same manner as the larger borosilicate glass insulators. However, there were not enough measurements performed here to provide any additional information.

7.2.6 Further analysis on HV feed failure data

In this section we will look at the data in the runs which were excluded due to HV feed failures. In the data presented it is hinted that despite damage to the HV feed, the breakdown could have still occurred between the parallel faces of the electrodes. A large amount of data, which was cut previously, mostly contains partial breakdowns. This was generally attributed to HV feed failures, but there are some full breakdowns hinted between the partial breakdown data points. Therefore, for this section further analysis will be performed to look more closely at the problem runs.

In this case data will be classified in three categories: highest quality (A), mixed quality (B), and unusable (C). The highest quality data is where the HV feed was undamaged after the measurement. Mixed quality is where HV feed failed during the run but some full breakdowns occurred at fields that would be expected for this separation; partial breakdowns will be classified as conditioning effects so not counted for this category. This is done to eliminate any breakdowns due to the HV feed which could shift the mean breakdown voltage. Poor quality is where the data is almost all partial breakdowns at fields lower than expected.

The runs in which the HV feed was damage were the following: 3, 4, 5, 8, 9, 10, 20, 23, 24. Every other run is considered class A data.

Figure 6.2 for run 3 shows that the first data point is at 100 kV with the following data all well below on both polarities. This is quite a large separation insulator, 18 mm in length, therefore, fields of the order of 100 kV would be expected. The data points after the first breakdown do contain some full breakdowns towards the end of the negative polarity application but they generally lie below the first breakdown voltage. After switching to positive polarity there are only partial breakdowns, on average at 70 kV. Therefore this

run will be classed as class C data.

Run 4 indicates an initial conditioning effect due to the first 5 breakdowns. However, it takes 13 further breakdowns to get to 120 kV, with only 5 of the 18 total being full breakdowns. The consistency of the breakdowns at 100 kV, events 5-10, is not consistent with an extremal process stated by Weber (108). This implies that the breakdown could have been occurring on the HV feed for these data points. Therefore, the positive polarity events for this run will be classed as C. The negative data shows a better picture, with the first three breakdowns low, at 100 kV, but subsequently the values are at the expected breakdown level. Only 2 partial breakdowns are present on the 2nd and 3rd event number of this polarity for this run, the rest are full breakdowns. This will be classed as B data. The final switch to positive polarity gives all full breakdowns which start dropping off, possibly due to the HV feed, but they are not partial breakdowns so are classified as B grade data.

Run 5, shown in Figure 6.5, was designated as an HV feed failure run, however, no partial breakdowns were observed. The start of the run has full breakdowns occurring at very low values which then increase quickly to drop off again and remain low. Therefore, as there is no evidence of partial breakdowns which could mean the HV feed is failing, it will be classified as B. It should be noted that where the feed broke down is on the room temperature side so could represent a different behaviour. The data is still given in Figure 7.3 for comparison.

Run 8, shown in Figure 6.9, starts out with 6 full breakdowns at fields expected for 4.94 mm separation from spacerless data. This is followed by 4 partial breakdowns at lower values, after which it recovered back to similar values previously seen for 4 breakdown events. After this the final two events are very low partial breakdowns, indicating that the HV feed has most probably failed. This will be class as type B.

Run 9 starts out with lower breakdown values already compared to run 8, and with partial breakdowns. There are 20 breakdown events in total with 15 of them being partial breakdown. The values are also all diminished as well. The implication is that the HV feed was limiting the voltage from the beginning, therefore, this will be classified as type C data.

In run 10, the highest breakdown occurs at the start ~ 70 kV but then the following values are all 45-50 kV and mostly partial breakdowns. The total number of partial breakdowns is 11 of 15 events, which indicates that the HV feed was probably the limiting cause. Therefore, this will be classified as type C. Afterwards the polarity was switched

from negative to positive. This seems to make a significant difference as the number of partial breakdowns (3/13) decreased and the breakdown voltages increased to values expected with this separation, 4.94 mm. Therefore, this will be classified as B data.

In run 20, shown in Figure 6.18, only one full breakdown occurred which even though was at a very high value ~ 100 kV, this clearly was on the HV feed as it was unable to charge up the electrodes after this event. Therefore, this will be classed as C data.

Run 23, shown in Figure 6.20, starts with just partial breakdowns for 7/11 events. The values of these breakdowns vary but they tend to be lower than the expected field for this separation of ~ 124 kV; they can be attributed to conditioning of the damaged HV feed. The final 4 events are all full breakdowns and are close to the expected breakdown value, therefore, this will be classified as type B.

In run 24, shown in Figure 6.22, the breakdown events start with fairly consistent full breakdowns with high values, and only two partial breakdowns at event number 1 and 3. After event number 7 there are only partial breakdowns of increasingly lower voltage values until the final event which is a full breakdown. Therefore, after run 7 it could be inferred that the HV feed failed hence the partial breakdowns that followed. This will be classified as type B data.

The category A and B data is plotted for Al_2O_3 in Figure 7.9. The data in run 5 is omitted as this is discussed in Figure 7.3. Comparing this to the data presented in Figure 7.6, shows that the 18 mm insulators are all lower then the spacerless trendline. The explanation for this is that these breakdown voltages represent conditioning of the setup; as previously stated, the maximum field with the power supplies is achieved frequently in this geometry, therefore, the mean breakdown field will be higher. The inclusion of the measurements at 18 mm bring the gradient down below the spacerless data, 16.90 ± 1.19 kV/mm. This data is still viable as it gives the lower bounds to breakdowns on that separation.

The positive polarity measurements for the category A with B data all lie on the linear regression fit giving a breakdown field of 16.25 ± 0.47 kV/mm, this is comparable to before adding these runs (16.82 ± 0.40 kV/mm). Therefore, this data is good and shows that the despite the HV feed failures usable breakdown data was still generated.

With the BG insulator, only one run had a HV feed failure, run 24. This has been added to the plot shown previously in Figure 7.5, and now given in Figure 7.10. The additional data point on the negative polarity lies in the same place as the previous 16 mm BG

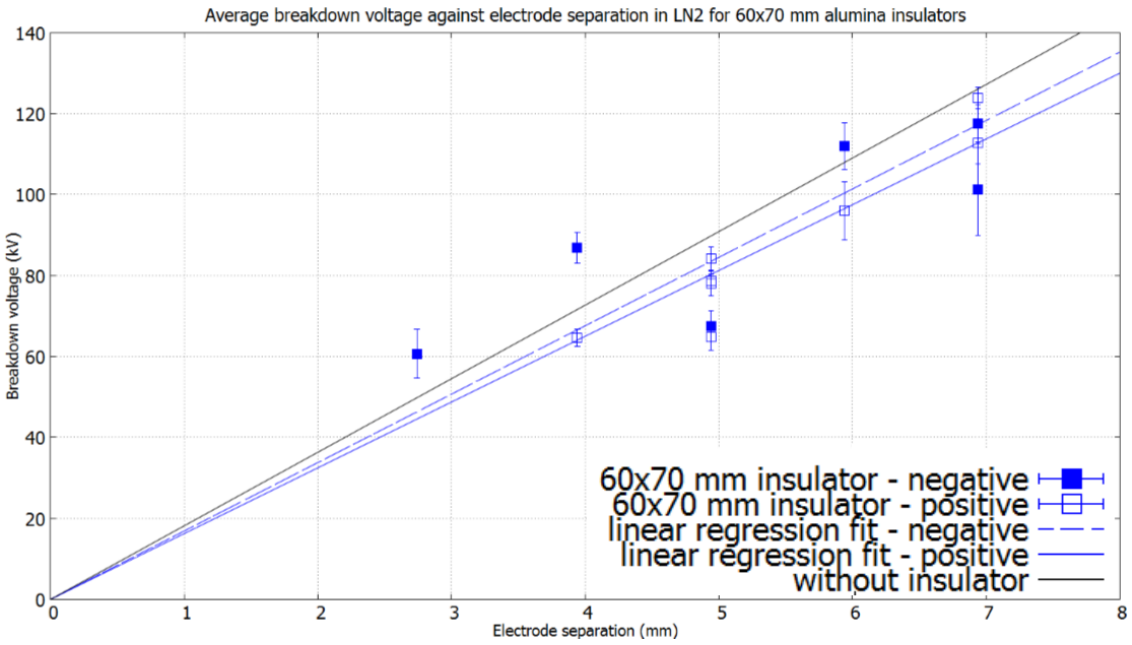

Fig. 7.9 Average breakdown voltage versus separation between DKHl electrodes with and without 60x70 mm Al_2O_3 insulators of various lengths (including measurements by Davidson (2) and category B runs, category C data cut). The standard error on the mean breakdown voltage is shown. Data shows 60x70 mm Al_2O_3 insulator runs in LN_2 and is compared with data from the spacerless breakdown data for DKHl electrodes given in Hill (3) and Davidsons (2) work. Blue squares, filled: V_{bd} LN_2 (negative polarity) Blue squares, not filled: V_{bd} LN_2 (positive polarity); Blue line (dashed) is linear regression fit to the data with intercept set to zero, gradient for negative values is 16.90 ± 1.19 kV/mm; Blue line (solid) is linear regression fit to the data with intercept set to zero, gradient for positive values is 16.25 ± 0.47 kV/mm; Black trend line with gradient of: 18.17 ± 0.37 kV/mm, is spacerless breakdown data with DKHl electrodes in LN_2.

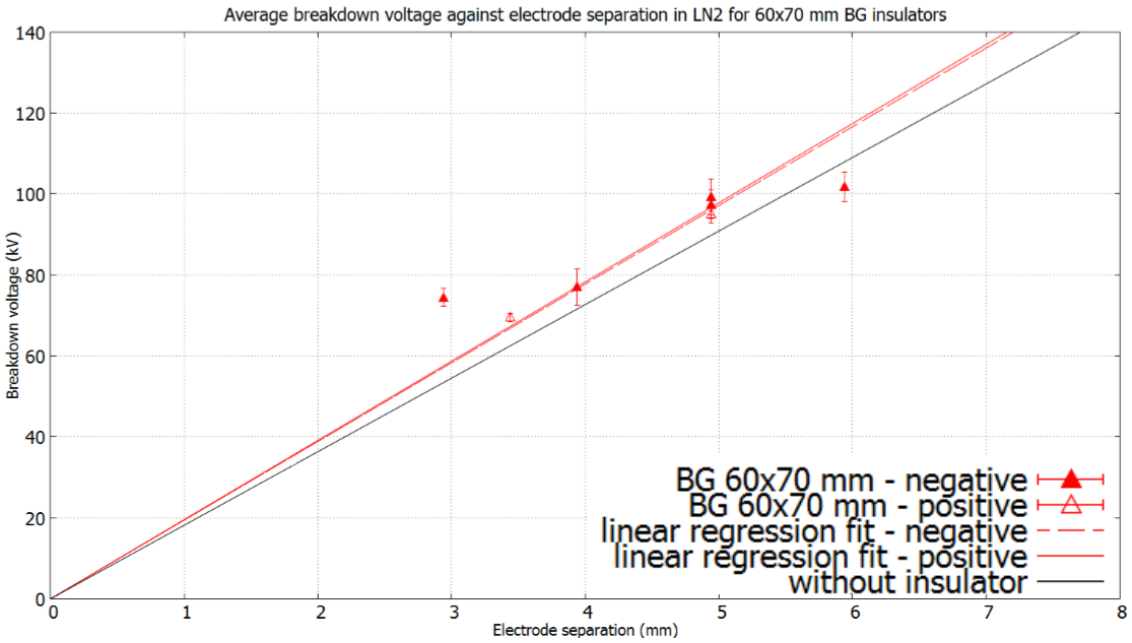

Fig. 7.10 Average breakdown voltage versus separation between DKHl electrodes with and without 60x70 mm BG insulators of various lengths (after cuts made and run 24 added). The standard error on the mean breakdown voltage is shown. Data shows all 60x70 mm insulator runs in LN_2 and is compared with data from the spacerless breakdown data for DKHl electrodes given in Hill (3) and Davidsons (2) work. Red triangles, filled: V_{bd} LN_2 (negative polarity); Red triangles, no fill: V_{bd} LN_2 (positive polarity); Red line (dashed) is a linear regression fit to the negative data with the intercept set to zero, giving a gradient of 19.44 ± 1.08 kV/mm; Red line (solid) is a linear regression fit to the positive data with the intercept set to zero, giving a gradient of 19.57 ± 0.45 kV/mm; Black trend line with gradient of: 18.17 ± 0.37 kV/mm, is spacerless breakdown data with DKHl electrodes in LN_2. Four breakdown runs removed.

insulator measurement, showing that with run 24 prior to the many partial breakdowns, the data was of reasonable quality and most likely broke down between the electrodes. The gradient has changed to 19.44 ± 1.08 kV/mm, compared to 19.30 ± 1.40 previously.

Generally, this analysis shows that while the partial breakdowns observed in the KEK setup are associated with insulator damage or HV feed failures, inclusion of some of the runs of decent quality where this has occurred does not significantly change the final mean breakdown voltage versus electrode separation results compared to fully cutting out the problematic runs. This shows that the breakdown fields measured in this apparatus are reasonably robust given the cuts that have been applied, even if there were minor issues with the HV feed or spacer insulators that escaped notice by inspection.

7.3 Analysis of Blue Elbow measurements

7.3.1 LN_2 measurements

The JT electrodes had a significantly larger surface area compared to the DKHl electrode, a factor of ~ 3 greater. Measurements by Hill and Davidson hinted that the larger surface area would result in a reduced breakdown voltage in LN_2 and LHe. However, this was not quantifiable due to the lack of data points. In these measurements the geometry can be directly compared to the DKHl electrodes with the borosilicate glass insulator present.

No cuts were made to this data set as the HV feed worked without damage occurring and the number of craters correlated to the number of breakdown events. In Figure 7.11 there is a clear indication of a surface area effect, since the JT electrodes show a reduction in breakdown voltage compared to that with the DKHl electrodes. Obviously the breakdown voltage for equivalent separations becomes smaller for the larger JT electrodes compared to the DKHl electrodes, giving a mean breakdown of 100 kV at 8 mm separation for the JT electrodes, but for the DKHl electrodes 100 kV is reached when the separation is ~ 5 mm. The interesting conclusion from this is that the gradient (kV/mm) in the breakdown field is logarithmically proportional to the surface area.

The DKHl electrode breakdown data indicates that the presence of the insulator for these geometries does not reduce the breakdown voltage. Therefore, a comparison can be made with the spacerless data from Hill (3), DKHl breakdown measurements, and JT electrodes to produce a plot to determine the kV/mm gradient versus the surface area of the electrodes. This can then be compared to the equation produced by Hayakawa,

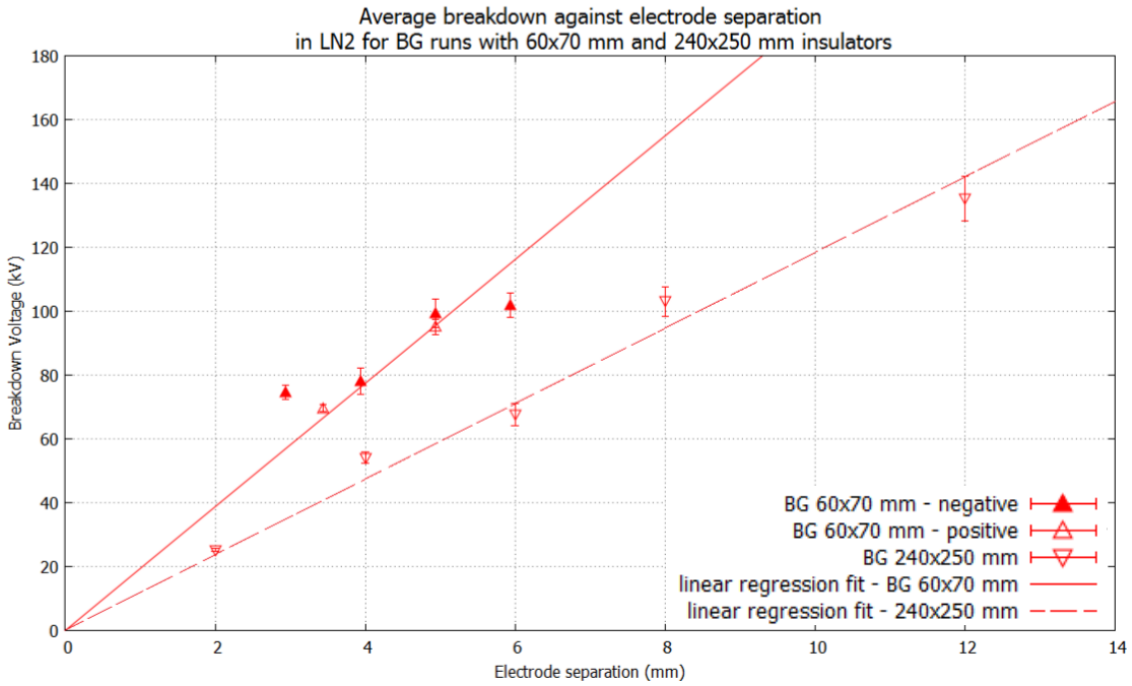

Fig. 7.11 Average breakdown voltage versus separation between JT electrodes with BG insulator 240x250 mm and 60x70 mm measurements. The standard error on the mean breakdown voltage is shown. Data shows 240x250 mm BG insulator measurements in LN_2 and is compared with data from BG 60x70 mm DKHl electrode measurements shown in Figure 7.7. Red triangles: V_{bd} LN_2 (60x70 mm insulators with mix of negative and positive polarity); Red line is linear regression fit to the BG KEK data with intercept set to zero, gradient 19.42 ± 0.92 kV/mm; Dark red triangles: V_{bd} LN_2 (240x250 mm insulators used positive polarity up till 8 mm, 12 mm used double polarity); Dark red line is linear regression fit to the JT electrode data with intercept set to zero giving a gradient of 11.82 ± 0.41 kV/mm.

$E_b = 105 \times SEA^{(-1/6.23)}$, where SEA is stressed electrode area (109). This comparison is shown in Figure 7.12.

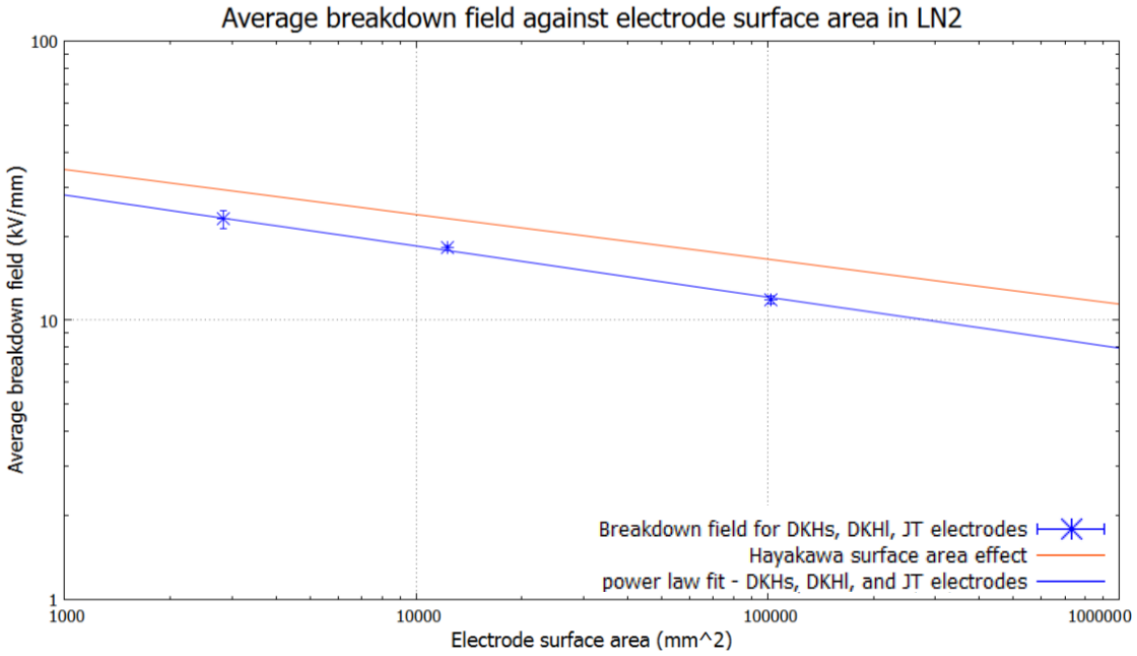

Fig. 7.12 Average breakdown voltage versus electrode area for JT, DKHl, and DKHs runs. The DKHs and DKHl gradients are taken from a linear regression fit from Davidson (2) and Hill (3) spacerless measurements. Blue dots are the various breakdown fields for each electrode data set; Orange line is produced from Hayakawa (109) data for peak breakdown fields $E_b = 105 \times SEA^{(-1/6.23)}$.

The values found for this thesis are comparable to the breakdown voltages at the lowest end on Figure 4.36. The values found here are slightly below what Hayakawa highlights as the trend for the surface area effect, however, his data is for different geometry (sphere to plane and coaxial) and is also based on the peak breakdown field rather than the mean achievable voltage as is measured in this thesis. It should also be noted that the condition of the electrode surfaces for these breakdown measurements was not perfect in each run, however, it seems not to have affected the result in a significant way, indicating that the cratering damage, at least to the extent present on the JT electrodes, did not significantly reduce the breakdown voltage.

One issue with the JT electrode breakdown data is that the larger separations capable with this geometry may extend into a region where a linear fit might not be applicable. At some point volume effects will also play a role and reduce the breakdown voltage resulting in a power law behaviour for larger separations. Hayakawa (109) demonstrated that the volume effect is proportional to $E_b = 83.1 \times SLV^{(-1/7.30)}$, where SLV is the stressed liquid volume. Calculating the breakdown electric field with this equation for the JT

electrodes at the maximum separation measured, 12 mm, would give 17.2 kV/mm. The fields that are found in this thesis are lower than that, implying if the field was to start to become non-linear it would probably be due to some liquid purity effect. It is not clear that this is occurring with JT breakdown data, though the 12 mm breakdown is slightly lower than expected based on a linear trend line. Breakdowns at larger separations would be required to confirm if this is occurring. There is a possibility that the peak voltage will always be much higher then the average breakdown, and that the deviation between these numbers increases with larger surface areas. This could explain why the error bars for the JT electrode measurements is ever increasing with larger separations. This data is generally more consistent than the DKHl data, which is probably due to the lack of insulator damage and no HV feed failures during these measurements.

The KEK data has a large amount of variation in comparison, which could be due to many variables in the system leading to the lower than expected breakdown voltage. These variables could be the electrode condition, insulator condition, and geometry of the setup. The JT electrode breakdown data is quite clean in comparison. In this setup the geometry is completely different in the groove region which has resulted in the breakdowns presumably always occurring across the plane-plane area of the electrodes. If the CTJ is exposed (like with the DKHs and DKHl electrodes) then the high field region could be in the base of the groove which may result in the lower breakdown values. In the case of the JT electrodes the CTJ is in a low field region by being buried in the electrode which could play a critical role in avoiding the breakdown occurring from that region. The shallower DKHl electrode groove could mean that the CTJ is more exposed to higher fields, which could result in larger separations having a slight drop off in breakdown voltage.

The radial separation needs to be consider for both setups for explanation of what is occurring. The KEK measurements had relatively large separations on the outside and inside of the groove to insulator for the 60x70 mm insulators. The breakdown damage to the insulator would also tend to be present around a particular side of the insulator surface, implying that the insulator was not centred, leading to a quite small radial separation on that side. This could explain why the damage on the insulator was not always seen in every run. The 50x60 mm insulators were damaged in every run they were used, which could back up this claim as they were very tight to the inside groove, and thus were very well centred in that setup causing the damage. The damage to the insulators in most cases resulted in a drop in breakdown voltage which would be expected if there is material floating around in the volume or a conductive track formed along the insulator surface. For the most part, the damage was eliminated if borosilicate glass was used instead of alumina. There was one case of a broken borosilicate glass insulator

after a breakdown run, but this very likely occurred due to mechanical compression rather than a breakdown event as it only occurred once. The polishing of the end faces of the borosilicate glass insulators seems to remove the issue of chipping on the insulator edges which may weaken the insulators potentially causing them to shatter. The best polishing method was flame polishing as it completely eliminated the chipping while the mechanical polishing reduced but did not completely remove the chipping issue.

In general this data shows that the breakdown voltage was not limited by the presence of the insulator as the breakdown values (excluding the ones where damage occurred) are within a reasonable spread around the trend line for spacerless measurements. This result is counter intuitive as the CTJ is a known to be the limitation for breakdown in a vacuum medium from the presence of the insulator. The runs in which the breakdown did occur on the insulator cause significant damage and limited the breakdown voltage. However, it was preventable with adjustments to insulator material and preparation resulting in a preference to bulk liquid breakdown in LN_2.

7.3.2 LHe measurements

Presented in Figure 7.13 is the LHe breakdown data in the Blue Elbow cryostat. Measurements were performed with LHe at 4.2 K SVP using variable separation geometry electrodes. Only 3 breakdowns runs were performed. The average breakdown voltages have very shallow slope with gradient of 2.1 kV/mm with intercept of 61.2 kV (represented by the blue line). This seems like a nonphysical result for breakdown voltages as it would be expected at an electrode separation of 0 mm there would be 0 voltage applied. The gradient is also very low for LHe which is different to past data presented in Chapter 4, which implied that values of order >100 kV/cm could be expected. There are two possible explanations for these results: as the separation increases the drop off in electric field is more dramatic than measured previously on smaller separations or the spacer plates are causing a high field region near the insulator which is limiting the achievable field.

The Opera simulations shown in Figure 5.39 indicated that as the spacer plates are added there is a high field region (similar magnitude to the E_0 field) present along the groove profile. This is further enhanced with small radial separations between the insulator wall and the groove wall. In the simulations an ideal situation existed where the insulator would be 0.1 mm away from the groove wall, however, in reality this is not the case. The insulator can be a bit closer on one side than the other as the BG insulator used is not perfectly circular but slightly elliptical. This tight geometry could result in premature breakdown voltages. A good test would be to replace the BG insulator

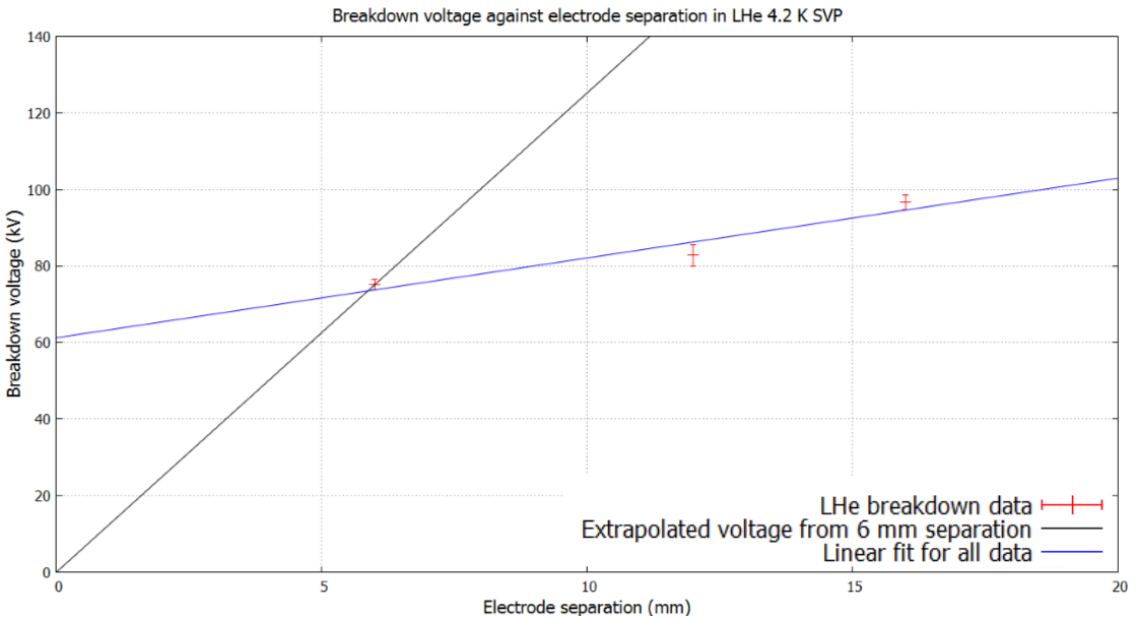

Fig. 7.13 Average breakdown voltage versus separation between JT electrodes with BG insulator 240x250 mm in LHe. The standard error on the mean breakdown voltage is shown. Red crosses: V_{bd} LHe; Black line is linear regression fit through 6 mm data only and intercept forced through zero, gradient 12.52 ± 6.04 kV/mm; Blue line is linear regression fit through all the data with gradient of 2.08 ± 0.60 kV/mm and intercept 61.23 ± 7.19 kV.

with the other available alumina or quartz versions as they have larger internal radial separations which could avoid this potential problem. Another test would be to measure the breakdown voltages at the maximum separation for these electrodes, 26 mm. This would remove the spacer plates and avoid this issue. If the spacer plates are the cause of this lower than expected breakdown voltages then at 26 mm separation over 100 kV should be able to be applied to the electrodes without breakdown occurring.

If the breakdown is occurring between the planes of the electrodes and not due to the spacer plates then this presents a problem for a cryogenic nEDM experiment. Extrapolating using a logarithmic fit to an expected separation for a cryogenic nEDM experiment of 45 mm gives an electric field of 20 kV/cm, which is similar to what's achieved in a room temperature experiments.

The data in Figure 7.13 is also plotted with a black line through one data point and forcing the intercept through zero (gradient of 12.52 kV/mm). The reason for demonstrating this is that if the spacer plates are the limitation then the expected electric fields for a real cryogenic nEDM experiment would be above the 100 kV/cm goal.

Ito (64) achieved 100 kV/cm on ϕ 120 mm electrodes without breakdown being ob-

served at separation of 1 cm, however, with the JT electrodes which are ϕ 360 mm breakdown fields where observed at ~ 70 kV/cm at separation of 1.2 cm. There is strong evidence that a surface area effect will be present, therefore, a result like this could be considered to be expected. If the surface area effect has a similar drop off in LHe as it does in LN_2 then take the ratio of the two gradients shown in Figure 7.11 gives a breakdown field in Ito's cell at 1 cm to occur at ~ 140 kV/cm if we use the blue line in Figure 7.13. The critical measurement that would help inform what is exactly happening here would be when Ito performs the measurements again but at 2 cm. If he is able to achieve 100 kV/cm again without a breakdown event on the same electrode geometry then it would indicate that the spacer plates could be the limitation for the setup presented in this thesis.

7.4 Suggested breakdown mechanisms

7.4.1 LN_2

The data presented in this thesis implies that the breakdowns occur primarily from the electrode surface. This is evident as there is a surface area effect which limits the breakdown voltage. The origin of the breakdown coming from the electrode surface is consistent with that found by Hara (114), Yoshino (152) (100), and Hayakawa (109) in LN_2. Blaz (118) (119), Hayakawa (109), and Hong (117) all suggest that that the breakdown is initiated by the generation of vapour bubbles on the electrode surface. However, in their case they used heaters to generate those bubbles. Yoshino, using a point-plane geometry, suggests that the creation of a streamer is the result of the breakdown mechanism via electron field emission when having the point at a negative polarity.

In the data in this thesis there is an additional issue of the insulator. Butcher (127) (126), Rodrigo (123) (125), Blaz (128), Kim (129) all indicate that the presence of the insulator will limit the breakdown voltage. In this data the presence of the insulator does not make a difference if geometry and material is optimised. However, when damage did occur to the insulator surface, then a reduction was generally observed in the breakdown voltage, which is consistent with the insulator presence being a limiting factor. The factor that could be overcoming this reduction could be the optimised geometry of the grooves for the JT and DKHl electrodes, and that the insulators were placed at a relatively large radial separation from the groove wall. These factors would have decreased the local field enhancement at the groove to insulator region, potentially overcoming the reduced breakdown issues observed by other experiments. The conclusion can be drawn that the high fields, and hence breakdowns occurred, most of the time between the plane-plane area of the electrodes, which was evident when

counting the cratering damage to the electrode surface and comparing to the number of breakdown events. However, the cases where the insulator failed is evidence that the breakdown had to have occurred along that insulator surface instead of the bulk fluid between the electrode plane faces.

If electron field emission was the primary breakdown mechanism then the type of damage observed on the insulator surface would not be so destructive. The electrons would travel up the insulator and liberate more electrons in a type of avalanche event. This would eventually lead to a conductive track along the surface in a manner that is observed in breakdowns in a gas atmosphere at room temperature along the surface of solids (81). However, in a liquid the damage observed is very destructive, with material blown out in a discontinuous manner along the tracking length. Pitting on the insulator surface is also observed around the damaged region. In some cases the tracking marks are discontinuous which would not occur in the case of electron field emission as the electrons would remain along the insulator surface to ground.

The proposed mechanism for the damage that is observed in this thesis is as follows.

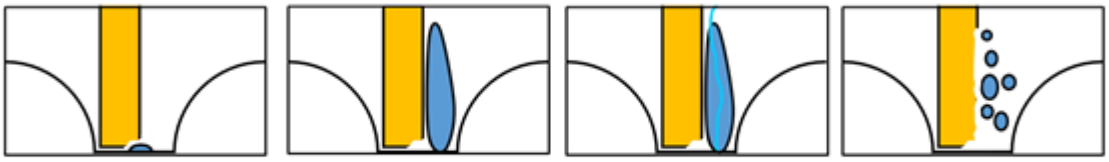

Fig. 7.14 Suggested mechanism for the damage resulting from a discharge in the LN2.

The high fields caused by the CTJ seeds a bubble at its base. This bubble then is able to grow and expand becoming ionised in the process. At some point the bubble is able to almost or completely span the gap to the opposite electrode which then results in a flash over of charge from one electrode to the other. The flash over is able to occur as the gas inside the bubble is of much lower dielectric strength then that of the liquid, gaseous breakdown. This then causes the bubble to collapse which leads to cavitation damage on the surface of the insulator. This would also explain why the track only occurs in a discontinuous manner in some cases. The process of bubble cavitation in normal fluids is explained by Brennen (110). This bubble formation is similar in behaviour to that described by Hong (117) and Hara (114). This damage did not always occur which implies that a variable in the system was causing the breakdown to change from originating at the CTJ to the plane-plane between the electrodes. The only variable that

changed during each run consistently was the radial separation which is attributed to be the reason for the large spread of breakdown values in the KEK measurements.

7.4.2 LHe

The theory of how LHe would breakdown is thought to follow the same bubble and cavitation idea presented previously but with preference for the discharge to occur over the insulator surface. There are two possible reasons for this: LHe suppresses free electrons and positive ions traveling through the bulk liquid but if there is a surface which these particles can travel along, it may act as a path and result in a breakdown more like a vacuum breakdown. The other possible mechanism is that due to such lower latent heat of vaporisation of LHe, bubbles are more easily formed due to high E fields on the electrode surface. These bubble then travel the gap and create a bridge resulting in the breakdown mechanism described above.

In previous work by Davidson (2) and Hill (3) showed the Al_2O_3 insulator damage observed was not as destructive as that seen in LN_2, instead would mostly create tracking on the surface (thought there was some chipping occurring but difficult to distinguish if this came from mechanical damage or not). The lack of cavitation damage observed implies that either the bubbles formed does not collapse or bubble formation is not the reason for the damage but instead free electrodes or positive ions traveling over the insulator surface. However, these measurements have only been made on DKHs electrodes, therefore, the translation of this behaviour to the JT electrodes with BG insulator (which had improved breakdown voltages in LN_2 and minimised damage) is unknown.

Ito (64) demonstrated a stable field of 100 kV/cm at 1 cm separation with electrodes ϕ 120 mm in LHe at 0.4 K either pressurised or at SVP. The insulator material used in that setup was PMMA which has a dielectric constant of 3.06 to 3.92 (153), similar to that of borosilicate glass. The electrode geometry was also improved using finite element meshing software in order to minimise the high fields at the groove walls. The optimisation of the geometry for Ito and measurements presented in this thesis seem to overcome the issue observed in previous work with Hill and Davidson.

Chapter 8

Conclusion and suggestion for further work

This thesis described measurements in a small test setup (the KEK cryostat) that were used to help inform electrode design, optimisation, and material choice for a larger scale setup (the Blue Elbow cryostat) that used electrodes comparable in size to what would be required for a cryogenic nEDM apparatus. Blue Elbow measurements in LN2 verified the surface area effect measured by previous authors, and were followed by initial measurements with LHe. Both the KEK and Blue Elbow measurements helped to further the main goal of this thesis: measuring LHe breakdowns in a cryogenic nEDM Ramsey cell size.

8.1 Conclusions on KEK breakdown measurements in LN_2

Breakdown measurements for a parallel ϕ 125 mm stainless steel electrode geometry with an insulator separating them have been performed in LN_2. Breakdowns were performed with different sized insulators and materials. The insulator sits in a recess in the electrode which forms the groove. Similar damage was observed to that found by Davidson (2) and Hill (3) but on insulators a factor of 6 larger in diameter than in that work. The damage would be in the form of carbon tracks along the surface of the insulator and in some cases material being blown out. In measurements performed in this thesis, Al_2O_3 insulators were the most susceptible to damage. The tendency of the damage to the insulators was dependent on the radial separation to the electrode groove geometry. However, Al_2O_3 has a high dielectric constant, ~ 9, and if this was lower, similar to the surrounding medium, it would help in overcoming this damage. This was experimentally tested with borosilicate glass (BG), which has a dielectric constant ~ 4, and no damage was observed on these insulators if the ends were properly treated by polishing.

Interestingly for these electrode separations (3-7 mm), the presence of the insulator does not lower the breakdown voltage of the system compared to breakdown measurements made without an insulator, as was expected to be the case.

8.2 Conclusions on Blue Elbow breakdown measurements in LN_2

The breakdown measurements in the Blue Elbow cryostat in LN_2 used parallel ϕ 360 mm stainless steel electrodes with a BG insulator separating the two plates. The internal electrode separation could be varied from 2-26 mm. Breakdowns were performed with electrode separations up to 12 mm. The breakdown voltages were consistently lower than those achieved with the ϕ 125 mm electrodes. Comparing these measurements with those performed by Davidson (2) and Hill (3) shows a trend that as the electrode surface area is increased the breakdown voltage decreases logarithmically, hence a surface area effect is present similar to the results by Weber (108) and Hayakawa (109).

8.3 Conclusions on Blue Elbow breakdown measurements in LHe

Breakdown measurements performed in LHe at 4.2 K SVP used the same electrode and insulator geometry as was used in LN_2. Measurements were carried out at 6, 12, and 16 mm electrode separation. While the average breakdown voltage at 6 mm was at about 75 kV, this value did not increase linearly as expected, and only increased to an average of 95 kV at 16 mm separation. This could possibly imply a much more dramatic volume effect that was not observed in the LN_2. If this is due to a limitation intrinsic to LHe, then this would possibly limit the gains in electric field strength possible for a cryogenic nEDM experiment. However, there is an indication from field modelling simulations, that the electrode geometry and spacer plates at 12 and 16 mm may have reduced the breakdown voltages, rather than this being a volume effect. If this is the case then from the 6 mm electrode separation results, electric fields of order 100 kV/cm are indeed achievable.

8.4 Suggestions for further work

The work performed with the DKHl electrodes only took a few measurements using the polished BG insulators. It would be informative to expand on these measurements

and see if at larger separations the damage will start to occur again. In that case, optimisation of the geometry of the groove would perhaps need to be changed to achieve the required fields without damaging the insulator. By increasing the separation of the electrodes further one could also measure the volume effects shown by Hayakawa (109).

Due to limitations of the side HV feed for the Blue Elbow cryostat, the LN_2 measurements on the large JT electrodes were only able to be performed with up to −40 kV on the lower electrode instead of the planned −130 kV. With +130 kV applied on the top electrode, this limited the maximum potential across the electrodes to 170 kV instead of 260 kV, which meant that LN_2 breakdown measurements could only be effectively carried out at separations up to 12 mm, as larger separations would likely require larger voltages to reliably achieve breakdown. If the side feed can be improved to deliver up to −130 kV, then this would allow the maximum design electric field of 100kV/cm at 26 mm separation, and would enable LN_2 breakdown measurements at separations larger than 12 mm. This could then indicate if the breakdown voltages continue to follow a linear behaviour against electrode separation, as has been assumed in this thesis.

An important next step would be to perform additional measurements at various separations in the Blue Elbow cryostat in LHe at 4.2 K SVP varying the electrodes separation between 2-26 mm. This could then be analysed the same way as on the LN_2 measurements and compared to previous work by Davidson (2) and Hill (3) in LHe to measure the surface area effect and better understand the breakdown mechanisms in LHe. These additional LHe measurements would also be able to confirm if the spacer plates are the limitation for the 12 and 16 mm separation LHe data. Determining the maximum electric field achievable in LHe at the maximum 26 mm electrode separation would also be especially interesting as this is of a similar size as what would be used in a cryogenic nEDM apparatus.

An additional improvement would be to develop the SV in order to allow pressurisation at 0.5 K in a similar manner to that presented in Davidson's (2) thesis but with an insulator present between the electrodes. Based on (2), the achievable electric field is expected to be the same as in LHe at 4.2 K SVP with an insulator, however, this should ideally be fully experimentally proven. Success of this measurement would demonstrate that a realistic cryogenic nEDM experiment is able to achieve required fields under these conditions. This would be a big step in concretely establishing the usable electric field in a cryogenic nEDM apparatus.

Additional work should also be carried out on investigating the electric field homogeneity and if it contributes to a $v \times E$ effect which could limit a nEDM experiment

which aims for a sensitivity of 10^{-28} ecm. This can be performed by using the simulation data that was already produced for this thesis. The simulations produce the vector components of the electric field. These components can then be compared with a "uniform" magnetic field and determine the average values of $\theta_{v\times E}$. This can determine the magnitude of $v \times E$ systematic effect.

Beyond electric field measurements in LHe one can next consider the configuration of a complete cryogenic nEDM experiment. Ideally the UCN source might be in the same volume as the cryogenic Ramsey chamber in order to reduce transport and dilution reductions in UCN density. The presence of an UCN source (in the setup) could provide additional heat input into the liquid volume when the necessary cold neutron beam is applied. Therefore, it may affect the achievable electric fields. It would be very interesting to see this type of experiment and its output.

It is very important for the advancement of nEDM sensitivity that this type of experiment is carried out, so that one of the keys to baryogenesis and the matter/antimatter asymmetry might be discovered.

References

[1] J. C. Long et al. High voltage test apparatus for a neutron EDM experiment and lower limit on the dielectric strength of liquid helium at large volumes. *arXiv 0603231*.

[2] A. J. Davidson. *High Voltage Breakdown in the Ramsey Cell of the CryoEDM experiment. - An experimental study of some relevant parameters.* PhD thesis, University of Sussex, 2011.

[3] D. Hill. High voltage breakdown across solid dielectrics in cryogenic. Master's thesis, University of Sussex, 2010.

[4] P. A. Bolokhov, M. Pospelov, and M. Romalis. Electric dipole moments as probes of CPT invariance. *Phys. Rev.*, D78:057702, 2008.

[5] I. B. Khriplovich and S. K. Lamoreaux. *CP violation without strangeness - electric dipole moments of particles, atoms, and molecules.* Springer, 1997.

[6] P. G. Harris. The Neutron EDM Experiment. *arXiv 0709.3100*.

[7] P. Schmidt-Wellenburg. The quest for an electric dipole moment of the neutron. *AIP Conf. Proc.*, 1753:060002, 2016.

[8] M. Goldhaber, L. Grodzins, and A. W. Sunyar. Helicity of neutrinos. *Phys. Rev.*, 109:1015–1017, Feb 1958.

[9] C. S. Wu et al. Experimental test of parity conservation in beta decay. *Phys. Rev.*, 105:1413–1415, Feb 1957.

[10] T. D. Lee and C. N. Yang. Question of parity conservation in weak interactions. *Phys. Rev.*, 104:254–258, 1956.

[11] L. Landau. On the conservation laws for weak interactions. *Nuclear Physics*, 3(1):127 – 131, 1957.

[12] J. H. Christenson et al. Evidence for the 2π Decay of the K_2^0 Meson. *Phys. Rev. Lett.*, 13:138–140, 1964.

[13] H. Burkhardt et al. First evidence for direct CP violation. *Physics Letters B*, 206(1):169 – 176, 1988.

[14] K. Abe et al. Observation of large *CP* violation in the neutral *B* meson system. *Phys. Rev. Lett.*, 87:091802, 2001.

[15] B. Aubert et al. Observation of *CP* violation in the B^0 meson system. *Phys. Rev. Lett.*, 87:091801, 2001.

[16] G. Lüders and B. Zumino. Some consequences of TCP-invariance. *Phys. Rev.*, 106:385–386, 1957.

[17] P. Wolfgang. *Niels Bohr and the Development of Physics*. London, Pergamon Press, 1955.

[18] M. Ahmadi et al. Observation of the 1S-2S transition in trapped antihydrogen. *Nature*, 541:506, 2016.

[19] J. P. Lees et al. Observation of time-reversal violation in the B^0 meson system. *Phys. Rev. Lett.*, 109:211801, 2012.

[20] Csaba Balazs. Baryogenesis: A small review of the big picture. 2014.

[21] R. H. Cyburt et al. Big bang nucleosynthesis: Present status. *Rev. Mod. Phys.*, 88:015004, 2016.

[22] J. Ellis, T. K. Gaisser, and G. Steigman. Exotic relics from the big bang. *Nuclear Physics*, B177:444, 1980.

[23] A. D. Sakharov. Violation of cp invariance, c asymmetry, and baryon asymmetry of the universe. *Soviet Physics Uspekhi*, 34(5):392, 1991.

[24] G. R. Farrar and M. E. Shaposhnikov. Baryon asymmetry of the universe in the minimal Standard Model. *Phys. Rev. Lett.*, 70:2833–2836, 1993.

[25] G. L. Greene et al. A new measurement of the magnetic moment of the neutron. *Physics Letters B*, 71(2):297 – 300, 1977.

[26] M. Kobayashi and T. Maskawa. CP violation in the renormalizable theory of weak interaction. *Prog. Theor. Phys.*, 49:652–657, 1973.

[27] L. Maiani. CP violation in purely lefthanded weak interactions. *Physics Letters B*, 62(2):183 – 186, 1976.

[28] J. Ellis, M. K. Gaillard, and D.V. Nanopoulos. Left-handed currents and cp violation. *Nuclear Physics B*, 109(2):213 – 243, 1976.

[29] B. W. Lee. Gauge theories of microweak CP violation. *Phys. Rev. D*, 15:3394–3406, 1977.

[30] S. L. Glashow, J. Iliopoulos, and L. Maiani. Weak interactions with lepton-hadron symmetry. *Phys. Rev.*, D2:1285–1292, 1970.

[31] I. B. Khriplovich and A. R. Zhitnitsky. What is the value of the neutron electric dipole moment in the Kobayashi-Maskawa model? *Physics Letters B*, 109(6):490 – 492, 1982.

[32] I. B. Khriplovich V. M. Khatsymovsky and A. S. Yelkhovsky. Neutron electric dipole moment, T-odd nuclear forces, and nature of CP-violation. *Annals of Physics*, 186:1–14, 1988.

[33] V. M. Khatsymovsky and I. B. Khriplovich. CP-odd interaction of light quarks and the neutron electric dipole moment. *Physics Letters B*, 296(1):219 – 222, 1992.

[34] I. I. Kogan and D. Wyler. A sum rule calculation of the neutron electric dipole moment from a quark chromoelectric dipole coupling. *Physics Letters B*, 274(1):100 – 110, 1992.

[35] V. Baluni. CP-nonconserving effects in quantum chromodynamics. *Phys. Rev. D*, 19:2227–2230, 1979.

[36] R. J. Crewther et al. Chiral estimate of the electric dipole moment of the neutron in quantum chromodynamics. *Phys. Lett.*, 88B:123, 1979.

[37] J. M. Pendlebury et al. Revised experimental upper limit on the electric dipole moment of the neutron. *Phys. Rev. D*, 92:092003, 2015.

[38] R. D. Peccei and H. R. Quinn. CP conservation in the presence of pseudoparticles. *Phys. Rev. Lett.*, 38:1440–1443, 1977.

[39] R. D. Peccei. The strong CP problem and axions. *Lect. Notes Phys.*, 741:3–17, 2008.

[40] M. Pospelov and A. Ritz. Electric dipole moments as probes of new physics. *Annals of Physics*, 318(1):119 – 169, 2005. Special Issue.

[41] C. Abel et al. Search for axionlike dark matter through nuclear spin precession in electric and magnetic fields. *Phys. Rev. X*, 7:041034, 2017.

[42] T. Inui et al. Neutron electric dipole moment in the minimal supersymmetric standard model. *Nucl. Phys.*, B449:49–68, 1995.

[43] T. Fukuyama. Searching for new physics beyond the Standard Model in electric dipole moment. *Int. J. Mod. Phys.*, A27:1230015, 2012.

[44] J. Papavassiliou. CP violation in the Weinberg multi - Higgs model. In *Beyond the standard model. Proceedings, 4th International Conference on High-Energy Physics, Tahoe City, USA, December 13-18, 1994*, pages 509–513, 1995.

[45] S. Weinberg. Gauge theory of CP nonconservation. *Phys. Rev. Lett.*, 37:657–661, 1976.

[46] G. Senjanovic and R. N. Mohapatra. Exact left-right symmetry and spontaneous violation of parity. *Phys. Rev. D*, 12:1502–1505, 1975.

[47] B. H. J. McKellar XG. He and S. Pakvasa. $\frac{\epsilon'}{\epsilon}$ and the electric dipole moment of the neutron in left-right-symmetric models. *Phys. Rev. Lett.*, 61:1267–1270, 1988.

[48] T. Chupp and M. Ramsey-Musolf. Electric dipole moments: A global analysis. *Phys. Rev. C*, 91:035502, 2015.

[49] S. A. Murthy et al. New limits on the electron electric dipole moment from cesium. *Phys. Rev. Lett.*, 63:965–968, 1989.

[50] B. C. Regan et al. New limit on the electron electric dipole moment. *Phys. Rev. Lett.*, 88:071805, 2002.

[51] J. Hudson et al. Improved measurement of the shape of the electron. *Nature*, 473:493–6, 05 2011.

[52] J. Baron et al. Order of magnitude smaller limit on the electric dipole moment of the electron. *Science*, 343:269–272, 2014.

[53] B. Graner et al. Reduced limit on the permanent electric dipole moment of ^{199}Hg. *Phys. Rev. Lett.*, 116:161601, 2016.

[54] M. A. Rosenberry and T. E. Chupp. Atomic electric dipole moment measurement using spin exchange pumped masers of ^{129}Xe and ^{3}He. *Phys. Rev. Lett.*, 86:22–25, 2001.

[55] D. Cho, K. Sangster, and E. A. Hinds. Search for time-reversal-symmetry violation in thallium fluoride using a jet source. *Phys. Rev. A*, 44:2783–2799, 1991.

[56] J. M. Pendlebury. Fundamental physics with ultracold neutrons. *Annual Review of Nuclear and Particle Science*, 43(1):687–727, 1993.

[57] N. F. Ramsey. A molecular beam resonance method with separated oscillating fields. *Phys. Rev.*, 78:695–699, 1950.

[58] R. Golub, D. Richardson, S. K. Lamoreaux. *Ultra-Cold Neutrons*. IOP Publishing Ltd, 1991.

[59] R. Golub and J. M. Pendlebury. Ultra-cold neutrons. *Reports on Progress in Physics*, 42(3):439, 1979.

[60] B. R. Martin and G. Shaw. *Particle Physics*. Wiley, 2003.

[61] R. Golub and J.M. Pendlebury. The interaction of Ultra-Cold Neutrons (UCN) with liquid helium and a superthermal UCN source. *Physics Letters A*, 62(5):337 – 339, 1977.

[62] C. R. Brome et al. Magnetic trapping of ultracold neutrons. *Phys. Rev. C*, 63:055502, 2001.

[63] E. Korobkina, R. Golub, B. W. Wehring, and A. R. Young. Production of UCN by downscattering in superfluid He^4. *Physics Letters A*, 301(5):462 – 469, 2002.

[64] T. M. Ito et al. An apparatus for studying electrical breakdown in liquid helium at 0.4 K and testing electrode materials for the neutron electric dipole moment experiment at the Spallation Neutron Source. *Rev. Sci. Instrum.*, 87(4):045113, 2016.

[65] O. Zimmer, F. M. Piegsa, and S. N. Ivanov. Superthermal source of ultracold neutrons for fundamental physics experiments. *Phys. Rev. Lett.*, 107:134801, 2011.

[66] I. Altarev et al. An improved measurement of the electric dipole moment of the neutron. *Nuclear Physics A*, 844(1):47c – 52c, 2010. Proceedings of the 4th International Symposium on Symmetries in Subatomic Physics.

[67] M. Seidel et al. Production of a 1.3 MW proton beam at PSI. In *Proceedings of IPAC'10, Kyoto, Japan*, 2010.

[68] D. A. Ries. *The Source for Ultracold Neutrons at the Paul Scherrer Institute: Characterisation, Optimisation, and International Comparison*. PhD thesis, ETH Zürich, 2016.

[69] M. Wohlmuther and G. Heidenreich. The spallation target of the ultra-cold neutron source UCN at PSI. *Nuclear Instruments and Methods in Physics Research Section A: Accelerators, Spectrometers, Detectors and Associated Equipment*, 564(1):51 – 56, 2006.

[70] L. Göltl. *Characterization of the PSI ultra-cold neutron source*. PhD thesis, ETH Zürich, 2012.

[71] J. Zenner. *The search for the neutron electric dipole moment*. PhD thesis, Johannes Gutenberg-Universität, Mainz, 2013.

[72] B. Lauss. Status of the apparatus for the next phase of the neutron EDM search at PSI – n2EDM. nEDM workshop, 2017.

[73] P. Ageron, W. Mampe, and A. I. Kilvington. The temperature dependence of ultra-cold neutron confinement times. *Zeitschrift für Physik B Condensed Matter*, 59(3):261–263, 1985.

[74] E. Korobkina et al. Temperature dependence of ultracold neutron loss rates. *Phys. Rev. B*, 70:035409, 2004.

[75] S. M. Clayton et al. Cavallo's multiplier for in situ generation of high voltage. *arXiv 1803.07665*, 2018.

[76] R. Golub and S. K. Lamoreaux. Neutron electric-dipole moment, ultracold neutrons and polarized ^{3}He. *Physics Reports*, 237(1):1 – 62, 1994.

[77] T. Kikawa. Developments for the next generation neutron EDM search at TRIUMF. nEDM workshop, 2017.

[78] T. Hayamizu. Xe/Hg dual-comagnetometer for the TRIUMF neutron EDM experiment. nEDM workshop, 2017.

[79] S. Degenkolb. SuperSUN and PanEDM: a new superthermal UCN source for a new nEDM measurement. nEDM workshop, 2017.

[80] M. A. Lieberman and A. J. Lichtenberg. *Principles of plasma discharge and materials processing*. Wiley, 2005.

[81] D. C. Faircloth. Technological Aspects: High Voltage. In *Proceedings, CAS - CERN Accelerator School: Ion Sources: Senec, Slovakia, 2012*, pages 381–419, 2013.

[82] D. Tommasini. Dielectric insulation and high-voltage issues. In *Proceedings, 2009 CAS-CERN Accelerator School: Specialised course on Magnets: Bruges, Belgium*, 2011.

[83] R. Latham. *High Voltage Vacuum Insulation*. Academic Press, 1995.

[84] E. F. Peschke and R. von Olshausen. *Cable Systems for High and Extra-High Voltage*. Pirelli, 1999.

[85] M. S. Naidu and V. Kamaraju. *High Voltage Engineering*. McGraw-Hill, 1995.

[86] E. Kuffel, W. S. Zaengl, and J. Kuffel. *High Voltage Engineering: Fundamentals*. Newnes, 2000.

[87] D. Kind and K. Feser. *High Voltage Test Techniques*. Newnes, 2001.

[88] J. Wilks and D. C. Betts. *An Iintroduction to Liquid Helium*. Oxford Unversity Press, 1987.

[89] A. A. Townsend. Liquid helium. *Journal of Fluid Mechanics*, 7(3):479–480, 1960.

[90] H. J. Maris. Electrons in liquid helium. *Journal of the Physical Society of Japan*, 77(11):111008, 2008.

[91] A. A. Belevtsev. Electron multiplication coefficients in liquid rare gases. *Nuclear Instruments and Methods in Physics Research Section A: Accelerators, Spectrometers, Detectors and Associated Equipment*, 327(1):18 – 24, 1993.

[92] Z. Li et al. Ionization and charge transport phenomena in liquid helium induced by corona discharge. *Journal of Electrostatics*, 66(5):263 – 274, 2008.

[93] J. R. Karamath. *He-II under High Electric Field Conditions for the Cryogenic Neutron Electric Dipole Moment Experiment*. PhD thesis, University of Sussex, 2007.

[94] P. V. E. McClintock. Field emission in liquid helium. *Physics Letters A*, 29(8):453 – 454, 1969.

[95] P. V. E. McClintock. Field-emission and field-ionisation in liquid ^{3}He. *Physics Letters A*, 35(3):211 – 212, 1971.

[96] C. Blank and M. H. Edwards. Dielectric breakdown of liquid helium. *Phys. Rev.*, 119:50–52, Jul 1960.

[97] W. F. Schmidt et al. Electronic conduction and breakdown in liquid helium and liquid neon. *IEEE Transactions on Dielectrics and Electrical Insulation*, 10(6):1012–1021, 2003.

[98] D. May and H. Krauth. Influence of the electrode surface condition on the breakdown of liquid helium. *IEEE Transactions on Magnetics*, 17(5):2089–2092, Sep 1981.

[99] J. Gerhold, M. Hubmann, and E. Telser. Gap size effect on liquid helium breakdown. *Cryogenics*, 34(7):579 – 586, 1994.

[100] K. Yoshino et al. Dielectric breakdown of cryogenic liquids in terms of pressure, polarity, pulse width and impurity. *Journal of Electrostatics*, 12:305 – 314, 1982.

[101] C. Olivier. Performance of electrodes at the first voltage breakdown in liquid helium. *IEEE Transactions on Magnetics*, 17(5):2086–2088, Sep 1981.

[102] J. L. Wu. *Cryogenic dielectric testing performed for the SMES-ETM program*. Springer US, Boston, MA, 1996.

[103] M. Hara et al. DC breakdown voltage characteristics of saturated liquid helium in the presence of metallic particles. *IEEE Transactions on Dielectrics and Electrical Insulation*, 13(3):470–476, 2006.

[104] M. Hara, H. Nakagawa, T. Shinohara, and J. Suehiro. Generation, growth and collapse of bubbles on collision of particle with electrode in DC electrically stressed liquid helium. *IEEE Transactions on Dielectrics and Electrical Insulation*, 9(6):910–921, Dec 2002.

[105] G. Colletti et al. Some data on the AC breakdown strength of liquid helium in the millimetre gap range. *Journal of Electrostatics*, 12:297 – 304, 1982.

[106] J. D. Cobine. *Gaseous Conductors: Theory and Engineering Applications*. McGraw Hill, 1958.

[107] S. Kim et al. Conditioning effect of dielectric breakdown in liquid helium. *Japanese Journal of Applied Physics*, 22(6R):952, 1983.

[108] K. H. Weber and H. S. Endicott. Area effect and its extremal basis for the electric breakdown of transformer oil. *Transactions of the American Institute of Electrical Engineers*, 75(3), 1956.

[109] N. Hayakawa et al. Breakdown mechanism of liquid nitrogen viewed from area and volume effects. *IEEE Transactions on Dielectrics and Electrical Insulation*, 4(1):127–134, Feb 1997.

[110] C. E. Brennen. *Cavitation and Bubble Dynamics*. Oxford Univerity Press, 1995.

[111] C. G. Garton and Z. Krasucki. Bubbles in insulating liquids: stability in an electric field. *Proceedings of the Royal Society of London A: Mathematical, Physical and Engineering Sciences*, 280(1381):211–226, 1964.

[112] J. Gerhold. Dielectric breakdown of cryogenic gases and liquids. *Cryogenics*, 19(10):571 – 584, 1979.

[113] H. Abe et al. Visual observation of the bubble dynamics in normal ^{4}He, superfluid ^{4}He and superfluid ^{3}He–^{4}He mixtures. *Journal of Fluid Mechanics*, 619:261–275, 2009.

[114] M. Hara et al. Electrical breakdown mechanism of liquid nitrogen in the presence of thermally induced bubbles. *Cryogenics*, 27(2):93 – 101, 1987.

[115] M. Hara et al. D.C. electrical breakdown of saturated liquid helium at 0.1 MPa in the presence of thermally induced bubbles. *Cryogenics*, 27(10):567 – 576, 1987.

[116] M. D. Cevallos et al. Imaging of negative polarity dc breakdown streamer expansion in transformer oil due to variations in background pressure. *IEEE Transactions on Plasma Science*, 33(2):494–495, 2005.

[117] T. P. Hong et al. Influence of vapor bubbles initiated by steady heating on the breakdown of liquid nitrogen. In *Annual Report Conference on Electrical Insulation and Dielectric Phenomena*, pages 313–316, 2003.

[118] M. Blaz and M. Kurrat. Studies of breakdowns in liquid nitrogen at different pressures between rogowski electrodes. *Physics Procedia*, 36(Supplement C):1330–1336, 2012.

[119] M. Blaz and M. Kurrat. Influence of bubbles in pressurized liquid nitrogen on the discharge behavior in a homogeneous electric field. *IEEE Transactions on Applied Superconductivity*, 23(3):7700804–7700804, 2013.

[120] J. Gerhold. Properties of cryogenic insulants. *Cryogenics*, 38(11):1063 – 1081, 1998.

[121] A. Neuber et al. The role of outgassing in surface flashover under vacuum. In *Digest of Technical Papers. 12th IEEE International Pulsed Power Conference*, volume 1, pages 441–445 vol.1, 1999.

[122] H. C. Miller. Surface flashover of insulators. *IEEE Transactions on Electrical Insulation*, 24(5):765–786, 1989.

[123] H. Rodrigo et al. Surface flashover of cylindrical G10 under AC and DC voltages at room and cryogenic temperatures. *IEEE Transactions on Applied Superconductivity*, 21(3):1409–1412, 2011.

[124] F. M. Bruce. Calibration of uniform-field spark-gaps for high-voltage measurement at power frequencies. *Electrical Engineers - Part II: Power Engineering, Journal of the Institution of*, 94(38):138–149, 1947.

[125] H. Rodrigo et al. AC flashover voltages along epoxy surfaces in gaseous helium compared to liquid nitrogen and transformer oil. *IEEE Transactions on Applied Superconductivity*, 24(3):1–6, 2014.

[126] M. Butcher et al. Surface flashover of dielectrics immersed in super-cooled liquid nitrogen. In *12th IEEE International Pulsed Power Conference*, volume 1, pages 450–453 vol.1, 1999.

[127] M. Butcher et al. Surface flashover in liquid nitrogen. In *Annual Report Conference on Electrical Insulation and Dielectric Phenomena*, volume 2, pages 654–657 vol.2, 1999.

[128] M. Blaz, M. Hilbert, and M. Kurrat. Investigation of the surface flashover behaviour of cylindrical insulators in liquid nitrogen. 2016.

[129] SY. Kim et al. Surface flashover characteristics in liquid nitrogen for application of superconducting pancake coils. *Cryogenics*, 42(6):415 – 418, 2002.

[130] A. Migliori, R. I. Schermer, and M. D. Henke. Dielectric tracking in liquid helium. *Cryogenics*, 18(7):443–445, 1978.

[131] J. Gerhold. Dielectric breakdown of helium at low temperatures. *Cryogenics*, 12(5):370–376, 1972.

[132] J. L. Wu and J. F. Roach. *DC dielectric breakdown tests of liquid helium at temperatures 1.8 K to 4.2 K*. Springer US, Boston, MA, 1992.

[133] Friatec. Frialit-Degussit technical ceramics. https://www.degussit.co.uk/Properties.htm.

[134] Materion. Material properties, BeO. https://materion.com/-/media/files/ceramics/datasheets/cc-002ceramicsmaterialpropertieschart.pdf.

[135] L. Munday. Microscopic investigation of surface damage after high voltage breakdown in cryogenic liquids. Master's thesis, University of Sussex, 2010.

[136] Vector Fields. Opera 3D finite element meshing software v17. https://operafea.com/.

[137] Lake Shore Cryogenics. Silicon diodes, Si410, CU/CU-HT data sheet. https://www.lakeshore.com/Pages/PackagesSI.aspx#.

[138] A. G. Katsika. *Magnetic aspects of the cryo-nEDM experiment*. PhD thesis, University of Sussex, 2011.

[139] Emerson & Cuming. Stycast 2850FT Blue. https://lartpc-docdb.fnal.gov/0000/000059/001/stycas2850.pdf.

[140] RS. CAL 9900 PID temperature controller. https://uk.rs-online.com/web/p/pid-temperature-controllers/0354925/.

[141] Spellman. SL10W Part Number SL130PN10/10002 Model SL130PN10/FGLL/230. https://www.spellmanhv.com/en/Products/SL.

[142] hivolt. High voltage cable, model no. 2121. http://www.hivolt.de/hochspannungskabel/hochspannungskabel-x-ray/.

[143] Vishay. Metal oxide resistors, special purpose, high voltage data sheet. https://www.mouser.co.uk/datasheet/2/427/rox-222769.pdf.

[144] J. Lux. Calculations for Rogowski profiles. http://home.earthlink.net/~jimlux/hv/rogowski.html.

[145] R. M. Ness. Engineering technical data Rogowski profile electrodes. http://www.nessengr.com/techdata/rogowski/rogowski.html.

[146] Dassault Systems. Solidworks CAD design software, 2014. https://www.solidworks.com/.

[147] B. Filippone. The search for a neutron electric dipole moment. In *JLAB User Group Meeting*, 2014.

[148] M. Kuźniak. *The neutron electric dipole moment experiment: research and development for the new spectrometer.* PhD thesis, Jagiellonian University, Marian Smoluchowski Institute of Physics, Nuclear Physics Department, 2008.

[149] Schott glass tubing. Duran: technical data sheet. http://www.us.schott.com/d/tubing/7fa95e87-38d4-4b93-9774-2f214a59563f/schott-tubing-datasheet-duran-english.pdf.

[150] H.Baumbach & Co. Fused Quartz: technical data sheet. http://www.h-baumbach.co.uk/Quartzproperties.htm.

[151] S. F. Ho. High voltage breakdown across cylindrical insulating spacer in liquid nitrogen. Master's thesis, University of Sussex, 2017.

[152] K. Yoshino et al. Electrical breakdown in cryogenic liquids. *Journal of Electrostatics*, 7:103 – 112, 1979.

[153] Prospector. Acrylic typical properties (PMMA) data sheet. https://plastics.ulprospector.com/generics/3/c/t/acrylic-properties-processing.

[154] B. Lauss. n2EDM Collaboration meeting, technical specifications. 2016.

[155] Emerson & Cuming. Stycast 1266 A/B. https://webaps.ellsworth.com/edl/Actions/GetLibraryFile.aspx?document=7975&language=en.

[156] Attwater & Sons Ltd. G10 technical specifications. https://www.attwater.com/products/datasheet/g10.pdf.

[157] Huntsman. Araldite 2014 technical specifications. https://polyestershoppen.nl/download/araldite-2014-1-epoxylijm/araldite-2014-1-datasheet-181.pdf.

[158] Huntsman. Araldite CW1312 technical specifications. http://www.farnell.com/datasheets/89718.pdf.

[159] Huntsman. Araldite CW1302 technical specifications. http://www.farnell.com/datasheets/1458623.pdf?_ga=2.249591558.1031960672.1529068274-70436761.1442244022.

[160] Essex X-ray. Technical data and specifications. http://www.essex-x-ray.com/.

[161] R. C. Richardson and E. N. Smith. *Experimental techniques in condensed matter physics at low temperature.* Advanced Book Program, 1998.

[162] J. P. Holtzhausen and W. L. Vosloo. *High voltage engineering practice and theory*. CRC Press, 2000.

[163] Rexolite. Technical specifications. http://www.rexolite.com/specifications/.

[164] CMR. GE Varnish IMI 7031 data sheet. http://www.cmr-direct.com/en/ge-varnish-2/cmr-gevar-25ml.

[165] Pico Technology. Thermocouple 8 channel data logger, TC-08, technical data sheet. https://www.picotech.com/data-logger/tc-08/thermocouple-data-logger.

[166] T. Rehaag. Investigate of the opera house effect in mercury magnetometry. Master's thesis, University of Sussex, 2017.

[167] Pfeiffer Vacuum. Operating instructions and technical data, model no. TSH 071 E/TSU 071 E. http://208.112.27.152/files/Pumps/Turbo%20Pumps/Pfeiffer%20E-Station_A%20Turbo%20Pumping%20Station%20Manual.pdf.

[168] Y. Chibane. *A new magnetometer for the neutron EDM experiement*. PhD thesis, University of Sussex, 1990.

[169] Ocean Optics. HR2000+ PMT data sheet. http://oceanoptics.com/wp-content/uploads/OEM-Data-Sheet-HR2000plus.pdf.

[170] Hamamatsu. Photomultiplier tubes 1986. https://archive.org/stream/HamamatsuPhotomultiplierTubes1986/HamamatsuPhotomultiplierTubes#page/n77/mode/2up.

[171] Solvay Solexis. Fombin PFPE: greases data sheet. https://www.idealvac.com/files/brochures/FomblinYVAC3Grease.pdf.

[172] Z. Chowdhuri et al. Experimental study of ^{199}Hg spin anti-relaxation coatings. *Appl. Phys.*, B115(2):257–262, 2014.

[173] Maflon. S.P.A Fluorwax F20 data sheet. http://www.maflon.com/.

Appendix A

Magnetic scanning of epoxies for n2EDM

A.1 Materials testing

The n2EDM (154) experiment requires a custom design for a HV feedthrough to deliver up to ±200 kV to the central electrode in a vacuum of order 10^{-6} mbar. The magnetic requirements of a feedthrough is that the gradient in the Ramsey Chamber is affected by a maximum of 1 pT/cm in any component, hence near zero magnetic susceptibility. There is also the possibility that a discharge occurs which can create a large local magnetic field, therefore, it also must be non-magnetisable. These requirements mean that careful selection of epoxies to bond the conductor in the feedthrough have to be considered.

The sample materials were measured using the PSI magnetic gradiometer (71). The magnetic gradiometer consists of a cylindrical two-layer magnetic shield. A solenoid coil produces a magnetic field, along the cylindrical axis of the gradiometer, of about B=2.2 μT. Two CsM, that use discharge lamps, are located in the centre of the cylindrical shielding, both separated by 200 mm. The samples are carried past the two CsM by a wooden cart which stops at various positions to take readings of the CsM. The magnetic field at the CsM from the sample is determined by the differential signal of the two CsM, which is measured twice, forward and back. Typical background values of the field (without the sample) is ~ 12 pT. The scanner can have occasional spikes in data due to: a nearby lift, SULTAN (German acronym for Supraleiter Test Anlage) neighbouring superconducting magnetic test facility, cars passing by, etc. The discrepancy between forward and backward signals is ~ 2 pT.

Testing of the samples was performed with multiple scans in order to get the cleanest

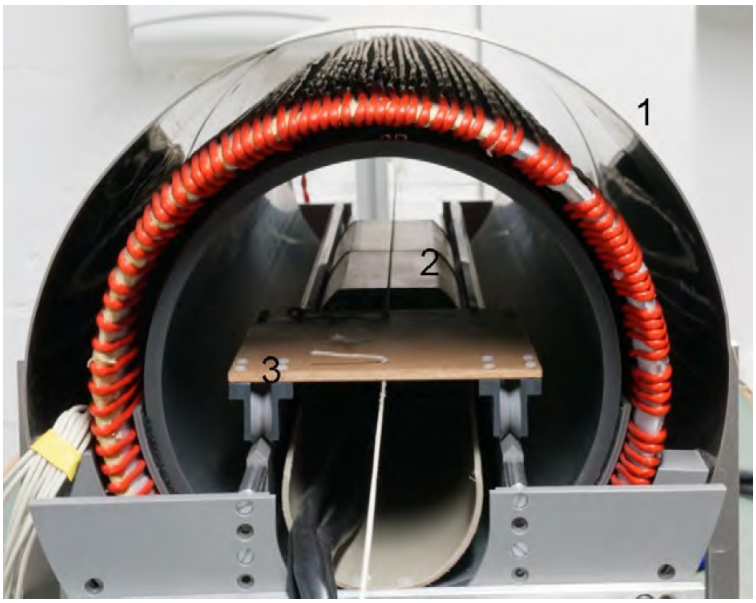

Fig. A.1 Front view of the two layer cylindrical shield (1). The red wires represent the degaussing coil of the system wrapped around the inner shield. Two CsM are in the centre of the shield (2). The non-magnetic cart which the samples sit on is carried by a pulley system (3).

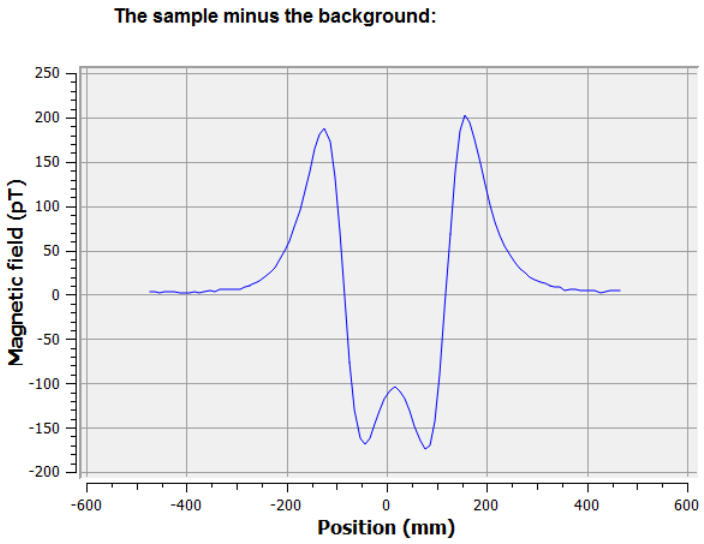

Fig. A.2 Example graph which the scanner produces. This is a scan done with one of the Araldite CW1312 samples, not cleaned. To produce this graph the software has done a background measurement, i.e. without the sample, then two forward and backward movements of the cart with the sample on it and the average of the two is taken, then the background data is subtracted. This scan shows there is a dipole present in the sample. In this case G_{p2p} = 380.9 (374.3) pT.

signal possible. Samples were also wiped clean with isopropanol before placement on the scanner to remove any contamination from dust. The cleanest run was then used to produce the following in Table A.1.

Sample material	Volume (cm^3)	$G_{p2p}(pT)$	Vacuum capability (mbar)	Magnetisable	Dielectric strength (kV/cm)
Stycast 2850FT (139)	42.5	51.2 (54.8)	10^{-9}	Y	144-150
Stycast 1266 (155)	91.8	17.6 (19.1)	-	N	157
G-10 (156)	77.4	33.1 (22.2)	10^{-5} - 10^{-6}	N	200
Araldite 2014-1 (157)	-	-	-	Y	173.2
Araldite CW1312/HY1300 (158)	98.9	177.7 (188.9)	-	-	135-155
Araldite CW1302/HY1300 (159)	81.5	408.0 (416.3)	-	-	150
Essex X-ray HV epoxy (160)	161.0	>1000	$<10^{-9}$	Y	-
Essex X-ray HV epoxy (no filler) (160)	44.3	55.1 (54.5)	$<10^{-9}$	-	-

Table A.1 Peak to peak (G_{p2p}) measurements for samples of given epoxies. All samples (apart from the G10 which was square) are a cylindrical block of stated volume. Magnetisability is determined by placing the sample on a ~ 0.1 T magnet for a few hours and if the signal changed from the previous measurement, by ~ nT, it is magnetisable. The sample was carefully cleaned and isolated from the magnet surface to ensure no magnetic contamination would transfer to the sample. Araldite 2014-1 was only tested to see if it was magnetisable, it did not pass the test so was not worth measuring further. All epoxies were chosen for their well known HV applications in various environments.

Results were surprising for a number of samples. The Stycast 2850FT was unusual, if prepared properly and left to cure inside a 2 layer mu-metal shielding it would result in the values stated in Table A.1. However, if placed on a magnet for a few hours or left to cure outside the shielding it would result in a magnetic field of order nT instead. Richardson et al. (161) mentions this problem with Stycast 2850FT and 2850GT but states Stycast 1266 as the alternative. Richardson also discusses varies properties of these glues as well.

The same problem was also found for the samples of epoxy that Essex X-ray (supplier of custom feedthroughs for X-ray applications) provided, which they use as standard in construction of high voltage cables and connectors (160). It was found that the large cylinder of epoxy with filler present gave a very large signal in the scanner while the one without a filler was much lower. This result is similar to Stycast 2850FT and 1266 where one has a filler (to change its thermal expansion coefficient to match that of steel) but the clear one seems to be non-magnetisable and produces a much lower magnetic field in the scanner. The major issue with Stycast 1266 is it can only be made in small batches due to exothermal runway in larger volumes, making constructing a feedthrough out of it very difficult.

The magnetisability of some of the epoxies seems to indicate that some material is added to the epoxy to give it a property (normally to match the thermal expansion coefficient of a given metal) which may be ferromagnetic. For example if try to match the thermal expansion coefficient of steel then the epoxy could have iron added which would explain why it exhibits a magnetic response after being placed on a magnet.

A.2 Maximum field limit for a feedthrough

Upper limits for the epoxies' magnetic field which would be acceptable for use in the feedthrough can be determined by using:

$$\vec{B} = -\frac{\mu_0 M_0}{2}\left(\frac{z-L/2}{\sqrt{a^2+(z-L/2)^2}} - \frac{z+L/2}{\sqrt{a^2+(z+L/2)^2}}\right)\hat{z}. \tag{A.1}$$

Equation A.1 is the magnetic field generated by a uniformly magnetised cylinder of length L and radius a, along its axis. Assuming the samples are cylindrical blocks of 4 cm height and 4 cm diameter, which pass over the Cs vapour cells about 7 cm away, for this case it would produce a G_{p2p} = 100 pT, which corresponds to a magnetisation of M_0 = 0.0033 A/m. Taking this value and extrapolating to the dimensions of a standard 160 kV receptacle (160), 30 cm long and 10 cm diameter, produces Figures A.3 and A.4.

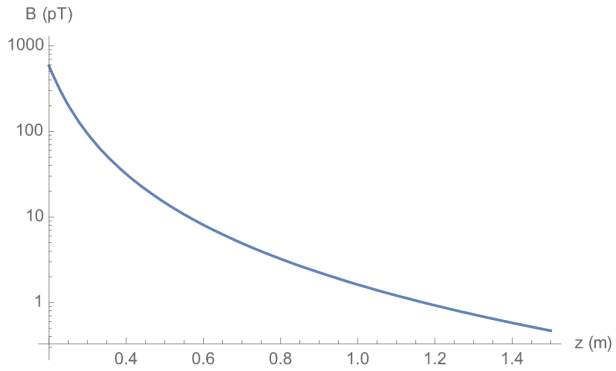

Fig. A.3 Magnetic field generated by the feedthrough if it was constructed of these samples. The field is along the z axis which is along its length.

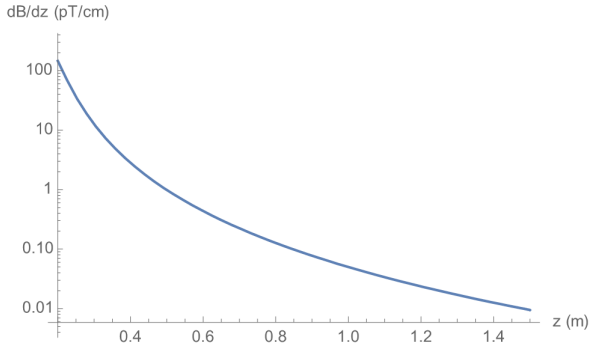

Fig. A.4 Magnetic field gradient generated by the feedthrough if it was constructed of these samples. The gradient is in the z axis which is along the length of the feedthrough.

Figure A.4 indicates that at a distance of 50 cm the samples would produce field gradients of 5 pT/cm, with is unacceptable. On a side note is that it is quite possible that the feedthrough could be much closer then 50 cm to the Ramsey Chamber.

This calculation only covers one configuration and field component but as an approximation it should be similar, by a factor of order unity (or less), to the value calculated is a worse case situation.

Appendix B

n2EDM feedthrough design and simulations

B.1 Introduction

Requirements for the HV feedthrough for n2EDM is to deliver 200 kV to a central electrode with a separation of 12 cm to two ground electrode on either side. The setup is placed within a vacuum chamber pumped to order of 10^{-5} mbar. In order to not generate a false EDM in the chamber, the magnetic field gradient inside the UCN volume must be less then 1 pT/cm. As shown in Appendix A, standard epoxies for HV feedthroughs contain some ferromagnetic properties. As the vacuum chambers' inner diameter is still to be determined, there is a possibility that the body of the feedthrough could be quite close to the central electrode. If, for example, Stycast 2580FT was used, a field at 10 cm was detected to be ~ 1 nT. This is unacceptably high, therefore, careful consideration of material choice is critical. Hence, materials such as PTFE, aluminium, PEEK (Zenner (71) measured its magnetic field in the same scanner as mentioned in Appendix A), Stycast 1266 and G10 are the acceptable materials with little to no magnetic field detected at 7 cm separation. These material also have very good dielectric strength and performance under high electrical fields. The materials also have good vacuum performance (though G10 outgasses).

The following was designed with the above considerations.

The design of this feedthrough is based of the current oil based 200 kV feedthrough at PSI. As this feedthrough was vertical it was acceptable to have it oil filled, but for n2EDM the central electrode is at HV, therefore, a horizontal feedthrough which would require less maintenance (the cable would absorb oil over time so would need periodic replacement) and not oil filled was required.

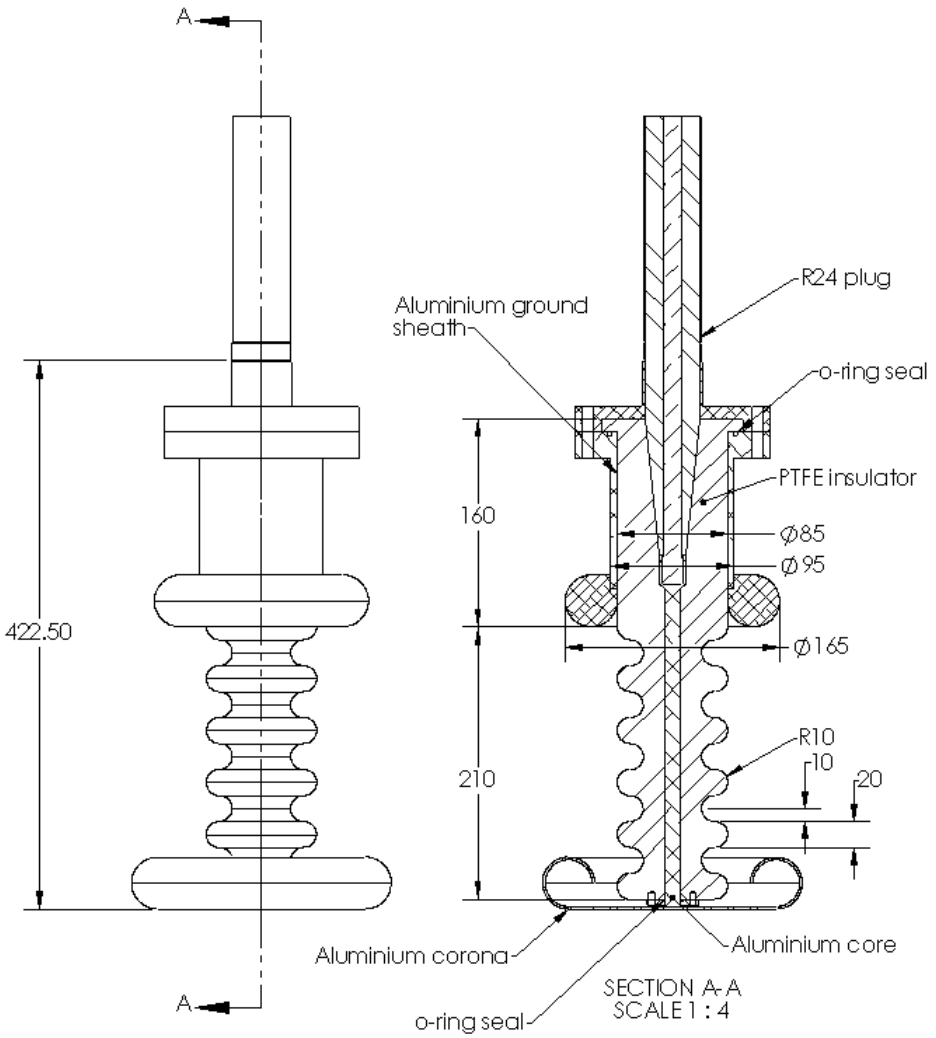

Fig. B.1 CAD design of n2EDM feedthrough.

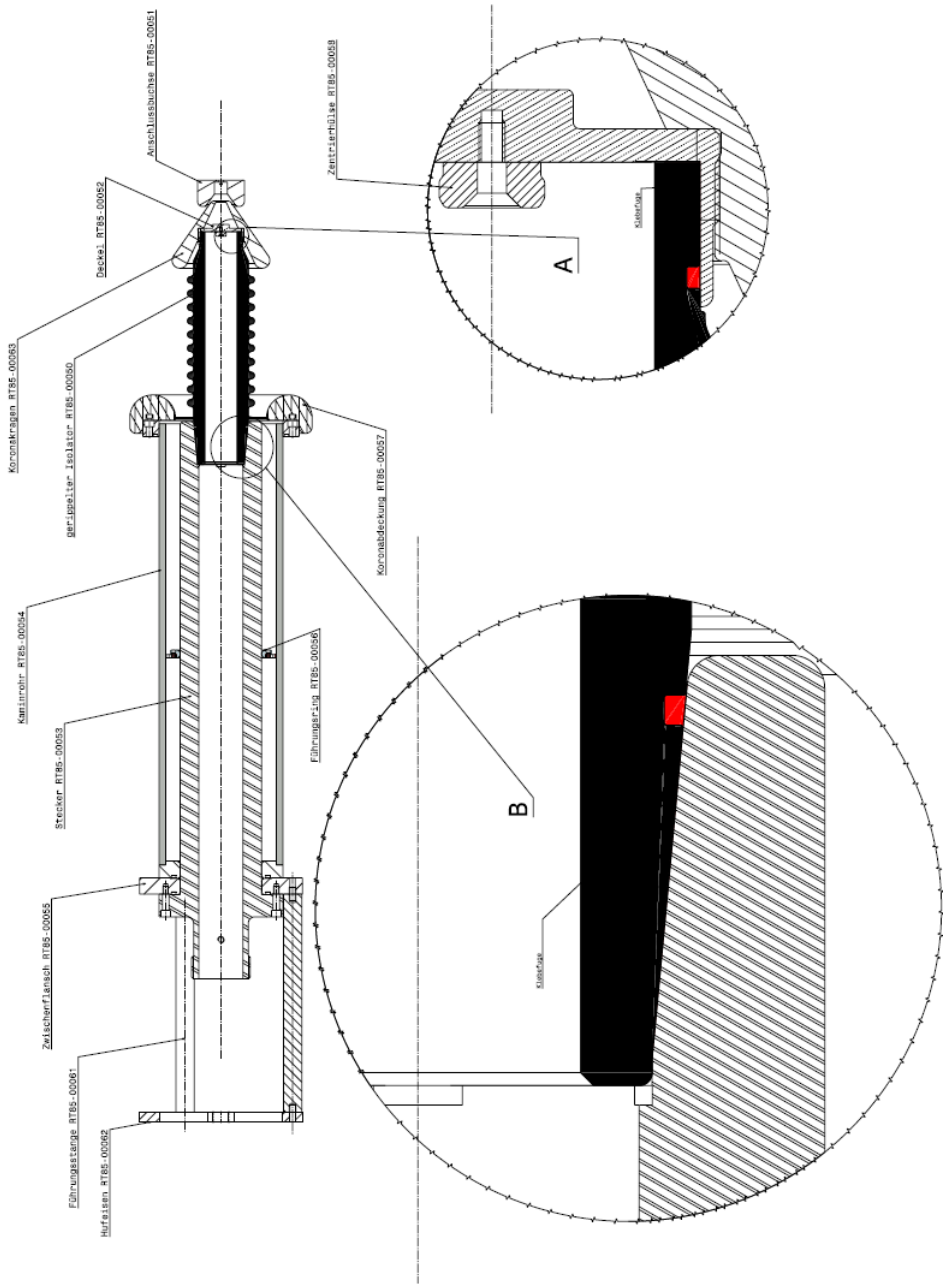

Fig. B.2 CAD design of nEDM feedthrough, oil filled.

B.2 Design comments

B.2.1 HV corona size

The size of the corona is determined by the radius of curvature. The size should always be such that the field on the surface is the lowest it can be. The biggest cause of breakdown on this surface could be due to machining burrs so proper treatment of the surface will ensure it could hold a sufficient field. The size of the corona is determined through Opera simulations in which the E fields are minimised on the surface within the constraints on the geometry. Fields can be higher than the separation between electrodes as under vacuum conditions it would require E fields of > 100 kV/cm to breakdown, while the presence of an insulator between two plane-plane surfaces will limit the field between the electrode to 10-30 kV/cm.

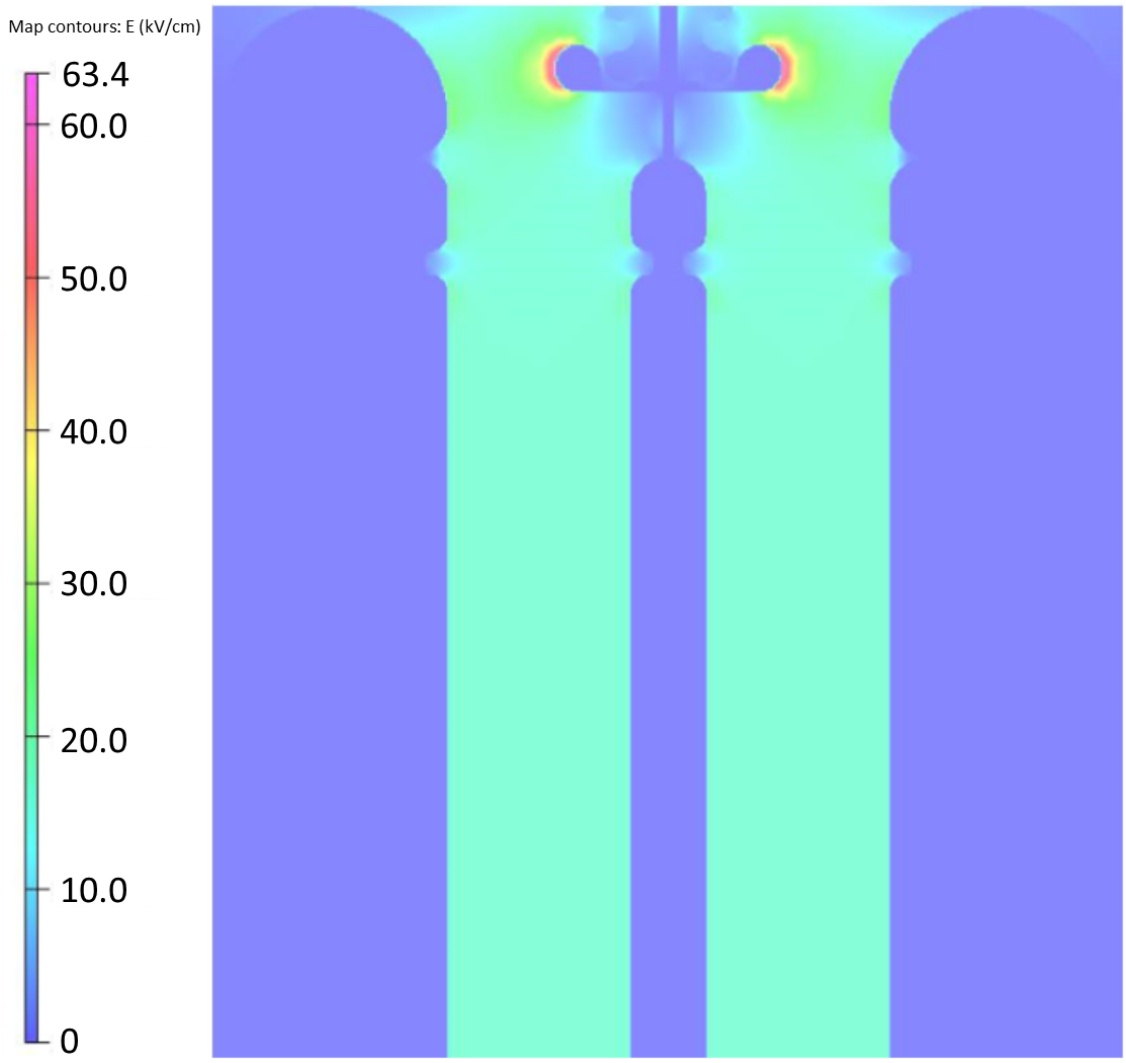

Fig. B.3 Opera simulation of n2EDM feedthrough and the electrode stack, E is in kV/cm.

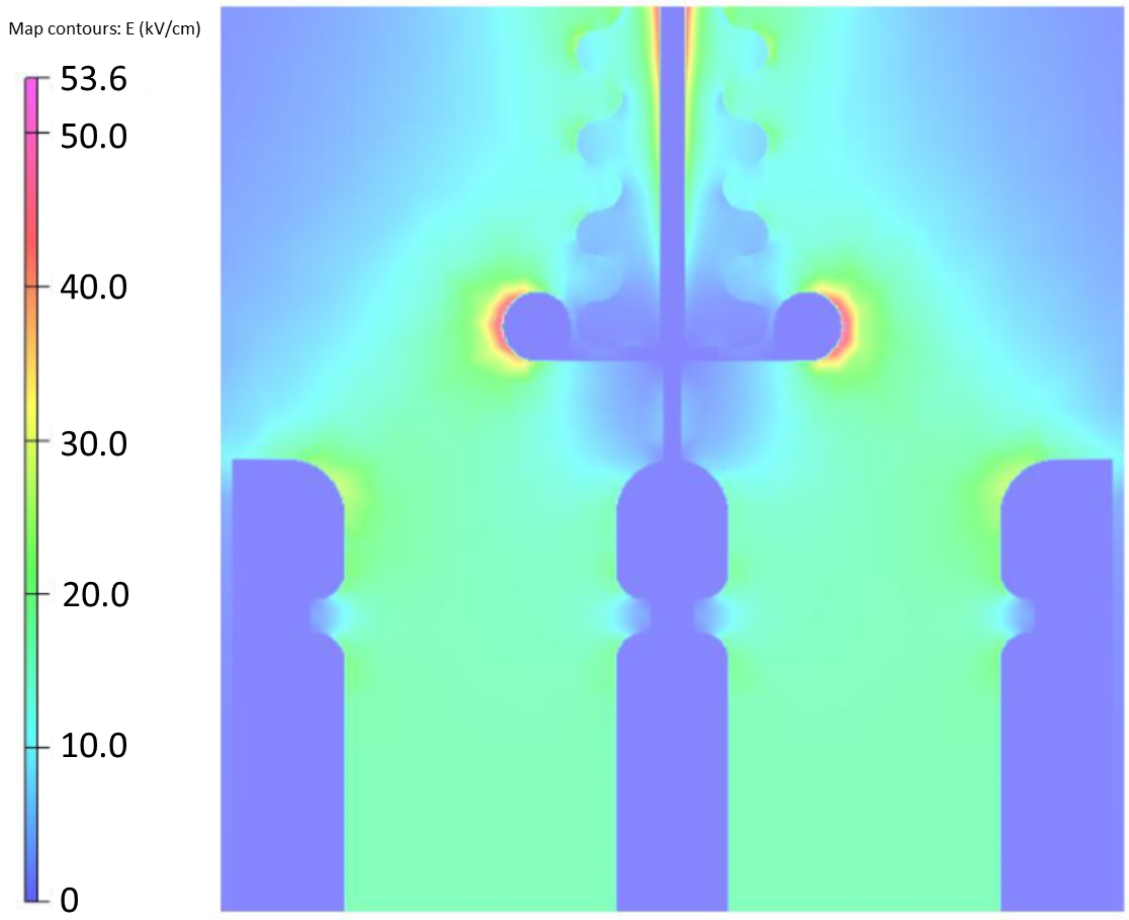

Fig. B.4 Opera simulation of n2EDM feedthrough with electrode stack but no corona domes on the ground electrodes, E is in kV/cm. Hence some form of corona domes on the ground electrodes will be required.

B.2.2 Vacuum seal on electrode side

The vacuum seal on the HV electrode end of the feed is required so that there is no leak down the conductor. The plan for this would be to machine the bore of the insulator very tight to the conductor and coat in vacuum grease to ensure there are no voids present. Even though this could then be vacuum tight there may be a leak with a long conduction path so this still needs to be sealed off to the main volume. The screws in to the insulator can be metal or plastic, whatever would ensure a good seal on the o-ring. This does mean the feed will require a corona dome to operate otherwise it will cause electron emission from the sharp edges of the metal sealing plate. There is a possibility that a virtual leak could occur from sealing this volume off, and this would need to be checked experimentally.

B.2.3 Size of the castellation

The size was determined from the current feedthrough, but as space is restrictive, the length was halved. This will still work to 200 kV as the current feed uses 2 – 4 mm/kV creepage length. These numbers are also backed up by various commercial ceramic ones.

B.2.4 Ground corona

The ground corona will need to be attached from inside the vacuum chamber, which should be possible once the feedthrough is installed. It is necessary to have a corona ring attached to the ground sheath of the feedthrough as there would be sharp edges on the vacuum tank and this will mitigate that.

B.2.5 Insulator material

The insulator is PEEK which has a dielectric strength of 20 MV/m. The thickest part of the feed is where the R24 plug interface sits which has sharp edges, hence needs more material to hold such a voltage. The sharp edges are there as it is difficult to machine a curved surface to match another without any voids, specially trying to machine something inside an object. At this thickest part the voltage should hold to 730 kV so if the sharp edges exceeds this value then there is a problem (only issue could come from tracking in this region to ground along surfaces). The bottom of a castellation to the HV conductor is 16.5 mm which should hold a voltage of 330 kV. It has been designed to hold 100 kV more than will be required in case there are any flaws in the material or construction.

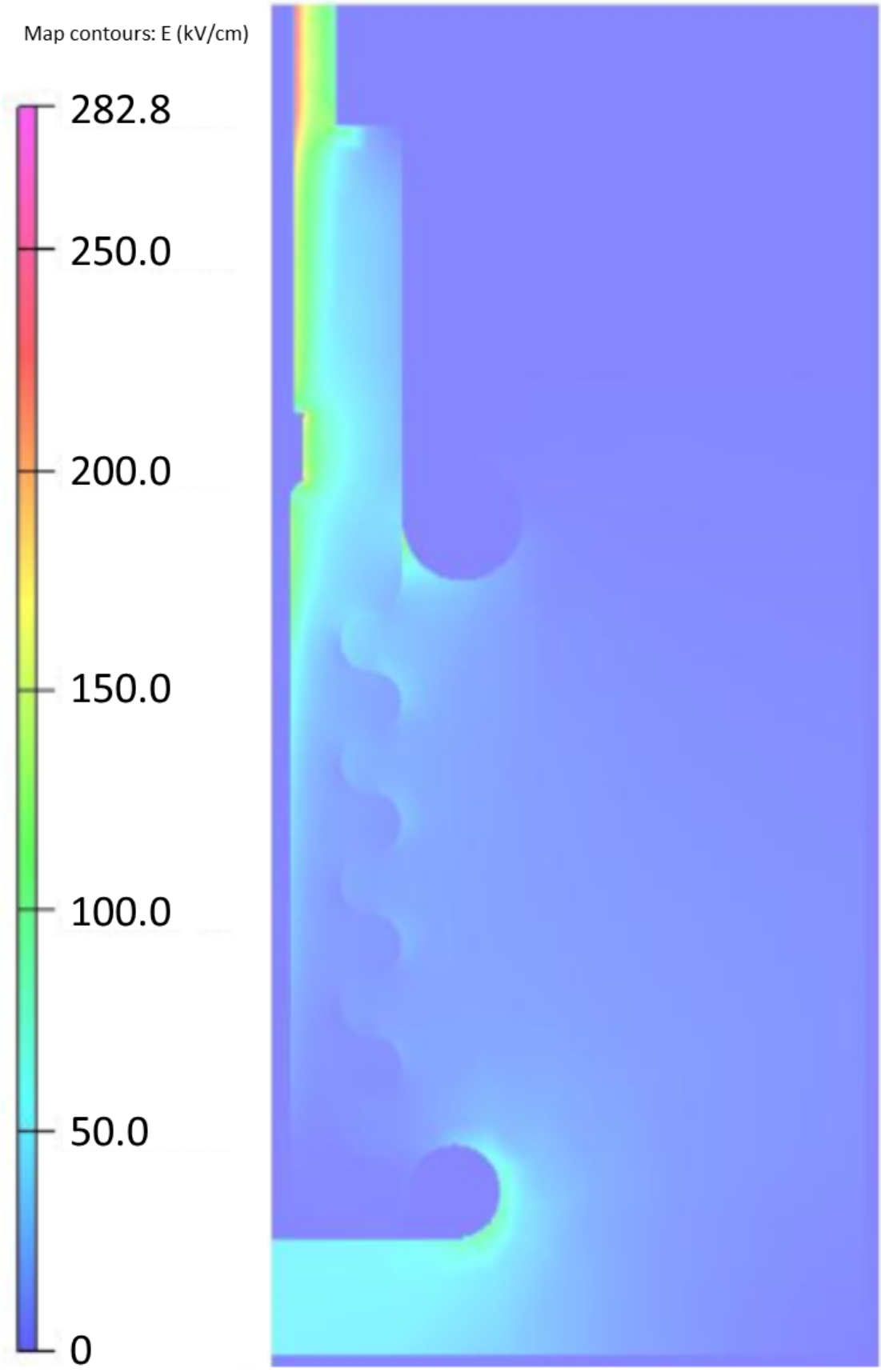

Fig. B.5 Opera simulation of n2EDM feedthrough, E is in kV/cm.

B.2.6 Internal HV interface

The internal HV interface is designed to match the thickness of the dielectric of the R24 plug, which will suppress any sharp edges on the connector, a standard thing to do in feedthroughs. The interface also creates a zero field region for the R24 plug connection.

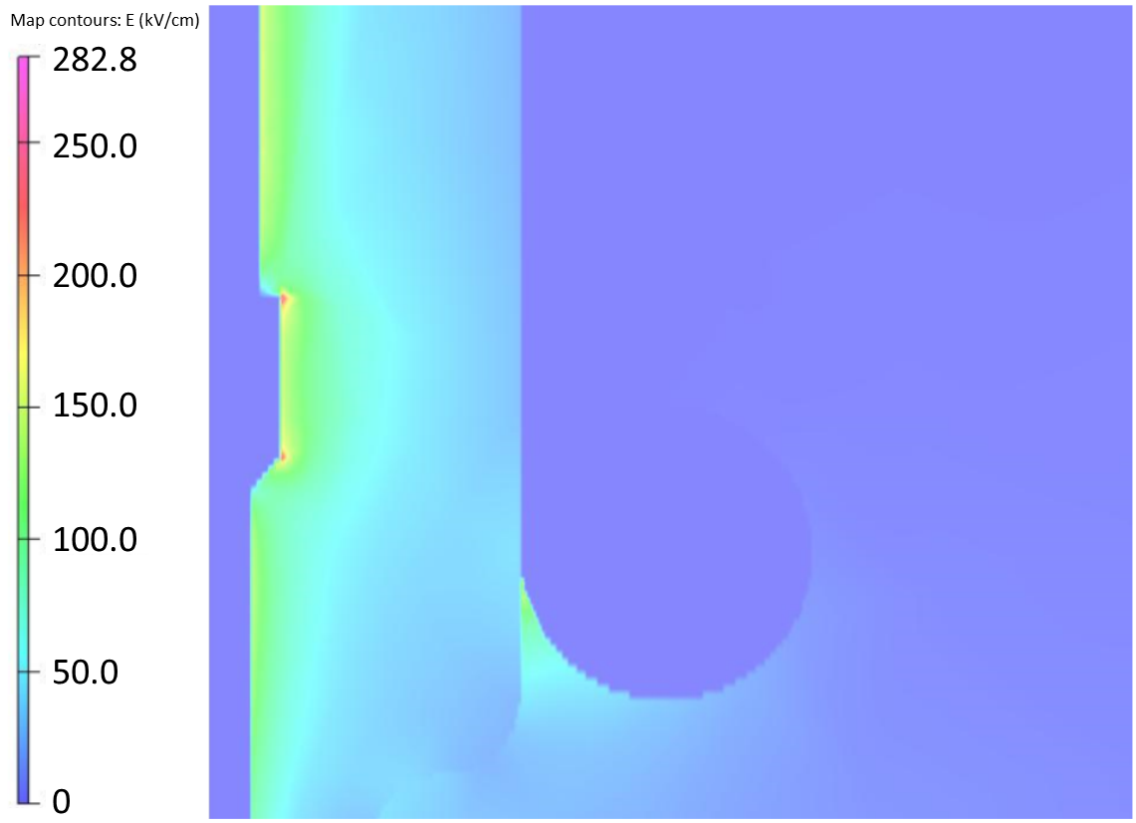

Fig. B.6 Opera simulation of a close up of the n2EDM feedthrough interface with the R24 connector, E is in kV/cm.

B.2.7 Ground sheath to CF/KF 150/200 flange

The construction of the feed is to take an aluminium tube which has been ideally bored from a large tube (ensures very accurate dimensions) or the easier way is to weld a sheet into a cylinder (this may lead to voids as you cannot guarantee its accuracy). This tube then needs to be welded to a CF/KF 150/200 flange. The larger flange choice is better as it then enable the whole feedthrough (coronas included) to be placed inside the tank in one go, while the small flange will not (HV and ground corona will need to be attached from inside the vacuum chamber). The bore of CF/KT 150 is 102 mm and CF/KT 200 is 152 mm.

The ground corona vacuum end will need to be threaded or else have some other form of connection to hold the ground corona in place. The insulator should be ma-

chined to be a very accurate outer diameter so it fits very tight into this tube, again to fill any voids (vacuum grease is also an option), however, the current design has a virtual leak along this tube so will need a correction at some point. Another possibility would be to cryo fit them together. This can be done by cooling the insulator in LN_2 which shrinks it, then forcing it into the tube. This method results in a fit that is near vacuum tight so would be the preferred construction. Either way the CF/KT 150/200 flange sits behind the ground corona.

The atmosphere/plug side of the feedthrough at the end of the tube will have an o-ring seal for contact against the insulator body, which is then clamped down with the clamping flange. The ground sheath may need to be thickened to add support for the weight of the feedthrough.

B.2.8 Notes

There is potentially an alternative for the HV corona, which would be to use a ball electrode instead but some thought needs to go into this because the vacuum sealing for inner conductor may need to be adapted.

B.2.9 References for design

The following references were used to help understand and develop the design for the feedthrough: (85), (83), (87), (86), (84), (162).

B.3 Conclusion

In conclusion the design is based around sound principles and tested geometries. There is some experimental work that needs to be done in order to determine if virtual leaks are present, if so then changes can be made to fix this. There is also the question of material choice; PTFE or PEEK. Either of these materials would work for the task, but PTFE is easier to work with. This design needs to be made and tested, but from a design stand point the feedthrough should operate to the required applied voltage of 200 kV.

Appendix C

nEDM E field analysis

C.1 Introduction

As the nEDM sensitivity is proportional to the E field, it raises an important question about the uniformity. If the E field between the two electrode is lower than expected from the applied voltage, the sensitivity to the nEDM could be lower, but can also lead to potential systematic limitations. The systematics can originate from the vxE effect. This occurs as the UCN pass through a non-homogeneous field which will create an additional local magnetic field changing the precession and mimicking the presence of a nEDM. As part of the contribution to PSI nEDM, an Opera simulation was performed on the apparatus to determine how uniform the E field is for these experiments.

C.2 Opera simulation for nEDM

The geometry for the simulation was taken from the detailed drawings of the setup at PSI. It consisted of; the ground electrode with corona ring, insulator with quartz windows, HV electrode with corona ring (electrodes are bolted to the corona rings). The electrode are made of aluminium and the insulator of Rexolite (163). Rexolite has very good HV properties, its dielectric constant is very low (2.53) and it has a very high dielectric strength (196.9 kV/cm). Simulations done in section 5.5 indicate that higher dielectric constant will produce higher E fields at the groove to insulator wall region, but in this setup Rexolite as a low dielectric constant, therefore the field at the groove wall is low in comparison to using normal insulator materials for UCN, such as BeO and quartz. The insulator has two hole machined into the horizontal axis for the mercury probe light to pass through. The probe light is in the UV spectrum, therefore, quartz windows have to be used. In order to seal the UCN volume the windows are glued in place. This creates a change in dielectric constant which could potentially be detrimental for HV application.

The ground electrode has two holes for mercury filling, and the other for UCN filling and extraction. The ports are covered by a plug, in order to seal off the internal volume during the measurement. The plug normally sits flush with the ground electrode surface. However, the position of the plug was not well known at the time of the simulation, therefore, the field in that region will be lower then actually achieved. Therefore, one can consider the uniformity in this simulation as a worse case situation.

The groove radius of the electrodes is 12 mm with a depth of 15 mm for the insulator to sit. The remaining 3 mm has a cut into the electrode, ~ 2 mm, for an o-ring which will seal against the insulator to keep it vacuum tight.

The HV electrode has the same geometry as the ground but there are no holes in the plane surface.

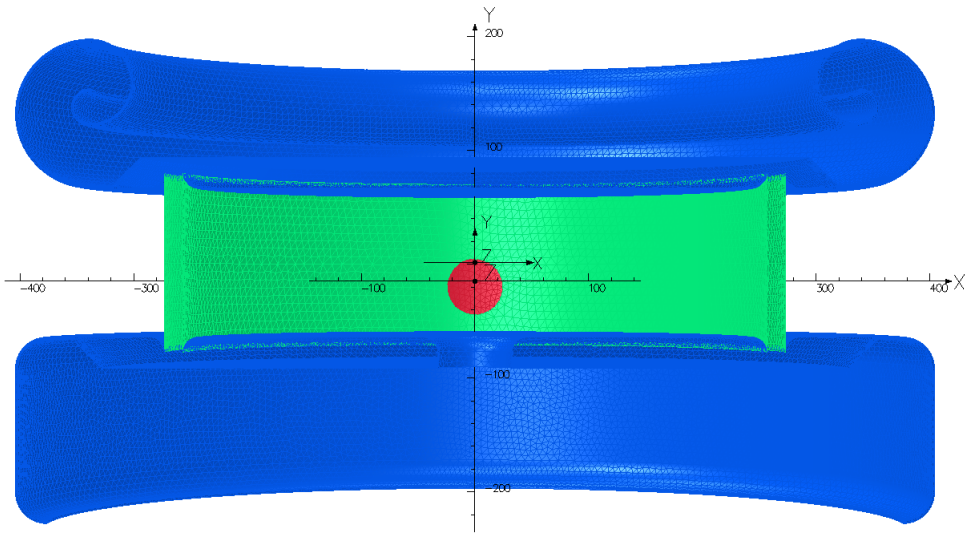

Fig. C.1 Cross sectional view of the Opera model of the nEDM Ramsey Cell. Blue components are made of aluminium (electrodes with corona rings), green is Rexolite (insulator separating the electrodes), and red quartz (windows for mercury probe light). The axes shown are in millimetres.

C.3 Determination of the E field

Opera is able to simulate the E field between the electrode, which also take into account variation in the field due to the presence of dielectric mediums. The simulation has conditions for the top electrode set to 140 kV and the bottom to ground with a separation of 120 mm. The expected field is therefore 11.67 kV/cm which is the average used in

the PSI nEDM experiment. The insulator uses the dielectric constant for Rexolite and quartz for the windows. This results in the following field shown in Figure C.2 and C.3.

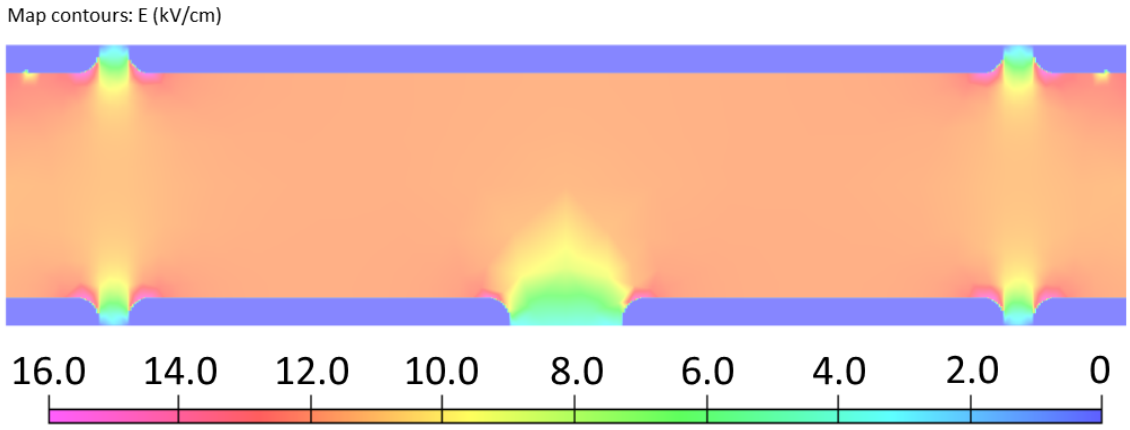

Fig. C.2 E field simulation of the nEDM experiment in the XY plane. The E field is in kV/cm.

The simulation shows that the highest fields are in the groove to wall region which is in agreement with simulations done in section 5.5. The interesting difference with those simulations is the field in the centre of the insulators is almost the same as the applied field of 11.67 kV/cm, showing the insulator hardly diverges the field. The big issue is the hole in the middle of the ground electrode. This hole creates a large, non-uniform region which the UCN's will occupy. The E fields at the grooves seem to be larger then the applied field, which could contribute to the non-uniformity of the volume.

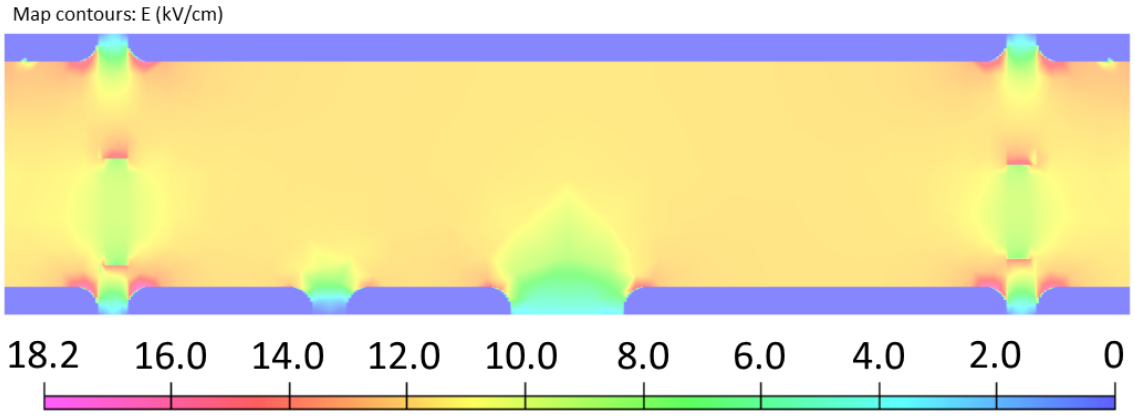

Fig. C.3 E field simulation of the nEDM experiment in the YZ plane. The E field is in kV/cm. This different orientation shows the affect of the quartz windows and mercury port on the E field. The highest field is now located at the edge of the quartz window, closest to the ground electrode, creating a potential weak point in the system.

The plane shown in Figure C.3 is more non-uniform then that shown in Figure C.2.

However, this is a small cross section of a very large cylinder, therefore, the contribution to the uniformity will be minimal.

C.4 nEDM E field uniformity

Opera is able to extract the E field at intervals over a 3 dimensional space. The intervals used were every 5 mm in x, y, and z extracting the magnitude of E at each point. The choice of 5 mm intervals was due to the size of the data file created when doing it every 1 mm, which would make it difficult to use.

The programme creates a box using these intervals, with the limits being the surface of the ground electrode, HV electrode, and insulator walls (the UCN volume). The box will have data points outside the cylinder so these numbers are removed for the analysis. The groove region is ignored as it contributes a very small volume towards the overall UCN volume. The field is also higher then the applied field which would cause the determined uniformity to be closer to the applied field from averaging with the lower field regions. The volume of the mercury and UCN ports are also not taken into account as they would normally be sealed flush with the ground electrode surface.

The uniformity is determined from this box by calculating the average E field. The average field can be considered the average field that the UCN will pass through during a nEDM measurement. The simulation gives a result of |E| = 11.54 kV/cm, compared to the expected field of E_0 = 11.67 kV/cm. This gives a non-uniformity to 1% of the UCN volume. However, this does include low field regions above the UCN and mercury ports. In the actual PSI nEDM experiment, this region does not exist as a plug sits flush to the ground electrode surface. For further consideration the groove region should be taken into account as UCN will get trapped there for considerable amount of time which may contribute to a systematic effect. Therefore, this non-uniformity number can be considered the worse case estimate.

C.5 Further analysis to be done

In Kuzniak (148) an analysis is performed on the vxE effect for a non-uniform E field on the PSI nEDM setup. This simulation uses a 2D model with perfect geometry (no grooves or holes in the ground electrode). This analysis produces an approximation for the vxE systematic effect, assuming a bulk rotational velocity of the UCN. This could be considered the lowest value for these particular systematic as any deviation of the E field will increase this systematic limit by changing uniformity of the E field. Therefore, a step beyond this using the 3D model and detailed geometry would be necessary in

order to investigate this effect further.

Another aspect that would be critical to be investigated, is the reversibility of the E field. This field is required to be reversible to order 10^{-4}, but the effect on a false nEDM and how to measure this reversibly is important to investigate.

Appendix D

Ballast Resistors

The power supplies used for the breakdown measurements presented in this thesis are designed for ±130kV discharge. However, running them back to back carries a risk that they could be damaged when twice the voltage is passed through them. In order to try to prevent this, two ballast resistors were constructed.

D.1 Ballast resistors construction

The body of the resistors are made of two aluminium plates, with 141.5 cm separation, that sit parallel from each other, supported by wooden stands. A threaded connector on the outside of the resistors, which the ground sheath of the Spellman HV (142) cable is connected to is bolted in the centre of each plate. On the inside a PVC tube, similar diameter of the HV cable, is bolted on, extending 37 cm from the aluminium plate. The end of the tube has a brass cap with a barrel connector attached, glued in place. Around the outside of this smaller tube is a larger PVC tube, 7.5 cm diameter and 0.5 cm wall thickness. This is also bolted onto the aluminium plates. The reason for the smaller tube is to act in the same manner as the cable connection to the power supply (141). The two larger PVC tubes are then connected to each other by a G10 tube 67 cm long, diameter 6.5 cm and wall thickness of 0.5 cm. The G10 is then bolted into the PVC tubing on both sides.

In order to shield the connections with the cable and the brass cap from high field regions, corona rings are added on both sides. This gives a zero field region where the cable will meet the resistor chain, electrically connected to the two brass caps. The corona rings are held in place with aluminium disks bolted onto the G10 tube. The corona domes are made of two halves which sit on the aluminium disk. The rings are electrically connected to the brass cap with a braided metal strip, bolted onto the brass

cap and the aluminium disk. The resistor chain is then attached to the two brass caps with barrel connectors. This chain sits freely inside the G10 tube.

Fig. D.1 Image of the constructed ballast resistor.

D.2 Determination of the required resistance

The required resistance for the circuit is determined by finding a suitable charging current, large enough to prevent damage, but still able to trigger the shutdown operation of the power supply if too much current flows between the electrodes. The final point is the most important, otherwise a breakdown could occur but the power supply will keep charging it back up again, causing more breakdowns when the fluid may be in a disturbed state.

In order to satisfy these conditions some calculations are required for information about the power supply (± 130 kV at 10 W (141)):

$$P = IV = 10 = I \times 130\,\text{kV}, \tag{D.1}$$

$$I = 76.9\ \mu\text{A}. \tag{D.2}$$

This is the maximum charging current that can be supplied by the Spellman power supply.

The power supplies have a current overload option built into them to shutdown the power supply when an external fault is detected. This is stated as an overcurrent greater than 104% of maximum output current produced by the power supply. This setting not only indicates if a breakdown has occurred but will also protect the power supply in case such an event occurs, giving a overcurrent of:

$$1.04 \times 76.9\mu\text{A} = 80\mu\text{A} \tag{D.3}$$

In some of the KEK breakdown measurements, the current supplied by the Spellman does show numbers above this value which does lead to shutting down the power supply. Therefore, in order to match that overcurrent with ballast resistors included in the circuit, one finds:

$$R = \frac{V}{I} = \frac{130 \cdot 10^3\,\text{V}}{80 \cdot 10^{-6}\,\text{A}} = 1.625\,\text{G}\Omega. \tag{D.4}$$

This resistance is quite large, therefore, it was a concern that the charging current would be affected (capacitance is ~ 1 nF as stated in section 5.4):

$$\tau = RC = 1.625 \cdot 10^9 \times 1 \cdot 10^{-9} = 1.625\ s. \tag{D.5}$$

There was concern that this resistance was too large and would limit the cratering damage to the electrode surface, therefore, it was decided that 1.2 GΩ would be more

appropriate:

$$\tau = RC = 1.2 \cdot 10^9 \times 1 \cdot 10^{-9} = 1.2 \text{ s}, \tag{D.6}$$

$$I = \frac{V}{R} = \frac{130 \cdot 10^3 \text{ V}}{1.2 \cdot 10^9 \ \Omega} = 108.3 \ \mu\text{A}. \tag{D.7}$$

This still gives a reasonable overcurrent value which should still protect the power supplies from any potential discharge. Therefore, two resistor chains were constructed using 12 Vishay 100M Ω 25 kV 10 W HV resistors in two series chains of 6 (143). The ballast resistors are then placed between the positive and negative power supplies and the HV feed.

D.3 Performance

Initial charging of the resistors after construction, with the HV feed side disconnected, resulted in a lot of discharging and sparks occurring up to the maximum voltage of 130 kV. A large leakage current was present throughout. The resistors took half a day before the leakage current disappeared and the voltage stabilised at 130 kV. One resistor struggled to achieve the maximum voltage at positive polarity, limited to 110 kV, constantly breaking down somewhere internally. However, for this particular resistor running at negative polarity worked without incident. Therefore, this resistor would only operate on the negative polarity side.

As these resistors were prone to large amounts of leakage current (> 1 μA) it was best to condition them for 15 minutes before performing any breakdown measurement. After this time at 130 kV the leakage current would completely disappear, therefore, not hide any potential leakage which may come from the HV feeds.

Appendix E

Blue Elbow performance

E.1 Introduction

The performance of the Blue Elbow cryostat will be discussed here when used with LN_2 and LHe in the SV. The temperature of the cryostat is monitored in a number of places using K type thermocouples.

The use of the temperature monitoring is only performed during the cool down and warm up and not during the breakdown measurements. The reason is that the discharge is unpredictable as to where it will travel to ground, therefore, all the sensors are disconnected from the mains and computers to protect all electronic devices.

E.2 LN_2 cooldown and warm up

During the LN_2 runs the temperature of these sensors was monitored by a Fluke 51 K/J thermometer. The only sensors that were present at the time were C, D, E, F, G, and H. The silicon diodes and thermocouple were not added in the system till LHe runs. This initial cooling of the cryostat was performed during the first LN_2 runs as the radiation load from a warm shield would contribute ~ 13 W at 200 K heat input which would cause significant boil off of the volume. The side feed could also contribute heat input to the bottom electrode which could have resulted in bubbling on the inner surface of the electrode, reducing breakdown voltages. The initial cooling of the shields provided the base temperatures of the cryostat thermometry:

The cooling of the shields was found to take ~ 100 litres of LN_2 to cool to 100 K. However, the shields operated as expected, getting down to 100 K for measurements and remaining at that temperature for ~ 24 hours when the tank is filled with 25 litres of LN_2. When the insert is connected to the cryostat shields via the copper straps from the

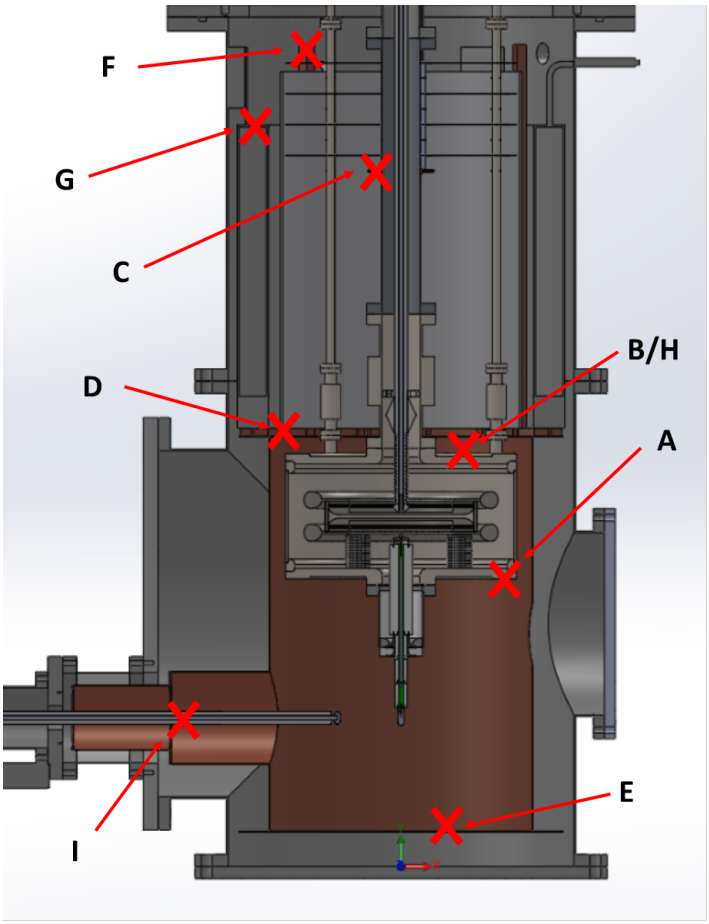

Fig. E.1 Location of the thermocouples and silicon diode placement on the Blue Elbow cryostat. The silicon diodes are as follows: A is bolted on to a copper plate which is in turn fixed to the bottom of the SV with indium and B is bolted to the heater copper plate on the top of the SV, glued with Stycast 2850FT. The K-type thermocouples are attached in various places as follows: C is varnished to the copper heat sink underneath the bottom radiation baffle; D is taped to the copper feet underneath the LN_2 tank of the cryostat; E is taped to the bottom of the 100 K copper radiation shield; F is bolted onto the copper bar which is attached to the inner aluminium radiation shield, these bars are bolted to the copper feet of the LN_2 tank; G is varnished to the top of the LN_2 tank; H is also attached to the copper plate with the heater (this is in order to monitor temperature for heater operation); I is bolted in place with indium on the thermal clamp which is clamped around the side feed.

Temperature sensor	Ultimate temperature (K)
C	117.7
D	91.2
E	111.0
F	105.1
G	98.8
H	86.6

Table E.1 Ultimate temperatures recorded for the various sensors.

copper clamp on the baffle assembly to the copper bars, the system would warm at a rate of 2-3.3 K/hr with the SV at 77 K and the shields at 100 K.

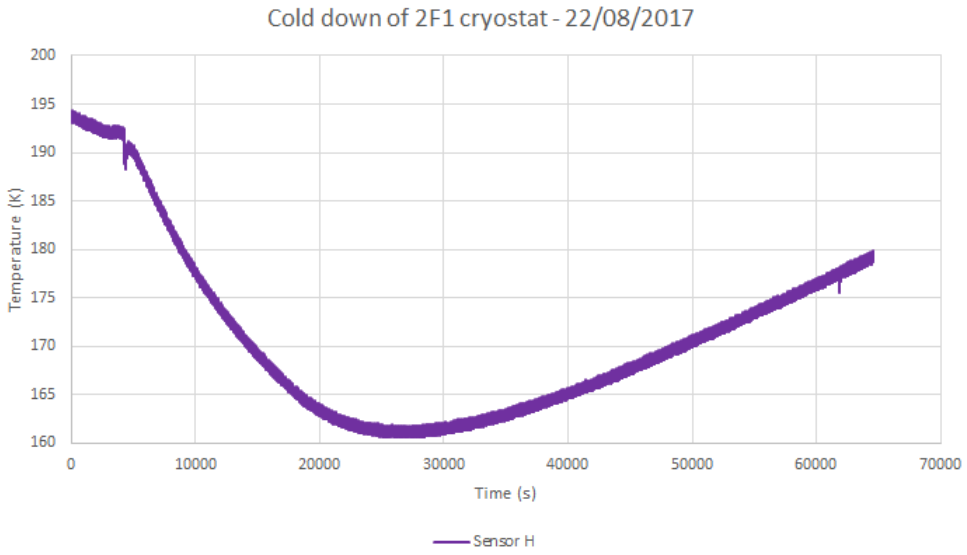

Fig. E.2 Example of cooldown to warming of sensor H on the copper heater plate. At ~ 5000 seconds the SV is filled with LN_2

E.3 LHe performance

Before performing the cooldown with LHe, better thermometry was required, therefore, 2 silicon diodes (A and B) were added as well as an additional thermocouple I. The silicon diodes were calibrated and found to have an offset at their base temperature (4.2 K for sensor A is 6.00 K and sensor B is 5.79 K). The reason for adding I was to check if the feed was cold enough when moved into contact with something at 4.2 K and if this would make a difference to the temperature of the bath. The heater wires and silicon diode wires were thermally anchored on the baffle assembly in various points by GE/IMI 7031 varnish (164). Three thermocouples (C, G, and F) contact points were changed in order to try to improve thermal contact with the shields and insert. C was previously bolted via a CuBe nut and bolt with some indium, however, this connection was observed to be loose after the final LN_2, therefore, it was instead kept in contact with the copper clamp by varnishing it to the plate. G previously was taped down with mylar and this was changed to varnish. F was clamped between the copper strap, indium, and copper bar. This proved to be problematic as this connection was broken each time the insert was removed, therefore, it was instead bolted into the side of the copper bar between some indium. The transfer tube used to get the LHe into the SV had a sintered metal filter attached on the dewar side.

The performance of the cryostat, during cooldown and warm up, was monitored, as

shown in Figure E.3.

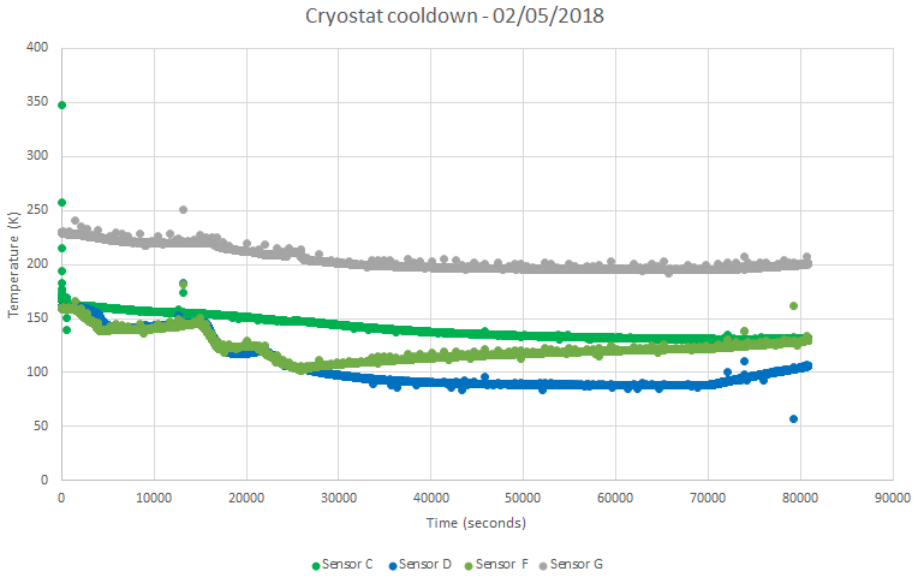

Fig. E.3 Temperature of the various sensors against time for pre-cooling for LHe cooldown 1. Monitoring of the cryostat was started after cooling half way to the ultimate temperature of the shield. 4 fills of LN_2 were performed which are indicated by the sensor D and F dropping.

The performance of the thermometry is questionable from these plots as lower values would be expected, closer to that of 77 K. The heat input to the chamber was calculated to be 1.38 W during these nitrogen cool downs.

E.3.1 LHe cooldown 1

The procedure of this cooldown is to get the shields to the base temperature with LN_2 filled up in the tank and the SV cooled with LN_2 to the level required for LN_2 breakdown runs (the liquid is 1-2 cm above the stress cone of the HV feed). At this point the LN_2 in the SV is siphoned out by pressurising the chamber to ~ 5 Psi. The SV will warm slightly to 80 -100 K till the LHe is transferred out, which ensures all the nitrogen is not present in the SV. It is noticeable on sensor A when the nitrogen has all been blown off by a sharp rise in temperature.

After the removal of the nitrogen from the SV, it warmed to 100 K and transfer of LHe was performed. At this point the use of a multi channel thermocouple data logger (Pico USB TC-08) (165) was used for 8 channel monitoring in real time.

The LHe was filled into the SV a couple of times (indicated by the saw tooth shape of sensor A data in Figure E.7) and allowed the gas pressure in the dewar to decrease while

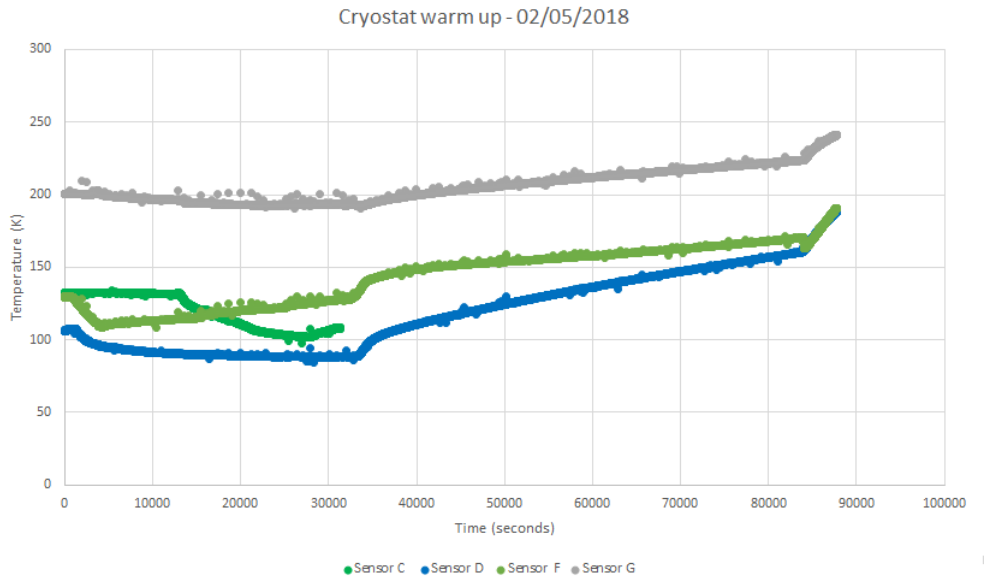

Fig. E.4 Temperature of the various sensors against time during a warm up. This data continues after the previous cooldown, with one fill at the beginning to reach lowest temperature. After 10000 seconds the SV is filled with LN_2 which is indicated by the drop in temperature of sensor C. Sometime after the filling of the SV the thermocouple stopped working for an unknown reason. The shields start to warm at ~35000 seconds as all the LN_2 was blown off. At 85000 seconds the vacuum is broken with dry N_2 to 100-200 mbar in order to speed up the warming process.

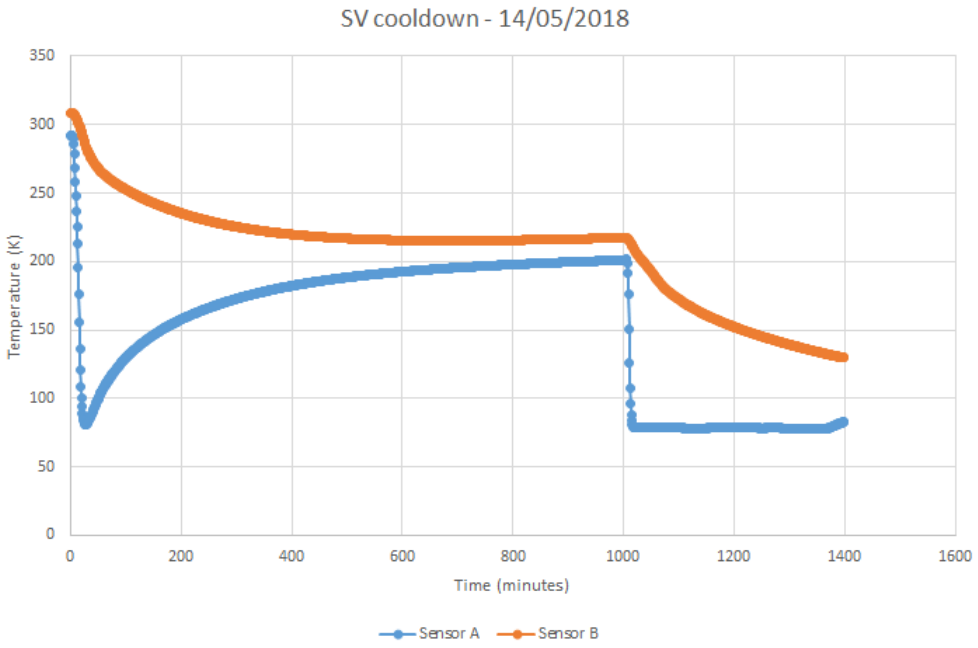

Fig. E.5 Temperature of the various sensors against time during a cooldown of the SV. The cooldown starts at room temperature, filled with 10 litres of LN_2, then left in order to gas cool the setup. This procedure is performed twice. At the end of the data, sensor A begins to rise, indicating all the nitrogen has boiled off. Leaving it overnight, SV is then filled to the experimental level with 20 litres of LN_2.

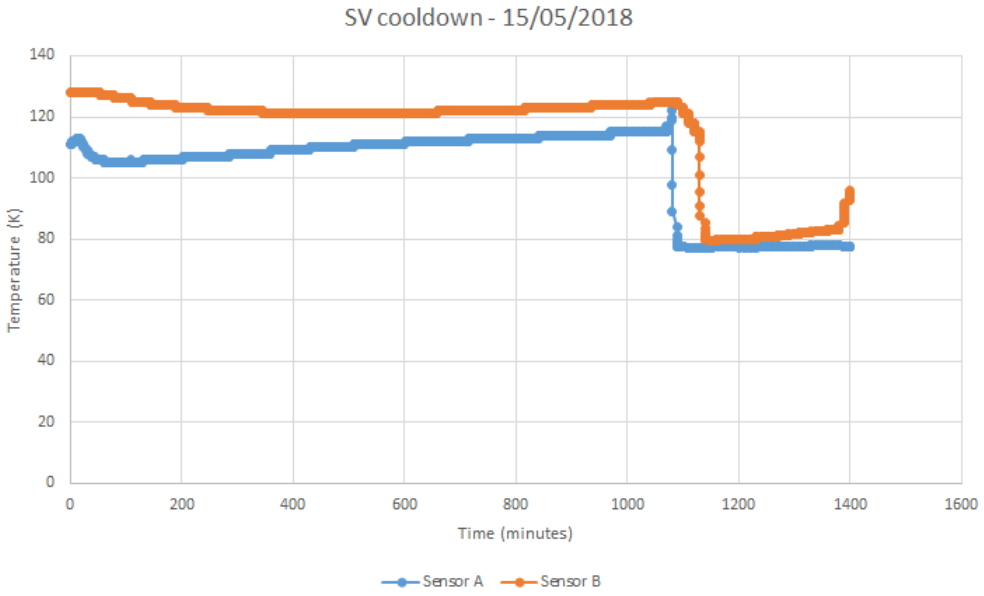

Fig. E.6 Temperature of the various sensors against time following on from the previous cooldown of the SV. The SV is ready at this point to fill to the experimental level with 20 litres of LN_2. This cools the top plate to a sensible temperature for LHe. Once at the correct temperature, the LN_2 is siphoned. Once it has all been siphoned sensor B rises. There is a volume in the G10 feedthrough on the bottom plate which cannot be removed, therefore, once that boils off the sensor A will rise indicating it is ready for LHe transfer.

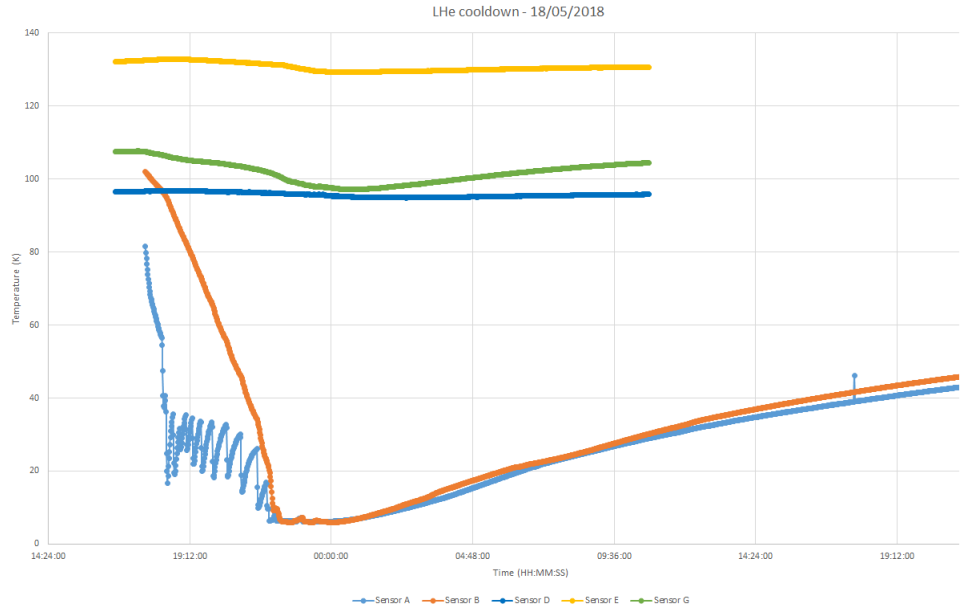

Fig. E.7 Temperature of the various sensors against time. Sensor A, B, D, E, and G were the only ones monitored as sensor C failed previously.

the top plate cooled, therefore, periodic filling. The issue found with the procedure used was that an in line flowmeter and gas meter was restricting the filling of the chamber, potentially causing back flow of LHe into the dewer. Eventually the top plate cooled to LHe temperatures and small amount of LHe was present at the bottom of the SV.

This process was not very efficient and used up ~ 60 litres of LHe without being able to fill the SV to experimental level. There is some noticeable features in the data. Sensor F (copper bar) observed a large drop in temperature which seems to be correlated with the falling temperature of the top plate. The other two sensors D and E also show a slight drop, of a few degrees. At this point this feature was not noted and another LHe fill was performed.

E.3.2 LHe cooldown 2

The shields were kept cold from the previous cooldown and the vacuum was not broken.

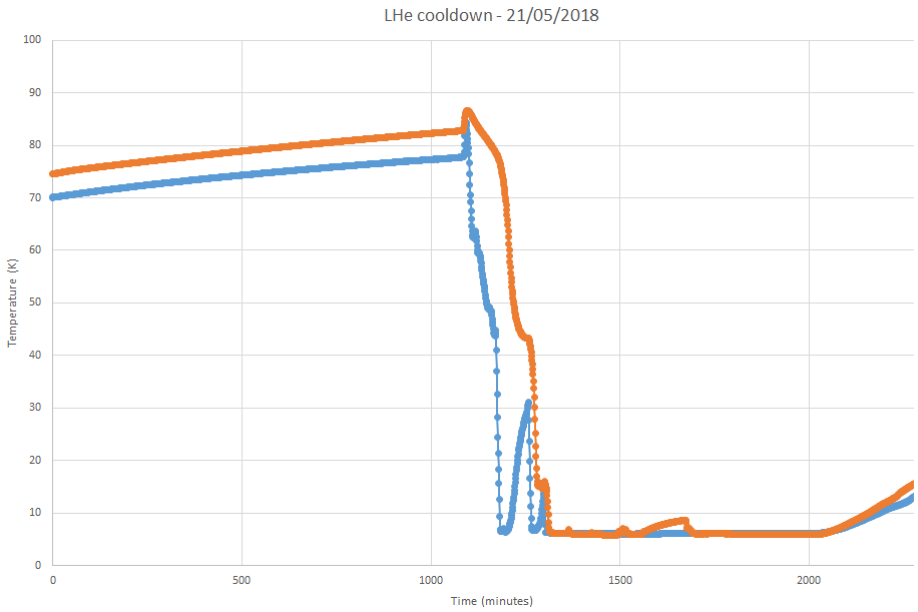

Fig. E.8 Temperature of the various sensors against time. Sensor A and B where the only ones monitored, due to an issue with the data logger.

In Figure E.8 the SV started at 75 - 85 K. The initial increase in temperature was due to warm gas through the transfer tube. The SV was filled with small amounts of LHe 3 times, until the top plates temperature drops to within a degree. The liquid level this time was monitored and found to reach approximately half way up the SV and potentially reaching the top plate. This is approximately 10-15 litres of liquid in the SV. Again during this run gas restriction on the blow off port was causing problems. Unfortunately the SV was unable to be filled as the LHe dewar was emptied before the

liquid reached the experimental level.

As the dewar was empty but liquid was present in the SV the effect of putting the HV feeds into contact could be looked at. First the side feed was moved in to contact with the ball electrode on the G10 feedthrough. It was left in this position for 20 minutes, with the temperature monitored. The temperature of the bath did not change. This result was somewhat expected, as to make electrical contact it requires very little force so not much heat can transfer between the two electrodes. The central feed was moved into contact with the top electrode. It resulted in a jump in temperature of the top plate, hence the feature in Figure E.8 for sensor B. The feed was then removed from contact with the top electrode and the temperature of the top plate dropped back to the previous temperature. The conclusion is that the HV feed may have came into contact with something on the insert or top plate implying the feed was too warm. Davidson (2) had similar problems with the HV feeds in his setup initially.

The liquid remained in the chamber for approximately 11 hours, giving a heat input of 0.8 W to the liquid volume.

At this point the method of filling the SV was very wasteful, therefore, a heater was added to the LHe dewar instead of pressurising to gas cool in a more controlled manner.

E.3.3 LHe cooldown 3

This cooldown was done with a gas cool in order to be more efficient with the LHe use. The shields and cryostat was kept cold from the previous LHe cool down attempt.
In Figure E.9 the bump at the beginning of the data was due to the cryostat warming as LN_2 had blown off in the tank, but was quickly cooled back down again. An initial He gas transfer occurred, indicated by the decrease in sensor A and B. The liquid transfer was unable to occur, therefore, it was then left overnight and warmed to 40 K. The next day the transfer tube was pre cooled by blowing liquid through it before being put back into the SV. Then a gas transfer was performed till both sensors reached < 10 K, at which point liquid was transferred. After attempting to cool with liquid it was stopped as sensor B had a sharp rise in temperature indicating something connected to the top plate was still not cold enough. The cooldown was stopped at this point having used up 60 litres.

The He gas transfer worked better in cooling the top plate more efficiently, using only 15 litres instead of 60 to reach the same temperature, however, something in the system was clearly not cold. The features present on sensors D, E, F, and G that was seen in the

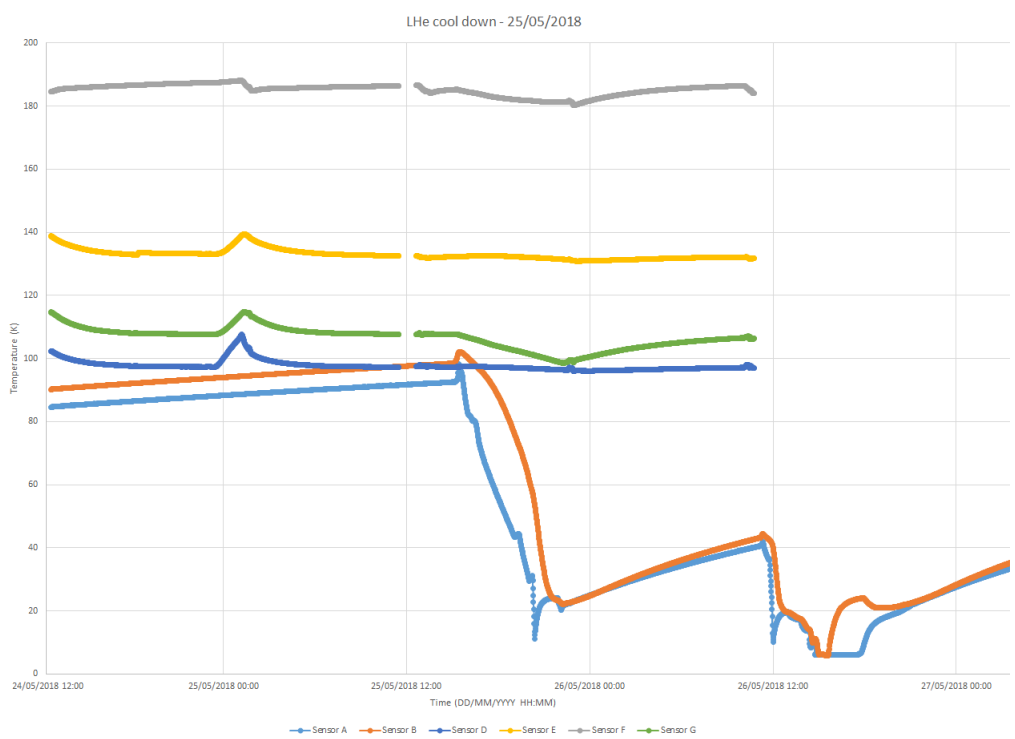

Fig. E.9 Temperature of the various sensors against time. This run sensor A, B, D, E, F, and G where used. The data logger again had problems before filling the SV with LHe, hence temperature data was not recorded for sensors D, E, F, and G after LHe fill.

temperature data in the first cooldown is also visible here. Taconis oscillations were present in the transfer line feedthrough, only this tube was closed off. The conclusion was that there may have been Taconis oscillations in the feedthrough with the transfer line and possibly the HV feed. A tee piece was added to the transfer line and the HV feed was filled with super-insulation and a brass thread screwed in at the HV cryogenic side to try to overcome the oscillations. This insert was also thermally anchored to the cryostat via copper straps from the copper bars to the copper clamp underneath the bottom radiation baffle. Its possible the He was cooling the shield indicated by the drop in temperature of sensor F, therefore, for the next run these straps were removed.

E.3.4 LHe cooldown 4

Before performing this run, there were concerns that the PTFE stress cone on the HV feed was not getting cold enough. Therefore, in order to guarantee that the feed would not be the problem, CuBe thermal clamps were made and attached to the feed. These clamps are of a similar design to what Davidson (2) used in his setup. Radiation baffles were also fixed to the HV feed to minimise thermal radiation down the central bore of the insert which have been could be causing problems. Sensor C was also fixed at this point. The copper wires for the heater were also disconnected and then wrapped around the thin wall tube underneath the bottom baffle in order to remove further heat

input to the SV.

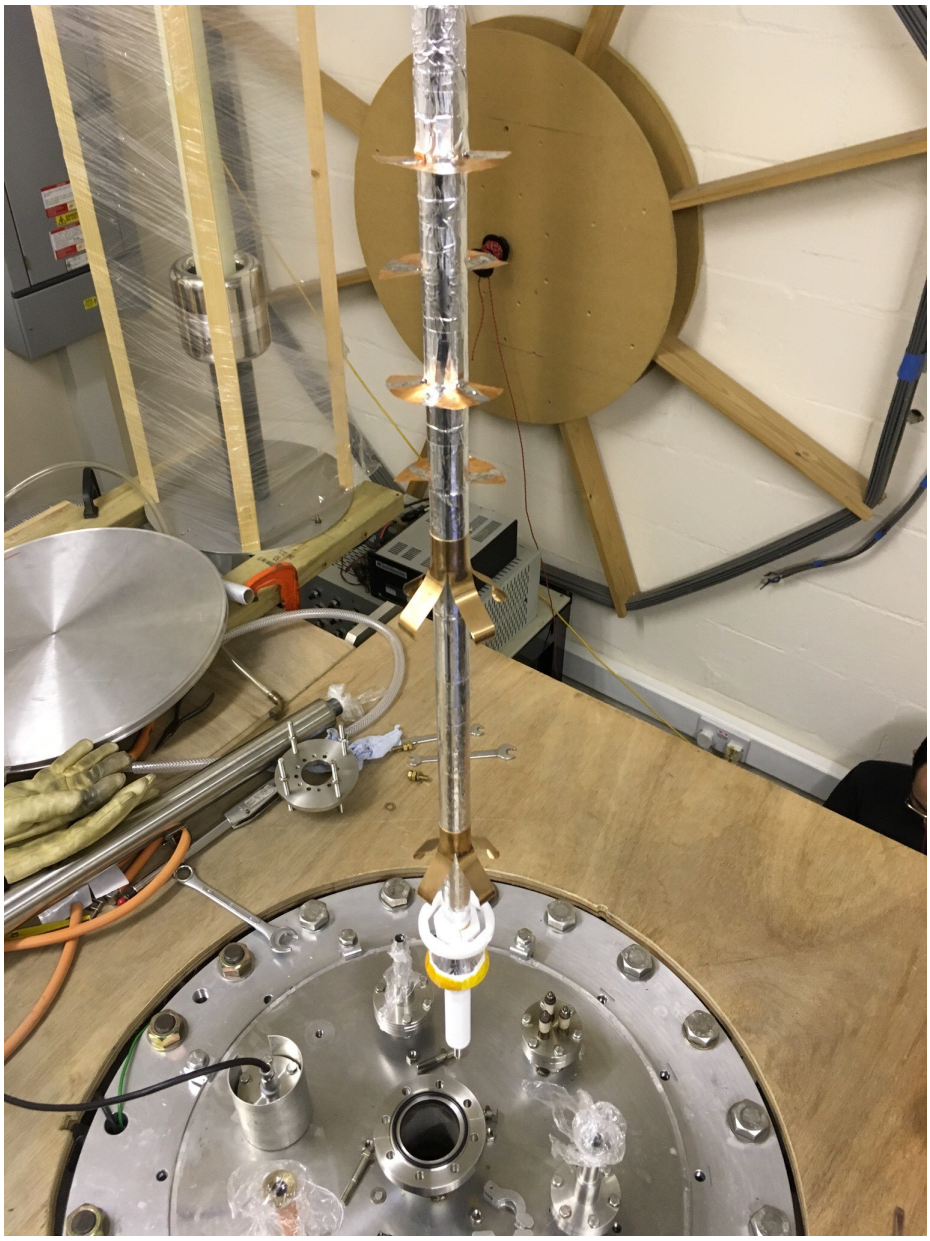

Fig. E.10 HV cryogenic feed with the CuBe clamps in two positions and radiation baffles. The bottom clamp would be in contact with the top of the CF63 bellows above the SV, the second is in contact with the copper clamps around the bottom of the baffle assembly. The four half noon radiation baffles are placed in the same position as the inserts baffles.

The system was pre cooled with LN_2. The performance of the cryostat was no different to that before the modifications. As the cryostat got cold, the temperatures of the SV was compared and both were clearly isolated from each other. The SV was pre cooled by filling of LN_2 then siphoned out. However, upon siphoning of the LN_2 it was found to take significantly longer to boil off the remaining liquid at the bottom of the SV. It is

likely that only1-2 litres of LN_2 remained in the SV, however, it took ~ 16 hours (compared to 30 minutes before) till this completely boiled off and sensor A started to rise. The implication is that the changes made a large difference to the heat input of the SV. Once the LN_2 had boiled off the temperature had risen to ~ 90 K, at which point He gas transfer was performed again.

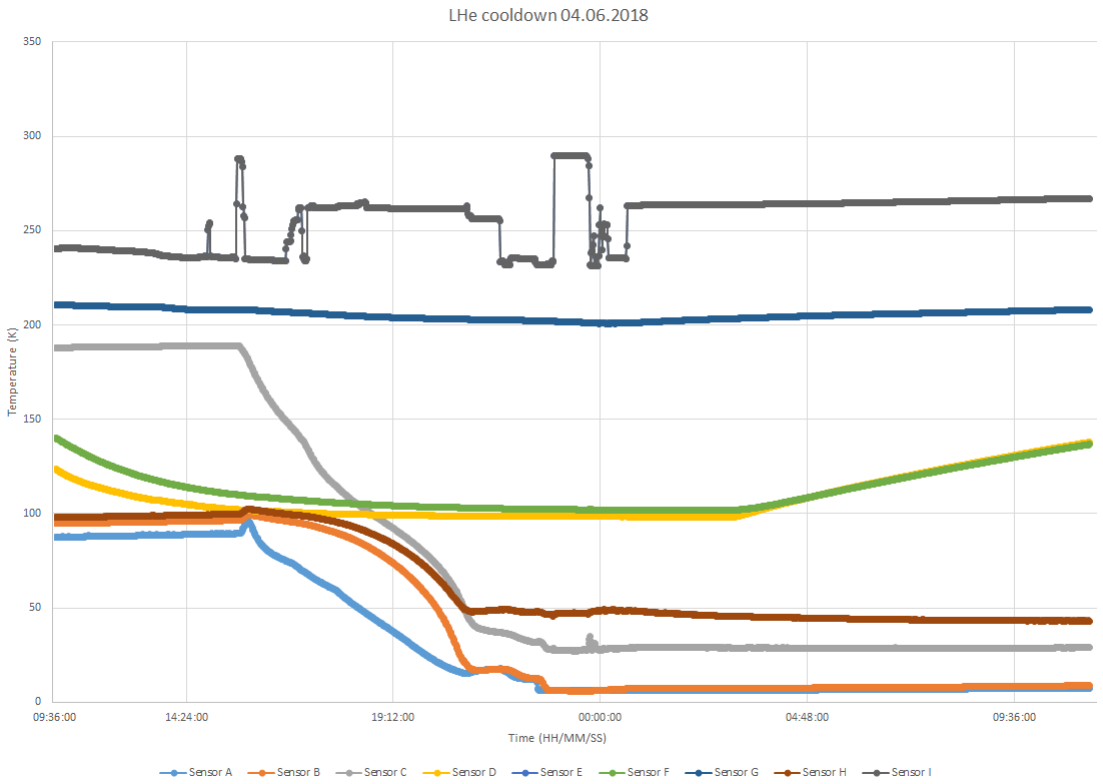

Fig. E.11 Temperature of the cryostat and SV versus time for LHe cooldwon 4. Sensor I was clearly not responding as expected possibly some poor connection between the thermocouples. Sensor G still had the same response as before, dropping a few degrees. Its unclear why this was occurring.

In Figure E.11 the gas transfer again initially caused a rise in temperature before falling. This gas transfer took 4 hours, compared to 5 on the previous cooldown, again only using ~ 15 litres to cool the SV. Sensor C and H clearly responded better this time to the He gas, dropping to less than < 50 K at the bottom of the baffle assembly, implying that the copper strapping to the shield was causing problems previously. The gas transfer was only able to drop the temperature to ~ 15 K before leveling off, and at this point liquid was transfered. The filling of the chamber had issues, the blow off ports were again connected to the gas meter. Upon filling the level was taking a long time to reach the top of the chamber. It was noticed that the pressure on the dewar side was too high, implying that back siphoning was occurring, therefore, the gas meter was disconnected and this seemed to correct the problem.

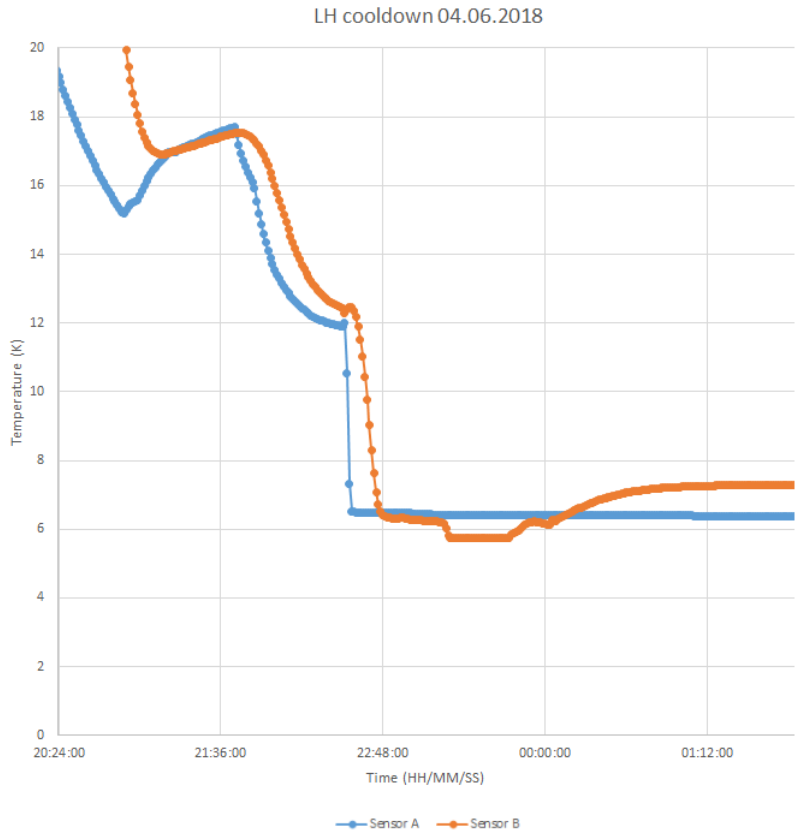

Fig. E.12 Close up of temperature of the SV versus time. The first rise in temperature is from moving the transfer tube closer to the liquid level. This is followed by a sharp fall which is when liquid was transfered.

In Figure E.12 the temperature of sensor B tracked much better to that of sensor A. The SV filled up to the top plate, however, the blow off tube on the level sensor was blocked so it was unclear if the liquid start to fill up the central bore of the insert, but this probably occurred. However, at this point the blow off rate of the liquid increased, implying something higher up was still warm. Unfortunately the dewar run out of LHe so was unable to force cool whatever was still warm and get liquid up the past the stress cone of the HV feed. At this point to find out what the actual level was, one of the tubes from a side port was opened up. This caused a huge amount of gas to shoot up the port, there was definitely liquid oscillations on this port. The level was dipped on this port. The liquid was found to be covering the top electrode. The implication is that the liquid was probably at the top plate and above that into the tubes, having lost a lot from dipping and the liquid oscillations. After this the top plate started to rise as can be seen in Figure E.12. There is a slight dip in the temperature, implying that whatever was warm above the top plate had finally gotten cold.

At this point it was decided that the flanges on the insert were probably what was

keeping the top plate still warm. They are large pieces of stainless steel which are not necessarily well connected to the rest of the system. Therefore, once the system had warmed, the insert was extracted and the flanges put into thermal contact to the rest of the SV with copper straps.

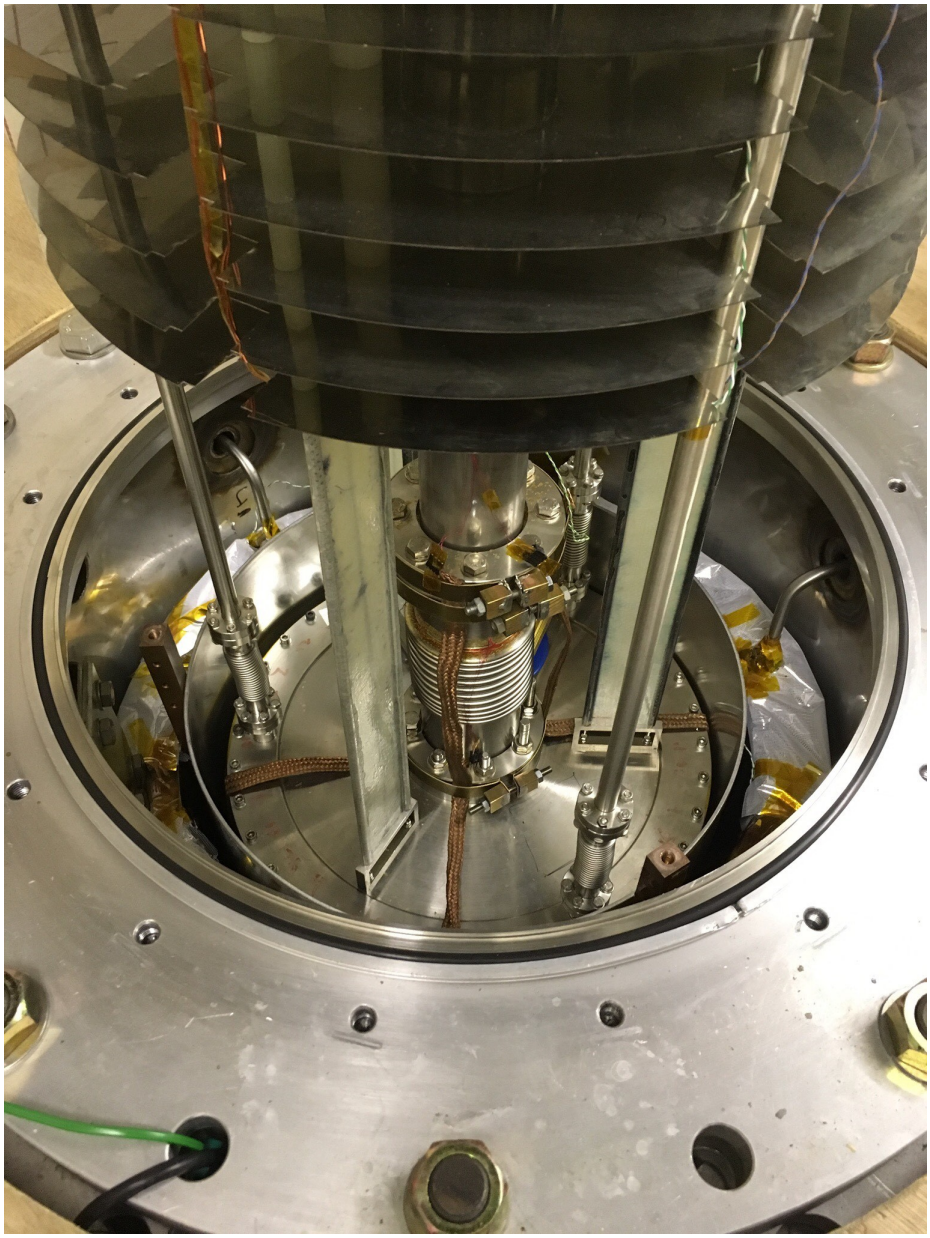

Fig. E.13 Insert being placed into the cryostat. Thermal straps are visible on the top plate of the SV. They are clamped in place by brass sheet, bend and bolted together. The two flanges for the bellows and flange at bottom of the thin wall tubing for the insert are thermally clamped with four copper straps. The straps then go on the outside of the SV to the bottom plate, where they are clamped to the extension tube above the G10 feedthrough.

Appendix F

Breakdown data tables

In this section the data for all the breakdown measurements are presented. The two measurements are split into those performed in the KEK cryostat and those in the Blue Elbow cryostat in LN_2. The methodology for these measurements are given in Chapter 5 and discussion of the results is given in 7.

F.1 KEK cryostat data

All these measurements where performed in LN_2.

Run number	Electrode used	Insulator material	Insulator dimensions (IDxOD mm)	Separation (mm)	Polarity	Mean breakdown voltage (kV)	Error (± kV)	Feed damaged?/Insulator damage?	Number of breakdowns	Number of craters: HV/G (initial)
1	DKHl	Al_2O_3	60x70	4.94	-	67.54	3.84	N/N	11	
2	DKHl	Al_2O_3	60x70	4.94	+	78.01	3.07	N/N	15	
3	DKHl	Al_2O_3	60x70	6.94	-/+	64.87/72.21	3.63/1.24	Y/N	18/29	
4	DKHl	Al_2O_3	60x70	6.94	+/-/+	97.51/113.76/112.71	1.87/2.72/5.06	Y/N	17/10/5	
5	DKHl	Al_2O_3	50x60	4.94	+/-	52.32/35.11	6.10/2.97	Y/N	10/11	
6	DKHl	Al_2O_3	50x60	4.94	+/-	53.71/79.27	4.47/2.57	N/Y	13/7	
7	DKHl	Al_2O_3	50x60	6.94	-	114.22	1.60	N/Y	10	
8	DKHl	Al_2O_3	60x70	4.94	+	54.72	4.18	Y/N	16	
9	DKHl	Al_2O_3	60x70	4.94	-	56.50	1.99	Y/N	20	
10	DKHl	Al_2O_3	60x70	4.94	-/+	50.47/77.41	1.52/1.51	Y/Y	15/13	
11	DKHs	Quartz	10x15	2.96	-	49.15	3.12	N/Y	17	
12	DKHs	Al_2O_3	11x12	2.96	+	54.65	2.14	N/Y	16	
13	DKHs	Quartz	10x15	2.96	-	41.65	4.86	N/Y	13	
14	DKHl	BG	60x70	2.94	-	102.32	3.68	N/Y	4	(36/25)
15	DKHl	BG	60x70	2.94	-	74.50	2.24	N/Y	16	46/52
16	DKHl	BG	60x70	3.94	-	77.00	4.57	N/Y	13	67/68
17	DKHl	BG	60x70	4.94	-	99.30	4.45	N/Y	17	86/84
18	DKHl	BG	60x70	5.94	-	35.46	12.74	N/Y	3	5/5 (0/2)
19	DKHl	BG	60x70	5.94	-	101.87	3.65	N/Y	10	13/10
20	DKHl	BG	60x70	6.94	-	98.64		Y/Y	1	
21	DKHl	Al_2O_3	60x70	3.94	-	86.88	3.88	N/N	8	
22	DKHl	Al_2O_3	60x70	5.94	-	112.05	5.76	N/Y	11	26/27
23	DKHl	Al_2O_3	60x70	6.94	-	103.28	5.24	Y/N	11	36/31
24	DKHl	BG	60x70	4.94	-	87.40	2.55	Y/Y	19	38/37
25	DKHl	Al_2O_3	60x70	4.94	+	84.18	2.87	N/N	13	50/49
26	DKHl	Al_2O_3	60x70	5.94	+	96.02	7.20	N/N	9	56/57
27	DKHl	Al_2O_3	60x70	3.94	+	64.56	2.08	N/N	12	65/70
28	DKHl	Al_2O_3	60x70	6.94	+	123.86	2.74	N/N	5	76/74
29	DKHl	BG	60x70	3.44	+	69.54	1.09	N/N	14	79/75
30	DKHl	BG	60x70	4.94	+	95.16	2.37	N/N	12	91/90

Table F.1 Table of KEK data including geometry, breakdown voltage, and damage to electrode surface. The double line break in the table represents the polishing of the electrodes.

F.2 Blue Elbow cryostat

These Blue Elbow measurements where done in LN_2 to follow on from the KEK data but also as a preliminarily tests for LHe runs.

Run number	Electrode used	Insulator material	Insulator dimensions (IDxOD mm)	Separation (mm)	Polarity	Mean breakdown voltage (kV)	Error (± kV)	Feed damaged?/Insulator damage?	Number of breakdowns	Number of craters: HV/G (initial)
31	JT	BG	240x250	6	+	67.70	3.51	N/N	13	10/10 (0/0)
32	JT	BG	240x250	4	+	54.08	1.85	N/N	14	24/23
33	JT	BG	240x250	2	+	25.12	0.48	N/N	39	61/64
34	JT	BG	240x250	8	+	103.05	4.55	N/N	15	76/80
35	JT	BG	240x250	12	+ & -	135.30	7.03	N/N	13	86/89
36	JT	BG	240x250	12	+ & -	82.79	2.83	N/N	10	95/91
37	JT	BG	240x250	6	+ & -	75.11	1.33	N/N	11	102/105
38	JT	BG	240x250	12	+ & -	96.64	1.94	N/N	10	

Table F.2 Table of Blue Elbow cryotat data including geometry, breakdown voltage, and damage to electrode surface in LN_2/LHe.

Appendix G

Mercury magnetometer performance under E field application

G.1 Introduction

The purpose of this investigation was to study the effect where by the reversal of the E field causes a drop in spin relaxation time of the mercury co-magnetometer in the PSI nEDM experiment. The reversal of the E field would drop the relaxation time from say 220 seconds to 150 seconds (one particular case) which would then recover back to a slightly diminished original value. After repeated cycles of HV reversal the maximum relaxation time would have permanently diminished to 160 seconds. This is shown in Figure G.1.

In order to stop the relaxation time diminishing, the cell is discharge cleaned. This process involves a steady leak of O_2 into the Ramsey Cell while still being roughed by a scroll pump. The pressure of the Ramsey Chambers pressure is set to 1.25 mbar, then the HV is is applied to 1.5 kV with current of 80 μA. This is done for 2000 seconds, reversing the polarity every 500 seconds. Afterwards the mercury generally recovers back to its peak value. It is not clear why this works.

For the nEDM experiment this problem has been mitigated with the discharge cleaning, however, there is a possibility that this problem could cause limitations for n2EDM, as it is planned to run at higher voltage, which causes a larger reduction in relaxation time. All work in this Appendix was done in conjunction with Rehaag (166) as part of his master's thesis.

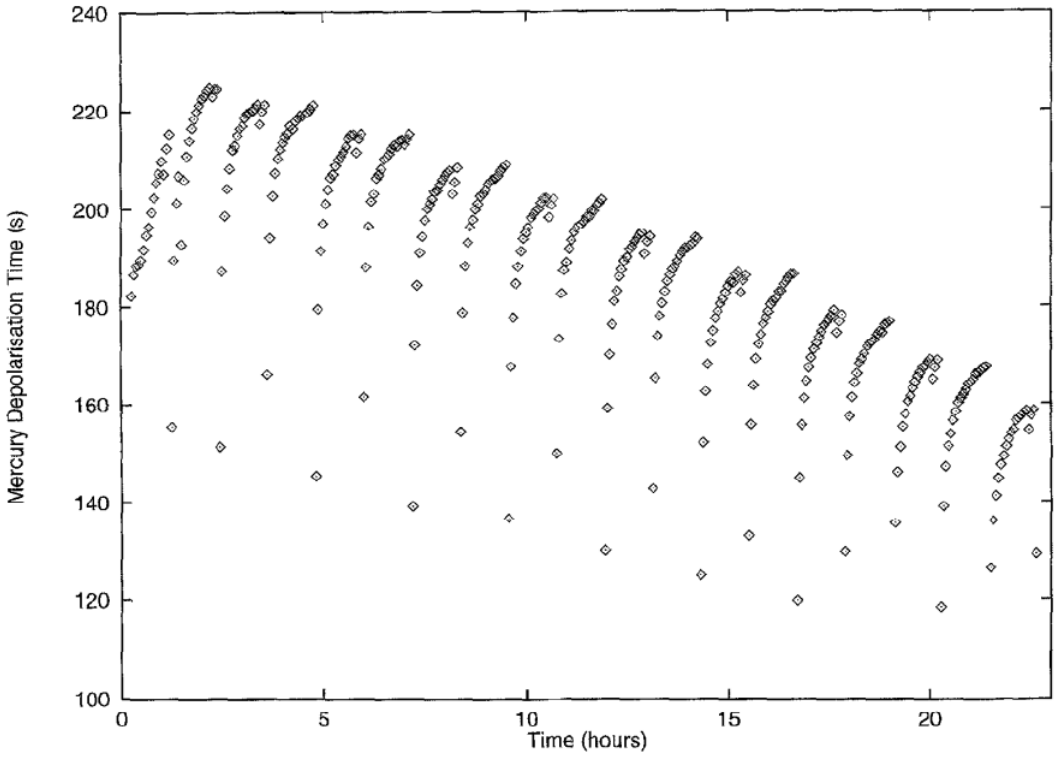

Fig. G.1 Relaxation time vs time for the mercury co-magnetometer at PSI in the nEDM experiment. Upon the reversal of the HV field, the mercury relaxation time drops, but quickly recovers back to the original value. However, there is some memory present from the previous reversal as it causes a ever decreasing value for the relaxation time after repeated cycles.

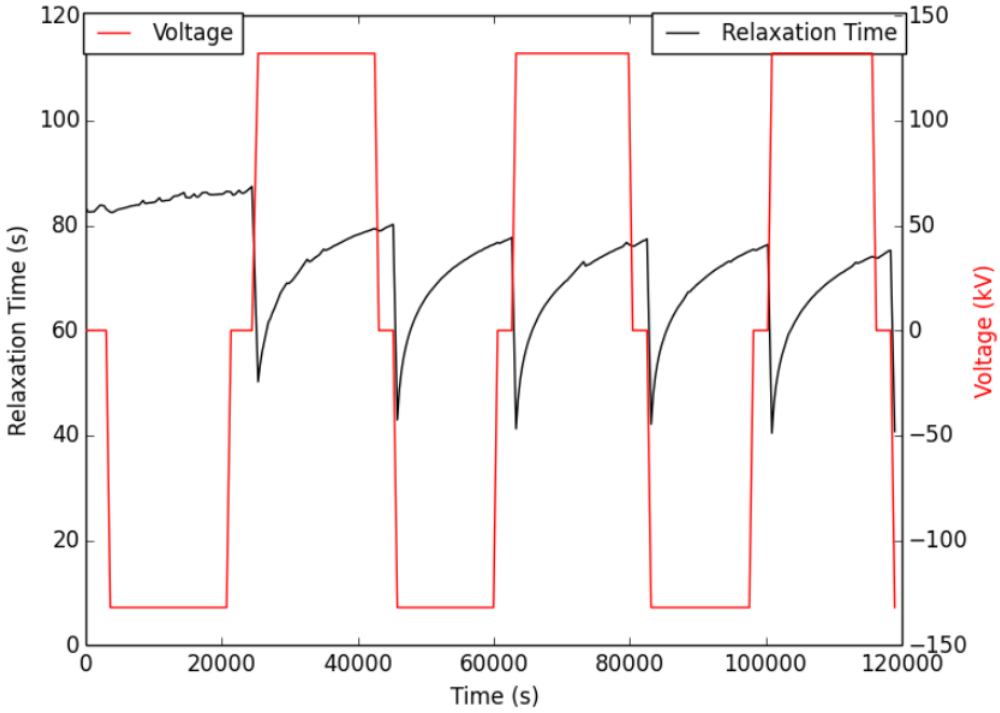

Fig. G.2 Overlap of mercury relaxation and HV ramp against time at the nEDM experiment at PSI.

G.2 PSI mercury relaxation time analysis

Rehaag (166) as part of his project, did an analysis of data from the mercury relaxation time at PSI in which a number of voltage ramps at different values were performed in order to understand this effect causing the drop in relaxation time with reversal of the E field.

G.2.1 HV conditioning effects

HV applications generally require conditioning in order to achieve their maximum designed voltage. This is due to microscopic contamination on surfaces which are very difficult if not impossible to remove even with extensive cleaning. The PSI nEDM experiment is no different, after initial application of HV there will be some conditioning present.

The HV conditioning results in small sparks, due to electrons traveling along surfaces, till the contamination is gone and a path to ground disappears. The removal of the contamination in the volume could release martial which will spin-spin interact with the mercury, causing the depolarisation. In Figure G.3, the conditioning effect is clearly correlated with the magnitude of the applied voltage, therefore, higher the electric fields that are present must accelerate the electrons giving them greater kinetic energy poten-

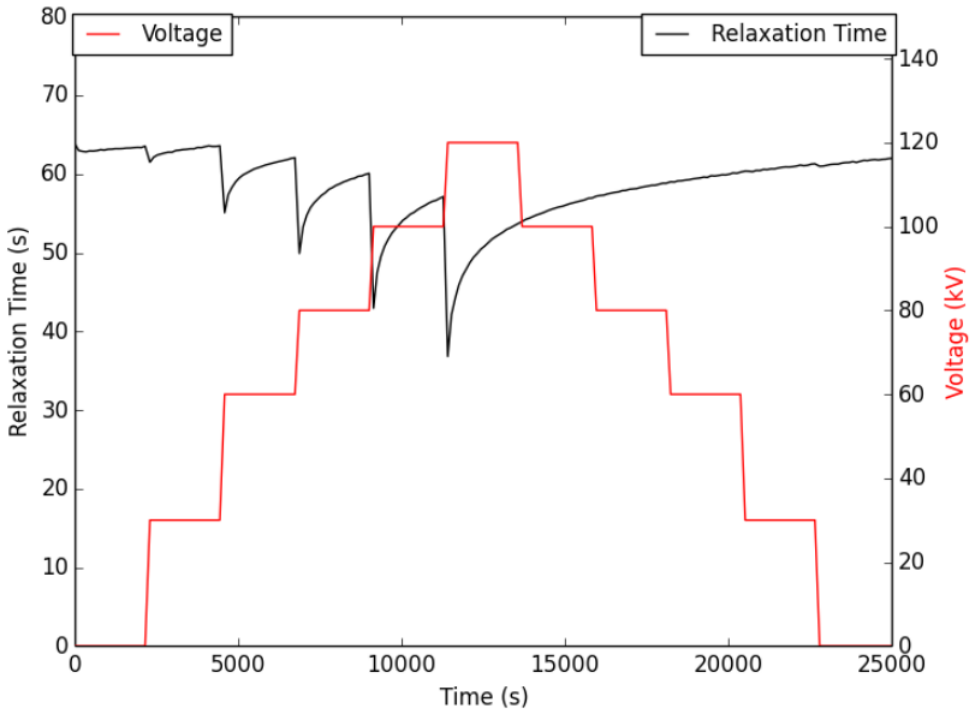

Fig. G.3 Comparison of the mercury relaxation time and voltage ramping against time at the PSI nEDM experiment. As the voltage is ramped, relaxation time drops off until the system is conditioned, then the mercury behaves normally (166).

tially displacing more material. Over a period of time, the system starts to condition, therefore the amount of sparking drops off as the system cleans off the contamination. Then, as the voltage is ramped up to 55 kV, the sparking comes back and mercury relaxation time drops off again. Further details of breakdown in gases are given in section 4.1.2.

G.2.2 Asymmetry of HV reversal on the relaxation time

The reversibility of the HV is clearly what causes this drop in relaxation time of the mercury, therefore, the two polarities can be compared to give an insight into what is happening. During a particular HV ramp at PSI the HV was cycled between the two polarities at ever increasing steps till a maximum voltage of 132 kV, then it was decreased with the same steps. The method of HV application can be seen in Figure G.5.

The drop in the relaxation time shown in Figure G.5 does not occur every time with the same magnitude. The smallest drop in relaxation time is from positive to negative polarity with the largest drop consistently happening from negative to positive. From Figure G.4 the naive conclusion could be drawn that the reversal of the HV could result in a conditioning effect from the rapid transition to the opposite polarity. In Figure G.5 this is not as clear as a conditioning process should diminish over time. In order to

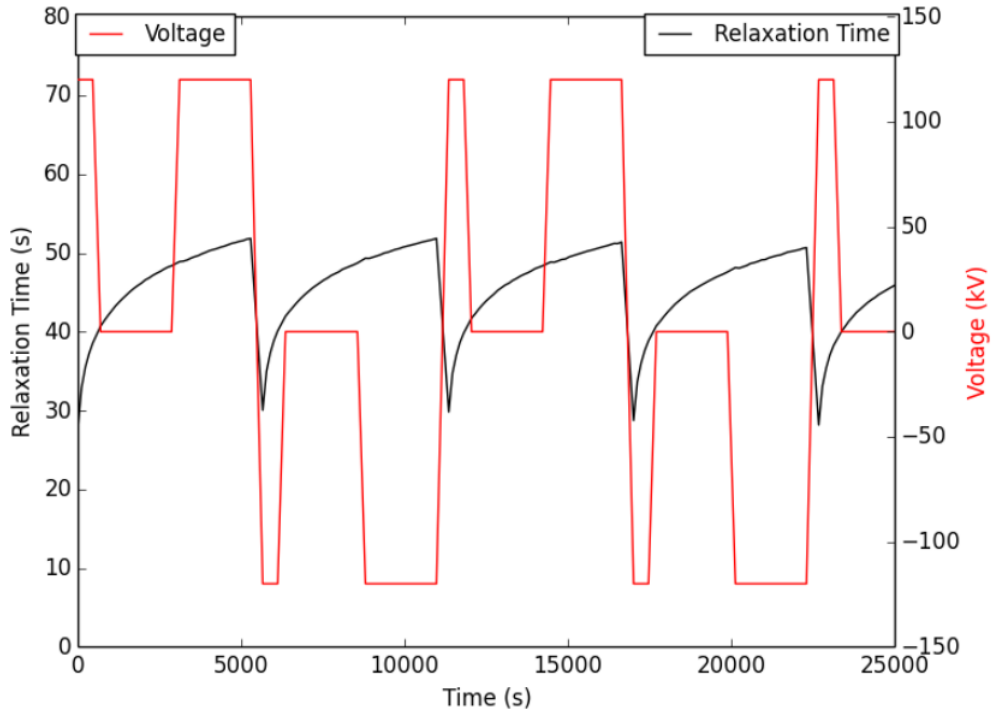

Fig. G.4 Comparison of the mercury relaxation time with reversal of polarity. The voltage is ramped twice up to the same polarity after the system is conditioned. It is clear that the relaxation time does not change after the same voltage is applied to the system. However, when the voltage is reversed, the relaxation time drops off again (166).

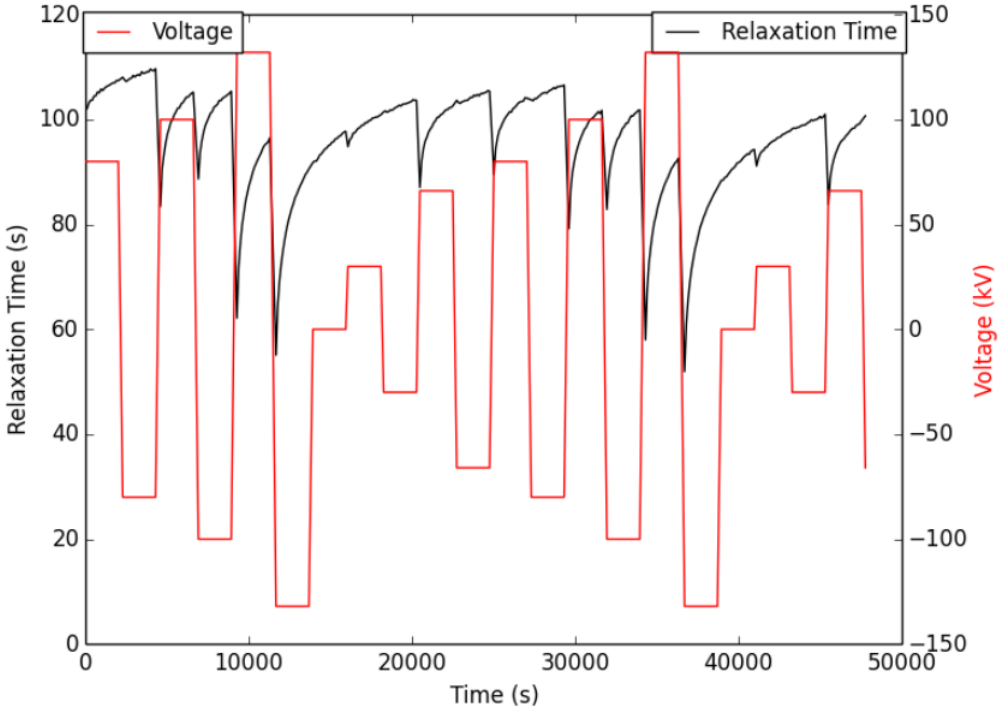

Fig. G.5 Mercury relaxation time and HV ramping against time at PSI on the nEDM experiment. The HV cycle is ramped up to a particular voltage then reversed to the opposite polarity with the same magnitude, then back to the previous polarity but having increased the voltage by 10-20 kV (166).

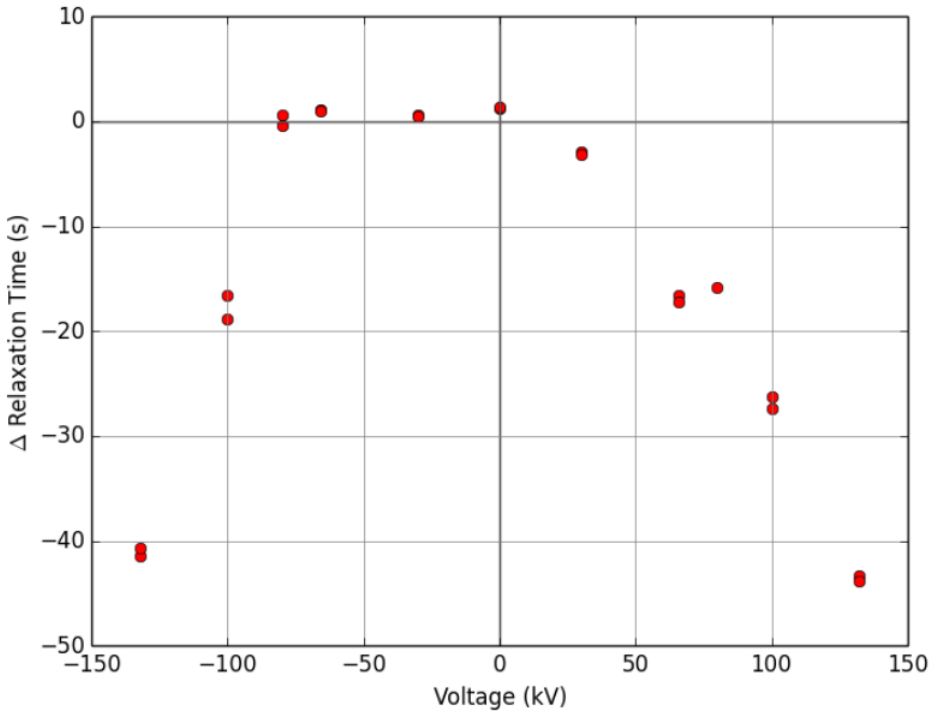

Fig. G.6 The drop in relaxation time against the applied voltage for the data shown in Figure G.5 (166).

visualise the effect, the reduction in relaxation time against the applied voltage is given in Figure G.6.

Figure G.6 shows the asymmetry much more clearly. There is a threshold voltage present on the application of the negative polarity. The positive, however, occurs from almost zero voltage, following an almost linear correlation. The magnitude of the drop in relaxation time is also different for the given polarity; at ±100 kV there is a difference of 10 seconds in the drop in relaxation time between the two polarities. This gap between the two polarities decreases to ~5 s at the 132 kV region.

One explanation for this effect occurring was thought to be due to out-gassing on the electrode surface. The high E fields could be drawing out particles like hydrogen which could spin-spin interact with the mercury, causing a drop in the relaxation time. However, this should result in a more symmetric pattern (general out-gassing would effect breakdown on either polarity). It could be due to bad vacuum conditions resulting in a breakdown: positive ions taking higher E field to draw them out for negative polarity, while positive polarity would emit electrons at a constant rate.

The effect is clearly HV correlated, therefore, a good question to ask would be: could the geometry be causing the asymmetry? In Appendix C the nEDM electrode geometry

is looked at and simulated in Opera. The HV electrode has no features on it, just the groove region in contact with the insulator. This region could be the cause, however, the same is true for the ground electrode; this feature is symmetric. The ground electrode has two holes in the surface for the mercury and UCN ports, however, Figure C.2 and C.3 show that the field on the groove edges are quite low compared to the field at the insulator wall region. The E field is quite low above the holes so it is likely this is not the problem.

This leaves the quartz windows in the insulator. In Figure C.3 the highest field present is on the bottom edge of the windows closest to the ground electrode. There are also very high fields present on the top edge of the windows too. There are two possible issues with this geometry that could explain the asymmetry. The quartz window is an insulator isolated from ground and HV in a vacuum. In vacuum, electrons can travel along surfaces as there are very limited collisions with gas molecules. Therefore, it is possible that charge can accumulate on the windows, then when the field is reversed the charge will discharge to the HV or ground depending on the polarity. The other possible cause is that the high fields cause sparking in the volume from contamination. This possibility seems to be the most probable as sparking on the ground side would occur more due to the highest E fields in the geometry being at the bottom of the quartz windows. The threshold is occurring as the top edge of the window is further from HV than the bottom, therefore, the higher fields are required in order to cause sparking.

G.3 Mercury magnetometer test setup

At Sussex a test setup exists: consisting of a simple vacuum system, pumped by a Pfeiffer TSH 071E unit (167). The turbo is then connected to a tee which has a penning gauge attached. The mercury cell is then connected to the other side of the tee piece. The mercury oven is connected to the vacuum pump through the cell. Inside the cell is a PTFE plate with holes, with o-ring seal on either side, which acts like a valve to seal the vacuum pump and/or the mercury oven for the given measurement. This plate is rotated by a servo motor which sits some distance underneath the mercury cell. This system is shown in Figure G.7.

The oven uses a resistive heater on the outside of a quartz tube to bake HgO powder which is then released into the mercury cell. The temperature is monitored by a K-type thermocouple to control the heat input to the mercury which varies the amount released into the cell. The temperature is varied between 353 - 373 K depending on the amount of Hg required. The HgO powder releases various elements when heated. The required isotope for the mercury magnetometer is ^{199}Hg, however, natural mercury is

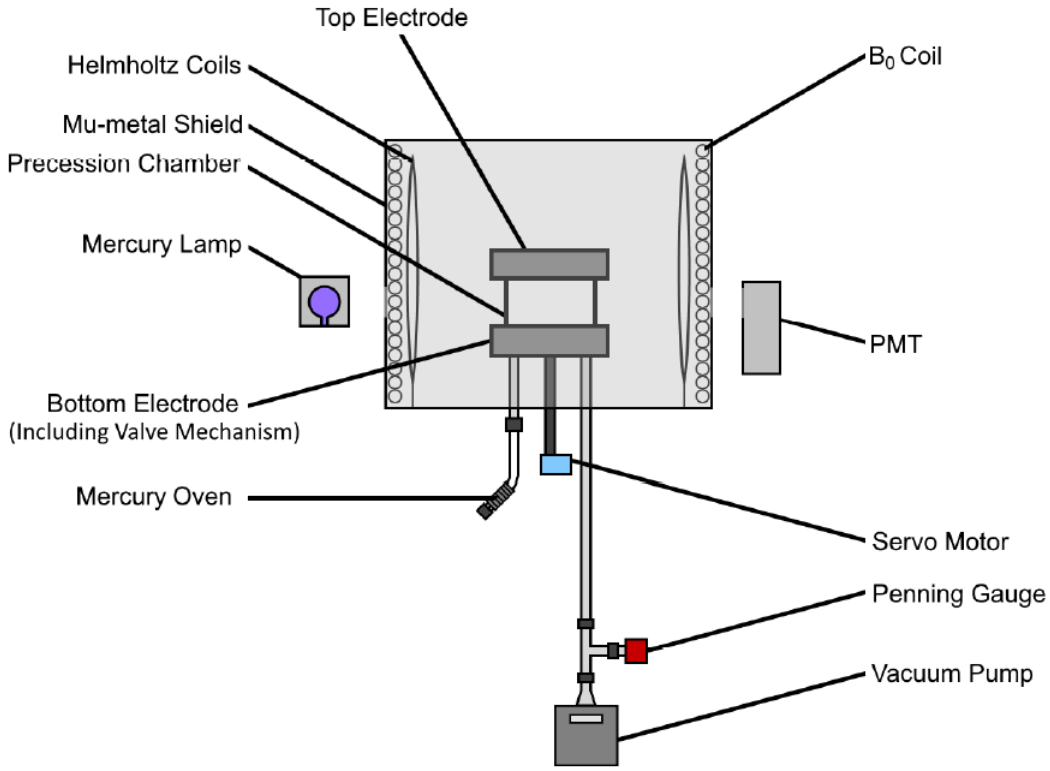

Fig. G.7 Diagram of the mercury magnetometer setup (166). The light guide tube which contains the polariser and 1/4 wave plate is not shown though it sits between the lamp and quartz cylinder. The light guide tube passes through a hole in the mu-metal shield.

only composed of 16.94% of this isotope. This makes it not the most efficient method but is the cheapest and still practical for our application.

The mercury cell is made of two cylindrical aluminium electrodes with square edges on the top (HV) and bottom (ground) of a quartz cylinder. The cell is made vacuum tight by o-ring seals on the electrodes. The seals comprise of an aluminium ring that the o-ring sits, this is then bolted on to the electrode body, creating a compression seal. These rings create high E fields at their edges being square, producing a high field region on the inside edge of the quartz cylinder, which could act like something similar to the sharp edges of the quartz windows in the PSI nEDM setup.

The mercury cell is centred in the middle of a single layer mu-metal shield. The shield has a solenoidal B_0 coil wrapped on the inside; there are also a pair of Helmholtz coils which create a uniform field through the mercury cell perpendicular to the mercury probe light. The magnetic environment was measured inside the mu-metal shield with a flux gate to understand if the relaxation time was not affected by fluctuations in the field from outside sources.

The probe light used to excite the ^{199}Hg is generated from a mercury ^{204}Hg lamp. The

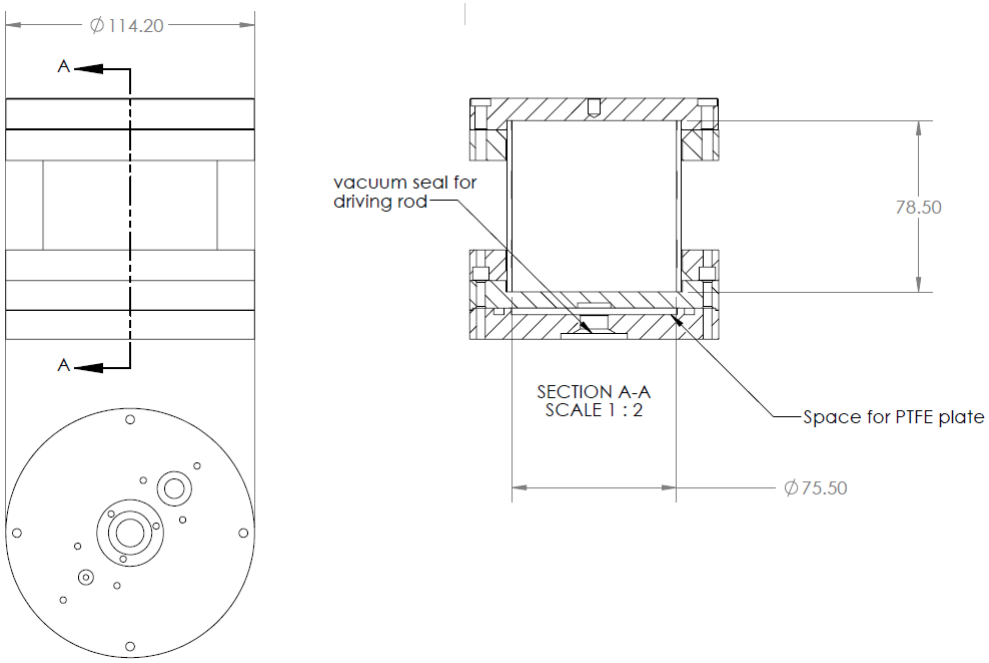

Fig. G.8 Dimensions of the mercury volume, all numbers are in millimetres. The PTFE plate is rotated by a rod that is sealed with an o-ring in the bottom of the ground electrode.

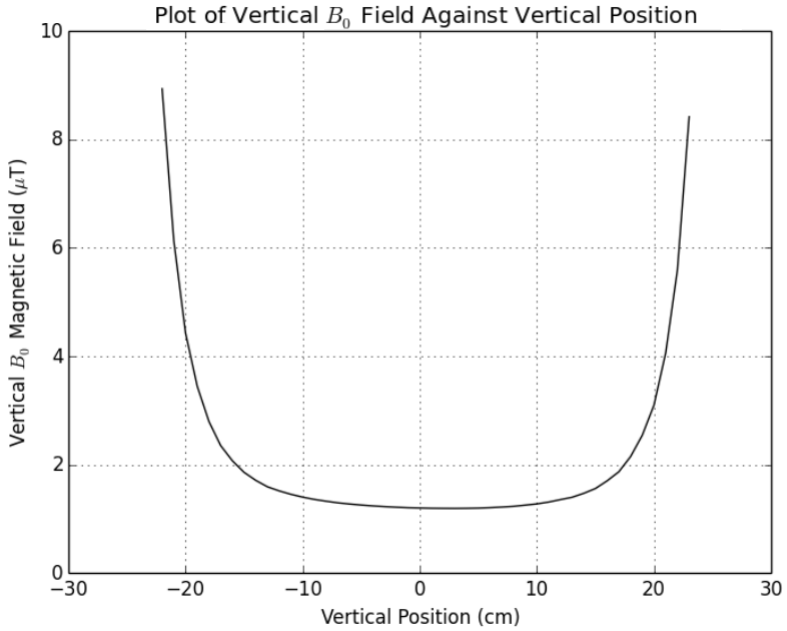

Fig. G.9 Plot of magnetic field vs vertical position inside the mu-metal shield. The measurement is taken with a single axis Fluxgate which is passed vertically through the mu-metal shield while the B_0 field is left one. The 0 cm position is the centre of the mercury cell. The measurement here is performed without the penning gauge on the vacuum system which has a very large magnet on it and may interfere with the field (hence it was moved further away from the tee piece during measurements) (166).

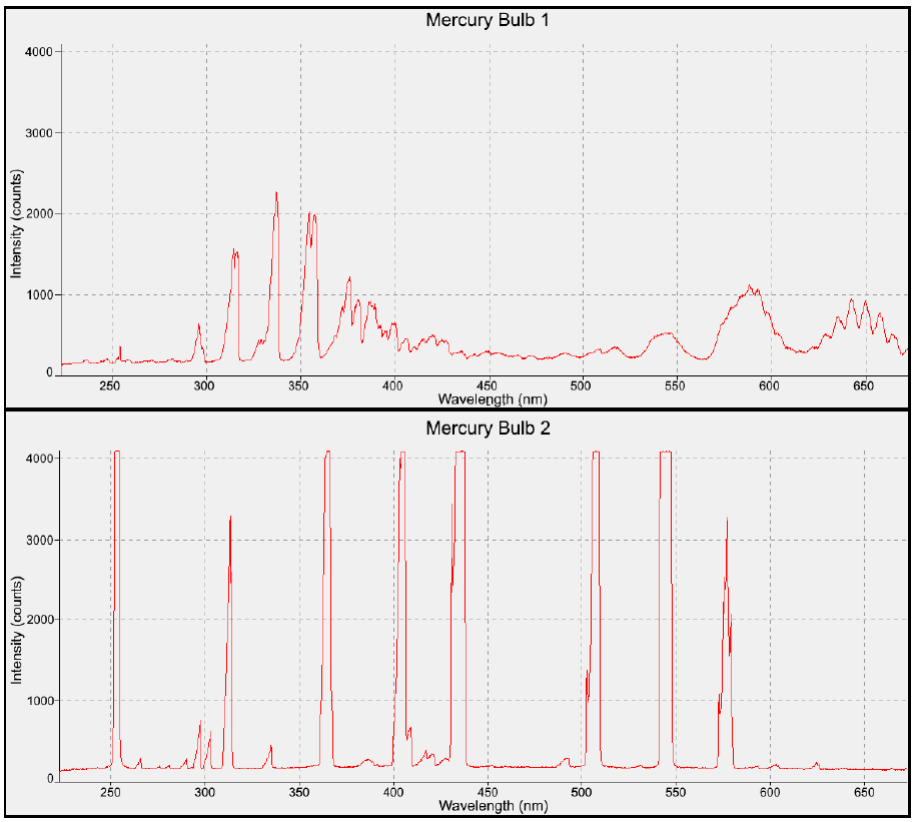

Fig. G.10 Example of the emission spectrum of two different mercury bulbs measured with Ocean Optics HR2000 high resolution spectrometer (169) (will not measure exactly the 253.7 nm wavelength but at least measure the total emission for quality comparison). Bulb 1 is poor with only emission in the 300-400 nm region, and critically, no emission at 253.7 nm. The colour of the bulb was pink during the measurement which implies the ^{204}Hg has solidified on the surface of the glass or has completely escaped. Bulb 2 glows a bright blue and has strong emission at 253 nm, good indication of bulb quality. Bulb 2 also has emission between 500-600 region which is from light emission of argon (166).

lamp uses mercury bulbs which contain a mix of gaseous ^{204}Hg and argon, details of construction are given in (168). The lamp is powered by a mircowave generator at 2.4 GHz into a cavity via an optical cable. The bulb sits in this cavity and its position is adjusted till the light emission is in the correct place in the bulb and a mercury signal is detected. The bulb should emit light at 253.7 nm which is for the hyper-fine splitting of the ^{199}Hg in the mercury cell. The bulb is first ignited with a discharge; the mircowave cavity then maintains this ionisation process. The optimisation of the lamp is notoriously tricky, with a number of variables which maximise light output but not necessarily emission at 253.7 nm. There is also the issue that each bulb is different, so upon replacement, everything has to be adjusted again. The free parameters for tuning this are: power of the source, temperature of the lamp, position of the bulb (x, y, and z positioning), and the size of the cavity.

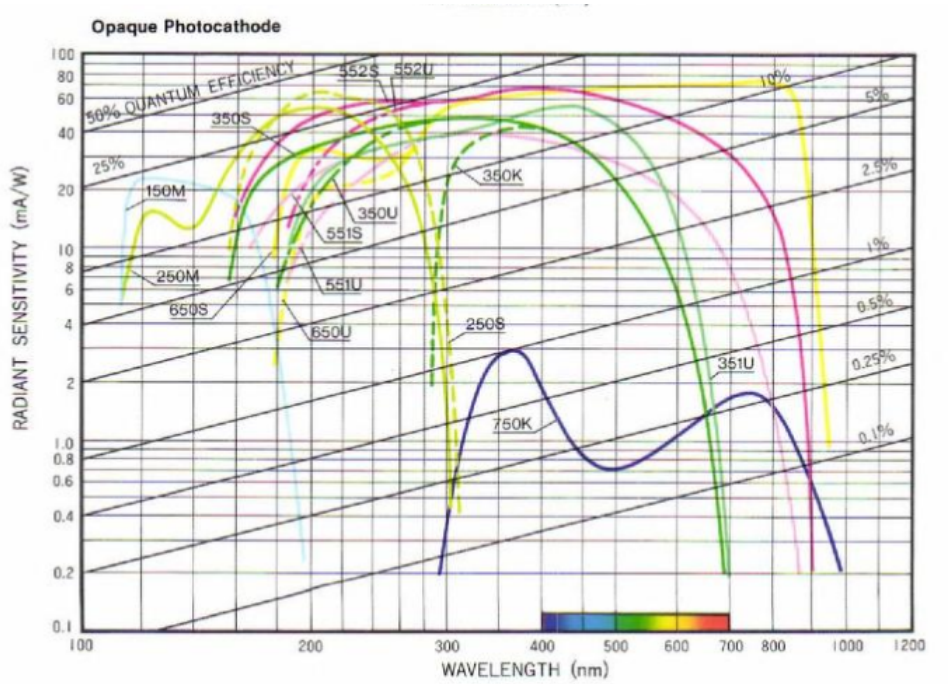

Fig. G.11 Sensitivity of models of Hamamatsu PMT's to various wavelengths of light. The model used is R166 which followed the dashed yellow line labeled 250S. This PMT has a peak sensitivity at ~ 200 nm but falls off sharply after 260 nm which makes it ideal for detecting the particular wavelength require while filtering out any other light emission (170).

In order to get the best light emission in the bulb, the cavity is adjusted so the majority of the light is in the tail. Further optimisation of the bulb is purely done by trial and error till a maximum mercury signal is detected. The light is then passed through a polariser and a 1/4 wave plate in between the lamp and mercury cell.

G.4 Procedure

During the measurement, the mercury cell and oven are pumped out to 10^{-5} mbar on the penning gauge. The oven is also heated at this point to ~ 370 K. The bulb is ignited and the position adjusted to maximise emission of the light. The emitted light is seen by a PMT on the opposite side of the mu-metal shield.

The position of the PMT is modified in order not to saturate it as the lamp produces substantial amounts of UV light.

Once sufficiently pumped, the PTFE plate is rotated which seals the oven to allow mercury to accumulate. After some time the vacuum pump is sealed and the mercury oven is opened to allow the cell to fill. At this point a dip in the detected light by ~ 30% (amount of absorption) means there is enough mercury in the cell. When this condition

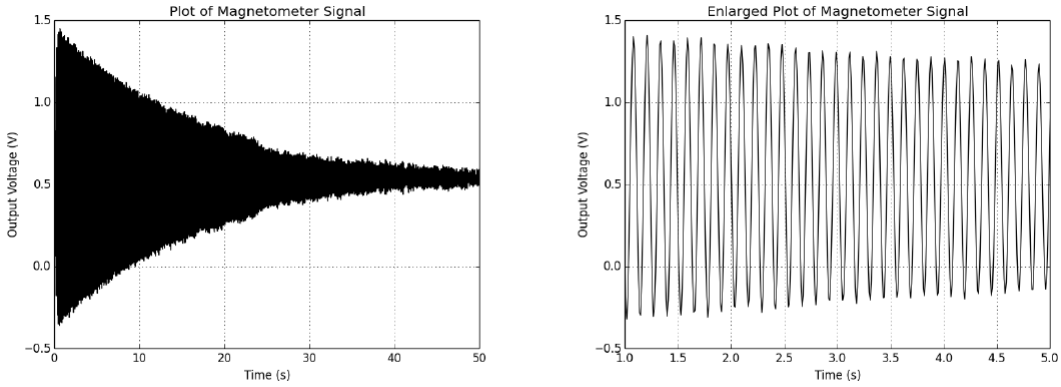

(a) (b)

Fig. G.12 Example of a typical signal from the mercury magnetometer of output voltage against time. (a) is the complete signal for which the relaxation time is determined. (b) is an enlarged view of the signal, showing the oscillation of the mercury signal (166).

is met the oven and vacuum pump are sealed off. The mercury is then polarised in the cell for 30 seconds with the Helmholtz coils switched on. Then the coils are switched off and the precession of the mercury is detected by the PMT.

The signal for the PMT is processed in real time by CAMAC modules. First the voltage signal from the PMT is amplified by order of 1000. Then it is sent through a bandpass filter at ~ 8 Hz (or the Larmor precession frequency). Details of this process is given in (166) (168). This produces a typical waveform as seen in Figure G.12.

The relaxation time of this signal will vary due to a number of parameters which are detailed in (168). However, for the purpose of this experiment, the surface coatings and application of HV on the signal will be looked at to see if there is any variation in the relaxation time correlated with reversibility of the E field.

G.5 Limitations of the setup

G.5.1 Application of HV

Testing the system under atmosphere at first was done in order to determine the maximum E field that could be expected and if there are limitations to the breakdown field from the geometry. The mercury cell was set up outside the mu-metal (to give good visibility and avoid magnetisation of the shields) then positive HV was applied to the top electrode. The electrodes were coated with Fomblin oil (171) which is known to give good mercury relaxation times (172). The typical time with this coating is ~ 20 seconds in the cell shown in Figure G.8. The power supply was set to 200 μA and ramped up in steps of 5 kV/min. The breakdown would occur multiple times between 30-40 kV

through a discharge. The breakdown was occurring on the outside of the cell, between the aluminium clamping plates for the o-rings. On closer inspection, it was caused by a sharp edge on a protruding screw (after the tests the screw was smoothed down and sunk in).

After this test the cell was pumped out. The vacuum on the penning gauge was at 6 x10^{-5} mbar before the HV was applied. The same current and voltage rate is applied again, however, this time there was leakage current present throughout and breakdown occurred at ~25 kV. This breakdown run was repeated 8 times resulting in about the same breakdown value even when the polarity was switched to negative. It was noticed that the penning gauge would rise before the breakdown occurred and fall back off again afterwards. However, this is inconclusive, due to the E field potentially creating more ions in the cell which triggers the penning gauge to produce a false value. The breakdown was not a sudden flashover like before, but instead occurring on the inside with no flash visible. But, it could be seen before breakdown occurred that there were sparks at the centre of the volume. It appeared that gas inside the volume was being ionised and causing the breakdown. The conclusion was that the Fomblin oil was out gassing heavily under application of HV, raising the pressure inside the cell close to the Paschen curve 4.1. The likely cause of this problem was the fact that this oil has a very low vapour pressure. After this the electrode surface was cleaned in acetone and a top layer was skimmed to remove any presence of the oil. The clean electrodes were tested with the same setup as before, achieving breakdowns at ~30 kV this time under vacuum. The indication from these breakdowns was that the vacuum was not good enough in the cell to achieve the voltages that were possible under atmosphere.

G.5.2 Vacuum condition

To be able to apply high voltages, which were required in order to get to the threshold voltage (~8 kV/cm negative and ~3 kV/cm positive) for the mercury effect observed at PSI, the vacuum needed improvements. The lowest pressure achieved on the system was 4 x 10^{-5} mbar just above the pump. The mercury cell is connected to the vacuum pump by a small hole, ~1 cm diameter, therefore, creating an impedance for the pumping system which could result in the pressure in the mercury cell being higher then at the pump. The hole to the mercury oven is even smaller ~1 mm. The oven when heated also creates a lot of gas which could also increase the pressure in the cell.

It was also found that there were some leaks coming from the rod which rotates the PTFE plate and the seals around the holes on the PTFE plate. These leaks were fixed resulting in a new lower pressure of 2 x 10^{-5} mbar. The conclusion is that in order to get

the system to the optimal operation with HV the cell would need to be redesigned. One possible way of doing this would be to instead remove the electrode surface from the vacuum side and have the plates in atmosphere on either side of a sealed quartz cylinder.

In order to get some measurements with the setup available, a limit of 25 kV was placed on what could be applied to the HV electrode, giving a field of 3.18 kV/cm, just enough to potentially observe the threshold effect from the mercury with positive polarity. However, as Fomblin had proved problematic, a different coating was required.

G.5.3 Coatings

The problem observed with Fomblin coating when HV is applied to the cell, meant that a replacement which would not out gas was required. A number of materials were considered that are known to have good behaviour with mercury (168): PTFE, polystyrene, and perfluorinated paraffin (173).

The PTFE coating was applied with a PTFE spray onto the surface of the electrode and allowed to dry overnight. It was found that the coating would not adhere to the surface under application of HV for very long, only getting a few cycles of measurements before holes appeared.

The polystyrene came in form of pellets which needed to be dissolved in toluene, at ratio of 1:10 by volume, over the course of several hours before being applied. The mixed solution is then spread with a paintbrush onto the aluminium surface till completely smooth and evenly spread. This was then allowed to dry overnight. This coating also had problems with adhesion; it started to separate from the electrode in one complete disc after several cycles in vacuum.

The paraffin was different, it came in a powdered form. In order to apply it to the surface evenly, electrodes were placed on a hot plate to allow to heat up to above 363 K. Then the paraffin was spread on to the surface with a brush, and the powder would melt, producing a lot of gas but leaving behind a coating on the surface. This coating was much better; it would not flake off and no holes appeared during measurements with it.

After measurements with each coating the electrodes are cleaned in an Ultra sonic bath with acetone. Table G.1 shows the results of the relaxation time in the mercury cell with different coatings applied.

Coating	No. of cycles	Average T_2 (s)	Error (± s)	Average reduced χ^2
Fomblin	40	21.59	0.25	1.59
PTFE	60	9.02	0.20	0.69
Polystyrene	39	4.21	0.21	2.83
Perfluorinated paraffin	40	23.78	0.44	1.24

Table G.1 Table of average relaxation times for various coatings in the mercury test cell. The number of cycles is a measurement of one T_2 time. The cycles selected are the best achieved relaxation times which is generally recorded just after the coating has been applied.

The performance of the PTFE and polystyrene was surprising. These materials have been demonstrated to perform well with mercury previously (172). However, in this cell they did not seem to work. The likely reason for the PTFE performance is the coating was not thick enough which is seen in the fact that the relaxation time is half what the Fomblin achieved. The polystyrene was difficult, as it took a number of attempts to get the coating uniform. However, the relaxation time was still very short which was probably due to the poor adhesion to the surface. There is also the chance that this particular polystyrene did not suit the mercury or if there was some residual toluene in the coating.

The best coating was the paraffin which even out performed the Fomblin, therefore, it was the coating of choice going forward. This result is also comparable to that found by Chowdhuri et al. (172). They found that the perfluorinated paraffin would give the largest T_2 times in a quartz cell of similar size to the one presented in this thesis.

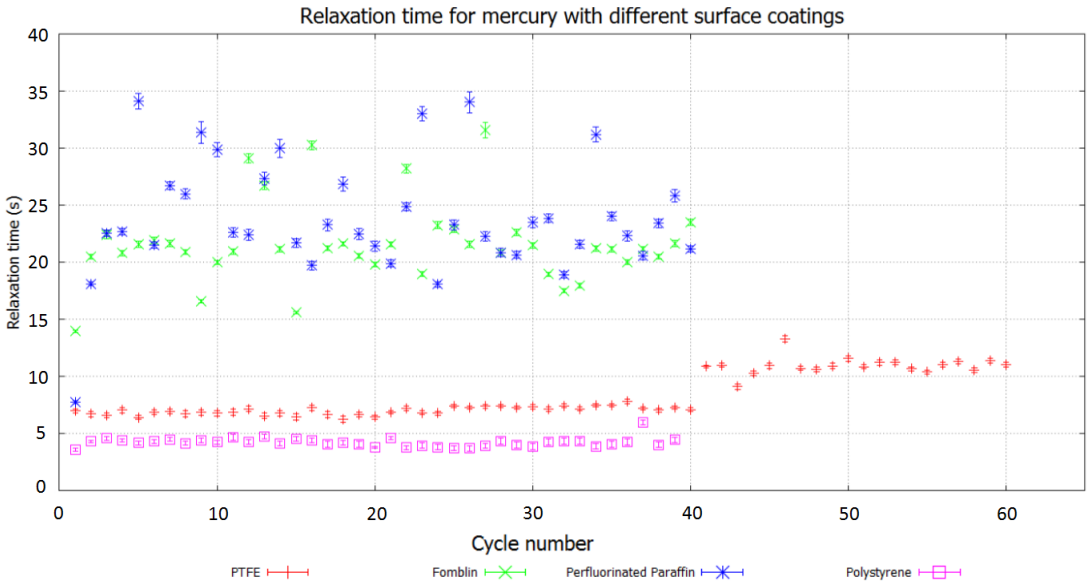

Fig. G.13 Relaxation time against cycle number for various electrode coatings. The jump on the PTFE measurements are a result of the lamps position being adjusted.

G.5.4 Relaxation time measurements with HV cycling

Having found a suitable coating to replace the Fomblin, HV could again be applied to test the aforementioned correlation of the relaxation time with the reversibility of the E field. As stated before, the vacuum condition of the cell is poor; the rotating PTFE valve traps volumes of gas which when moved are released into the vacuum system. It was found when testing with Fomblin coating that the pressure would rise when the valve was rotated. If HV was applied at the same time as this was occurring a breakdown would be triggered, even at lower voltages of say 10 kV.

In order to bypass this problem, the HV is only applied when the cell is being pumped by the vacuum system, i.e. the oven and cell are both open to the vacuum pump. This does not exactly represent the same process in the nEDM experiment but if the effect is due to only the application of HV on the system then these tests will possibly provide information.

First a baseline for the paraffin was determined by taking measurements of the relaxation time over the course of two days.

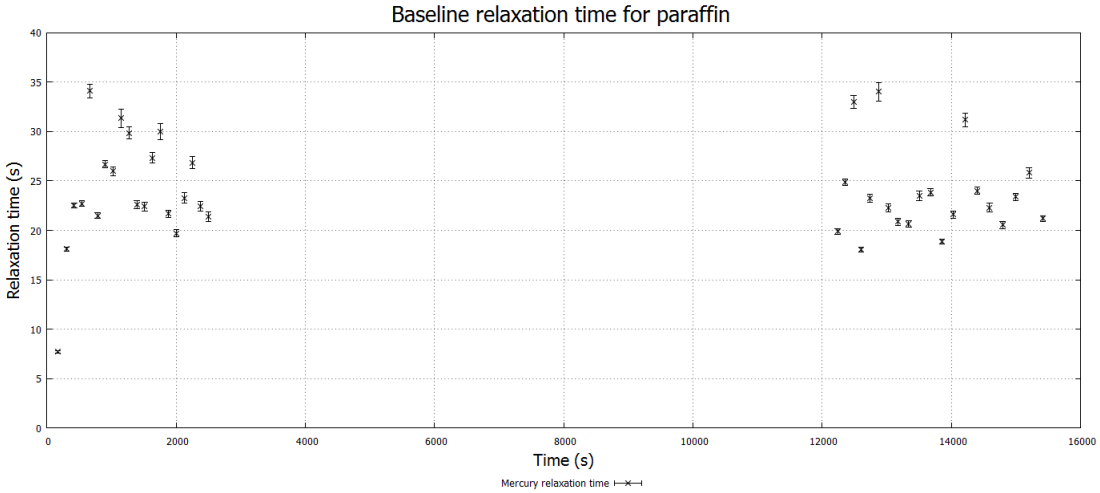

Fig. G.14 Relaxation time against time with the perfluorinated paraffin coating. Average value of the relaxation time is given in Table G.1.

After this measurement positive HV was applied to the cell the for 10 minutes to gauge the field which would be achievable for the following measurements. It was found that 25 kV was stable, therefore, this will be the field used throughout. Higher voltages were not attempted as a breakdown could have magnetised something inside the mu-metal. The system was left under vacuum and then run two days later.

Figure G.15 starts with the relaxation time slightly lower then the baseline measurement,

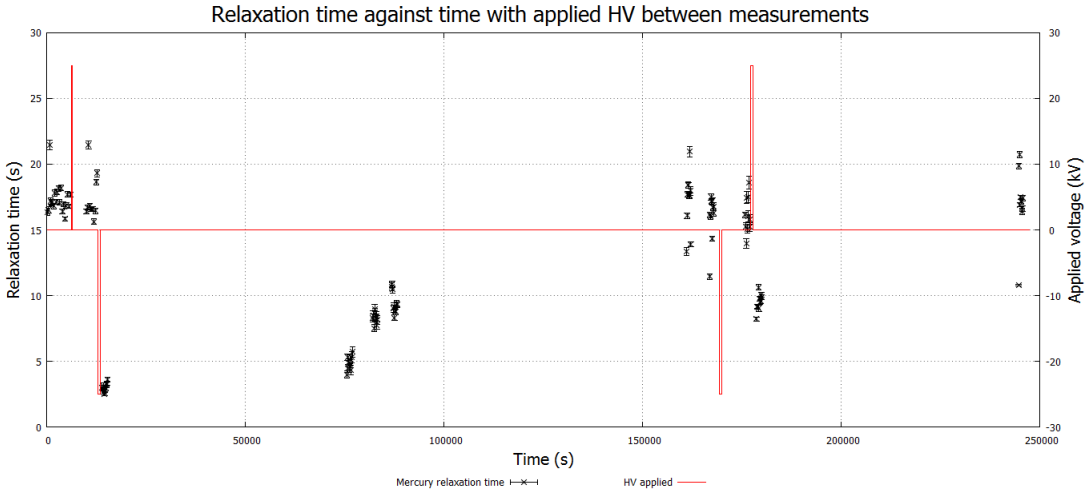

Fig. G.15 Relaxation time against time with applied HV overlaid.

by about ~2-3 seconds. The application of the HV to gauge the E field performance several days previous seems to have changed the relaxation time of the mercury despite being left to pump. This could be due to some conditioning effect of the HV. Then, positive polarity is applied again to the cell for the same time period as before. The relaxation time does not change after the positive HV is applied. Then, negative polarity is applied to the cell. After turning off the HV, the relaxation time is measured and it has dropped to ~3-4 seconds. The cell did not clearly breakdown, however, the negative power supply used does not have a current limit setting, therefore, the supplied current as much as to 80 μA at 25 kV.

It is unclear what happened, but the relaxation time was significantly reduced and it proved difficult to recover. It took a number of days, and multiple venting of the vacuum system to get to ~10 seconds. After this the system was left open to atmosphere for a few days which seemed to recover it back to ~15 seconds.

Once the relaxation time had recovered, HV application was again performed. This time negative was applied first. This seemed to have no effect on the relaxation time. Therefore, the polarity was switched to positive. The application of HV this time dropped the relaxation time to ~ 9-10 seconds. It was noted that the power supply tripped (voltage drop, implying a breakdown) during this HV application.

The data presented in Figure G.15 can at first glance be believed to show a similar HV reversibility behaviour as seen at PSI. However, the fact that breakdowns could have occurred means the measurements needed to be repeated with careful monitoring of the cell to see if a breakdown had or had not occurred.

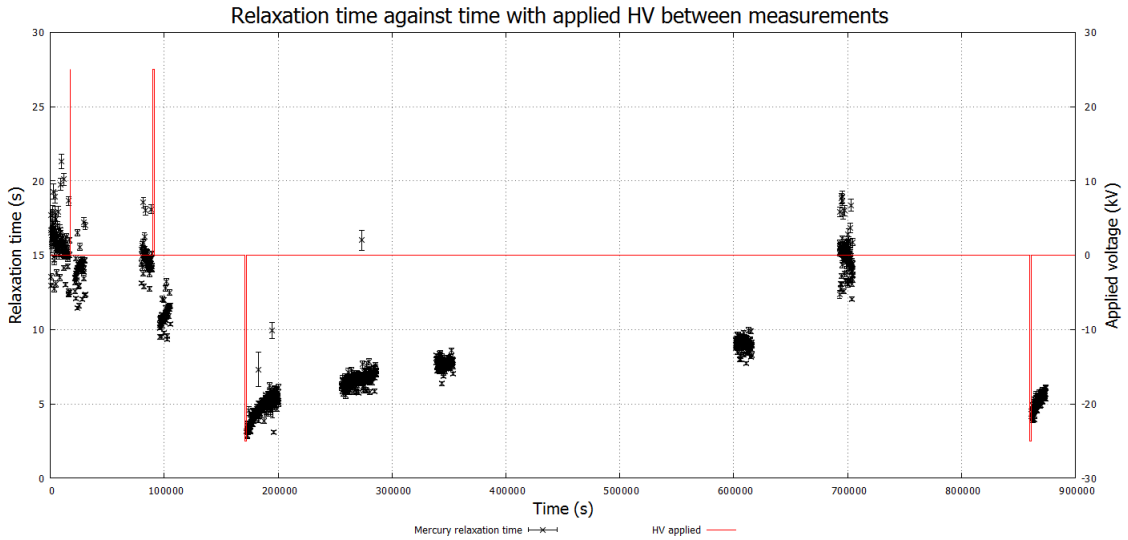

Fig. G.16 Relaxation time against time with applied HV overlaid, this was performed after the previous data set in Figure G.15.

After the relaxation time had recovered from repeated venting the system and leaving it to atmosphere, HV was applied to the cell again.

The relaxation time recovered to ~ 16 seconds, at which point positive polarity was applied once again. This resulted in a slight drop in relaxation of ~ 1-2 seconds. There was no evidence of any discharging occurring in the cell. Positive polarity was again applied after the relaxation time recovered slightly back to 15 seconds. This time a discharge occurred in the cell, evident by additional current being drawn from the power supply. This discharge dropped the relaxation time of the mercury to ~ 11-12 seconds. After this the polarity was again switched.

Negative polarity was applied to the cell. Again discharges occurred in the cell with 1 μA required to get to 25 kV. However, this disappeared after a few minutes. The signal drops down to ~ 3-4 seconds due to this. The relaxation time is recovered, but it required constant venting and leaving at atmosphere to get it back to ~ 15 seconds.

Negative polarity was again applied to change the HV pattern, however, this time multiple catastrophic breakdowns occurred with sparks between the electrodes. The relaxation time dropped down to ~ 4 seconds due to this breakdown. After this the relaxation time would not recover back to ~ 15 seconds. It was assumed that the breakdowns had damaged the coating too much and created holes in the surface or something inside the cell had become magnetised.

G.5.5 Conclusion

The initial application of HV will result in a slight drop in the relaxation time which can be attributed to conditioning effects as also demonstrated in the PSI nEDM data in Figure G.3. The cause is due to sparks in the cell during this conditioning process.

The HV pattern used in the experiment indicates that the polarity reversal causes a reduction in the relaxation time. In Figure G.15 the positive then negative polarity applied at the beginning causes a drop in relaxation time; this is then followed by negative polarity then positive which also causes a drop but with reduced magnitude. After that, shown in Figure G.16, positive is applied then negative which gives a similar drop in relaxation time as the previous HV pattern. This could be argued is the reversibility effect seen at PSI, however, it is more likely that what was seen here is due to discharging in the cell. This can be seen in the final measurement with negative polarity, where it discharged and killed the relaxation time even before the application of positive polarity. The fact that the application of HV has some residual effect even after the power supply is turned off, implies that the discharge has either magnetised something inside the mu-metal or created some residual material which coats the paraffin, depolarising the mercury during the measurement. This latter seems more likely as the mercury relaxation time is improved by venting the system and leaving it at atmosphere for some time potentially flushing this system of this material. This could also explain why discharge cleaning in the PSI experiment works.

As for asymmetry, negative polarity results in a greater drop in relaxation time for the mercury over the positive. This is different for the PSI results, where negative would only effect the relaxation time after a threshold field of ~ 8 kV/cm while the positive should apply at almost any field. This discrepancy is more likely due to the power supplies used. The positive has a limiting current, therefore, if a discharge occurs it will limit the current in that breakdown. The negative supply did not have this feature, therefore, it supplies current proportional to the supplied voltage, giving the discharge more energy in the breakdown.

In conclusion there is not enough data points here to determine if the effect observed in the test setup is the same as that at PSI. There are also too many limitations in the system which means pin pointing the cause is difficult. The system needs improvements in vacuum condition and a more controlled method for HV application in order to replicate the PSI setup better and investigate the effect. However, if the drop in relaxation time observed at PSI is due to the same causes observed in the test setup in this lab, then this points to improving the E field in the PSI setup as a way to overcome this issue. It should

be noted that PSI has a ballast resistor between the power supply and the cell, therefore, if a discharge occurs then the current supplied will be limited reducing the spark in the setup which could explain why sparks are not observed, also why the relaxation time is not completely reduced to zero.

Appendix H

Blue Elbow drawings

The following drawing are of the SV and the electrodes.

H.1 SV drawings

The SV was designed to hold the electrodes with an insulator between them for a maximum electrode separation of 26 mm. The electrodes are sitting on 3 G10 castellated rods, leaving a separation to ground for the corona rings of 26 mm to the wall and to the ground lid by 45 mm.

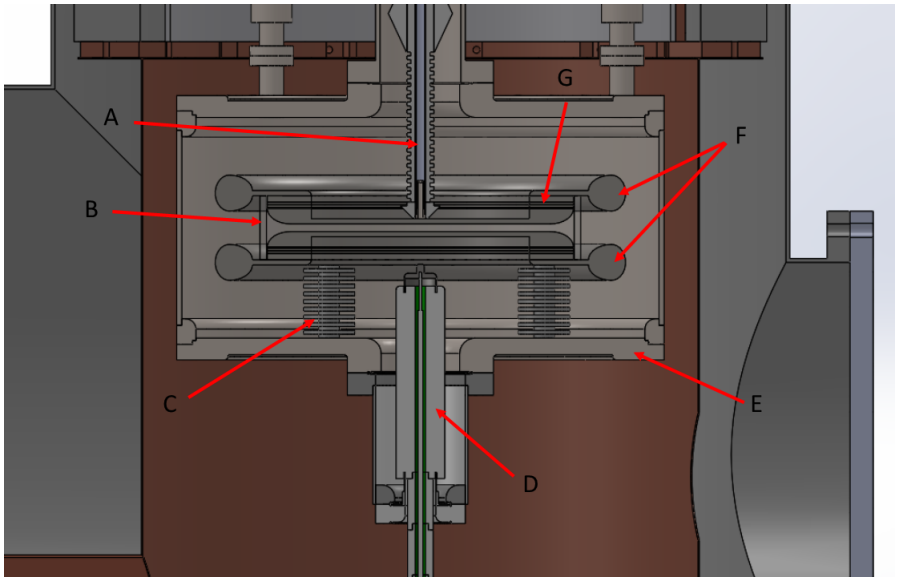

Fig. H.1 CAD model of the SV inside the Blue Elbow cryostat. The G10 feedthrough is connected to the bottom of the SV and the top HV feed is in contact with the top electrode.

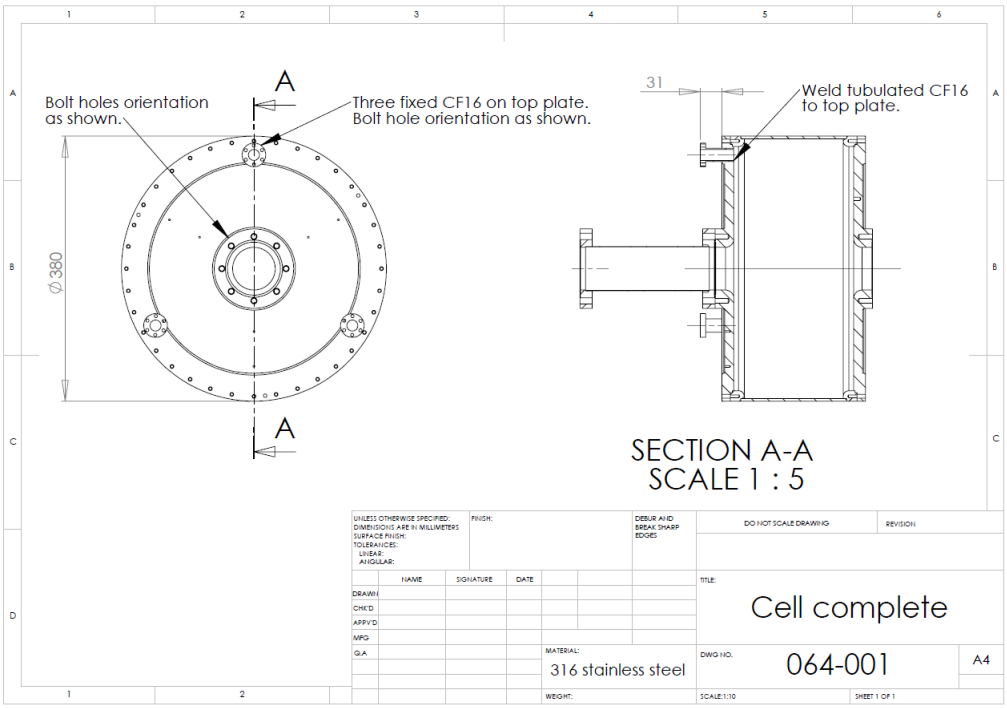

Fig. H.2 Drawing of the SV with a CF63 extension tube attached to the top plate.

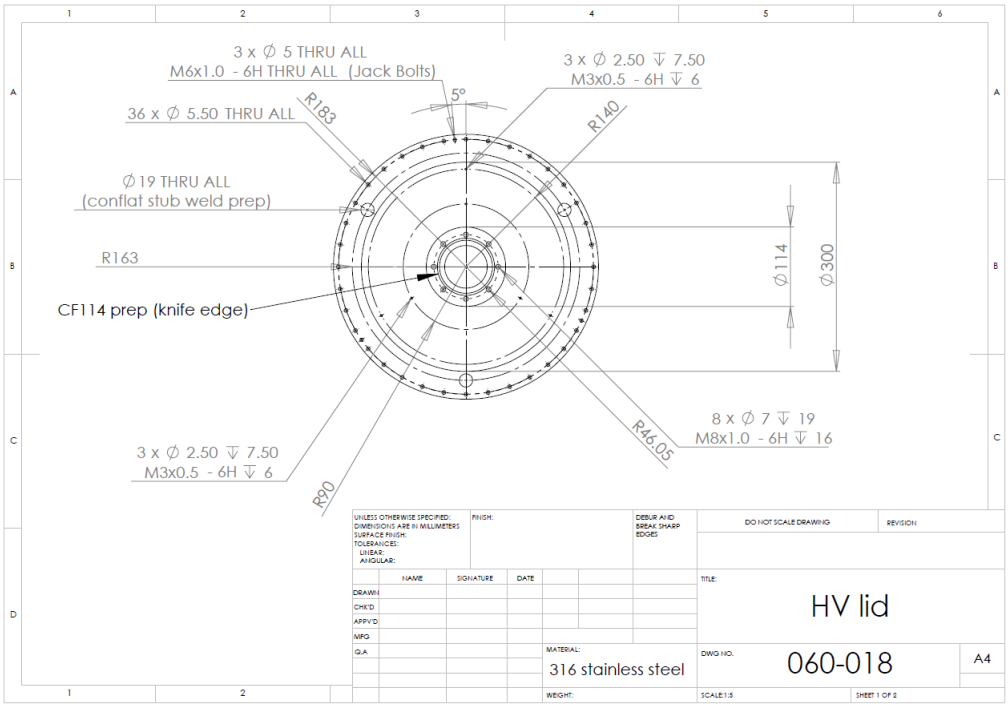

Fig. H.3 Top lid of the SV.

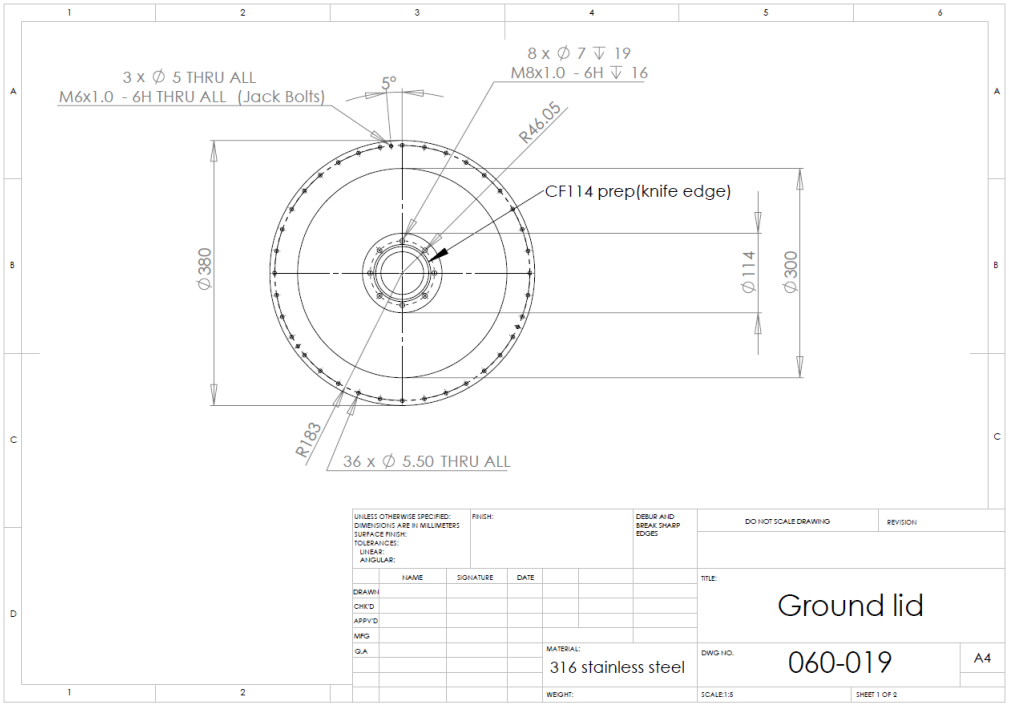

Fig. H.4 Bottom lid of the SV.

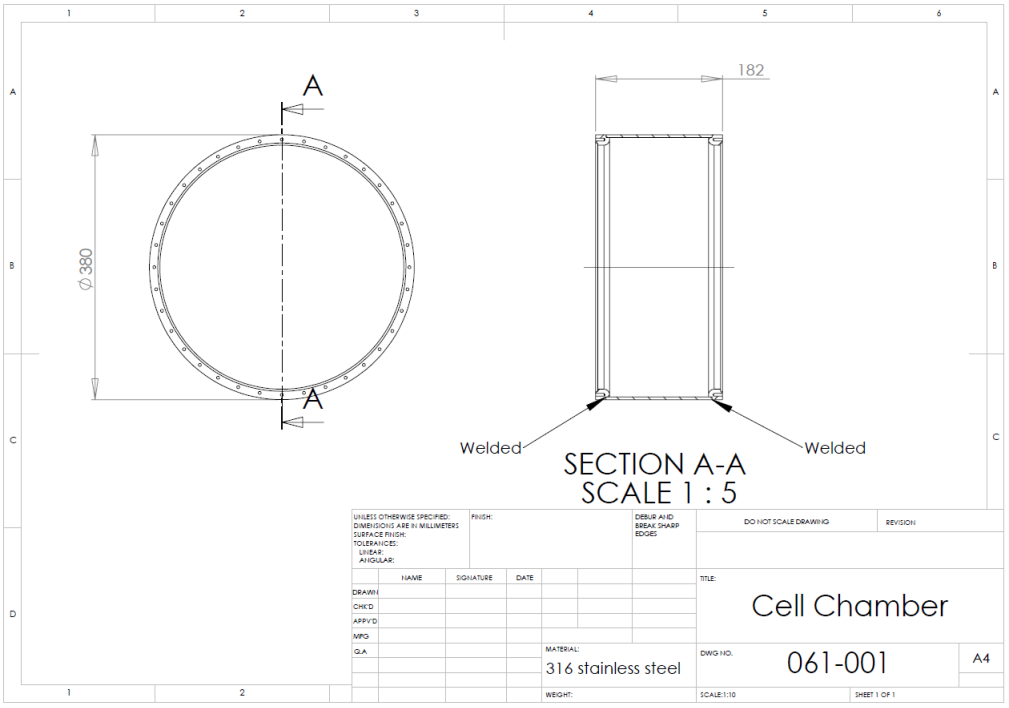

Fig. H.5 Drawing of the SV without the lids. Chamber walls have two flanges welded in place for an indium seal with the lids to create a vacuum tight environment.

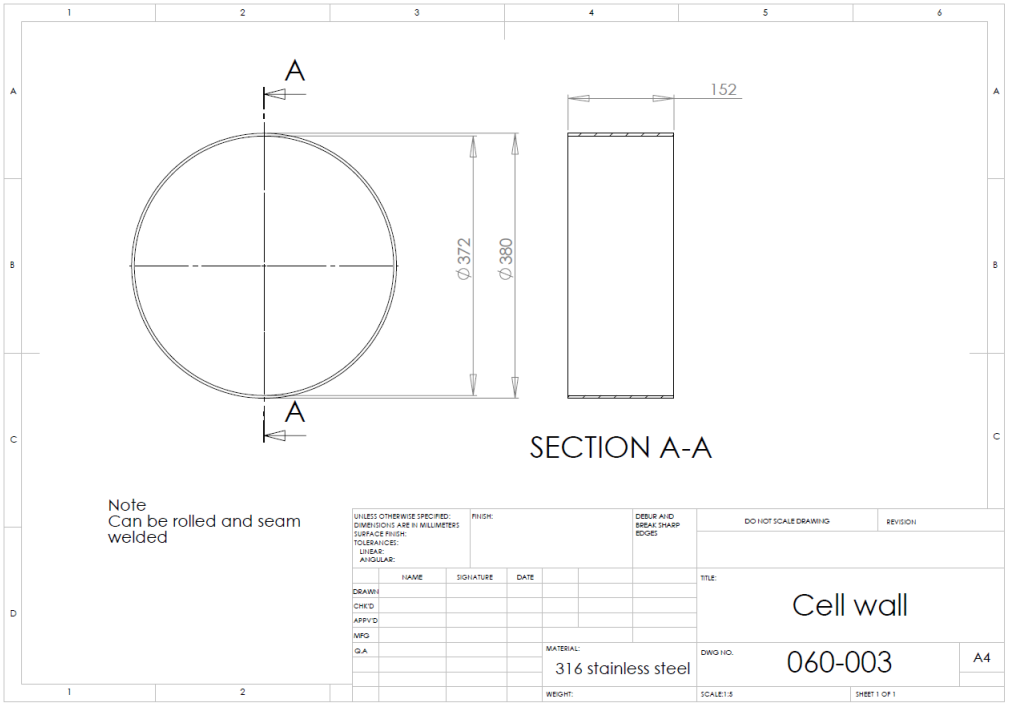

Fig. H.6 Drawing of the SV wall.

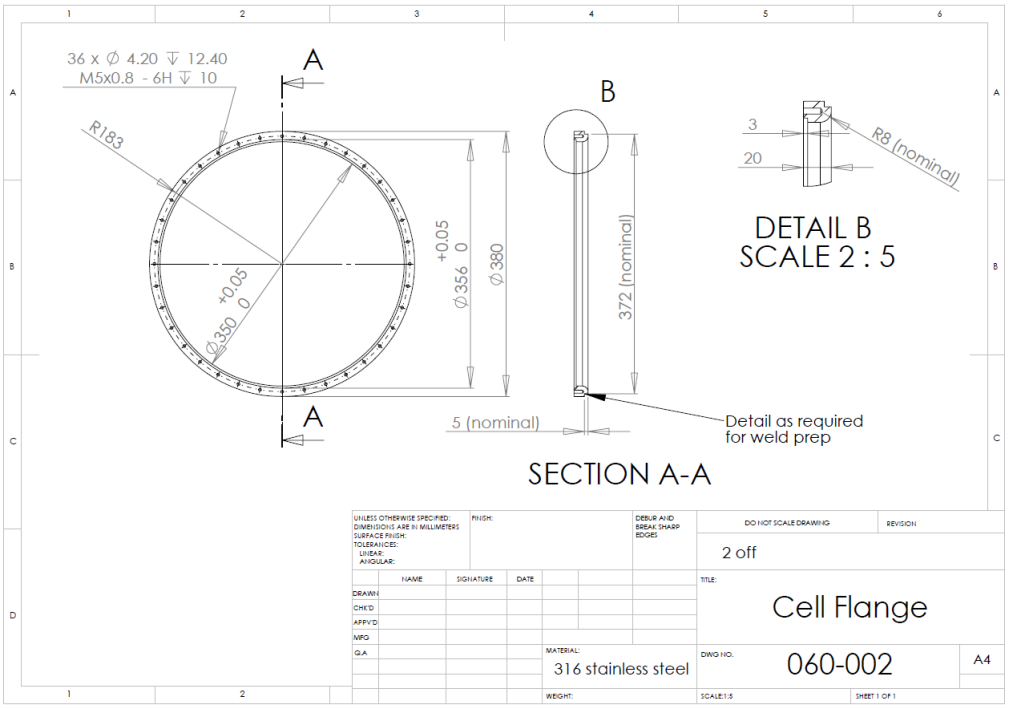

Fig. H.7 Drawing of the vacuum flanges for the indium seal, was welded onto the chamber walls.

H.2 Electrode drawings

The geometry of the electrodes given here is determined from the simulations given in section 5.5.

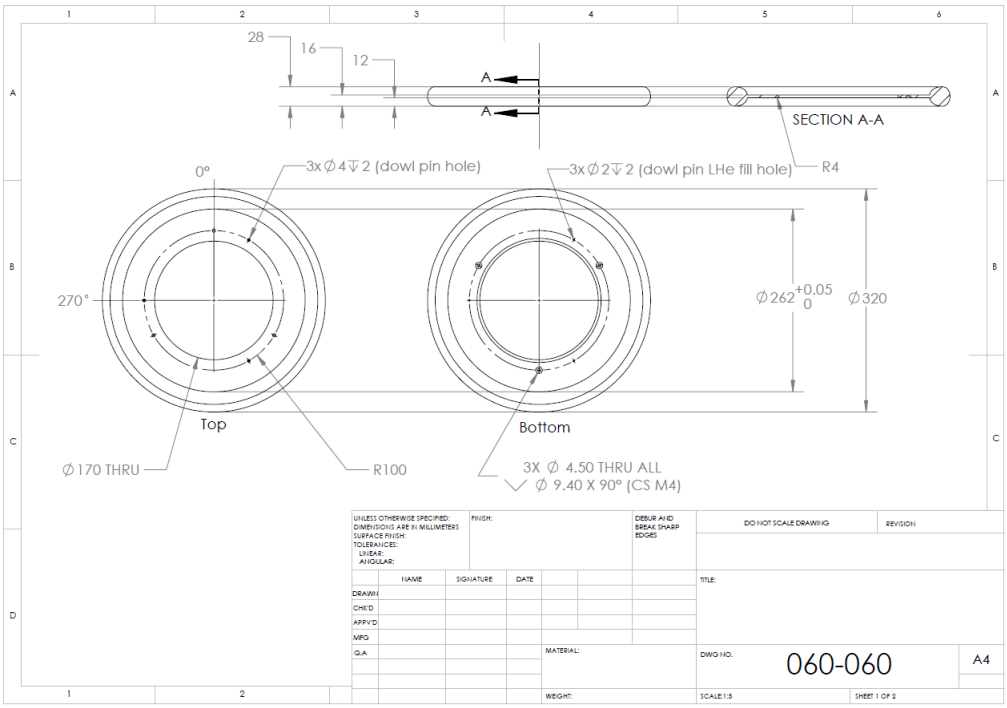

Fig. H.8 Drawing of the HV electrode corona ring. The spacer plates are bolted into this ring and aligned using dowel pins.

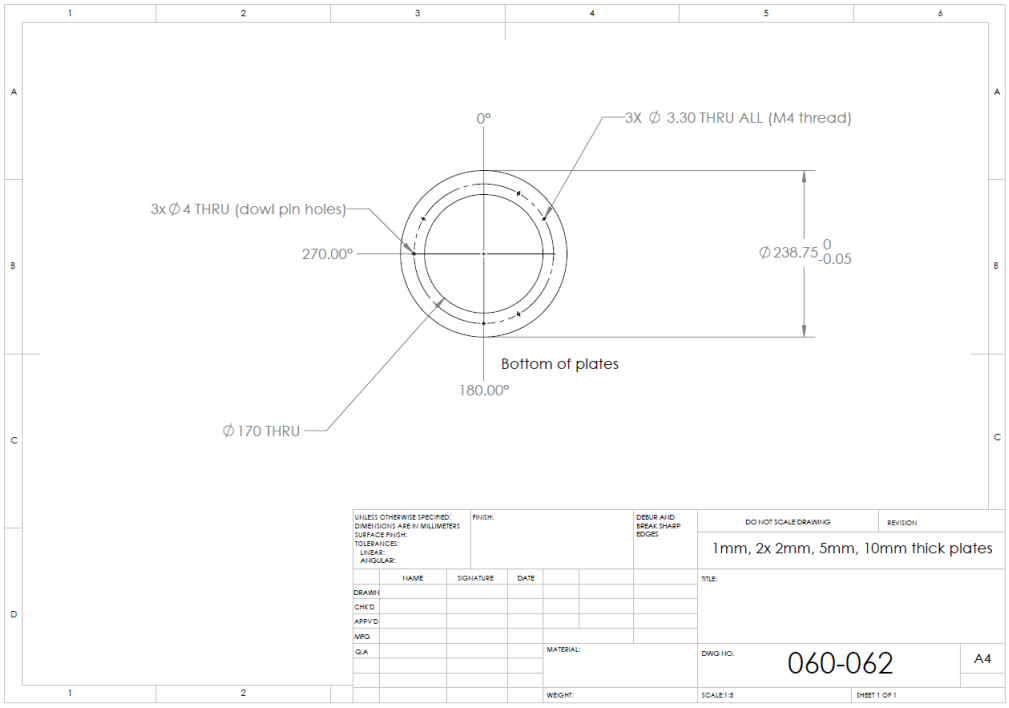

Fig. H.9 Drawing of the spacer plates for both the HV and ground electrode.

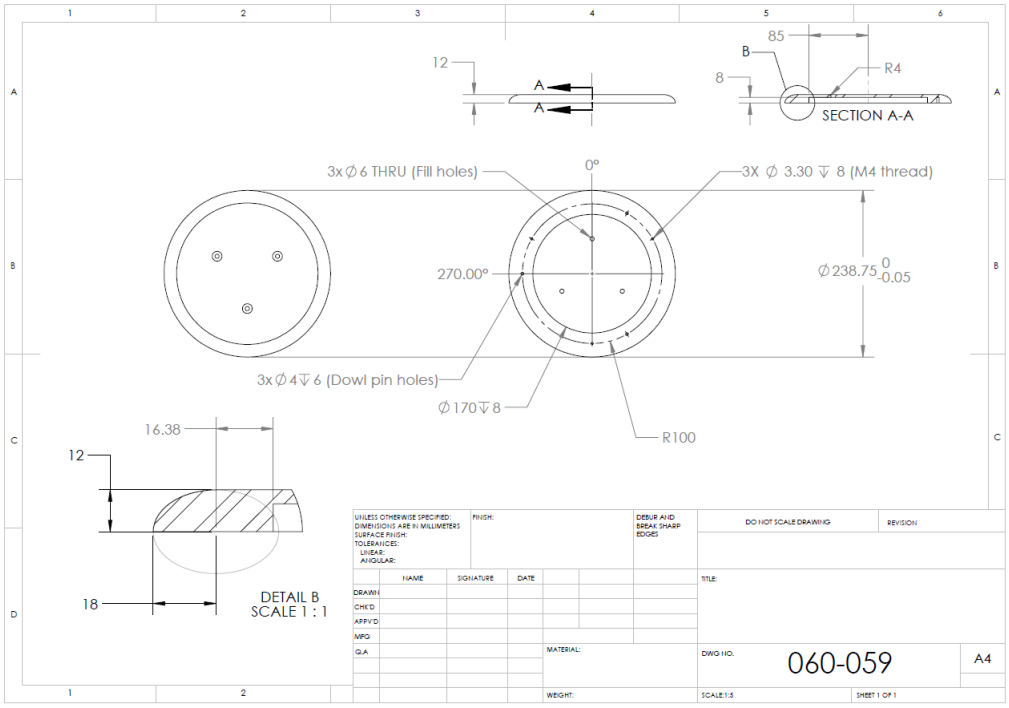

Fig. H.10 Drawing of the face plate for the HV and ground electrodes. The radius of the groove is optimised for this geometry.

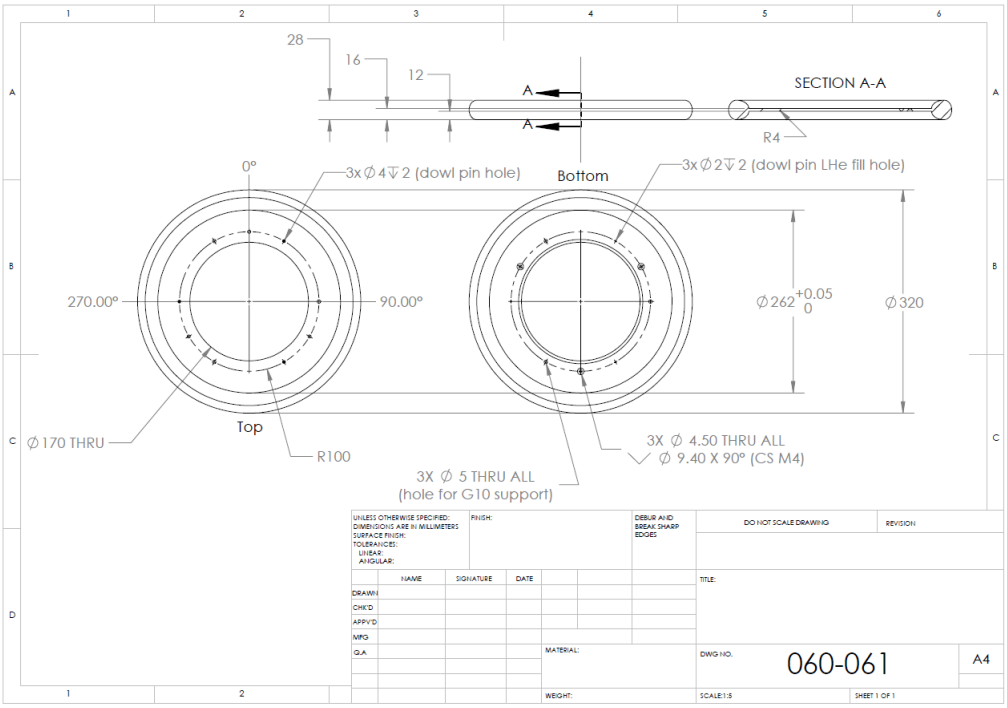

Fig. H.11 Drawing of the ground electrode corona ring. This ring has additional holes for the G10 support rods.